UNIVERSITY OF SOUTHAMPTON

FACULTY OF ENGINEERING AND THE ENVIRONMENT

CIVIL, MARITIME & ENVIRONMENTAL ENGINEERING AND SCIENCES UNIT

Synergistic Response of Steel Structures to Thermal and Blast Loading

by

Laurence Clough MEng (Hons)

Thesis for the degree of Doctor of Philosophy

February 2017

UNIVERSITY OF SOUTHAMPTON

ABSTRACT

FACULTY OF ENGINEERING AND THE ENVIRONMENT

Civil, Maritime & Environmental Engineering & Sciences Unit

Thesis for the degree of Doctor of Philosophy

Synergistic Response of Steel Structures to Thermal and Blast Loading

By Laurence George Clough

This research project investigates the thermo-mechanical non-linear response of steel structures to combined long duration (> 200msec) blast and thermal loads. Depending upon explosive size and standoff distance the thermal load can reach, and degrade a structure prior to the arrival of the blast load. The thermal load produced by explosive events can damage steel structures such that the damage from the combined thermal and subsequent blast load would be greater than or different to, the damage from the blast load alone.

Parametric studies presented in this thesis examine the response of structural steel columns to a range of blast and thermal loading regimes and investigate the effect of parameters including connection type, compressive loads and thermal conductivity. Data from previous research is used to develop predictive algorithms calculating the thermal and blast load regimes from explosive events. Transient, non-linear, coupled (thermal and structural) analyses using the finite element analysis (FEA) program, LUSAS are performed on the structural steel columns. The design of, and results from a series of trials recording temperatures, thermal flux and pressures, and observing the response of 2mm thick steel plates, within a 41kg TNT equivalent (eq.) explosive fireball, is presented. The design of, and results from experimental trials investigating the response of structural steel columns to combined thermal, compression and long duration blast loads within an Air Blast Tunnel (ABT) are also presented. Results from both sets of trials are compared to predictive non-linear FEA models of the steel plates and columns, developed to provide verification of computational procedures used throughout the research project.

Resistance curves for the vulnerability analysis of whole buildings to explosive events are presented. The curves represent the elastic and plastic failure mechanisms of structural columns to thermal and blast explosive loads. This research project demonstrates that under specific loading regimes steel structures can exhibit a thermo-mechanical, synergistic response to combined thermal and blast loads from explosive events. This has been achieved through detailed investigation into previous research, thorough and comprehensive parametric studies and a series of innovative experimental trials using M.O.D national testing facilities.

Contents

List of Tables

List of Figures

Academic Thesis: Declaration of Authorship

I, Laurence George Clough declare that this thesis and the work presented in it are my own and has been generated by me as the result of my own original research.

Synergistic Response of Steel Structures to Thermal and Blast Loading

I confirm that:

1. This work was done wholly or mainly while in candidature for a research degree at this University;

2. Where any part of this thesis has previously been submitted for a degree or any other qualification at this University or any other institution, this has been clearly stated;

3. Where I have consulted the published work of others, this is always clearly attributed;

4. Where I have quoted from the work of others, the source is always given. With the exception of such quotations, this thesis is entirely my own work;

5. I have acknowledged all main sources of help;

6. Where the thesis is based on work done by myself jointly with others, I have made clear exactly what was done by others and what I have contributed myself;

7. Either none of this work has been published before submission, or parts of this work have been published as: [please list references below]:

- CLOUGH, L.G., Synergistic Response of Structures to Thermal and Long Duration Blast Loading, Poster Presentation: First Prize, *Institution of Structural Engineers Young Researcher's Conference 2014*, London, UK,
- CLOUGH, L. G., CLUBLEY, S.K. 2013. Gauging the Fireball: Simulation and Testing. *Internation Symposium on Interaction of Effects of Munitions with Structures.* Potsdam, Germany.
- CLOUGH, L. G., CLUBLEY, S.K. 2014. Response of Steel Plates to Thermal and Blast Load from Within the Fireball of an Explosive Event. *Structures under Shock and Impact.* New Forest, UK.

Signed:

Date:

Acknowledgements

The author would like to express gratitude to UK MOD for use of the facilities and help of staff at MOD Shoeburyness. All data reported herein is property of the MOD. The author would also like to express thanks to the sponsor.

The specific assistance and support of Dr S. Clubley throughout this research project is gratefully acknowledged as is the support of Mr R. Keys, Dr R Johns, Dr W.M.G Lakshitha, and Mr J. Denny.

Chapter 1

Introduction

1.1 Overview

This research project investigates the thermo-mechanical non-linear response of steel structures to combined long duration blast and thermal loads. Depending upon the explosive size and standoff distance the thermal load can reach and degrade a structure prior to the arrival of the blast load. The thermal load produced by explosive events can damage steel structures such that the damage from the combined thermal and subsequent blast load would be greater than or different to, the damage from the blast load alone.

Recent events including the Buncefield oil refinery disaster (2005), (Burgan, 2009), (Atkinson, 2011b), the West Texas fertiliser factory explosion (2013) and the Tianjin warehouse explosions (2015) have highlighted a growing need to understand the response of structures to equivalent high explosive events. The radiating thermal load from such explosive events is significantly more damaging to structures than the equivalent thermal load from smaller explosive events. It is therefore important to understand and appreciate the synergistic response of structures to the combined intense thermal loads and long duration loads from explosive events. The little existing research in this field (Gregory, 1982) shows that a synergistic response may occur; this project significantly extends this research to develop a holistic understanding of this synergistic response and forms quantitative output for the analysis of structures and buildings to such loads.

There has been a significant amount of research undertaken regarding the response of steel structures to blast loads over recent decades; however little or no research has been undertaken regarding the synergistic response of steel structures to combined blast and thermal loads. Research such as the effect of static compressive loads on the response of steel columns has been

investigated in (Nassr, 2013), and (van Netten, 1997) investigated the response of cantilever columns to long duration blast loads. Research has shown that the response of structural columns can be highly varied due to blast load parameters and structural conditions such as static loads and column end restraints. There has also been significant research regarding the response of steel under high strain rate loading, leading to guidance for structural designers detailed in (Yandzio, 1999).

The response of steel structures to thermal loads such as fire loading is a large research field. Existing research into the response of structural columns to fire loads shows that steel columns can exhibit a wide variety of response to thermal loads from fires dependent on parameters such as static loading, end connections, fire intensity, duration and application. Design codes, such as BS EN 1993-1-2-2005 (BSi, 2005c) have been used, developed and adopted for several decades to enable designers to analyse structures subject to fire loading. Investigations into the effect of temperature on the properties of steel and relative strain rates have been also undertaken by (Burgan, 2001).

This research project investigates how thermal loads propagate out from explosive events in relation to blast waves, and the subsequent response of structural steel columns to these loads. The relation of the duration, intensity and arrival times of the thermal loads to the blast loads determines the extent of the potential thermo-mechanical response. The response of whole buildings or structures to extreme thermal and blast loads from explosive events is complex due to different thermo-mechanical responses occurring concurrently such as loss of stiffness, load distribution and reduction of connection strength. This research investigates the response of single column elements to a range of blast and thermal loading regimes. To enable extrapolation of single element results to whole buildings, this research also investigates the effects of parameters including connection type, compressive load and thermal conductivity. Computational models of structural columns, using transient, non-linear, coupled (thermal and structural) finite element analyses are developed using the FEA program, LUSAS

Studies into existing research including thermal energy emission from explosive events, explosive thermal simulation, blast phenomenology and structural response to blast and thermal loading helped form the basis of the parametric studies and experimental trials. Existing theoretical data based on previous research regarding thermal and blast loads from explosive events is used to develop predictive algorithms to calculate the thermal and blast loads from explosive events. These loads are applied to the structural column computational models.

The design of and results from a series of trials recording temperatures, thermal flux and pressures, and observing the response of 2mm thick steel plates, within a 41kg TNT equivalent (eq.) explosive

fireball are presented. A series of experimental trials investigating the response of structural steel columns to combined thermal, compression and long duration blast loads were undertaken in the Air Blast Tunnel (ABT) at M.O.D Shoeburyness. The ABT is a unique testing facility which is able to produce long duration blast waves (≈200msec) akin to those produced by high explosive events such as the Buncefield oil refinery disaster (2005), (Burgan, 2009), (Atkinson, 2011b), the West Texas fertiliser factory explosion (2013) and the Tianjin warehouse explosions (2015). The ABT is owned and maintained by the M.O.D, who granted access and use for this research project.

It is not feasible to directly observe the response of structures to explosive events of equivalent size to those observed at Buncefield, Tianjin or West Texas. Therefore, it is necessary to simulate the loading regimes from these events. Thermal loads from explosive events rise very quickly over several hundred milliseconds, and decay slowly over several seconds following a parabolic decay profile. Due to the extreme temperatures inside and close to a fireball of an explosive event it is beyond the practical remit to perform experimental simulations re-creating the exact thermal environment. Previous small scale experimental simulations were able to create an intense parabolic thermal load profile but only on small test specimens (30mm). Previous large scale simulation experiments produced high thermal loads over large areas; however, they were not able to replicate the parabolic decay shape and the presence of combustion products caused detrimental effects to the thermal and subsequent blast loads. Due to the difficulties of replicating the intense thermal load from explosive events the columns in the ABT trials were subject to a long, lower thermal load with temperatures akin to fire loading (≈500^{o}C, 20mins).

Plate deformation results from the arena trials are analysed and compared to non-linear FEA models of the steel plates. Non-linear FEA models are developed and compared to the response of columns within the ABT. Modelled columns showed a reasonable correlation to the actual trial columns, providing verification of the adopted computational procedures used throughout the research project.

Resistance functions, used for the vulnerability analysis of whole buildings to explosive events are developed and presented. The resistance functions represent the elastic and plastic failure mechanisms of structural columns under specified explosive loads. Functions such as these will be utilised within fast running single degree of freedom (SDOF) analysis programs. This research project shows that under specific loading regimes steel structures can exhibit a synergistic, non-linear thermo-mechanical response to thermal and blast loads from explosive events. Given the highly complex and original nature of the research project, further research areas are highlighted for future development.

1.2 Research Hypothesis

The hypothesis central to this research project is that the thermal load from explosive events reaches and degrades a structure before the arrival of a subsequent blast load from the same explosive event causing a synergistic response. The majority of thermal load from explosive events is emitted in radiation, travelling at the speed of light. The blast load propagates at a slower rate (approximately speed of sound) and therefore reaches a structure after the arrival of thermal radiation. Steel structures will also absorb heat energy, thermally degrade and exhibit a thermo-mechanical response quicker than their structural response to an equivalent blast load. Although the onset of thermal degradation and thermo-mechanical behaviour is before the blast arrival, the extent of thermal degradation and thermo-mechanical response varies depending on parameters such as explosive size and standoff distance which relate to the extent of absorbed thermal energy prior to blast arrival.

The applied thermal load in regions very close to centre of an explosive will be of short duration before the blast arrival therefore there will be lower thermal degradation prior to blast. The blast pressure is also so large in these regions that it typically the dominant load case. A far distances the thermal load is lower as it has been reduced through the atmosphere, therefore there is also lower thermal degradation prior to blast arrival. Structures in a middle range of standoff distances will exhibit the most thermal degradation before the blast arrival and exhibit significant synergistic response to the blast and thermal loads. This middle range is determined and examined in this research project through an extensive parametric study verified with a series of high explosive experimental trials.

1.3 Aim

The primary aim of this doctoral research is to investigate the combined effects of long duration blast loads and thermal loads from explosive events on the response of steel structures. The response of steel columns is investigated in this context for a range of explosive sizes and standoff distances. The following aim is set in order to develop capabilities of predicting the response of steel structures to the combined loading regimes.

“To what extent does the intense thermal load from an explosive event degrade a steel structure and how does the thermomechanical behaviour exhibited by the structure alter the response to the subsequent blast load”.

1.4 Research Objectives

1. Determine the extent and duration of the emitted thermal radiation within, on the edge, and at far distances from explosive fireballs of a range of sizes.
2. Determine the equivalent long duration blast loading regimes relative to the explosive sizes investigated in (1).
3. Perform experimental trials recording the intense temperatures, thermal flux and pressures within, and on the edge of an explosive fireball.
4. Develop predictive structural models investigating the effect of thermal and long duration blast loads on structural steel columns.
5. Validate predictive structural models with a series of combined thermal, compressive and long duration blast load experimental trials within the ABT.
6. Production of resistance curves for use in SDOF analysis programs.

1.5 Research Methodology

There are two main aspects to this research project: The first aspect is the development of an extensive parametric study investigating the response of steel columns to intense thermal and long duration blast loads. The second aspect is the design of, and undertaking of experimental trials to a) record the intense heat and blast loads within an explosive fireball and b) observe the response of steel columns to combined compressive, thermal and long duration blast loads. The design of the experimental trials and basis of the parametric study are formed from an extensive literature review investigating existing research. Numerical verification modelling provides the link between the experimental trials and parametric study.

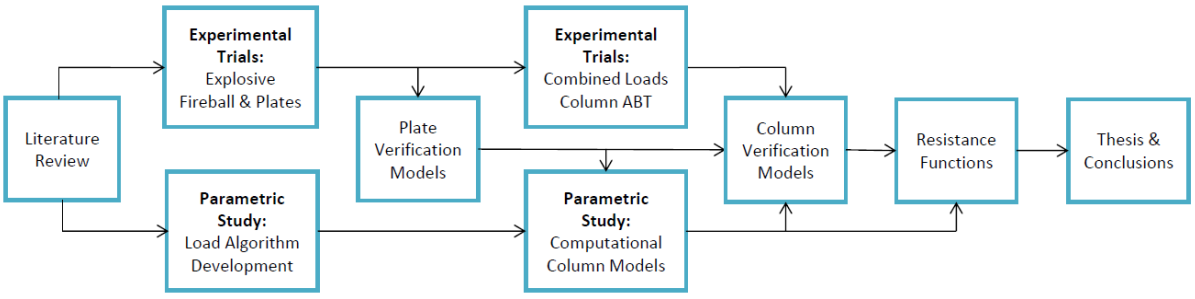

Figure 1.5.1: Flowchart of Research Methodology

The literature review investigates thermal energy emitted from explosive events, experimental simulation of thermal energy emitted from explosive events, blast phenomenology, response of structures to blast loads, response of structures to fire and thermal loads and the synergistic response of structures to combined thermal and blast loading. Theory regarding thermal energy

emission from explosive fireballs and blast load parameters is used to form predictive loading algorithms for adoption within the parametric study. Data from previous combined thermal and blast load experimental trials enable the design of the combined compressive, thermal and long duration blast load ABT trials.

The first phase of experimental trials records the pressures, thermal flux and temperatures within and adjacent to a fireball of a 41kg TNT eq. explosive event. The response of 2mm thick steel plates subject to the intense loads within and on the edge of the fireball is also observed. The second phase of trials investigates the response of structural steel columns to combined compressive, thermal and long duration blast load within the ABT. Six ABT trials are undertaken with nine columns (three section types) in each trial with varying levels compressive and thermal load applied before the blast load.

The computational analysis serves two purposes, the first to model response of the plates and columns from the explosive fireball and ABT experimental trials, and second to predict the structural response of columns under intense thermal and long duration blast loads from explosive events. Coupled (thermal and structural) non-linear models are developed using the finite element analyses (FEA) program LUSAS (LUSAS, 2013) throughout the research project.

Algorithms predicting the thermal energy emission from explosive events (2.1) are developed to produce thermal flux (cal/cm^2/sec) and temperature (^{o}C) history profiles. An algorithm to predict the applied pressures on column sections subject to long duration blast loads is also developed for use within the parametric study. A Johnson-Cook material model for steel under high temperatures, high strains and high strain rates is adopted within the predictive FEA models of the steel columns in the parametric study and ABT trials. Comparing results from the computational analyses and experimental trials provides verification for the numerical procedures adopted throughout the research.

Resistance functions are developed using the results from the parametric studies verified with the predictive models of the columns from the ABT trials. The resistance functions describe the elastic and post elastic response of structural columns under combined thermal and blast loads from explosive events. The functions developed indicate the differing response of the columns under blast load alone compared to the response under combined thermal and blast loads.

Chapter 2

Literature Review

2.1 Thermal Energy Emission from Explosive Events

A key area of research for this project is emitted thermal energy from explosive events. Of particular interest is the emitted thermal energy across, at the edge of, and beyond the fireball of an explosive event with an equivalent long duration blast load. It is within and at the edge of the fireball that a high amount of thermal energy is emitted producing extremely high temperatures over a very short time. The relation with the propagating blast wave is important in determining the effects that the combined thermal and blast loads will have on a structure. The absorbed thermal energy from an explosion may significantly weaken a structure so that when the subsequent blast arrives it could lead to significant deformation and failure of a structure that when subject to the blast alone could survive. The applied heat onto a steel structure will degrade material properties including the Young's Modulus and Yield Strength thus the weakening the structure so the deformations from the subsequent blast load are of a higher magnitude. This section investigates the emitted thermal energy from explosive fireballs in order to extract data to assist in the parametric studies.

The thermal power from explosive fireballs can be emitted in multiple pulses, as an example a fireball of a nuclear detonation emits thermal power in two pulses as shown in Fig.2.1.1. The initial pulse is typically very quick and radiates extremely high temperatures but only contributes to 1% of the total emitted thermal energy. Subsequent pulses are longer, up to several seconds, reaching lower temperatures but have a greater effect on material and structural degradation. In terms of effective thermal radiation the first pulse is ignored. The effective thermal radiation accounts for approximately 35% of the total energy emitted from a long duration explosive event. For example, for 1T of TNT if 0.35T is emitted as thermal energy a total $3.5x10^8$ calories will be emitted (Glasstone,

1977). The remaining portion of explosive energy consists of blast wave energy, long distance thermal energy and late time radiation.

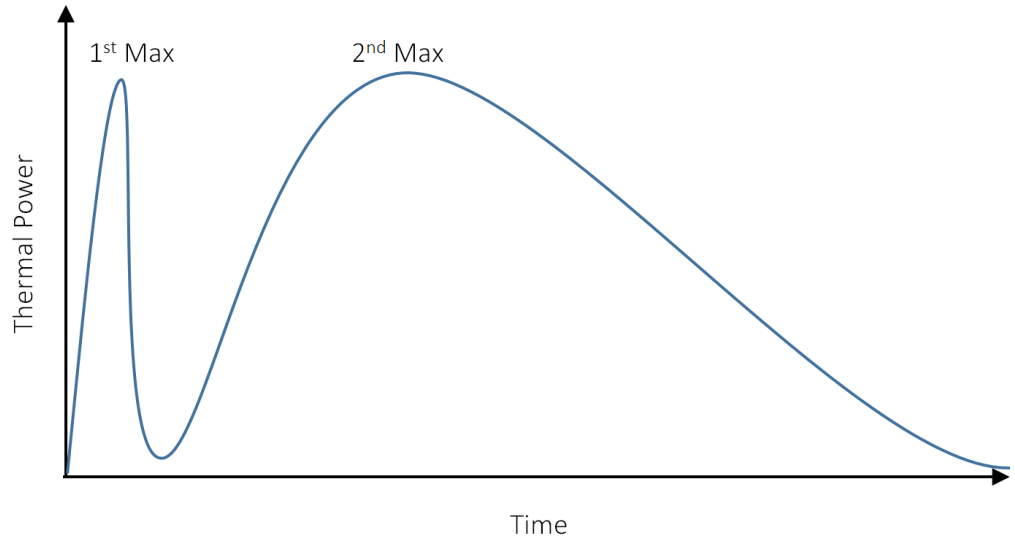

Figure 2.1.1: Thermal Radiation vs. Time

2.1.1 Fireball Development (0 – 80msec)

In the initial stages of an explosive event temperatures in the region of tens of millions of degrees are reached in fractions of a second as the energy diffuses into the surrounding air. During this time the explosive material and immediate surrounding air dominate the early radiation characteristics.

The initial radiations are in the Gamma and X-ray region, the amount of which is determined by the explosive material. The air immediately adjacent to the explosive source is heated to millions of degrees and becomes transparent to X-rays as they escape. Cold air surrounding the hot air is opaque until it has reached several millions of degrees when the air molecules are ionised, once this has occurred the air is transparent and cannot absorb more radiation (Brode, 1964).

The initial rate of fireball expansion is very quick up to 1µsec after the initial explosion, after which the rate of expansion decreases due to decreased radiation from increased opacity causing a temperature differential on the edge of the fireball. Behind the fireball front, the explosive vapours are also expanding with the case shock at a slower rate. The early initial fireball takes the form of a very hot sphere with a uniform temperature throughout until the edge where the temperature quickly drops.

After 1µsec the very hot air re-radiates rapidly into the surrounding cold air as the fireball grows. At approximately 34µsec the early fireball has a maximum constant temperature of approximately 700,000°K across the radius, until the edge where it rapidly drops to zero. The density is also

relatively constant across the radius at 0.25kg/m^3, with a sharp peak near the centre (explosive material). The pressure across the fireball radius at this time is also relatively constant. There is a high peak pressure near the centre just behind a constant pressure until the fireball edge where there is a significant drop. This high peak forms the start of the shock wave which will pick up air and become a non-adiabatic isothermal shock.

At approximately 100µsec the shock wave expands further and engulfs air which due to its incandescence radiates very strongly but it is restricted to the interior areas of the fireball due to surface opacity of the front. The explosive source vapours drop away as the shock expands to the edge of the fireball where a strong adiabatic shock is formed and speeds up expansion of the fireball. The surface of the fireball now radiates as a black body. At approximately 74msec the fireball has grown and the temperature across can be up to a constant of approximately 80,000^{o}K in the centre dropping to 4000^{o}K at the edge with a sharp drop to zero.

2.1.2 Fireball Development (After 80msec)

After 80msec, surface temperature decreases to several thousand degrees as the fireball expands. The shock front, which was previously opaque, becomes transparent due to decreasing pressure. Due to increased transparency the hot interior radiates more freely and the rate of thermal energy radiation rapidly increases. The shock wave then continues to grow as the late fireball stops growing, when the shock wave reaches the front of the isothermal sphere the fireball temperature is close to the second maximum (Fig2.1.1) (Bethe, 1964). Thereafter the shock wave is independent of the fireball and continues forward. The radiation now decreases to zero over several seconds, during which the majority of fireball energy is dissipated (Brode, 1963). At 0.51 seconds the centre of the fireball is at approximately 12,000^{o}K whilst the edge radiates at approximately 700^{o}K. This continues to drop as the fireball stops growing and cools.

2.1.3 Radiant Power from the Fireball

For the purposes of this research project it is assumed that the fireball radiates as a black body, as described in (Freeman, 1963), this assumption is justified for the majority of the fireball. In transitional areas this assumption is not perfect as combustion products can obstruct a homogenous radiation. As the temperature varies so does the radiant energy spectrum; low temperatures are dominated by longer wavelengths and higher temperatures are dominated by shorter wavelengths. Therefore, extremely high temperatures recorded at the very start of the explosion are in the X-ray region. At the maximum radiant power the dominant wavelength is in

the visible spectrum (3,850Angstrom), the equivalent temperature is 7,500°K which closely relates to the maximum surface temperature of the fireball (approximately 8,000°K).

The Stefan Boltzmann law (eqn. 2.1) derived from general physics, is used to calculate the total thermal energy radiated by a black body (J/cm^2/sec), where σ is the Stefan Boltzmann Constant (Appendix A) and T is the absolute temperature:

$$\boldsymbol{J = \sigma T^4} \tag{2.1}$$

Therefore, the total rate of emission of a fireball of a given size is the product of the total energy and surface area ($4\pi R^2$), this is the total radiant power = P (cal/sec), (T in Kelvin, R in cm):

$$\boldsymbol{P = 4\pi\sigma T^4 R^2 = 1.71 \times 10^{11} T^4 R^2} \tag{2.2}$$

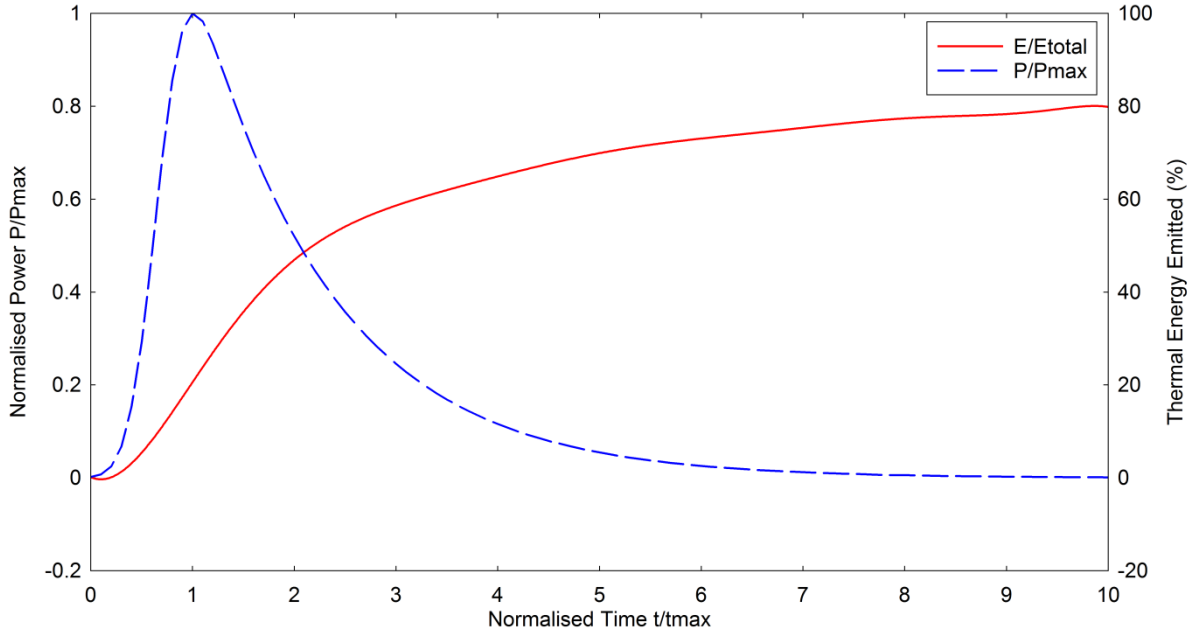

Figure 2.1.2: Normalised Power vs. Normalised Time of Thermal Energy Emitted from an Explosive Fireball

Fig.2.1.2 shows the normalised thermal power emitted from an explosive fireball over normalised time (time to max = 1). Approximately 28% of thermal energy is radiated before the maximum power is reached, increasing to 80% at $10t_{max}$. Beyond $10t_{max}$ the rate of thermal emission (radiant power) is so low that the remaining 20% of thermal energy still to be radiated does not significantly contribute to any material or structural damage. For the purposes of this research it is therefore assumed that $10t_{max}$ is the time when the emitted thermal energy returns to zero. The maximum power (P_{max}) and time to maximum power (T_{max}) can be calculated using equations 2.3 and 2.4.

$$\boldsymbol{P_{max} = 3.18 W^{0.56}} \text{ (kT/sec)} \tag{2.3}$$

$$\boldsymbol{T_{max} = 0.0417W^{0.44}}\text{(sec)} \quad (2.4)$$

To convert this calculated power from kT/sec to cal/sec the value is multiplied by 10^{12}. This conversion is used for explosive sizes described using TNT equivalence. Equations 2.3 and 2.4 have been derived from previous experimental and computational research and are not dimensionally homogenous. The detailed derivation of such calculations is not an open source material. Equation 2.5 (Dolan, 1972) is the total incident radiant energy per unit area (radiant exposure: cal/cm^2), (τ= Transmittance, D= Distance (cm), R= slant distance, $E_{tot} = fW$, W= yield, f= Thermal Energy Ratio):

$$\boldsymbol{Q = \frac{E_{tot}\tau}{4\pi D^2}} \quad (2.5)$$

This can be re-arranged with R in km as:

$$\boldsymbol{Q = \frac{7.96\,Wf\tau}{R^2}} \quad (2.6)$$

The slant distance (R) is the direct distance from the centre of the explosion to the object of interest. The thermal energy ratio (also known as thermal efficiency) is the portion of the explosive size which is expelled as thermal radiation (E_{tot}/W). At increasing explosive heights the thermal energy ratio increases. For surface explosions the thermal energy ratio is less due to dust from the ground. A typical thermal energy ratio at ground level is 0.19.

2.1.4 Atmospheric Effects

In a simplified situation where there is no attenuation of thermal radiation from the atmosphere the energy will be spread out over an ever increasing (hemi)-spherical area. The energy at a given distance would be proportional to the inverse square of the total thermal energy, ($E/4\pi D^2$); however, thermal radiation can be attenuated in the atmosphere by absorption and scattering. It is typically the shorter wavelengths that are absorbed and scattered more readily. Therefore the initial X-Rays and UV Rays are quickly absorbed after initial explosion and do not travel far. Scattering can also reduce the radiation by diverting rays into different directions, and hitting dust or other airborne particles. If the relative density of air is high with low visibility there is likely to be multiple scattering, therefore an object may be exposed to thermal radiation from several directions.

The “Daylight Visibility Range” (Visibility) is used to measure the state of the atmosphere. The daylight visibility distance can be quantified as the “Distance to a Large Dark Object on Horizon to be Discernible in Daylight”. Table 2.1 gives vales for visibility for various atmospheric conditions.

Table 2.1: Visibility for Atmospheric Conditions

Atmospheric Condition	Visibility	
	Kilometres	**Miles**
Exceptionally Clear	280	170.0
Very Clear	50	31.0
Clear	20	12.0
Light Haze	10	6.0
Haze	4	2.5
Thin Fog	2	1.2
Light to Thick Fog	1 or less	0.6 or less

Further away from the centre of the explosion the atmospheric attenuation and scattering becomes more prominent and the accuracy of the calculated radiation decreases. The term transmittance (τ) is used to describe how well the radiation propagates through the atmosphere or how much radiation is absorbed. Transmittance is a function of visibility, absorption, explosive height and distance. Transmittance can be calculated using equation 2.7. The units for transmittance are dimensionless.

$$T = e^{-2.9\frac{R}{V}}\left(1 + 1.9\frac{R}{V}\right) \tag{2.7}$$

R = Slant Distance, V = Visual Distance

2.1.5 Surface Explosions

When an explosion occurs on the ground the radiating energy is decreased to 50% of an equivalent air explosion. The fireball is semi-spherical with a “shock-skirt” at the front (produced from ground dust and debris). The material kicked up from the ground reduces the temperatures inside the fireball and gives the fireball an opaque appearance which reduces the thermal radiance.

2.1.6 Reliability of Thermal Calculations

The numerical procedures detailed in 2.1.3 to 2.1.5 were largely developed from computational modelling of long duration explosive events validated against observations of historical explosive testing. Previous research describes good agreements between the computational codes and experimental data for thermal radiation parameters including the radius-time data, and the reproducibility of fireball evolution details. The parameters showing less agreement included the

thermal energy ratio and extent of radiation during the first maximum. This was due to unknowns regarding the interaction of shock pre-cursor and thermal radiation.

2.1.7 Late Time Fires

It is not only direct radiation from the explosive event that causes thermal damage, but frequently and potentially more damaging, are the late fires that occur. This could occur at far distances from the explosive fireball. The initial radiation or blast wave could produce late time fires by secondary effects such as burning combustible materials or damaging electrical lines, fuel tanks etc. The likelihood of any late-time fires developing after an explosive event is very difficult to quantify. Factors such as density of fuel, combustibility, fire breaks (rivers), topography and any meteorological effects would be taken into account. If an explosion causes many small fires across an area there is a likelihood that those individual fires can coalesce into one massive fire to produce fire storms or conflagrations.

2.2 Experimental Simulation of Thermal Radiation from Explosive Events

In order to simulate the thermal energy and blast loads within an explosive fireball several experimental simulation techniques have been developed. The following section discusses these techniques, investigating the practicalities in a testing environment, the accuracy of replicating an actual thermal load and the shortcomings with subsequent improvements on the design of each technique.

2.2.1 Rocket Propellant

The first testing undertaken with the principal notion to simulate thermal loads from high explosive events was by N.Griff and J.F.Proctor in 1972 using a burning sheet of rocket propellant. The aim of the rocket propellant tests was to create a thermal radiance history similar to the one shown in Fig.2.2.1.

The propellant mixture constituted an ammonium perchlorate as oxidiser with copper chromite to speed up the burning rate. The mixture was ignited by heating (to incandescence) lengths of Nichrome wire which were cemented to the surface of propellant sheets. The surface was coated in paint of pyrotechnic powder and nitrocellulose and butyl acetate. The sheets produced a thermal flux of 15cal/cm^2/sec and were able to heat up the rear surface of 2.4mm thick aluminium plates to 400^{o}C in 8 seconds (Fig.2.2.2).

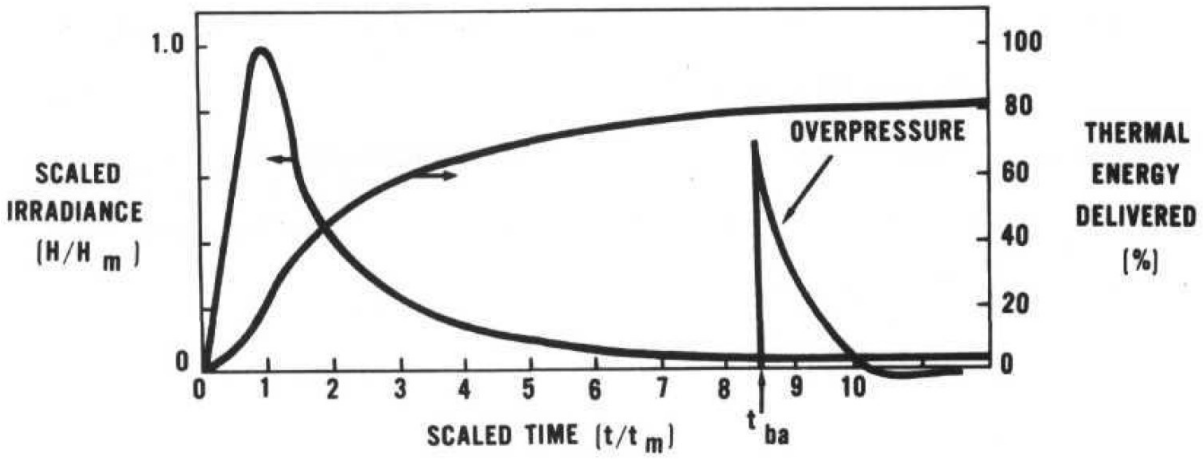

Figure 2.2.1: Typical Simulated Scaled Thermal Irradiance (Griff, 1972)

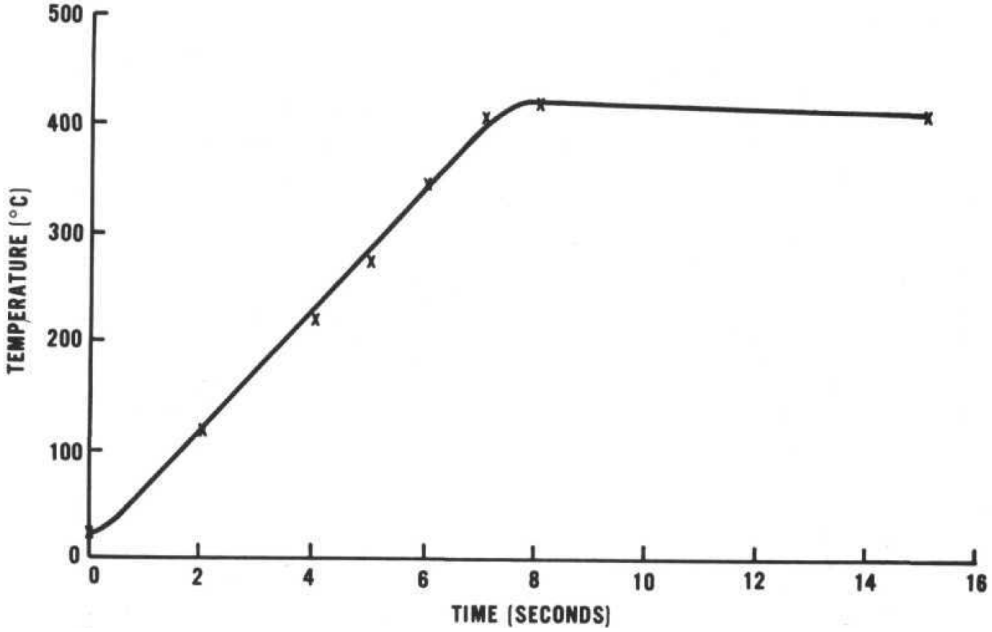

Figure 2.2.2: Rear Surface Temperature of Aluminium Plate Subject to Sheet Propellant (Griff, 1972)

A Conical Shock Tube (CST) was used to test the aluminium plates to blast loading following exposure to the rocket sheet propellant. The CST creates blasts with an amplification factor of approximately 30,000 and can produce long duration blast loads. The tests were conducted outside the rear open end of the shock tube where a pressure of 10psi (68.95kPa) was achieved. The aluminium plates tested were 406mm x 406mm x 2.4mm. The maximum deflection of the combined thermal and blast loaded plate was 10.4mm, larger than the thermal only (8.6mm) and the blast only (2.54mm). The initial direction of movement of the plate under heat load only was not consistent over several trials due to material and manufacturing variances.

2.2.2 Aluminium Oxidation & Rotating Table

In order to test full size structural elements (aluminium circular hollow sections) to intense thermal and long duration blast loads a large thermal simulator was constructed. Due to non-uniform heating of the rocket sheet propellant (2.2.1) on large structural elements an alternative was investigated involving the oxidation of aluminium powder.

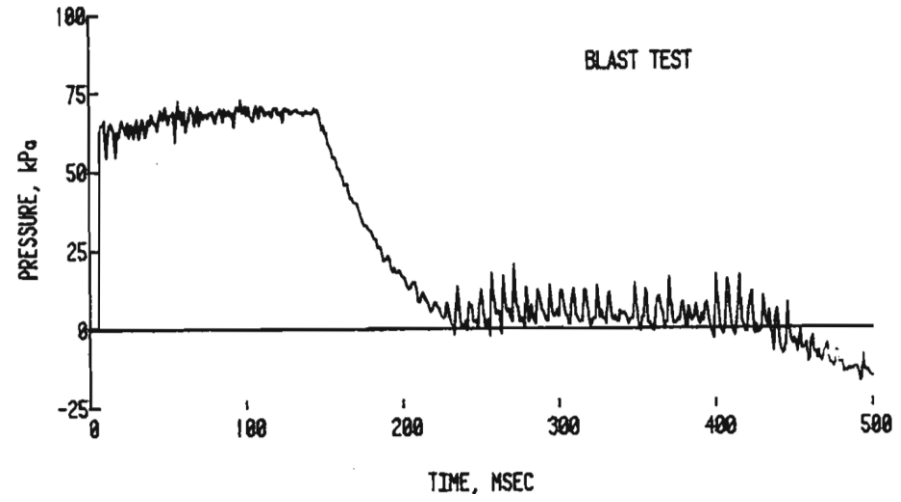

(a) Blast Only

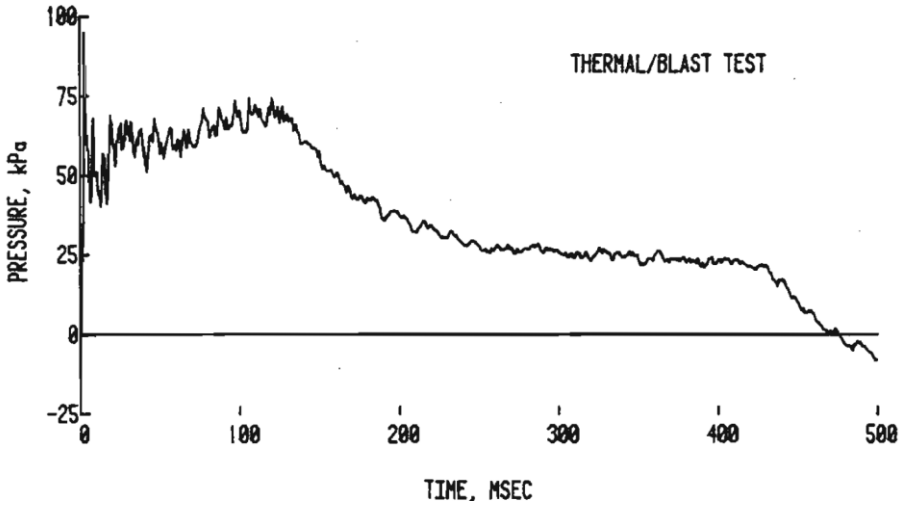

(b) Combined Thermal and Blast

Figure 2.2.3a & b:Shock Pressure For Blast Only (a) & Combined Thermal & Blast (b) (Teel, 1981)

The thermal simulator tested at the Ballistic Research Laboratory (BRL) used an aluminium fluidiser which, after ignition, expelled fluidised aluminium into oxygen producing a controlled thermal flux of approximately 25cal/cm^2/sec. An issue occurred in the form of a cloud of combustion products adjacent to the target for several seconds after the thermal load. The combustion products perturbed the subsequent shock wave before reaching the target. In order to negate this effect the

aluminium fluidiser was placed downstream of the target which was placed on a “rotating table”. The target was subject to the thermal load turned through 180 degrees and subject to the blast load. Despite the efforts of the rotating table to eliminate the effects of the combustion products, the blast wave still had minor perturbations. Figs. 2.2.3a) and 2.2.3b) shows a comparison of pressures from the blast only and combined tests. When a blast wave travels through hot combustion products its waveform characteristics can be modified. The blast wave can be attenuated by up to 30% by the thermal products, such as in the Miser’s Bluff experiment (Fig.2.2.4), where the blast wave was modified as it passed through combustion products.

Figure 2.2.4: Miser's Bluff Test with Perturbed Wave Front (Kitchens, 1981)

As a shock wave passes through a region of heated combustion products the properties of the air behind, inside and in front of the products is changed. The speed of sound within the combustion products is several times higher than ambient air, therefore the shock wave moves faster within the products. At the entry boundary part of the wave is reflected back as a rarefaction wave into the previously shocked air reducing the positive phase pressure. The shock wave that passes through is also significantly reduced. As the shock wave arrives at the rear (exit) boundary of the combustion products a portion of the shock wave is also reflected back into the combustion products and a reduced shock sent forward into the ambient air. The reflected wave can be reflected several times back and forth on each boundary. Fig.2.2.5 is a diagrammatical representation of the interaction of the shock wave and combustion products.

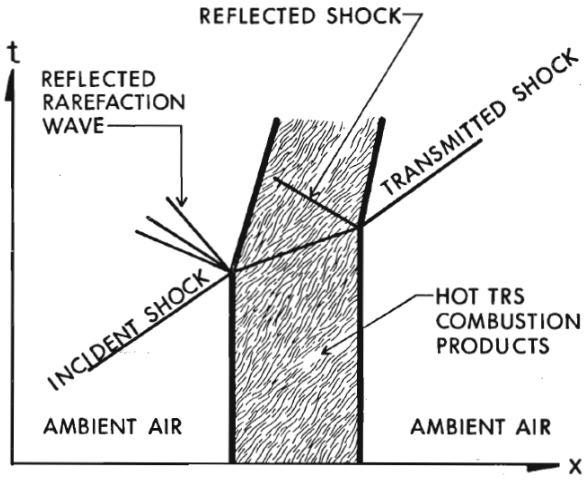

Figure 2.2.5: Diagram of Shock Wave & Combustion Products Interaction (Kitchens, 1981)

2.2.3 CEG Flux & Multi-Nozzle TRS within the Air Blast Tunnel

Experiments were conducted at the Centre d'Etudes de Gramat (CEG) in order to observe the flux, fluence and spectral distribution of an aluminium and liquid oxygen thermal simulator (Three Burner TRS-LOX). Ten seconds of liquid oxygen followed by aluminium powder were both ejected under nitrogen pressure followed by the combustion of aluminium for a specified duration. Free-field tests were performed to enable the calibration of the flux spectrum. Figs.2.2.6a and 2.2.6b show the flux and fluence levels at 3m from the burners.

The TRS-LOX simulators were tested in the 2.4m shock tube at CEG, as a precursor to further TRS-LOX simulation in the Air Blast Tunnel (ABT). Removal of the majority of the combustion products was achieved using a 1m width slot in the shock tube wall above the burners. Some combustion products still remained upon shock arrival; however these did not interfere with the main shock.

In order to improve the accurate simulation of a thermal pulse in the shock tube a diverter valve was located at the nozzle to control the aluminium oxide flow. This shortened the potential delay from the end of combustion to the start of the shock. The valve initially diverted the flow of aluminium to a tank away from the burner until a constant flow was reached then diverted the flow to the burner. This reduced the rise time from 400msec to 100msec with a decay of 50ms (compared to 800msec previously). Figs. 2.2.7a and 2.2.7b show the thermal flux before and after the use of the diverter valve.

As the simulated thermal pulse shapes were trapezoidal using the TRS-LOX, unlike parabolic thermal pulse shapes (typical of explosive events), it was necessary to perform a calibration on the test subjects. A solar furnace was used to calibrate the samples using an accurate parabolic thermal pulse. Samples were initially exposed to a parabolic flux profile in the solar furnace. Identical

samples were then exposed to a trapezoidal flux profile equivalent to the TRS-LOX. After comparing temperature, damage and thermal energy levels the TRS-LOX was adjusted to match the parameters of the parabolic thermal pulse.

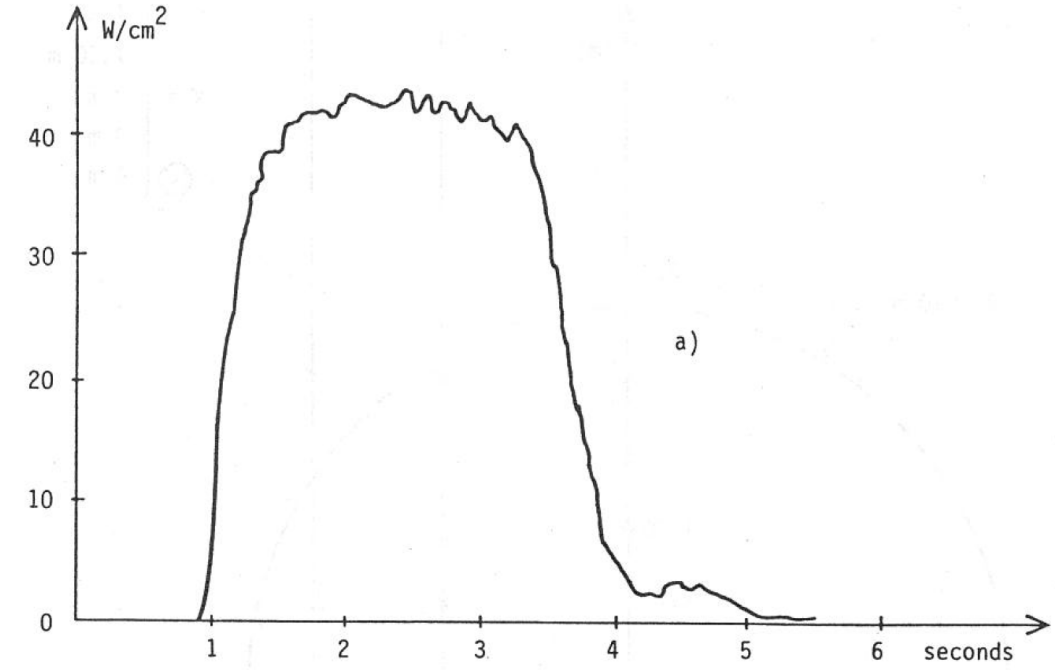

(a): Flux

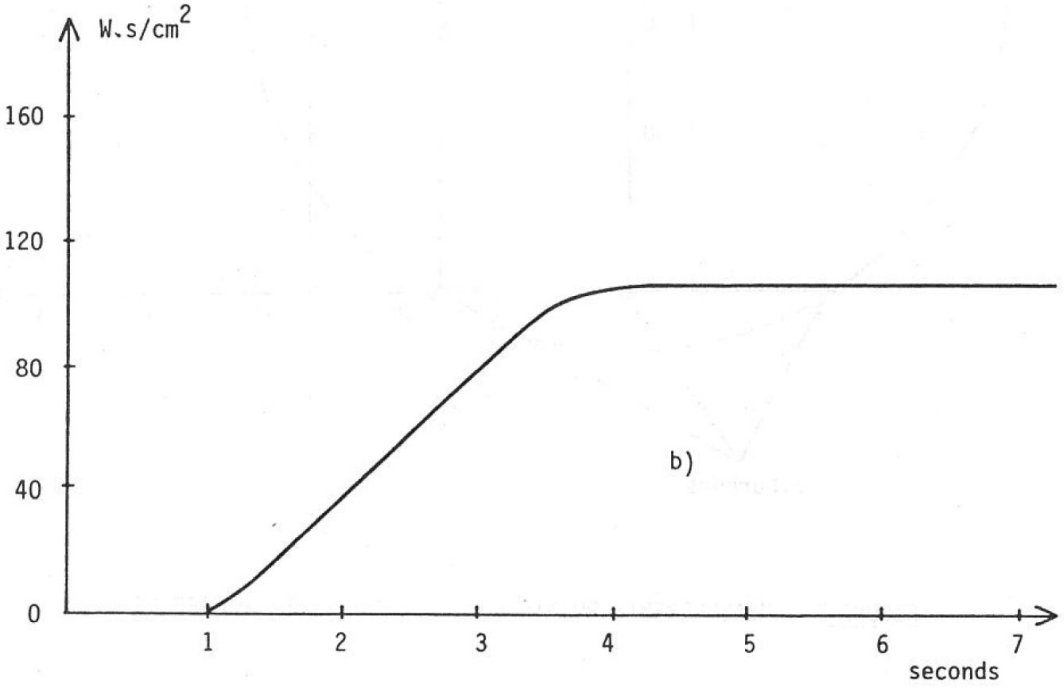

(b): Fluence

Figure 2.2.6a & b: Flux (a) & Fluence (b) Levels at 3m from TRS-LOX (Gratias, 1983)

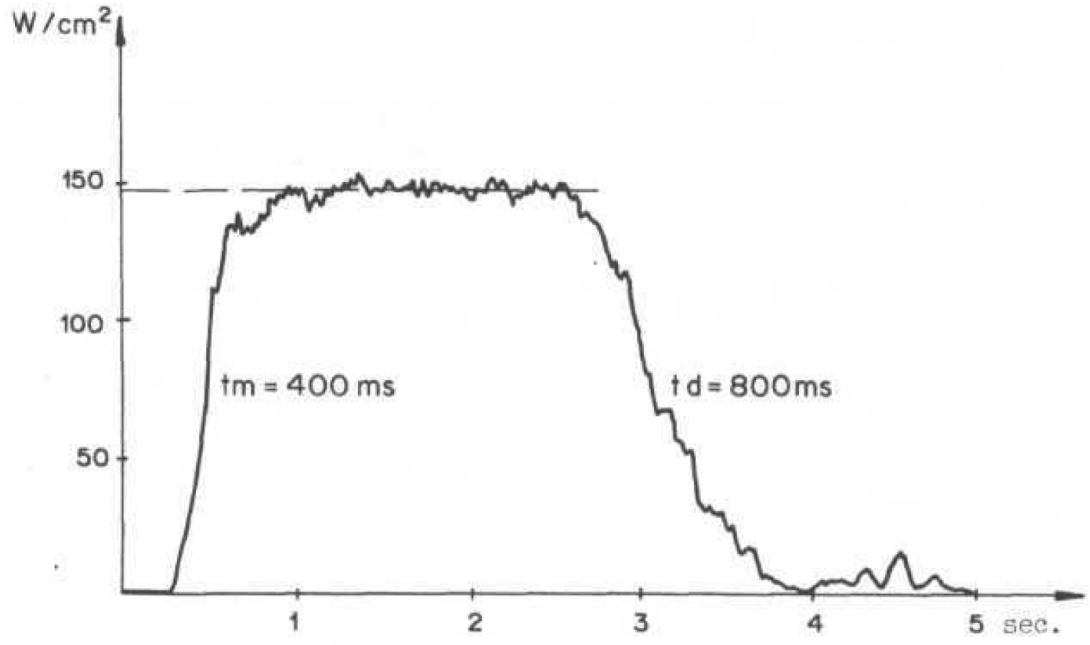

(a): Before Diverter Valve

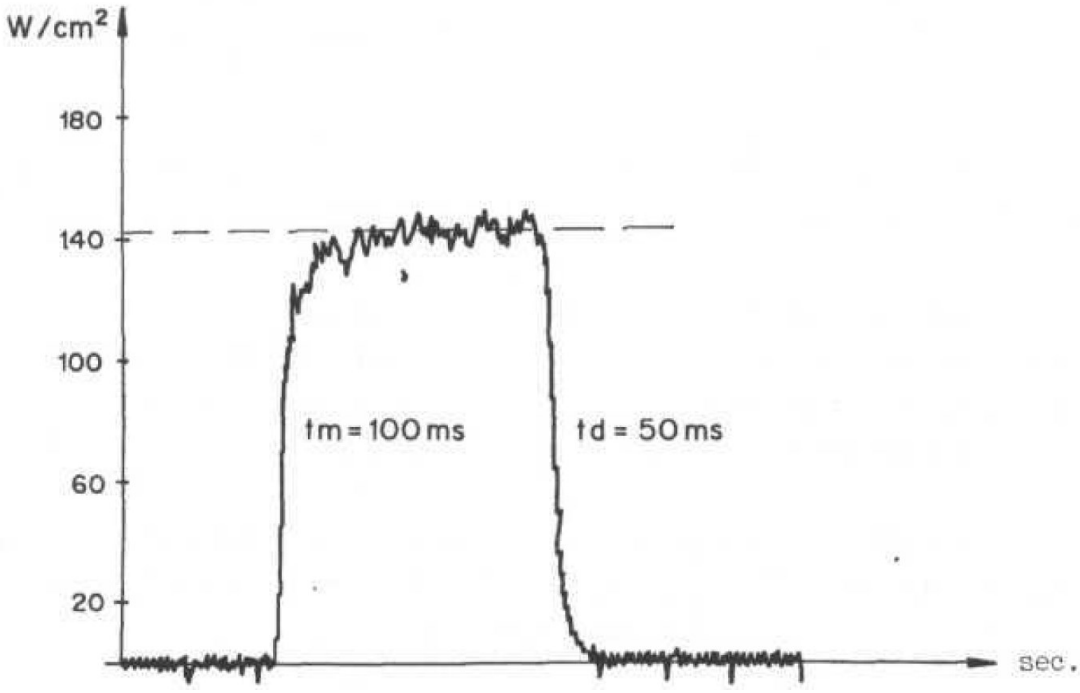

(b): After Diverter Valve

Figure 2.2.7a & b: Flux values before (a) & after (b) the use of diverter valve (Gratias, 1987)

Following the TRS-LOX testing at CEG the TRS was tested inside a 10.2m diameter section of the Air Blast Tunnel (ABT) at Foulness Island. A blast pressure of 50kPa was combined with a fluence from the TRS of 100cal/cm^2. Initial calibration tests were undertaken using a single TRS nozzle upstream of the 10.2m section with a test piece at 2m. During the calibration it was observed that the test

piece became obscured by a dense freezing mist during the initial ejection of liquid oxygen affecting blast wave and recording equipment. (Borgartz, 1985)

With no extraction of combustion products there were significant differences between the recorded pressures during the blast only trial and the blast and thermal trial. Pressures recorded near the floor had an enhanced shock; due to the higher density cold gas. The pressures recorded near the roof show the shock moving faster through the high temperature zone, also with a pronounced disturbance. To remove the combustion products Jetflow Airmover, Type 200E fume extractors were installed in roof of the tunnel, with three extractors positioned above each TRS nozzle.

2.2.4 Large Blast / Thermal Simulator

Similarly to the ABT at Foulness Island, the large blast / thermal simulator at White Sands, New Mexico produces a long duration shock wave akin to a large explosive event. The shock wave is produced by releasing compressed gas from several high pressure tubes into a large tunnel (Opalka, 1989). Constructed within the tunnel is a thermal radiation simulator (TRS), mounted under the floor upstream of any test items. To contain the combustion products within the TRS, air currents are fed through nozzles on either side. Several jet pump ejectors are also fixed to the ceiling above the TRS extracting the combustion products to ensure minimal disturbance to the shock wave.

2.2.5 Summary of Thermal Simulation Facilities

Small laboratory simulators such as Xenon lamps or solar furnaces can simulate accurate thermal parabolic pulse shapes using complex computer controlled systems such as at WIS, Munster. Larger scale tests are undertaken using the TRS (2.2.3) in free field, shock tube and the ABT.

The small heat flash thermal simulator at WIS, Munster uses a 2.5kW Xenon arc lamp overdriven to 10kW. Thermal energy from the lamp is reflected by an adjacent elliptical mirror into an auxiliary mirror, positioned to improve luminous efficiency. Thermal radiation is then homogenised through a honeycomb filter on to a 15mm usable circular zone with a maximum illumination of 2.0MW/m^2. The duration of the flash can be from 0.5secs to 4secs in 0.01sec steps with a peak thermal flux of 38W/cm^2. The large thermal heat flash simulator at WIS, Munster uses an 80kW short-arc Xenon lamp, stabilised by a dynamic Xenon gas flow. The size of the usable homogenous irradiation is 25cm^2 and the illumination can reach 4MW/m^2. A benefit of the xenon lamp simulator is the ability to produce accurate parabolic thermal pulse shapes.

The solar furnace twice reflects thermal rays from the sun concentrating and modulating the thermal flux before reaching a target (see Fig.2.2.8). Thermal rays from the sun are reflected off a heliostat; a 17.5m x 14m assembly of plane mirrors which track the sun. The rays pass through an attenuator and reflect again of a concentrator which focuses the rays to a 100mm box. The flux can be modified by the attenuator. Uncertainties and inaccuracies with the flux levels from solar furnaces can be due to the actual solar flux from the sun and reduction in mirror reflectance due to dust.

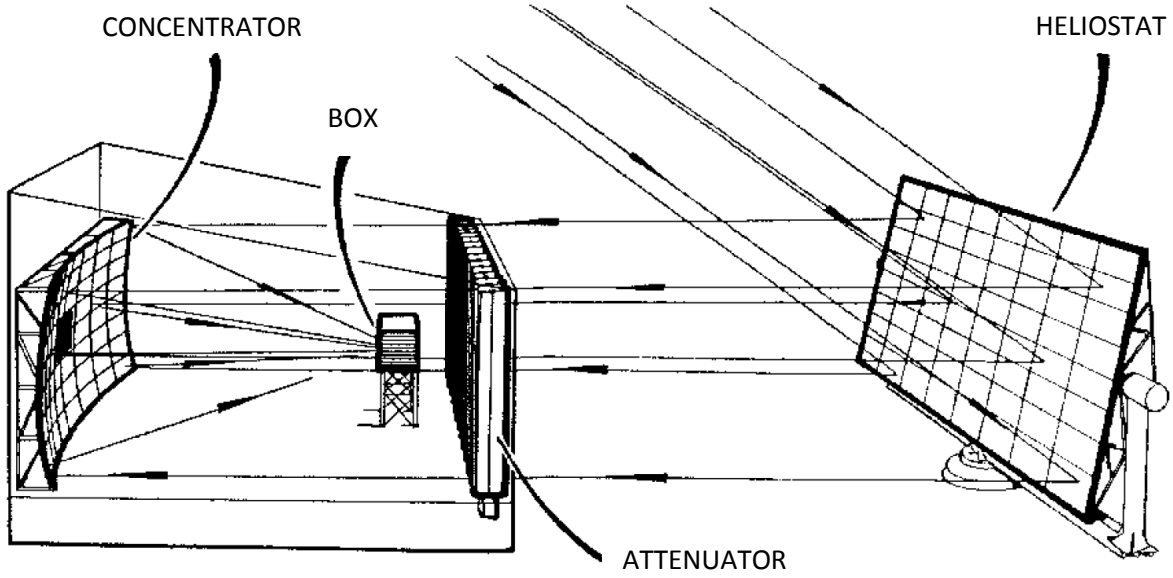

Figure 2.2.8: Diagram of the Solar Furnace (Simon, 2008)

The four burner TRS heat flash facilities at WIS, Munster can produce thermal radiation from vertically ejected aluminium powder and liquid oxygen up to an area of $10m^2$ (Fig.2.2.9). The maximum flux is $2.0MW/m^2$ at 1.5m. The TRS can achieve an illumination which is homogeneous to ±20% over a $10m^2$ area and with a flux reproducibility of ±15%.

For good accurate simulation and good reproducibility of explosive thermal flux profiles the solar furnace and xenon heat lamp are the choice facilities; however they can only be used on small samples. The open air TRS facility is the best method of subjecting large structures to an intense thermal flux, however reproducibility and homogeneity is lower than lab trials due to uncontrollable environmental effects.

Figure 2.2.9: TRS Field (Simon, 2008)

2.2.6 Thermal Tile Development

An initial aim of this research programme was to perform a series of trials using the high thermal simulator "Thermal Tile". The thermal tile was previously developed by the Defence Special Weapons Agency (DSWA, US) with the intention of using the thermal tile as a high thermal simulator combined with a subsequent blast wave (Zavitsanos, 1998). The tile consists of two metallic elements (Boron and Titanium) which when ignited produce a highly exothermic reaction. The metallic elements were combined in powder form, formed into slurry and poured into trays. Set within the slurry is a palladium cladded aluminium wire which when ignited initiates the Boron/Titanium reaction (Fig.2.2.11).

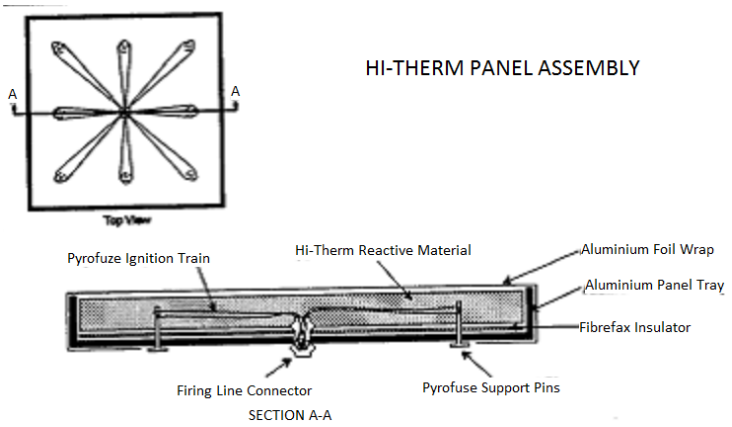

Figure 2.2.10: Thermal Tile Configuration (Zavitsanos, 1998)

A singular tile (1ft x 1ft) produced a peak thermal flux of 155Cal/cm^2/sec with little observable combustion products. A larger array of tiles (3ft x 3ft) produced a lower peak flux of 46cal/cm^2/sec, with increased combustion products obscuring the radiation. Further development of the tiles was required for full scale testing; the use of a lower porosity mixture to reduce the volatility of the constituent materials was recommended. The use of the thermal tiles during this research project was not pursued further due to the high volatility and instability of the materials involved.

2.2.7 Ceramic Heating Elements

The use of the thermal tile or other high thermal simulation techniques to produce an intense heat flux applied to structural elements was investigated at the early stages of this research project. After exploring several options a decision to use a slower thermal simulator which emits a lower thermal load was made. The use of ceramic heating elements was pursued as the preferred option (Fig.2.2.11).

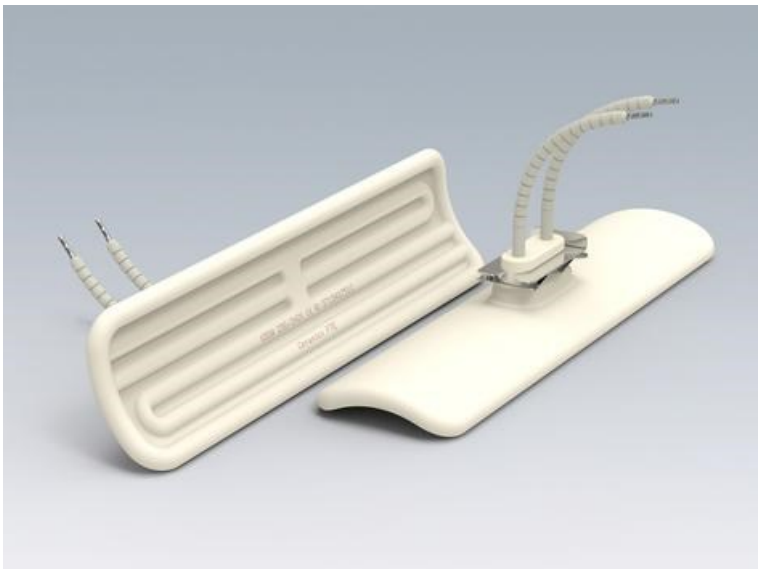

Figure 2.2.11: Ceramicx Heating Elements (Ceramicx, 2015)

Ceramic heating elements have been widely used in a range of industries including plastic thermoforming and multi-material bonding which require high levels of concentrated, controlled infra-red heating, (Ceramicx, 2015); however, there has been little use of ceramic heating elements for structural fire or thermal research. The thermal performance of the ceramic heating elements is shown in Fig.2.2.12 (heating up and cooling down curves) and Table 2.2 (performance parameters).

Given the controllable temperatures of the ceramic heating elements they were selected as the preferred option for thermal testing undertaken during this research project. Further information

regarding the experimental testing of the ceramic heating elements during this research project is detailed in 3.3.

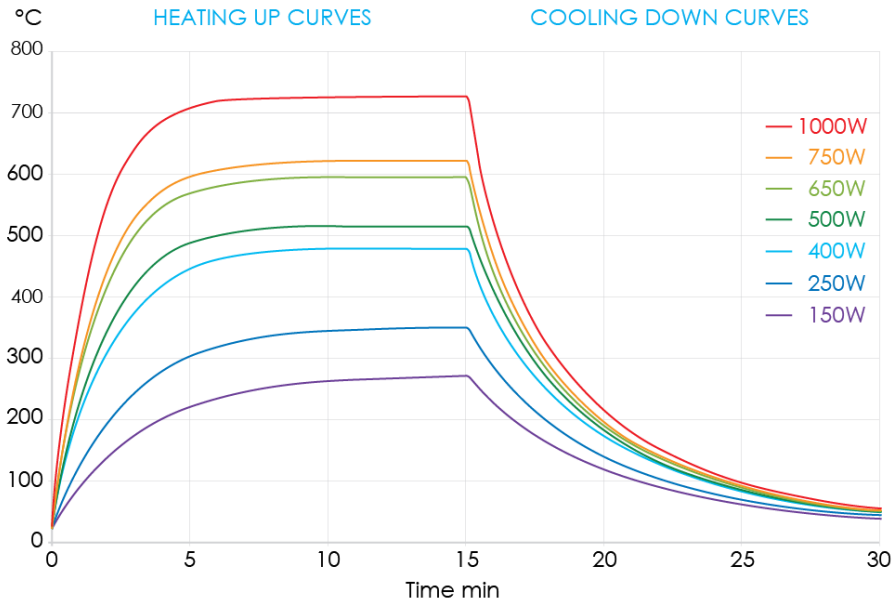

Figure 2.2.12: Heating Up & Cooling Down Curves for Ceramicx Heating Elements (Ceramicx, 2015)

Table 2.2: Ceramic Heating Elements: Performance Parameters (Ceramicx, 2015)

FTE Full Trough Element	**150W**	**250W**	**300W**	**400W**	**500W**	**650W**	**750W**	**1000W**
Mean surface temperature	262ºC	354ºC	400ºC	464ºC	486ºC	589ºC	634ºC	722ºC
Max permissible operating temp.	750ºC							
Max power density kW/m² (w/inch²)	0.9 (5.8)	1.5 (9.7)	1.8 (11.6)	2.4 (15.5)	3.0 (19.4)	3.9 (25.2)	4.5 (29)	6.0 (38.3)
Radiant Watt density at 100mm (W/cm²)	0.10		0.26		0.48	0.69		1.14
Dimensions	245 x 60 x 35 mm							

2.3 Blast Phenomenology

2.3.1 Typical Blast Waves

A blast wave is created by the rapid expansion of gases after the detonation of explosive materials, resulting in a shock pressure. Immediately after the initial explosion, conventional explosives can produce very high pressures and temperatures in the region of 30GPa and 4000^{o}C. The air surrounding the initial explosion becomes compressed and is forced out, this produces an imbalance between the air in the blast wave and the undisturbed air in front, forcing the blast to move outwards (Mays, 2009). The rapid expansion of the blast wave causes overexpansion and the air behind the blast inhibits a negative pressure below atmospheric levels. This typically displays itself as a negative suction phase after the positive blast wave has past.

When the highly compressed air reaches an object a region of high pressure is created by the energy from the reflection of the blast wave on the surface. At the front of the blast wave the maximum pressure caused by the compression of the air is termed the peak overpressure. The duration which the overpressure is sustained is the positive phase duration.

Once the incident overpressure has passed it is closely followed by a negative pressure and dynamic pressure. The dynamic pressure is the product of a "blast wind", created by the acceleration of air particles from the initial blast wave. It is calculated using the kinetic energy of the air (equation 2.8). For conventional explosions the dynamic pressure is usually negligible in terms of scale and effect compared to the peak overpressure. Depending on explosive size, location, dimensions of interacting object and time after initial explosion the negative suction phase can significantly reduce the magnitude of the dynamic pressure.

$$\text{Dynamic Pressure} = \frac{1}{2}\rho u_s^2 \tag{2.8}$$

ρ = Air Density (kg.m^{-3}), u_s = Particle Velocity (m.s^{-1})

2.3.2 Calculations for Blast Wave Parameters

To assess the magnitude of a given blast and the effects that the blast will have on a structure the blast parameters are calculated. The original parameters, derived from first principles, were calculated by Rankine and Hugoniot (Rankine, 1870), describing shocks in ideal gases. The blast wave front velocity and peak dynamic pressures are calculated using the ambient air pressure, peak static overpressure and speed of sound (equations 2.9 and 2.10).

Blast Wave front Velocity = $\boldsymbol{U_s = a_0\sqrt{\frac{6p_s+7p_0}{7p_0}}}$ (2.9)

Peak Dynamic Pressure = $\frac{\mathbf{5p_s^2}}{\mathbf{2(p_s+7p_0)}}$ (2.10)

p_s = peak static overpressure, p_0 = ambient air pressure, a_0 = speed of sound (ambient conditions)

For conventional sized explosives, the peak static overpressure can be calculated using equations 2.11 and 2.12. The constants adopted in these equations have dimensions such that the division n/Z^m, where n is the constant and Z is the scaled distance (equation 2.13), produces a value with the units of pressure. The blast wave scaling laws adopted by Brode use the Hopkinson-Cranz cube root scaling law (equation 2.14) in which two charge masses of a particular diameter (d) and charge size (W) can be related. Two explosive events at given distances (R) and charge size (W) can also be related as shown in equation 2.14. The overpressure time history profile can be calculated using the Friedlander equation 2.15 in relation to the static peak overpressure.

Peak Overpressure (Near Field - > 1MPa):

$$p_s = \frac{6.7}{Z^3} + 1bar \ (p_s > 10bar) \quad (2.11)$$

1 bar = 100kPa

Peak Overpressure (Med to Far Field - 10kPa to 1MPa):

$$p_s = \frac{0.975}{Z} + \frac{1.455}{Z^2} + \frac{5.85}{Z^3} - 0.019bar \ (0.1 < p_s < 10bar) \quad (2.12)$$

Scaled distance = $Z = R/W^{1/3}$ (m/T$^{1/3}$) (2.13)

(R = Distance, W = Charge Size)

Hopkinson-Cranz Blast Wave Scaling Laws: $\frac{d_1}{d_2} = (\frac{W_1}{W_2})^{\frac{1}{3}} \quad \frac{R_1}{R_2} = (\frac{W_1}{W_2})^{\frac{1}{3}}$ (2.14)

Time Related Overpressure (Freidlander) = $p(t) = p_s\left[1 - \frac{t}{t_d}\right] exp\left\{-\frac{bt}{t_d}\right\}$ (kPa) (2.15)

t_d = Positive Phase Duration, b = waveform parameter

The impulse (equation 2.16) is the product of the incident pressure (kPa) and the time (sec) over which the pressure acts. A high impulse indicates a long duration blast load; the damage to buildings and structures, from which, is often much higher than an equivalent conventional explosive with the same peak overpressure.

Positive Phase Impulse = $\boldsymbol{i_s = \int p_s(t)dt}$ (2.16)

The impulse is the integration of a curve (Fig.2.3.1) defined using the Freidlander equation. Instead of the exponential decay that is shown from the Friedlander equation, it is simpler and often adequate to use a triangular decay shape. The impulse for a triangular decay shape is described in equation 2.17.

$$\text{Simplified Impulse} = \boldsymbol{i_s = \frac{1}{2} t_d p_s} \tag{2.17}$$

The effect of the negative phase (suction) pressure is important for analysing building structures to blast loads. Equations 2.18 and 2.19 calculate the peak negative phase overpressure and equivalent negative impulse. The negative phase curve can also be estimated as two triangular shapes (Mays, 2009).

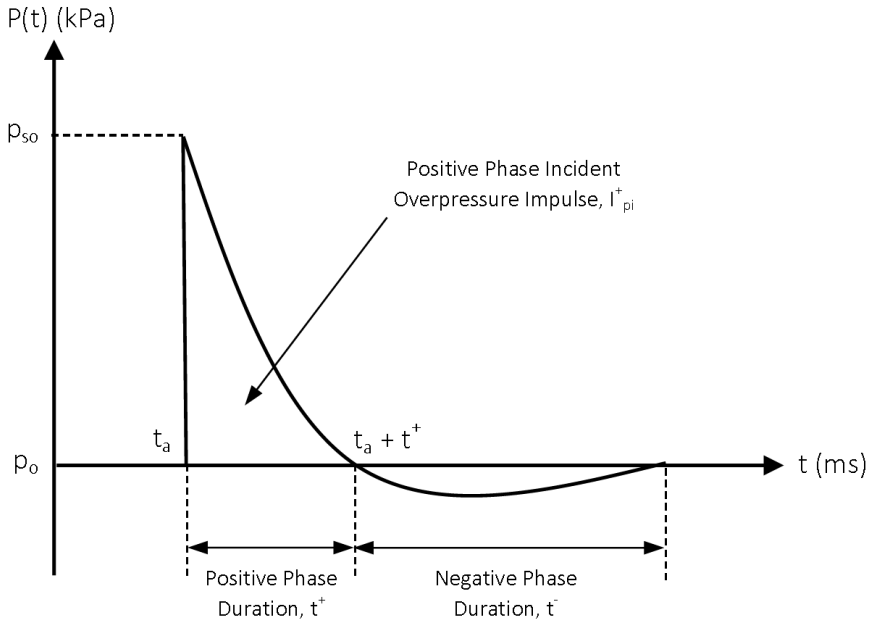

Figure 2.3.1: Typical Blast Wave Profile

$$\text{Peak Negative Overpressure} = \boldsymbol{p^-_{so} = \frac{0.35}{Z}} \tag{2.18}$$

(Z>1.6, p^-_{so}(bar))

$$\text{Negative Phase Impulse } \boldsymbol{i^-_s = i_s \left[1 - \frac{1}{2Z}\right]} \tag{2.19}$$

To take account of blast reflected off the ground for surface and near surface explosions the blast parameters are enhanced by a factor of 1.8, this assumes 20% of the pressure is absorbed into the ground. Some ground surfaces will reflect more pressure than others, such as concrete as opposed to sand. An ideal reflective surface that doesn't absorb any blast energy increases the pressure by a factor of two; this value is conservatively used in the design of structures subject to blast when ground surfaces are unknown.

As the blast wave hits a surface the wave is reflected back and an area of increased pressure above the normal incident pressure develops, this is the reflected pressure. Equation 2.20 calculates the reflected pressure in relation to the peak pressure and ambient density (Rankine, 1870).

$$\text{Reflected Peak Overpressure} = \boldsymbol{p_r = 2p_s\left[\frac{7p_o+4p_s}{7p_o+p_s}\right]} \qquad (2.20)$$

A particular phenomenon that occurs when a blast wave reflects off the ground at angles over 40° is the creation of a Mach stem. After reflection the wave travels closer to the surface and catches up with the original incident wave at a point termed the "Triple Point", forming a Mach stem (Fig.2.3.2). The Mach stem is a near planar blast wave with equal pressure to the incident overpressure travelling parallel to the ground.

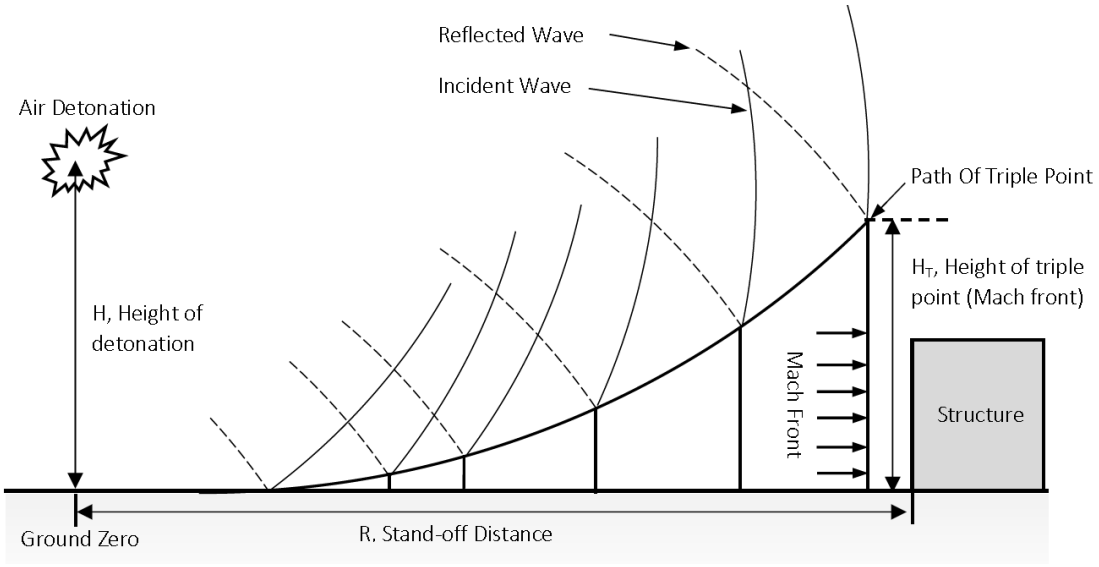

Figure 2.3.2: Visual Representation of Mach Stem Formation

2.3.3 Blast Parameters

Long duration blast loads parameters including time of arrival, positive phase duration and decay of dynamic pressure and overpressure are calculated in accordance with (Kingery, 1984) and (UFC, 2008). The normalised curves shown in figures 2.3.3a and 2.3.3b are used to calculate the pressure decay profiles for a 1000 Tonne explosive event. Figure 2.3.4 is used to calculate the arrival times at given distances and explosive heights for a 1000 Tonne explosive event. Figure 2.3.5 is used to calculate the peak overpressures at given distances for a 1000 Tonne explosive event.

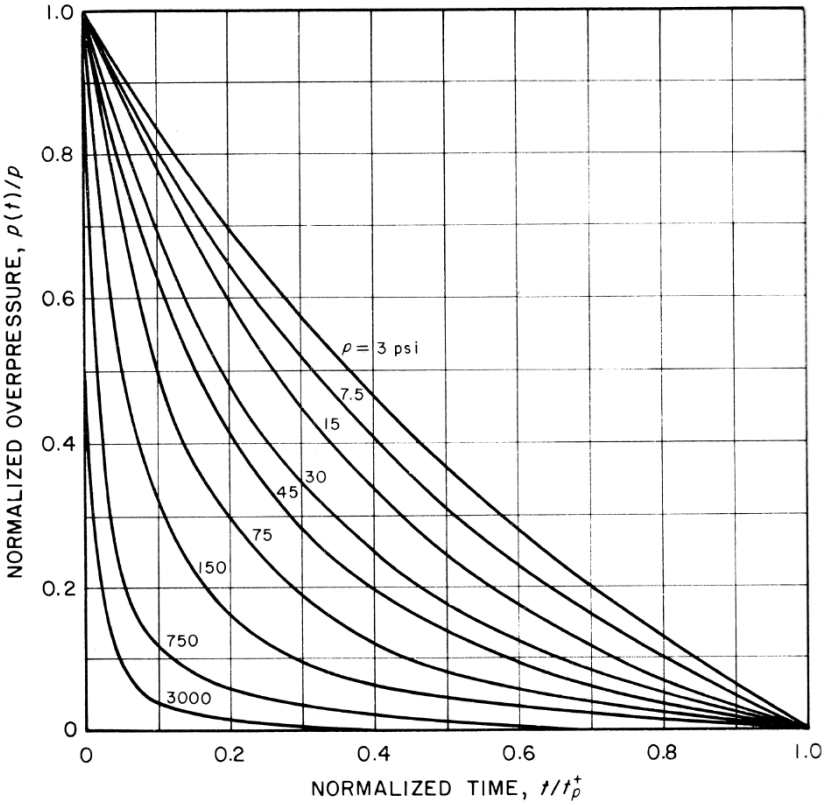

a): Normalised Overpressure

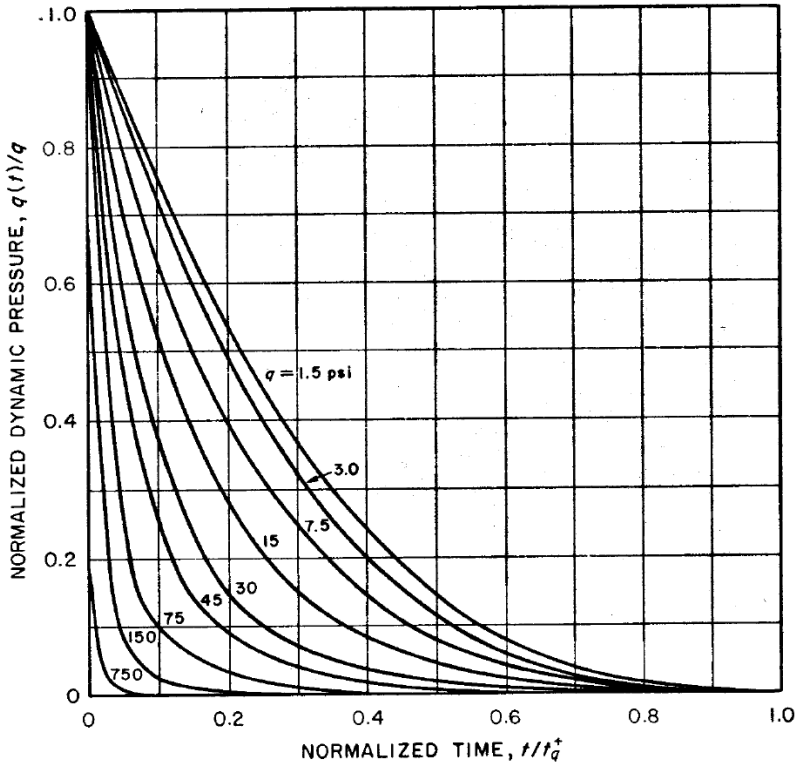

b): Normalised Dynamic Pressure

Figure 2.3.3a & b: Normalised Pressures for a 1000T Explosive Event (Glasstone, 1977)

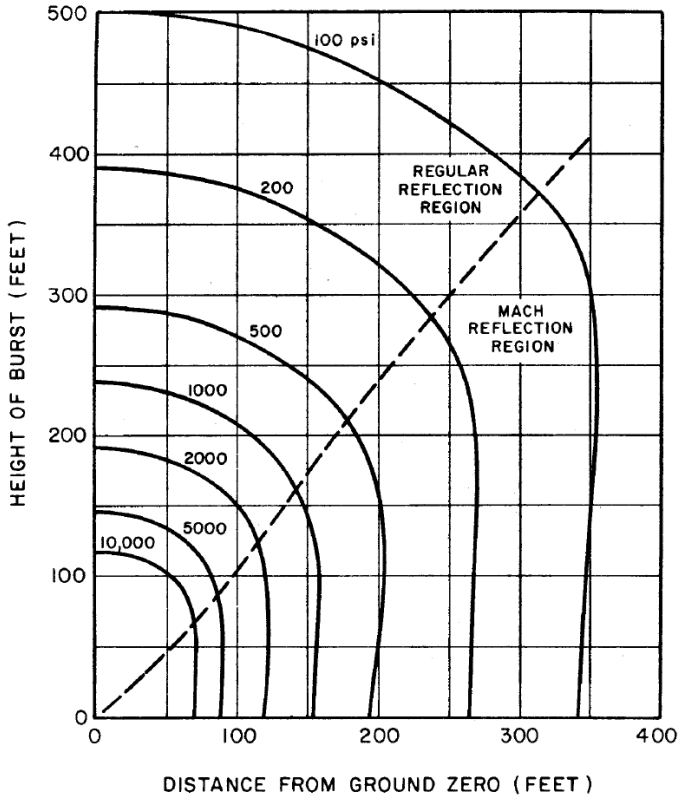

Figure 2.3.4: Arrival Times for a 1000T Explosive Event (Glasstone, 1977)

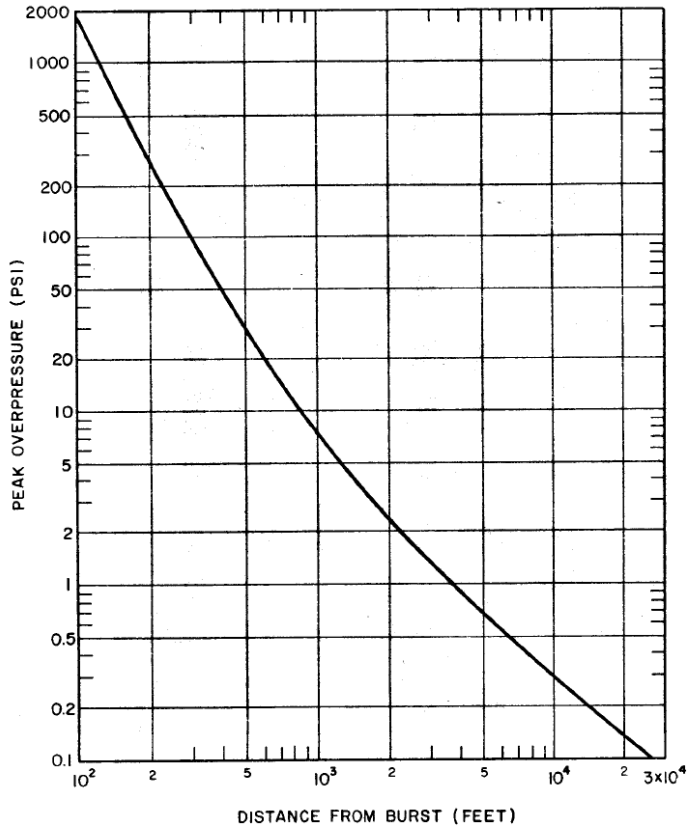

Figure 2.3.5: Peak Overpressure for a 1000T Explosive Event (Glasstone, 1977)

The blast wave scaling law (equation 2.14) is used to convert these parameters for a 1000 Tonne explosive event to other explosive sizes. These blast parameters are used in parallel with calculations regarding the blast wave interaction with structures as detailed in (UFC, 2008) to develop pressure time histories of structures subject to long duration blast loads. Full calculation procedures are detailed in 4.3.

2.4 Structural Response to Blast Loads

This section discusses methods of calculating the response of structures, specifically steel, to blast loading. A whole building response to blast loads is complex, factors such as the strength of the cladding panels, structural members, building use and geometry require consideration. If the cladding panels, (whether glass, masonry or profiled steel sheet) do not fail when the blast is applied the load will be transferred to the main structural elements. If the cladding is removed by the blast the main structural elements will be subject to a reduced blast load, however complex internal pressures will develop within the building. This research project focuses on the response of singular primary structural elements as opposed to whole buildings. A holistic understanding of how whole buildings and structures respond to blast and thermal loads will be gained by applying the conclusions from this research regarding singular elements to other structural configurations and full structures.

The positive phase pressure from a blast wave is often simplified as a triangular impulse (equation 2.21, Fig.2.4.1) (Ngo, 2007). The intensity and duration of the impulse determines the structural response. The ratio of impulse duration (t_d) to the natural period of a structure (T) determines if a structural response regime is quasi static, dynamic or impulsive (eqns. 2.22 to 2.24). It will in turn govern the subsequent methods adopted for structural design and analysis (Mays, 2009). If a structural response is either impulsive or quasi-static the solution can be determined using energy balance methods (2.4.2), however if the structural response is dynamic, complex computational analysis methods are required. Energy balance methods can only be used to predict maximum deflections and stresses. If a response is quasi static (often for long duration blast loads) the displacement of a structure can be simplified as function of load (F) and stiffness (K). A conservative assumption is that the load can be applied as constant. For an impulsive response the displacement is a function of impulse, stiffness and mass.

$$\text{Impulse} = \boldsymbol{F(t)} = \boldsymbol{F}(\mathbf{1} - \frac{\boldsymbol{t}}{\boldsymbol{t_d}}) \tag{2.21}$$

($F(t)$ = Time Varying Force)

$$\text{Impulsive: } t_d/T < 0.1 \tag{2.22}$$

Dynamic: 0.1 < t_d/T < 10 (2.23)

Quasi-Static: t_d/T > 10 (2.24)

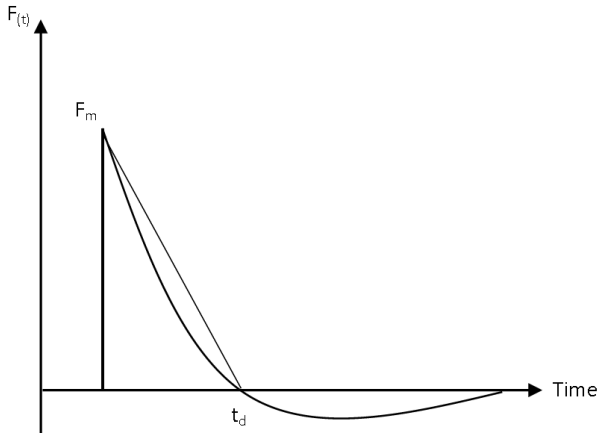

Figure 2.4.1: Triangulated Positive Impulse

2.4.1 SDOF Method

The most widely adopted and simplest method to analyse a structure under blast loading is the Single Degree of Freedom (SDOF) method (Fig.2.4.2). The structure, whether it is a beam, column, plate or frame is simplified as a lumped mass system from which the equation of motion is used to relate the mass (M), damping (C), stiffness (k), and load ($F(t)$) to the acceleration ($\ddot{x}$), speed ($\dot{x}$) and displacement (x), (equation 2.25).

$$\boldsymbol{M\ddot{x} + C\dot{x} + kx = F(t) = F\left(1 - \frac{t}{t_d}\right)} \quad (2.25)$$

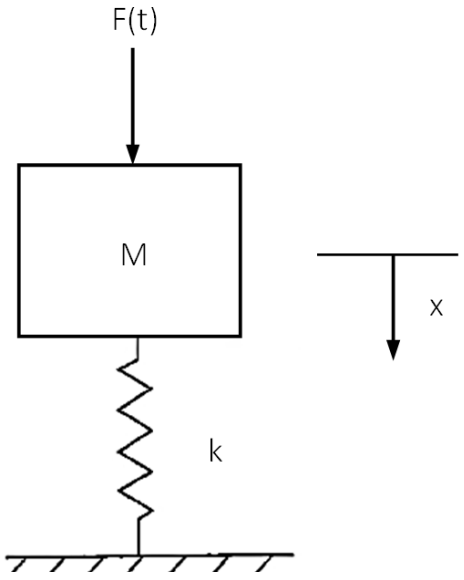

Figure 2.4.2: SDOF System

To calculate peak deflections the damping parameter is removed as it has a minimal effect on the peak response. When the velocity of the structure is zero the structure has reached its maximum displacement, therefore equation 2.25 can be rearranged to represent the dynamic deflection (equation 2.26). The natural frequency can then be calculated using equation 2.27

$$\boldsymbol{x(t) = \frac{F}{k}(1 - \cos \omega t) + \frac{F}{kt_d}} \quad (2.26)$$

$$\text{Natural Frequency} = \boldsymbol{\omega = \sqrt{k/M}} \quad (2.27)$$

In order to relate the properties of a structural system to a dynamic analysis of the system a series of transformation factors are adopted. The factors shown in equations 2.28 to 2.31 are for a simply supported beam with a uniformly distributed load. Factors for other structural configurations are detailed in (Biggs, 1964).

$$\text{Mass Factor: } \boldsymbol{K_M = \frac{M_E}{M} = 0.5} \quad (2.28)$$

$$\text{Load Factor: } \boldsymbol{K_L = \frac{F_E}{F} = 0.64} \quad (2.29)$$

$$\text{Stiffness Factor: } \boldsymbol{K_S = \frac{K_E}{K} = 0.64} \quad (2.30)$$

$$\text{Load-mass Factor: } \boldsymbol{K_{lm} = \frac{K_M}{K_L}} \quad (2.31)$$

M_E = Equivalent Structural Mass, F_E = Equivalent Structural Force, K_E = Equivalent Structural Stiffness

Using these factors the natural period of a structure can be calculated:

$$\boldsymbol{T = \frac{2\pi}{\omega_u} = 2\pi\sqrt{\frac{M_E}{K_E}}} \quad (2.32)$$

2.4.2 Energy Balance Method

For structural responses in the quasi-static region, the energy balance solution uses the relation of work done by the structure (equation 2.33) to strain energy (equation 2.34) in order to determine the maximum deflection of the structural response (Hetherington, 1994). This method is appropriate for simple one directional stress and strain relationships to calculate maximum deflections (x_{max}).

$$\text{Work Done: } = \boldsymbol{Fx_{max}} \quad (2.33)$$

$$\text{Strain Energy: } \boldsymbol{U = \frac{1}{2}Kx_{max}^2} \quad (2.34)$$

Rearranging these equations a solution calculating the maximum dynamic displacement using the equivalent static displacement (x_{st}) for the same force is formed. Equation 2.35 is termed the Dynamic Load Factor (DLF) which relates dynamic deflection to static deflection.

$$\frac{x_{max}}{F/k} = \frac{x_{max}}{x_{st}} \tag{2.35}$$

If the response is impulsive the momentum transferred from the blast to the structure imparts kinetic energy which is converted into strain energy and the structure acquires a velocity (eqn. 2.36).

$$\text{Kinetic Energy: } KE = \frac{1}{2}M\dot{x}_0^2 = \frac{I^2}{2M} \tag{2.36}$$

$\dot{x}_0$ =Initial Velocity, I= Impulse, M= Structural Mass

Equating the kinetic energy equation (2.36) and the strain energy equation (eqn. 2.34) a solution can be formed for the maximum deflection:

$$\frac{x_{max}}{F/k} = \frac{x_{max}}{x_{st}} = \frac{1}{2}\omega t_d \tag{2.37}$$

x_{max}= Maximum Dynamic Displacement

2.4.3 Plastic Analysis

When a structure responds plastically to a blast load it deflects beyond its elastic limit and permanently deforms. Finite Element Analysis (FEA) packages can be used to accurately analyse structures for plastic deformation but have high computational running times. A simple approach uses the Rayleigh-Ritz method in order to calculate the maximum displacement for impulsively loaded structures assuming a rigid-plastic stress response (Mays, 2009).

$$\frac{x_{max}}{L} = \frac{i_r^2 L}{4\sigma_y \rho d^3} \tag{2.38}$$

i_r = Reflected Impulse, L = Length, ρ = Density, σ_y = Yield Strength, d= depth

Given the higher non-linear and quasi-static nature of the loading regimes investigated in this research FEA will be used to accurately analyse structural response and deformations.

2.4.4 Resistance Function

Resistance functions are described as “the measure of resistance during response regimes” (Yandzio, 1999). The resistance R_m equates to the maximum load applied to a structure at the point

of failure. The definition of failure varies for different structural systems and materials. For steel structures R_m could represent the idealised fully plastic failure (strain increase with no stress increase). The resistance function would therefore have three gradients representing the elastic, elasto-plastic and fully plastic ranges of structural response (Fig 2.4.3).

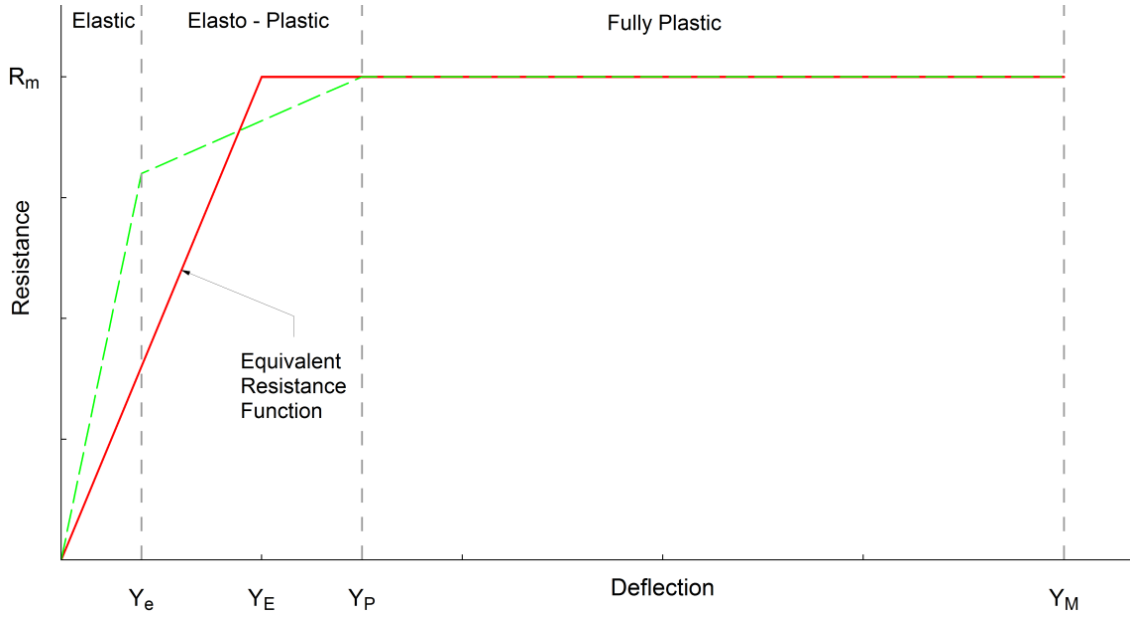

Figure 2.4.3: Resistance Function Tri and Bi-Linear Structural Response

In order to simplify this further the tri-linear (green) resistance function can be simplified to a bilinear (red - elastic-plastic) response (Yandzio, 1999). Other structural failure definitions can include lateral torsional buckling, cracking of concrete and fracture of glass or masonry. Each failure mechanism has a different resistance function. For the purposes of this research, failure is defined as irrecoverable fully plastic failure for individual elements.

2.4.5 Material Response

The behaviour of materials subject to blast loads is dependent on material strength and ductility. The strength of materials subject to blast loading can be magnified due to the increased material strain rate during blast loading. A simple method used to quantify the increase in strength due to the high strain rates (>50ε^{s-1}) is the use of Dynamic Increase Factors (DIF). They are used to modify the yield and ultimate tensile strengths of a material under blast loads. The values and application of the DIFs for structural steel are shown in equations 2.39, 2.40 and table 2.3 (Yandzio, 1999).

$$\boldsymbol{DIF} = \frac{\boldsymbol{\sigma_{dyn}}}{\boldsymbol{\sigma_y}} \tag{2.39}$$

σ_{dyn} = Dynamic Yield Stress, σ_y = Static Yield Stress

Dynamic Design Yield Stress (Bending):

$$\boldsymbol{\sigma_{y,des} = a\,(DIF)\,\sigma_y} \tag{2.40}$$

a = 1.1 for S275 and S355

Table 2.3: Dynamic Increase Factors for Structural Steel (Yandzio, 1999)

Time to Reach Yield Stress	Dynamic Increase Factors for Yield Stress	Dynamic Increase Factors for Ultimate Tensile Strength
>1 sec	1	1
100 msec	1.1	1.05
10 msec	1.6	1.05
1 msec	1.9	1.05

As strain rates increase above $1\varepsilon^{s-1}$ (typically $>50\varepsilon^{s-1}$) the yield strength of steel increases, there is also a relatively low increase in the ultimate tensile strength and no effect on the Young's Modulus. Figs.2.4.4 and 2.4.5 show the effect of strain rate on the relationship of stress vs. strain for steel. The initial gradient (Young's modulus) is negligibly affected; however post yield the stress states vary greatly with higher strain rates.

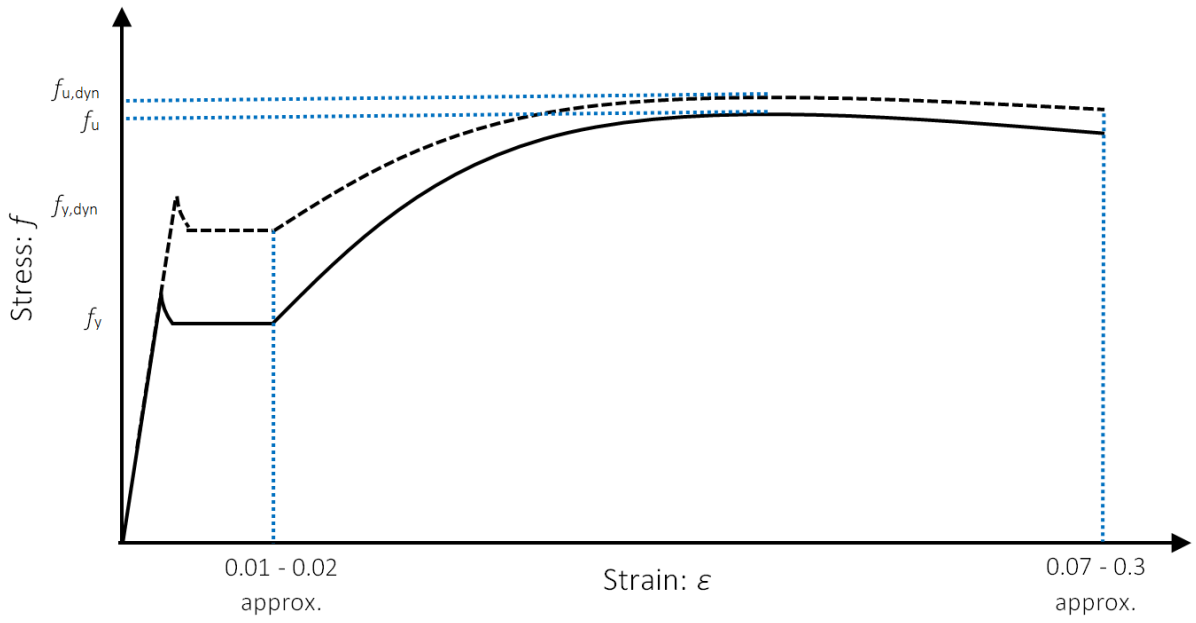

Figure 2.4.4: Stress/Strain Curve with Rapid Strain Rate

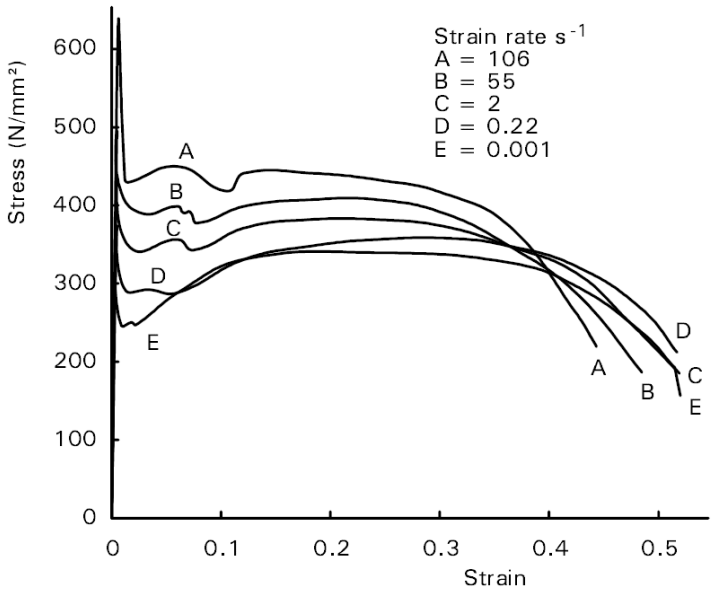

Figure 2.4.5: Effects of Strain Rate on Behaviour of Mild Steel (Burgan, 2001)

The relationship between dynamic increase factors and strain rates is shown in Fig.2.4.6; as the strain rate increases, so does the dynamic increase factor. The Cowper-Symonds relationship is used to describe this relationship (equation 2.41).

$$\boldsymbol{\sigma_d/\sigma} \;=\; \boldsymbol{DIF} \;=\; \mathbf{1} \;+\; (\dot{\boldsymbol{\varepsilon}}\,/\boldsymbol{D})^{\mathbf{1/q}} \tag{2.41}$$

D = 40, q = 5, $\dot{\varepsilon}$ = uniaxial plastic strain rate (Burgan, 2001)

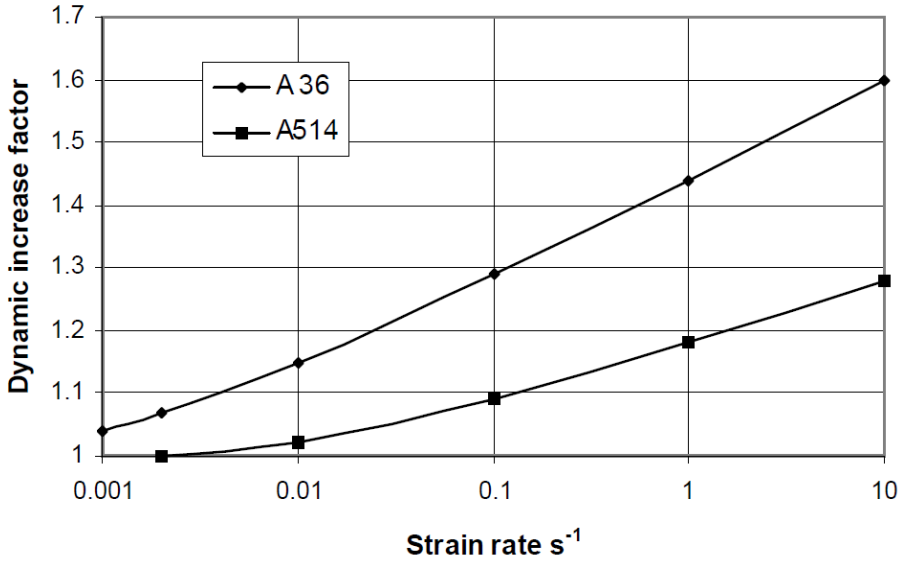

Figure 2.4.6: Dynamic Increase Factor for Yield Strength of Mild and High Strength Steel vs Strain Rate (Burgan, 2001)

2.4.6 Steel Column Response to Blast and Compressive (Axial) Loads

The response of steel columns under short duration blast loads and compressive loads is investigated in (Nassr, 2013). SDOF and FEA parametric studies were performed and results compared to full scale column tests. It was found that columns with a higher percentage of applied axial load to the axial load capacity required less peak pressure for the column to fail; however the level of impulse required for column failure remained relatively unchanged with increasing axial load.

2.4.7 Long Duration Blast Load Response

Long duration blast loads can be very destructive due to a large relative impulse. Prior investigations into the effects of long duration blast loads on structures have been undertaken by retrospective inspection of the damage to the structures at the Buncefield disaster in (Atkinson, 2011a) and (Atkinson, 2011b). These papers showed that significant damage was observed on a warehouse structure at long distance from the explosive centre. Large vents were created when the lightweight wind posts on the front face of the warehouse were overmatched allowing the inward passage of pressure. This allowed a build- up of internal pressure on the opposite wall (to the blast onset direction) subsequently damaging the cladding by forcing it out (Fig.2.4.7). The damage to this warehouse and other structures at large distances confirmed the theory that long duration pressures were present at the Buncefield refinery disaster.

Figure 2.4.7: Outward Displacement of Cladding on Back Wall of Warehouse (Atkinson, 2011a)

(Clubley, 2014) investigated the response of cylindrical shell structures to long duration blast loading. Experimental trials were undertaken at the Air Blast Tunnel (ABT), M.O.D Shoeburyness, and computational analysis performed using the FEA program, LUSAS. Local buckling and crushing

failures were observed in both trials and computational analysis (Fig.2.4.8). Analysis undertaken after the trials using accurate pressure profiles recorded adjacent to the cylinders gave a good correlation of the actual cylinders deformations.

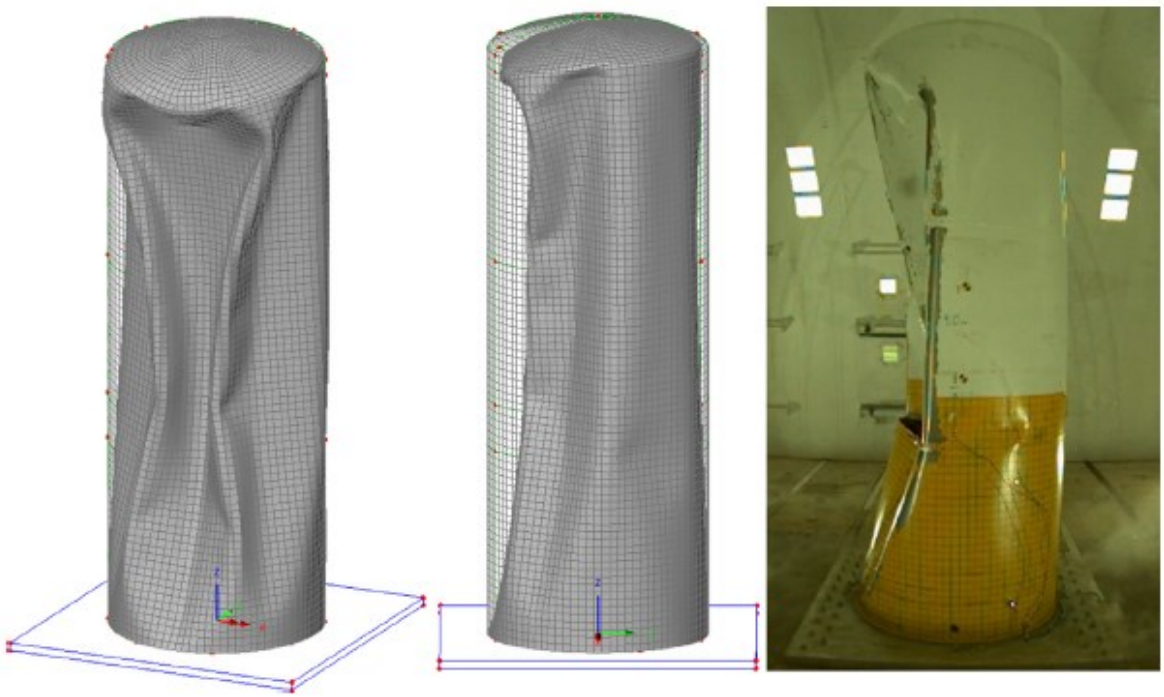

Figure 2.4.8: Damage to Cylindrical Thin Walled Shells (Clubley, 2014)

The effect of long duration blast loads on elastic-plastic and rigid-plastic cantilever columns and the influence of drag load on columns was investigated in (van Netten, 1997). When a blast load reaches a column the difference of the high reflected pressure on front face and ambient pressure on back face causes an initial acceleration in the direction of the blast. If the positive phase duration (t_d) equals the time for the blast wave to pass the column the structural response is dominated by the initial reflected pressure loading mechanism (diffraction phase). If the positive phase duration is longer than the time to pass the column, a drag type loading is experienced (dynamic pressure dominant). Fig.2.4.9 (reproduced from (van Netten, 1997)) shows the flow of high pressure around a circular column. As a cantilever column deforms the front face is no longer at 90^o to the blast direction, this reduces the drag coefficients and subsequent applied pressure. The region of high pressure will have a reducing effect as the column continues to deform. Fig.2.4.10 shows the deflection of one a cantilever column after it is subject to a long duration blast load.

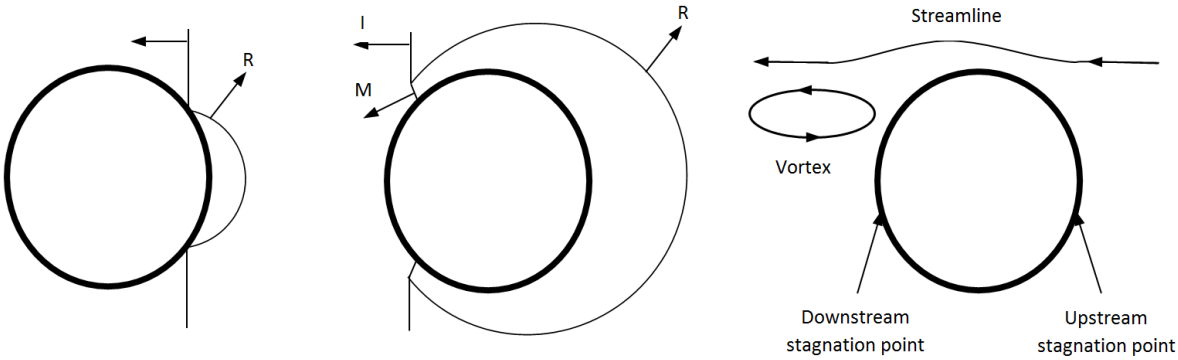

Figure 2.4.9: Pressure Flow around a Circular Column

Figure 2.4.10: Deformation of Cantilever Column (van Netten, 1997).

Dynamic pressures variances surrounding structural sections subject to long duration blast loads was investigated in (Clubley, 2013). Testing on shielded and unshielded square and circular hollow structural sections (SHS and CHS) inside the Large Blast Thermal Simulator (LBTS), White Sands, New Mexico, was performed to record drag pressures around the sections. The flow around circular sections was found to be laminar in nature, producing a complex series of drag coefficients and pressures. When a square section was rotated at 45^{o} compared to 0^{o} to the blast a 50% increase in the drag coefficients was observed. Forces on unshielded sections, compared to shielded, were also found to be lower due to the absence of flow stagnation in front of the section.

The damage criteria for structures affected by drag loading is described in Table 2.4. The three levels of damage criteria described are “Severe”, “Moderate” and “Light”. In relation to steel frame structures the severe criterion is described as “Severe distortion or collapse of frame”, the

moderate criterion relates to some minor distortions of frame and the light criterion assumes no primary frame damage, but damage to windows, doors and partitions.

Table 2.4: Damage Criteria for Structures under Drag Loading

Structure Description	Description of Damage		
	Severe	Moderate	Light
Light steel frame industrial building, single storey; low strength walls which fail quickly. 5 ton crane capacity.	Severe distortion or collapse of frame	Minor to major distortion of frame; cranes if any not operable until repairs made	Windows and doors blown in, light siding ripped off
Heavy steel frame industrial building, single storey; lightweight, low strength walls which fail quickly. 25 to 50 ton crane capacity	Severe distortion or collapse of frame	Some distortion to frame; cranes not operable until repairs made	Windows and doors blown in, light siding ripped off
Heavy steel frame industrial building, single storey; lightweight, low strength walls which fail quickly. 60 to 100 ton crane capacity	Severe distortion or collapse of frame	Some distortion to frame; cranes not operable until repairs made	Windows and doors blown in, light siding ripped off
Multi-storey steel frame office type building, 3 to 10 storeys; lightweight, low strength walls which fail quickly, earthquake resistant construction	Severe distortion, incipient collapse	Frame distorted moderately, interior partitions blown down	Windows and doors blown in, light siding ripped off, interior partitions cracked
Multi-storey steel frame office type building, 3 to 10 storeys; lightweight, low strength walls which fail quickly, non-earthquake resistant construction	Severe distortion, incipient collapse	Frame distorted moderately, interior partitions blown down	Windows and doors blown in, light siding ripped off, interior partitions cracked

2.5 Structural Response to Fire and Thermal Loading

The behaviour of structures under long term thermal loads from fires has been well documented and researched for several years; from full scale fire tests (BRE, Cardington (Kirby, 1998)), to the effects of fires on concrete slabs (membrane action, (Gillie, 2004)) and response of individual steel members. This section discusses structural and material response to thermal loads.

2.5.1 Structural Design to Fire Loading

Most structural degradation from heat occurs when a fire burns inside or adjacent to a building for a long period of time. The load carrying ability of the structure is reduced as the temperature of the material rises. In order to quantify the temperatures experienced from such fires equation 2.42 describes a standard internal fire (time) curve, as detailed in BS EN 1991-1-2-2002 (BSi, 2013).

$$\text{Gas Temperature in Fire Compartment} = \boldsymbol{\theta_g = 20 + 345\log_{10}(8t + 1)} \qquad (2.42)$$

BS EN 1993-1-2-2005 (BSi, 2005c) describes reduction factors that can be applied to the steel material parameter at elevated temperatures (eqn. 2.43 to 2.45). These factors are applied to the equivalent properties of the steel at ambient temperatures.

Fig.2.5.1 and Table 2.5 show how the reduction factors relate to steel properties at different temperatures. The proportional limit factor relates to the elastic limit of the structure. Fig 2.5.2 shows an idealised stress vs. strain curve for mild steel with reduced properties from fire loading: an elastic response to the proportional limit ($f_{p,\theta}$) is followed by an elasto-plastic response of increasing stress and strain until the effective yield strength ($f_{y,\theta}$). A perfectly plastic response is shown after the yield strength until the limiting strain ($\varepsilon_{t,,\theta}$) for the yield strength, after which the stress decreases with increasing strain. Further research into the effects of high temperatures on the properties of steel is detailed in 2.5.6.

Effective Yield Strength Factor: $\boldsymbol{k_{y,\theta} = f_{y,\theta}/f_y}$ (2.43)

Proportional Limit Factor: $\boldsymbol{k_{p,\theta} = f_{p,\theta}/f_y}$ (2.44)

Slope of Equivalent: $\boldsymbol{k_{E,\theta} = E_{a,\theta}/E_a}$ (2.45)

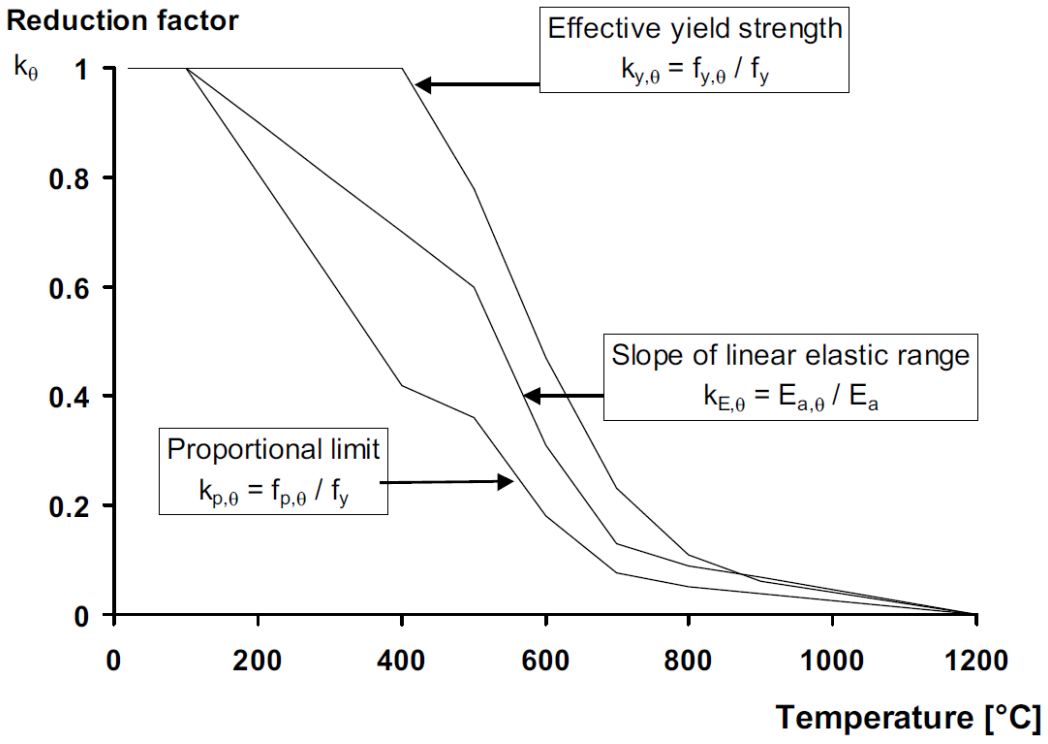

Figure 2.5.1: Reduction Factors vs. Temperature (BSi, 2005c)

Table 2.5: Steel Reduction Factors at Varying Temperatures (BSi, 2005c)

Steel Temperature (°C)	Reduction Factors Relative to Value of f_y or E_a at Ambient Temperature		
	Reduction Factor (relative to f_y) for effective yield strength	Reduction factor (relative to f_y) for proportional limit	Reduction factor (relative to E_a) for the slope of the linear elastic distance
20°C	1.0	1.0	1.0
100°C	1.0	1.0	1.0
200°C	1.0	0.807	0.90
300°C	1.0	0.613	0.80
400°C	1.0	0.42	0.70
500°C	0.78	0.36	0.60
600°C	0.47	0.18	0.31
700°C	0.23	0.075	0.13
800°C	0.11	0.05	0.09
900°C	0.06	0.0375	0.0675
1000°C	0.04	0.025	0.045
1100°C	0.02	0.0125	0.0225
1200°C	0.0	0.0	0.0

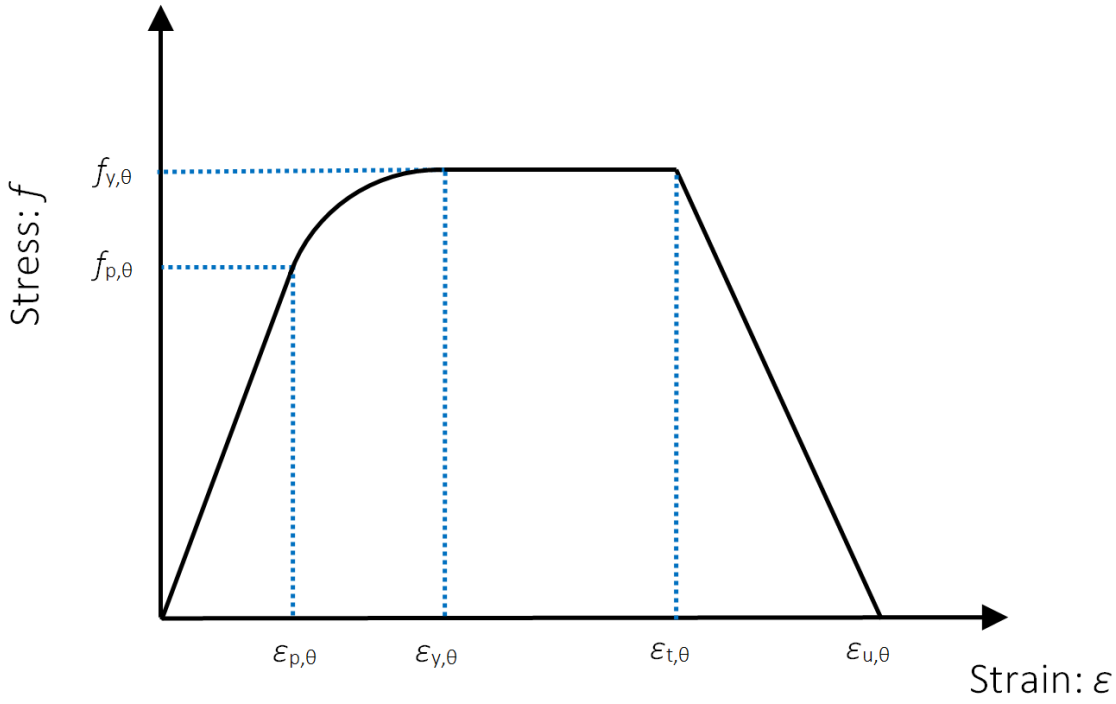

Figure 2.5.2: Stress/Strain Graph for Reduced Steel Properties (BSi, 2005c)

$f_{y,\theta}$ = Effective Yield Strength, $f_{p,\theta}$ = Proportional Limit, $\varepsilon_{p,\theta}$ = Strain at Proportional Limit, $\varepsilon_{y,\theta}$ = Yield Strain, $\varepsilon_{t,\theta}$ = Limiting Strain for Yield Strength, $\varepsilon_{u,\theta}$ = Ultimate Strain,

2.5.2 Physical Effects on Structures from Thermal Loading

The following section discusses behaviour of structures when subject to thermal loading including expansion, bowing and material degradation.

2.5.2.1 Thermal Expansion

As a structural element is heated the material will expand, if the element is restrained at both ends against longitudinal displacement (Fig.2.5.3) high compressive stresses will develop. No thermal strain is developed from the thermal expansion; therefore any strain is mechanical. If the steel element is heated sufficiently the Young's Modulus will decrease and the structure will become unstable. Longitudinally unrestrained elements (Fig.2.5.4) will experience thermal expansion strains when heated (Usmani, 2001).

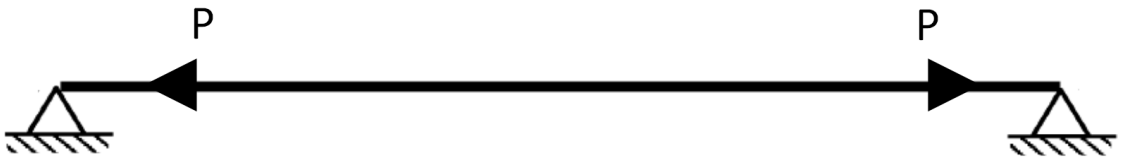

Figure 2.5.3: Axially Restrained Beam with Uniform Temperature Rise

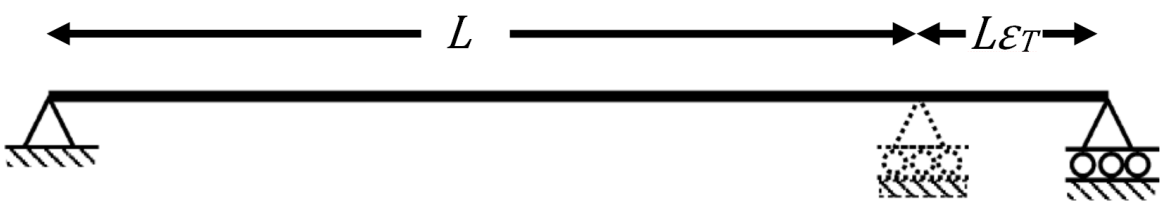

Figure 2.5.4: Axially Un-Restrained Beam with Uniform Temperature Rise

The total strain experienced by a structure under thermal loading is a combination of mechanical and thermal strain. For axially restrained structures the structural stresses depend purely on the mechanical strains. Thermal strains are a product of thermal expansion and the curvature created by a potential temperature differential across a structural section. Equation 2.46 and Fig.2.5.3 show that with no thermal strain from a uniform increase in temperature (ΔT), the stress and longitudinal restraint force are functions of the mechanical strain only (in axially restrained structures).

$$\boldsymbol{P = AE\varepsilon_m = -AE\varepsilon_T = AE\alpha\Delta T} \tag{2.46}$$

If a column is stocky an increasing temperature will cause axial stresses to increase until the yield stress of the material is reached (equation 2.47). Slender elements will buckle before yielding as the Euler buckling load and critical buckling temperature is reached (equations 2.48 and 2.49). This

approach can only be used for simple axially loaded sections. P-Delta effects (secondary moments) can occur due to the increasing out of plane deflection and axial force; if these are prominent a more complex analysis is required. 2.5.4 and 2.5.5 details the effect of axial restraint and the post buckling analysis of steel structures under thermal loads.

$$\text{Yield Temperature: } \Delta \boldsymbol{T_y} = \frac{\boldsymbol{\sigma_y}}{\boldsymbol{E\alpha}} \tag{2.47}$$

α = Coefficient of Thermal Expansion

$$\text{Euler Buckling Load: } \boldsymbol{P_{cr}} = \frac{\boldsymbol{\pi^2 EI}}{\boldsymbol{l^2}} \tag{2.48}$$

Equated to the longitudinal restraint force P gives the critical buckling temperature:

$$\Delta \boldsymbol{T_{cr}} = \frac{\boldsymbol{\pi^2}}{\boldsymbol{\alpha \lambda^2}} \tag{2.49}$$

(λ = Slenderness ratio)

Structural restraints are rarely purely rigid, a column in a building can be restrained axially at each end but the restraints are not infinite and some movement would be allowed. Therefore, it is useful to take the restraint stiffness into account when calculating the stresses, buckling loads and temperatures within a structure. Equations 2.48 and 2.49 can be rearranged to take into account a connection spring stiffness k_t, giving the critical buckling temperature as:

$$\Delta \boldsymbol{T_{cr}} = \frac{\boldsymbol{\pi^2}}{\boldsymbol{\alpha \lambda}} \left(\mathbf{1} + \frac{\boldsymbol{EA}}{\boldsymbol{k_t L}}\right) \tag{2.50}$$

E = Young's Modulus, A = Cross-Sectional Area, k_t = Spring Stiffness, L = Length

2.5.2.2 Thermal Bowing

If a structural element is heated from one side only; which is often the case for internal fires and composite beams, a thermal gradient will be present across the structural section depth. This may lead to bowing of the structure. When a structural element bows, one side is in compression whilst the opposing side is in tension. If the element is axially restrained this tension can potentially cancel the compression that has developed in the element from thermal expansion against the supports. The thermal gradient ($T_{,y}$) across the depth of a section is described using equation 2.51.

$$\boldsymbol{T_{,y}} = \left(\boldsymbol{T_2} - \boldsymbol{T_1}\right) / \boldsymbol{d} \tag{2.51}$$

If an element bows under a thermal gradient the support reaction will be tensile (if pinned); however the support reaction from a uniformly heated element is compressive. If an element has fixity at the supports a moment is induced which can reduce the curvature in the element from the thermal gradient. It may be possible for the element to remain straight but with a constant moment along its length. The support conditions may also change during a fire so that a restraint which was initially fixed could degrade to act as a pinned. This would significantly alter the structural behaviour of the element.

2.5.3 Effects of High Temperatures on Steel

(Cooke, 1988) describes changes to the mechanical properties of structural steels at elevated temperatures including thermal expansion, phase transformation, elastic modulus, Poisson's ratio and stress / strain relationships. Constant values of 0.3 for the Poisson's ratio and 12 x 10^{-6}/^{o}C for the coefficient of thermal expansion were found to be suitable.Fig.2.5.5 shows the effect of temperature on the stress vs. strain relationship of structural steel (1000 lb/in^2 = 6.895MPa, in/in = ε).

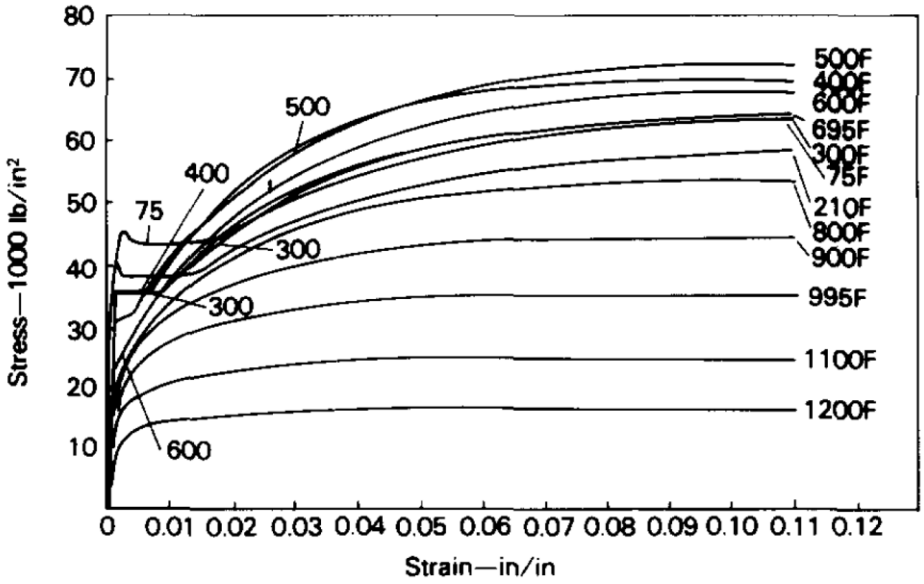

Figure 2.5.5: Stress - Strain Curves for Steel at Elevated Temperatures (Cooke, 1988)

The phenomena of phase transformation occurs when steel material composition changes from pearlite to austenite accompanied by the atomic structure changing from body centred cubic to face centred cubic. Structurally, phase transformation refers to a sudden shrinkage in the steel structure as it is heated and expands, before it expands again. This is more likely to occur in lightly stressed than highly stressed structures, as highly stressed structures may experience local buckling or reach yield stress before reaching the phase transformation temperature (approximately 800^{o}C).

The HSE report (Burgan, 2001) describes how elevated temperatures effect and relate to high strains with reference to EC3-1.2 (BSi, 2005c) and BS5950-8 (BSi, 2003). Fig.2.5.6 shows strength reduction factors at elevated temperatures at three strain values of 0.5%, 1.5% and 2%. At low strain the strength reduction factors are lower than for higher stain rates at equivalent temperatures. The mechanical properties of structural steel during and after heating are detailed in (Outinen, 2002). After heating S355 grade steel to 950°C it was found that the Young's Modulus returned to nominal values once cooled; however the yield and ultimate strengths were lower than the initial strengths steel before heating (Fig 2.5.7). It was also found that the high strength of cold formed sections remained constant at high temperatures until approximately 600°C.

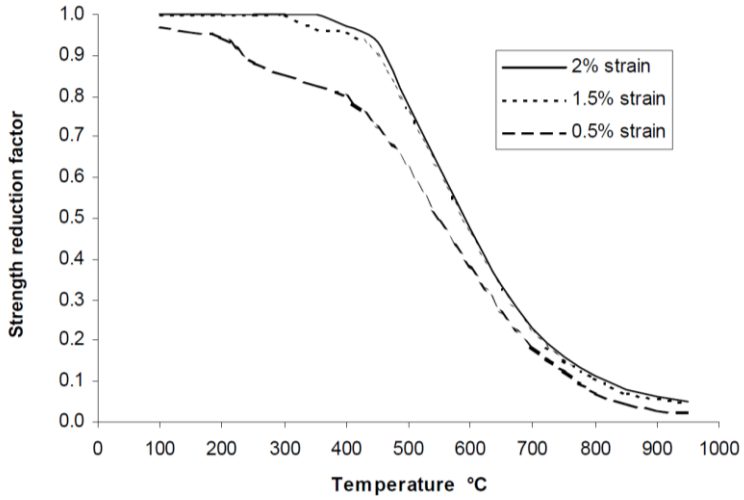

Figure 2.5.6: Strength Reduction Factor with Increasing Temperature at Various Strains (Burgan, 2001)

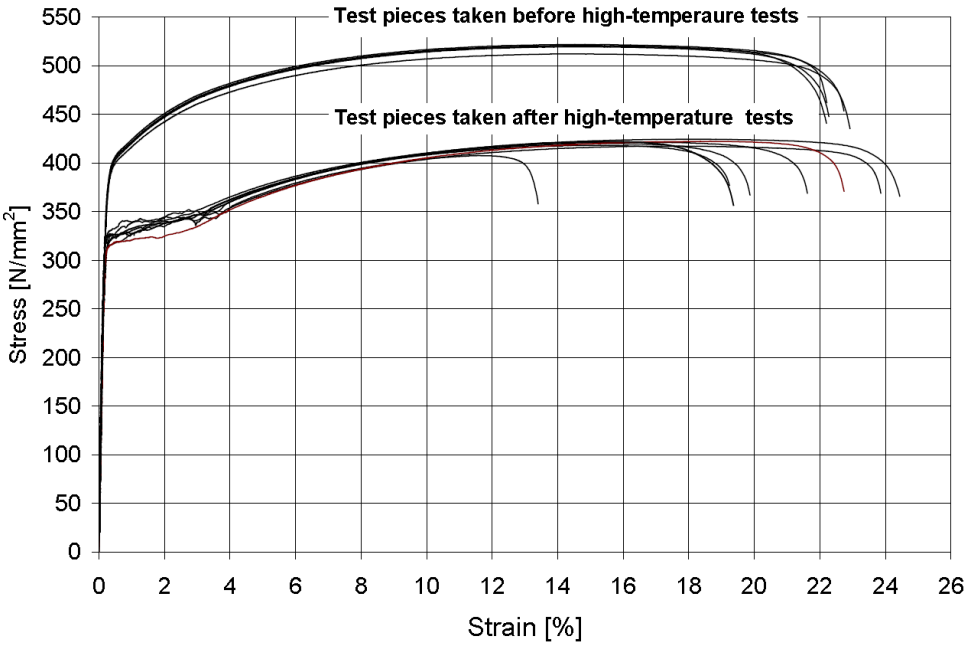

Figure 2.5.7: Tensile Test of S350 Steel Before and After High Temperatures (Outinen, 2002)

2.5.4 Axial Restraint on Steel Beam-Column Behaviour

The behaviour of steel beam-columns under thermal loads (with significant axial force) is documented in (Kodur, 2009). It was found that the behaviour depends on several factors, dominantly the level of end axial restraint. Axial restraints can be detrimental to the fire resistance of steel beam-column structures as expansion induces a compressive axial stress which in turn increases the lateral deflection and P-Delta moment. Fig.2.5.8 shows the effect of increasing fire exposure time to the induced axial force with varying axial restraint (α = 1: high, α = 0: low). With a higher axial restraint the compressive axial force increases throughout the initial stages of a fire. When phase transformation is reached the compressive axial force in the column is released and the relative effect of the axial restraint level is negligible.

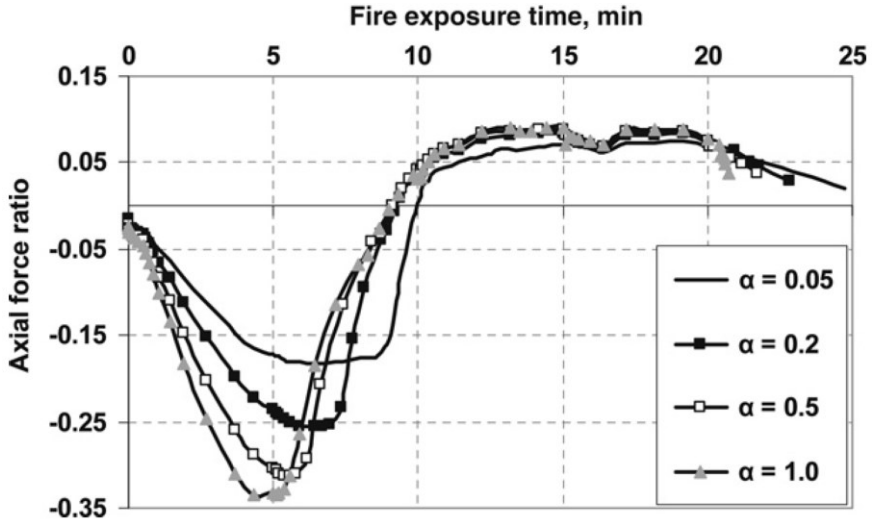

Figure 2.5.8:Effect of Axial Restraint on Fire Induced Axial Force (Kodur, 2009)

2.5.5 Steel Column Post Buckling Response

The buckling response of axially restrained steel columns to fire was investigated in (Shepherd, 2011). Using the FEA program VULCAN, steel columns under fire loads were modelled with an increasing axial load representing the increasing axial restraint from a surrounding cooler structure. The post buckling behaviour of the steel column was modelled; showing column re-stabilisation and snap back behaviour phenomenon. Columns with high axial restraint reached buckling loads sooner than with low restraint. It was also observed that all columns pass through the same point (50^{o}C) where initial shortening is overcome (Fig.2.5.9). After buckling the column loses stiffness and is effectively hanging. Over the course of a typical fire the temperature will eventually decrease as the fire dies out during which the axial force in a steel column will increase as the material properties are restored (snap back).

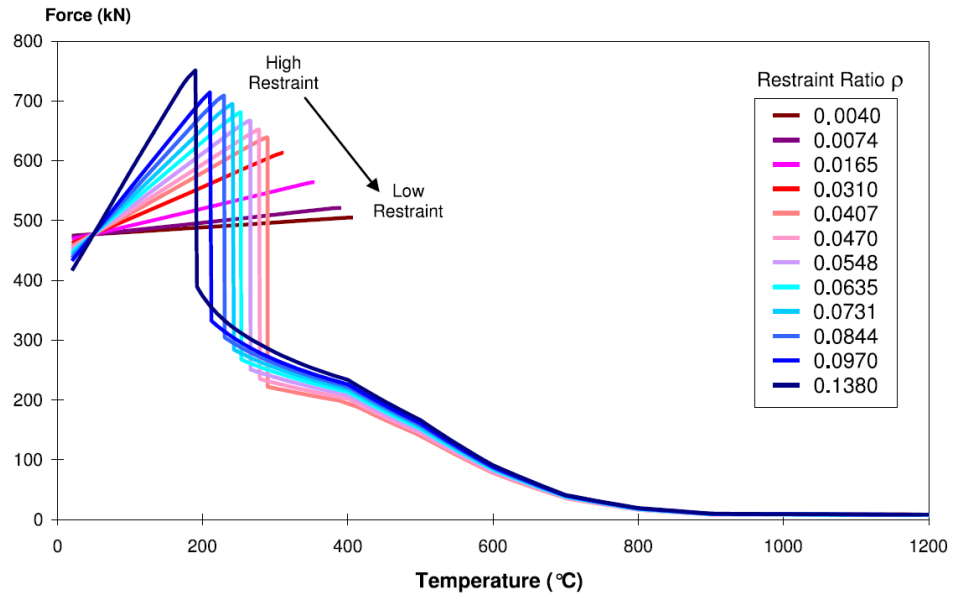

Figure 2.5.9: Axial Force in Columns Vs Temp at Varying Restraints (Shepherd, 2011)

2.5.6 High Strain Rates at High Temperatures

Given the high strain rates (50 – 100ε^{s-1}) and high temperatures (500 - 1000°c) investigated in this research project it is important to gain a full understanding of how steel behaves under these combined load regimes. (Laasraoui, 1991) investigated the stresses in steels at high strain rates and temperatures with reference to hot rolling of steel sheet. Figs.2.5.10a and 2.5.10b show the stress vs. strain profiles at various temperatures under two strain rates: (a) = 0.2 s^{-1}, (b) =2 s^{-1}. The shape of the profiles between the two strain rates is similar; with the higher strain rate reaching a stress 210MPa, compared to 180MPa for the lower strain rate at 800°C. The relevance of temperature increase from the steel under high strain rates without an external additional source of heat is also described in (Laasraoui, 1991). Localised temperatures of up to 100°C can be experienced in areas of high strain, which could have a significant effect on stress vs. strain profiles and deformations.

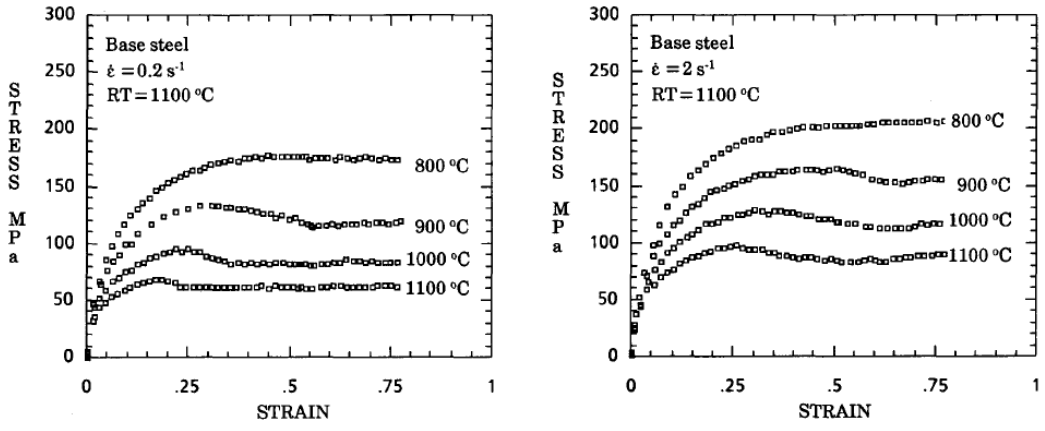

Figure 2.5.10a &b: Stress/ Strains at Various Temperatures (Laasraoui, 1991)

2.5.7 Thermal Damage from Explosive Events

The relative size of an explosive event can be calculated by observing the depth of penetration of heat damage in certain materials. In a classic approach to the conduction of heat through solids it is assumed that the heat (in the form of light radiation) penetrates a surface to a short distance until it is scattered, refracted absorbed or diffracted. With specific material constants such as conductivity and thermal capacity the extent of radiation can be calculated by inspecting the heat damage to a given material. Knowing the temperature required to produce damage to certain materials the thermal flux can be calculated with an assumed radiation emissivity (Penney, 1987).

Scaling laws can then be applied to the thermal flux to determine the size of explosion. The scaling laws are based on either of the assumptions: “two explosions will give equal thermal damage to a particular type of receptor if total heat accepted is the same” or “equal thermal damage will be caused when the two maximum surface temperatures are the same” (Penney, 1987). An issue with these laws occurs if the colour of the surface changes due to physical or chemical reactions, as the absorption of heat will change. This approach also makes no allowance for the loss of heat by re-radiation into air from the material surface.

Quantifying the thermal degradation of structures is a complex problem which can be divided into the following specialist areas: coupling of thermal load into structure, mechanisms for loss of energy through convection and re-radiation, effect of absorbed energy, change in material properties and effects of changes in material properties on the structural resistance to blast loading.

The thermal energy emitted from explosive events as detailed in 2.1 can be absorbed by a structure; the percentage of the energy that is absorbed is defined by the absorption coefficient. The absorption coefficient is a product of surface colour, roughness etc. The absorption coefficient may change throughout the application of the thermal energy if the surface characteristics change during absorption of thermal energy. The angle of incidence can also alter the thermal energy absorbed by the structure (equation 2.52).

$$Q_a = QA_e \cos\theta \tag{2.52}$$

Where, Q = Incident energy (cal/cm^2), Q_a = absorbed energy, (cal/cm^2)

Radiation losses are considered negligible in relation to applied thermal energy as the heat loss through radiation is relatively small. Convective losses are also most likely to occur in a forced convection situation such as moving aircraft surrounded with a flow of air; subsequent blast winds will also provide forced convective cooling.

If a structure is regarded as thermally thin the temperature gradient between front and back surfaces is negligible, leading to the assumption that no thermal gradient exists. The following describes a procedure for determining if a structure is thermally thin, followed by a series of calculations to determine the increase in temperature of the structure;

The factor η is calculated from the ratio of specific time of interest (t) to the time to maximum thermal radiation (t_{max}) (equation 2.53):

$$\eta = t/t_{max} \tag{2.53}$$

A second factor is calculated from the ratio of time to thermal maximum to the square of the thickness (b) of the irradiated structure, multiplied by the parameter α (equation 2.54):

$$\alpha t_{max}/b^2 \tag{2.54}$$

The parameter α is the ratio of thermal conductivity (k) to the product of material density (ρ_m) and specific heat (C_p) (equation 2.55):

$$\alpha = k/\rho_m C_p \tag{2.55}$$

The "thermal thickness" of a plate can be determined using Fig 2.5.11 with equations 2.53 and 2.54. A thermally thin plate has a temperature difference from the front to back of less than 10%. A thermally thick plate indicates no temperature rise on the back and a finite plate describes situations between thermally thin and thick. If a plate is thermally thin the following calculations can be performed to determine the temperature rise. If a plate is thermally thick or finite, complex computational codes are required. Fig. 2.5.12 and equation 2.56 are used to calculate the thermal response (temperature increase) of a thermally thin plate exposed to thermal radiation from explosive events.

$$\frac{h_{cv} t_{max}}{\rho C_p b} \tag{2.56}$$

h_{cv} = convective heat loss (cal/cm^2.sec.^{o}C), ρ = specific gravity of material (g/cm^3).

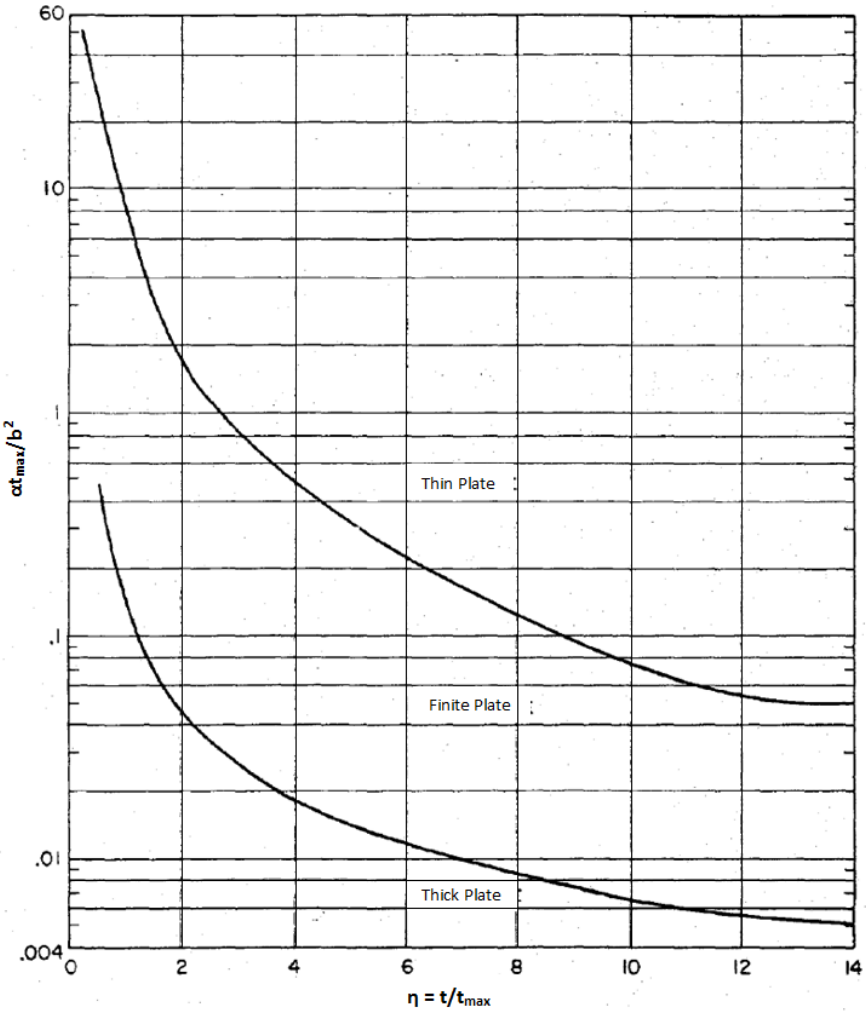

Figure 2.5.11 Thermal Thickness of Plate (Dolan, 1972)

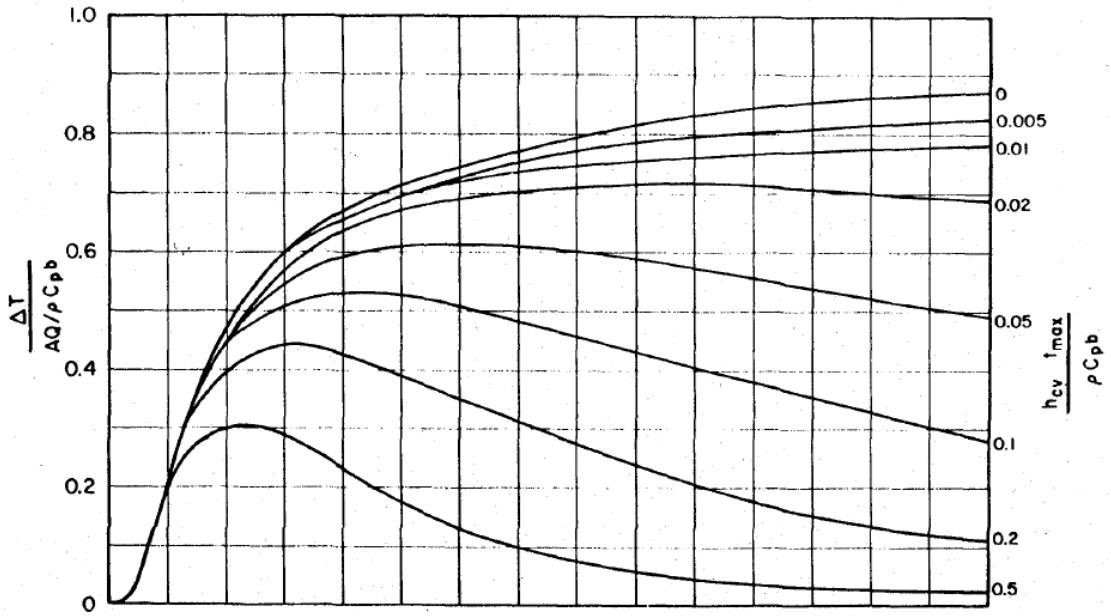

Figure 2.5.12 Thermal Response of Thin Plate (Dolan, 1972)

Extracting a value for equation 2.57 from Fig.2.5.12 and re-arranging gives the temperature rise of the plate. Adding this to the initial temperature gives the actual temperature at the time of interest.

$$\frac{\Delta T}{AQ/\rho C_p b} \tag{2.57}$$

Where, ΔT = Temperature rise (°C), Q = Thermal Exposure (cal/cm^2)

Limitations with using the above procedure include the assumption the plate temperature is consistent across its depth and the use of total thermal exposure (fluence); Q (cal/cm^2) opposed to the thermal flux: q (cal/cm^2/sec).

2.6 Synergistic Response to Thermal and Blast Loads

The aim of this research project is to investigate the synergistic response of structures subject to thermal and blast loading. Previous research in this area is very limited; this section details some of the research which has been undertaken. The synergistic response of structures does not necessarily refer to the fact that the loads are synergistic i.e. act together, but that the response of the loads can act together. The principle in the context of this research is that the synergistic response of the structure is greater than or different to the response of the structure under the separate loading regimes.

2.6.1 Cylinder Testing with Aluminium Oxide and Rotating Test Table

The aluminium oxide and blast (with rotating table) trials undertaken at the Ballistic Research Laboratory (BRL), detailed in 2.2.2, tested a series of aluminium circular hollow sections (CHS) with clamped ends. The cylinders were subject to a 25cal/cm^2 thermal pulse as a precursor to a 42kPa shock wave. Cylinders were instrumented with flux gauges, thermo-couples and strain gauges. Pressure gauges were also installed adjacent to the cylinders and pre and post shot deflection measurements were taken.

Separate blast, thermal and combined trials were undertaken in order to observe specific differences. To observe a similar level of response between the combined and separate trials, the combined trials used slightly less load than the separate cases. Figs.2.6.1a), b) and c) show a 3D representation of post shot cylinder deformations under blast only (a), thermal only (b) and blast and thermal loads (c). (Pearson, 1981).

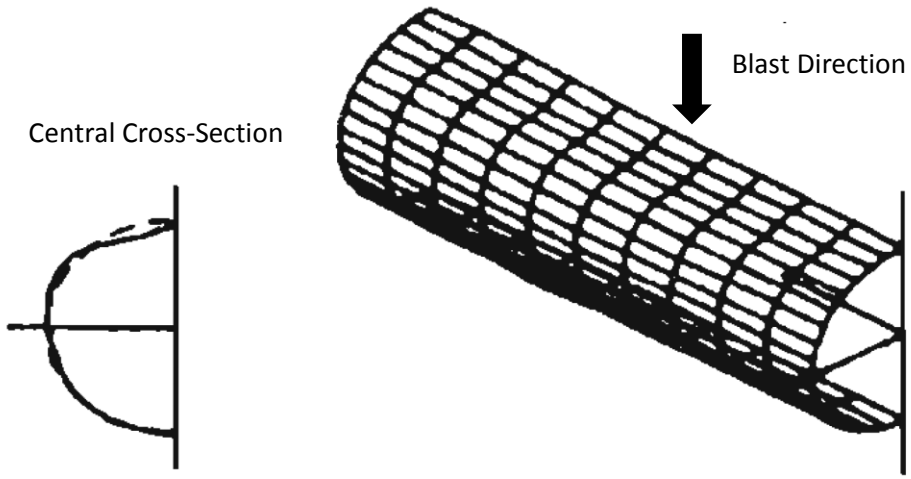

a) Blast Only

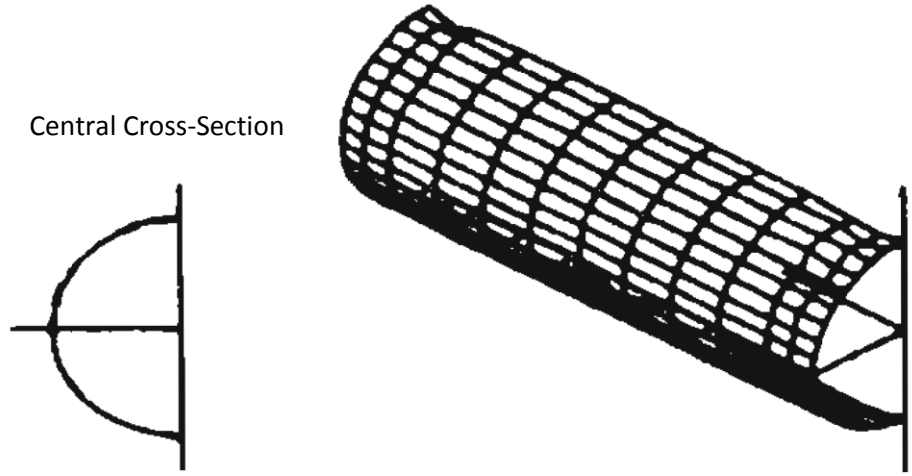

b) Thermal Only

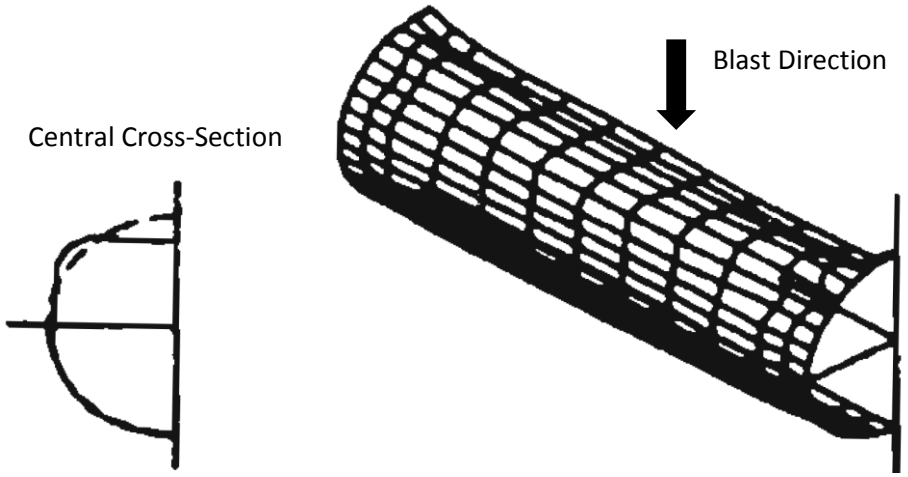

c) Blast and Thermal

Figure 2.6.1a, b & c: 3D Representations of Post-Shot Cylinder Deformations (Pearson, 1981)

The blast only trial showed a small tensile strain at the shock arrival, followed by compressive strain. The compressive strains increase to a maximum at the first rarefaction wave then slowly decrease to an unrestrained condition. The strain history for the thermal only trial shows a rising compressive strain until one second when the target buckled. The strain then dropped to a third of its peak value followed by a small compressive rise until the end of the trials, settling at 50% of its peak value. The buckling occurred near the clamped ends of the cylinder whilst the centre did not experience significant deformations. Temperature measurements taken on the inside of the cylinder showed a rapid thermal absorption followed by a slow thermal loss and redistribution. See (Pearson, 1981) for detailed strain history plots of the aluminium cylinders

During the combined test the shock wave arrived at the cylinder 3.5 seconds after the start of the thermal pulse. During the thermal portion of the trial there was an increasing compressive strain followed by a bucking and sharp swing to tensile strain at one second, very similar to the thermal only test. Post buckling, there was an increasing compressive strain due to thermal load followed by another sharp tensile strain swing at the arrival of the shock wave. At the end of the trials the compressive strain was 33% of its maximum. The final deflected shape of the cylinder revealed buckling at the clamped ends, similar to the thermal trial but with an additional large central deformation which did not occur in the separate tests.

The magnitude and character of the combined trials differed considerably from the linear combination of the two separate trials. This showed that thermo-mechanical non-linear degradation does produce a significant synergistic effect when combined with a blast load.

2.6.2 Analysis of Aluminium Cylinders from Thermal and Blast Simulation

The response of lightweight aluminium structures to intense thermal loads and subsequent blast loads was investigated in (Gregory, 1982). Aluminium cylinders were tested in a thermal & blast tunnel in three states: blast only, thermal only and combined. To avoid interaction with combustion products the thermal source (aluminium powder and oxygen) was placed downstream of the target which was placed on a rotating table.

The thermal source heated the near side of the cylinders to 200^{o}C. The cylinders were 30.48mm in diameter, 1.016mm thick and 800mm long. Subsequent modelling was performed using FEA program ADINA with a von-Mises kinematic material hardening model. The peak pressure was 104kPa and the peak fluence was 25cal/cm^2. The ADINA program did not allow true thermal and structural coupling to be performed so an initial displacement equivalent to the effect of the temperature increase was used. This method made the assumption that the cylinder reached its

maximum deformation from the thermal load before the blast arrival. This also assumes the temperature reaches equilibrium through the thickness of the aluminium almost instantaneously. These assumptions are not correct as any effects of a thermal gradient are ignored and the aluminium is likely to have a slower temperature rise and cooling time compared with duration of the thermal load.

A slight buckling was observed at the ends of the cylinder after the thermal trial, contradicting the numerical analysis. The combined blast and thermal trial produced a midpoint radial deflection four times larger than the blast only and ten times larger than the thermal only trials. The deformed shape was also significantly different between the trials: the thermal only cylinder deformed outwards on both near and far sides, whereas the combined trials produced a curvature away from the thermal source and blast wave.

2.6.3 Blast and Subsequent Fire: Analysis Methods

A method of analysing steel frame structures to explosive and subsequent fire loads was detailed in (Song, 2000) and validated in (Izzuddin, 2000). The adaptive method used allows the two load cases to be modelled together and separately. A non-linear analysis was performed on steel frames initially using elastic elements which were re-meshed during the analysis into elasto-plastic elements when the stresses reached yield values. Three material models were adopted into the analysis: the bilinear stress vs strain model (Fig.2.6.2: reproduced from (Song, 2000)), the variation of Young's Modulus with Temperature (Table 2.6) and the tri-linear variation of thermal strain with temperature (Fig.2.6.3: reproduced from (Song, 2000)), based on EC3 values. The bilinear stress vs. strain model shows an elastic-plastic response with a linear return when unloaded.

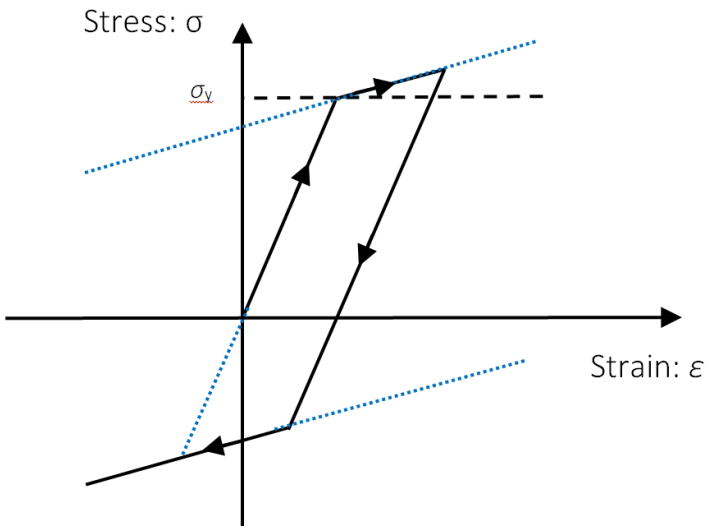

Figure 2.6.2: Bilinear Stress - Strain Response

Table 2.6: Young's Modulus Variation with Temperature

Temperature (°C)	Young's Modulus (GPa)
20	210.0
300	210.0
600	42.0
1200	0.0

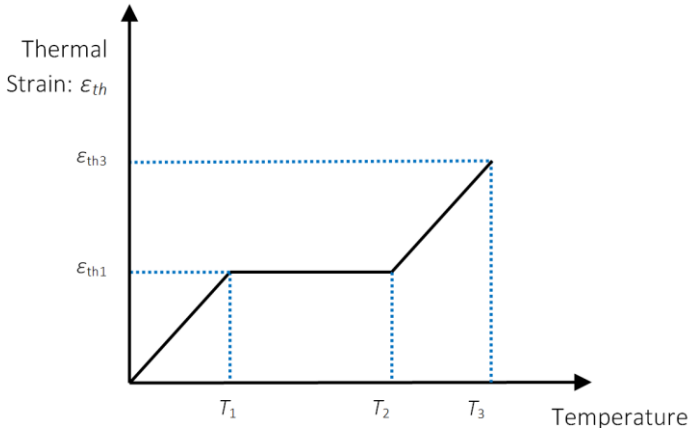

Figure 2.6.3: Tri-linear Variation of Thermal Strain with Temperature

These material models were incorporated into non-linear, thermal and structural analyses (using ADAPTIC). It was found that the initial blast loads reduced the fire resistance of the steel structures by 40%. Elliptical stress vs. strain material models were also found to be more appropriate than the bilinear model (Izzuddin, 2000). Fig.2.6.4 shows the horizontal displacement of a column under thermal only and combined loads. As both columns are heated they reach yield at similar temperatures however, post yield the non-blasted column can sustain much further deformation before complete failure.

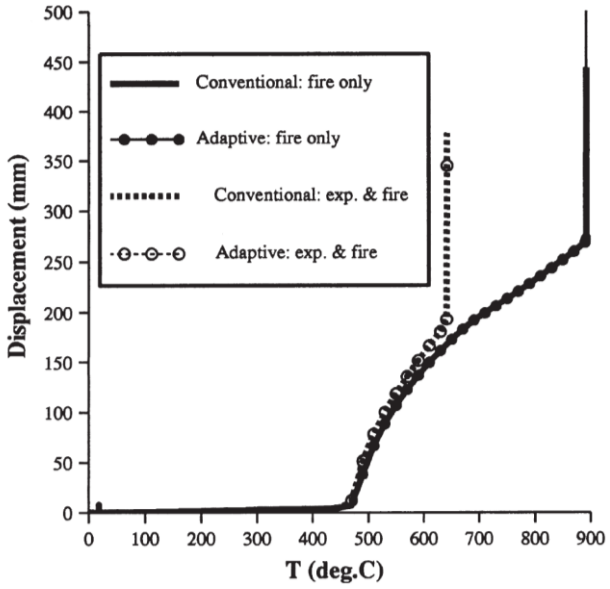

Figure 2.6.4: Displacement Vs Temp of Column Post Explosion (Izzuddin, 2000)

A similar method to the adaptive method was the mixed element approach used in (Chen, 2005) where a whole frame was analysed with beam elements (away from a localised blast) and shell elements (near blast). A strain rate dependent material plasticity model was adopted for the steel (Perzyna model - see Appendix A). Using only beam elements the response of the steel frame was over-estimated. The shell models experienced inelastic local buckling at critical cross sections and high strain rates.

In (Quiel, 2013) steel columns subject to fire and explosive loading were modelled using a multi-hazard approach. The columns were analysed under an initial blast load using a blast analysis module code. The deformed column properties were subsequently input into a structural fire analysis. The fire analysis was undertaken by using a fibre-beam and simplified lumped mass method. This approach is computationally inexpensive and is only suitable for columns with no local buckling or large p-delta effects and doesn't model combined effects. (Liew, 2007) used a mixed element approach to model steel frames to blast and subsequent fire loads. By using detailed finite element analysis on elements subject to both blast and thermal loading regimes the local member and total frame instability was accurately predicted.

The effect of passive fire protection on a structural frame when subject to an explosive or impact event (leading to the removal of one perimeter column), followed by a fire is investigated in (Quiel, 2012). By investigating a prototype building model it was found that the structure with no fire protection lost stability after only 11 minutes, whereas the structure with fire protection remained stable for an extra 30 minutes.

2.7 Literature Review Summary

This literature review was undertaken to gather the essential background knowledge of subject areas relating to the research project. This information is used throughout the research project to aid the numerical and experimental studies and provide reason to the conclusions drawn. The existing research into thermal energy emission from explosive events enables the calculation of thermal load profiles for the parametric study. The previous research investigating experimental thermal radiation simulation highlights the limitations and difficulties encountered whilst attempting to accurately replicate an intense thermal load from an explosive event. Some experimental designs shown are used to benefit the design of the experimental trials undertaken during this research project.

The background research into blast phenomenology assists in the calculation of blast loads and their interaction with structures. This information is adopted during the parametric study to

calculate the loads applied to the structural columns. The existing research regarding the structural response to blast loads aids the holistic understanding of structural response and details methods that are used to analyse structures under blast loading. The information relating to steel material response to dynamic loading will help form realistic material models for numerical modelling. The research into structural response to thermal loads helps in understanding the physical and material response of steel structures to thermal loads and material degradation. There is little existing research into the synergistic response of structures to thermal and blast loading; however, the minimal research that has been undertaken has shown a potential synergistic response and can be used to aid the numerical and experimental studies.

Chapter 3

Experimentation

3.1 Introduction

This chapter describes the experimentation undertaken as part of the research project. It is divided into two subsections: Part A discusses two 41kg equivalent (eq.) TNT explosive arena trials that were completed from April to June 2013. Part B details the combined thermal, compression and long duration blast trials performed within the Air Blast Tunnel (ABT) that were undertaken during spring 2015 and the pre-requisite trials that were undertaken prior to the combined ABT trials as part of the full testing programme.

3.2 Part A: High Explosive Arena Trials

The purpose of the arena trials was to record the intense temperatures, thermal flux and pressures within the fireball of a conventional explosive event and observe the response of thin steel plates within the explosive fireball. A new method of recording pressures, temperatures and thermal flux from within the explosive fireballs was developed using bespoke Heavy Structural Boxes (HSBs). The plate response was compared to numerical models, as discussed later in section 4.3, to draw conclusions regarding the synergistic response of the plates and for validation of the computational methods used for the subsequent parametric study. During April to June 2013 two open air 41kg TNT eq. (equivalent: 39kg TNT flakes, 2kg PE4 explosive) controlled explosions were undertaken at the M.O.D national testing facility on Foulness Island, M.O.D Shoeburyness.

3.2.1 Experimental Trial Design

For each trial six HSBs were placed at 4m (x2), 6m (x2) and 8m (x2) radial locations across and beyond the edge of the explosive fireball, these positions were determined after inspection of high speed video from a previous explosive trial of the same size (41kg TNT eq.). Fig.3.2.1 shows a plan of the arena trial with HSB positions in relation to explosive charge centre, cameras and maximum fireball diameter.

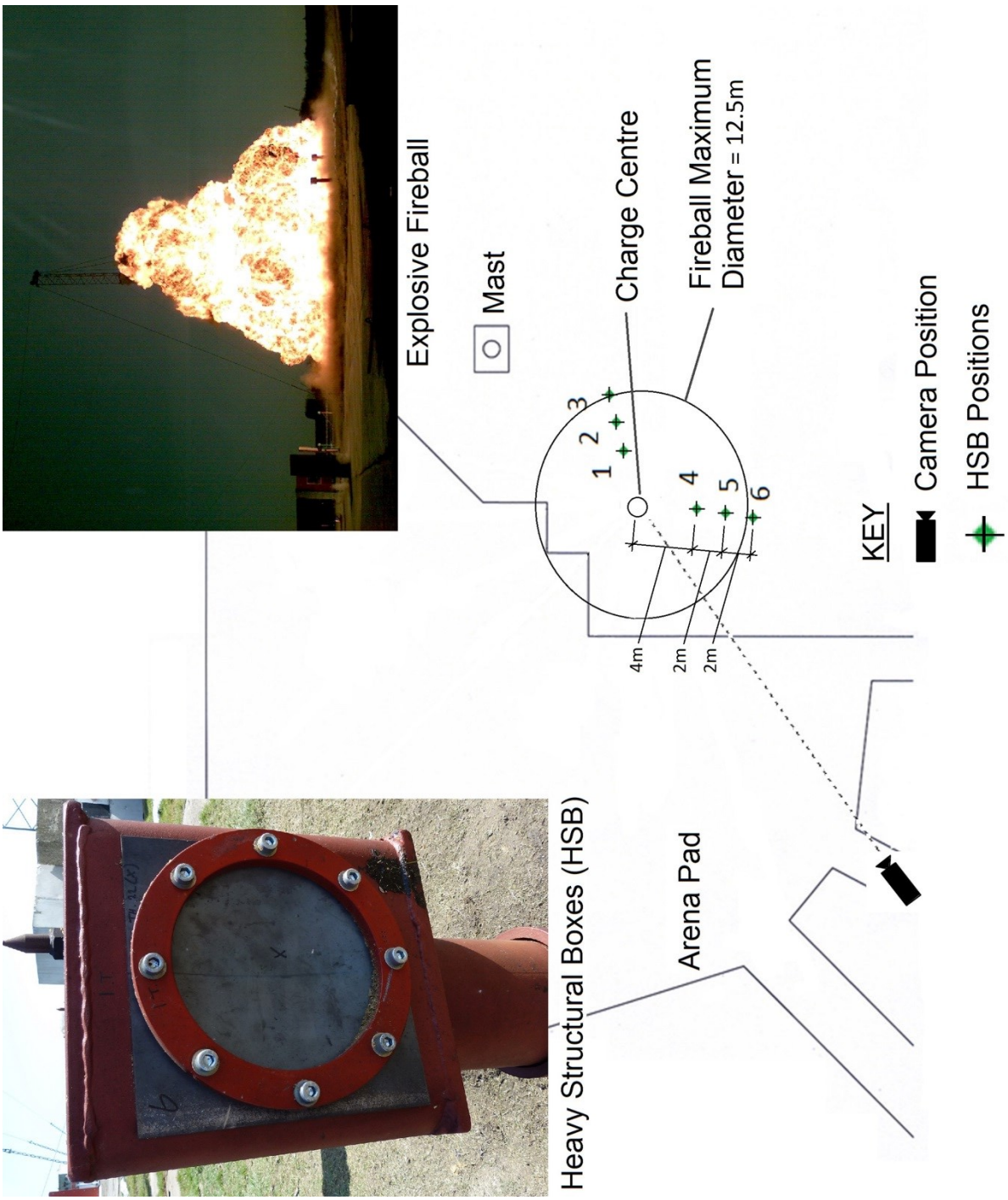

Figure 3.2.1: Plan of Arena Trial

Steel plates, 150mm diameter, 2mm thick were bolted to the front of each HSB using a circular collar (Fig.3.2.2, Fig.3.2.3 and Fig.3.2.4). The HSBs were instrumented with thermocouples (K-Type) and thermal flux gauges (Seqouia) positioned on the top external face and pressure gauges (Endecvo 8510c-100) on the front external face. Three of the HSBs (positions 1, 2 and 3) were fitted with plates instrumented with strain gauges (Rossette) and thermocouples (K-Type) glued with epoxy on the rear (inside) of the plates.

Figure 3.2.2: Heavy Structural Boxes (HSB Positions 1, 2 & 3)

The remaining three HSBs (positions 4, 5 and 6) were fitted with un-instrumented plates. During the first trial the HSBs with instrumented plates faced the blast and the HSBs with un-instrumented plates faced away. For the second trial the HSBs were rotated by 180^{o} with the un-instrumented plates facing towards the blast and the instrumented plates facing away. The HSBs were welded to heavy circular hollow sections (CHSs), which fitted inside larger diameter CHSs allowing ease of rotation between the two trials and affording protection to the instrumentation cabling which passed through undamaged (Clough, 2013). The HSBs were designed to withstand the extreme pressures (4.3MPa) and temperatures (480^{o}c) within the explosive fireball. Fig. 3.2.2 shows the HSBs in-situ at 4m, 6m and 8m radial positions (1, 2 and 3) facing the blast and Fig 3.2.1 (inset) shows the explosive fireball and a deformed plate bolted to the front of a HSB at 4m radial position after the first explosive trial.

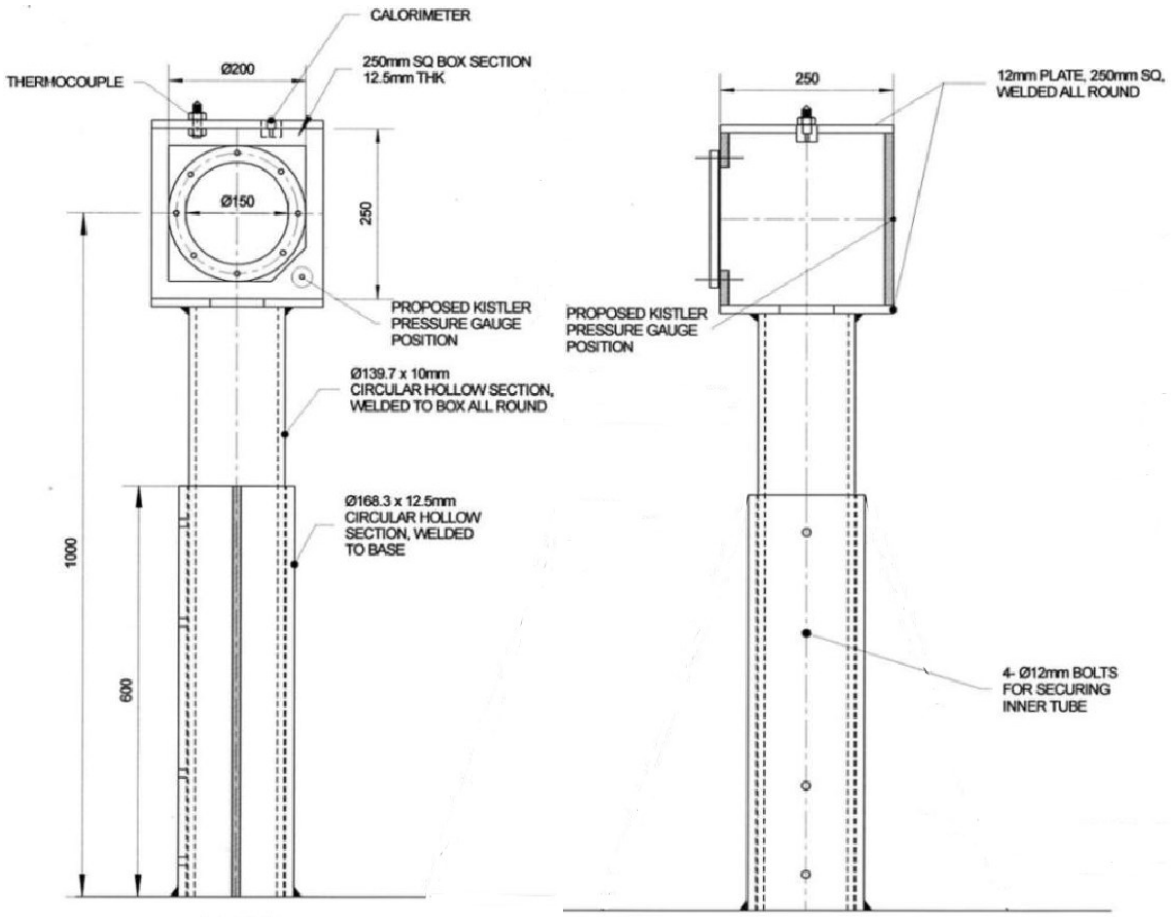

Figure 3.2.3: Design of Heavy Structural Boxes (Front & Side Views)

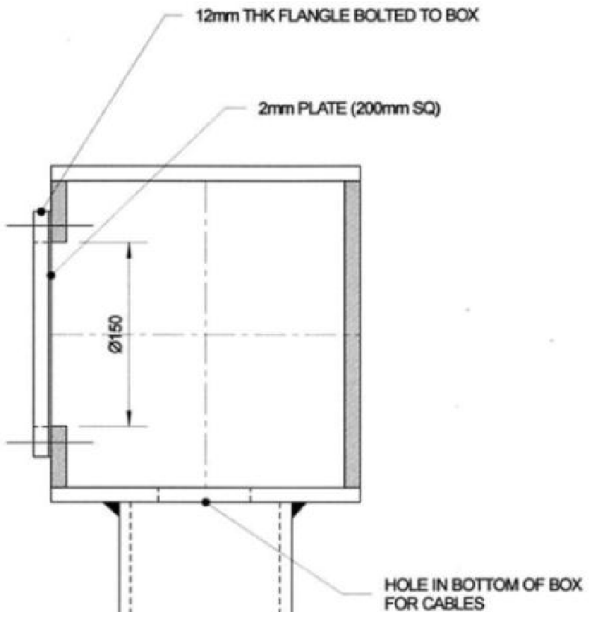

Figure 3.2.4: Design of Heavy Structural Boxes (Section Detail View through Box)

The steel grade used for the plates was Hot Rolled Steel for Forming (BSEN 10111:DD11) (BSi, 1998). The yield strength was 162MPa, ultimate strength was 266MPa and the Young's modulus was

202GPa. These values were determined by tensile coupon tests performed on the plates. Table 3.1 shows results from the tensile testing conducted by the author at the University of Southampton.

Table 3.1: Tensile Test Data

Sample	Yield Strength / 0.2% Proof Stress (MPa)	Ultimate Tensile Strength (MPa)	Young's Modulus (GPa)
1.1	160 / 165 (Low Strain Rate)	260	212
2.1	152 / 156	266	213
3.1	160 / 167	269	200
1.2	156 / 164	267	213
2.2	152 / 154	266	183
3.2	162 / 167	270	188
Mean	**157 / 162**	**266**	**202**

3.2.2 Fireball Evolution and Recorded Temperatures

The total recorded duration of the explosive fireball evolution and dissipation was less than one second for both trials. The fireball reached a maximum diameter of 12.5m at 39msec. The HSBs at 4m (8m diameter) were inside the fireball at maximum diameter, at 6m (12m diameter) they were on the edge of the fireball and at 8m (16m diameter) they were outside the fireball. Figs.3.2.5a to 3.2.5k are still images taken from the high speed phantom cameras during the first trial showing the fireball evolution after the initial explosion. Temperature, pressure, thermal flux and strain data was successfully recorded by the HSBs across the diameter of the fireball.

(a): Fireball at 0.81msec after Ignition

(b): Fireball at 1.0msec after Ignition

(c): Fireball at 2.2msec after Ignition

(d): Fireball at 8.2msec after Ignition

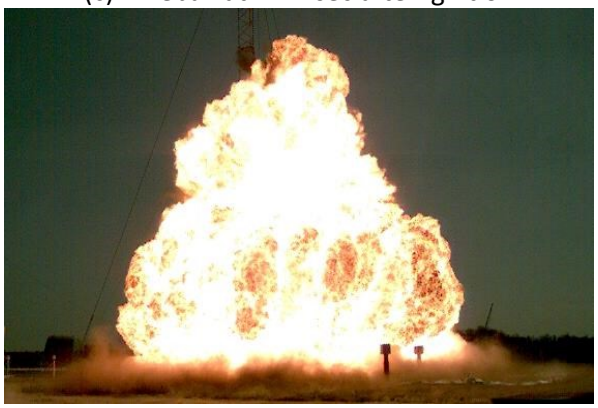

(e): Fireball at 39msec after Ignition

(f): Fireball at 100msec after Ignition

(g): Fireball at 300msec after Ignition

(h): Fireball at 450msec after Ignition

(j): Fireball at 600msec after Ignition

(k): Fireball at 915msec after Ignition

Figure 3.2.5a to k: Evolution of Fireball after Ignition

Fig.3.2.6 shows the recorded temperatures for both trials at the 4m, 6m and 8m radial locations. The temperatures between the two trials are generally comparable but there are differences between the peak temperatures and cooling rate. At 4m the peak temperature was 480°C for the first trial and 465°C for the second. After the peak, the temperature decrease was slower for the first trial compared to the second. At 6m the recorded peak temperatures were 106°C and 64°C for the first and second trial respectively. At 8m the recorded peak temperature for the first trial was 75°C compared to 46°C for the second trial. The differing values are due to the highly volatile nature of the fireball and atmospheric effects. The figures of recorded trial data included in this thesis are smoothed data curves from raw gauge data. Smoothing was undertaken using fast Fourier transform to low-pass filter the data.

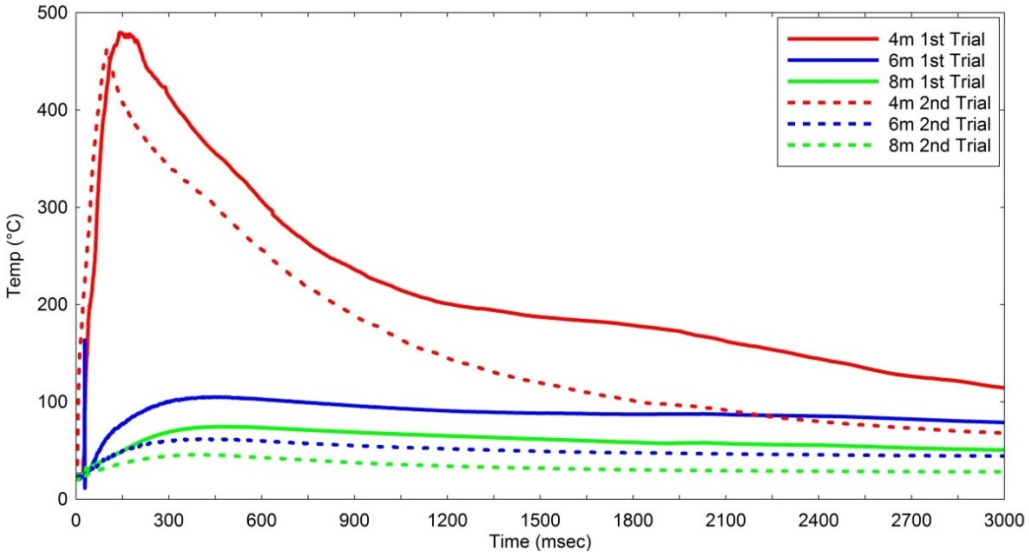

Figure 3.2.6: External temperature at 4m, 6m & 8m radial positions.

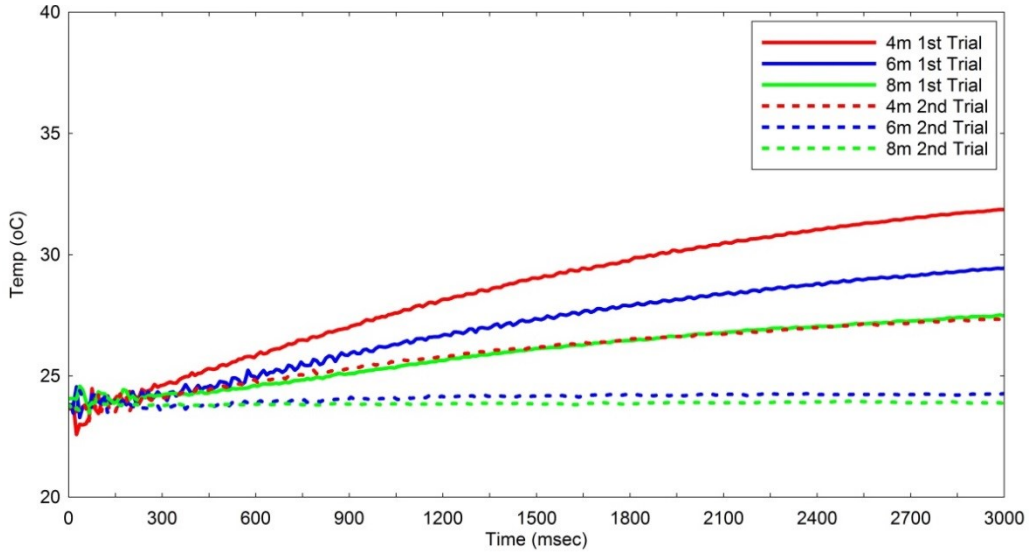

Figure 3.2.7: Internal temperature at 4m, 6m & 8m radial positions

Thermocouples inside the HSBs recorded the temperature increase on the rear face of the steel plates. Fig.3.2.7 shows the recorded temperatures on the rear face of the steel plates. At 4m the temperature increase was 8.2°C for the first trial and 3.75°C for the second trial. This difference was due to the plates facing the explosive charge during the first trial and facing away during the second. The plates facing away were shadowed from the thermal radiation; therefore, less thermal energy reached the plates resulting in a lower temperature. By comparing Fig.3.2.6 and 3.2.7 a steep thermal gradient is observed across the thickness of the plates for the duration of the trial.

3.2.3 Thermal Flux

Seqouia flux gauges recorded the thermal flux across the explosive fireball during both trials (Fig.3.2.8). Similarly to the recorded temperatures, the recorded thermal flux was higher during the first trial than the second. The peak flux values recorded at 4m were 145W/cm^2 (first trial) and 115W/cm^2 (second trial). The rapid increase and slow decrease in the recorded temperatures and thermal flux apparent in Fig.3.2.6 and Fig.3.2.8 are attributed to a combination of the rapid thermal radiation pulse followed by the slower expansion and cooling of the combustion products. This is in agreement with (Stepanov, 2011), who states "The radiation from a conventional explosive fireball has a short term pulsed character due to the fast radiative cooling of the fireball and mixing of combustion products". The initial high peak flux recorded at 4m during the first trial at 25msec is due to an electrical disturbance.

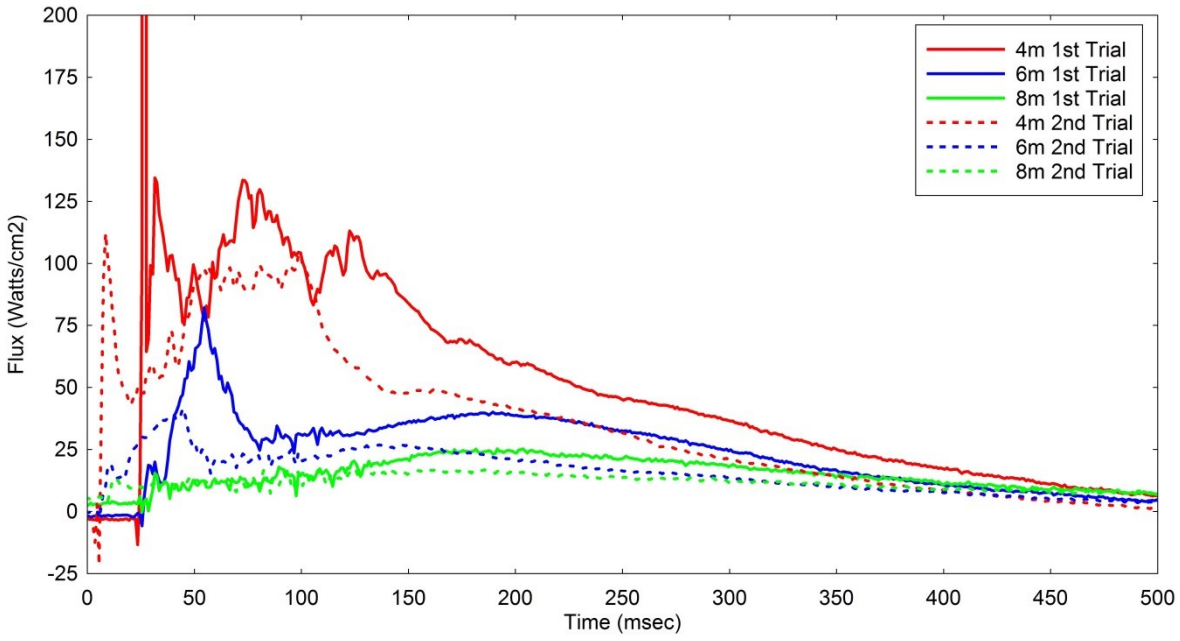

Figure 3.2.8: Recorded Flux at 4m, 6m & 8m Radial Locations.

3.2.4 Reflected Pressure

Endecvo 8510c-100 pressure gauges were positioned adjacent to the steel plates on the front face of the HSBs to record the pressure during the explosive trials. Fig. 3.2.9 shows the recorded reflected pressures on the HSBs facing the blast for both trials at 4m and 8m radial locations. The peak recorded reflected pressures at 4m were 4.04MPa (Trial 1) and 4.29MPa (Trial 2).

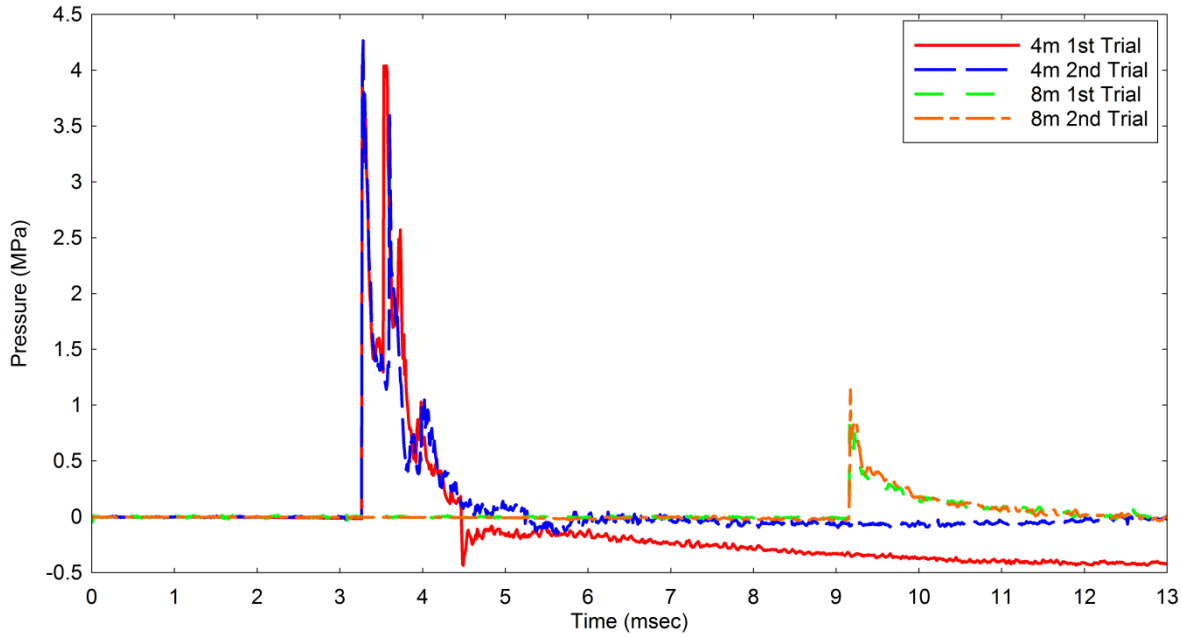

Figure 3.2.9: Recorded Reflected Pressures at 4m and 8m Radial Locations During a 41kg TNT Eq. Explosive Trial: Facing Blast

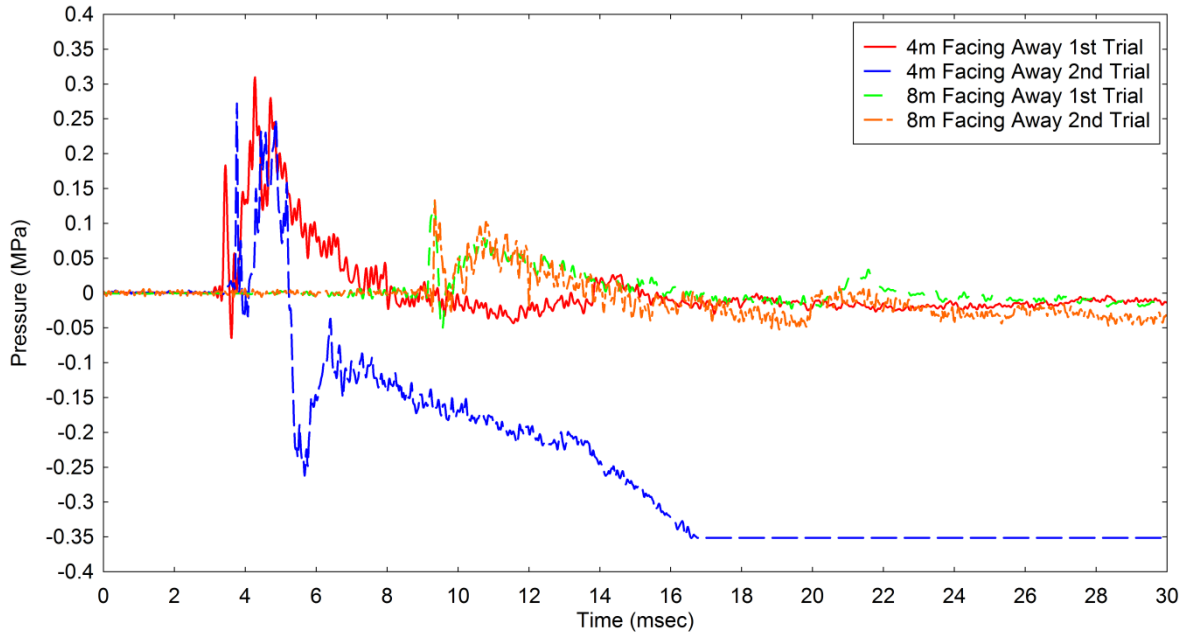

Figure 3.2.10: Recorded Reflected Pressures at 4m and 8m Radial Locations during a 41kg TNT Eq. Explosive Trial: Facing Away From Blast

A double peak pressure was observed at 4m facing the blast. The exact reason for this is unknown; however after examination of the duration between the peaks and the speed of the blast wave the most reasonable explanation is due to the combustion products reaching the pressure gauge separately to the blast wave. This theory is verified further as the double peak was not observed at 8m due to the combustion products (fireball) expanding to a distance between the 6m HSBs and 8m HSBs. There was reasonable repeatability of the recorded reflected pressures between the two trials. Reflected pressures recorded on the boxes facing away from the blast were lower than the reflected pressures on the boxes facing the blast. An average peak value of 0.3MPa at 4m was recorded over both trials (Fig.3.2.10).

3.2.5 Recorded Strain

Rossette strain gauges were glued with epoxy to the rear of the steel plates on three HSBs for each trial. Fig.3.2.11 shows the recorded vertical and horizontal strain history in the plates at 4m, 6m and 8m radial locations during the trials. The recorded strains for trial two have been offset by 29msec for ease of comparability. There was a large difference in the peak and final strain values between the two trials, due to the plates facing away from the blast during the second trial. The final strains recorded on the plates facing the blast (trial one) were 750µstrain (micro-strain) at 4m, and 205µstrain at 6m. The final strain values recorded on the plates facing away from the blast (trial two) were 380µstrain at 4m, 15µstrain at 6m and -38µstrain at 8m.

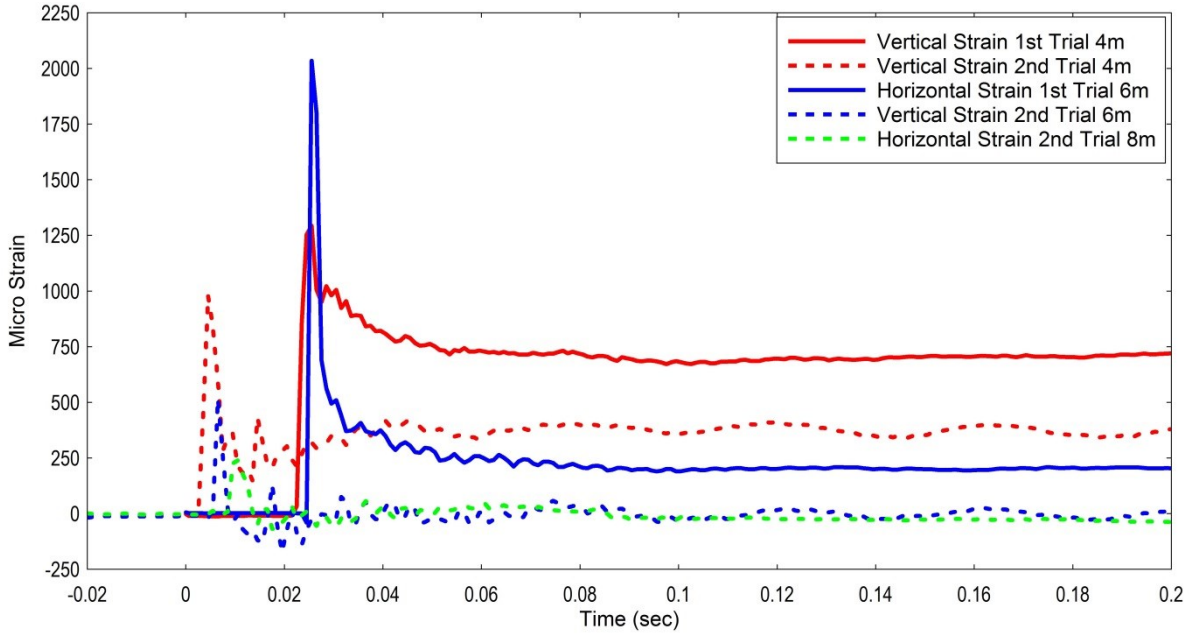

Figure 3.2.11: Recorded Strain at 4m, 6m & 8m Radial Positions

The recorded peak strain at 6m (2035µstrain) for the first trial was higher than the recorded strain at 4m (1300µstrain) during the same trial. During both trials the strain gauges were affected by an

electrical disturbance at approximately 25msec, leading to unrealistic recorded peak strains. Assuming a two dimensional stress state, with a Young's Modulus of 202GPa (Table 3.2), the peak of 1300μstrain equates to an equivalent yield stress of 262MPa. Oscillations are also observed in the recorded histories indicating a dynamic response to the blast load.

3.2.6 Final Deflected Shapes

The final deflection profile of the plates was recorded manually using Vernier callipers after the completion of the explosive trials and removal of the plates from the HSBs. The plates with visible permanent deformations were at 4m (both trials) and 6m (trial one) radial positions facing the blast. The plate at 6m facing the blast during the second trial facing the blast had no visible permanent deformations. Fig.3.2.12 shows the final deflection profile recorded across the plate centre line for the plates facing the blast at 4m (both trials) and 6m (trial one). Polynomial fits (10^{th} order) are used to smooth manual errors encountered using Vernier callipers. The maximum permanent deflections at 4m were 10.5mm (trial one) and 7.5mm (trial two). The peak deflection at 6m was 5.25mm (trial one).

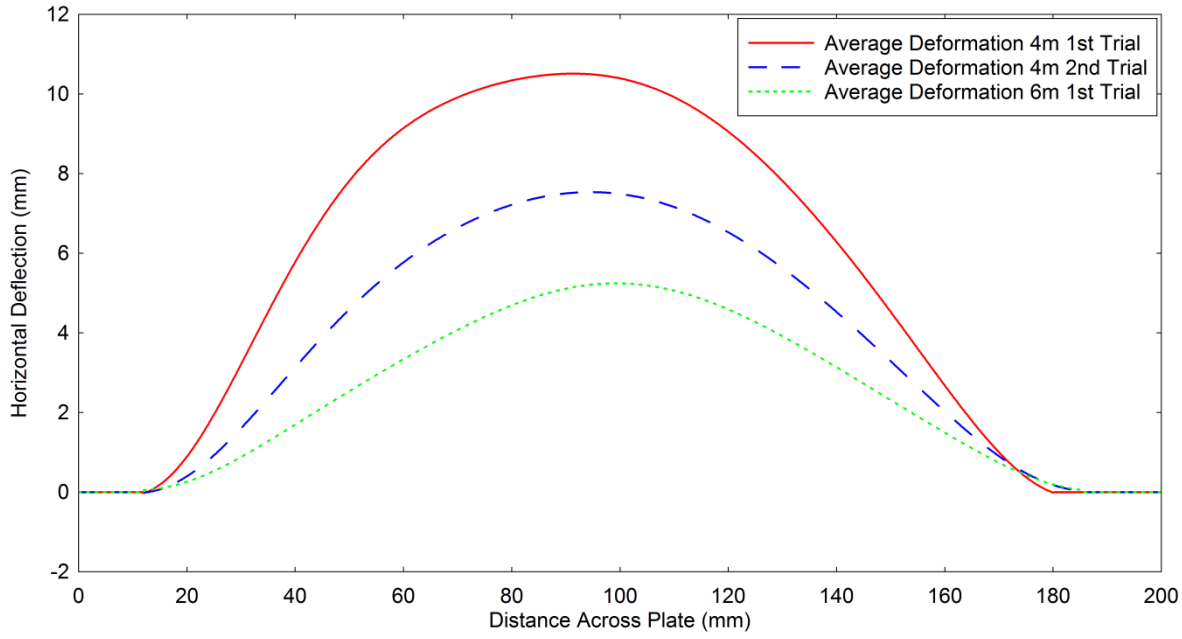

Figure 3.2.12: Permanent Plate Deflection Profiles at 4m and 6m Radial Positions (Centreline)

The permanent plate (facing blast) deformations observed in the first trial were higher than the second trial. The reasons for the difference between the two trials include fireball volatility, trial reproducibility and fixity of plates. There were no observed permanent deformations or damage to

the HSBs or the CHSs therefore the local plate deformations observed are assumed to be equal to the total global deformations.

3.2.7 Arena Trials Summary

Two arena trials were successfully undertaken recording the temperatures, thermal flux and pressures within a fireball of a high explosive event. The response of thin steel plates within the explosive fireball was also successfully observed. Recordings at such close proximities to high explosive events had not been achieved prior to this research project. The heavy structural boxes were successfully used to position the gauges and steel plates within the fireball without unforeseen damage. The recorded data from the trials is used throughout this research project for numerical analyses and the conclusions drawn help verify the theory adopted for the computational studies. The trials also have set a benchmark for future testing and recording of pressures within high explosive fireballs.

3.3 Part B: Combined Air Blast Tunnel (ABT) Trials: Thermomechanical Response

The following section details the combined thermal, compression and long duration blast tunnel trials that were undertaken during spring 2015 as part of the full research programme. Prior to the combined ABT trials two sets of pre-requisite trials were performed. The first pre-requisite trial investigated the use of ceramic heating elements to increase the temperature of structural steel column hollow sections (3.3.1). The second pre-requisite trial examined the response of the structural column hollow sections as cantilever structures subject to long duration blast loads inside the Air Blast Tunnel (ABT) at M.O.D Shoeburyness (3.3.2).

After the initial pre-requisite trials the main series of trials was undertaken observing the response of the structural steel columns subject to compressive, thermal and long duration blast loads within the ABT. There were six ABT separate trials forming the main series. The aim of the ABT trials was to determine if the steel columns exhibited a greater or different response when subject to thermal and compressive loads preceding a long duration blast load compared with the response of columns subject to a long duration blast load alone. The trials and subsequent numerical analysis validate the numerical methods adopted throughout the research project. Table 3.2 shows a simplified overview of the trial order; further detail is shown in 3.3.1, 3.3.2 and 3.3.3 for each trial series.

Table 3.2: Trial Overview

#	Trial Series	Location	Target Overpressure	Duration	Test Structures	Variability
1.	**PR.1: Ceramic Heating Element Trials**	Controlled Lab	N/A	N/A	3m CHS, SHS & RHS Steel Columns	Heat Load: Extent & Duration
2.	**PR.2: ABT Pre-Cursor Trial**	10.2m ABT	55kPa	180msec	3m CHS, SHS & RHS Steel Columns	N/A
3.	**ABT Trials #1 to #6**	10.2m ABT	55kPa	180msec	3m CHS, SHS & RHS Steel Columns	Heat Load & Compressive Load
PR = Pre-Requisite. CHS, RHS & SHS (Circular, Rectangular and Square Hollow Sections)						

3.3.1 Pre-Requisite Trials: Ceramic Heating Elements

The aim of the first pre requisite trials was to test the suitability of the ceramic heating elements (Fig.3.3.1),(Ceramicx, 2015) to heat structural column hollow sections to temperatures akin to those reached in a typical fire (850^{o}C in 30min (BSi, 2013)). The response of the columns subject to combined heat and compression loading was also observed.

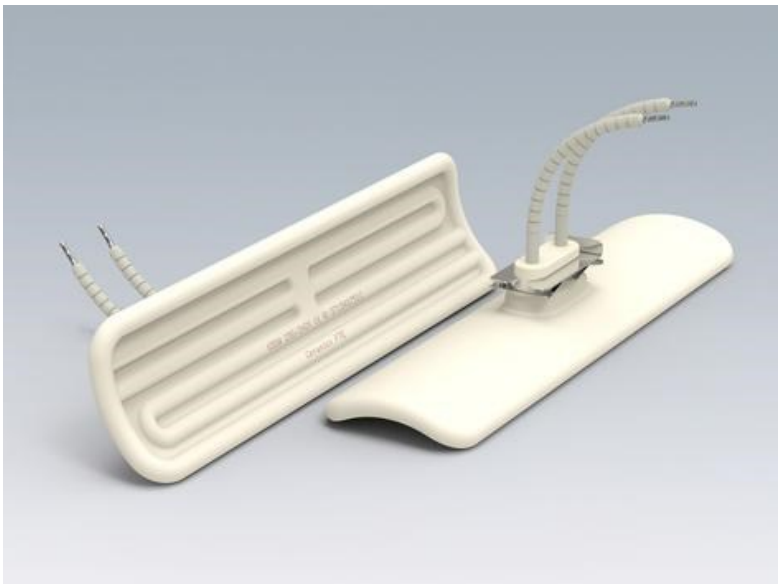

Figure 3.3.1: Ceramicx Heating Elements (Ceramicx, 2015)

3.3.1.1 Design and Diagnostics

A circular array of eight ceramic heating elements fixed inside a thermally insulated box were used to heat the 3m long steel structural hollow sections. Fig.3.3.2a) and b) shows detail of the array and a plan view schematic of the thermal boxes.

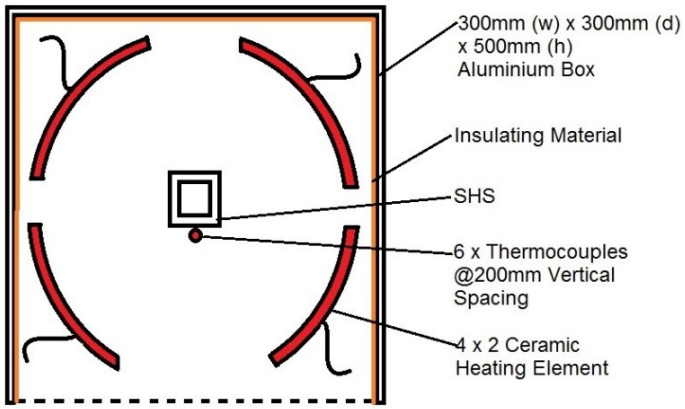

(a) **(b)**

Figure 3.3.2a & b: Ceramic Heating Element Array (a) Schematic Plan View of Thermal Box (b)

Four (by two) heating elements were positioned around the column section to heat the column evenly from all sides. The elements were positioned at a distance of 100mm maximum from the surface of each column. Insulating fabric was used on the inside of the aluminium boxes to maintain high temperatures. The aluminium box was 500mm (h) x 300mm (w) x 300mm (d). The front of the box (blast facing) was left open to allow observation of the column during the trial.

The ceramic heating trails were performed in controlled laboratory conditions (not ABT), so the effects of external environmental temperature could be minimised. The rig supporting the columns and thermal box was designed as a prototype for the subsequent ABT trials. The thermal box was fixed to a drop-down frame (Fig.3.3.3), this would allow the box to be positioned vertically during the heating phase and dropped back once the target temperature was reached prior to the passing of the subsequent blast wave (for ABT trials). The column was fixed inside a heavy structural rig with a pinned sleeve connection at the top and a sleeved spring connection at the base (Fig.3.3.3). The base spring connection applied a compressive load into the column (Table 3.3), thus replicating a structural column as used in service.

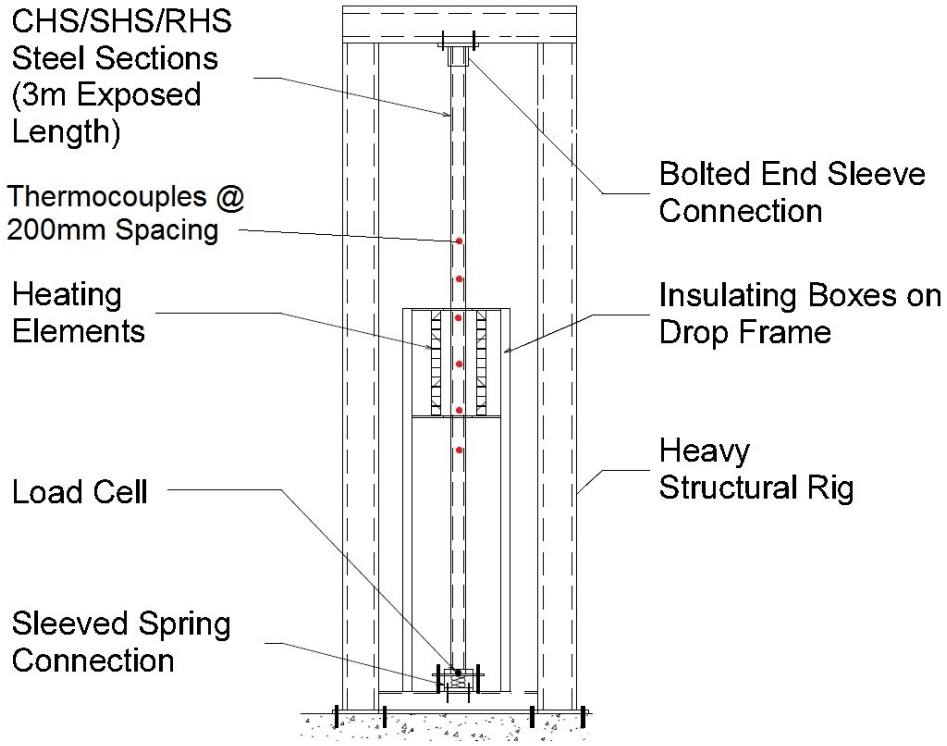

Figure 3.3.3: Ceramic Heating Pre-Cursor Trial Rig: Elevation View

Three column sections were tested; a 50x25x2mm Rectangular Hollow Section (RHS), a 25x25x2mm Square Hollow Section (SHS) and a 33.7x3mm Circular Hollow Section (CHS). The steel grade used for the columns was S355 J2C, cold formed (BSEN 10219) (Bsi, 2006). Figs.3.3.4a), b) and c) show the configuration of the rig, thermal box, heating elements, and sleeved compression spring support in the controlled laboratory during the heating trials. Six thermocouples (K-type) were positioned at 200mm centres (1100mm to 2100mm) to record the temperatures along the length of each column (Fig.3.3.3.). The compressive load from the springs was monitored during the heat testing using load cells (Zemic BM24R-C3-1T-3B (Zemic, 2015)).

(a) **(b)** **(c)**

Figure 3.3.4a, b & c: Ceramic Heating Trial: Full Rig (a), Drop Down Rig with Insulated Box (b), Sleeve with Compression Spring at Column Base (c)

3.3.1.1.1 Ceramic Heating Element

The ceramic heating elements, supplied by Ceramicx, were used to heat the steel columns to temperatures akin to those reached in a typical fire (850^{o}C in 30min (BSi, 2013)). Their use in industry and performance is further detailed in 2.2.7. The heating element specified for these trials was a 245mm x 60mm 1000 Watt Full Trough Element (FTE) (Fig.3.3.5). The FTE was specified due to the curved profile. The curved profile could produce a more focused high intensity thermal load, compared to a flat heating element. The curved shape was also suitable for positioning in a circular array surrounding a column section. Fig.3.3.6 shows the radiative heat flux profile produced by a 245mm x 60mm 1000 W FTE. The radiative heat flux is maintained at 1W/cm^2 across the width of the elements at 100mm from the surface of the element. The flux drops to approximately 0.4W/cm^2 at the longitudinal ends of the element. When positioned in the circular array used during the heating element trials these flux levels were at a constant and higher level across the length and width of each element.

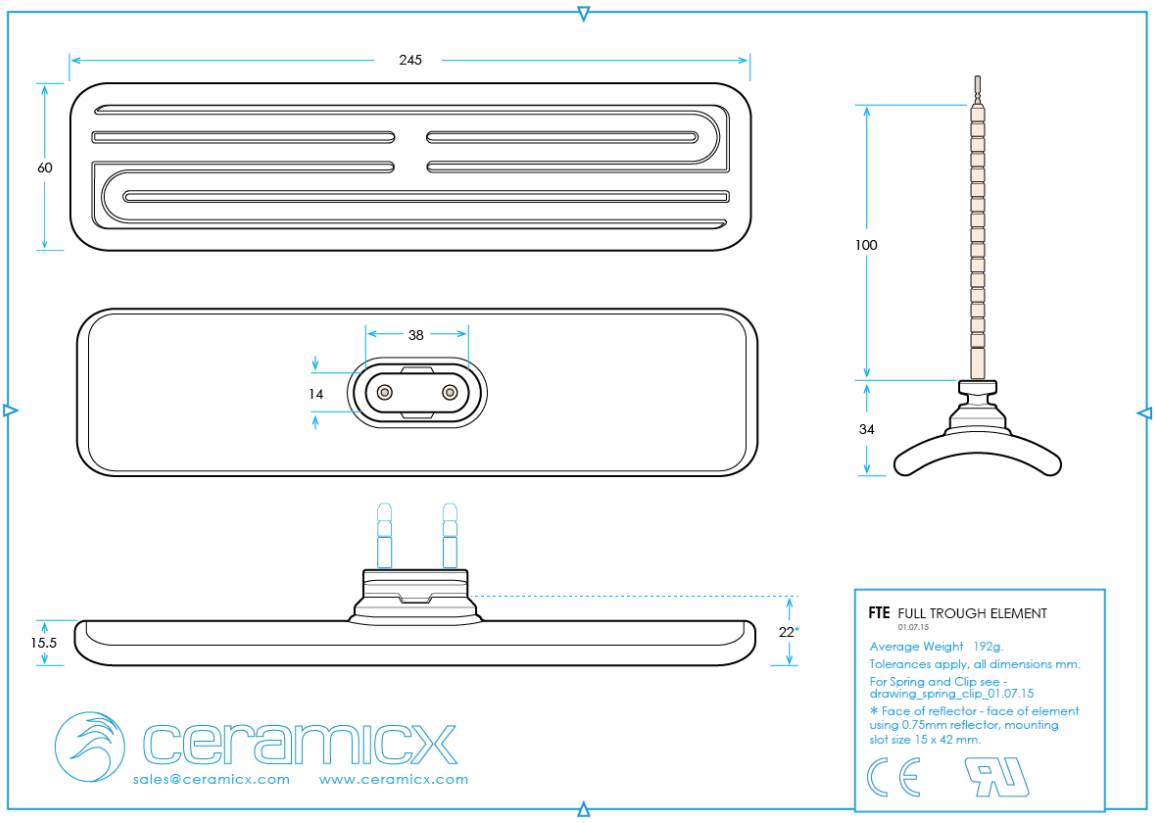

Figure 3.3.5: Full Trough Element (FTE) (Ceramicx, 2015)

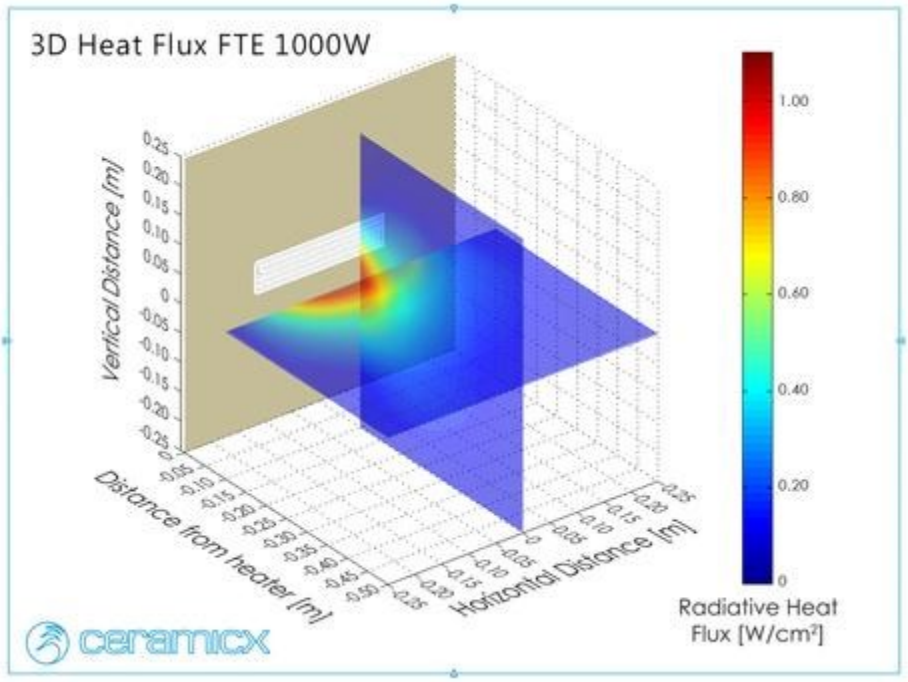

Figure 3.3.6: Radiative Heat Flux Profile Produced by 1000W FTE (Ceramicx, 2015)

3.3.1.2 Results and Observations

The ceramic heating pre-requisite trials served two purposes: the first to test the performance of the ceramic heating element to heat the steel columns to levels akin to fire loading, the second to observe the response of the SHS, RHS and CHS steel columns to the thermal and compressive loads alone. The trials were performed in a controlled laboratory environment. Lateral movement (bending) of the columns was observed during the heating trials and permanent mid-span deflections were recorded after the columns had cooled and were removed from the rig. During heating the circular hollow sections bent laterally towards the rig until they touched the drop down rig preventing any further movement.

The largest permanent mid-span deflection was observed in the SHS (17mm). The load cells recorded increasing compressive loads in all three columns during the heating. This indicated that the longitudinal column expansion was causing an increase in the applied compressive load. The RHS load cells recorded the largest increase in applied compressive load of 0.5kN. The recorded compression, lateral movement observations, maximum temperatures and permanent mid-span deflections are shown in Table 3.3.

Table 3.3: Thermal Trial Results

	Column		
	RHS	**SHS**	**CHS**
Compressive Load at Start of Heating	4.15kN	3.35kN	4.8kN
Compressive Load at Max Temperature	4.65kN	3.6kN	5.0kN
Observed Movement During Heating	Not Visible	Visible	Visible
Max Temperature Reached	572^{o}C	561^{o}C	546^{o}C
Permanent Mid-Span Deflection	5mm	17mm	n/a

Thermocouples (K-type) recorded the increasing temperatures during the heating trials. The highest temperatures recorded along the length of the 3m columns were either at 1500mm or 1700mm (trial variance). A shallow decrease in recorded temperatures along the column length was observed above the column centre; below the column centre a steep decrease along the length was observed. The recorded temperatures are shown in Figs. 3.3.7 to 3.3.9. Comparing these temperatures to standard fire design curves (BSi, 2013); at 30mins the standard fire temperature is 850^{o}C; at 15mins the heated RHS column reached a maximum temperature of 572^{o}C. The

temperature increase slows after 15min and stays below 600°C, therefore not reaching the target temperature of 850°C.

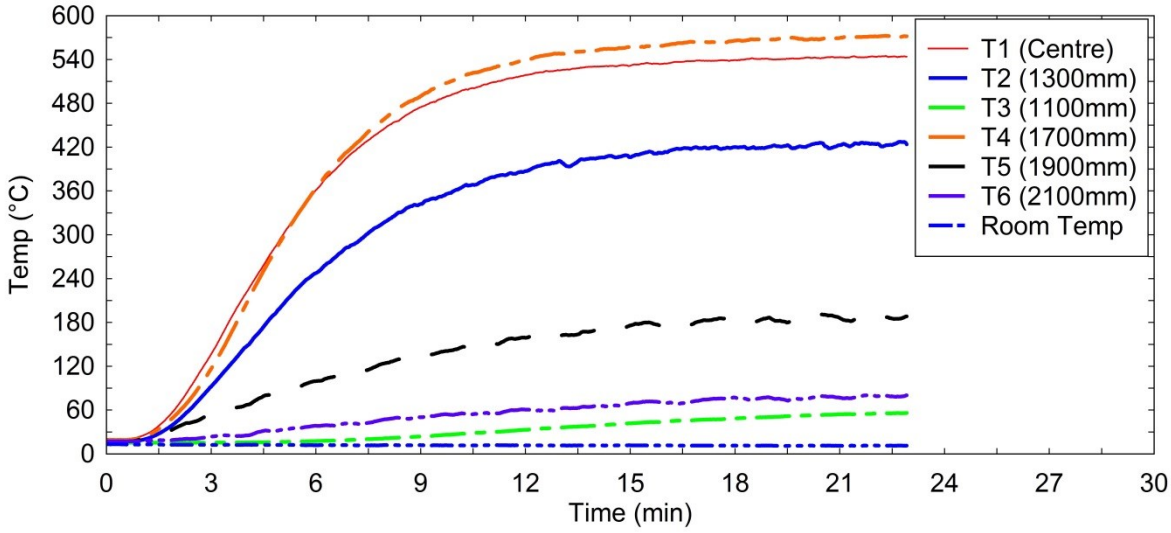

Figure 3.3.7: Recorded Temperatures during Ceramic Heating Element Trials: RHS

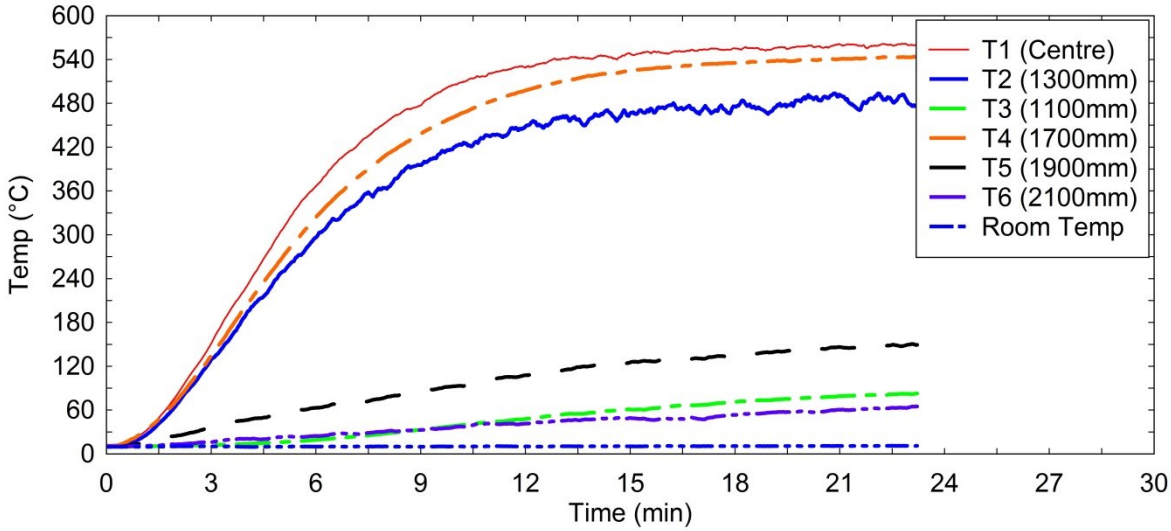

Figure 3.3.8: Recorded Temperatures during Ceramic Heating Element Trials: SHS

After completion of the pre-requisite ceramic element heating trials, the heating elements were deemed suitable for heating the columns tested during the subsequent combined ABT trials (3.3.3). However, alterations were made to the thermally insulated box included introducing a thermally insulated front panel, to increase the peak temperature, and increasing the width of the gaps at the top and bottom of the box for the columns to fit through with additional space for bending. The drop down rig was adjusted to allow the columns to bend without pressing against a horizontal steel bar on the lower end of the rig. These improvements were incorporated to the rig and thermally insulated box design prior to the combined ABT trials (3.3.3)

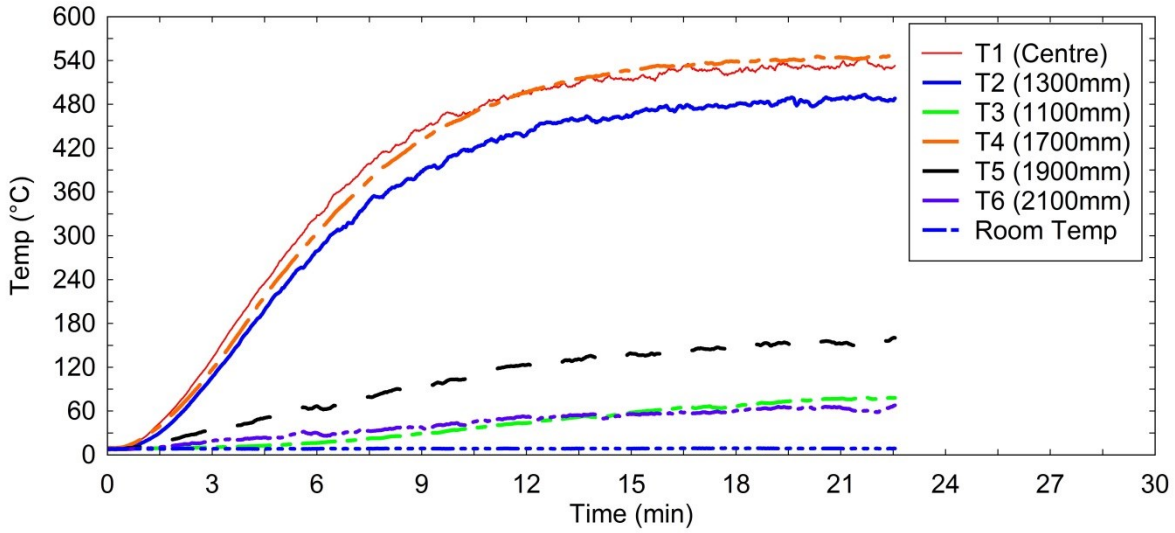

Figure 3.3.9: Recorded Temperatures during Ceramic Heating Element Trials: CHS

3.3.2 Pre-Requisite Trials: ABT Pre-Cursor Trial

The purpose the ABT pre-cursor trial was to observe the response of the selected column sections (50x25x2RHS, 25x25x2SHS and 33.7x3CHS) as cantilevers subject to a long duration blast load. If the columns showed large elastic and/or permanent deformations the selected column sections would be adopted for the full combined trials. If the columns exhibited no visible deformation during or after the pre-cursor trial alternate (weaker) column sections would have been specified for the subsequent combined ABT trials. The ABT (Fig.3.3.10) is designed to produce long duration blast loads with a peak pressure of approximately 110kPa in the 4.9m diameter section, or 55kPa in the 10.2m diameter section with a positive phase duration of approximately 150msec. It is possible to simulate explosive events equivalent to 450T of TNT at 250m. At the open end is a Rarefaction Wave Eliminator (RWE), this prevents any rarefaction (negative pressure) wave re-entering the tunnel.

Figure 3.3.10: Air Blast Tunnel, MOD Shoeburyness: Viewed from RWE Eliminator End

3.3.2.1 Design and Diagnostics

The ABT was configured to fire at maximum power producing a peak overpressure of 55kPa (10.2m section). The columns were fixed as cantilevers at the base using a sleeve and plate bolted to the concrete base of the tunnel (Fig.3.3.11). Fig.3.3.12 shows the relative column positions during the ABT pre-cursor trial.

Figure 3.3.11: 3m High Column Sections in ABT (View Facing Upstream)

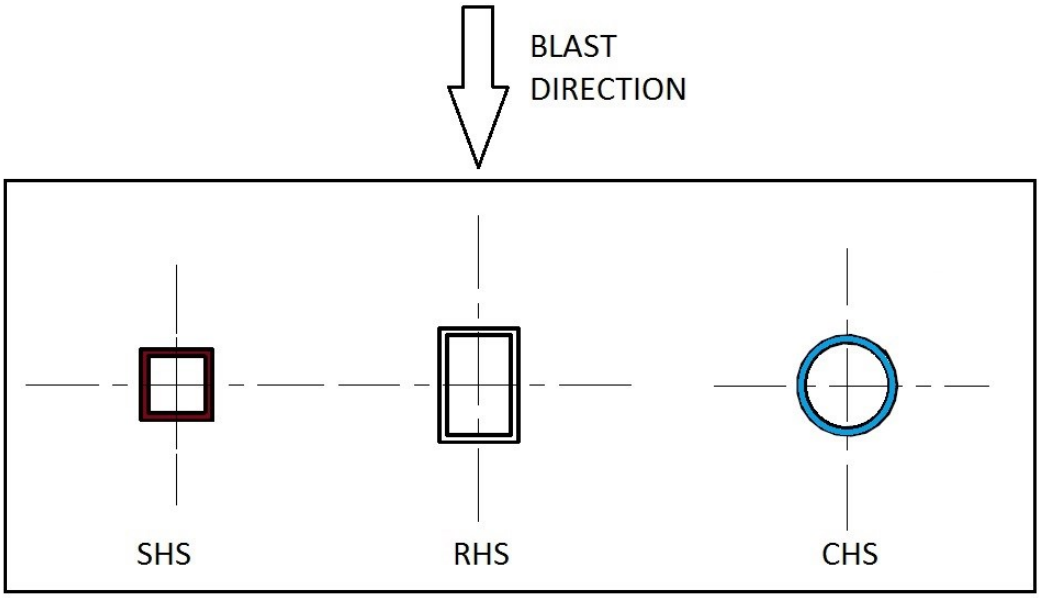

Figure 3.3.12: Post-Shot Deformation of Steel Columns in ABT

The 3m high columns were steel grade S355 J2C, cold formed (BSEN 10219) (Bsi, 2006). Incident (Endevco -8510) and dynamic (Kulite-20D) pressure gauges recorded pressure data adjacent to the columns. High speed phantom (2000 frames per second (fps)) cameras were used to record the deflections of the columns during the event. The column sections tested were specified as they were wide enough to absorb kinetic energy from the blast wave, but weak enough to exhibit significant deformations under the long duration blast loads.

3.3.2.2 Observations and Results

The incident and dynamic pressures were recorded adjacent to the columns within the 10.2m section during the trial. Fig.3.3.13 shows the recorded incident pressure, Fig.3.3.14 shows the recorded dynamic pressure (different scales).

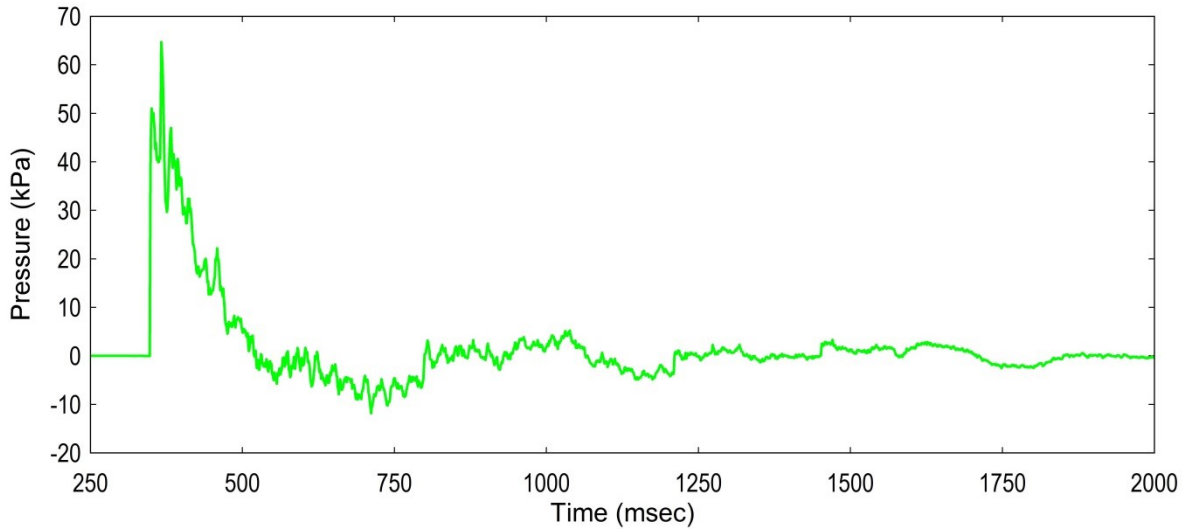

Figure 3.3.13: Incident Pressure in ABT

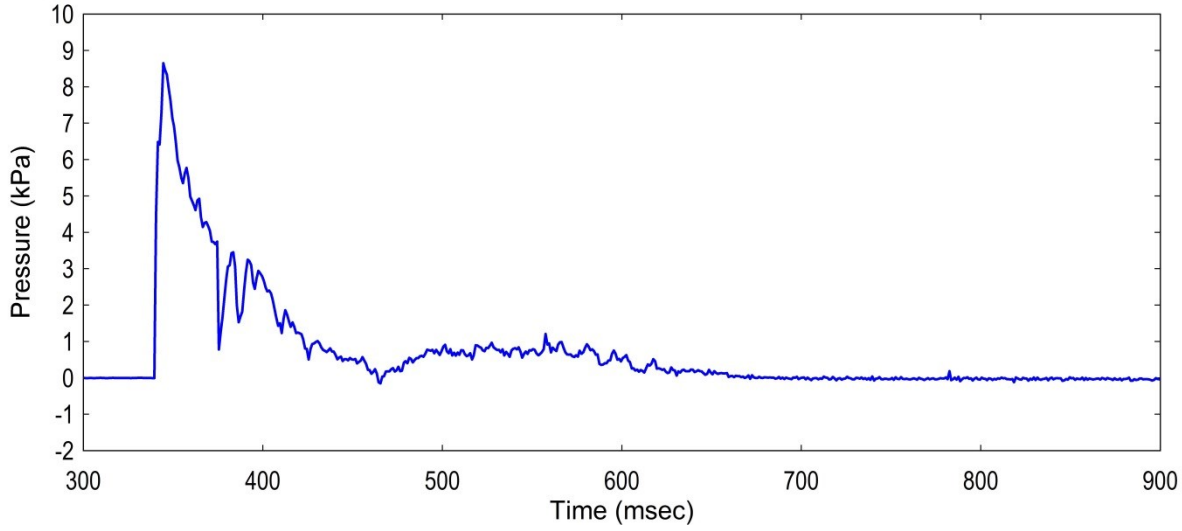

Figure 3.3.14: Dynamic Pressure in ABT

Raw data has been decimated with 1000 point average to produce these curves. The peak incident pressure was 64.67kPa (sharp peak) with a positive phase duration of 173msec. The peak dynamic pressure was 8.65kPa with a total positive phase duration of 329msec (ignoring the small negative pressure of -0.15kPa at 465msec).

The SHS deformed permanently away from the oncoming blast load with a peak of approximately 125mm at 3m height. The CHS and RHS had no visible permanent deformations. Fig.3.3.15 shows the post-shot deformations of the columns. The red column is the SHS, the blue column is the CHS and the white column (partially obscured by the CHS) is the RHS. During the pre-cursor trial the RHS was rotated so the major (stronger) axis was parallel to the blast. As the RHS exhibited no visible permanent deformation during the pre-cursor trial it was rotated 90^{o} during the subsequent ABT trials so the major axis was parallel to the direction of the blast, and therefore a higher chance of permanent deformation.

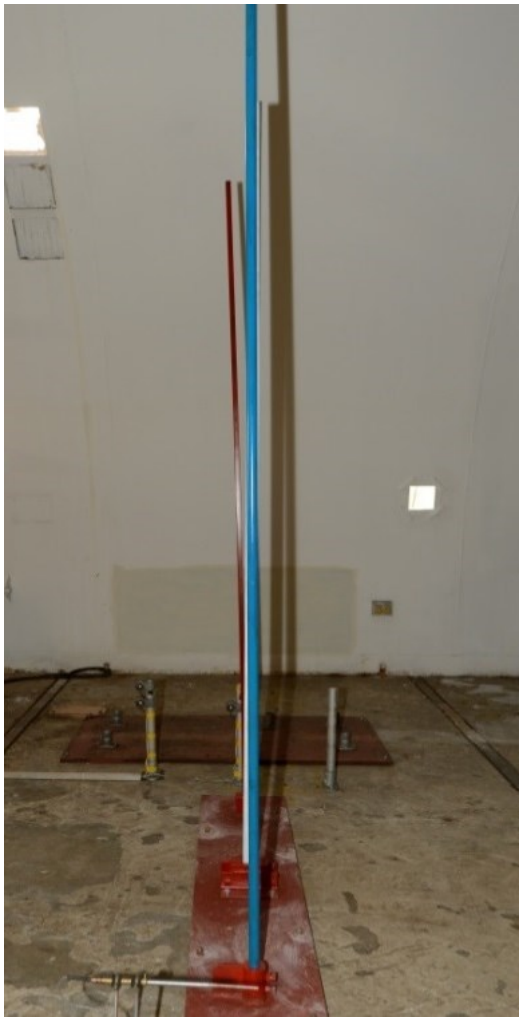

Figure 3.3.15: Post-Shot Deformation of Steel Columns in ABT

(a) 113msec **(b) 309msec** **(c) 492msec**

Figure 3.3.16a, b & c: Pre-Cursor ABT Trial High Speed Camera Stills (Times after Blast Arrival):

Deflections of the columns during the trial were recorded using high speed Phantom cameras. Figs.3.3.16a), b) and c) show stills from the video photography. Fig.3.3.16a) shows the maximum deflection of the SHS (red) at 113msec. Fig.3.3.16b shows the position of the columns at 309msec; the SHS and CHS have returned to straight. Fig.3.3.16c shows the deflections at 492msec; the SHS has deflected away from the blast again but to a lower magnitude than the first maximum at 113msec. The SHS continues to oscillate one second after the passing of the blast wave. Smaller elastic deformations are observed in both the CHS and RHS throughout the duration of the trial. The ABT pre-cursor trial was successful in demonstrating the selected column sections would deform both elastically and plastically in the ABT, providing confidence in using the same section sizes for the subsequent combined ABT trials.

3.3.3 Combined ABT Trial: Thermomechanical Response

The aim of the combined ABT trials was to observe the response of structural steel columns subject to combined compressive, thermal and long duration blast loads. Six ABT trials were undertaken with nine steel columns (S355 J2C, cold formed, BSEN 10219, (Bsi, 2006)) in each trial. The response of three different hollow steel sections was investigated: 50x25x2RHS, 25x25x2RHS and 33.7x3CHS.

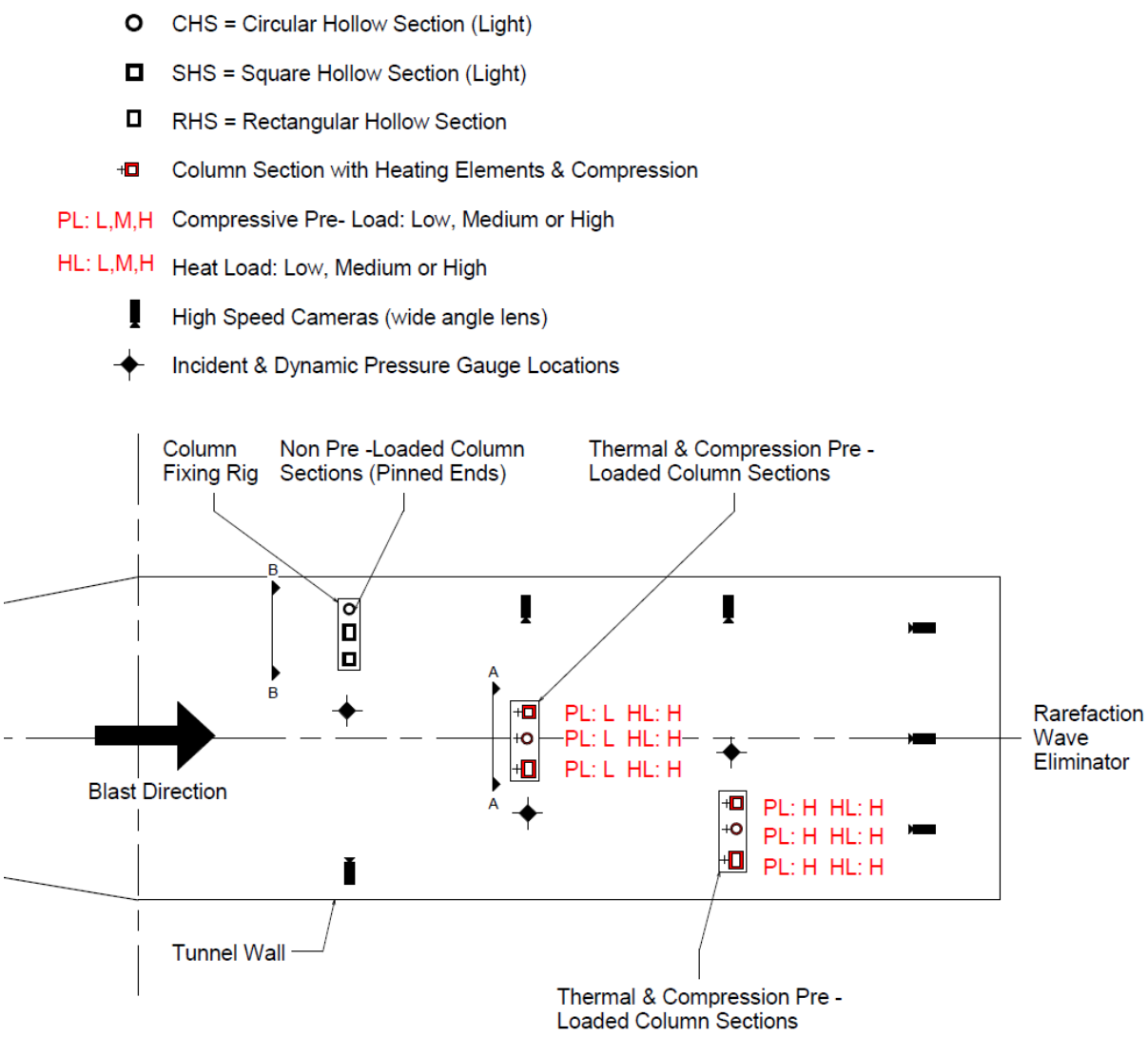

Figure 3.3.17: ABT Trial: Plan View

The columns were subject to compressive and thermal loads which varied throughout the six trials. Three columns per trial were pinned at both ends with no thermal or compressive load. The tunnel was calibrated to fire at maximum power, with a 55kPa target pressure for each trial. Fig.3.3.17 shows a plan view of the ABT trial with column rigs positioned in the 10.2m diameter section. The configuration of the six trials differed with varying compressive (PL) and thermal (HL) loads.

3.3.3.1 Design and Diagnostics

Three testing rigs were designed and constructed for the ABT trials. Two rigs applied thermal and compressive loads to the columns and the third rig held the columns with pinned connections at both ends with no additional thermal or structural loads. The rigs were bolted into the concrete tunnel base with additional bracing enabling re-use for all six trials. The thermal and compression rigs had a smaller drop down rig within each frame. The drop down rigs had thermally insulated boxes fixed over the central 500mm section of the columns (Fig.3.3.18). Each rig held three columns (RHS, SHS and CHS).

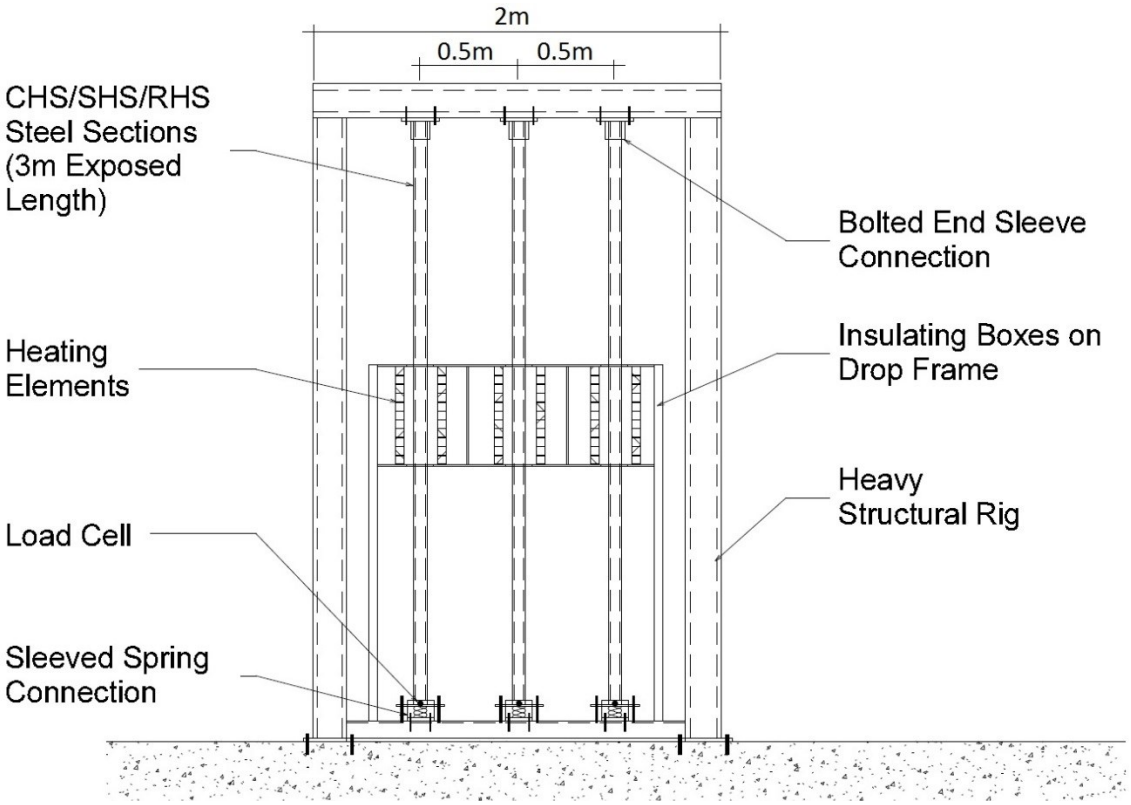

Figure 3.3.18: ABT Trial: Compression and Thermal Rig Elevation

The two compression and thermal rigs used heavy duty compression springs (IST "Closed and Ground" (IST, 2015) in BS5126 Patented Carbon (Bsi, 1991)) to apply compressive load to the columns. The springs were placed inside circular sleeves at the base of each column. At each spring connection a 250mm (l) 50mm (w) x 10mm (t) steel bar with two 22mm diameter threaded holes at 200mm spacing was placed above the spring sleeve. Two 22mm diameter bolts fixed (welded) to the base of the frame were positioned either side of spring sleeve. The spring was torqued by tightening 22mm diameter nuts on the bolts through the threaded holes against the 10mm thick steel bar. Each column was subsequently fixed in place using sleeve connections welded to the steel bar at the base and the top (the spring was only at the base connection). Once the columns were in place the nuts on the 22mm diameter bolts were loosened therefore transferring the spring load into the columns. Fig.3.3.19 shows the plan and side view of the spring sleeve base connection detail for the RHS and Fig 3.3.20 shows the base of a compression and thermal rig (columns in place) with the spring sleeve connections; the bolts used to torque each spring are shown either side of the circular sleeve. Figs.3.3.21 to 3.3.22 show the sleeved connection detail at the top of each column used in the compression and thermal rigs.

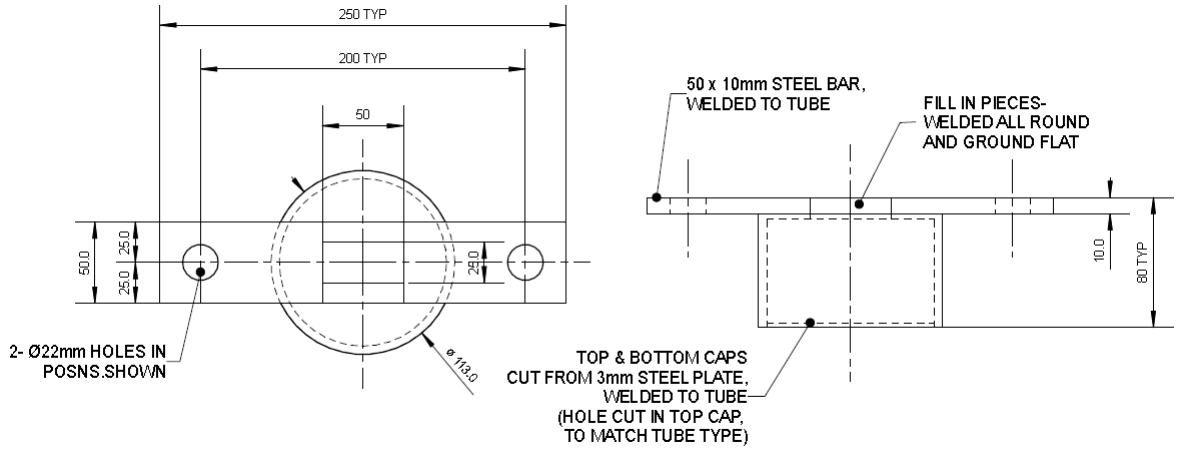

Figure 3.3.19: ABT Trial: Spring Sleeve Detail of for Compression & Thermal Rig: RHS

Figure 3.3.20: Compression Sleeves at Base of Columns

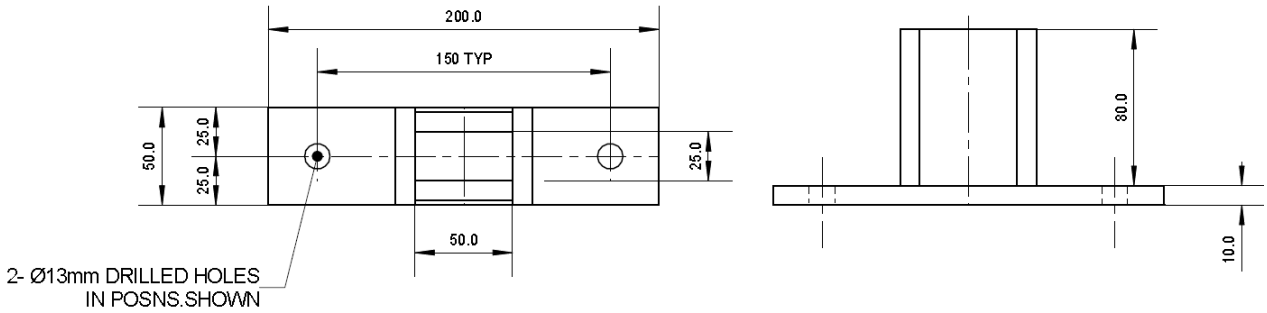

Figure 3.3.21: ABT Trial: Top Sleeve Detail for Compression & Thermal Rig: RHS

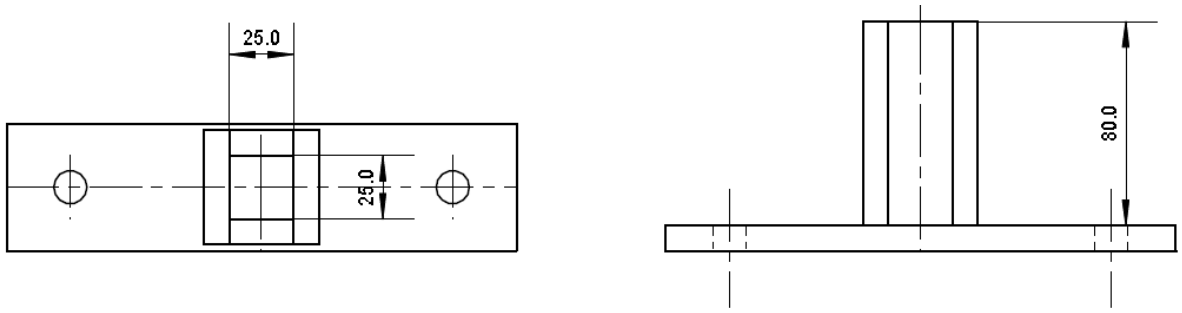

Figure 3.3.22: ABT Trial: Top Sleeve Detail for Compression & Thermal Rig: SHS

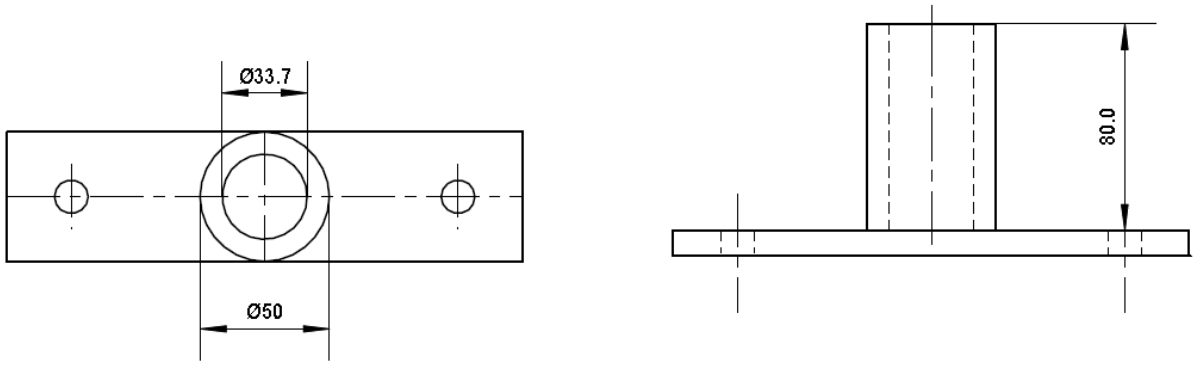

Figure 3.3.23: ABT Trial: Top Sleeve Detail for Compression & Thermal Rig: CHS

The third rig held the structural columns with sleeved pinned connections at the top and bottom (Figs.3.3.24-3.3.26). The sleeved pinned connections were designed with a 20mm diameter hole at mid-height to allow a bolt to pass through the column. To allow “pinned” rotation of the column at the bolt location there was a 10mm gap between the column and the inside surface of the sleeve. The sleeves were made using 5mm thick steel.

During trials one to three the columns were tested with no additional wings in order to directly compare results to the columns in the compression and thermal rigs. For trials three to six the columns were tested with 250mm wide, 3mm thick steel wings (Hot Rolled Sheet Steel: BS EN 10025, 2004 S275JR,(BSi, 2004)) fitted over the central 1m length of the columns. The wings were fitted to reproduce the additional effect of cladding adjacent to structural columns. The wings, fitted with u-bolts, were designed to transmit a higher area of blast load to the columns resulting in higher deflections and stresses. Fig.3.3.24 shows the pinned column rig, Fig 3.3.26 shows the pinned rig with columns fitted with wings and Fig.3.3.25 shows the pinned sleeve end connection used at the top and bottom of the RHS.

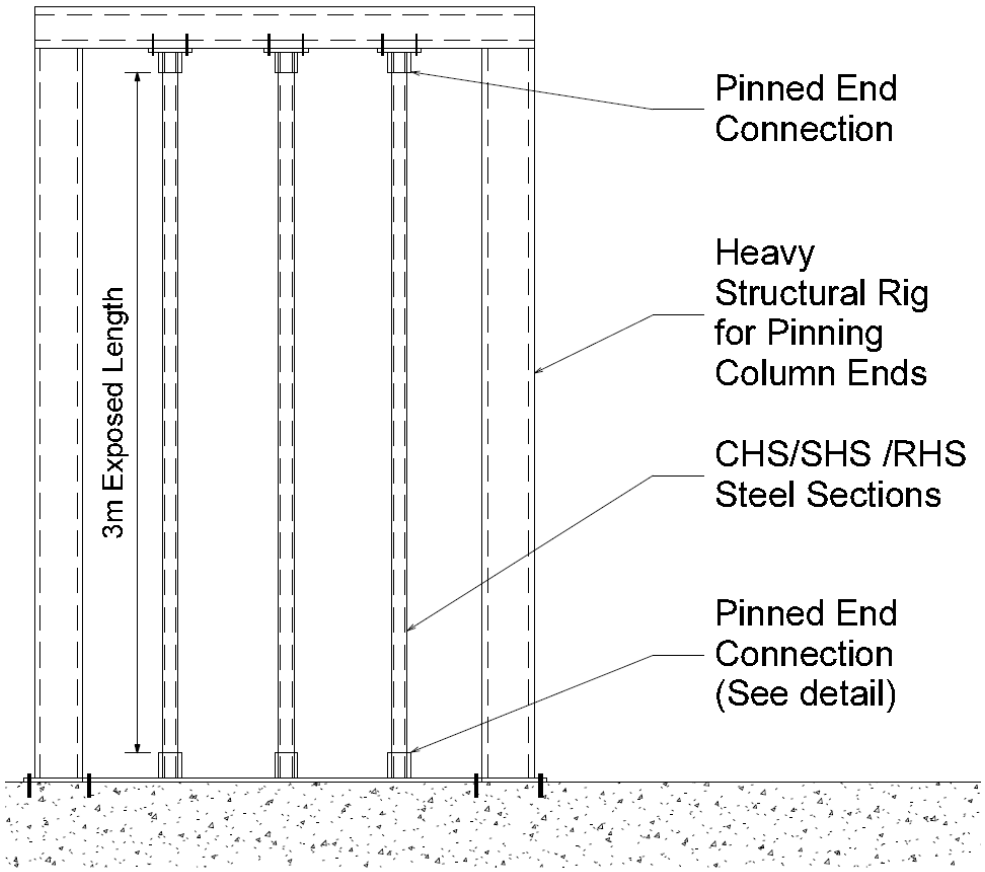

Figure 3.3.24: ABT Trial: Pinned Rig Elevation

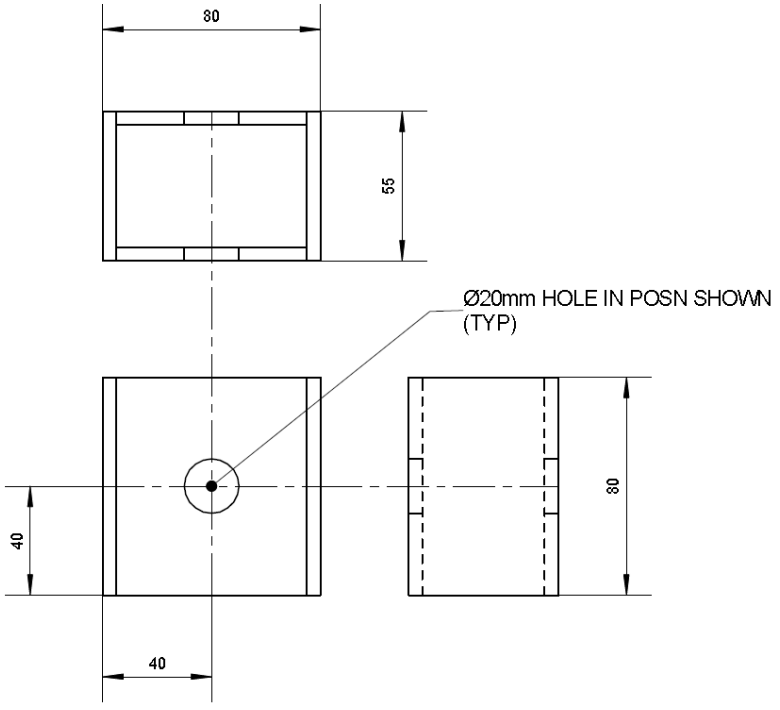

Figure 3.3.25: ABT Trial: Sleeve Detail for Pinned Rig: RHS

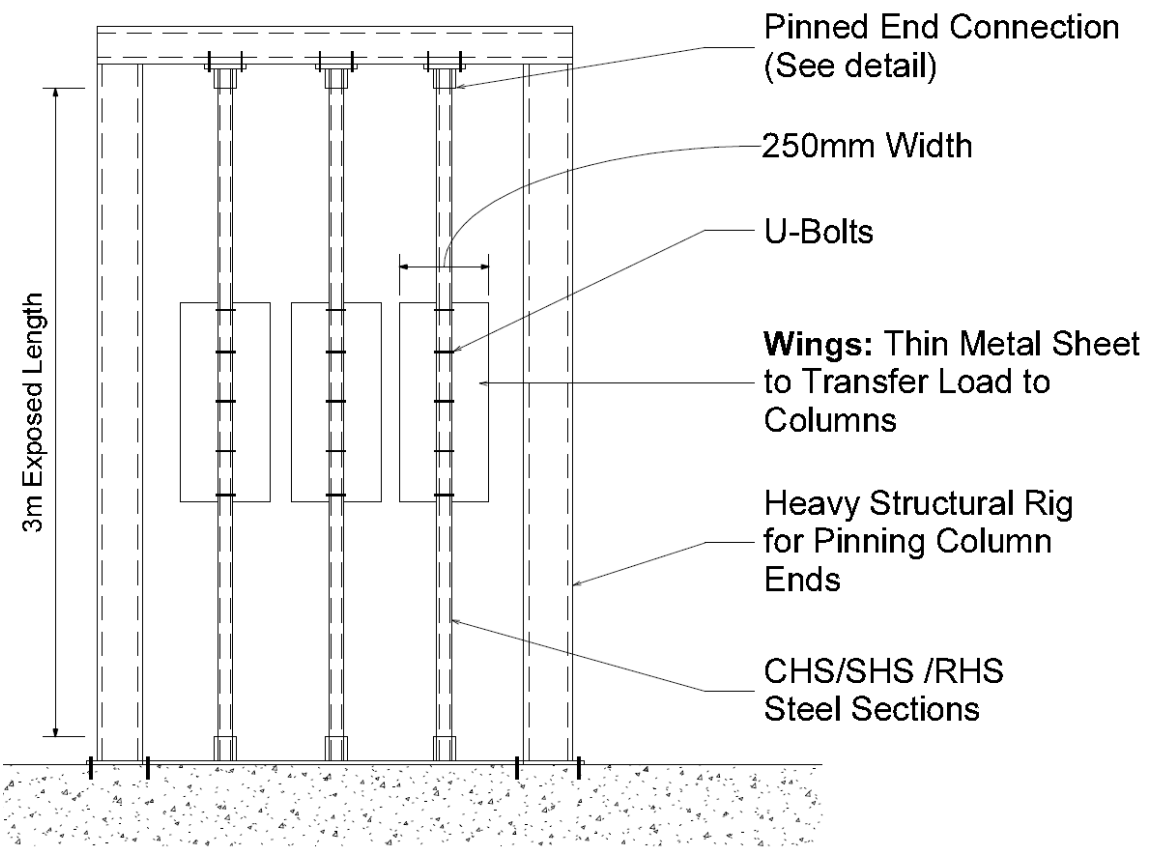

Figure 3.3.26: ABT Trial: Pinned Rig with Column Wings Elevation

3.3.3.1.1 Heavy Duty Springs

Heavy duty springs (IST "Closed and Ground" (IST, 2015) in BS5126 Patented Carbon (Bsi, 1991)), were mounted inside sleeves at the base of the columns on the compression and thermal rigs. The springs applied compressive loads equivalent to 50%, 75% and 90% of the buckling capacity of each column section. This represented a range of compressive stresses typical of columns in service or near failure therefore replicating the typical stresses induced in columns in buildings and structures whilst in use.

Table 3.4 shows the compressive loads which were applied to the columns using the heavy duty springs. The buckling loads for each column section were determined using the "interactive blue book" (Tata, 2016). Load cells (Zemic BM24R-C3-1T-3B (Zemic, 2015)) were used to record the actual compressive load applied at the base of each column. The heavy duty springs were torqued to the required value using 22mm diameter threaded bolts either side of the column (Fig.3.3.20).

Table 3.4: Applied Compressive Loads

Column Section	Length	Low (50% Buckling)	Med (75% Buckling)	High (90% Buckling)
25 x 25 x 2 SHS	3m	1.54 kN	2.3 kN	2.8 kN
50 x 25 x 2 RHS	3m	2.86 kN	4.28 kN	5.14 kN
33.7 x 3 CHS	3m	3.48 kN	5.2 kN	6.26 kN

3.3.3.1.2 Ceramic Heating Elements

Ceramic heating elements were used to heat the structural columns to varying temperature levels; high, medium, low and none, over the six trials. The high, medium and low target temperatures were initially set to 550°C, 450°C and 350°C; however, due to varying environmental temperatures the ceramic elements were not able to reach and maintain these temperatures on each column over the six trials. The high, medium and low temperature values were subsequently used as approximate target values. Three thermocouples (K-type) were placed at 1250mm, 1500mm and 1750mm heights on the surface of each heated column during the trials. There were eight ceramic heating elements fixed inside a thermally insulated box positioned over each column. The boxes were 500mm high x 400mm wide. The heating elements were positioned to heat the columns uniformly across the section width.

(a) **(b)**

Figure 3.3.27a & b: Thermally Insulated Boxes: First Trial (a), Subsequent Trials (b), Camera View Facing Downstream

A drop down rig held three thermally insulated boxes in position over the centre of the columns during the heating phase. The drop down rig was held upright using elastic cord and high strength

wires. During each trial the rigs were dropped down after the columns had reached the target temperatures before the arrival of the blast wave. The rigs were dropped down using remote controlled cutting of the high strength wires allowing the elastic cord to pull the rig downstream on to cushioning air bags. During the first trial the target temperatures were not reached, therefore the design of the thermally insulated box was improved for trials two to six by introducing an insulated front panel to increase the maximum achievable temperature. Figs.3.3.27a) and b) show the thermally insulated box positioned over the centre of the columns for the first trial (a) and subsequent trials (b)

Table 3.5 shows a detailed trial overview for the six trials with the column types and levels of thermal and compressive load (*Actual applied compressive loading in parentheses). The order of the trials differs from the "round/trial number" referred to in the overview and other trial documentation. This re-arrangement of the trial order was to match the target temperatures to the actual temperatures reached during each trial.

Table 3.5: Trial Schedule

Final Trial Schedule										
Order	Round Number	Rig 1	Rig 2				Rig 3			
		Pinned Only	Steel	Compression	kN	Temp	Steel	Compression	kN	Temp
4th	1	Yes + Wings	Square	low	1.54	High	Square	High	2.8	High
		Yes + Wings	Rect	low	2.86	High	Rect	High	5.14	High
		Yes + Wings	Round	low	3.48	High	Round	High	6.26	High
2nd	2	Yes	Square	Med	2.3	Med	Square	low	1.54	None
		Yes	Rect	Med	4.28	Med	Rect	low	2.86	None
		Yes	Round	Med	5.2	Med	Round	low	3.48	None
5th	3*	Yes + Wings	Square	Med	2.3 (4.28)	High	Square	low	1.54 (2.86)	Med
		Yes + Wings	Rect	Med	4.28 (5.2)	High	Rect	low	2.86 (3.48)	Med
		Yes + Wings	Round	Med	5.2 (2.3)	High	Round	low	3.48 (1.54)	Med
3rd	4	Yes	Square	Med	2.3	None	Square	High	2.8	Med
		Yes	Rect	Med	4.28	None	Rect	High	5.14	Med
		Yes	Round	Med	5.2	None	Round	High	6.26	Med
1st	5	Yes	Square	High	2.8	Low	Square	low	1.54	Low
		Yes	Rect	High	5.14	Low	Rect	low	2.86	Low
		Yes	Round	High	6.26	Low	Round	low	3.48	Low
6th	6*	Yes + Wings	Square	Med	2.3 (4.28)	Low	Square	High	2.8 (5.14)	None
		Yes + Wings	Rect	Med	4.28 (5.2)	Low	Rect	High	5.14 (6.26)	None
		Yes + Wings	Round	Med	5.2 (2.3)	Low	Round	High	6.26 (2.8)	None

Figs.3.3.28a) and b) show the three rigs holding the structural columns in position prior to the fourth trial (round 1) and first trial (round 5). The downstream view shows the rigs positioned as followed: Left: Rig 1 (pinned), Centre: Rig 2 (compression and thermal) and Right: Rig 3 (compression and

thermal). Figs.3.3.29a) and b) show the pinned rig prior the fourth trial (round 1) and first trial (round 5). Figs.3.3.30a) and b) show the front (facing downstream) and side elevation (downstream direction: left) of the compression and thermal rig (number two) prior to the first trial (round 5). Once heating of the columns had taken place the thermal boxes dropped onto air-filled cushioned bags to minimise damage to heating elements. An angled wooden box was positioned upstream of the dropped boxes to divert the blast wave over the boxes whilst in a horizontal position.

(a)

(b)

Figure 3.3.28a & b: Overview of Three Rigs in ABT Trials: Round 1 (a), Round 5 (b)

(a) **(b)**

Figure 3.3.29a & b: Pinned Rig in ABT Trials: Round 1 (a), Round 5 (b)

(a) **(b)**

Figure 3.3.30a & b: Front (a), and Side (b) View of Compression and Thermal Rig (#2): Round 5

Incident (Endevco-8510) and dynamic (Kulite-20D) pressure gauges were positioned within the tunnel adjacent to each rig. A reflective (Endevco) pressure gauge was mounted to each heavy structural rig facing the oncoming blast load. Fig.3.3.31 shows a schematic drawing of the gauge

positions in relation to the rigs. Load cells were positioned between the springs and base of the columns to measure the magnitude of the applied compressive load throughout the trials. Six high speed (Phantom) cameras (3000 frames per second) were positioned in the tunnel to record the trial, Fig.3.3.17 shows the positions of the cameras in relation to each rig. Two high speed cameras per rig were positioned to record column deflections parallel and perpendicular to the blast direction. The cameras recording deflections perpendicular to the blast direction were placed downstream (lens facing upstream), and the cameras recording deflections parallel to the blast direction were placed adjacent to each rig. Post shot, in-situ, mid-span measurements were taken using a rule and spirit level. Deflection measurements were taken using Vernier calipers along the length of each column after removal from the rigs.

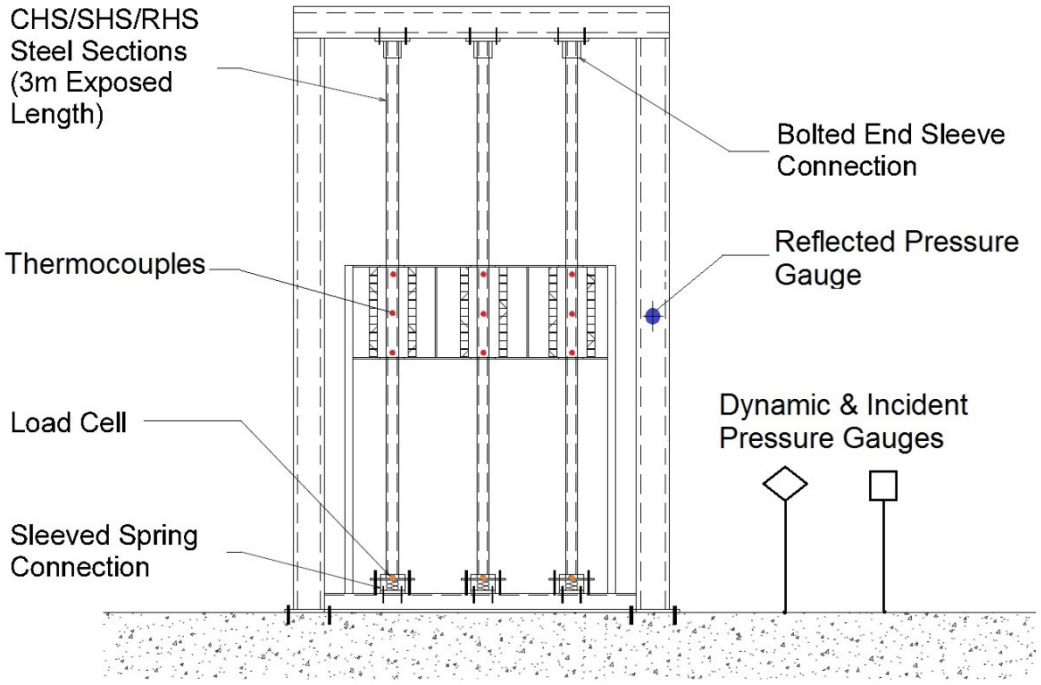

Figure 3.3.31 Schematic Drawing of Rig with Gauge Locations

3.3.3.2 Observations and Results

The six trials were successfully undertaken and large data sets were collected recording the deflections of the columns, temperatures, compressive loads and pressure-time histories. Initial observations showed the RHS deformations were the largest, the SHS exhibited smaller deformations and the CHS had the lowest.

After the first trial, improvements were made to the thermally insulated boxes to achieve higher peak temperatures by introducing a front panel. During the second trial the thermal box on rig two (medium thermal and compressive load) did not drop after the high strength wire was cut, prior to the arrival of the blast wave. At the arrival of the blast the drop rig fell back damaging the heating

elements. The data recorded from this rig during the second trial (round 2) is not presented in these results due to lack of parity with the other rigs and trials. After inspection of the high speed video for rig two, round two, observations showed the RHS exhibited large lateral deformations during the thermal loading phase. The RHS pressed against the thermal box preventing the box dropping on to the cushioned air bags upon cutting of the wire, prior to the blast. Further improvements were made to the thermal boxes by widening the gap at the top and bottom of each box for the columns to fit through and increasing the strength of the elastic cord. Repairs to the damaged thermal boxes were made using a new set of heating elements.

Nominal pin connections at the top and bottom of the columns in the pinned rig were orientated parallel to the blast direction. A 20mm diameter bolt (acting as a pin) passed through each sleeve and column parallel to the blast. This was an installation error as the bolts should have passed through the sleeves and columns perpendicular to the blast direction; however this did not affect the relative rotation of each column. Inspection of the high speed video showed that the columns responded as with pinned or near pinned connections at both ends. During the fourth trial a bolt acting as a pin connection sheared off a CHS fitted with wings.

3.3.3.2.1 Pressure History

The target incident peak pressure for the six trials in the 10.2m section of the ABT was 55kPa. Fig.3.3.32 shows the incident pressures recorded at each rig location during each trial, the raw gauge data was decimated with 8000 points average. Fig.3.3.33 shows the raw gauge data recorded at rig one during trial one (round “R” 5). There were eighteen incident pressure gauge recordings in total; the gauges showed good reproducibility of pressures across the six trials at each rig location. One gauge (trial 4, (R1) rig 1) recorded uncertain results with a large negative pressure of approximately -30kPa at 1400msec. This gauge data was subsequently not used during the trial analysis. Fig.3.3.34 shows a schematic plan drawing of the 10.2m section of the ABT with the rig numbers and locations.

The peak recorded incident pressures at each rig location across the six trials are shown in Table 3.6 (decimated with 8000 points average). The peak pressure taken from the raw gauge data at rig one during the first trial (R5) was 60.31kPa. The durations of the recorded incident overpressure at each rig during trial six (R6) were: Rig 1 = 189.5msec, Rig 2 = 165.4msec, Rig 3 = 144msec. There was an observed decrease in the duration of the positive pressure phase further away from the oncoming blast. There was also an observed decrease in peak pressure between rig one and rig two, at rig three there is a slight increase for the majority of the trials.

Table 3.6: Peak Incident Pressures (kPa)

Trial	Rig 1	Rig 2	Rig 3
1 (R5)	46.075	46.787	47.573
2 (R2)	48.936	44.997	47.132
3 (R4)	47.293	44.438	46.736
4 (R1)	47.660	47.439	47.669
5 (R3)	52.054	50.705	46.159
6 (R6)	51.630	44.240	46.680
Average	**48.941kPa**	**46.434kPa**	**46.992kPa**

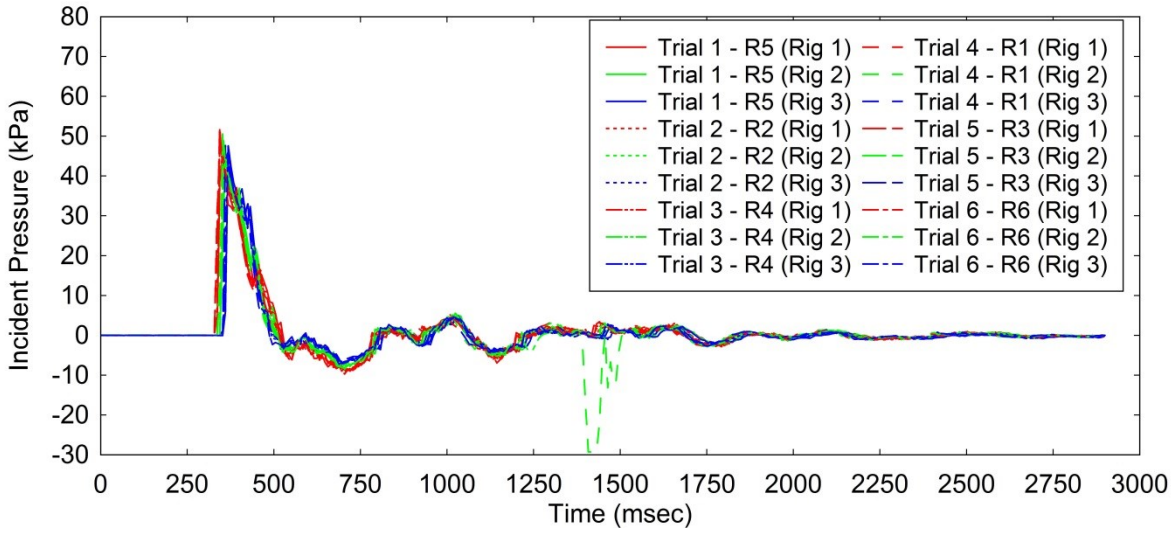

Figure 3.3.32: Incident Pressure (All Trials and Rigs, Decimated 8000 Average)

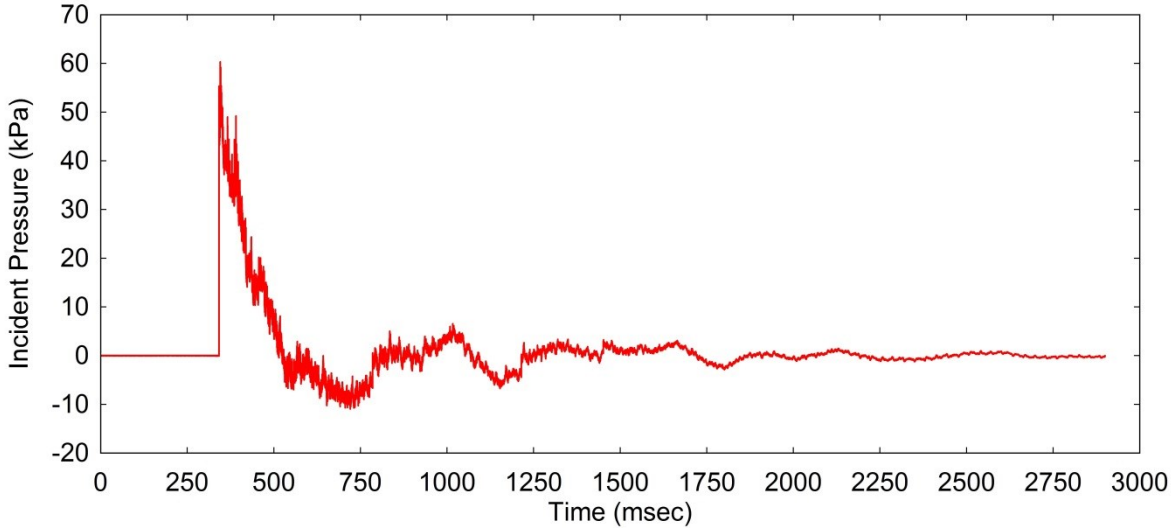

Figure 3.3.33: Incident Pressure (Trial 1 (R5), Rig 1, Raw Data)

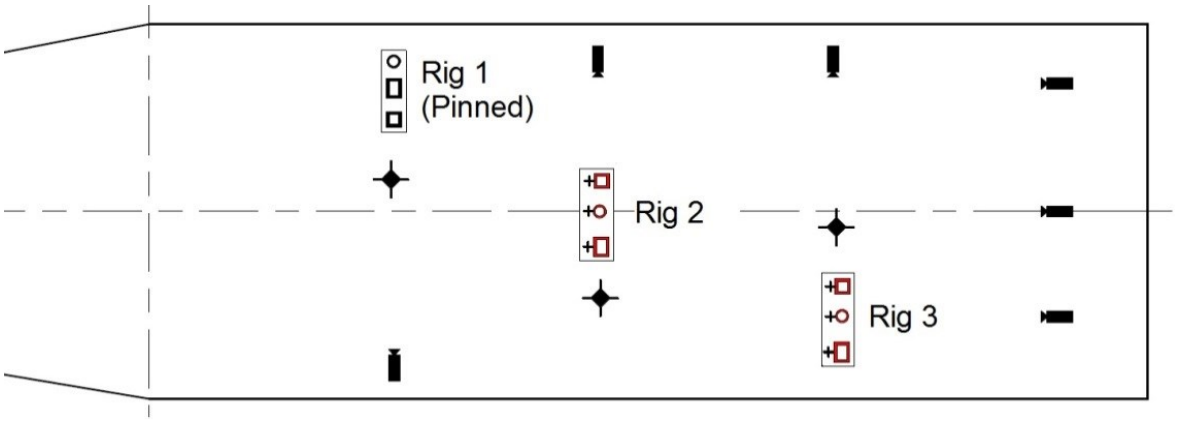

Figure 3.3.34: Incident Pressure (All Trials and Rigs, Decimated 8000 Average)

Fig.3.3.35 shows the recorded dynamic pressures at each rig location during the six trials. Due to an electrical gauge malfunction there were errors in the recorded data at rig two for trials three (R4), four (R1) five (R3) and six (R6). These errors were only observed during analysis of the data subsequent to the trials. This data has been omitted from Fig. 3.3.35 and Table 3.7. There was a good reproducibility of dynamic pressures across the trials. Fig.3.3.36 shows the raw data of the recorded dynamic pressure at rig one during the first trial (R5). The peak recorded dynamic pressures are shown in Table 3.7 (8000 points decimated average). The peak pressure from the raw gauge data at rig one during the first trial (R5) is 24.17kPa. This peak is caused by significant noise recorded by the dynamic gauge. The durations of the recorded dynamic pressure at each rig during trial one (R5) were: Rig 1 = 386msec, Rig 2 = 376.8msec, Rig 3 = 347.6msec. Similarly to the incident pressure, there is a decrease in the duration of the positive phase away from the oncoming blast. The average peak dynamic pressure reduces between rig one and rig two, but increases slightly at rig three.

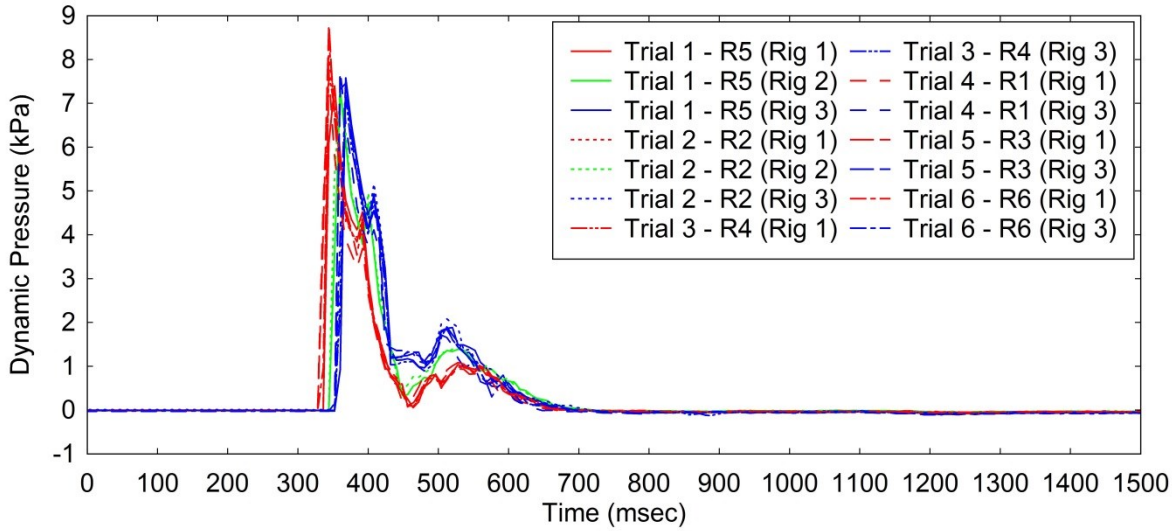

Figure 3.3.35: Dynamic Pressure (All Trials, Decimated 8000 Average)

Table 3.7: Peak Dynamic Pressures (kPa)

Trial	Rig 1	Rig 2	Rig 3
1 (R5)	7.398	7.327	7.581
2 (R2)	8.005	7.311	7.536
3 (R4)	7.706	n/a	7.181
4 (R1)	7.701	n/a	7.753
5 (R3)	8.793	n/a	7.459
6 (R6)	8.411	n/a	7.561
Average	**8.002kPa**	**7.319kPa**	**7.512kPa**

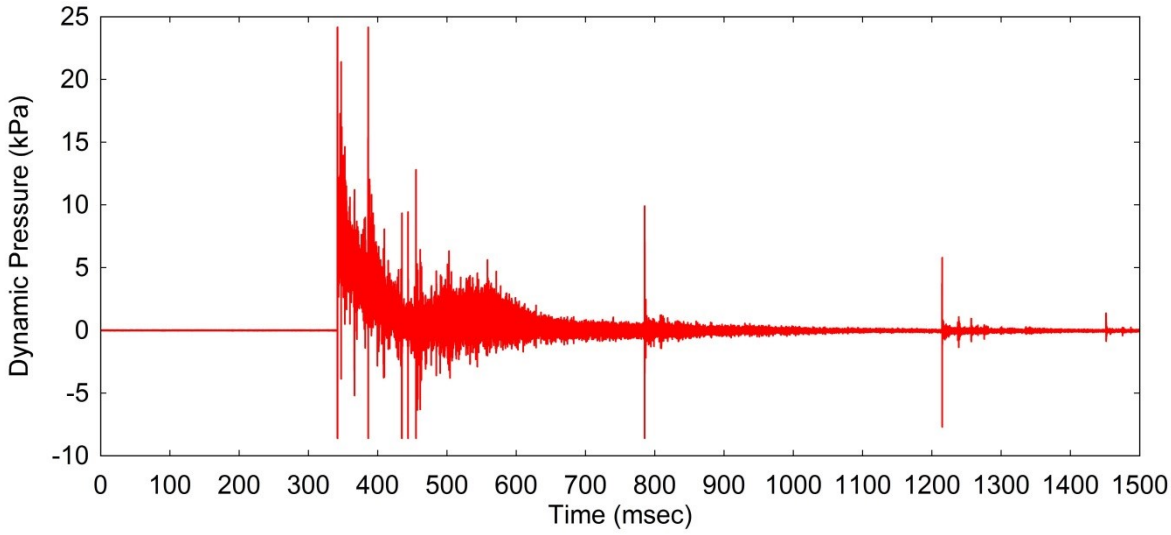

Figure 3.3.36: Dynamic Pressure (Trial 1 (R5), Rig 1, Raw Data)

Fig.3.3.37 shows the recorded reflected pressures at each rig location for all six trials with good reproducibility of reflected pressures across the trials. Fig.3.3.38 shows the raw data of the recorded reflected pressure at rig one during the first trial (R5). Fig.3.3.39 shows a detailed plot of the sharp peak reflected pressure at 341.25msec, the peak pressure recorded was 157.332kPa. The total duration of the initial sharp peak (before settling at 50.35msec) was 0.95msec. There are two discernible peaks forming the initial sharp peak, the duration of the first peak was 0.1msec.

Table 3.8: Peak Reflected Pressures (kPa)

Trial	Rig 1	Rig 2	Rig 3
1 (R5)	55.453	55.460	56.053
2 (R2)	64.114	52.864	55.252
3 (R4)	62.763	52.417	55.119
4 (R1)	55.210	56.125	55.228
5 (R3)	59.911	60.977	61.755
6 (R6)	62.414	58.923	54.237
Average	**59.978**	**56.128**	**56.274**

The peak recorded reflected pressures are shown in Table 3.8 (8000 points decimated average). The positive phase durations of the recorded reflected pressure at each rig during trial one (R5) were: Rig 1 = 190.8msec, Rig 2 = 177msec, Rig 3 = 172.8msec. There was also a decrease in the duration of the positive phase at each rig location further downstream. The average peak reflected pressure reduced between rig one and rig two, but slightly increased at rig three. This trend was repeated across the three types of pressure gauge.

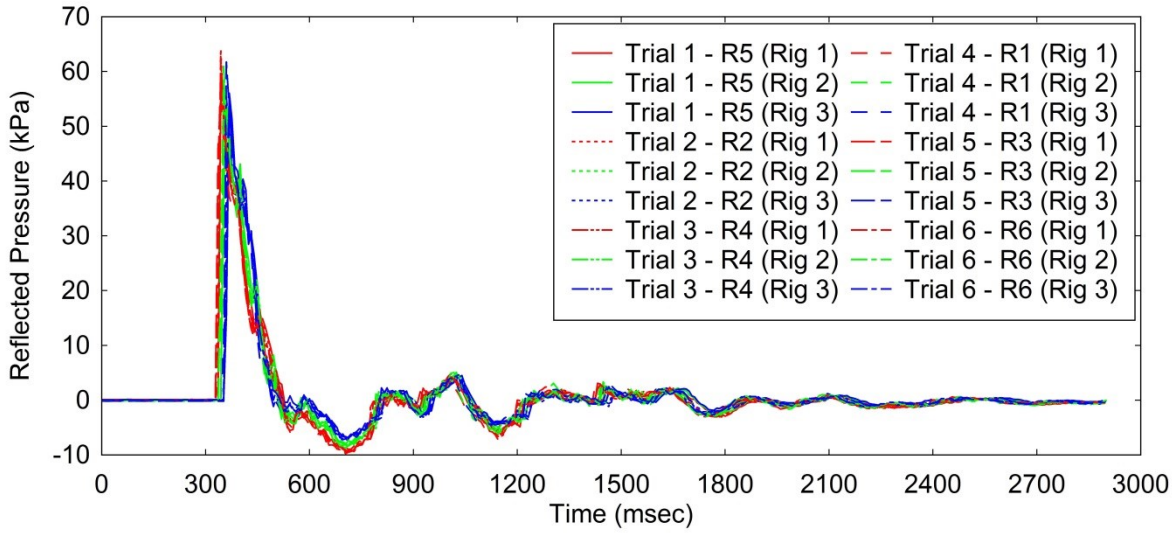

Figure 3.3.37: Reflected Pressure (All Trials and Rigs, Decimated 8000 Average)

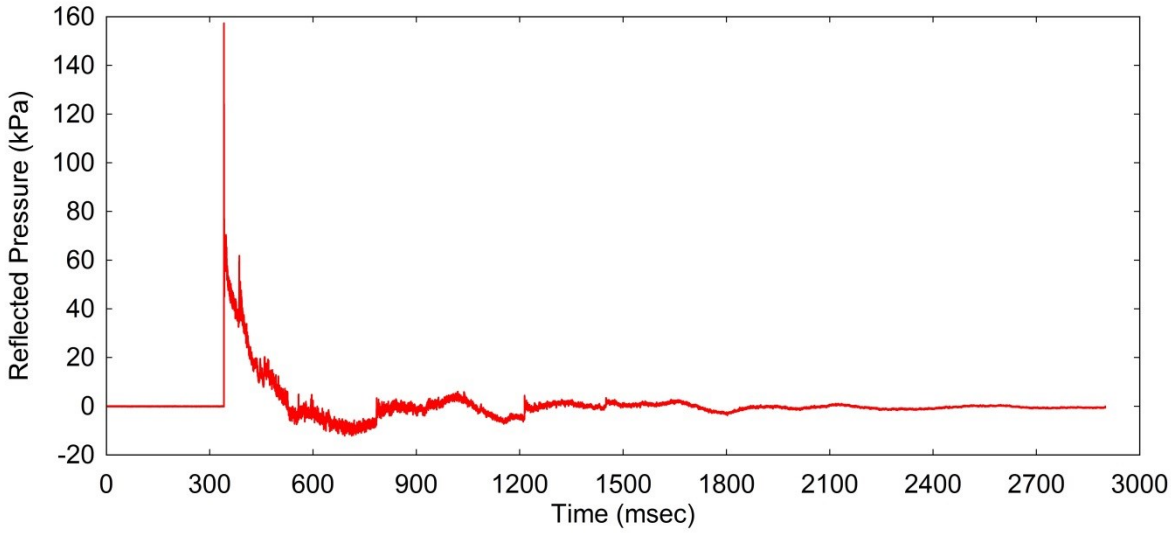

Figure 3.3.38: Reflected Pressure (Trial 1 (R5), Rig 1, Raw Data)

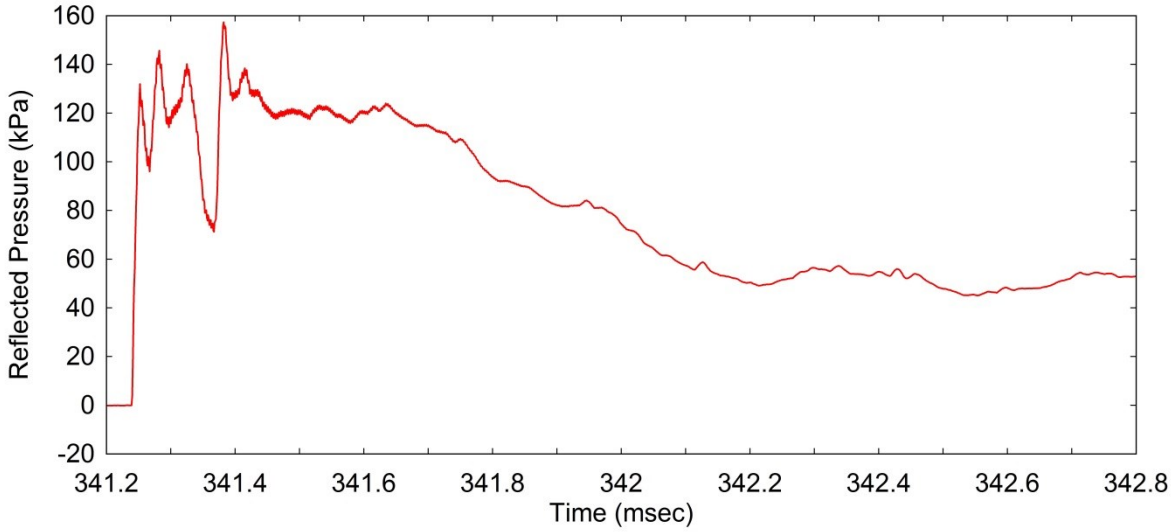

Figure 3.3.39: Reflected Pressure Peak (Trial 1 (R5), Rig 1, Raw Data)

3.3.3.2.2 Temperature History

Fig.3.3.40 shows the recorded temperatures during the heating phase at rig 2 during trial 2 (R2) (1000 point decimated average). Recorded temperatures on arrival of the blast (at 340msec approx.) and post blast are shown in Fig.3.3.41 (8000 point decimated average). The full recorded temperatures across the thermal rigs and trials are shown in Appendix B. There were no recorded temperatures during the initial heating phase of the first trial (R5).

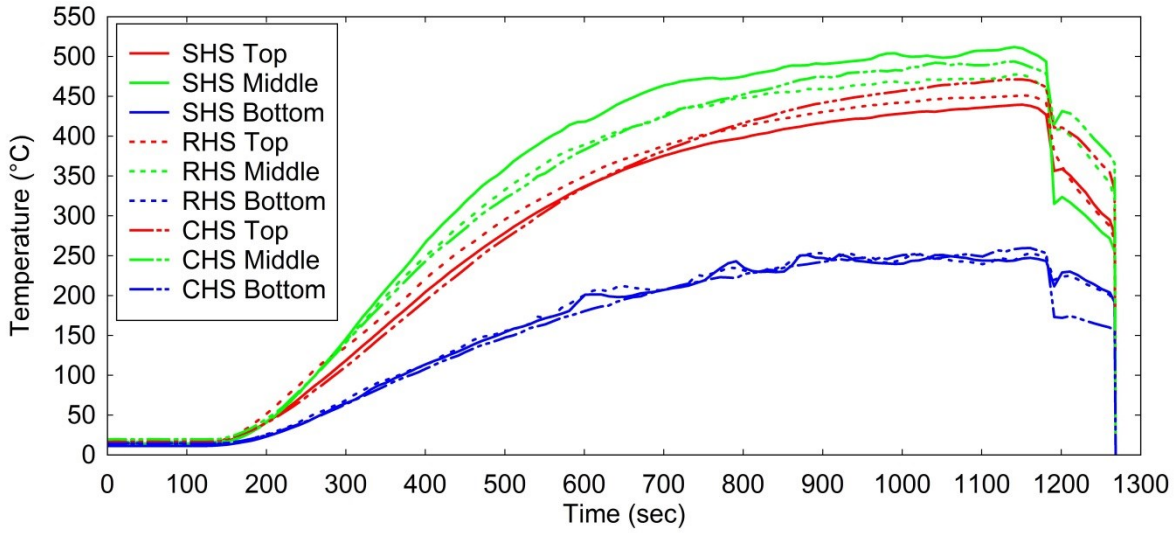

Figure 3.3.40: Pre-Shot Recorded Temperature (Trial 2, Rig 2, 1000 Decimated)

Table3.9 shows the peak recorded temperatures at each thermocouple position on each column during the six trials. The maximum pre-blast temperature is not equal to the temperature at the blast arrival due to cooling of the columns between dropping of thermal boxes and arrival of blast wave. Thermal boxes were dropped approximately eight seconds before the arrival of the blast to ensure the boxes were fully dropped and to minimise the cooling before the arrival of the blast.

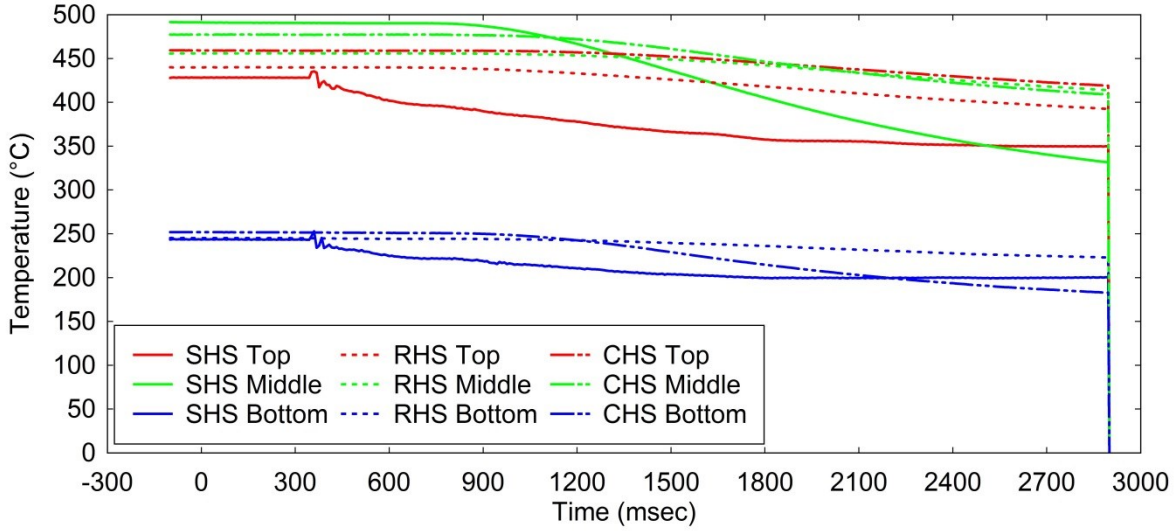

Figure 3.3.41: Post-Shot Recorded Temperatures (Trial 2, Rig 2, 8000 Decimated)

All thermocouples at 1500mm (mid) height (other than at 1750mm on the RHS during fourth trial (R1) and at 1750mm on the SHS during sixth trial (R6)), recorded the maximum temperature on each column. Ceramic elements were unable to achieve constant temperatures between the two rigs and across the trials due to the differing environmental conditions on each day and within the tunnel. The low, medium and high target temperatures were set at the start of each trial; however,

the target temperatures were often not reached. The maximum temperature recorded during trial four (R1) (rig two, CHS) was 483.8°C (for a "high" target temperature), for an equivalent "medium" target temperature (trial three (R4), rig three, CHS) the maximum temperature recorded was 531.4°C. Despite difficulties in achieving specific high, medium and low target temperatures there was a broad range of temperatures recorded during the trials. Therefore a large range of steel material degradation levels and structural response to the heat loads occurred and was observed.

Table 3.9: Maximum Temperatures of Steel Columns

Trial Order # (Round#)	Thermocouple Position	Maximum Pre-Shot Temperature Reached (°C)					
		Rig 2			Rig 3		
		RHS	SHS	CHS	RHS	SHS	CHS
First (5)*	1750mm	262.5	247.6	274.6	298.0	352.9	319.7
Rig 2: Low	1500mm	**344.5**	**347.7**	**353.6**	**360.9**	**382.8**	**385.3**
Rig 3: Low	1250mm	201.2	203.9	229.9	125.5	207.9	221.1
Second (2)	1750mm	451.2	439.7	471.4	-	-	-
Rig 2: Med	1500mm	**477.4**	**512.0**	**493.9**	-	-	-
Rig 3: None	1250mm	253.8	251.6	259.8	-	-	-
Third (4)	1750mm	-	-	-	462.4	504.6	448.6
Rig 2: None	1500mm	-	-	-	**495.8**	**536.5**	**531.4**
Rig 3: Med	1250mm	-	-	-	210.2	218.5	277.6
Fourth (1)	1750mm	**473.8**	438.1	460.3	488.2	565.0	500.4
Rig 2: High	1500mm	468.8	**517.3**	**483.8**	**526.4**	**572.4**	**572.2**
Rig 3: High	1250mm	262.5	295.5	272.1	297.1	295.8	328.4
Fifth(3)	1750mm	429.2	432.6	445.7	432.7	460.1	391.4
Rig 2: High	1500mm	**468.5**	**510.4**	**465.0**	**460.4**	**465.4**	**460.4**
Rig 3: Med	1250mm	251.8	261.7	232.2	215.8	234.1	239.2
Sixth (6)	1750mm	396.0	**415.2**	375.3	-	-	-
Rig 2: Low	1500mm	**410.1**	404.9	**405.9**	-	-	-
Rig 3: None	1250mm	197.8	231.8	206.1	-	-	-

*Temperatures at blast arrival, **Bold** = Maximum temperature at each column,
Rig #: High / Med / Low / None = Target temperature distances

3.3.3.2.3 Load Cell Data

The applied compressive loads recorded using the load cells during the heating phase of trial two (R2) are shown in Fig.3.3.42 (1000 points decimated average). The heated columns in rig two all show an increase in the compressive load during the heating phase (SHS: +0.15kN, RHS: +0.19kN, CHS: +0.22kN). The compressive loads were applied using heavy duty springs (IST "Closed and Ground" (IST, 2015)). Each spring was torqued to its design value relative to 50%, 75% or 90% of the column buckling capacity. The actual applied loads recorded by the load cells are not equal to these designed values but are a reasonable match. Fig.3.3.43 shows the compressive loads

recorded at the arrival of the blast and post blast, during trial two (R2), rigs two and three (decimated average of 8000 points). There is little change in the pre-blast and post-blast compressive loads; however, oscillations are observed indicating reductions and increases in compressive load during a dynamic response. Recorded compressive loads for all rigs and trials are shown in Appendix B. Table 3.10 shows the actual applied compressive loads at the start of each trial. At rig three, during trial three (R4) there was a spring / load cell error showing a much lower recorded compression load in comparison to the spring design load.

Table 3.10: Recorded Compressive Loads at Start of Each Trial (kN)

Rig : Column	Trial 1 (5)+		Trial 2 (2)		Trial 3 (4)		Trial 4 (1)		Trial 5 (3)		Trial 6 (6)	
	Spring	Actual	Spring	Actual	Spring	Actual	Spring	Actual	Spring	Actual	Spring	Actual
Rig 2: CHS	6.26	5.98	5.20*	4.23*	5.20	4.23	3.48	3.79	2.30	2.39	2.30	2.43
Rig 2: RHS	5.14	4.32	4.28*	4.29*	4.28	4.10	2.86	3.39	5.20	2.72	5.20	2.67
Rig 2: SHS	2.80	3.10	2.30*	2.49*	2.30	2.32	1.54	1.59	4.28	4.09	4.28	4.14
Rig 3: CHS	3.48	3.52	3.48	3.56	6.26	2.27^	6.26	5.73	1.54	1.48	2.80	2.86
Rig 3: RHS	2.86	3.19	2.86	3.10	5.14^	1.15^	5.14	4.15	3.48	3.53	6.26	5.28
Rig 3: SHS	1.54	1.60	1.54	1.55	2.80	2.15	2.80	2.91	2.86	3.02	5.14	4.19
*Thermal box didn't drop, + Compressive load before blast arrival, ^ Error with spring												

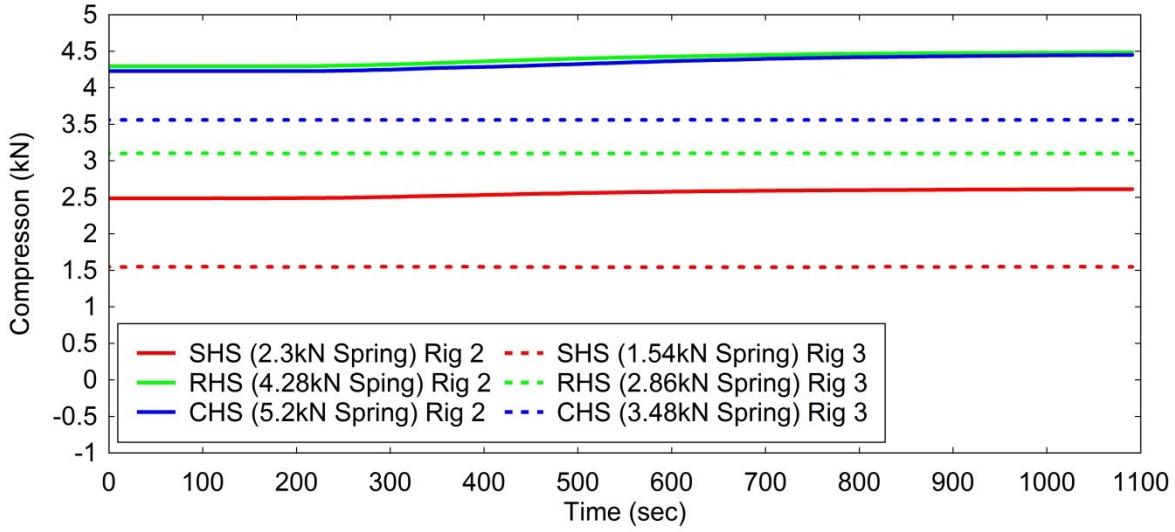

Figure 3.3.42: Recorded Compression during Heating Phase (Trial 2, 8000 Decimated)

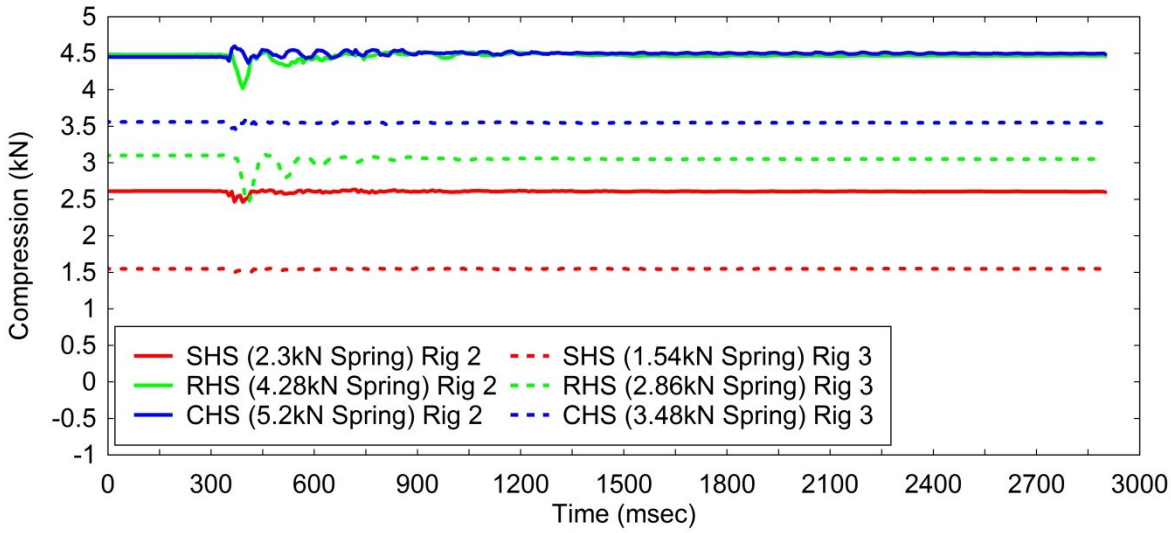

Figure 3.3.43: Post-Shot Recorded Temperatures (Trial 2 8000 Decimated)

3.3.3.2.4 Post-Shot Deflections

There were two sets of post shot deflections recorded during the ABT trials; the first set were in-situ midpoint deflections recorded immediately after each trial (after cooling of columns), the second set were taken at nine points along the length of each column (1100mm to 1900mm) after removal from the rigs. The first set were taken with a spirit level and scale rule, the second set were taken using a Vernier Caliper. Fig.3.3.44 shows the method of recording the post shot (in-situ) deflections using a scale rule and level. The measurement error for the in-situ deflections was +-3mm; due to a combined human error (1mm) and the error in the bend of the horizontal aligning bar (2mm) used as a marker. The measurement error for the post shot deflections (after removal from rig), recorded along the column lengths is +- 2mm; this is due to the combined human error using and reading the Vernier Caliper (+-0.5mm) and the error in the straightness of the tape used as a straight edge marker adjacent to the columns (1.5mm over a 3m length).

Table 3.11 shows the midpoint in-situ deflections taken at each column after each trial. The in-situ deflections were not taken at rig one after the first trial. There was an increase in the magnitude of the pinned column deflections in the 4th, 5th and 6th trials. This was due to the introduction of the wings on the central 1m length of each column in the pinned rigs. There was also significant variation in the magnitude of deflections across several trials with no variance in specified parameters (such as pinned columns: trials 1 to 3, and 4 to 6). This range of deflections is attributed to factors affecting trial repeatability, such as column connections, material and manufacturing tolerances and consistency of the applied blast load across the trials. The largest permanent in-situ deflections recorded on the columns with compression and thermal load are on the RHS during

trials three (R4) (Rig 3 = 120.5mm), four (R1) (Rig 3: 103.5mm) and five (R3) (Rig 3: 101.5mm). The recorded maximum temperatures on the RHS at rig three were 495.8°C (trial 3), 526.4°C (trial 4) and 460.4°C (trial 5). The equivalent applied compressive loads on these columns was 5.14kN (trials 3 and 4) and 3.48kN (trial 5).

Figure 3.3.44: Post-Shot Deflection Measurement

Table 3.11: Mid-Point In-Situ Column Deflections (mm)

Rig : Column	1st Trial	2nd Trial	3rd Trial	4th Trial	5th Trial	6th Trial
Rig 1: CHS	-1.85	-	14.15	104.15+	64.65	67.15
Rig 1: RHS	39.5	-	29	101.5	119.5	104
Rig 1: SHS	7.5	-	7	99	109	113
Rig 2: CHS	20.65	11.15*	8.65	13.15	12.65	13.15
Rig 2: RHS	64	22.5*	72	90.5	98	76
Rig 2: SHS	25.5	10.5*	15.5	14	72.5	65.5
Rig 3: CHS	6.15	9.15	13.65	12.65	7.15	8.65
Rig 3: RHS	43.5	52	120.5	103.5	66	101.5
Rig 3: SHS	-0.5	14	9.5	52.5	36.5	29.5
*Thermal box didn't drop, + Bolt sheared and column rotated						

Figs.3.3.45 to 3.3.50 show the deflections taken along the length of each column recorded after removal. The applied temperature is indicated by the legend Temp: L (Low), M (Medium), H (High) and N (None), the applied compressive load is indicated by Comp: L (Low), M (Medium) and H (High). There was no compressive or thermal load on the pinned rigs (1). There were no perceptible deflections in several columns, therefore no measurements were taken. The recorded data has been smoothed using Fourier transform smoothing. Smoothing windows (number of points which data is smoothed), of 10 to 100 were used. The total length of the columns varied due to differences

in the end connection details at each rig; columns in the pinned rig were 3145mm (average), columns in the compression and thermal rigs were 3085mm (average). Table 3.12 shows the maximum recorded deflections in each column after removal from the rigs. Maximum deflections after removal are typically lower than the in-situ mid-point recorded deflections. This is due to the release of the compressive loading causing out of plane bending in the columns.

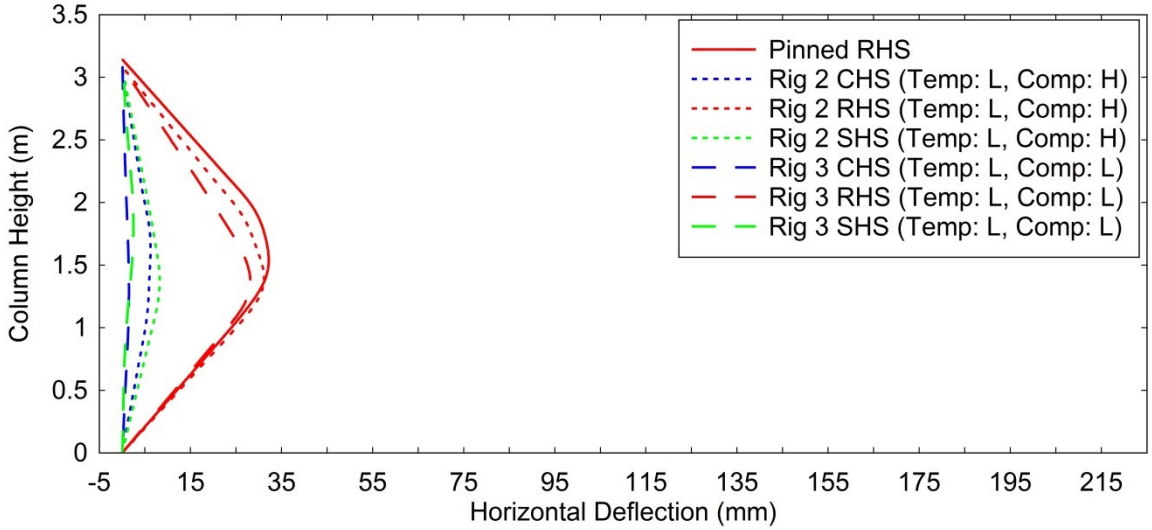

Figure 3.3.45: Post-Shot Deflections (First Trial)

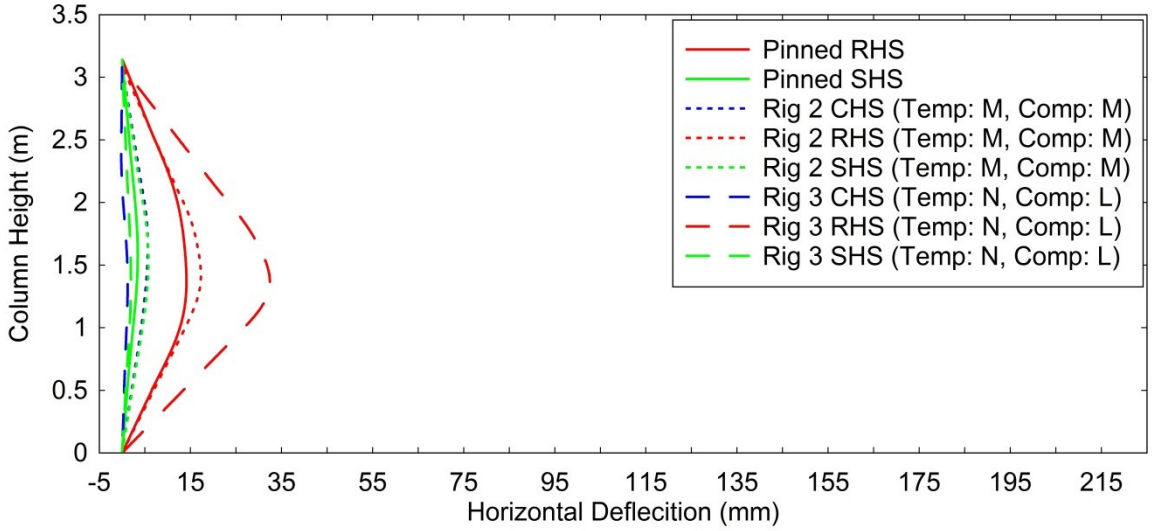

Figure 3.3.46: Post-Shot Deflections (Second Trial)

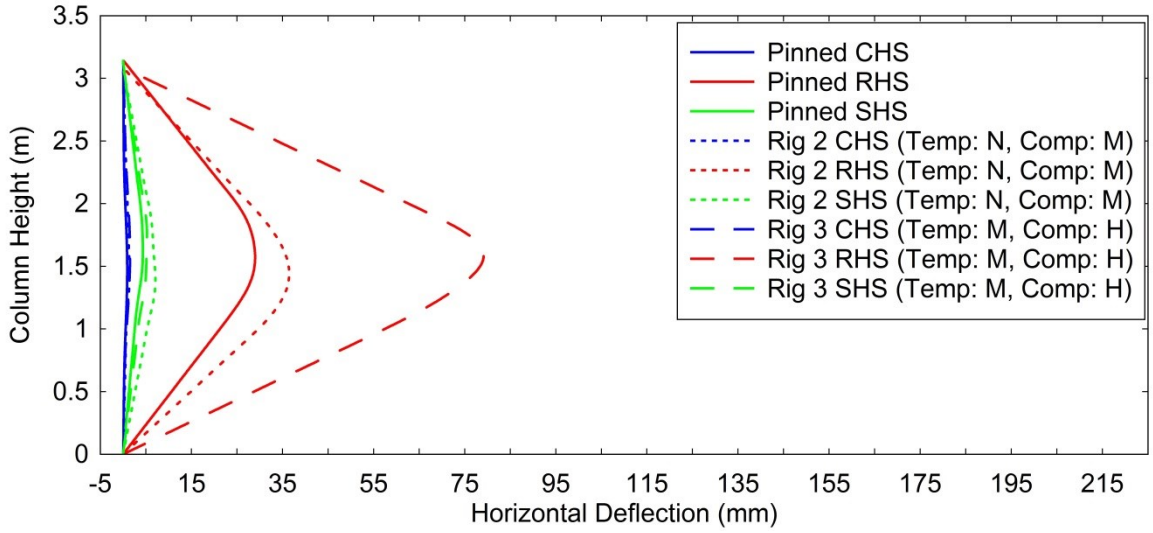

Figure 3.3.47: Post-Shot Deflections (Third Trial)

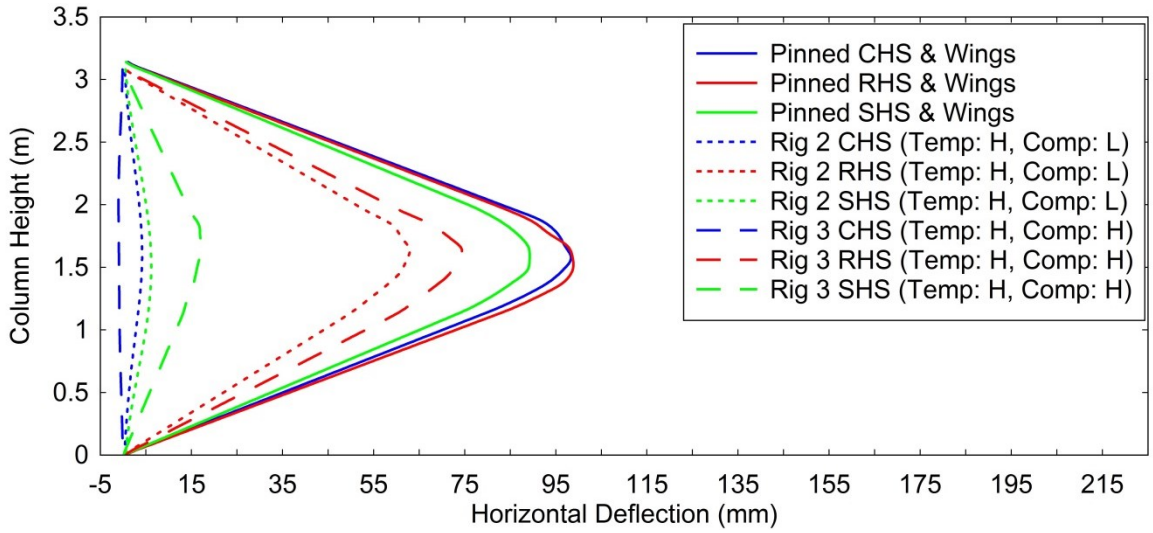

Figure 3.3.48: Post-Shot Deflections (Fourth Trial)

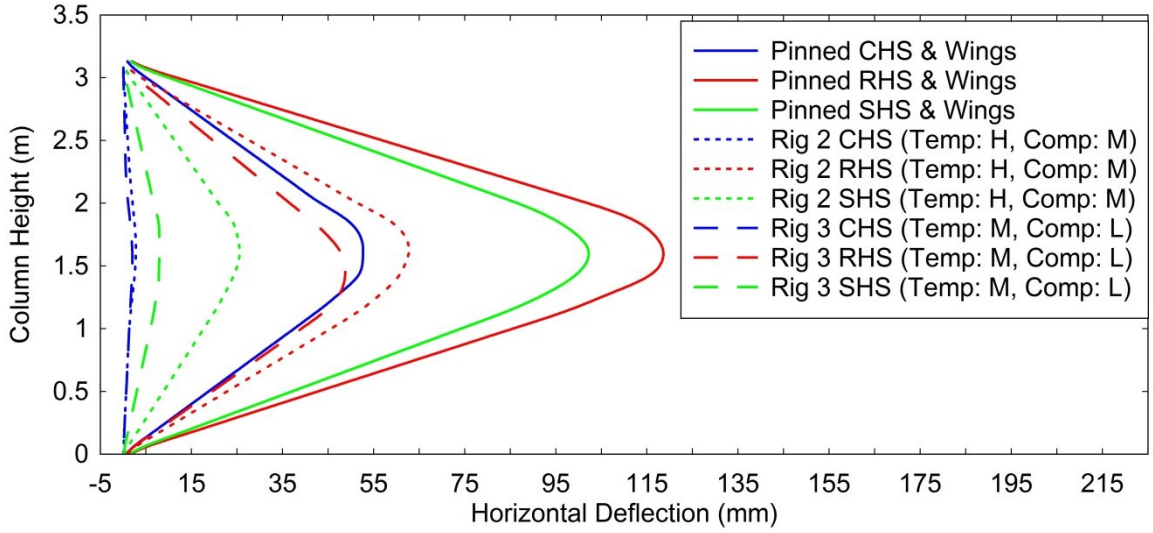

Figure 3.3.49: Post-Shot Deflections (Fifth Trial)

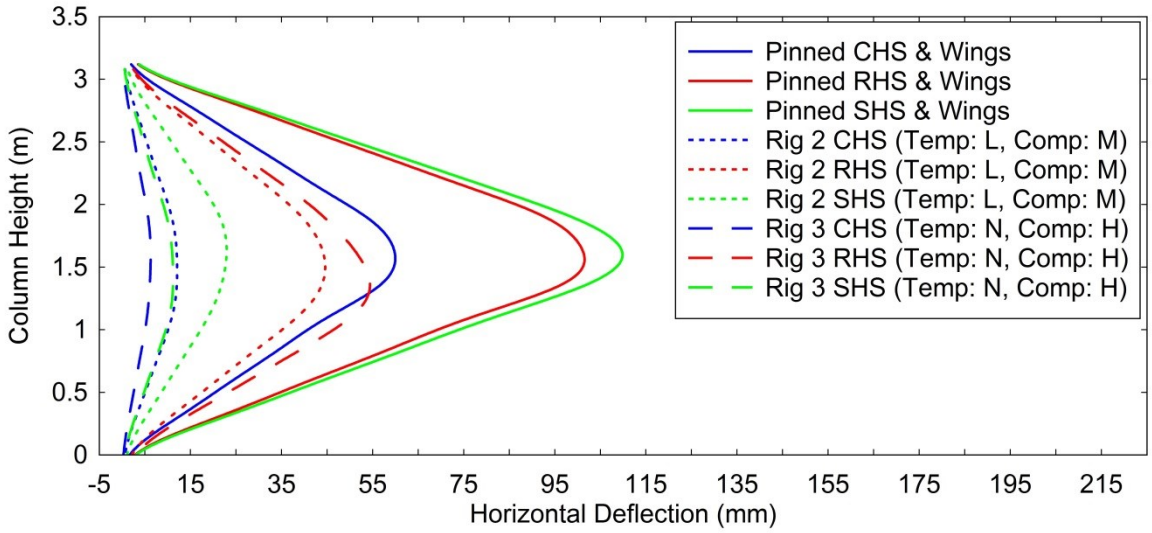

Figure 3.3.50: Post-Shot Deflections (Sixth Trial)

Table 3.12: Maximum Column Deflections (after removal) (mm)

Rig : Column	Trial 1	Trial 2	Trial 3	Trial 4	Trial 5	Trial 6
Rig 1: CHS	-	-	1.68	98.84+	53.16	60.41
Rig 1: RHS	32.68	15.31	29.2	98.74	118.71	102.73
Rig 1: SHS	-	4.02	4.55	89.31	102.5	111.69
Rig 2: CHS	6.34	5.89*	1.52	5.16	2.99	12.94
Rig 2: RHS	32.38	17.72*	37.33	63.21	63.45	45.96
Rig 2: SHS	8.37	5.82*	7.42	6.8	25.82	23.79
Rig 3: CHS	1.7	1.79	2.11	-1.35	2.23	7.16
Rig 3: RHS	28.47	32.97	80.74	74.9	48.85	56.61
Rig 3: SHS	2.94	2.43	5.57	17.4	8.21	12.11
*Thermal box didn't drop, + Bolt sheared and column rotated						

3.3.3.2.5 Deflection Time Histories

Figures 3.3.51 to 3.3.84 show the maximum and final deflected shape of the columns and the deflection - time histories recorded at each rig. Figs.3.3.67a), 3.3.73a) and 3.3.79a) show the near maximum deflected shape of the columns as the maximum deflected shapes are obscured by the heavy structural rigs. The deflection – time histories were recorded by inspection of the high speed video; the mid-height location of each column was selected using the collect points function (Phantom camera control software) at several time frame steps throughout the duration of each trial. The recorded points were graphically represented with Fourier transform smoothing (smoothing window = 20) applied to each data set. To account for the error introduced by camera movement the position of the LED on the heavy structural rigs, was subtracted from the absolute position of each column midpoint therefore plotting the relative position of the column midpoint to the heavy structural rig (assuming no lateral movement of heavy structural rig).

The RHS columns had the largest maximum and final deflected shapes and they exhibited a clear harmonic response to the blast load. The SHS exhibited high peak elastic deflections and exhibited a similar harmonic response to the RHS; however, the final deflected shapes were significantly smaller than the RHS. The CHS deformed the least of the three sections; however reasonable peak elastic deflections followed by a harmonic response and small permanent deflections were still observed.

The columns fitted with wings exhibited larger maximum and permanent deflections due to a wider (250mm) area subject to the blast over the central 1m length of the columns. There was large variation in the maximum deflections and final deflected shapes across the pinned columns and columns with wings. This was due to blast reproducibility and column fixity. The peak incident pressures ranged from 55.2kPa to 64.1kPa at the pinned rig over the six trials.

3.3.3.2.5.1 First Trial (Round 5)

- Rig One:
  - Pinned Only
  - No Wings

(a) **(b)**

Figure 3.3.51a & b: First Trial (5) Maximum (a) and Final (b) Deflected Shapes: Rig 1

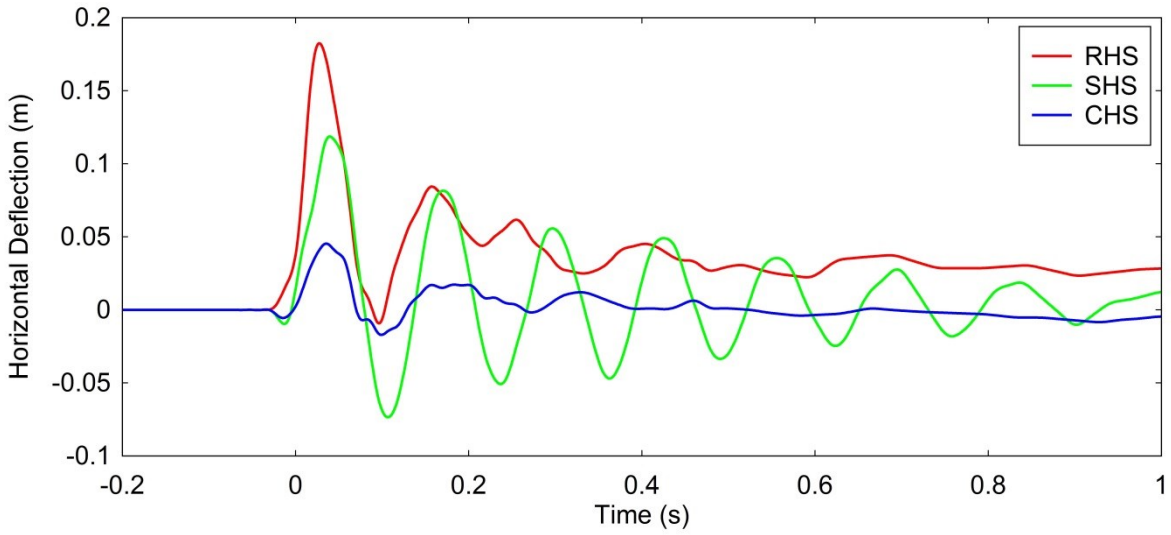

Figure 3.3.52: First Trial (5) Deflection - Time History: Rig 1

- Rig Two:

Recorded Maximum Temperature (°C)		Recorded Initial Compressive Load (kN)	
RHS	344.5	RHS	4.32
SHS	347.5	SHS	3.10
CHS	353.6	CHS	5.98

(a) **(b)**

Figure 3.3.53a & b: First Trial (5) Maximum (a) and Final (b) Deflected Shapes: Rig 2

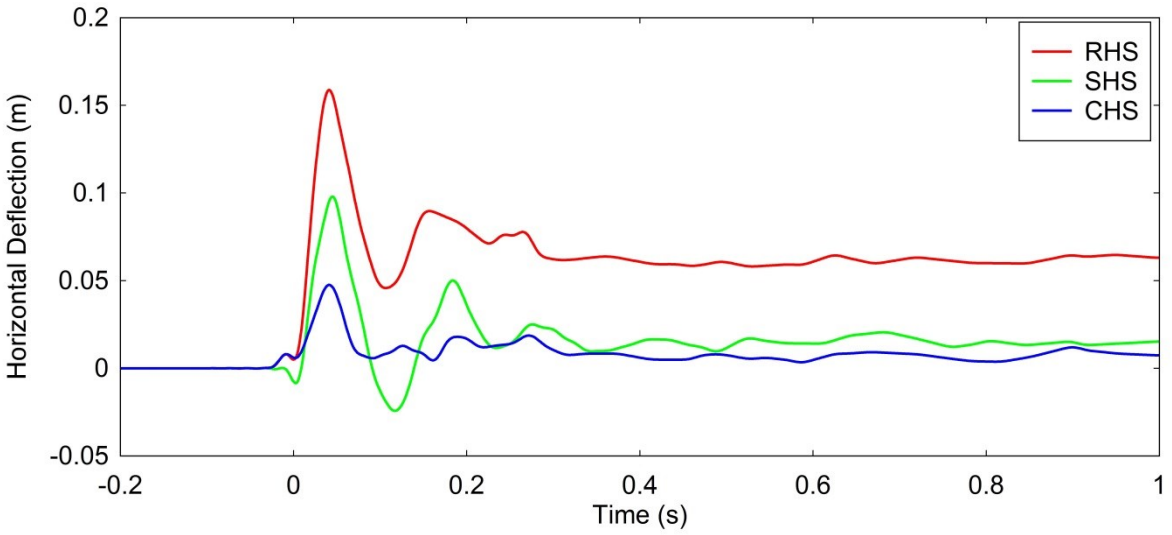

Figure 3.3.54: First Trial (5) Deflection - Time History: Rig 2

- Rig Three:

Recorded Maximum Temperature (°C)		Recorded Initial Compressive Load (kN)	
RHS	360.9	RHS	3.19
SHS	382.9	SHS	1.60
CHS	385.3	CHS	3.52

(a) **(b)**

Figure 3.3.55a & b: First Trial (5) Maximum (a) and Final (b) Deflected Shapes: Rig 3

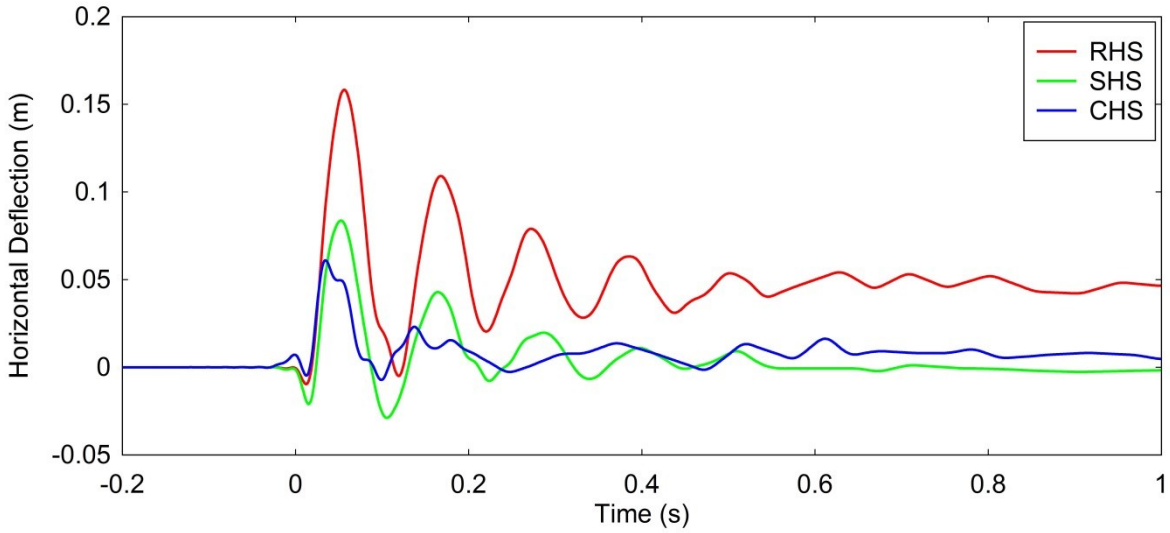

Figure 3.3.56: First Trial (5) Deflection - Time History: Rig 3

3.3.3.2.5.2 Second Trial (Round 2)

- Rig One:
    - Pinned Only
    - No Wings

(a) **(b)**

Figure 3.3.57a & b: Second Trial (2) Maximum (a) and Final (b) Deflected Shapes: Rig 1

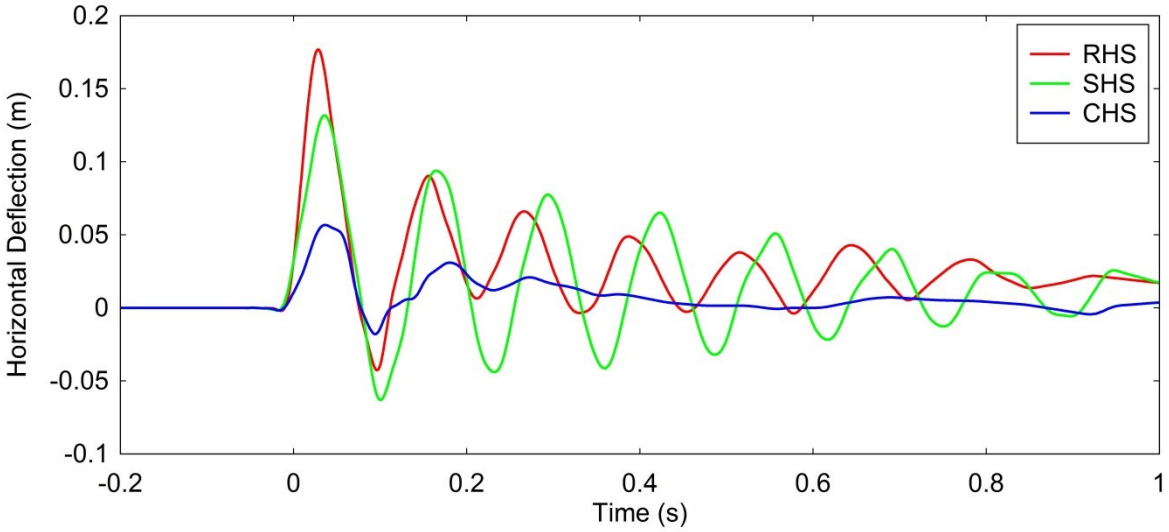

Figure 3.3.58: Second Trial (2) Deflection - Time History: Rig 1

- Rig Three:

Recorded Maximum Temperature (°C)		Recorded Initial Compressive Load (kN)	
RHS	-	RHS	3.10
SHS	-	SHS	1.55
CHS	-	CHS	3.56

(a) **(b)**

Figure 3.3.59a & b: Second Trial (2) Maximum (a) and Final (b) Deflected Shapes: Rig 3

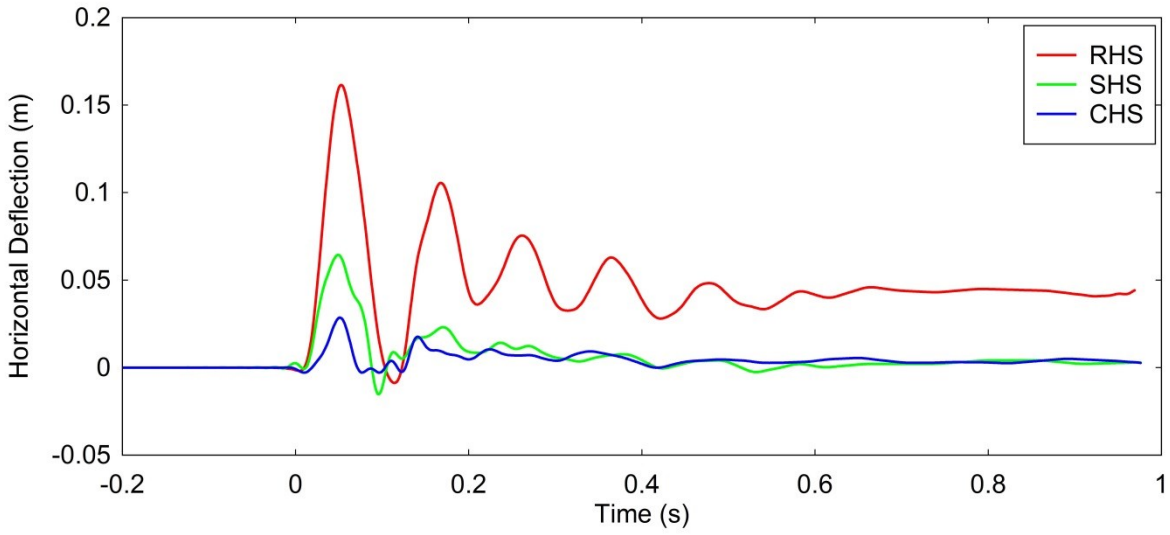

Figure 3.3.60: Second Trial (2) Deflection - Time History: Rig 3

3.3.3.2.5.3 Third Trial (Round 4)

- Rig One:
    - Pinned Only
    - No Wings

(a) **(b)**

Figure 3.3.61a & b: Third Trial (4) Maximum (a) and Final (b) Deflected Shapes: Rig 1

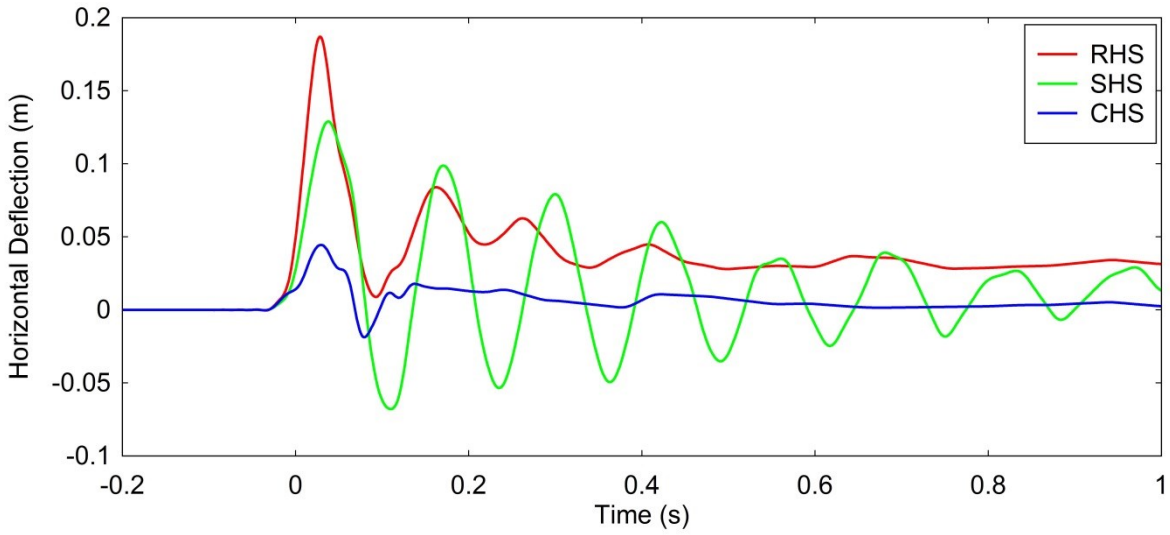

Figure 3.3.62: Third Trial (4) Deflection - Time History: Rig 1

- Rig Two:

Recorded Maximum Temperature (°C)		Recorded Initial Compressive Load (kN)	
RHS	-	RHS	4.10
SHS	-	SHS	2.32
CHS	-	CHS	4.23

(a) **(b)**

Figure 3.3.63a & b: Third Trial (4) Maximum (a) and Final (b) Deflected Shapes: Rig 2

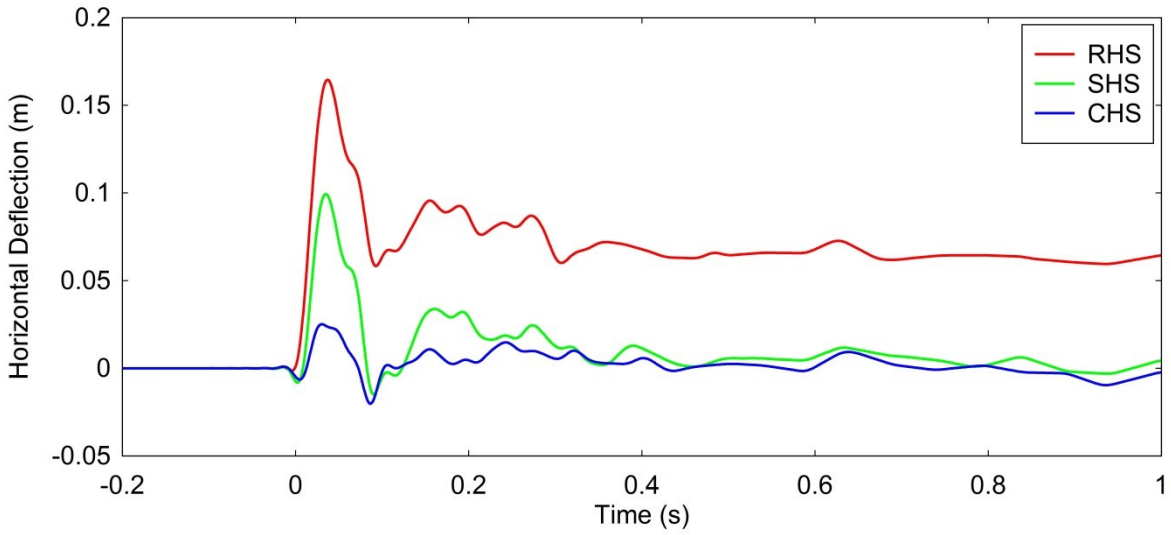

Figure 3.3.64: Third Trial (4) Deflection - Time History: Rig 2

- Rig Three:

Recorded Maximum Temperature (°C)		Recorded Initial Compressive Load (kN)	
RHS	495.8	RHS	1.15
SHS	536.5	SHS	2.15
CHS	531.4	CHS	2.27

(a) **(b)**

Figure 3.3.65a & b: Third Trial (4) Maximum (a) and Final (b) Deflected Shapes: Rig 3

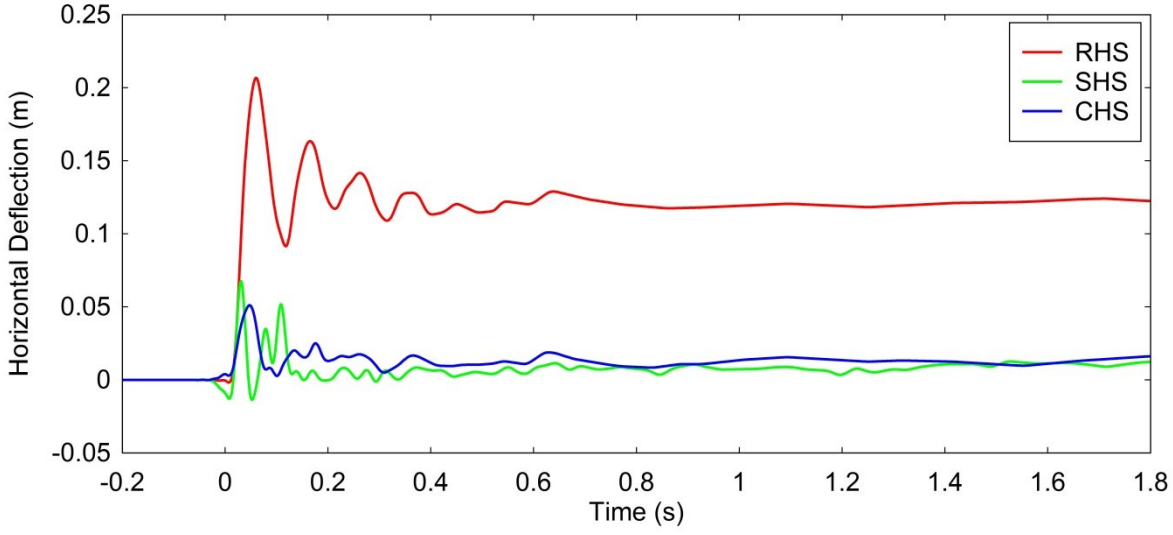

Figure 3.3.66: Third Trial (4) Deflection - Time History: Rig 3

3.3.3.2.5.4 Fourth Trial (Round 1)

- Rig One:
  - Pinned Only
  - With Wings

(a) **(b)**

Figure 3.3.67a & b: Fourth Trial (1) Near Maximum (a) and Final (b) Deflected Shapes: Rig 1

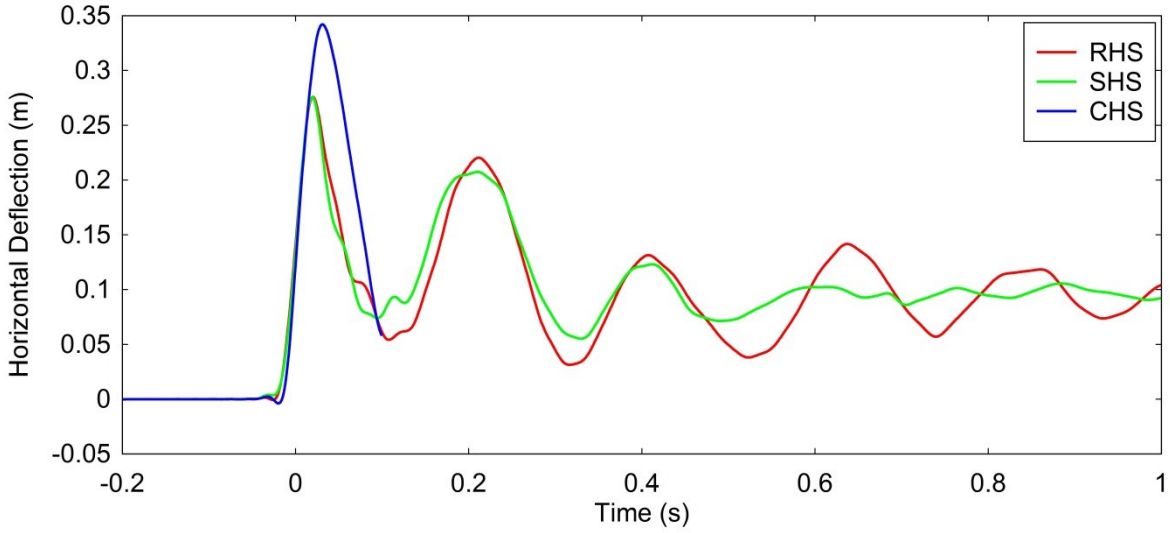

Figure 3.3.68: Fourth Trial (1) Deflection - Time History: Rig 1

- Rig Two:

Recorded Maximum Temperature (°C)		Recorded Initial Compressive Load (kN)	
RHS	473.8	RHS	3.39
SHS	517.3	SHS	1.59
CHS	483.8	CHS	3.79

(a) **(b)**

Figure 3.3.69a & b: Fourth Trial (1) Maximum (a) and Final (b) Deflected Shapes: Rig 2

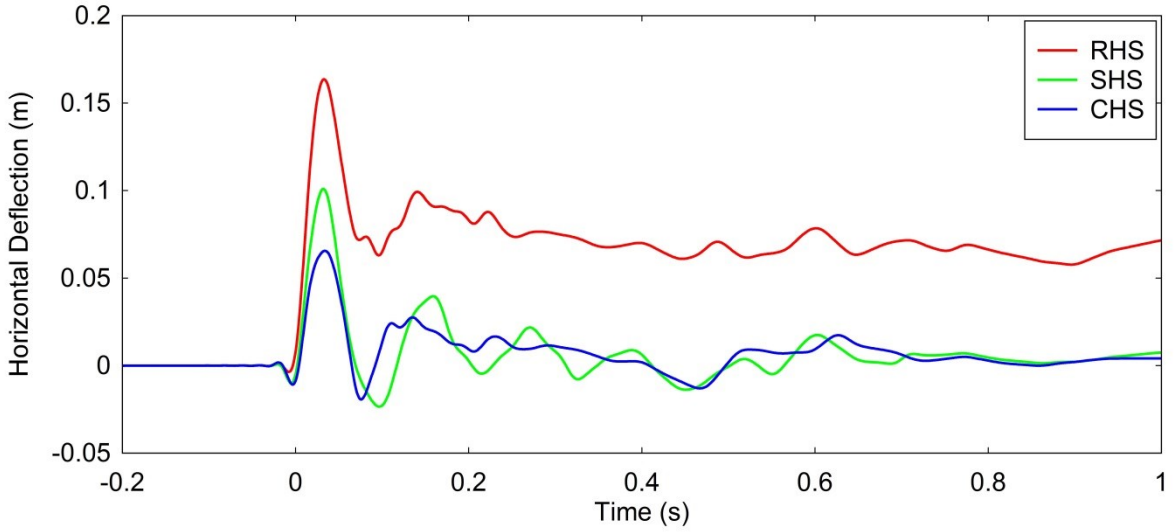

Figure 3.3.70: Fourth Trial (1) Deflection - Time History: Rig 2

- Rig Three:

Recorded Maximum Temperature (°C)		Recorded Initial Compressive Load (kN)	
RHS	526.4	RHS	4.15
SHS	572.4	SHS	2.91
CHS	572.2	CHS	5.73

(a) **(b)**

Figure 3.3.71a & b: Fourth Trial (1) Maximum (a) and Final (b) Deflected Shapes: Rig 3

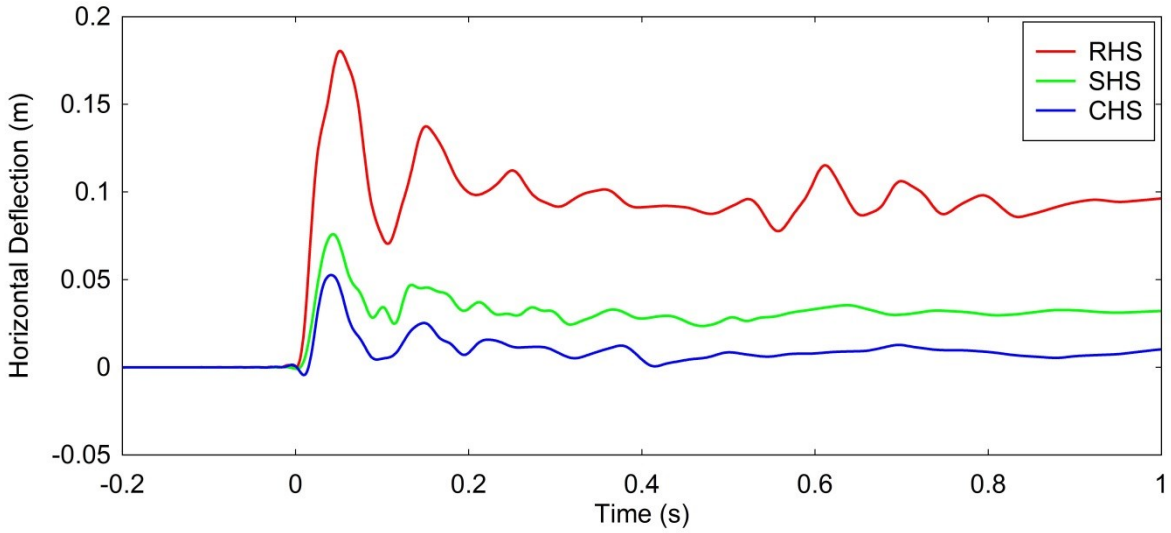

Figure 3.3.72: Fourth Trial (1) Deflection - Time History: Rig 3

3.3.3.2.5.5 Fifth Trial (Round 3)

- Rig One:
    - Pinned Only
    - With Wings

(a) **(b)**

Figure 3.3.73a & b: Fifth Trial (3) Near Maximum (a) and Final (b) Deflected Shapes: Rig 1

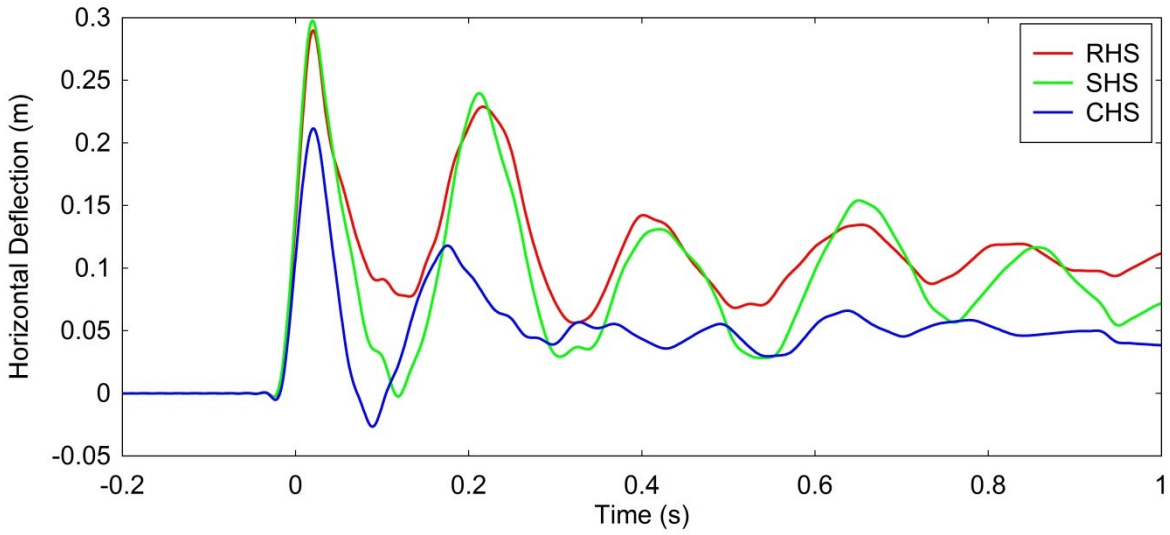

Figure 3.3.74: Fifth Trial (3) Deflection - Time History: Rig 1

- Rig Two:

Recorded Maximum Temperature (°C)		Recorded Initial Compressive Load (kN)	
RHS	468.5	RHS	2.72
SHS	510.4	SHS	4.09
CHS	465.0	CHS	2.39

Figure 3.3.75a & b: Fifth Trial (3) Maximum (a) and Final (b) Deflected Shapes: Rig 2

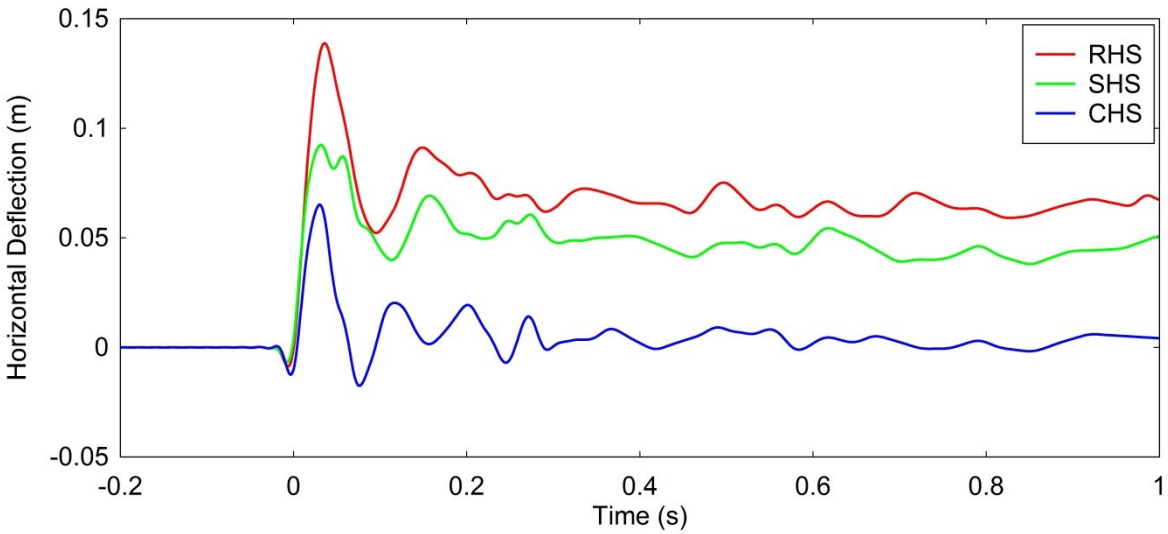

Figure 3.3.76: Fifth Trial (3) Deflection - Time History: Rig 2

- Rig Three:

Recorded Maximum Temperature (°C)		Recorded Initial Compressive Load (kN)	
RHS	460.4	RHS	3.53
SHS	465.4	SHS	3.02
CHS	460.4	CHS	1.48

(a) **(b)**

Figure 3.3.77a & b: Fifth Trial (3) Maximum (a) and Final (b) Deflected Shapes: Rig 3

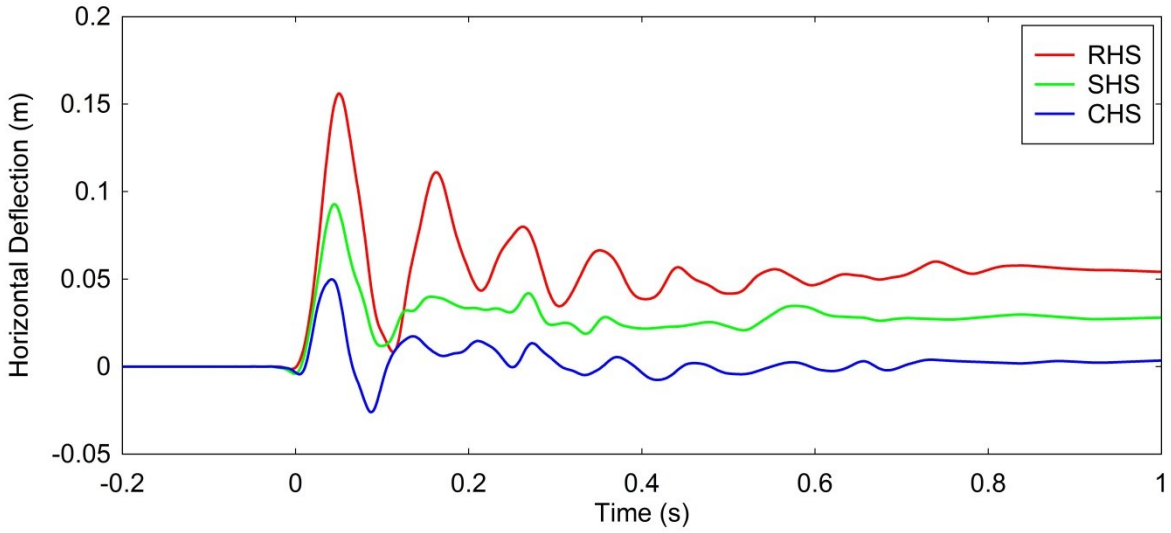

Figure 3.3.78: Fifth Trial (3) Deflection - Time History: Rig 3

3.3.3.2.5.6 Sixth (Round 6)

- Rig One:
    - Pinned Only
    - With Wings

(a) **(b)**

Figure 3.3.79a & b: Sixth Trial (6) Near Maximum (a) and Final (b) Deflected Shapes: Rig 1

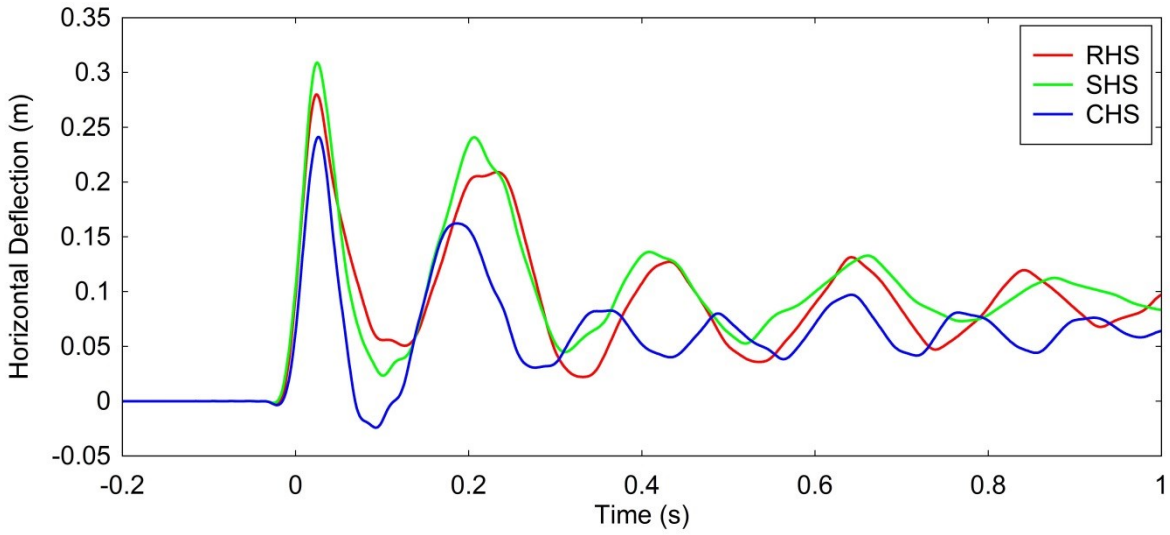

Figure 3.3.80: Sixth Trial (6) Deflection - Time History: Rig 1

- Rig Two:

Recorded Maximum Temperature (°C)		Recorded Initial Compressive Load (kN)	
RHS	410.1	RHS	2.67
SHS	415.2	SHS	4.14
CHS	405.9	CHS	2.43

(a) **(b)**

Figure 3.3.81a & b: Sixth Trial (6) Maximum (a) and Final (b) Deflected Shapes: Rig 2

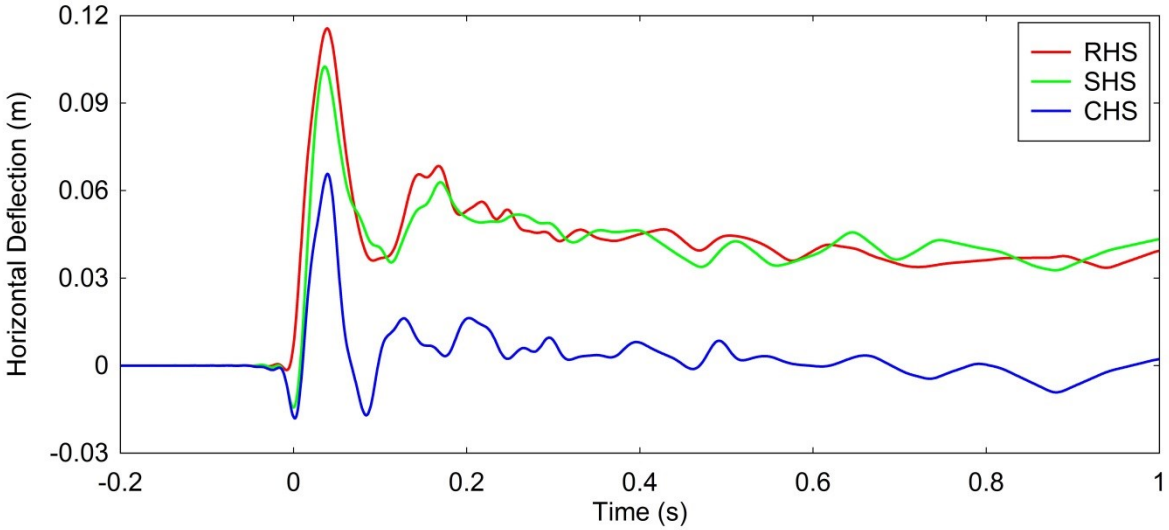

Figure 3.3.82: Sixth Trial (6) Deflection - Time History: Rig 2

- Rig Three:

Recorded Maximum Temperature (°C)		Recorded Initial Compressive Load (kN)	
RHS	-	RHS	5.28
SHS	-	SHS	4.19
CHS	-	CHS	2.86

(a) **(b)**

Figure 3.3.83a & b: Sixth Trial (6) Maximum (a) and Final (b) Deflected Shapes: Rig 3

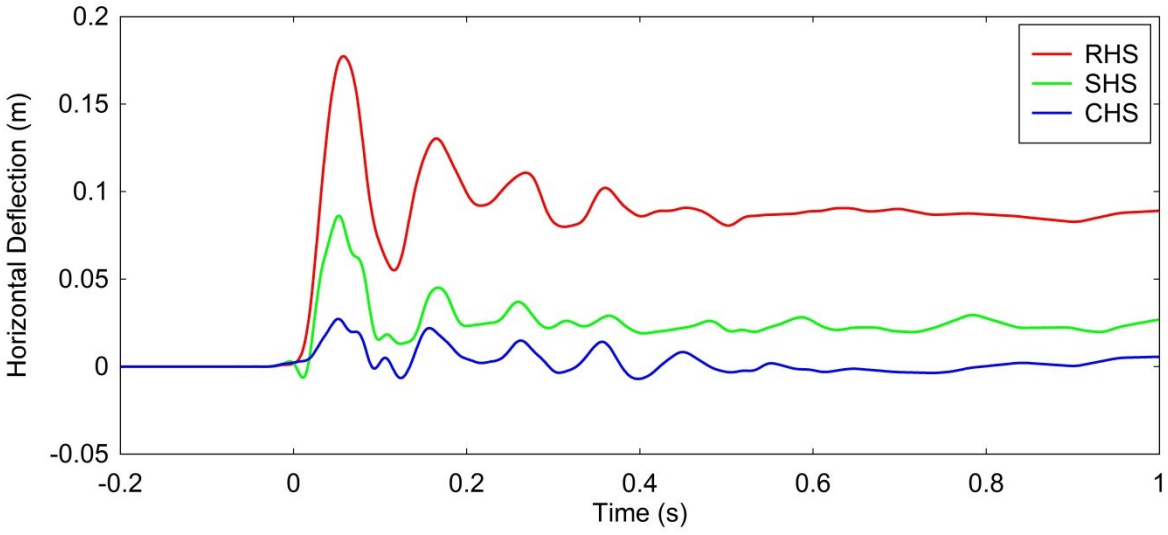

Figure 3.3.84: Sixth Trial (6) Deflection - Time History: Rig 3

Figs.3.3.85 to 3.3.87 show the final deflections vs maximum temperature for CHS, RHS and SHS (excluding columns in the pinned rig and rig 2 during the second trial; box did not drop). The CHS

and SHS show little correlation between increased temperature and increased deflection. The RHS showed the largest relative increase in deflection when subject to increasing thermal loads. This was due to RHS having the largest applied blast load. The largest elastic deformations were observed in the RHS in rig three (third trial (4) = 207mm, and fourth trial (1) = 181mm). The maximum temperatures reached on the RHS during these trials were: trial 3(4) = 496°C and trial 4(1) = 526°C. These results show that at higher temperatures the Young's Modulus has been reduced leading to larger elastic deflections compared with columns at lower temperatures.

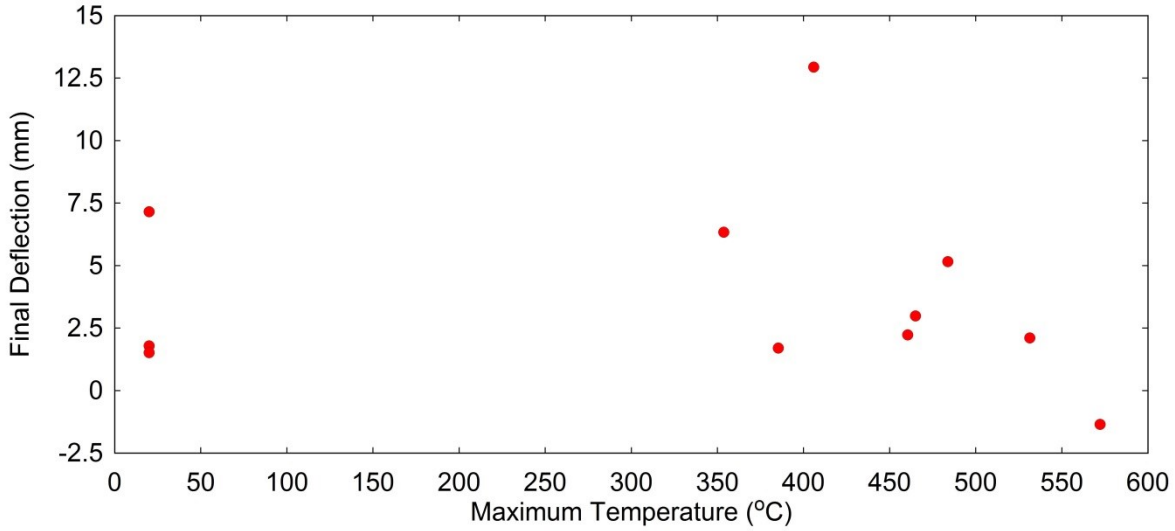

Figure 3.3.85: Final Deflection vs Maximum Temperature: CHS

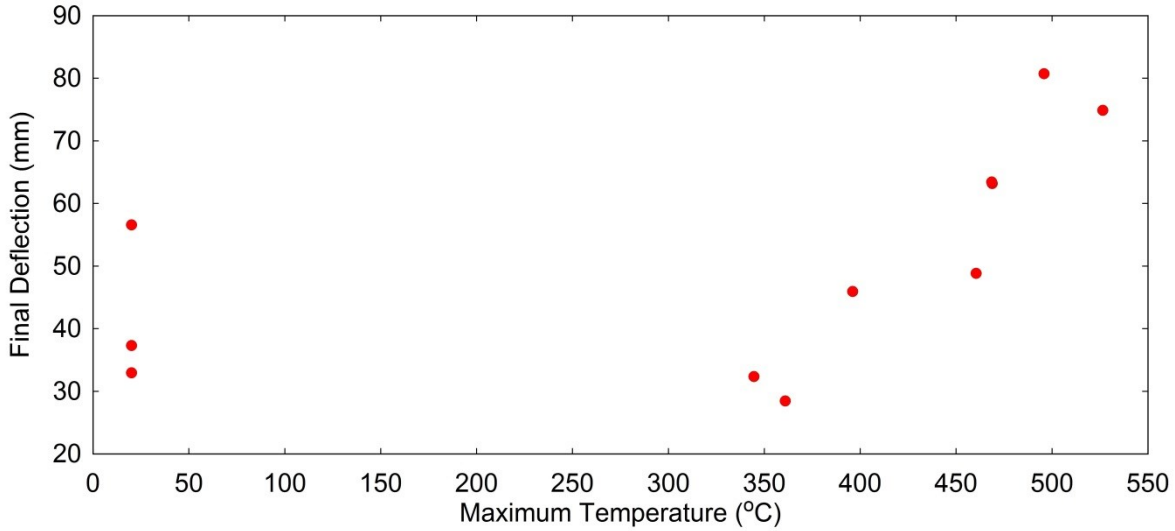

Figure 3.3.86: Final Deflection vs Maximum Temperature: RHS

The steel material properties across the three column sections would have degraded to relatively similar levels, with similar temperatures; however, as the load applied to the RHS is significantly larger than the SHS or CHS a larger relative elastic and permanent response is observed, therefore any response due to the thermal degradation of the material properties would be amplified.

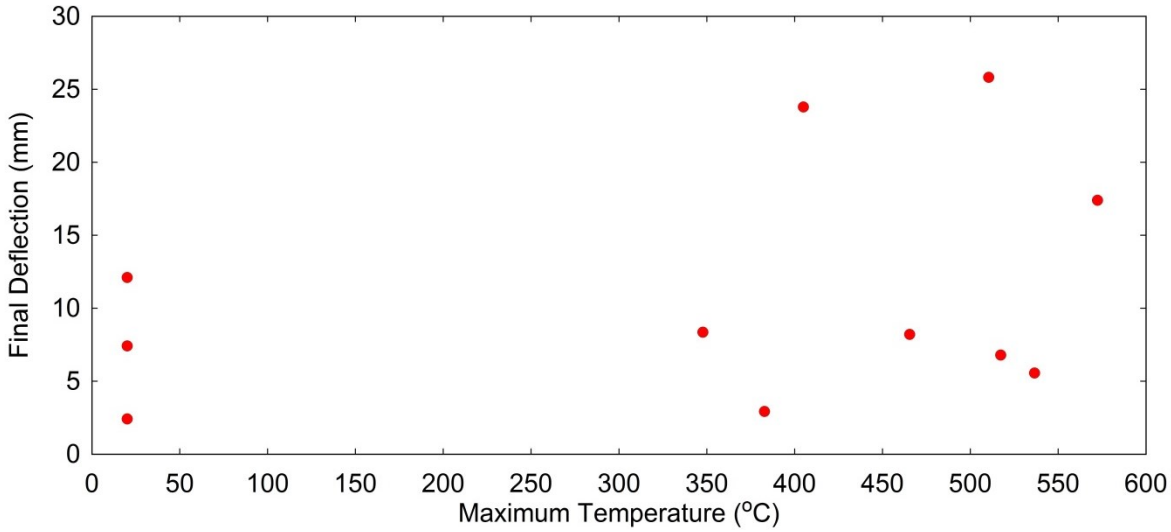

Figure 3.3.87: Final Deflection vs Maximum Temperature: SHS

Figs.3.3.88 to 3.3.90 show the final deflections vs applied compressive load for the CHS, RHS and SHS. There is minimal relation between increasing compressive loads and the final deflections for the CHS and RHS. There is a significant correlation between increasing compressive loads and final deflections for the SHS. This is due to the relative compressive weakness of the SHS compared to the CHS and RHS. The SHS with high compressive stresses were near buckling or had buckled at the arrival of the blast load. The blast subsequently deformed the columns laterally, increasing the effect of further deformations caused by the compressive load.

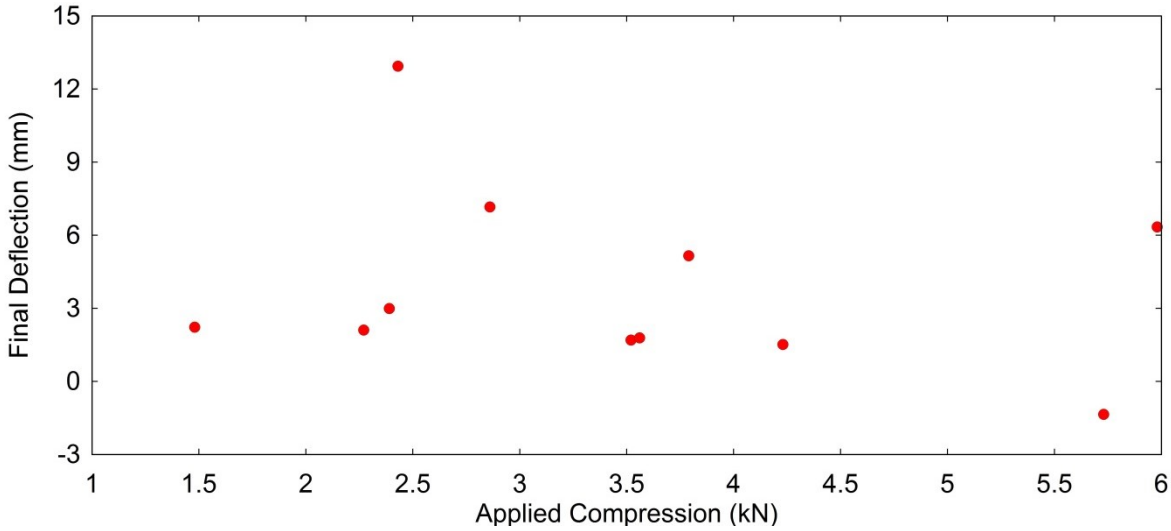

Figure 3.3.88: Final Deflection vs Applied Compressive Load: CHS

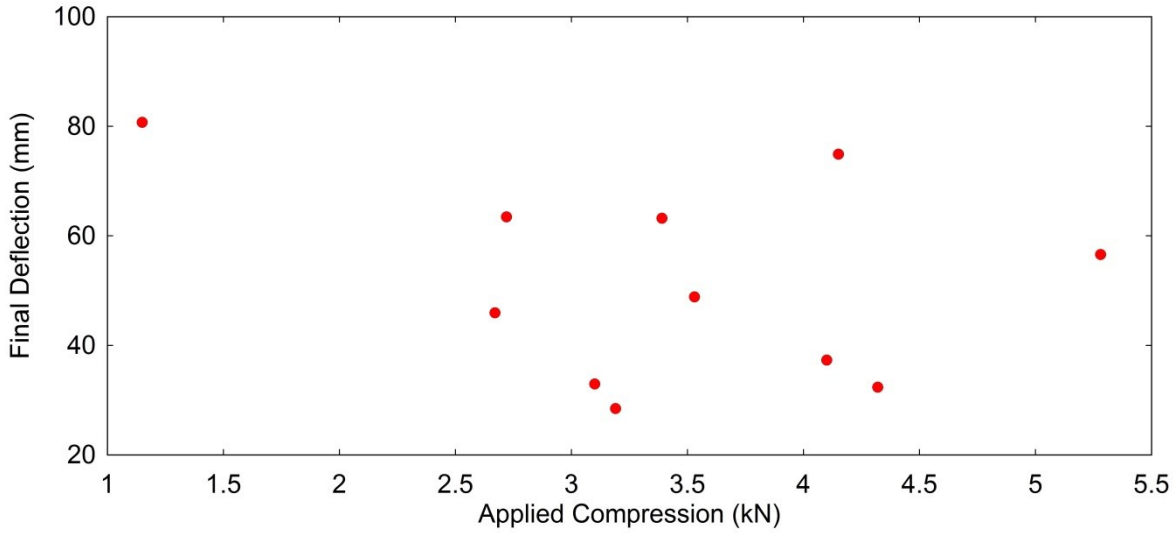

Figure 3.3.89: Final Deflection vs Applied Compressive Load: RHS

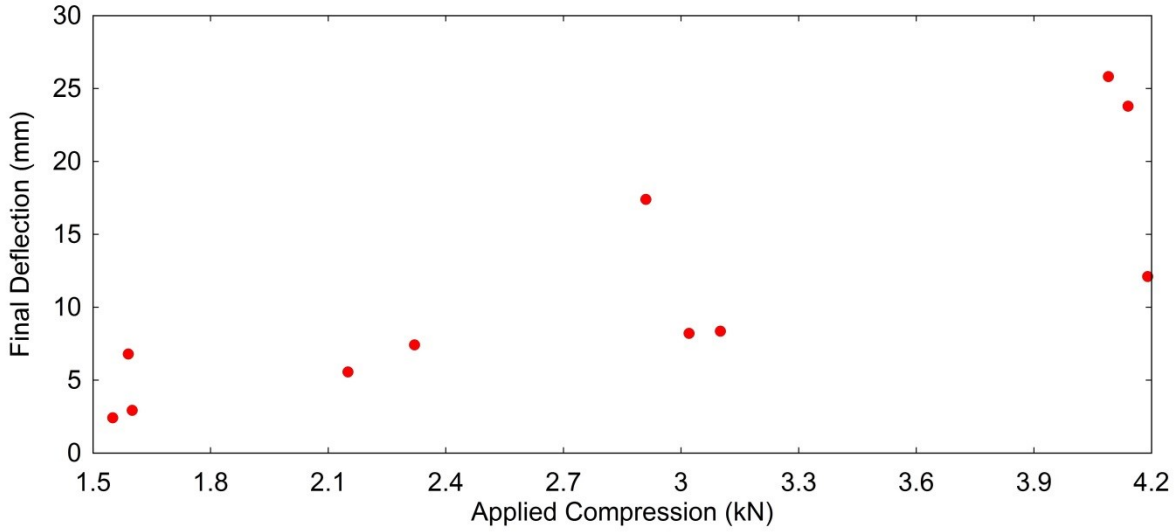

Figure 3.3.90: Final Deflection vs Applied Compressive Load: SHS

Figs.3.3.91 and 3.3.92 show the final deflections vs maximum temperature for varying compressive loads for the RHS and SHS. The RHS and SHS show an increase in final deflection with increased temperature and equal compressive load, this relationship is more significant for the RHS. There is a small (negative) difference in the final deflections between ambient temperature and 350°C; however, above 400°C the effect of the increasing temperature on the final deflections is more prominent. This relationship is attributed to the decreasing yield strength of the steel above 400°C; below this temperature the yield strength remains at or near the equivalent strength at ambient temperature.

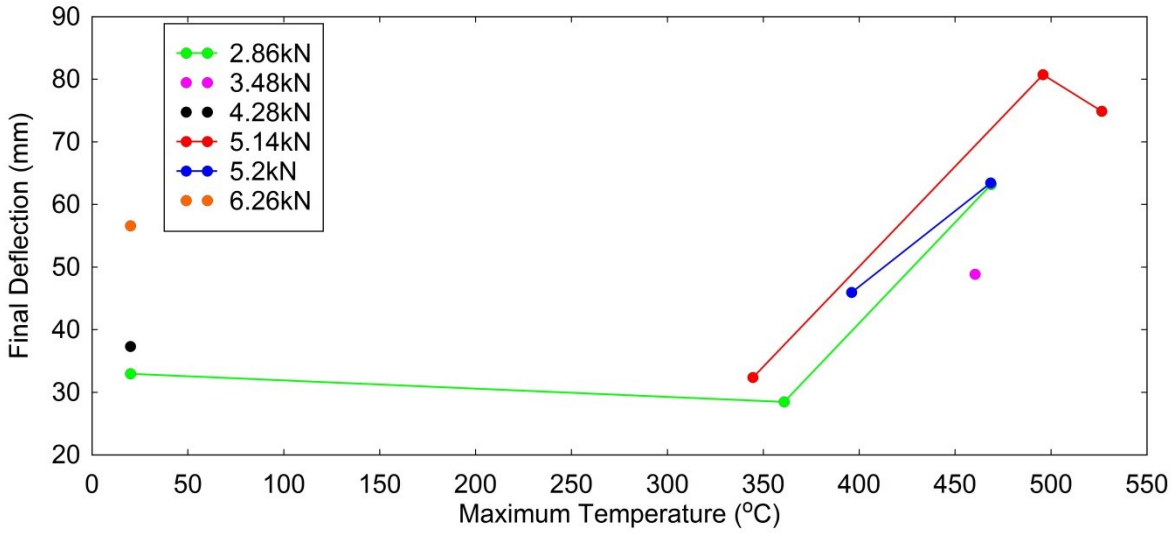

Figure 3.3.91: Final Deflection vs Maximum Temperature for Varying Compressive Loads: RHS

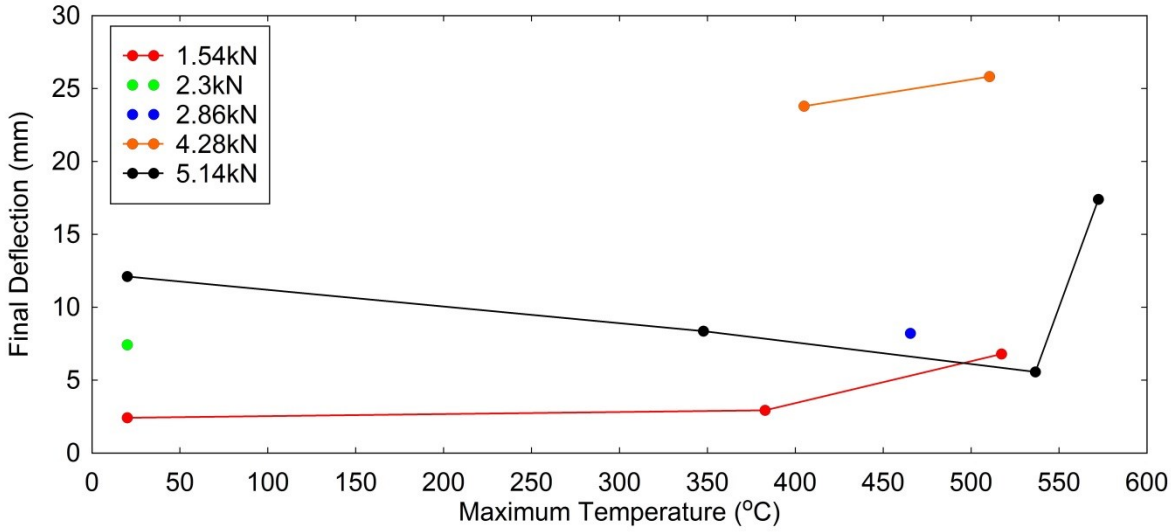

Figure 3.3.92: Final Deflection vs Maximum Temperature for Varying Compressive Loads: SHS

The observations made from Figs.3.3.85 and 3.3.92 show agreement with Fig.2.5.1 and Table 2.5, which display the reducing factors applied to the ambient yield strength at increasing temperatures; between 400°C and 500°C a factor of 0.78 is applied, between 500°C and 600°C a factor of 0.47 is applied, subsequent factors decrease with increasing temperature.

3.3.4 ABT Experimental Trials Summary

The ABT trials were successfully undertaken during spring 2015 as part of the research project. There were six combined thermal, compression and long duration blast load trials performed within the ABT observing the response of structural steel columns to combinations of these load regimes. The trials were a culmination of two years planning and design and are the foundations for future combined thermal and blast testing to be undertaken within the ABT. The RHS exhibited the largest

response from increasing temperatures combined with the long duration blast load. The SHS showed the largest response to increasing compressive loads combined with the blast load. The CHS showed minimal response to all loading regimes. This was due to the higher compressive strength of the column, thicker material and lower applied blast load due to a narrow, rounded profile. The columns with wings also had a larger response than without. There was also large variation in final deflections and deflection-time histories between identical column sections with pinned ends and no specified parameter variations. This was due to the reproducibility of blast loads, trial reproducibility and column fixity. The fixity of the end connections for the pinned columns allowed complete rotation of the column ends; however the sleeved connections for the columns in the heating and compression rigs provided a higher degree of fixity.

These trials are used to validate the numerical methods adopted in the parametric study for the research project. Models of the columns in the trials have been developed and the results compared to the trial results to give validation to the computational methods used throughout the research project (section 4.5).

Chapter 4

Computational Analysis

4.1 Introduction

This chapter details the computational analysis undertaken as part of the research project. Part A describes the finite element analysis adopted as the core computational modelling procedure, Part B discusses the computational modelling performed on the steel plates from the arena trials, Part C describes the numerical methods and results from the parametric studies and Part D details the computational analysis of the columns from the combined ABT trials.

4.2 Part A: Finite Element Analysis Procedure

Coupled (thermal and structural), non-linear, transient, dynamic analyses using the finite element analysis (FEA) program LUSAS, (LUSAS, 2013) were performed on the structural elements from the experimental trials and parametric studies. As part of the initial model development an eigenvalue analysis was undertaken on each structure to calculate the natural frequencies and Rayleigh damping parameters. The dynamic damping of a structure is calculated using the Rayleigh damping parameters (Chopra, 2014) for the structural stiffness and mass. For normal building use a damping ratio of 3%, (Davison, 2012) is adopted (typical buildings and structures use a range of 1-5%). Equation 4.1 is used to calculate the mass and stiffness damping parameters. To simplify the models constant damping parameters are specified throughout each analysis for this research.

$$C = \alpha M + \beta K \tag{4.1}$$

An implicit dynamic analysis was adopted for the non-linear analysis. An implicit analysis is relatively computational expensive as it requires stiffness matrix inversion at every time step; however it was preferred to an explicit analysis as explicit can only be used with consistent time steps, Rayleigh

damping parameters are not supported and there are no stress variations across an explicit element. To enable the coupling of the thermal and structural analyses, manually controlled time steps were used with no allowance for step reduction. This enabled larger time steps to be specified during low heating and low/no blast load phases. Smaller time steps were manually specified at the times of peak thermal and blast loading. Due to these extreme loading regimes convergence issues were prominent in the development of the numerical models. Issues including divergence or oscillation of the solution were resolved by setting the maximum number of iterations to 20 per step. Further iterations would produce inaccurate solutions and longer computational running times. Mesh inspection and refinement in areas of high stress and strain were undertaken and an element aspect ratio was maintained below 1:7.5.

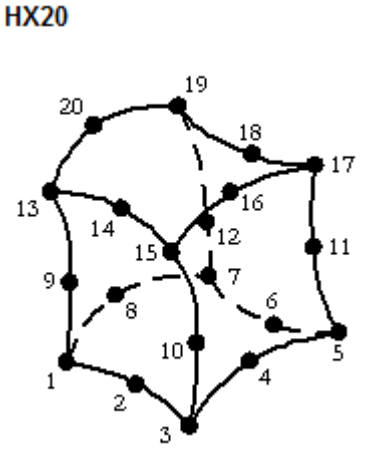

Figure 4.2.1: HX20: Quadratic Solid Element (LUSAS, 2011)

Investigations into the appropriate element type were undertaken at the start of the research project. Plate and shell elements were disregarded due to incompatibility with geometric and material non-linear and coupled analyses. A continuum quadratic solid element (HX20: Fig.4.2.1) was adopted throughout the research project. The HX20 is a standard high order iso-parametric element with mid-side nodes and linear stress variations, (LUSAS, 2011). The geometric non-linear analysis was performed using the Total Lagrangian method. As part of the development of the computational methods the use of Lagrangian and Eulerian methods were also investigated; the Total Lagrangian method was adopted as it was a robust formulation, which could compute the large rotations, displacements and strains exhibited in the elements under intense blast loading. The Eulerian formulation was not suitable as it was only appropriate for moderate strains and each time stepped solution was projected onto an un-deformed original element grid; this was deemed too inaccurate for this project.

Separate material models were developed for each part of the computational analysis; the arena trial plate models adopted dynamic increase factors (4.3) whereas the parametric study (4.4) and ABT trial columns (4.5) used the Johnson-Cook material model to describe the steel properties under high strain rates and high temperatures. The stress potential Von-Mises yield criterion was the chosen formulation for the steel material models.

Structural and thermal loads were applied to the column models using time-varying load curves replicating the recorded pressures and temperatures from the trials and the calculated pressures and temperatures for the parametric study. End constraints were typically pinned or roller pinned; however, spring supports were modelled during the parametric study and the ABT trial column modelling to replicate in service support conditions and the spring stiffness during the trials.

4.3 Part B: Analysis of Arena Trial Plates

The response of the steel plates under the intense blast and thermal loading regimes within an explosive fireball were modelled using the FEA procedure detailed in 4.2. The plates were 150mm diameter, 2mm thick with a bolted circular collar connection to the Heavy Structural Boxes (HSBs) (Fig.4.3.1).

Figure 4.3.1: 2mm Steel Plate Bolted to HSB

A pinned connection was modelled to represent the circular collar. The plates were subject to intense thermal and blast loads from a 41kg TNT eq. event (see 3.2 for full fireball trial details). In order to de-couple the effects of the thermal and blast load on the plates they were modelled under

separate and combined loading regimes. The temperatures and reflected pressures recorded during the trials (Figs.3.2.6 and 3.2.9) were applied to the surface of the plates. Load curves (load-time histories) were used to translate the variation of thermal and blast pressures over the duration of the explosive event into applied loads within the non-linear FEA model.

Under rapid loading scenarios the strain development in structural steels can occur at a very high rate. Steel under high strain rate loading can reach higher yields and ultimate strengths compared to steel under static or low strain rate loading. (Yandzio, 1999) describes the use of Dynamic Increase Factors (DIFs) applied to the yield and ultimate strength of structural steel to account for high strain rate loading. To account for the intense blast load (<10 msec duration) within, and adjacent to the explosive fireball DIFs were applied to the equivalent static steel strength of the plates. The static yield (162MPa) and ultimate (266MPa) strengths, and Young's modulus (202GPa) of the steel were determined from the tensile coupon testing (table 3.1). A DIF of 1.6 (Yandzio, 1999) was applied to the static yield strength and a DIF of 1.05 was applied to the ultimate tensile strength, giving values of 259MPa (yield) and 279MPa (ultimate). The modelled yield strength closely matches the actual yield strength (262MPa) calculated from the recorded strain (3.2.5) during the trials. A shallow strain hardening gradient was defined from the yield (259MPa) to the ultimate (279MPa) strength at 20% strain. An eigenvalue analysis was performed to calculate the mass (α = 170^{1}/s) and stiffness (β = $5.3x10^{-6}$s) damping constants using Equation 4.1. Fig.4.3.2 shows an extract from a FEA model of the 150mm diameter, 2mm thick steel plate. The area of elevated stresses at the corners is due to using a non-radial grid on a circular plate causing high localised stress irregularities.

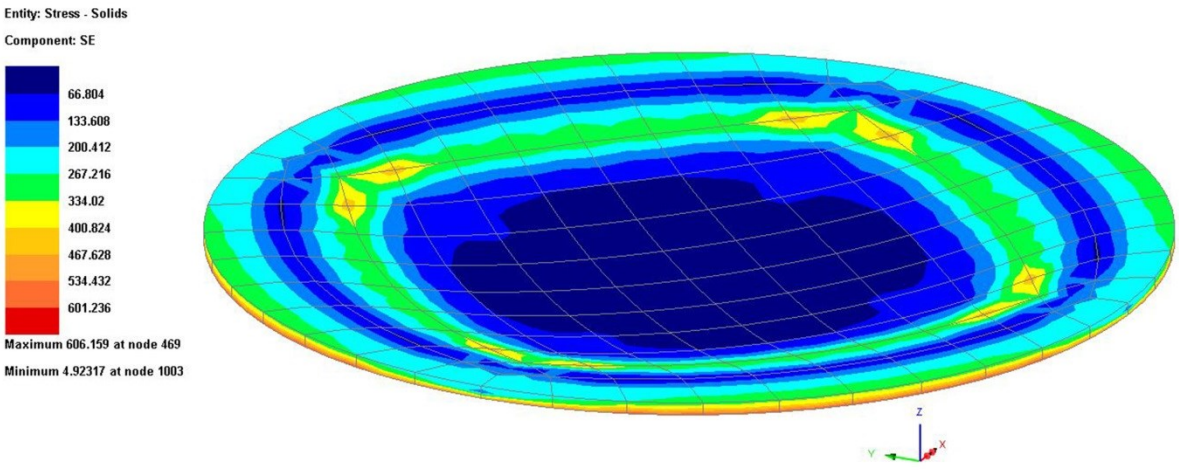

Figure 4.3.2: FEA model of deformed 2mm Thick Circular Plate with Principal Stresses

4.3.1 Model Results and Analysis

Computational models were developed of the steel plates at 4m, 6m and 8m radial locations from the centre of the explosive event. There were no pressure gauges at the 6m location, therefore predicted pressure were calculated using Air3D (Rose, 2001); a computational fluid dynamics (CFD) tool used for the calculation of blast parameters. Separate blast only, blast and thermal and thermal only models were run to de-couple the structural and thermal response and observe any potential synergistic effects. The following results show the horizontal deflection of the plates at the midpoint node of the plate.

4.3.1.1 4m Radial Position

Fig. 4.3.3 shows the deflection-time history of the modelled plates at 4m facing the blast (trial one and two). The deflection history of the plates under combined thermal and blast loads was equal to the deflection history of the plate under blast load alone. Therefore at 4m the response of the plates was blast dominant and no synergistic response occurred. This was due to the plates deforming beyond the plastic limit under the intense blast load, prior to any potential structural response from the explosive thermal load. Under the thermal load alone the plate deflects to a peak of 6mm (trial one), followed by a decrease to 3mm at 3secs. The response of the plates under the thermal load alone follows a similar profile to the recorded temperature (Fig.3.2.6) indicating a thermo-mechanical response which would have occurred under the explosive thermal load only.

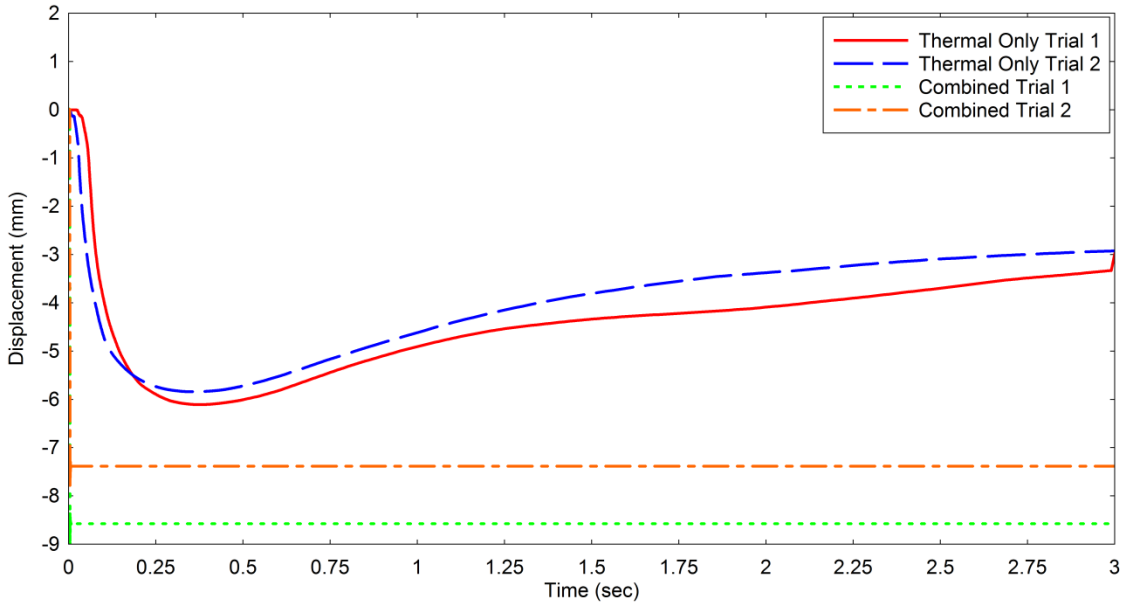

Figure 4.3.3: Displacement at 4m Radial Position: Facing Blast: Combined and Thermal Only

4.3.1.2 6m Radial Position

Fig.4.3.4 shows the deflection time history of the modelled plates at 6m (trial 1) under thermal only and combined blast (predicted) and thermal loading regimes for the plates facing the blast during trial one.

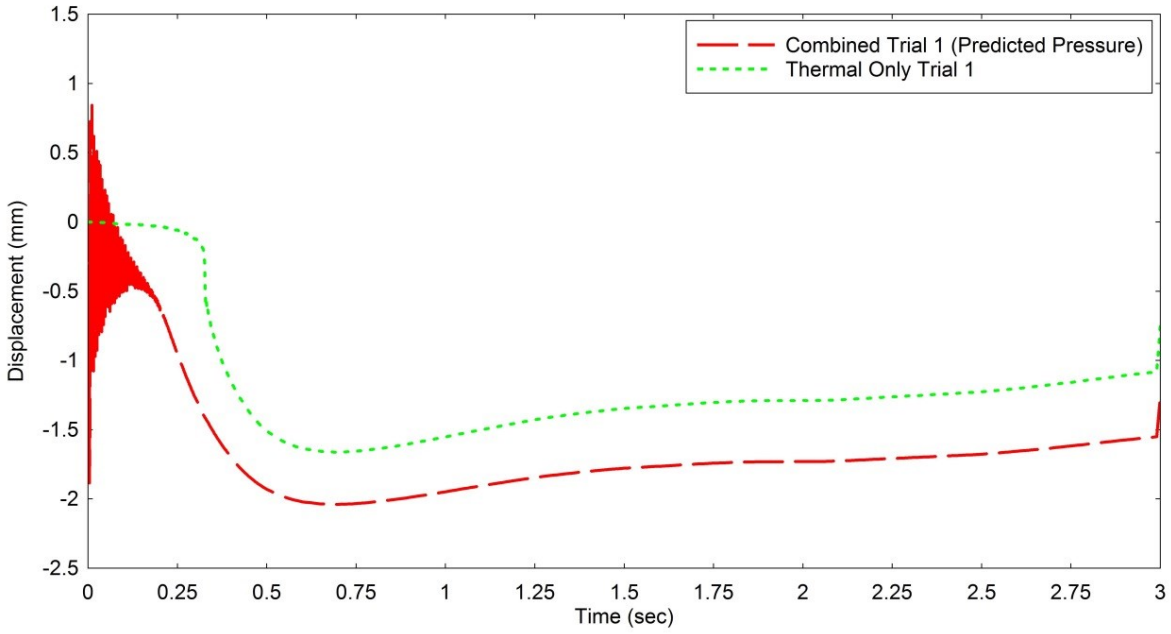

Figure 4.3.4: Displacement at 6m Radial Position: Facing Blast: Combined and Thermal Only

The profile of the deflection time history of the combined loaded model shows an initial intense peak deflection of -1.88mm followed by a decrease with a harmonic response and a second slower peak of -2.04mm, in line with the temperature profile. The thermal only deflection (trial one) follows a similar profile to the post blast (thermal) deflection of the combined model, with a lower peak of -1.66mm. The combined deflection profile indicated a potential synergistic response in the plates at 6m.

4.3.1.3 8m Radial Position

Fig.4.3.5 shows the deflection time histories for the modelled plates at 8m under blast only, thermal only and combined loads. Combined and blast only models (trial one) follow similar deflection profiles. Initial peaks are observed at -2mm with a subsequent harmonic decrease to -0.1mm at 0.03sec (blast only) and -0.29mm at 0.05sec (combined). The thermal only models show minimal deflections during the trials due to relatively low temperature recorded at the 8m location. The blast only model (trial two) peaked at -2.57mm with a subsequent harmonic decrease to 0.48mm at 0.03sec. Blast only and combined models of the plates at 8m all showed an elastic response with a subsequent return to a near zero deflection, this correlates to no visible (to naked eye) permanent deflections observed on the plates at 8m.

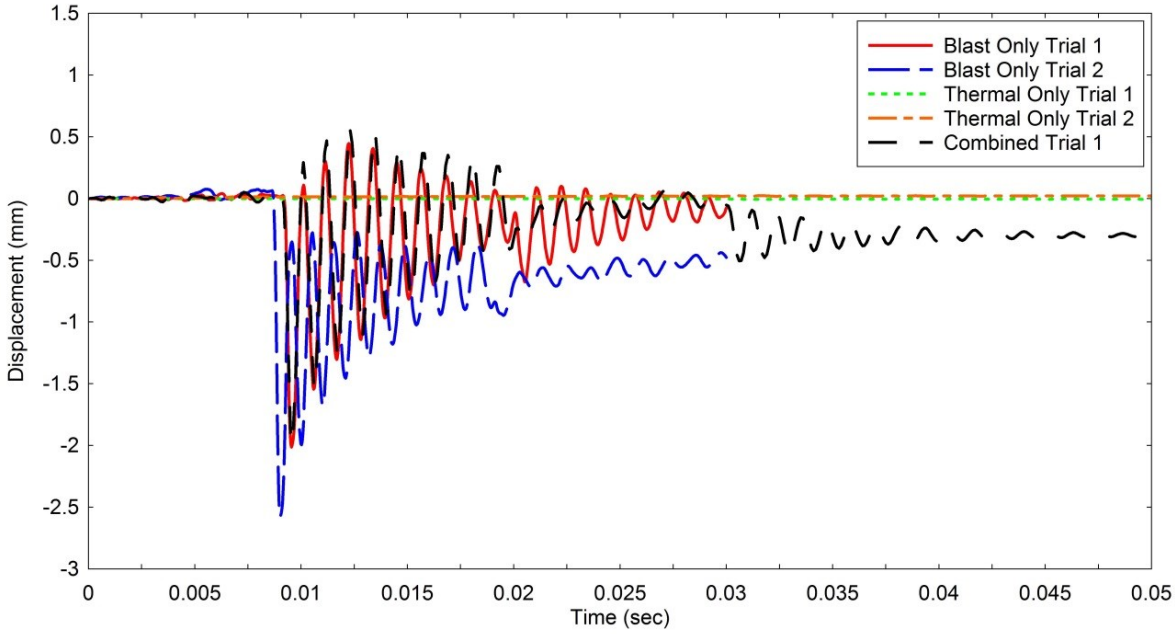

Figure 4.3.5: Displacement at 8m Radial Position: Facing Blast: Combined, Thermal and Blast Only

4.3.1.4 Summary of Arena Trial Plate Analysis

There was no synergistic response observed in the numerical models of the plates at 4m; however at 6m the plate models exhibited a potential synergistic response. The final deflections shapes predicted by the FEA models at 4m were 8.5mm (Trial 1) and 7.5mm (Trial 2). These deflections show reasonable agreement with the final measured deflections in the plates at 4m of 10.5mm (Trial 1) and 7.5mm (Trial 2). The correlation between the modelled and actual final deflections of the plates at 4m provides verification for the core computational procedures adopted for the arena trial modelling, parametric study and ABT trial modelling. Differences in the modelled and actual deflections can be attributed to differences in the plate supports and the variability and extreme volatility of the explosive fireball, (Clough, 2014). The explosive trials were successful in recording the near field pressures, thermal flux and temperatures within a high explosive fireball. The original method of using the heavy structural boxes enabled recording of the pressures, thermal flux and temperatures at very close proximities to the explosive centre. Data recordings at these distances had not previously been achieved for equivalent high explosive events. The data recorded during these trials was subsequently used to model the steel plates with reasonable accuracy and will benefit further research in this field.

4.4 Part C: Parametric Studies on Structural Columns

The parametric study investigated the response of structural column sections under combined intense thermal and long duration blast loads from explosive events. The numerical methods used

for the parametric study are verified with computational modelling of the steel plates from the arena trials (4.3) and the structural columns from the combined ABT trials (4.5). Structural columns were the chosen structural form for the parametric studies and ABT trials as the majority of primary key elements in multi-storey buildings are columns. A key element is a member which, if fails can cause disproportionate collapse of a whole or significant part of a building as opposed to localised damage (BSi, 2000). Key elements are designed to resist large "accidental" loads to prevent progressive collapse of a building (BSi, 1996).

A 193.7x5mm circular hollow section (CHS) was selected for the parametric study due to its thin (5mm) steel walls which facilitate the rapid conduction of thermal load. A universal column (UC) with a similar width, such as a 203x43mm UC has an 11mm flange thickness. In selecting a thinner section there was a higher probability of observing a synergistic response. The columns were 4m in length in order to replicate a typical column used in multi-storey buildings.

The primary parameters investigated during the study were the explosive thermal and blast load determined from parameters including explosive size and standoff distance. Once a sensitivity response envelope of primary loading parameters was formed, secondary parameters were investigated including column fixity, compressive loading, coefficient of thermal conductivity and element thickness. The following section details the numerical procedures used to formulate the full parametric study and results drawn from the study. The data presented in section 2.1 regarding the thermal energy emission from explosive events was used to develop a numerical algorithm for calculating the thermal load applied to the column section at a range of distances and explosive sizes. The algorithm allowed the input of basic explosive parameters in order to extract full thermal flux and temperature history profiles. The prediction of long duration blast loads and blast interaction with the column was undertaken using the methods detailed in (UFC, 2008). The choice and use of the appropriate steel material model under intense thermal and long duration blast loads is detailed in 4.4.4.

4.4.1 Predicting Thermal Profiles

The thermal load profiles are calculated using a numerical algorithm based on parameters relating to the thermal energy emission from explosive events. Thermal emittance data from explosive events detailed in section 2.1 is used to form the numerical algorithm for predicting thermal loads akin to explosive events such as the Buncefield oil refinery (2005), (Burgan, 2009), (Atkinson, 2011b), the West Texas fertiliser factory (2013) and the Tianjin warehouse (2015). The following section details the calculations forming the algorithm including any assumptions and mathematical conjecture that has been employed. The algorithm allows input of parameters including explosive

size W, standoff distance, air temperature, thermal to total energy ratio, Stefan Boltzmann's constant and visual distance. A limitation of the algorithm includes providing accurate data up to ten times the time to the peak thermal load. The calculation procedure used is detailed in the following steps.

The maximum thermal power (cal/sec) emitted from a explosive event is calculated using Equation 4.2:

$$\mathrm{P}_{max} = 3.18W^{0.56} \tag{4.2}$$

Time to reach the peak (maximum) thermal power (sec) is calculated using Equation 4.3:

$$\mathrm{T}_{max} = 0.0417W^{0.44} \tag{4.3}$$

The Stefan Boltzmann black body radiation equation (4.4) relates the thermal power per area (J – Cal/sec/m^2), to an equivalent temperature (T), using the Stefan Boltzmann constant σ, (5.6704x10^{-8} J/sec/m^2/^{o}k^4). If a hemispherical fireball (ground explosion) is assumed equation 4.4 can be rearranged to calculate the maximum temperature (^{o}K) at a given location (equation 4.5). Equation 4.5 assumes the fireball radiates as a black body, if the fireball radiates as a grey body the term ε, emissivity is introduced.

$$J = \sigma T^4 \tag{4.4}$$

$$\text{Max Temp} = (P_{max}/(4\pi\sigma R^2))^{\frac{1}{4}} \tag{4.5}$$

R = radial distance or slant distance from centre.

Equations 4.2 to 4.5 calculate the maximum thermal power, time to maximum power and maximum temperature without taking the thermal to total energy ratio f, and transmittance T, into account. The thermal to total energy ratio describes the percentage of emitted thermal energy to the total explosive size: E_{tot}/W. As the parametric study focused on ground explosions the ratio of E_{tot}/W was assumed as 0.19.

Transmittance (equations 4.6 and 4.7), calculated using the visual range V and slant distance R, describes the proportion of the total emitted thermal energy which reaches the distance of interest. The visual range is a factor which describes the atmospheric conditions. In clear weather, there is a long visual range therefore the thermal energy will radiate further than in cloudy or foggy weather when the visual range is low. The slant distance is distance from the centre of explosion to the location of the structure; this equals the standoff (ground) distance. Equation 4.6 is used to calculate transmittance.

$$T = exp^{-2.9R/V}(1 + 1.9\,R/V) \quad (4.6)$$

R = Slant Distance, V = Visual Range

To calculate the maximum thermal power per area, or peak flux (Equation 4.7 - cal/cm^2/sec) at the location of interest, the maximum power (P_{max} - Equation 4.2) is multiplied by the transmittance T, and thermal energy ratio (f). This is divided by the hemispherical radiated area at the distance of interest (Equation 4.7):

$$Peak\ Flux = \frac{fTP_{max}}{(4\pi R^2)} \quad (4.7)$$

The peak flux (Equation 4.7) is converted to a flux-time history profile using the normalised power (P/P_{max}) vs. time profile (Fig.4.4.1). Fig.4.4.1 also shows a profile representing the percentage of emitted thermal energy to total thermal energy (E/E_{tot}) over normalised time. The normalised power curve was incorperated into the algorithm by using a best fit Gaussian distribution curve with the parameters shown below (Equation 4.8). The peak flux at a specific location is multiplied by normalised power vs. time factors from equation 4.8 to give the thermal flux vs. time profile. Equation 4.5 is used to convert the thermal flux vs. time profile to a temperature vs. time profile.

$$f\ (x;\mu,\sigma,\lambda) = \lambda/2\, e^{\lambda/2(2\mu+\lambda\sigma^2-2x)} erfc(\tfrac{\mu+\lambda\sigma^2-x}{\sqrt{2\sigma}}) \quad (4.8)$$

Gaussian Distribution Parameters (μ = 0.7, σ = 0.05, λ = 0.7), $erfc$ = Complementary Error Function

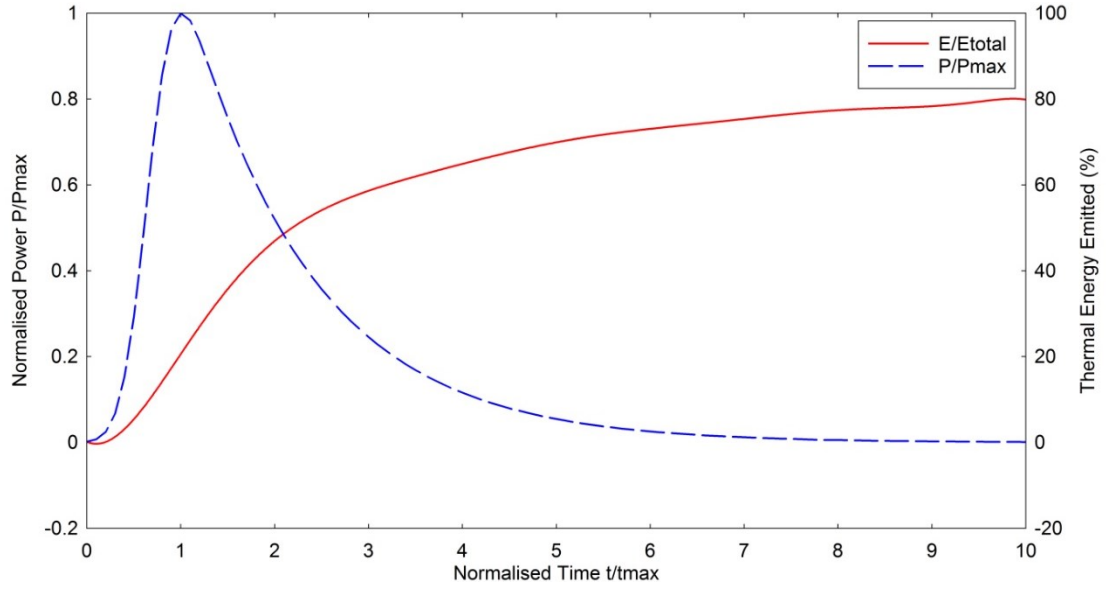

Figure 4.4.1: Normalised Power vs. Time of Thermal Energy Emitted

Figures 4.4.2 and 4.4.3 show the thermal flux and temperature vs. time profiles produced by the numerical algorithm. The numerical procedure uses theory regarding the thermal energy emission

from an explosive fireball as discussed in section 2.1. The extent and form of the thermal radiation from explosive fireballs is based on theoretical calculations with relation to past experimental trials as detailed in section 2.1.

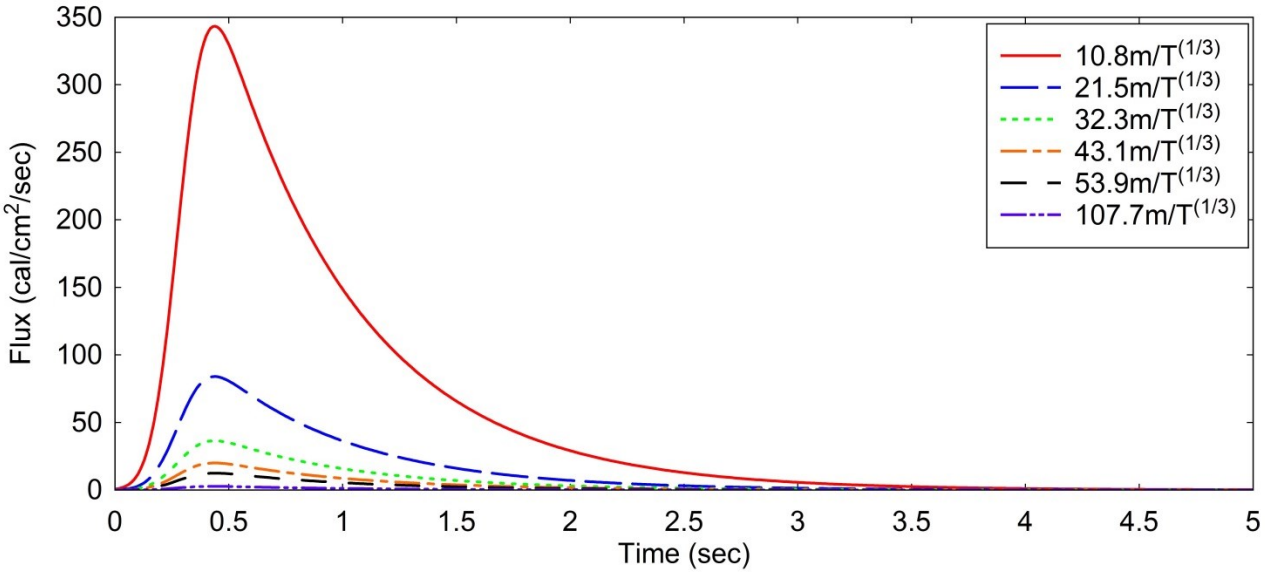

Figure 4.4.2: Thermal Flux vs. Time

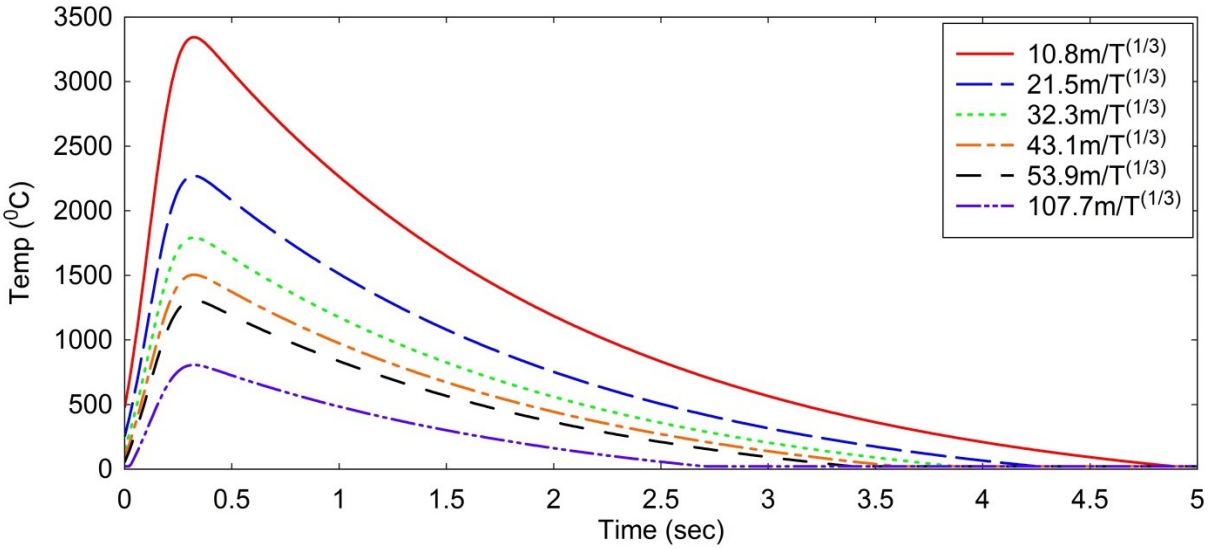

Figure 4.4.3: Temperature vs. Time

4.4.2 Structural Steel Column Temperature

The thermal energy from the explosive fireball is transferred to a structural steel column via radiation as the primary mechanism. The amount of thermal energy absorbed by the structure is determined by the surface colour and texture. This can be quantified by use of an absorption coefficient. Structural steel columns have an absorption factor of 0.79 (oxidised steel (Wang, 2013)),

this factor is applied to the incident thermal radiation. The absorption coefficient was used with the Stefan Boltzmann black body equation (4.4) to calculate the surface temperature. This thermal load (temperature) was applied to the external surface of the column within the computational models. The thermal analysis within the FEA calculates the absorption of this thermal load through the steel enabling the thermal gradient to affect the structural and material properties. This is a simplified assumption of the increase in surface temperature of the steel. Further work beyond the course of this research project could investigate the effect of varying thermal thicknesses upon the steel surface temperature and thermal gradient.

After the peak surface temperature is reached the steel will begin to cool via a combination of convection, conduction and (re)radiation. The convective cooling surface temperature of the steel is calculated using Newton's Law of Cooling which states "*the rate of heat loss of a body is proportional to the difference in temperatures between the body and its surroundings",* (Equation 4.9), (Incropera, 2007) and (Butterworth, 1977). For the parametric study a constant heat transfer coefficient of 5 W/m^2.^{o}K independent of the temperature difference between the steel surface and surrounding air was assumed.

$$\frac{dQ}{dt} = hA(T(t) - T_{env}) = hA\Delta T(t) \tag{4.9}$$

Q = thermal energy (J), h= convective heat transfer coefficient (free convection, steel to air: 5 W/m^{2}K), A= heat transfer surface area (1.217m^2), T = surface temperature (^{o}C)*, T_{env}= environmental temperature* (^{o}C)*, $\Delta T(t)$ = time-dependent thermal gradient between environment and object*

To solve equation 4.9 a lumped capacitance model was assumed (the conduction of heat through the steel is greater than the loss of heat via convection). The rate of convective heat transfer is therefore equated to the rate of change in internal energy of the block (Equation 4.10)

$$-hA_s(T - T_{env}) = \rho V_c \frac{dT}{dt} \tag{4.10}$$

Rearranging and solving the differential equation 4.10 leads to a solution for *t,* (Equation 4.11) the time taken for the steel surface to cool to a specific temperature (sec):

$$t = \frac{\rho V_c}{hA_s}\left[\ln\frac{(T - T_{env})}{(T_i - T_{env})}\right] \tag{4.11}$$

ρ = material density (7.7x10^{3}kg/m^3), V = volume (area of heated steel x thickness = 6.085x10^{-3}m^3), c = specific heat capacity (J/kg.^{o}K), T_i = initial temperature (^{o}C),

Prior to the blast arrival the convective cooling is assumed to be "free". The pressure from the blast load and subsequent blast wind will produce a forced convective cooling situation leading to the rapid cooling of the steel surface. For the purpose of the parametric study the latter forced convective cooling is ignored as the primary interest is the thermo-mechanical state of the steel column upon arrival of the blast. Radiative cooling is also ignored as the temperature drop between peak temperature and blast arrival is negligible. Thermal energy is also conducted through the steel column; the conduction of the thermal energy through the steel is calculated as part of the thermal analysis within the non-linear FEA.

To take account of the circular face of the CHS used in the parametric study, a smoothing variation was applied to the incident radiation across the face of the column. The smoothing variation used cosine factors equating to a maximum of 1 at 0^o (front face) and zero at 90^o (side face). The factor at 45^o was 0.7071. These factors were applied around the front circumference of the column.

4.4.3 Predicting Blast Load Profiles

A numerical algorithm combining blast parameters and the application of the blast loads on structures was developed for the prediction of blast loads on structural columns. The primary blast parameters including the peak dynamic pressure (Equation 4.12) and shock velocity (Equation 4.13), were calculated. Values for the peak static overpressure, arrival time and decay rate of the positive phase static and dynamic pressures were taken from (Figs.2.3.3 to 2.3.5). These parameters were used with the scaling laws according to (Brode, 1954) (Equation 2.14). The curves shown in Figs. 2.3.3 to 2.3.5 were incorporated into the numerical algorithm using best fit polynomial decay curves.

$$q = \frac{5}{2}\frac{p^2}{7P_0+p} \tag{4.12}$$

$$U = c_0\left(1+\frac{6p}{7P_0}\right)^{1/2} \tag{4.13}$$

P_0 = ambient pressure at sea level, p = static overpressure.

The applied blast pressure to the face of structural columns was calculated according to (UFC, 2008). If the column section is assumed to be "standalone" the incident pressure from the blast wave would rapidly equalise around the column shortly after the blast arrival, reducing the net pressure in the direction of the blast. This is due to the relatively shallow width and depth of the 193.7mm CHS in comparison to the length of the long duration blast wave. To negate the effects of the rapid equalisation of the blast pressure the following assumptions were made regarding the column's structural configuration. These assumptions can be directly related to the use of a column in a typical building.

- There is no cladding attached to, or directly in front of, the column; therefore the thermal radiation can reach the column face and no blast load would be directly transferred from the cladding to the columns.
- The building cladding is adjacent to the columns. Fixed at the top and bottom to horizontal beams or slabs.
- The cladding remains intact for the duration of the blast load, transferring the applied blast load to beams / slabs and preventing any equalisation of pressure around the adjacent column

Using these assumptions the dynamic and incident blast loads, with appropriate drag load coefficients were applied to the front half of the CHS structural column according to the methods shown in (UFC, 2008). For flat surfaces such as square or rectangular column sections, the applied pressure to the front face rises to an instantaneous peak upon arrival of the blast wave. For circular structures (such as CHS) the pressure applied to the front face rises over time until a peak of $2p$ (p = incident overpressure) is reached at time $D/2U$ (D = column diameter, U = shock velocity) (Fig.4.4.4). Following the peak the applied pressure drops linearly to the equivalent pressure after a decay time of $2D/U$. From this time to the end of the positive phase the applied pressure equals the sum of the decaying incident pressure (p) and the dynamic pressure (C_d) with an applied drag coefficient. The drag coefficient (q) used for the front face of the CHS was 0.8.

The pressure applied to the side face of the column increases linearly to p_{s1} after the arrival of the blast on the front face to a time (t) when the front of the blast wave has passed the whole column (D/U). The peak pressure p_{s1} is equal to the incident overpressure at time $t = D/U$. Due to complex vortex formations around the column this peak pressure drops linearly to a minimum pressure, p_{s2} at time $3D/U$, p_{s2} is equal to half the incident overpressure at that time. Following this minimum the pressure increases linearly again to the sum of the incident overpressure (p) and dynamic pressure with applied drag coefficient ($C_d q$) at time $t = 9D/2U$. The applied pressure subsequently decays to the end of the positive phase (Fig.4.4.5).

The drag coefficient (q) used for the side faces was 0.9. Linear smoothing was applied to the front and side pressures using the ratio of peak pressures on each face (split into front quarter and side quarters) to ensure there was no unrealistic load step across the surface of the CHS.

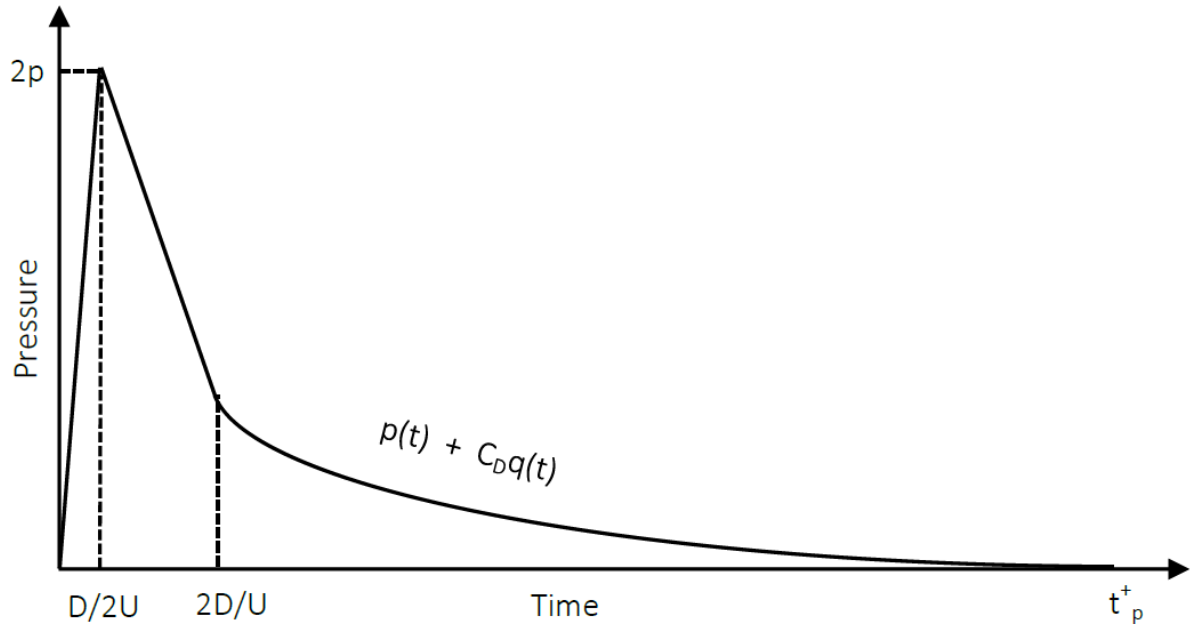

Figure 4.4.4: Front-On Pressure on Circular Structure

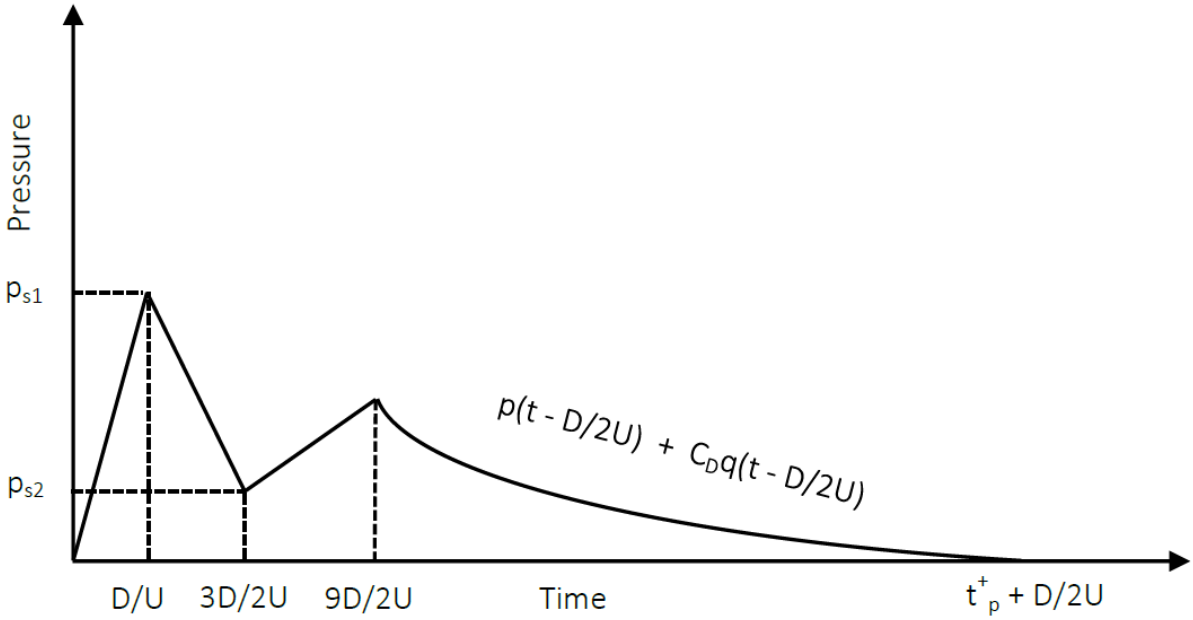

Figure 4.4.5: Side-On Pressure on Circular Structure

Figs. 4.4.6 and 4.4.7 show the pressures applied on the front and side face of the CHS for an explosive event with an equivalent peak static overpressure of 99.4kPa. Fig 4.4.6 shows a sharp peak pressure followed by a longer, lower decay phase. Despite a lower pressure the decay phase (dynamic and incident) is the dominant pressure phase as the duration and impulse are much larger. Fig.4.4.7 shows the variations in the peak pressures on the front and side of the CHS as the shock front passes, lasting less than 2.2msec. Equivalent pressure profiles were calculated for a range of explosive sizes and distances as part of the parametric study (Appendix C).

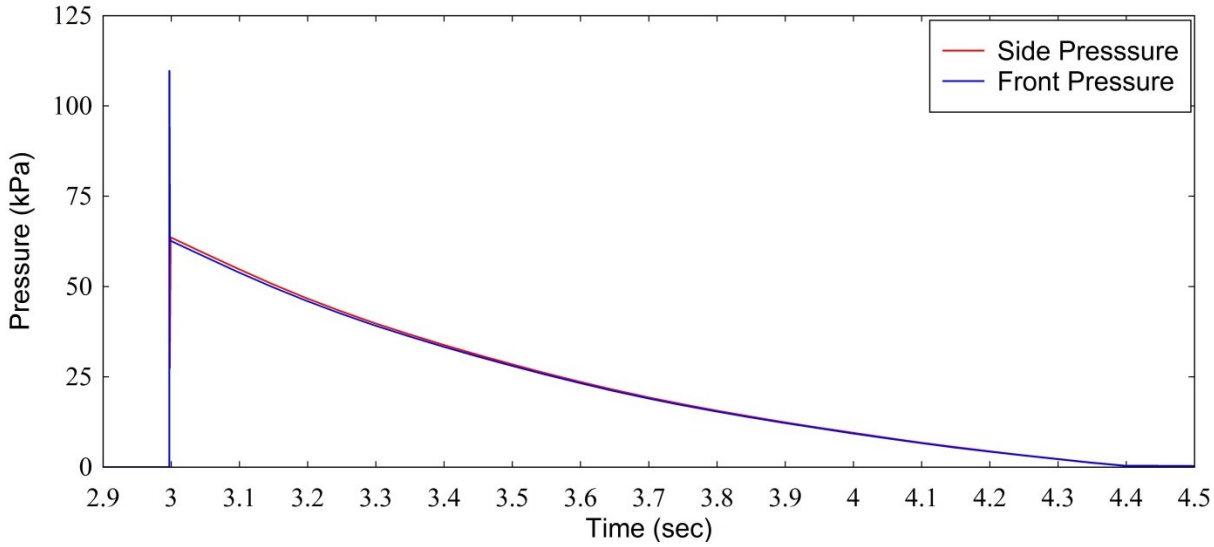

Figure 4.4.6: Front and Side-On Pressure on CHS

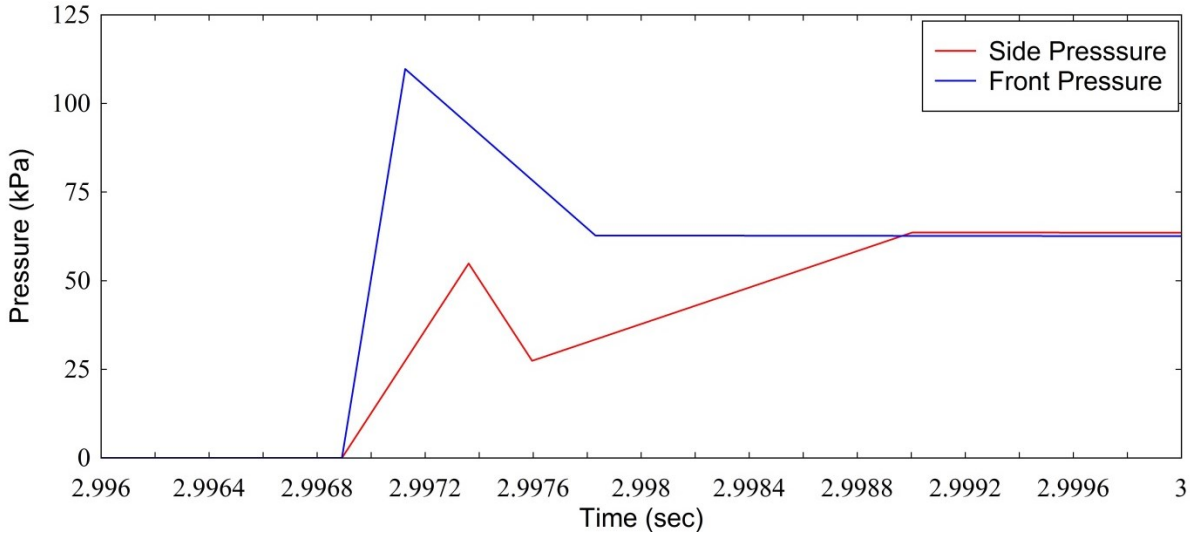

Figure 4.4.7: Front and Side-On Pressure on CHS (Zoomed at Peak)

4.4.4 Structural Material Model

The steel columns investigated were under extreme structural and thermal loading conditions. Therefore, it was necessary to ensure the most appropriate material model was used for the non-linear modelling of the columns. The specified material model needed to match, as close as reasonably possible, the response of steel under intense temperatures and blast loads. The use of the appropriate Young's Modulus, thermal conductivity, coefficient of thermal expansion, Poisson's ratio and specific heat coefficient were also investigated.

4.4.4.1 High Strain Rate and Temperature Effects on Steel

When subject to high temperatures the properties of steel change and degrade; BS EN 1993-1-2-2005 (BSi, 2005c) applies factors to the yield and ultimate strength of steel to account for this

degradation. These factors are independent of any high strain and strain rate effects of the properties of steel. (Cooke, 1988) describes the changes to steel properties at elevated temperatures including variations in the stress vs. strain relationship (2.5.3).

The combination of high temperatures and high strains on structural steels is investigated in (Burgan, 2001) with reference to BS EN 1993-1-2-2005 (BSi, 2005c) and BS5950-8-2003 (BSi, 2003) (2.4.5 and 2.5.3). At higher strains steel exhibits an increased strength when compared to steel under lower strains at the same temperature. (Laasraoui, 1991) investigated steel under high temperatures and two strain rates (0.2 εs^{-1} and $2\varepsilon s^{-1}$); the steel under higher strain rate loading reached higher yield stresses than the steel under a lower strain rate loading at an equivalent temperature. For simplified structural design to blast loads Dynamic Increase Factors (DIF) are used to increase the equivalent yield and ultimate tensile strength of steel under high strain rate loading, (Yandzio, 1999); however, the use of DIFs is inappropriate for the combined thermal and blast scenarios investigated in this parametric study.

The material model adopted for steel columns in the parametric study was the Johnson-Cook model (Equation 4.14, MPa), (Johnson, 1983). The material model is used to represent the post elastic stress state combining strain hardening [parenthesis one], strain rate hardening [parenthesis two] and thermal softening [parenthesis three].

$$\sigma_y = \left[A + B(\varepsilon_{eff}^{p})^N\right](1 + C \ln \dot{\varepsilon})[1 - (T_H)^M] \tag{4.14}$$

σ_y = Yield Stress, ε_{eff}^{p}= Effective Plastic Strain, A = Elastic Yield Stress, B & N = Strain Hardening Parameters, T_H = Homologous Temperature, M = Material Parameter, C = Strain Parameter

Table 4.1 shows the Johnson-Cook material parameters adopted for the structural columns in the parametric study. The steel grade S275 (mild steel) was specified. A constant strain rate of $80\varepsilon s^{-1}$ was used to calculate the model parameters. This strain rate was adopted as it is typically observed in steel structures under long duration blast loads, (van Netten, 1997) and (Clubley, 2014). The homologous temperature is calculated using equation 4.15.

$$T_H = \frac{T - T_R}{T_m - T_R} \tag{4.15}$$

T_m = melt temperature (1500°C), T_R = reference temperature (20°C), T = applied temperature (°C)

The specified parameters were determined for mild steel under high strain rate, high strain and high temperature loads. As no specific example using the Johnson-Cook model under the strain rates and temperatures have been previously investigated, the material model parameters were

determined from the following papers which had undertaken testing on steels under different strain rates and temperatures.

The strain parameter C (0.076) and strain hardening parameter N (0.643) were determined from (Vedantam, 2005) who had undertaken Split-Hopkinson bar tests on mild steel at room temperature (20°C). The homologous temperature T_H, was determined using the same reference temperature T_R = 20°C. The material parameter M, was determined from (Schwer, 2007), who investigated high temperature and strain rates on U.S structural steel (A36). Figure 4.4.8 shows the post elastic stress vs. strain profile calculated using the Johnson-Cook material model adopted for the steel columns in the non-linear analysis.

Table 4.1: Johnson-Cook Material Parameters

Parameter	Value	Unit
A: Elastic Yield Stress (at ambient temperature)	275	MPa
B: Ultimate Tensile Stress (at ambient temperature)	410	MPa
C: Strain Parameter (Vedantam, 2005)	0.076	n/a
N: Strain Hardening Parameter (Vedantam, 2005)	0.643	n/a
M: Material Parameter (Schwer, 2007)	0.917	n/a
T_H: Homologous Temperature	Varies (Eqn. 4.15)	°C
$\dot{\varepsilon}_0$: Reference Strain Rate	1.0	(sec^{-1})

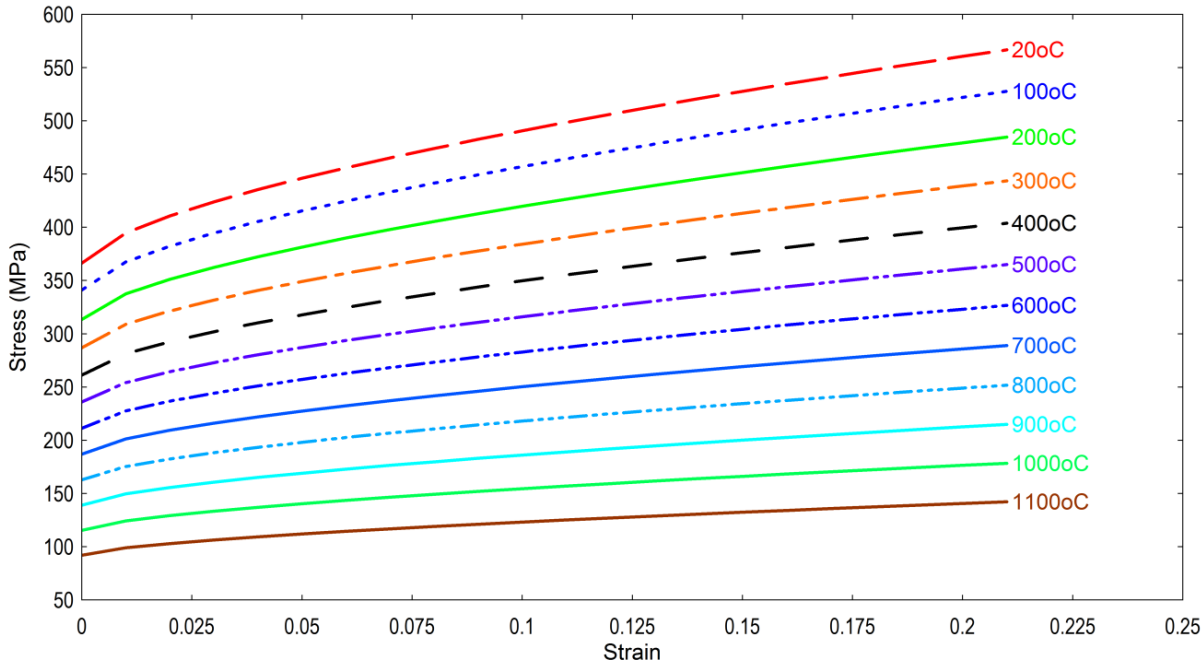

Figure 4.4.8: Structural Steel Material Model

The Young's Modulus is negligibly affected by high strain rate loading, but is significantly affected by high temperatures. The factors in BS EN 1993-1-2-2005 (BSi, 2005c) describe the reduction of the Young's Modulus at elevated temperatures. Table 4.2 shows the reduced Young's Modulus at elevated temperatures. These values were incorporated into the structural steel material model used in the non-linear analyses.

Table 4.2: Young's Modulus Reduction at Elevated Temperatures

Temperature (°C)	Young's Modulus (GPa)
0	205.0e3
100	205.0e3
200	184.5e3
300	164.0e3
400	143.4e3
500	123.0e3
600	63.60e3
700	26.70e3
800	18.50e3
900	13.80e3
1000	9.20e3
1100	4.60e3
1200	0.0

4.4.4.2 Additional Steel Material Properties

The mechanical properties of steel including Poisson's ratio, thermal expansion, specific heat capacity and thermal conductivity were assumed constant with increasing temperatures and high strain rates. These properties do exhibit some small variations under elevated temperatures however the changes were deemed negligible. Table 4.3 shows the specified values used throughout the parametric study. A study was performed as part of the full parametric study investigating the effect of thermal conductivity on the response of the column to blast and thermal loading (4.4.6.5). For the purposes of this research project the strength and stiffness of the column connections are assumed constant at increasing temperatures, remaining at the equivalent strength and stiffness at ambient temperatures.

Table 4.3: Mild Steel Material Properties

Material Property	Value	Unit
Poisson's Ratio	0.3	n/a
Coefficient of Thermal Expansion	$12.0e^{-6}$	$^{o}C^{-1}$
Thermal Conductivity	45	$W/m.^{o}K$
Specific Heat Coefficient*	4.68	$mJ/mm^3.^{o}C$

**Specific Heat Coefficient = Specific Heat Capacity x Density*

4.4.5 Non-Linear Modelling Process

The finite element analysis procedure detailed in 4.2 was used to model the structural columns under intense thermal and long duration blast loading regimes. Solid elements (HX20) were used to model the column. The ideal shape of a solid element in a structural analysis is cuboid with an aspect ratio of 1:1:1; however a 4m long, 193.7x5mm CHS column with this aspect ratio would have required approximately 150000 elements and three million nodes. This would have been very computationally expensive and impractical to perform a full parametric study. Each element modelled was approximately 30mm wide, 27mm deep and 5mm thick, equating to a maximum aspect ratio of 1:6. Each column model therefore consisted of 3000 elements and 60,000 nodes. The average approximate running time for a coupled thermal and structural analysis was 8 hours (2 hours thermal, 6 hours structural). The use of these thin solid elements increased the risk of shear locking (bending deformation mode requires energy from shear strain as well as normal strain leading to stiff bending and inaccurate deformations) (LUSAS, 2011). However no shear locking occurred throughout the parametric study.

After formation of the column geometry and selection of the element type and size, an eigenvalue analysis was performed to determine the natural frequency and calculate the Rayleigh damping parameters of the column. Using the typical damping ratio of 3% (for normal building use), (Davison, 2012) the damping parameters calculated were: mass damping constant(α)= 30^1/s, stiffness damping constant (β) = $1.0x10^{-6}$s. The stress potential, Von-Mises yield criterion model was adopted for the material continuum formulation. Von-Mises yield criterion was chosen as it was appropriate for use with ductile (steel) materials.

Separate blast only and combined blast and thermal models were developed as part of the parametric study in order to de-couple the effects of the two load regimes to form separate resistance functions (5.1). Two methods of thermal load application within the LUSAS modelling platform were investigated as part of the parametric study; applied thermal flux and prescribed temperature. The prescribed temperature application used the temperature profiles calculated

from the Stefan Boltzmann radiation equation and Newton's convective cooling equations (4.4.2). The calculated temperatures were directly applied to the surface of the steel columns. The thermal flux load was applied to the steel surface using the thermal flux profiles calculated from 4.4.1. The convective, radiative and conductive cooling of the columns subject to thermal flux was performed by the thermal analysis within the FEA program. Two thermal load application methods were initially investigated (flux and temperature) to determine the most appropriate and suitable method to apply the thermal load profiles calculated in 4.4.1 and 4.4.2. The blast loads calculated in 4.4.3 were applied to the surface of the column using face loads. Face loads are typically applied to faces of solid elements in the local element direction; therefore the applied blast pressure was always normal to the surface of the column around the circumference.

The blast pressures were applied using face loads assigned to load (varying) vs. time curves. In order to encourage the analyses to converge at the initial, intense stages of the applied blast pressure, nominal gradients (ramp functions) were applied to the pressure load curves instead of an immediate (vertical) increase to the peak pressures. The duration of the nominal gradients used were 25msec to 30msec dependent on the blast pressure arrival time. During the development of the trial models it was observed that the initial high peak pressure (2p) had little effect on the structure. This was due to its application over a very small duration (< 0.5msec). Consequently, very small time steps were required in order to enable the analyses to converge at the peak (2p) pressure values, this led to very high computational running times. Subsequently computational models were developed for the full parametric study using a lower equivalent peak pressure of $p + C_d q$ at time $2D/U$.

A study was conducted as part of the full parametric study investigating the effect of one and two element thick steel on the response of a smaller column to identical blast and thermal loads. This was performed to observe any noticeable differences in the stresses throughout the elements and any significant differences in the deflections. A singular element thickness was adopted for the columns in the majority of the parametric study to minimise the computational running times. If a two element thick model was used with a maximum element ratio of 1:6, the element dimensions would have been 15mm (w) x 13.5mm (d) x 2.5mm (t). This would have quadrupled the number of elements and nodes, significantly increasing the computational running times.

4.4.5.1 Column Supports & Compressive Load

As part of the full parametric study several types of column support were investigated; pinned support at base and top, pinned support at base with roller support at top, and pinned support at the base with spring support at top representing the stiffness imparted from an equivalent of one

and two storeys above the column. The response of the column under varying compressive loads was also investigated.

The applied compressive loads were calculated by estimating the load from a number of typical storeys above the column. Assuming a singular column supports 36m^2 (6m x 6m bay), with a dead load of 4.95kPa, live load of 2.0kPa the total load per storey, per column was 249kN (Serviceability Limit State, SLS) and 365kN (Ultimate Limit State, ULS). The ULS load was calculated using partial load factors of 1.4 (Dead) and 1.6 (Live) (BSi, 1996). Therefore two storeys of compressive load totalled 498kN (SLS) and 730kN (ULS). The compressive load capacity of a 4m long CHS193.7x5 column is 845kN (Bsi, 2005b). Therefore the single storey compressive load equates to 43% of the compressive capacity and the two storey load equates to 86%.The vertical load was applied as a compressive stress load to the solid elements forming the structural column. The compressive stress was calculated by dividing the total ULS vertical load by the sectional area of the column. For one storey load the applied compressive stress was 124MPa.

The columns investigated in the parametric study with spring support top connections used a spring stiffness representing one and two storeys of compressive load above the column. The spring stiffness was calculated according to (Shepherd, 2011). The support stiffness (K_r) of the column's top end connection supporting one or two storeys above was calculated using equation 4.16.

$$K_r = K_{floor1} + \frac{1}{\frac{1}{k_{column2}} + \frac{1}{k_{floor2}}} \tag{4.16}$$

The stiffness from the floor directly above the column (K_{floor1}), defined by equation 4.17, is dependent on the number of beams (N) framing into the top of the column.

$$K_{floor\ 1} = N\frac{12EI}{l^3} \tag{4.17}$$

Four, 6m structural beams are assumed to span into the top of the column each with a section size of 203x133x30UB. This is a simplified assumption for the parametric study; a typical building may have several different size and length beams framing into the top of a structural column. The sectional properties for a 203x133x30UB are: A (area) = 3820mm^2, and I (second moment of area) = 2896x10^{4}mm^4 (Bsi, 2005b). Therefore using equation 4.17 the stiffness from one floor directly above the column is 1.319kN/mm. If the structural layout is repeated for any floors above, the same structural stiffness can be used in equation 4.16 for K_{floor2} etc.

The stiffness imparted from a column supported directly above the column connection of interest ($K_{column2}$) is calculated using equation 4.18

$$K_C = \frac{EA}{L} \tag{4.18}$$

Assuming the column above has the same length and section size (193.7x5CHS: A = 2960mm^2, I = 1320x10^{4}mm^4, L = 4000mm), the stiffness K_c = $K_{column2}$ = 151.7kN/mm. Therefore, using equation 4.17, if the building was a single storey, with stiffness imparted only from roof beams the total spring support stiffness would be 1.319kN/mm. If the building had two storeys with a column above and a second level of beams, the total stiffness, calculated using equation 4.16, would be 2.627kN/mm.

4.4.6 Parametric Study Results

The key aim of the parametric study was to investigate the response of a circular steel column under a range of blast and thermal loads from explosive events. Table 4.4 shows the range of peak pressures and peak temperatures investigated.

Table 4.4: Peak Pressures and Temperatues

Case	Peak Pressure (*2p*) (kPa)	Equivalent Peak Temperature (°C)	Scaled Distance (m/T$^{1/3}$)
1	66.4	1464	58
2	95.1	1525	48
3	96.6	1465	47
4	107.1	1738	44
5	109.7	1701	43
6	111.5	1668	43
7	112	1536	43
8	127.9	1674	41
9	136.2	1594	40
10	153.1	1708	38
11	153.6	1682	38
12	182.4	1904	34
13	182.5	1762	34
14	184.8	1866	34
15	198.7	2013	32
16	198.8	1873	32
17	203.8	1827	32
18	260.9	1998	28
19	281.7	2126	27
20	290.3	2084	27
21	329.3	2247	26
22	329.4	2091	26
23	384.9	2166	24
24	477.9	2370	22
25	536.4	2504	20
26	912.7	2787	16

The cases shown in table 4.4 relate to specific size explosions and standoff distances, these can be related into a single parameter; scaled distance (m/$T^{1/3}$, TNT eq.), $Z = R/W^{1/3}$, which takes account of several explosive parameters into one parameter. The parametric study was performed using the blast and thermal load profiles relating to the peak pressures and temperatures shown in table 4.4.

At an early stage of the parametric study a sensitivity response envelope of peak pressures and temperatures was formed. This envelope was formed from the loading regimes which produced the most significant synergistic response. After forming the envelope further parameters were investigated including column support conditions, compressive loads and thermal conductivity of the steel. A study investigating the response of a short column with double and single element thickness was also undertaken to assess the suitability of using single element thickness column models for the majority of the parametric study. The cases within the sensitivity response envelope are shown in Fig.4.4.26 to 4.4.8 and discussed thereafter in 4.4.6.3 to 4.4.6.6.

Different methods of thermal load application (thermal flux and applied temperature), within the FEA modelling platform were initially investigated. The parametric study conducted on load cases within the critical envelope was completed using the prescribed temperature load application as it enabled manual calculation of convective cooling and direct input of temperature-time history profiles.

4.4.6.1 Individual Column Results

A column subject to a blast load with a peak pressure of 198.8kPa and equivalent thermal load with a peak temperature of 1873^{o}C fell within the sensitivity response envelope of results. The column had a pinned base and roller top connection. Figs 4.4.9 and 4.4.10 show the midpoint deflections and principle von Mises stress histories of this column. There are three curves per figure, one showing the blast only response and two showing the combined thermal and blast response using the prescribed temperature and thermal flux load application. The largest response is observed in the blast and thermal case (using prescribed temperature); a deflection under the thermal load towards the blast of -22.5mm is observed followed by a large peak deflection away from the blast of 187.4mm settling at a final deflection of 138mm, indicating a plastic response. A smaller elastic deflection occurred in the blast only model (13.9mm) and the thermal flux model exhibited a small thermal deflection (-2.8mm) followed by an elastic deflection (11.2mm) with the same relative magnitude to the blast only case.

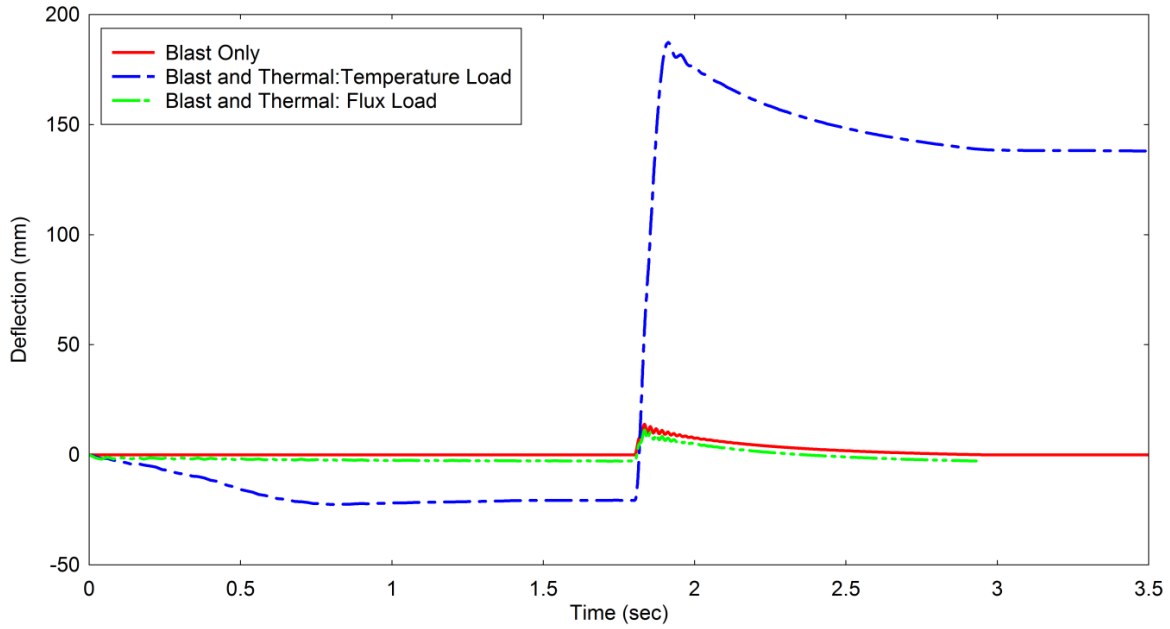

Figure 4.4.9: Midpoint Deflection vs. Time of Column (Peak Pressure = 198.8kPa)

The stress histories follow a similar profile to the deflections with stresses observed during the thermal loading phase in the prescribed temperature and thermal flux models, followed by a large increase in stress peaking at 380.62MPa (prescribed temperature), 200.45MPa (thermal flux) and 142.625MPa (blast only). The prescribed temperature model settles at a final stress of 287.43MPa compared with 53.94MPa for the thermal flux (similar to pre-blast thermal stress) and 2.07MPa for the blast only model.

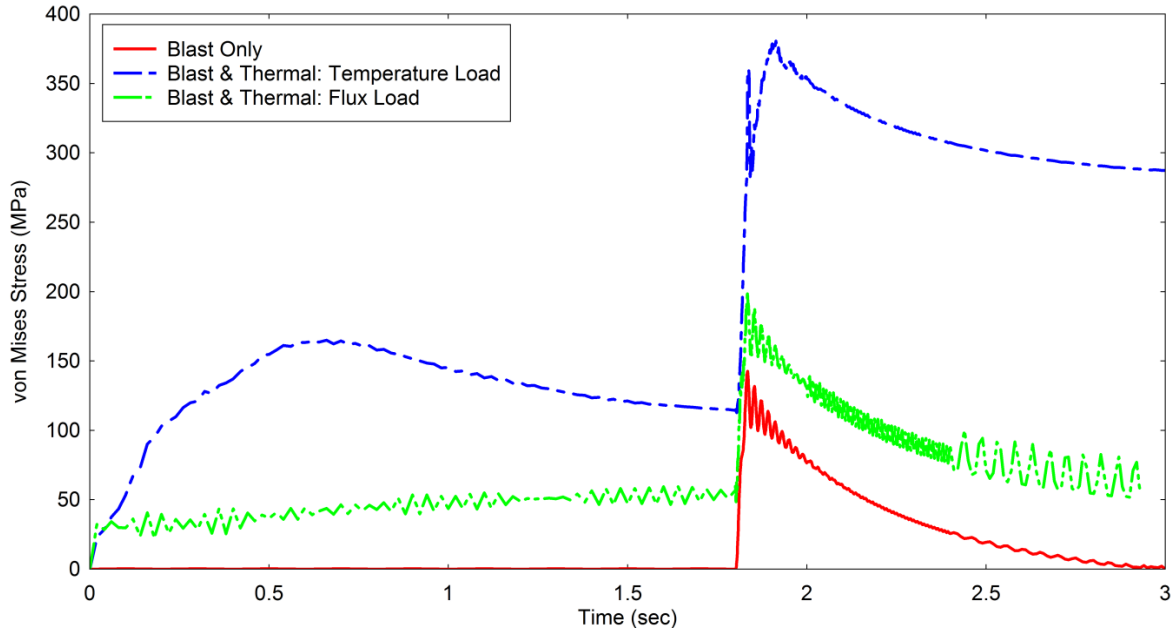

Figure 4.4.10: Midpoint (von Mises) Stress vs. Time of Column (Peak Pressure = 198.8kPa)

Figure 4.4.11 shows the deformed shape of the column and principle von Mises stresses under the combined loading regime (peak pressure = 198.8kPa, prescribed temperature). A plastic hinge (area

of high fluctuating stresses) has formed in the column. Figs.4.4.12 and 4.4.13 show the deflection and longitudinal stress vs. column height. The plotted lines represent the peak and final deflections for the blast only case and the peak and final deflections for the blast and thermal case (prescribed temperature). The peak deflection during the thermal (pre-blast) loading phase is also shown (thermal peak). Moderate peak elastic deformations of 14.5mm are observed in the blast only case. A longitudinal peak stress of 557MPa is observed at the column base for the blast case, with a peak stress of -230.7MPa at location of maximum deflection. The blast and thermal case shows a "thermal peak" deflection towards the direction of the blast, prior to the blast arrival, of -25.7mm at 2.62m height. A large peak deflection of 282mm at 2.28m height and final deflection of 227mm at 2.29m height was observed in the blast and thermal case. The deflection profile narrowed along the length of the column at the point of maximum deflection indicating the formation of a plastic hinge, also indicated by the high stress variation over a relatively short length of column.

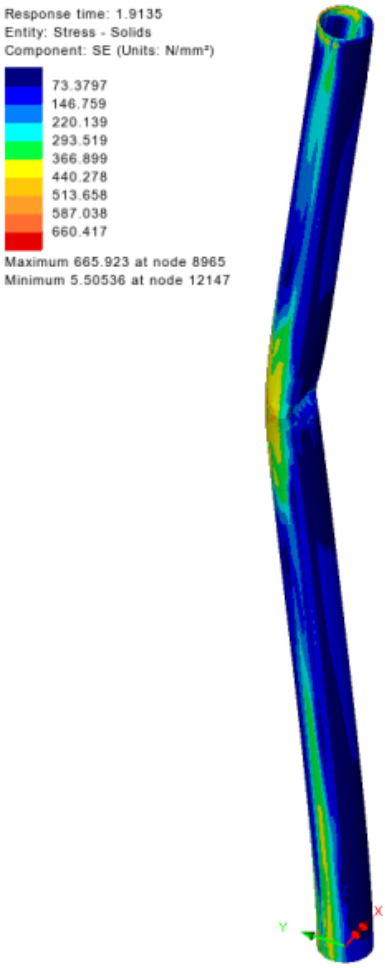

Figure 4.4.11: Column Deformations under Thermal and Blast Load (Peak Pressure = 198.8kPa)

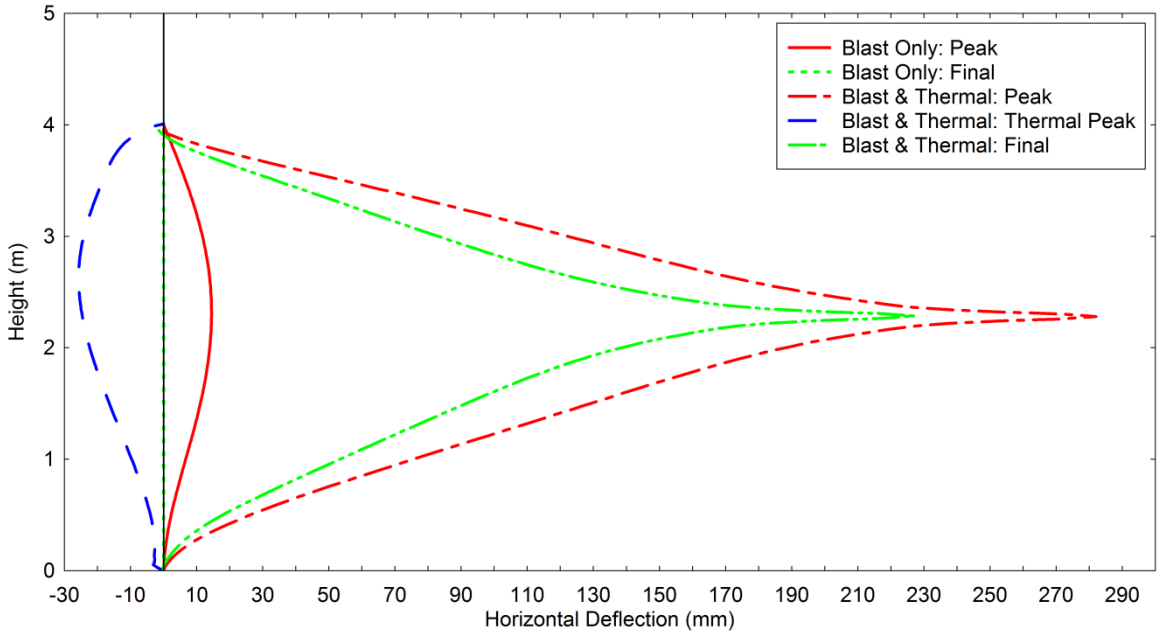

Figure 4.4.12: Deflection vs. Column Height (Peak Pressure = 198.8kPa)

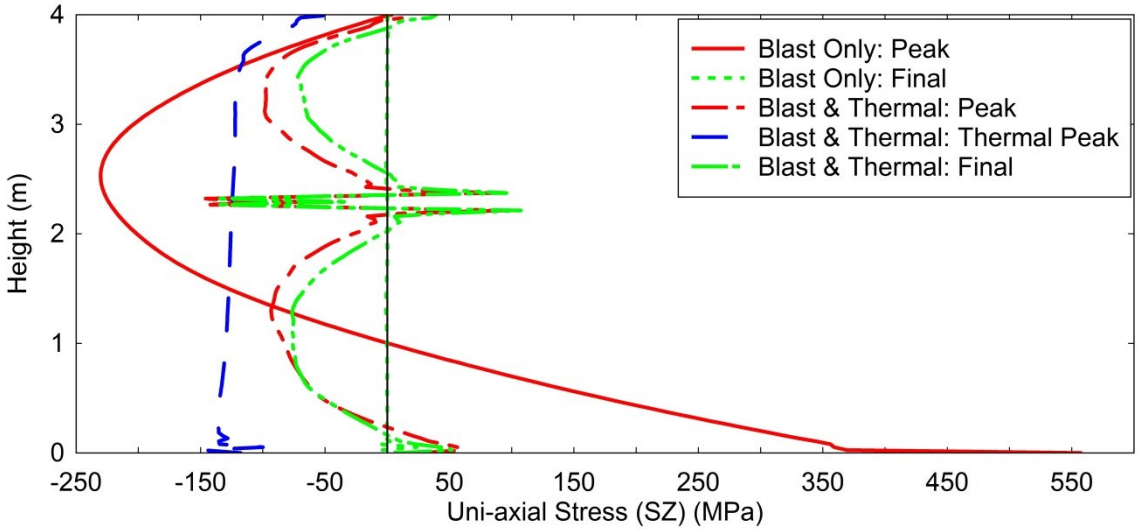

Figure 4.4.13: Uni-axial Stress vs. Height (Peak Pressure = 198.8kPa)

Columns outside the sensitivity response envelope of loading regimes were subject to either very high thermal and blast loading over a short duration or low thermal and blast loading over a long duration. The columns subject to the highest temperatures typically had shorter theoretical stand-off distances. Therefore the duration of the thermal load was much shorter and the time for the thermal energy to absorb into the steel columns before the arrival of the blast load was subsequently shorter leading to a reduced potential synergistic response. Columns subject to lower, longer duration thermal and blast loads typically had larger theoretical stand-off distances. The peak temperatures reached were lower and the relative response of the structure to the combination of the thermal and blast loads was reduced.

Figs.4.4.14 and 4.4.15 show the midpoint deflection and stress histories of a modelled column with a pinned base and roller top end connection, subject to very high thermal and blast loads outside the sensitivity response envelope. The three curves in Figure 4.4.14 show very large deflections of (1043.6mm: blast, 1069.9mm: flux, 612.3mm temperature); however, the analyses stopped before the peak deflections were reached. This was due to the very high stress gradients caused by the intense blast load.

The stress profile from the blast only column model in Fig.4.4.15 shows a peak stress of 462.3MPa. This is higher than the peak stress of 437.5MPa exhibited by the thermal flux loaded column model. The applied temperature model shows an initial peak stress of 383.3MPa followed by a drop and subsequent increase. The model stopped running before the second peak stress was reached. The response of the columns under the very intense pressures and temperatures are blast dominant. The thermal load does have an effect on the peak stresses and deflections reached; however, the applied blast load alone deforms the column well beyond its elastic limit to a fully collapsed state.

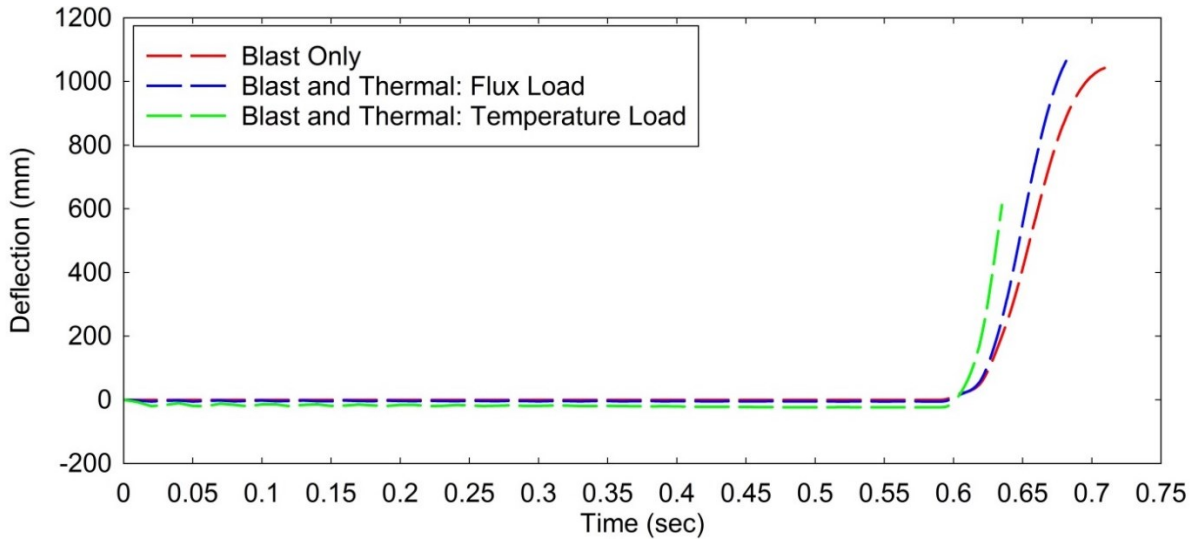

Figure 4.4.14: Midpoint Deflection vs. Time of Column (Peak Pressure = 536.4kPa)

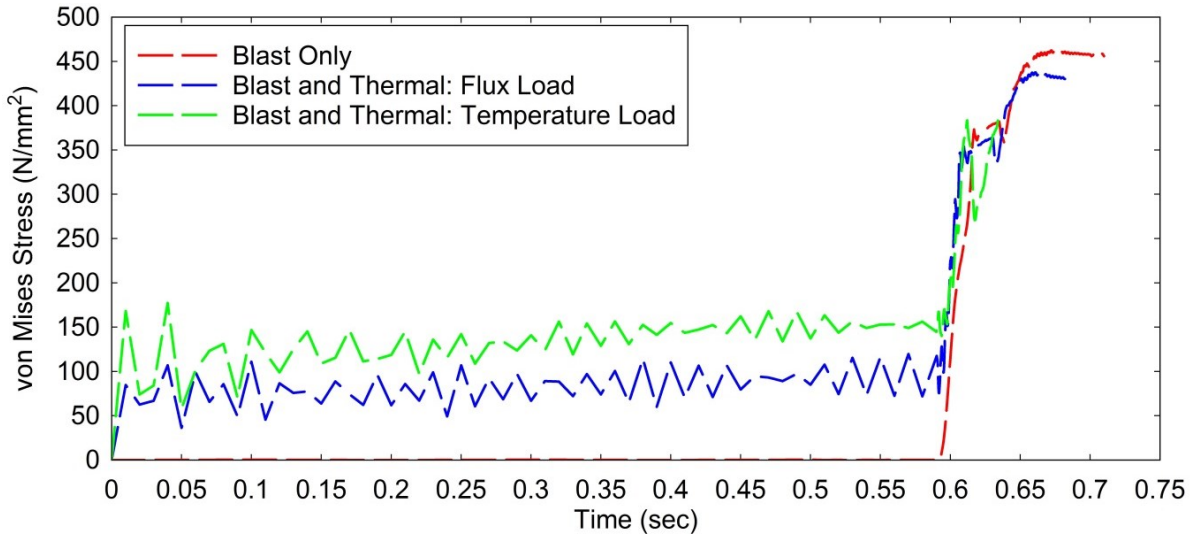

Figure 4.4.15: Midpoint (von Mises) Stress vs. Time of Column (Peak Pressure = 536.4kPa)

Fig.4.4.16 shows the midpoint deflection history of a modelled column with pinned base and roller top connections, subject to low and longer duration thermal and blast loads outside the sensitivity response envelope. An exponential decay curve fit has been applied to the blast and thermal curves as the analyses were stopped at approximately 2.5secs (see Appendix J for best fit curve equations). The blast and thermal temperature load curve shows a larger relative peak deflection (38.8mm) than the blast only curve (7.1mm); however the profile returns to a deflection of -17.1mm which is very close to the pre-blast (thermal) deflection of -20.8mm. This curve shows a deflection towards the explosive centre from the thermal load prior to arrival of the blast and a larger elastic deformation but minimal plastic (permanent) deformation.

There is a definite synergistic response observed in this column; however columns subject to higher, more intense thermal and blast loads in the parametric study exhibited a greater synergistic response, especially with regard to the post yield state. The midpoint deflection histories for each loading regime investigated are shown in Appendix D. Stress history plots are also shown.

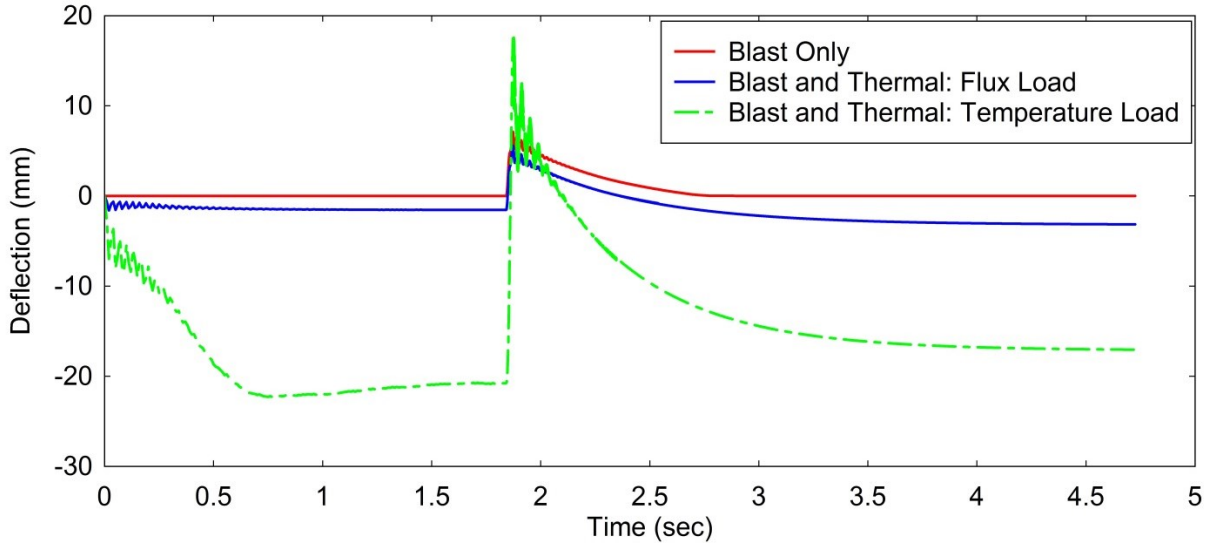

Figure 4.4.16: Midpoint Deflection vs. Time of Column (Peak Pressure = 111.5kPa)

Significant differences were observed between the flux load column deformations and the temperature load column deformations. The columns with flux load (and blast) exhibit the same relative deflection as the blast only model indicating no reduction in Young's Modulus or yield strength. The flux loaded columns, however do exhibit a thermal deflection (towards theoretical blast) due to thermal expansion. The temperature load column deformations are considerably larger indicating a reduced Young's Modulus and yield strength, they also exhibit larger thermal expansion deformations. Due to the clear difference in deformation between the temperature (and blast) load columns and the blast only columns the temperature load method was adopted for the parametric study detailed in 4.4.6.2 to 4.4.6.7. The temperature load method also allowed manual calculation of cooling via convection and direct input of temperature profiles.

4.4.6.2 Result Trends and Correlations

Figs.4.4.17 to 4.4.28 show the peak and final deflections and stresses of the columns under varying blast and thermal loads. These data sets enable observations to be made regarding any trends and correlations in the response exhibited by the columns under a range of combined thermal and blast loads compared to the blast loads alone. The figures use the results from the parametric study of columns with roller top or pinned top (both pinned base) connections.

Fig.4.4.17 and Fig.4.4.18 represent damage sensitivity curves showing the peak and final deflections of the columns under blast only and blast and thermal loading with roller top connections. The peak and final deflections and stresses are plotted against scaled distance (Figs. 4.4.17 to 4.4.20 and

4.4.25 to 4.4.28). Scaled distance (m/T$^{1/3}$, TNT eq.), $Z = R/W^{1/3}$ was used as the comparison parameter in these figures as it relates to the peak pressure, peak temperature and durations of the thermal and blast loads. Figs.4.4.21 to 4.4.24 show the correlation of peak deflections and stresses to peak pressures and temperatures. Figs. 4.4.17 to 4.4.20 and 4.4.25 to 4.4.28 show best fit correlation lines applied to each set of deflections and stresses.

The values of deflections and stresses follow the best fit curves with a degree of scatter. This scatter is attributed to multiple parameters described into one single parameter (scaled distance). The scaled distance relates to the explosive size and standoff distance of each explosive case. Therefore peak pressure and temperatures vary for each scaled distance. Time of blast arrival, time to peak temperature, total thermal energy absorbed before blast and blast duration also vary with differing scaled distances. In using a single parameter to describe several explosive parameters a degree of scatter is to be expected. Scaled distance is used as the main comparative parameter as it is widely used by blast practitioners and allows multiple complex parameters to be described by one meaningful value. It also aids the analysis of the combined effects of absorbed thermal energy and equivalent long duration blast load. Scaled distances for these cases are shown in table 4.4.

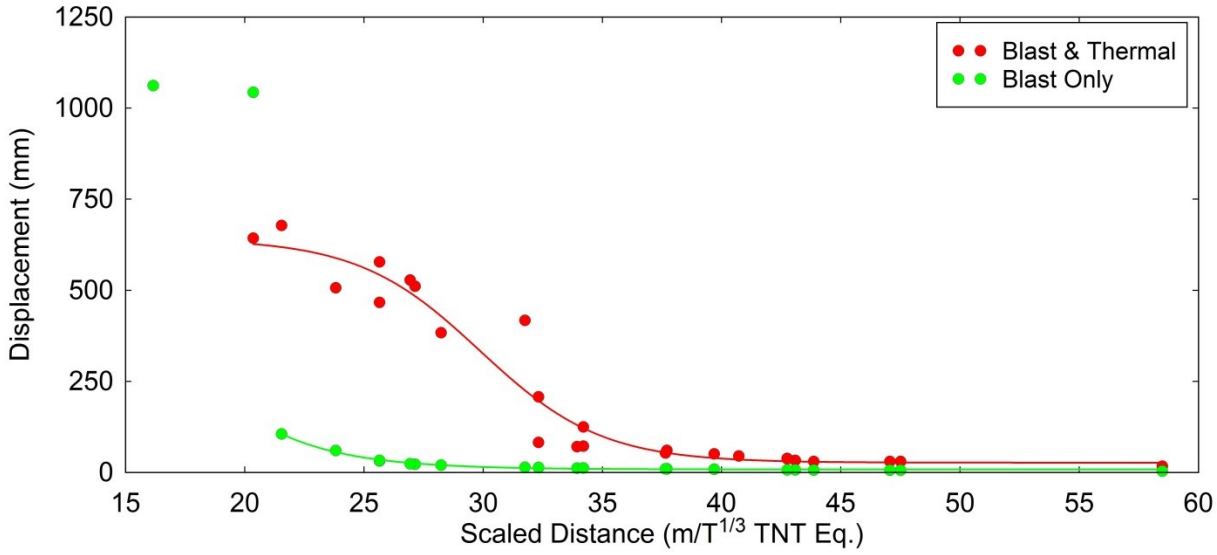

Figure 4.4.17: Peak Deflections vs. Scaled Distance (Roller)

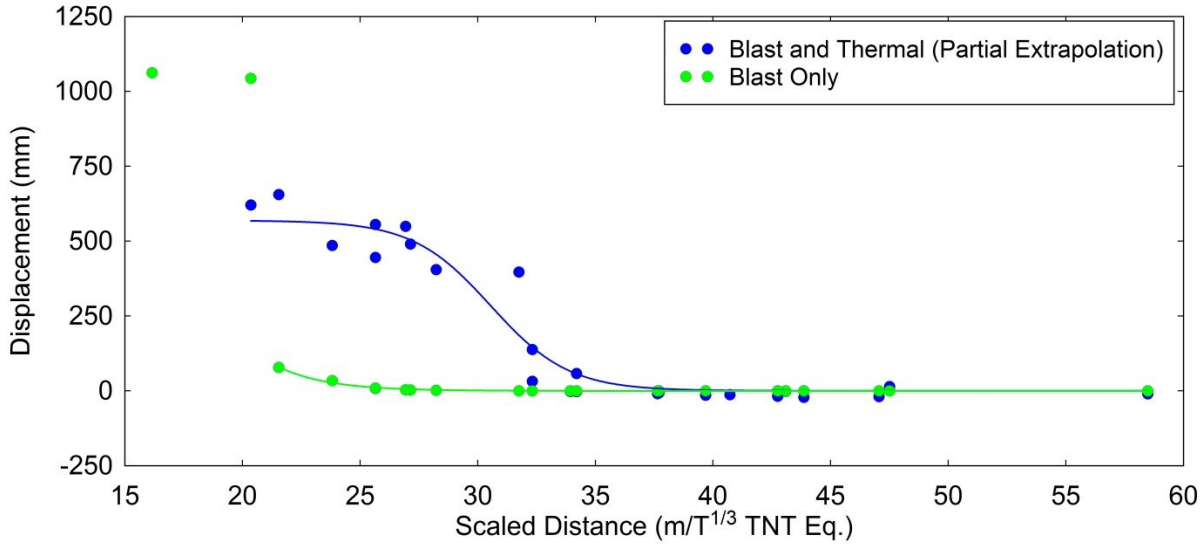

Figure 4.4.18: Final Deflections vs. Scaled Distance (Roller)

A significant difference is observed between the deflections of the blast only columns and the combined blast and thermal columns. This difference is most evident at scaled distances with corresponding peak thermal and blast loads which form the sensitivity response envelope. For smaller scaled distances the blast only loading models exhibit a dominant response and for larger scaled distances there is little or no difference between blast only and combined load deflections. Several final deflection values have been calculated through extrapolation of the curves using exponential decay best fit curves. The exponential decay equations are shown in Appendix J and the full set of deflection vs. time graphs are shown in Appendix D.

There is little difference between the peak and final deflections of the columns exhibiting a plastic response. There is a larger difference in the peak and final deflections of the columns exhibiting an elastic response (zero final deflections). Negative final deflections were observed in several of the blast and thermal loaded columns. This was due to a deflection towards to the theoretical explosive centre during the initial thermal loading phase. The trend lines for each plot were formed using best fit polynomial, exponential or logarithmic curves (depending on scatter trend). The equations for the best fit trend lines are detailed in Appendix J with standard errors and parameters.

Figures 4.4.19 and 4.4.20 show the peak and final midpoint von-Mises stresses in the columns under blast only and blast and thermal loading vs. scaled distance. The peak stress plots show several features of interest including blast only loaded columns with similar or larger peak stresses compared to equivalent blast and thermally loaded columns. This is due to a reduced yield and ultimate strength in the columns under elevated temperatures.

As the scaled distance increases the peak stresses of the blast only columns decrease below peak stresses of the blast and thermal columns. The blast and thermal trend lines follow a similar s-

shaped profile as observed in the peak and final deflection figures. This indicates a reduced effect from the thermal load at larger scaled distances and blast dominant loading at smaller scaled distances.

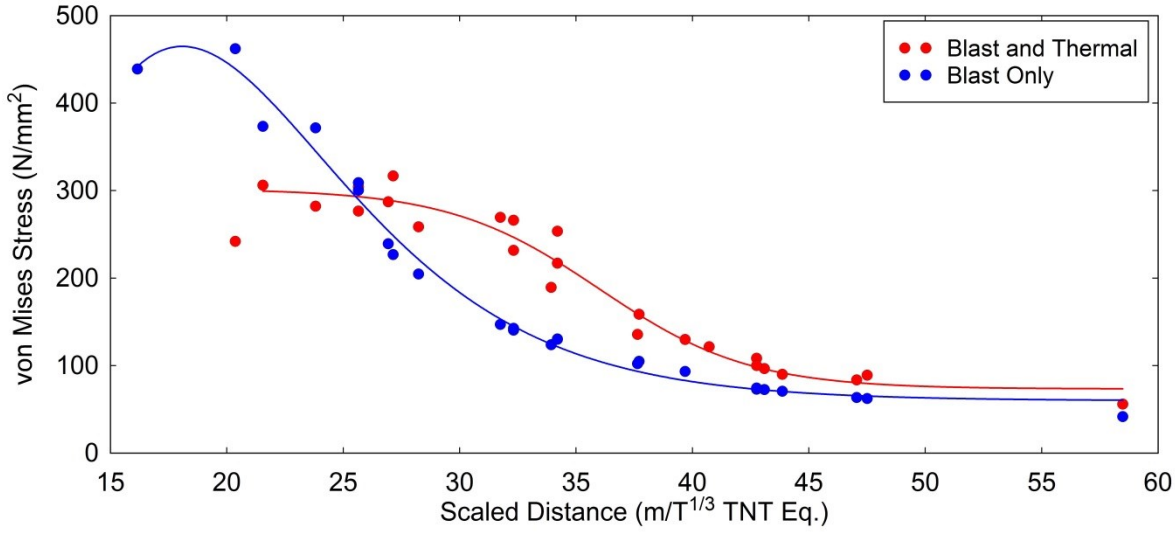

Figure 4.4.19: Peak Stress vs. Scaled Distance (Roller)

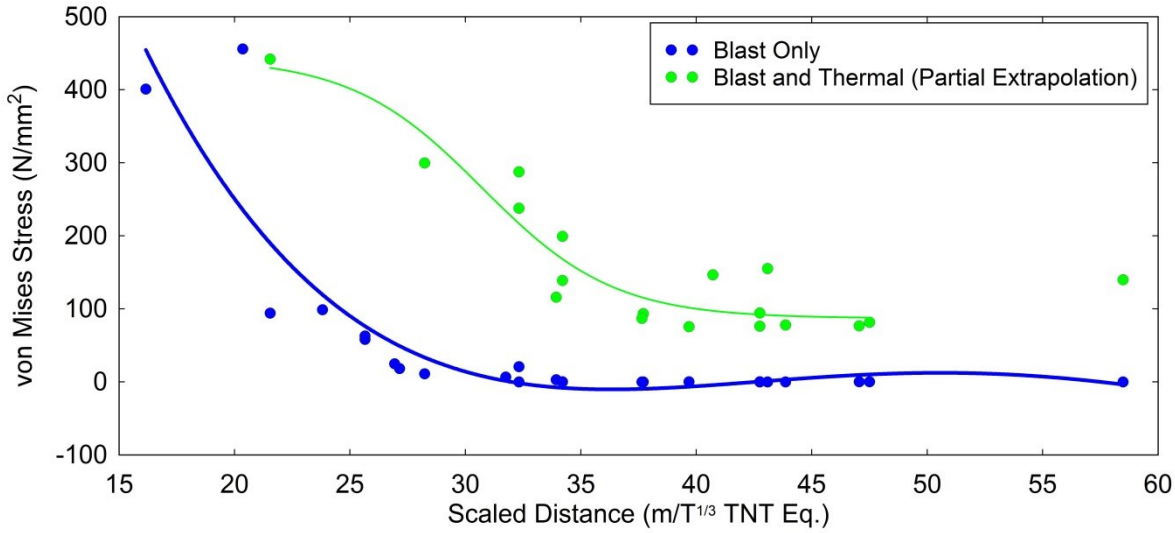

Figure 4.4.20: Final Stress vs. Scaled Distance (Roller)

Figs.4.4.21 and 4.4.22 show the peak deflections and stresses exhibited by the blast only and blast and thermal loaded columns vs. peak pressure. As the peak pressure increases the peak deflections and stresses increase under the combined and blast only loading regimes. The blast and thermal peak deflections and stresses are typically higher than the blast only peak deflections and stresses for the majority of cases. Above 535kPa peak pressure the peak deflections exhibited by blast only loaded columns show a significant increase. This trend is consistent with the smaller scaled distances where high pressures are present but the thermal loading is shorter with less relative effect.

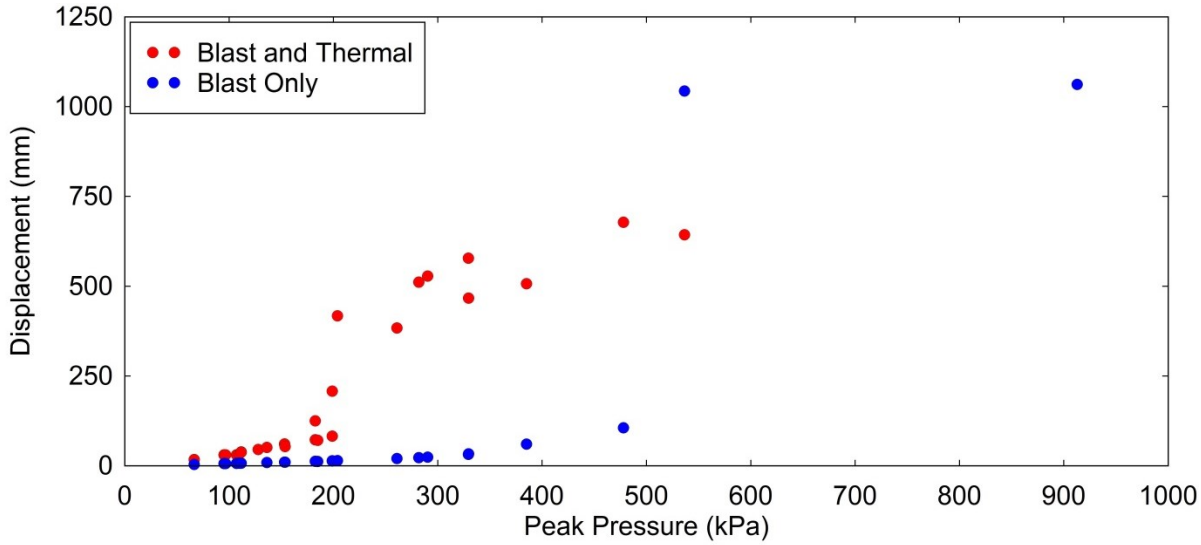

Figure 4.4.21: Peak Deflection vs. Peak Pressure (Roller)

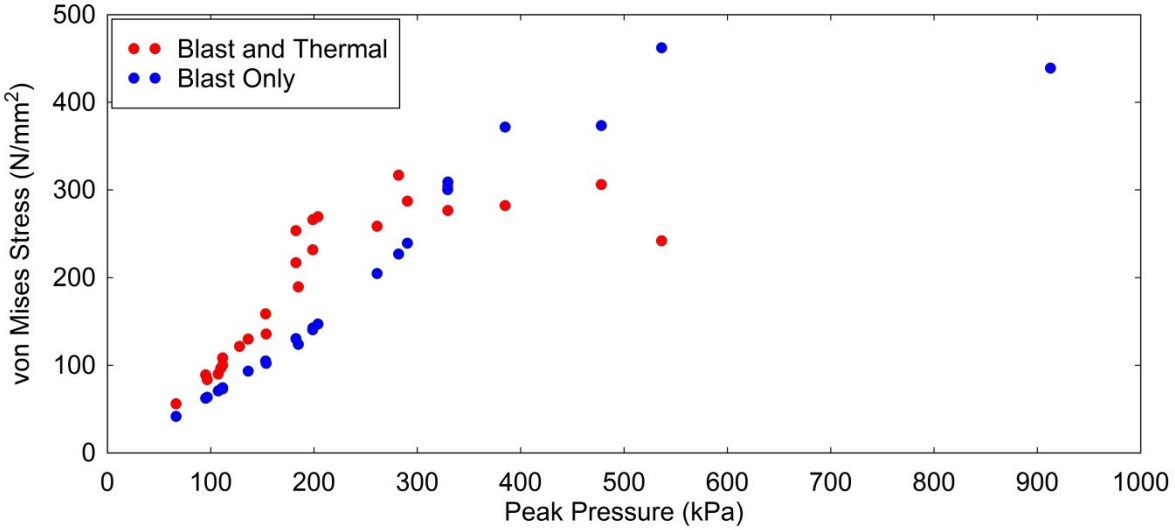

Figure 4.4.22: Peak Stress vs. Peak Pressure (Roller)

Figs.4.4.23 and 4.4.24 show the peak deflections and stresses exhibited in the blast and thermal loaded columns vs. peak temperature. The peak displacements and stresses increase with increasing peak temperature. The peak displacements increase at a relatively low level until 2000°C peak temperature, where significant increases are observed. The peak stresses increase linearly to approximately 317MPa at a relative peak temperature of 2000°C. Above 2000°C the peak stresses remain at a constant level or start to reduce. This is due to the reduction in yield and ultimate stresses at elevated temperatures. The peak temperatures shown equal the equivalent temperatures from radiated thermal energy applied to the front surface of the steel columns perpendicular to the direction of the blast. The temperatures of the columns significantly drop across the steel thickness and around the circumference, resulting in steep temperature gradients.

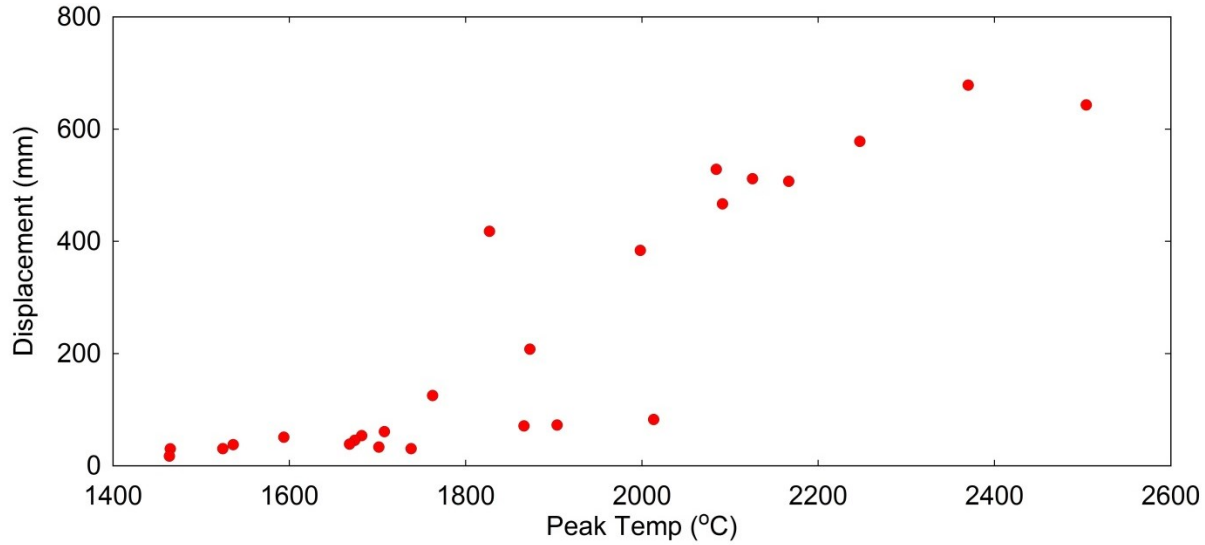

Figure 4.4.23: Peak Displacement vs. Peak Temperature (Roller)

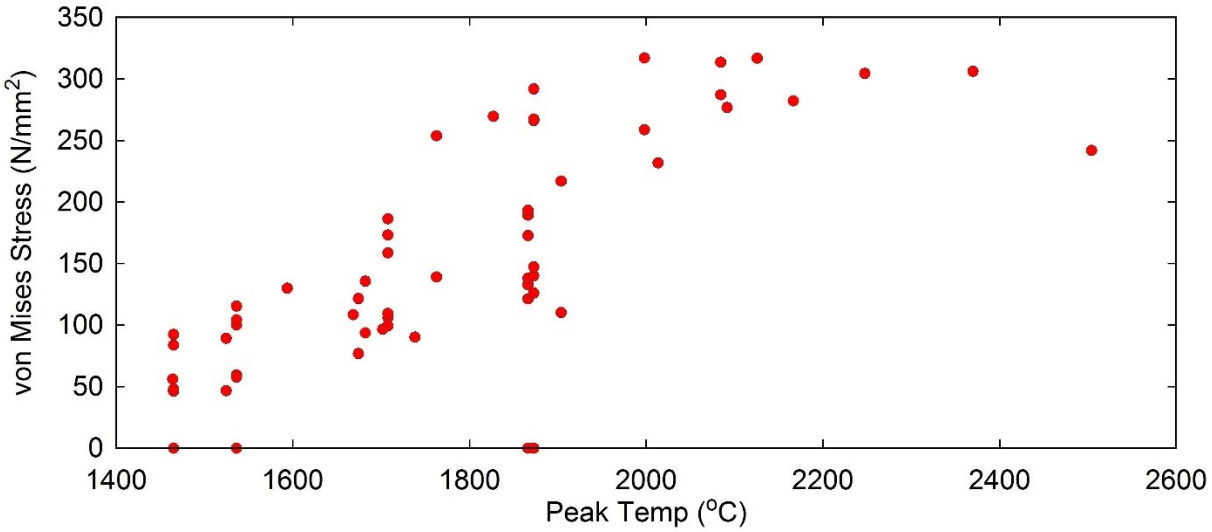

Figure 4.4.24: Peak Stress vs. Peak Temperature (Roller)

Figs.4.4.25 and 4.4.26 show the peak and final deflections of the blast only and blast and thermal loaded (pinned top) columns vs. scaled distance. There is a clear difference between the blast only and blast and thermal pinned top column deflections compared to the roller top deflections (Figs.4.4.17 and 4.4.18). The peak and final deflections are much lower for the pinned top columns under both loading regimes compared to the roller top deflections. This is due to the pinned top connection preventing the top of the columns dropping and the column "folding", forming a plastic hinge. There is also no permanent (plastic) deflection observed in the blast only columns with pinned top connections. A near linear increase in the peak and final deflections under blast and thermal load with decreasing scaled distance is observed until approximately $32.5m/T^{(1/3)}$. At lower scaled distances the peak and final deflections are significantly higher, not adhering to this linear trend.

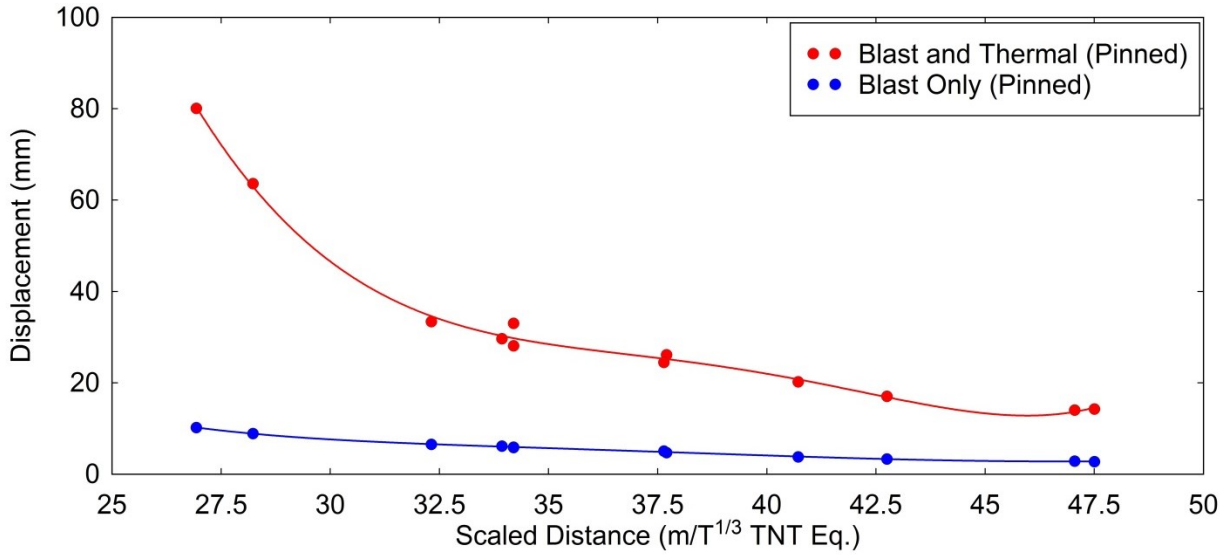

Figure 4.4.25: Peak Deflection vs. Scaled Distance (Pinned)

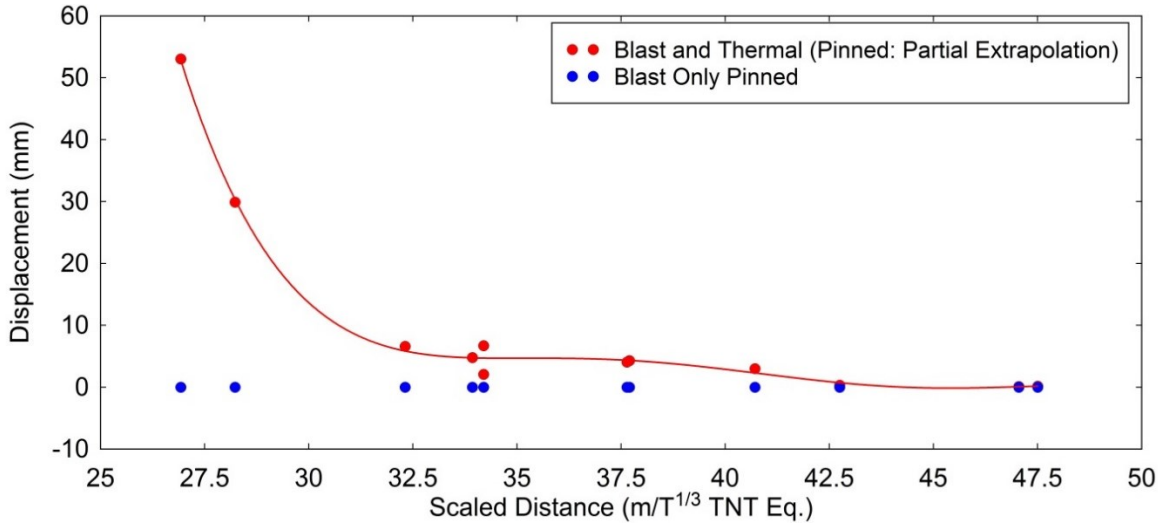

Figure 4.4.26: Final Deflection vs. Scaled Distance (Pinned)

These curves show that a clear synergistic response was observed in the columns at decreasing scaled distances. Column models with pinned top connections were developed using loading regimes within the sensitivity response envelope of cases. The trend curves aligned to the peak and final deflections shown in Figures 4.4.25 and 4.4.26 would take a different shape if the column deflections at lower or higher scaled distances (outside the sensitivity response envelope) were included in the scatter plot.

The curves fitted to the peak and final stresses plotted against scaled distance, shown in Figs.4.4.27 and 4.4.28, show a similar trend to the deflection curves shown in Figs.4.4.25 and 4.4.26. The peak stresses for the blast only pinned columns do not exceed 150MPa indicating the yield stress was not reached in the cases shown. There is a clear increase in the peak and final stresses subject to

blast and thermal loads compared to the blast loads alone. This difference decreases as the scaled distance increases.

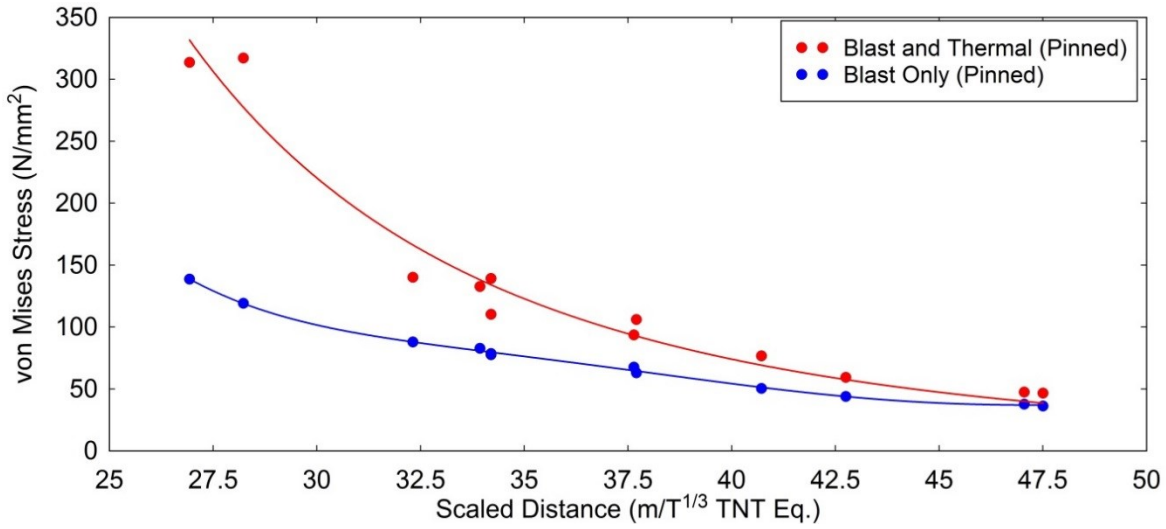

Figure 4.4.27: Peak Stress vs. Scaled Distance (Pinned)

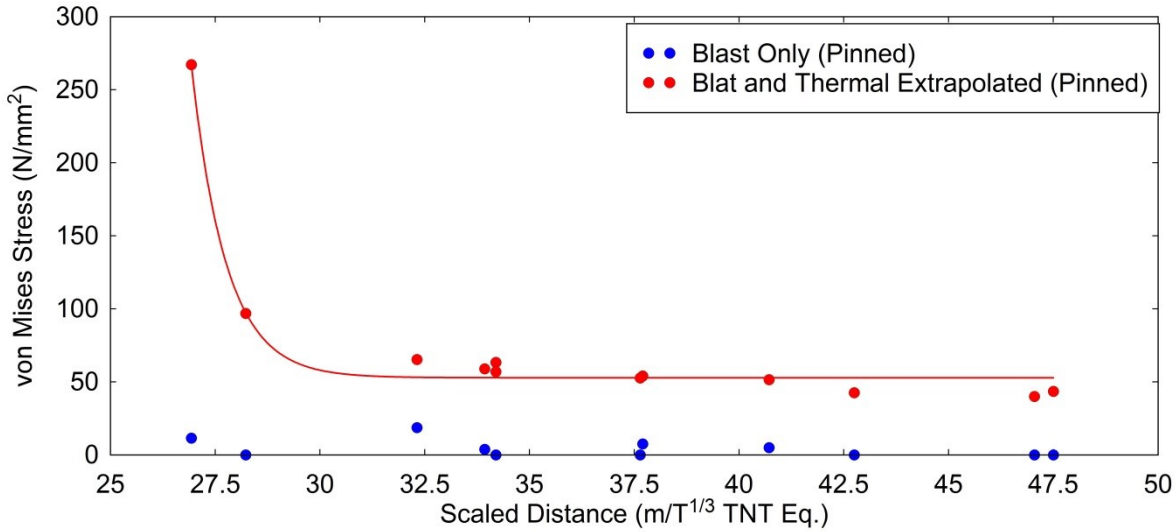

Figure 4.4.28: Final Stress vs. Scaled Distance (Pinned)

4.4.6.3 Pinned Top Connections

Once the sensitivity response envelope of blast and thermal loading regimes was determined on columns with roller top connections further column models were developed using pinned top connections (within the sensitivity response envelope). Figs.4.4.29 and 4.4.30 show the deflection and stress-time histories of a column under combined blast and thermal and blast only loading regimes using pinned and roller top connections. The peak and final deflections exhibited in the column models with pinned top connections are lower compared to column deflections with roller top connections. The columns with pinned top connection do not exhibit any lateral deflections during the thermal heating phase (prior to the arrival of the blast); however, the stress in the pinned

column during the heating phase follows a similar (but lower) profile to the roller top column. Both (roller and pinned) blast only column models show an elastic response under this particular loading regime (198.8kPa Peak Pressure).

These figures indicate the significant difference observed between columns with roller and pinned top connections under blast loading. If the pinned and roller top connection columns are modelled under static horizontal loading the structural response and behaviour would be identical and the beam would deform to the same extent; conversely, under transient non-linear blast loads the columns behave differently with wide ranging deformations. The effect of the thermal load upon the potential degradation of the column connections is not pursued further in this study as it is outside the scope of this project.

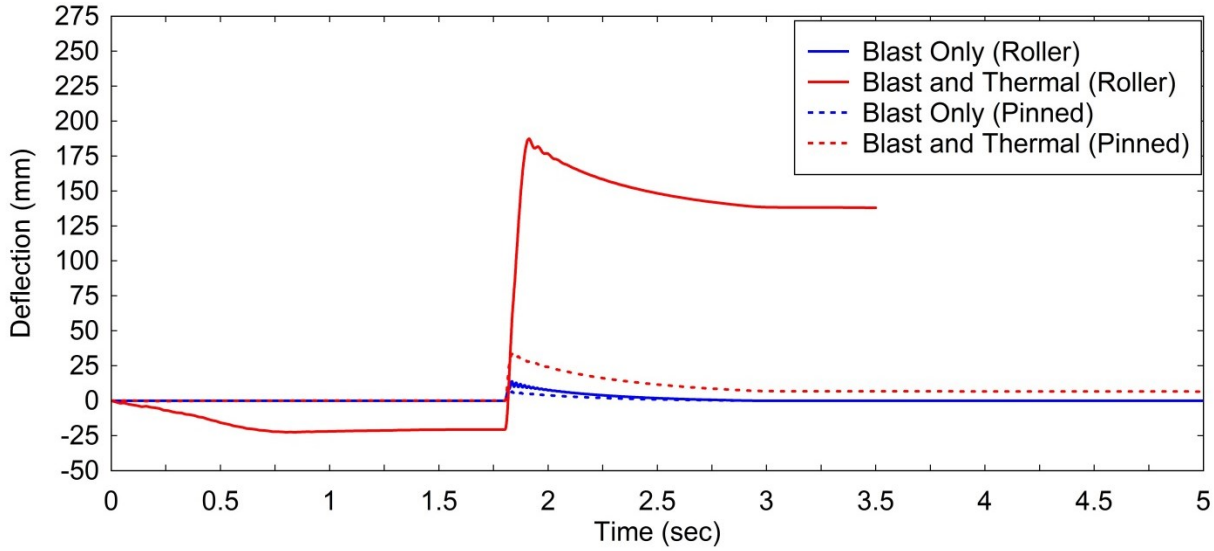

Figure 4.4.29: Midpoint Deflection vs. Time: Pinned & Roller (Peak Pressure = 198.8kPa)

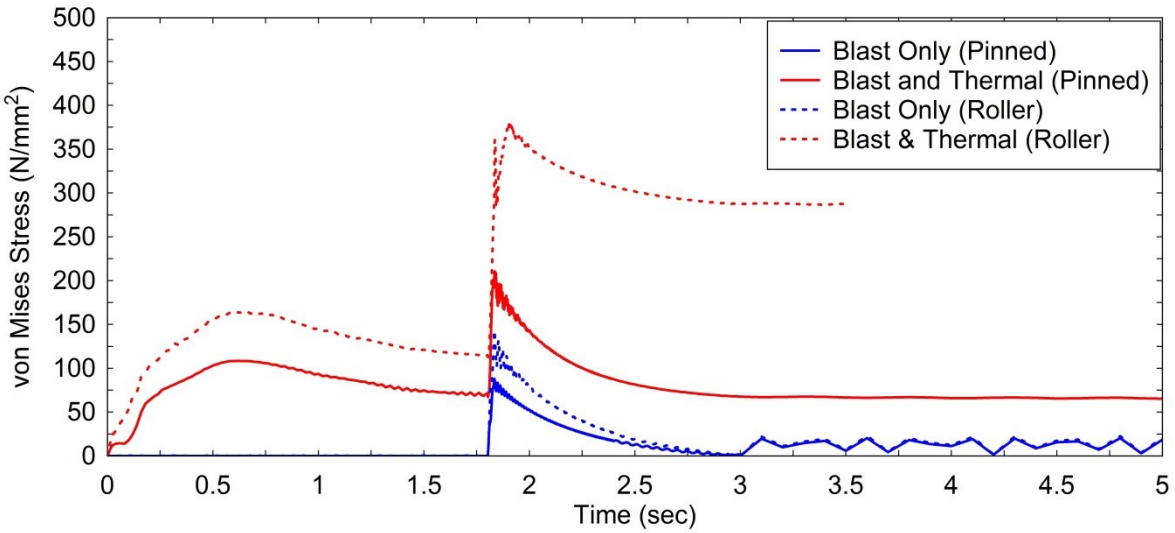

Figure 4.4.30: Midpoint Stress vs. Time: Pinned & Roller (Peak Pressure = 198.8kPa)

Figs.4.4.31 to 4.4.34 show the midpoint deflection history profiles of pinned columns under combined blast and thermal and blast only loads from a range of explosive events (peak pressures from 95.1kPa to 290.3kPa). The columns under blast only load show an elastic response with varying peak deflections. The columns under combined blast and thermal loads show a larger elastic response and several show a plastic (permanent) response. For the majority of cases (for the combined loading regime) the peak and final deflections decrease as the peak pressures decrease; however there are cases where higher peak and final deflections are observed with lower peak pressures. This is due to an increased thermal load which is not directly compared in Figs.4.4.31 to 4.4.34. A case with a small peak pressure may have a larger explosive size and greater stand-off distance than an equivalent case with higher peak pressure but a smaller explosive size and lower stand-off distance. There is no horizontal deflection observed in the columns during the thermal loading phase (prior to blast arrival). The columns modelled with pinned end conditions were developed from a sensitivity response envelope of column models with roller top connections. Columns subject to blast only loads outside this envelope (closer to explosive centre) would have exhibited larger permanent deformations.

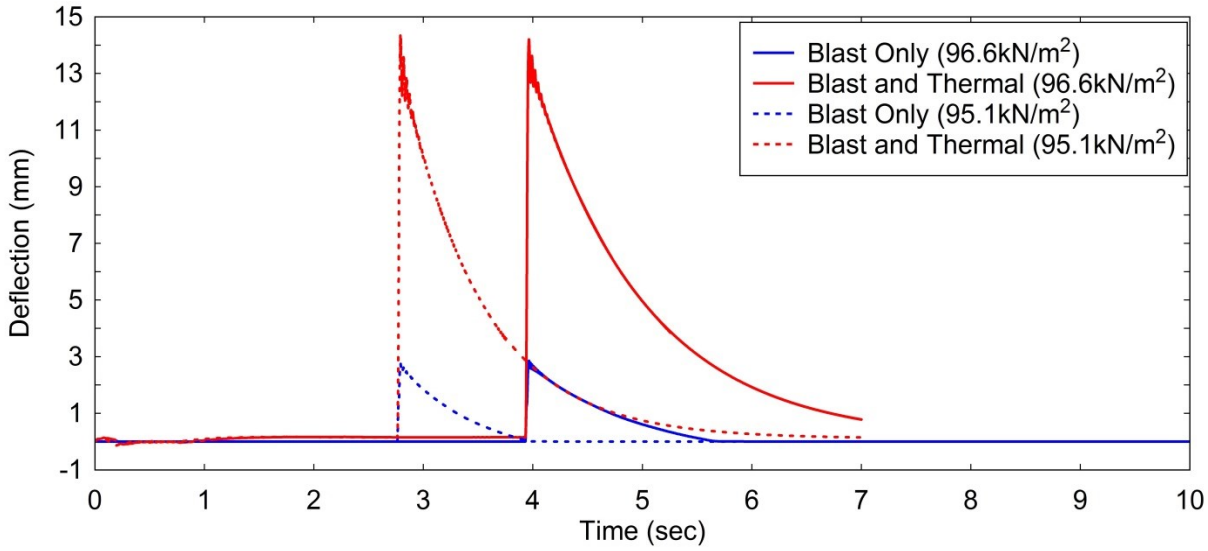

Figure 4.4.31: Midpoint Deflection vs. Time: Pinned (Peak Pressure: 0 – 100kPa)

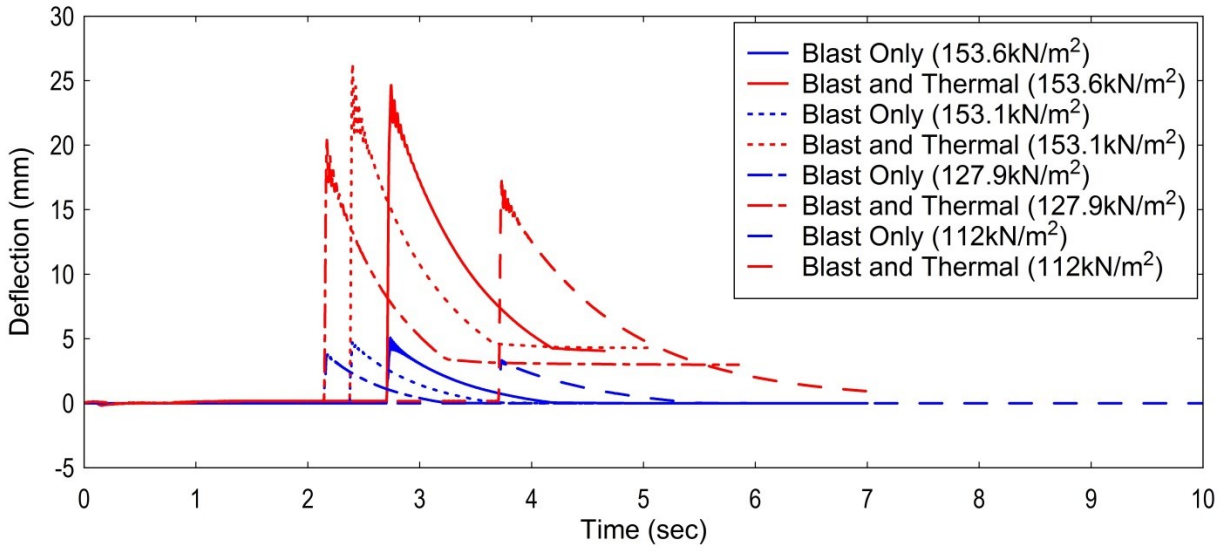

Figure 4.4.32: Midpoint Deflection vs. Time: Pinned (Peak Pressures: 100 - 160kPa)

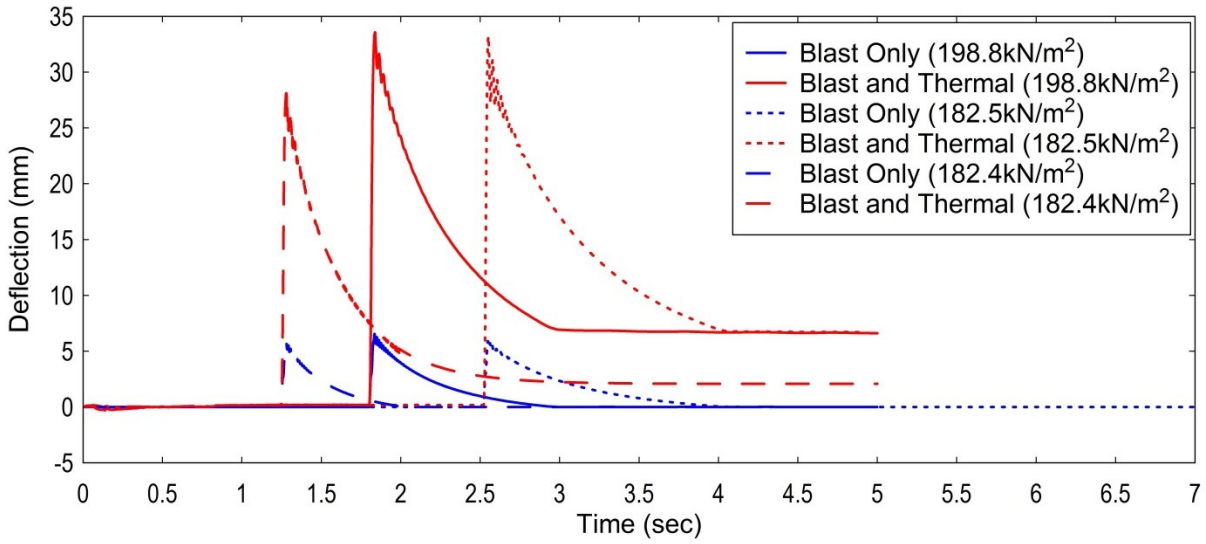

Figure 4.4.33: Midpoint Deflection vs. Time: Pinned (Peak Pressures: 160 - 200kPa)

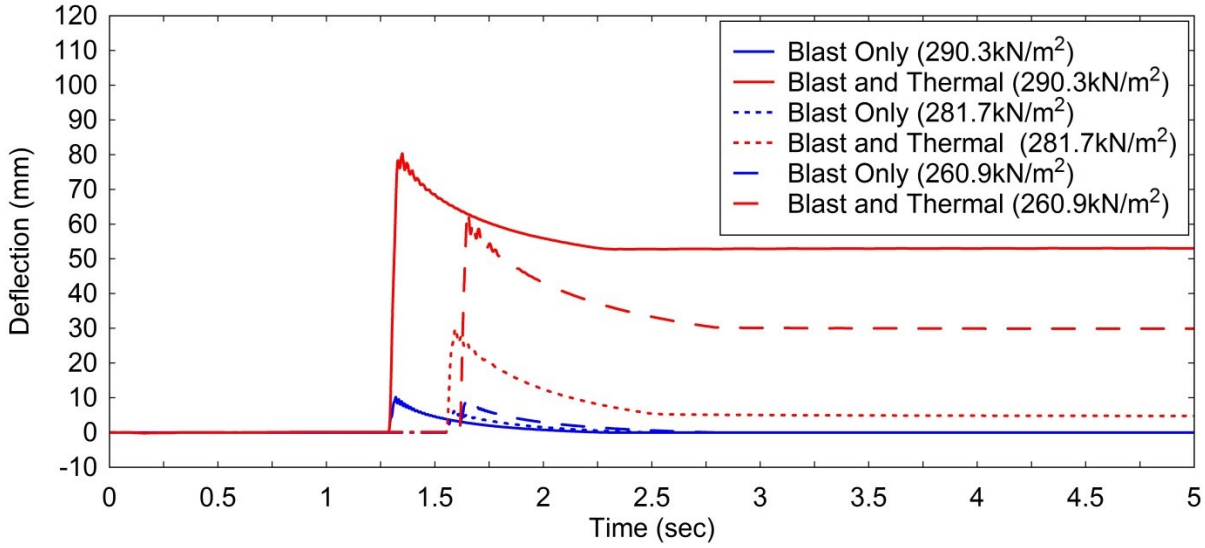

Figure 4.4.34: Midpoint Deflection vs. Time: Pinned (Peak Pressures: 200 – 300kPa)

4.4.6.4 Compressive Load / End Connection Fixity

During the parametric study the effect of varying levels of compressive load and end connection fixity on the response of the columns was also investigated. The end connection spring stiffness and levels of compressive load were calculated to represent one or two storey loading above the column. The compressive loading from two storeys equates to 86% of the selected column section compressive resistance (845kN). The calculations for compressive loads and end connection spring stiffness are detailed in 4.4.5.1. Figs.4.4.35 and 4.4.36 show the midpoint deflection histories for columns with pinned, roller top and one storey and two storey spring end connections. The columns with spring end connections were also subject to relative (one and two storey) compressive loads.

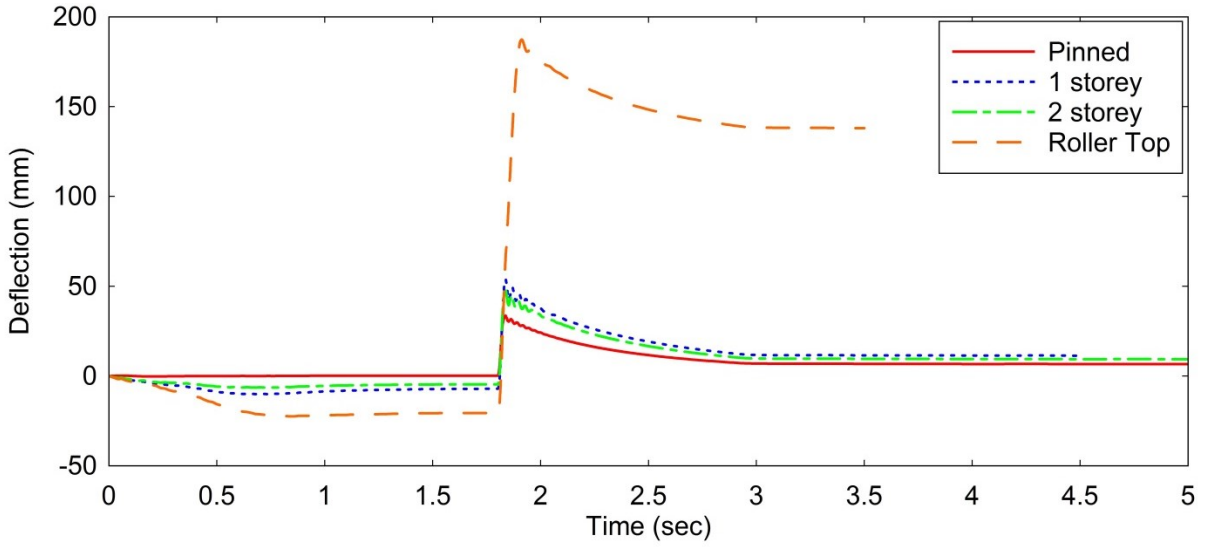

Figure 4.4.35: Midpoint Deflection vs. Time: Varying Compressive Load (Blast & Thermal: Peak Pressure = 198.8kPa)

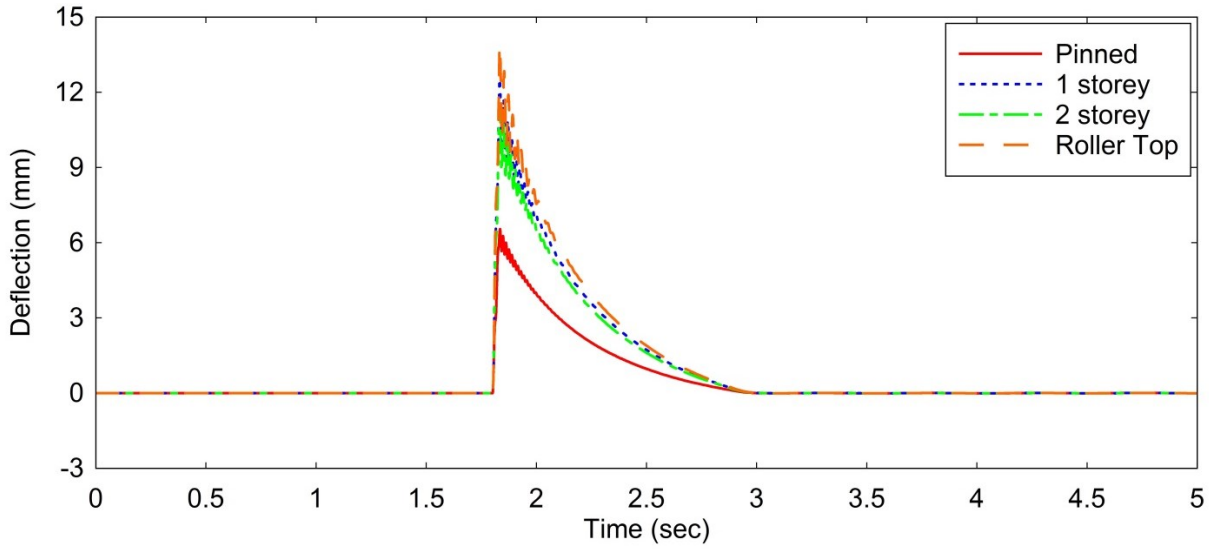

Figure 4.4.36: Midpoint Deflection vs. Time: Varying Compressive Load (Blast Only: Peak Pressure = 198.8kPa)

The blast and thermal loaded column with roller top connection shows a large peak of 187.4mm followed by a permanent deflection of 138mm, the pinned column exhibited a smaller peak of 33.8mm settling at a permanent deflection of 6.6mm. The columns with spring end connections and compressive load from one or two storeys showed deflections similar in magnitude and profile to the pinned column. The column with two storey compressive load showed a peak deflection of 48.9mm, the column with one storey compressive load showed a peak deflection of 53.9mm. Both one and two storey loaded columns exhibited a lateral deflection during the thermal loading phase; the thermal deflection of the column with one storey compressive load was slightly larger (12mm) than column with two storey compressive load (8mm). The column subject to higher compressive load deflected less (47mm) than the column with lower compressive load during the blast loading (56mm) due to the increased spring stiffness of the top support provided by the upper storey column and floor.

The columns under blast only load (Fig.4.4.36) exhibited an elastic deflection with pinned, roller top and one and two storey spring connections (and compressive loads). The column with roller top connection showed the largest peak deflection of 13.9mm, the pinned top connection showed the smallest peak deflection of 6.5mm. The peak deflections for the one and two storey loaded columns were 12.5mm and 11.6mm (respectively). The peak deflections for the one and two storey loaded columns were similar to the deflections exhibited by the column with roller top connection. The deflection of the one storey loaded column was larger than the two storey loaded column due to the increased spring fixity in the two storey loaded column. Further deflection time histories of columns subject to explosive loads within the sensitivity response envelope, with pinned, roller top

and one and two storey end equivalent connections and compressive loads are detailed in Appendix D.

4.4.6.5 Thermal Conductivity

The effect of varying the thermal conductivity of steel was investigated during the parametric study. The thermal conductivity of the mild structural steel used for the majority of the parametric study was 45W/m.°K (Cverna, 2002). As structural steel can be produced to different specifications (due to carbon content) dependent on geographical location, lower and higher bound values for the thermal conductivity were investigated during the parametric study. The lower bound value was 35W/m.°K and the higher bound value was 55W/m.°K. Figs.4.4.37 and 4.4.38 show the deflection and stress histories of a pinned end column with varying thermal conductivities under combined blast and thermal loads.

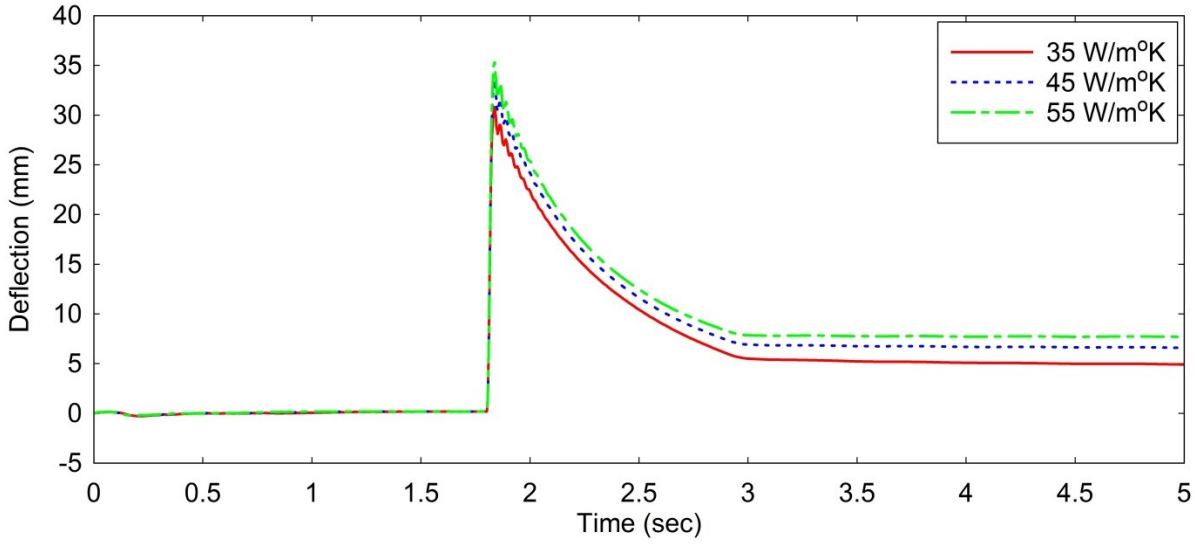

Figure 4.4.37: Midpoint Deflection vs. Time: Varying Thermal Conductivity: Pinned (Blast and Thermal: Peak Pressure = 198.8kPa)

The columns with the three levels of thermal conductivity show a similar deflection profile (Fig.4.4.37). The column with a thermal conductivity of 35W/m.°K exhibited the lowest peak deflection of 30.8mm, the column with a thermal conductivity of 45W/m.°K exhibited a peak deflection of 33.6mm and the column with a thermal conductivity of 55W/m.°K exhibited the largest peak deflection of 35.3mm. The percentage variation of the peak deflections was -8.3% to +5.1%. This variation is less than the variation in the values of thermal conductivity (±22%). This demonstrates that linear relationship does not exist between thermal conductivity and structural response. Further deflection time histories of columns subject to loads within the sensitivity response envelope, with varying thermal conductivities are detailed in Appendix D.

During the initial thermal loading phase the stress profiles differ with varying thermal conductivity; however, the post blast stress profiles are similar (Fig.4.4.38). During the heating phase the stress levels in the three columns rise equally until a stress of 67.2MPa is reached at 0.22sec. Subsequently, the stress in the 55W/m.^{o}K column increases rapidly to 108.4MPa at 0.54sec, the stress in the 45W/m.^{o}K column increases to 108.5MPa at 0.62sec and the stress in the 35W/m.^{o}K column rises to 108.9MPa at 0.76sec. Following these peaks the stress in each column drops. The stress in the 55W/m.^{o}K column drops to 63.2MPa (the lowest stress of the three columns), before the arrival of the blast. The stress levels in the columns with higher thermal conductivity increase rapidly due to the heat penetrating the steel at a quicker rate.

The three columns reached similar peak stresses during the thermal heating phase; this is due to the same thermal energy applied to each in the heating phase. After arrival of the blast the peak stresses reached were 201.8MPa (35W/m.^{o}K), 210.5MPa (45W/m.^{o}K) and 214.8MPa (55W/m.^{o}K). Higher stresses were reached in the columns with higher thermal conductivities. The percentage variation in the peak stresses was -4.1% to +2.0%, which is less than the percentage variation of the thermal conductivities.

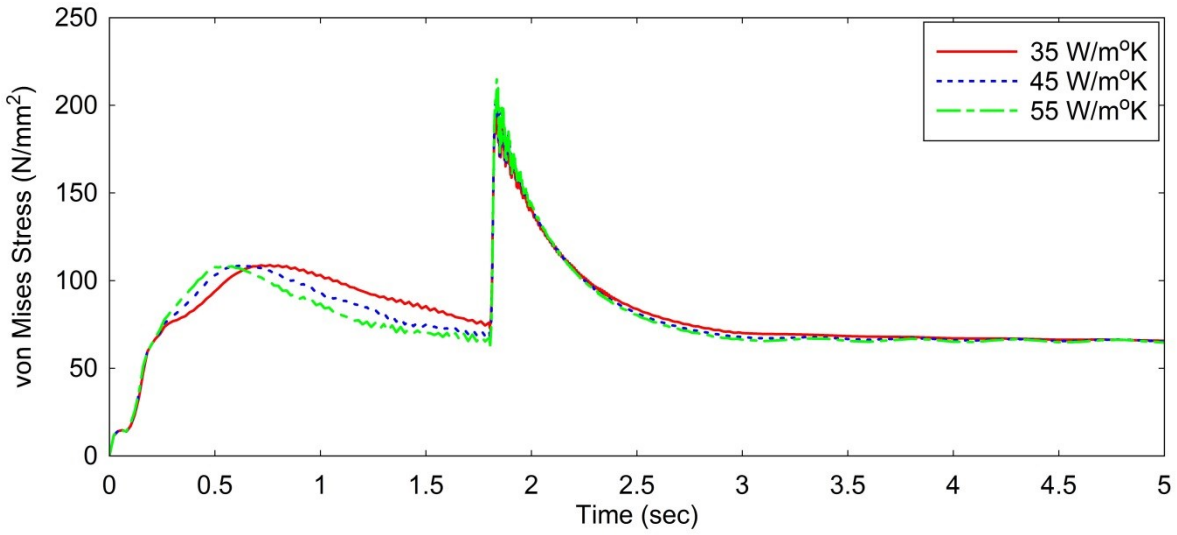

Figure 4.4.38: Midpoint Stress vs. Time: Varying Thermal Conductivity: Pinned (Blast and Thermal: Peak Pressure = 198.8kPa)

4.4.6.6 Two Element Study

The effect of using one or two elements across the thickness of the column section walls was investigated during the parametric study. The aim of the two element thick study was to observe if using two elements instead of one greatly altered the structural response of the column. The response of a short (0.5m long) column was investigated under the combined blast and thermal

loads detailed in 4.4.1 to 4.4.3. The response of a one element thick short column was compared to the two element thick short column under identical loads. A short column was analysed to minimise computational running times.

Figs.4.4.39 to 4.4.41 show the deflection and stress histories of the short column with one or two element thickness under blast and thermal loads (198.8kPa peak pressure, roller top support). Both the single and double element thick columns exhibited lateral deflections and stresses under the initial thermal load. The peak thermal deflections are -5.69mm (single thickness) and -5.83mm (double thickness); a percentage variation of 2.4%. There is little relative change in the deflections or stresses observed in the columns from the blast load (arrival at ≈ 1.82sec). Fig.4.4.40 shows the relative change in deflection observed in the one and two element thick columns at the blast arrival (narrowed time extents). The relative peak deflection is -0.4mm for the one element thick column and -0.5mm for the two element thick column. The one element column relative deflection is 20% less than the two element thick column relative column; however, both deflections are negligible in relation to the overall deflection of the column under combined thermal and blast loading.

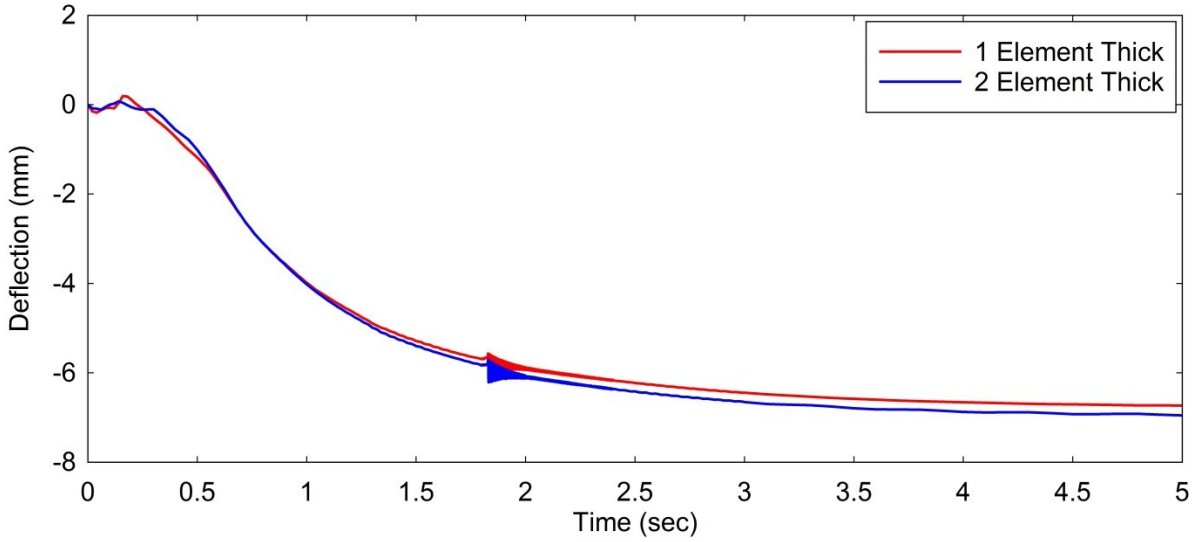

Figure 4.4.39: Midpoint Deflection vs. Time: One and Two Element Thick Short Column (Blast and Thermal: Peak Pressure = 198.8kPa)

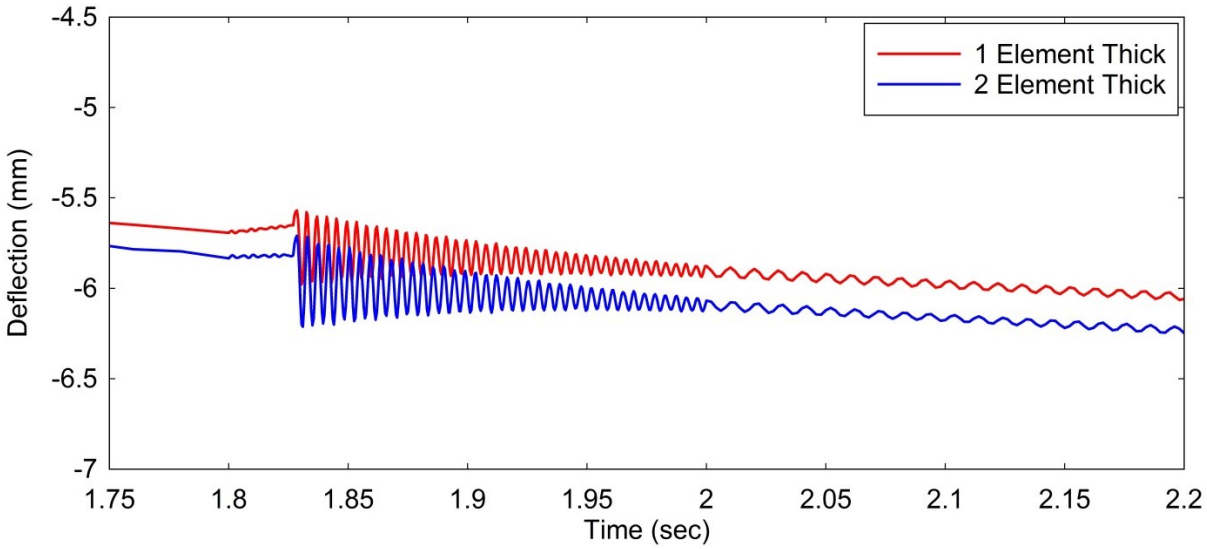

Figure 4.4.40: Midpoint Deflection vs. Time: One and Two Element Thick Short Column: Zoomed Extents (Blast and Thermal: Peak Pressure = 198.8kPa)

Fig.4.4.41 shows the midpoint stress history profile for the one and two element thick, short columns. The peak stresses under thermal load are rapidly reached in each column: 358.5MPa at 0.04sec (one element) and 355.8MPa at 0.02sec (two elements). Following these initial peaks there are high stress fluctuations observed in both the one and two element thick columns. After the fluctuations the stresses settle at 69MPa (one element) and 66.6MPa (two elements) before the blast arrival at 1.8 seconds. The overall stress profiles are negligibly affected by the blast load. Despite the large differences in the fluctuation of thermal stresses between the one and two element thick columns they both reach comparable peak thermal stress and settle at similar stress before the arrival of the blast.

The difference between the deflection and stress response of the short columns with one or two element thickness was negligible. This provided confidence for using single element thickness columns for the majority of the parametric study. The analysis time of the short column (0.5m long) with two element thickness was 8hr10min on a dual quad core PC. A 4m long column with two element thickness would have taken 65hr20min producing a result file of approximately 113GB. A typical analysis of a 4m long column with one element thickness ran for approximately 7hrs (on average) producing a results file of 14GB. Using one element thick columns for the majority of the parametric study allowed stable analyses to run without excessive computational running times and large data files.

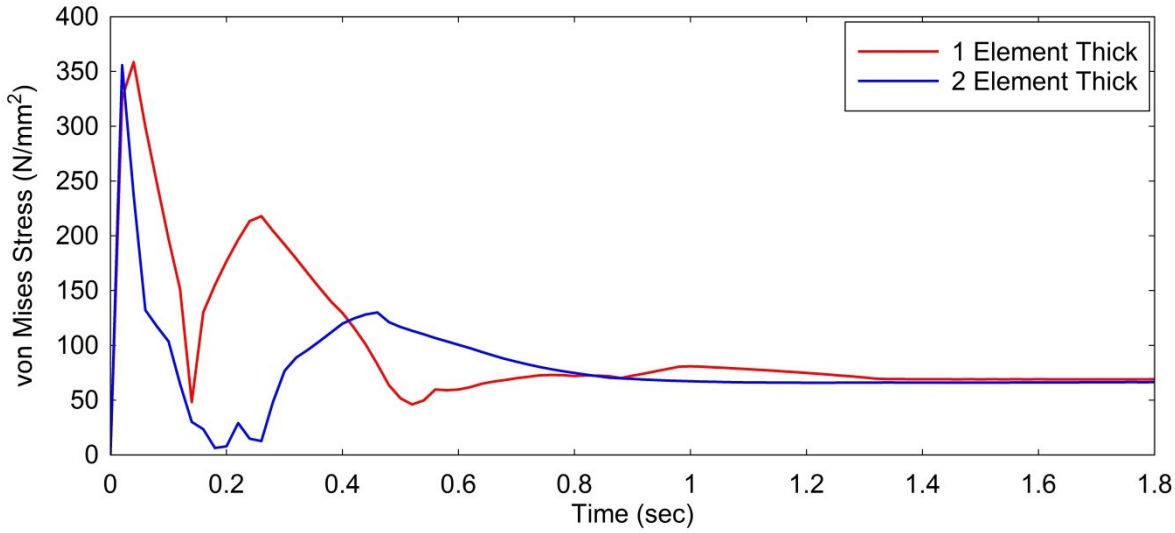

Figure 4.4.41: Midpoint Stress vs. Time: One and Two Element Thick Short Column (Blast and Thermal: Peak Pressure = 198.8kPa)

4.4.7 Parametric Study Summary

The methods, results and conclusions presented in 4.4.1 to 4.4.6 detail the full parametric study undertaken as part of this research project. The aim of the parametric study was to investigate the response of structural steel columns to high intense thermal and long duration blast load from explosive events. This has been achieved through rigorous numerical methods calculating the intensity, timing and duration of the blast and thermal loads from explosive events, the changing properties of steel under thermal and high strain rate loading and the non-linear FEA modelling procedures.

Results detailed show synergistic responses where the initial thermal load has significantly altered the material and structural properties of the steel column prior to the arrival of the blast. Relationships of scaled distance vs. deflection and stresses show a clear increase in this synergistic response as scaled distances decrease, until a razor (steep increase) is reached where the deflections and stresses are dictated by the blast load. There are also clear relationships observed between increasing peak temperatures and peak pressures vs. deflections and stresses.

Parameters investigated during the study includes support conditions, compressive loading, thermal conductivity and element mesh sensitivity. Results from the support conditions studied showed that columns with pinned supports deformed much less than columns with roller top support. The compressive load study showed that the deformations and stresses reduced with increasing compressive load. This relationship was due mainly to the increasing spring support stiffness replicating the column top support from one and storeys of typical floor load above. The results from the thermal conductivity study showed small increasing stresses and deformations

with increasing the thermal conductivity. This relationship was expected as higher thermal conductivities allow thermal loads to absorb further through steel. The degradation to the steel material properties was therefore higher and the response to the subsequent blast load was more prominent. The mesh sensitivity study investigated the effect of a two element thick steel column vs. a one element thick steel column. The results showed minor differences in the stress and deflection variations; however these differences were small in relation to the overall stresses and deflections providing confidence that a one element thick steel column was appropriate for the majority of parametric study.

4.5 Part D: ABT Column Modelling

In order to verify the computational methods adopted for the parametric study (4.4) computational models simulating the response of the columns from the ABT experimental trials were developed. Computational models of the ABT trial columns subject to compressive, thermal and long duration blast loads were developed using the FEA procedures detailed in 4.2.

Table 4.5: ABT Trial: Column Modelling Schedule

Trial	Rig	Column	Modelled	Trial	Rig	Column	Modelled
1 (5)	1	RHS	Modelled	**4 (1)**	1	RHS	Modelled
1 (5)	1	CHS	Modelled	**4 (1)**	1	CHS	Modelled
1 (5)	1	SHS	Modelled	**4 (1)**	1	SHS	Modelled
1 (5)	2	RHS	-	**4 (1)**	2	RHS	Modelled
1 (5)	2	CHS	-	**4 (1)**	2	CHS	Modelled
1 (5)	2	SHS	-	**4 (1)**	2	SHS	Modelled
1 (5)	3	RHS	-	**4 (1)**	3	RHS	-
1 (5)	3	CHS	-	**4 (1)**	3	CHS	-
1 (5)	3	SHS	-	**4 (1)**	3	SHS	-
2 (2)	1	RHS	-	**5 (3)**	1	RHS	-
2 (2)	1	CHS	-	**5 (3)**	1	CHS	-
2 (2)	1	SHS	-	**5 (3)**	1	SHS	-
2 (2)	2	RHS	-	**5 (3)**	2	RHS	-
2 (2)	2	CHS	-	**5 (3)**	2	CHS	-
2 (2)	2	SHS	-	**5 (3)**	2	SHS	-
2 (2)	3	RHS	Modelled	**5 (3)**	3	RHS	-
2 (2)	3	CHS	Modelled	**5 (3)**	3	CHS	-
2 (2)	3	SHS	Modelled	**5 (3)**	3	SHS	-
3 (4)	1	RHS	Modelled	**6 (6)**	1	RHS	-
3 (4)	1	CHS	Modelled	**6 (6)**	1	CHS	-
3 (4)	1	SHS	Modelled	**6 (6)**	1	SHS	-
3 (4)	2	RHS	Modelled	**6 (6)**	2	RHS	Modelled
3 (4)	2	CHS	Modelled	**6 (6)**	2	CHS	Modelled
3 (4)	2	SHS	Modelled	**6 (6)**	2	SHS	Modelled
3 (4)	3	RHS	-	**6 (6)**	3	RHS	Modelled
3 (4)	3	CHS	Modelled	**6 (6)**	3	CHS	Modelled
3 (4)	3	SHS	Modelled	**6 (6)**	3	SHS	Modelled

The recorded compressive loads, temperatures and blast pressures detailed in 3.3.3 were applied to the column models in order to replicate the response of the columns tested in the ABT. Table 4.5 details the column sections (RHS, CHS and SHS) from the ABT trials which were selected for computational modelling. Non-linear FEA models of 26 of the 54 columns from the ABT trial were developed during this research project. Due to time constraints the remaining 28 columns were not modelled during this project.

4.5.1 Modelling Procedure: Columns for ABT Trial

The modelling of the columns from the combined ABT trials was undertaken using the FEA procedures described in 4.2. Specific details for modelling columns from the ABT trials are shown in 4.5.1.1 to 4.5.1.4, including the application of pressure, thermal and compressive load and the material model details.

4.5.1.1 Pressure Load Application

Pressures applied to the faces of the column models were taken from a combination of the recorded reflected pressures and dynamic pressures with appropriate drag coefficients. The drag coefficients varied depending upon column section type. The reflected pressures detailed in 3.3.3.2.1 were applied to the front face of each column section. To remove unstable peaks from the raw pressure data the reflected pressure histories were decimated by 100 points average. Fig.4.5.1 shows the initial peak recorded reflected pressure (trial 1 (R5), rig 1) from 341.24msec to 342.64msec; the raw data and 100 point average decimated data are shown. It was necessary to decimate the raw data to reduce non-convergence during the analyses. The reflected pressure data was decimated by a further 10 points after the initial peak pressure duration. This was to reduce the size of the load curves and improve the running of the analyses. The recorded dynamic pressures were applied to the rear face of the columns using the following drag coefficients: SHS and RHS = 0.4, CHS = 0.3 (Clubley, 2013), (Bsi, 2005a). Linear smoothing was applied to pressure loads around the circumference of CHS column (using the ratio of the peak pressures on each face) to reduce any unrealistic and steps in the applied pressure.

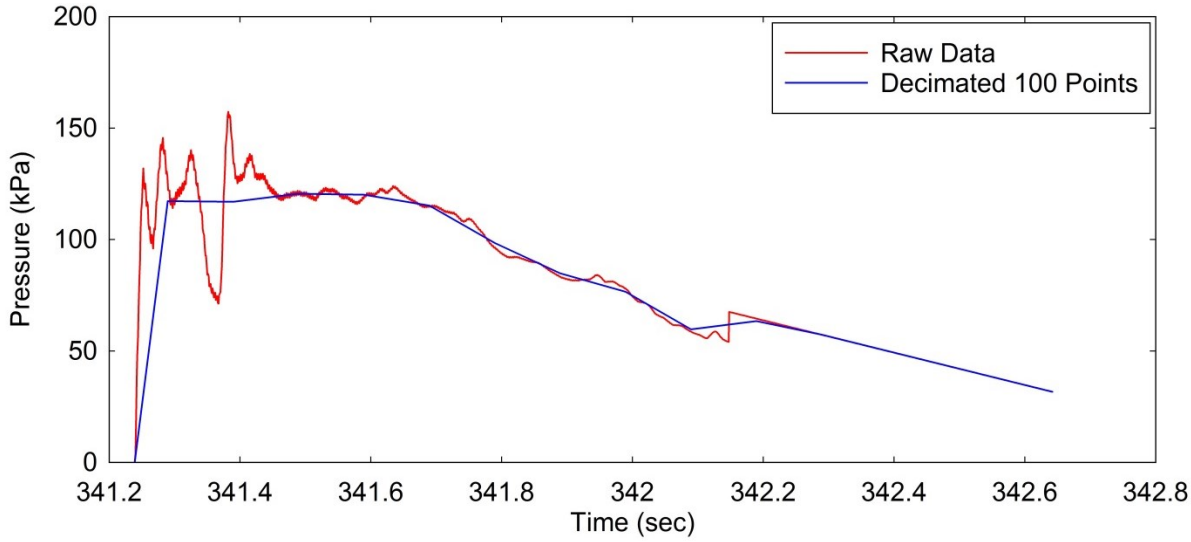

Figure 4.5.1: Reflected Pressure Peak: Raw and 100 Point Decimated (Trial 1 (5): Rig 1)

During the development of ABT column models dynamic pressures were applied to the front and rear faces of each column type (CHS, RHS and SHS) with appropriate drag coefficients; however, the magnitude of the modelled column's response was very low compared to the actual response. Modelled columns with a combination of reflected pressure on the front face and dynamic pressure on the rear face showed a reasonable correlation to the actual total deflections. The reflected pressures were recorded from gauges mounted to the front face of the heavy structural rigs. The gauges were mounted to a 150mm wide structural section. The trial columns were narrower (RHS: 50mm, SHS: 25mm and CHS: 33.7mm) therefore the actual applied pressures on the columns would differ from the reflected pressures recorded by the gauges on the heavy structural rigs. Future developments relating to this research could involve further detailed pressure mapping around the face of the columns.

4.5.1.2 Thermal Load Application

The temperatures were recorded during the trials using thermocouples placed at 1250mm, 1500mm (centre) and 1750mm along the length of the columns. These recorded temperatures were applied to the column models as prescribed temperatures using load varying time curves, in three sections: 0 – 1250mm, 1250mm – 1750mm and 1750mm – 3000mm. For each column (with thermal loading) the three recorded temperature profiles were applied with smoothing variations along the length. The smoothing variations adopted for each column were calculated using the peak recorded temperatures at each thermocouple location. As there were no thermocouples placed at the top and base of each column the actual temperatures were assumed to equal zero at the base

and half of the recorded temperature at 1750mm, at the top. These assumptions were based on higher recorded temperatures at 1750mm compared to 1250mm. This assumption is also substantiated by comparison of the temperatures along the length of the columns during the pre-requisite ceramic heating element trials (3.3.1). To model highly accurate temperature variations across the full length of the columns further heating trials would be necessary with a full set of thermocouples along the full length of each column with the same environmental conditions within the ABT.

The smoothing variations for each section (0 – 1250mm, 1250 – 1750mm and 1750 – 3000mm were calculated as follows (ex. Trial 3(4): Rig 3: RHS):

1. Peak temperature at 1250mm / Peak temperature at 1500mm = 210.21^{o}C / 477.06^{o}C = 0.44
2. Peak temperature at 1750mm / Peak temperature at 1500mm =462.38^{o}C / 477.06^{o}C = 0.97
3. From 0mm to 1250mm the smoothing variation = 0 - 1
4. From 1250mm to 1750mm the smoothing variation = 0.44 to 1 (midpoint) to 0.97
5. From 1750mm to 3000mm the smoothing variation = 1 to 0.5

The temperatures were applied using smoothing variations over 69 linear steps on each of the three sections of the modelled columns. To avoid doubling the applied temperature at nodes which connect the three sections the variation factors in the adjacent 69th and 1st step for each column section were halved. Fig.4.5.2 is an extract from a FEA column model showing the temperature variation along the length of the RHS from trial 3(4), rig 3.

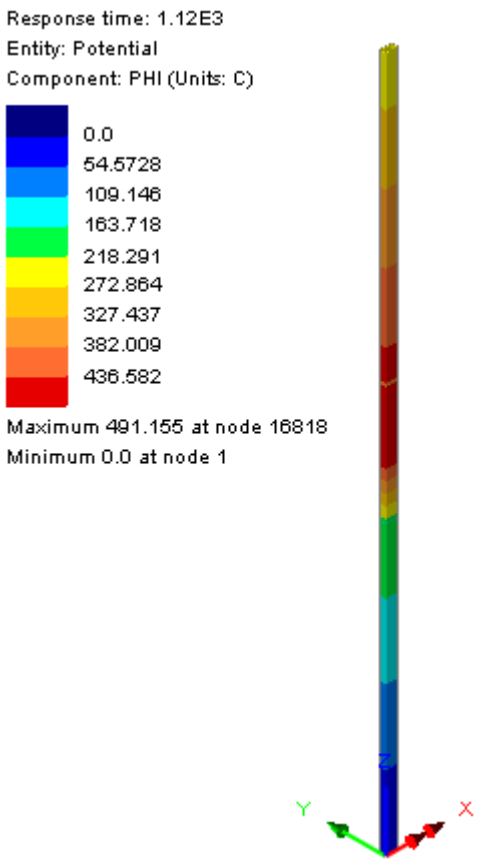

Figure 4.5.2: ABT Trial Column FEA: Temperature Variation (Trial 3 (4): Rig 3: RHS)

4.5.1.3 Compressive Load Application

The compressive loads applied to the columns in the ABT trials were recorded using load cells placed between the heavy duty compression springs and the base of each column (3.3.3.2.3). A small variation (increase) in the applied compression was observed over the duration of the initial heating phase, followed by minor fluctuations during the subsequent blast load. The compressive loads from the heavy duty springs were replicated in the column models using spring supports. The applied stiffness was equivalent to the spring rate of each heavy duty spring (IST, 2015). Table 4.6 shows the spring stiffness used for the column models for each applied compressive load.

Table 4.6: Experimental Specification Spring Stiffness

Compressive Load (kN)	Spring Stiffness (N/mm)
1.54	15.4
2.3	23.0
2.86	28.6
3.48	34.8
4.28	42.8
5.15	51.5
5.2	52.0
6.26	62.6

4.5.1.4 Material Model

The steel strength used for the ABT trial columns was S355 (Bsi, 2006) high yield structural steel. Static tensile tests were performed by Stead and Wilkins Ltd. on samples from the structural steel columns in accordance with BS EN ISO 6892-1:2009 (Bsi, 2009). Table 4.7 shows results from the tensile tests. The 0.2% proof (yield) stress and ultimate yield stress were incorporated into the Johnson-Cook material model for the steel columns. The steel material model was developed using the methods detailed in 4.4.4. Results from the static tensile tests showed the SHS had a much higher proof and ultimate tensile stress compared to the RHS and CHS. All proof stresses are above the lower bound limit of 355MPa assumed for S355 structural steel. The results from the static tensile tests on the steel column samples illustrate the importance of conducting separate material sample testing due to potential large variations from assumed design stresses.

Table 4.7: ABT Trial Columns Static Tensile Tests

Section	0.2% Proof Stress (MPa)	Ultimate Tensile Stress (MPa)
CHS 1.	411.0	466.0
CHS 2.	417.0	474.0
CHS Average.	**414.0**	**470.0**
SHS 1.	520.0	572.0
SHS 2.	537.0	574.0
SHS Average.	**528.5**	**573.0**
RHS 1.	371.0	431.0
RHS 2.	371.0	432.0
RHS Average	**371.0**	**431.5**

Figs.4.5.3 to 4.5.5 show the post elastic material models for the three structural steel column sections under high strain rates and high temperatures according to the Johnson-Cook formula (Equation 4.14). The average proof and ultimate tensile stresses shown in table 4.7 are used as parameters A and B for the material model formulation for each column section type.

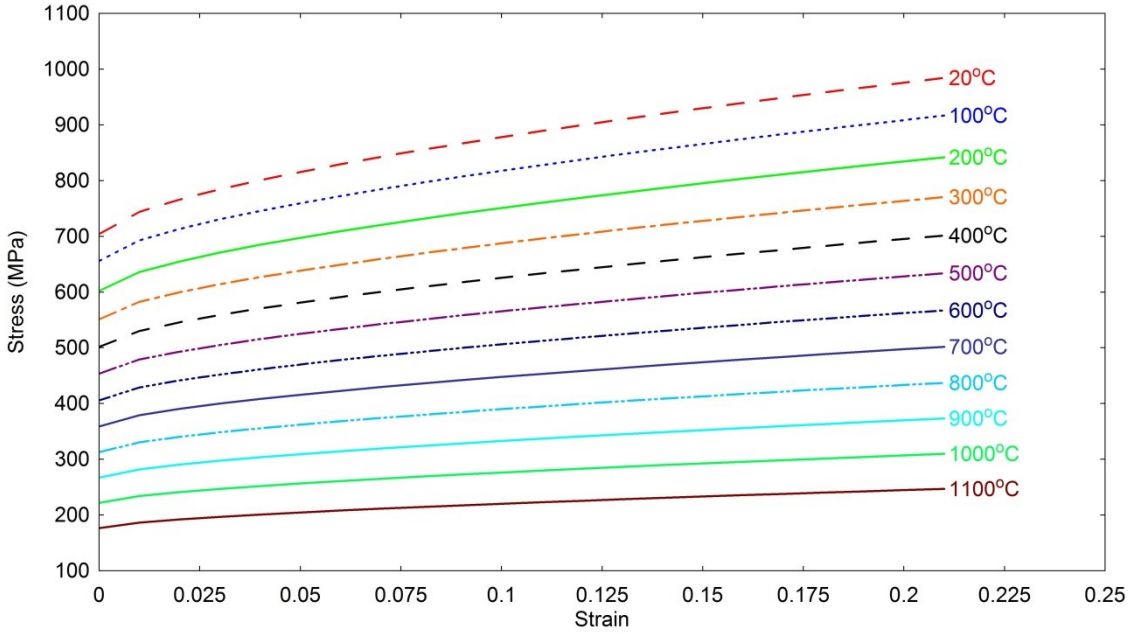

Figure 4.5.3: Structural Steel Material Model: SHS

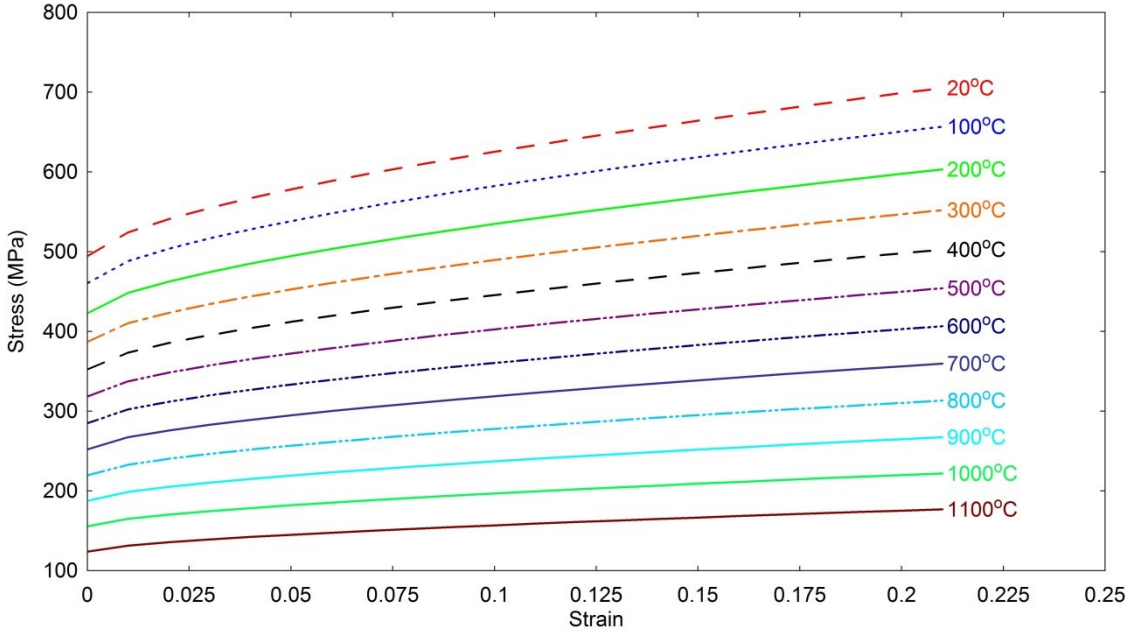

Figure 4.5.4: Structural Steel Material Model: RHS

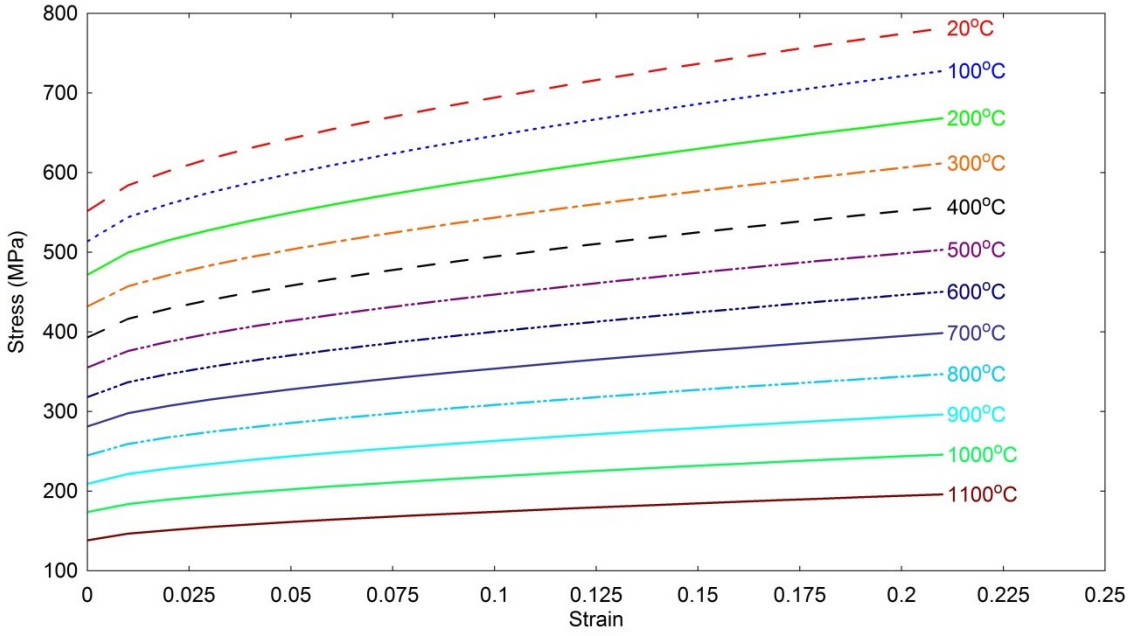

Figure 4.5.5: Structural Steel Material Model: CHS

4.5.2 ABT Trial Column Model Results

Figures 4.5.6 to 4.5.12 show the horizontal midpoint deflections of the columns from the ABT trials and the equivalent predictive computational models for each column. Each figure shows the actual horizontal midpoint deflections recorded using the high speed cameras and the horizontal deflections extracted from the post-processing of the predictive computational models. Due to time and data collection constraints several assumptions were made regarding the pressure and temperature distributions around each column and the fixity of the column end connections. As there was no recorded reflected pressure data from the surface of each column the recorded reflected pressures (on surface of heavy structural rig) and dynamic pressures were used to calculate the approximate applied pressure to each face of the columns. Temperatures were only recorded on the central 500mm of each column due to a limited number of thermocouples available. Despite the assumptions that were made during the computational modelling process the models reproduced, to a degree of reasonable accuracy, the structural response of the columns in the ABT trials.

Fig.4.5.6 shows the actual and modelled midpoint deflections of the RHS, SHS and CHS in the pinned rig during trial 1. There is a significant difference in the modelled and actual peak deflections and the harmonic response. The RHS peak deflection was 182.43mm during the trial, compared with 76.68mm (model). Average frequency of oscillations after the peak deflection observed in the RHS was 7.97Hz (trial) and 46.73Hz (model). Despite differing peak deflections and frequencies reasonable correlation was observed between the trial and model final deflections (after one

second). The final deflection of the RHS was 28.3mm (trial) and 38.1mm (model), the final deflection of the SHS was 12.29mm (trial) and 12.77mm (model) and the final deflection of the CHS was-4.5mm (trial) and 9.7mm (model). The clear difference between the midpoint deflections of the RHS, SHS and CHS trial columns was shown in the column model results; the RHS exhibited the largest response, followed by the SHS with the CHS showing the smallest response.

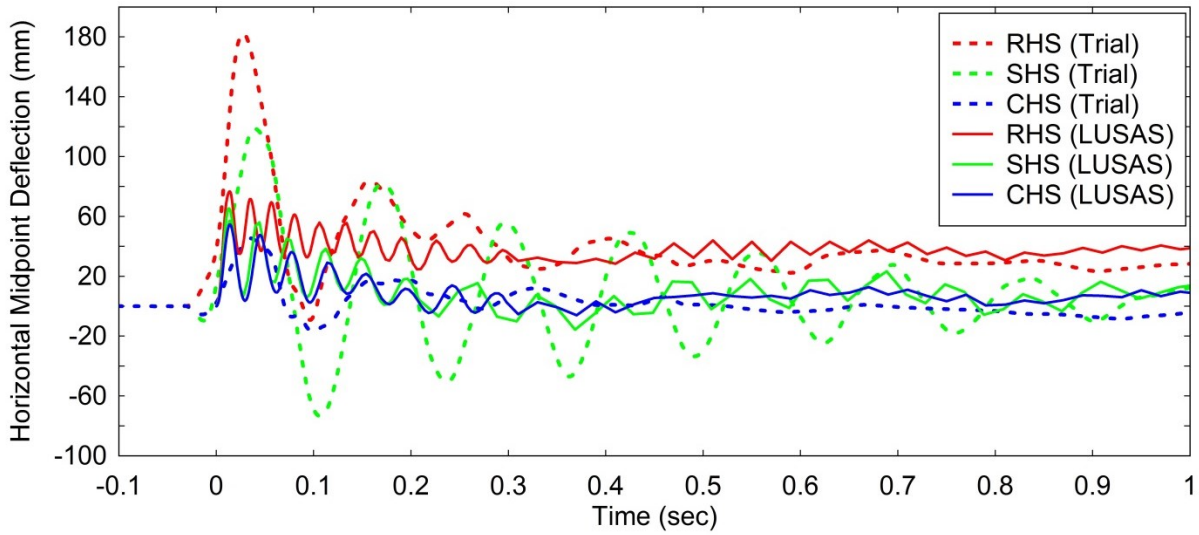

Figure 4.5.6: Trial 1(5): Pinned Rig Horizontal Midpoint Deflections

Fig 4.5.7 shows the actual and modelled midpoint deflections of the RHS, SHS and CHS in rig 3, during trial 2. The columns in this rig were under low compressive load and no thermal load. The peak deflection of modelled RHS was 131.4mm, compared with the actual RHS peak deflection of 161.53mm (< 20% difference).

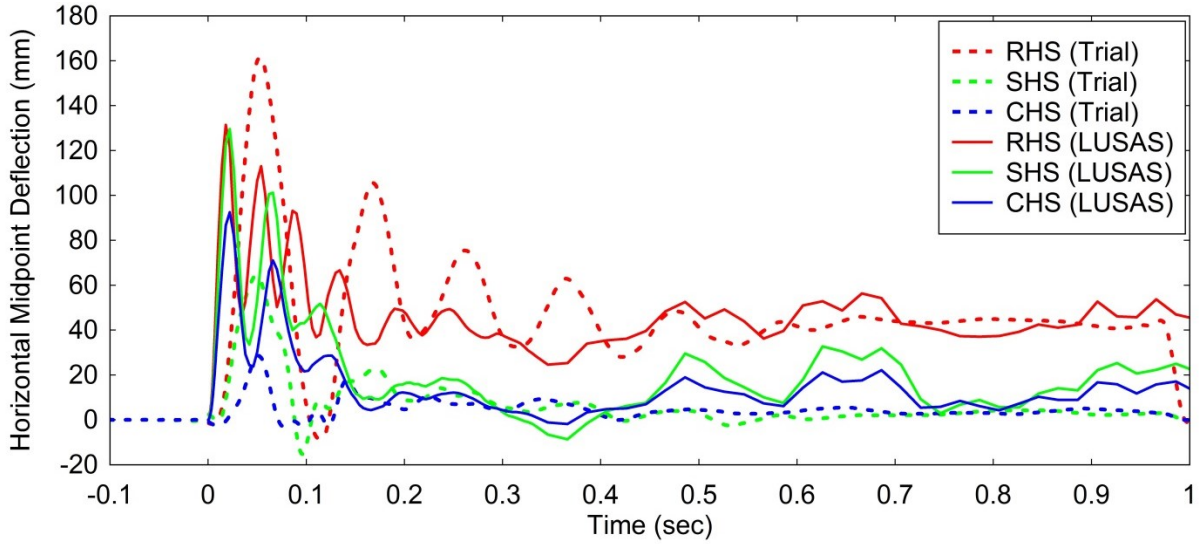

Figure 4.5.7: Trial 2 (2): Rig 3 Horizontal Midpoint Deflections

There is a reasonable correlation between the modelled and trial final RHS deflections; the final deflection of the trial RHS was 53.67mm (excluding camera error at 0.97sec) and the modelled RHS was 45mm. The SHS and CHS models over predicted the peak and final deflections. The correlation of the harmonic response of each trial column to modelled column is closer than the pinned rig (Fig.4.5.6) columns. The frequency of the trial RHS was 9.62Hz, compared with 22.73Hz for the modelled RHS. After the initial harmonic response the model and actual RHS deflection time histories are similar: (45mm trial, 48mm model)

Fig 4.5.8 shows the actual and modelled midpoint deflections of the RHS, SHS and CHS in rig 2, during trial 3. The columns were under medium compressive load and no thermal load. The modelled RHS under predicts the peak deflection (trial: 164.58mm, model: 120.57mm) but predicts the final deflection to a more reasonable degree of accuracy (trial: 64.44mm, model: 39.63mm). The modelled SHS peak deflection of 117.17mm is a reasonable correlation to the actual peak SHS deflection of 99.31mm. The profile of the SHS deflection time history is followed to a degree of reasonable accuracy between the model and trial columns.

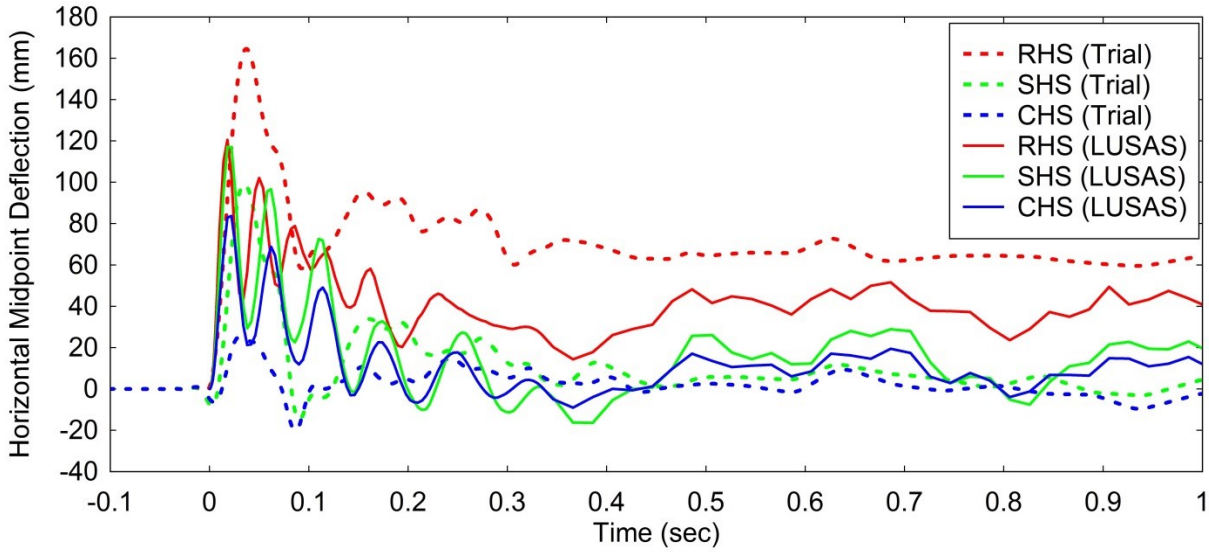

Figure 4.5.8: Trial 3(4): Rig 2 Horizontal Midpoint Deflections

Fig.4.5.9 shows the actual and modelled midpoint deflections of the RHS, SHS and CHS in the pinned rig during trial 3. Similarly to Fig.4.5.6 (trial 1, pinned) the numerical models do not accurately predict the peak deflections and harmonic response, however the final (settled) deflections are reasonably reproduced. The most reasonably predicted peak deflection was the CHS with values of 44.48mm (trial) and 54.0mm (model). The final (at one second) deflections for each of the modelled and trial columns were as follows: RHS: 31.65mm (trial), 48.14mm (model), SHS: 16.6mm (trial), 15.68mm (model), CHS: 2.78 (trial), 6.52mm (model). The difference between the response shown

in the computational models and actual columns is due to accurate modelling of the end connections.

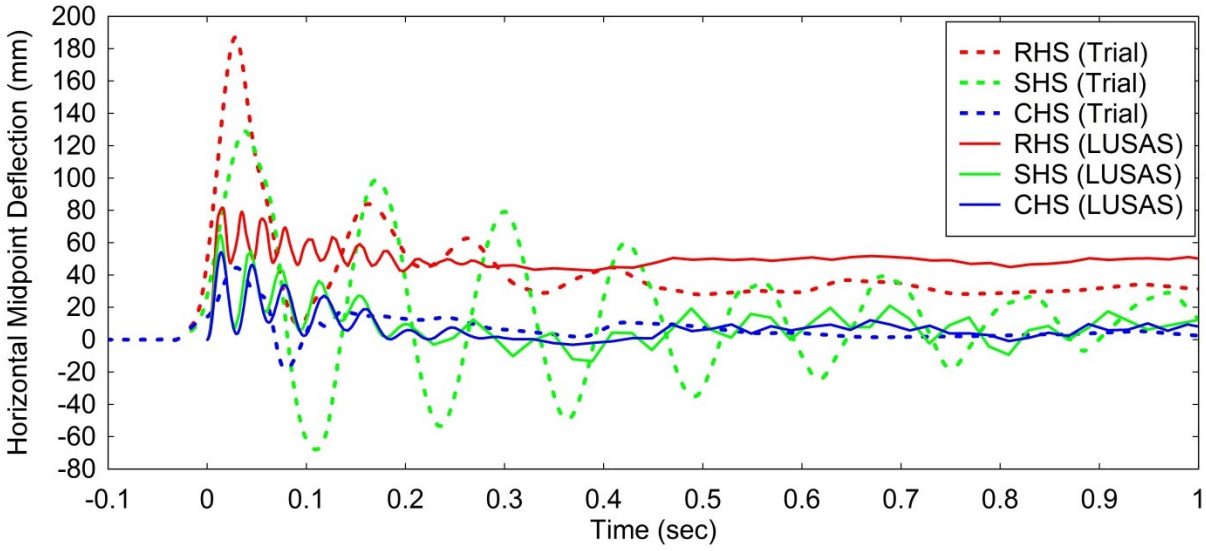

Figure 4.5.9: Trial 3(4): Pinned Horizontal Midpoint Deflections

Fig4.5.10 shows the actual and modelled midpoint deflections of the RHS, SHS and CHS in rig 2 during trial 4. The columns were subject to high thermal and low compressive loads prior to the blast arrival.

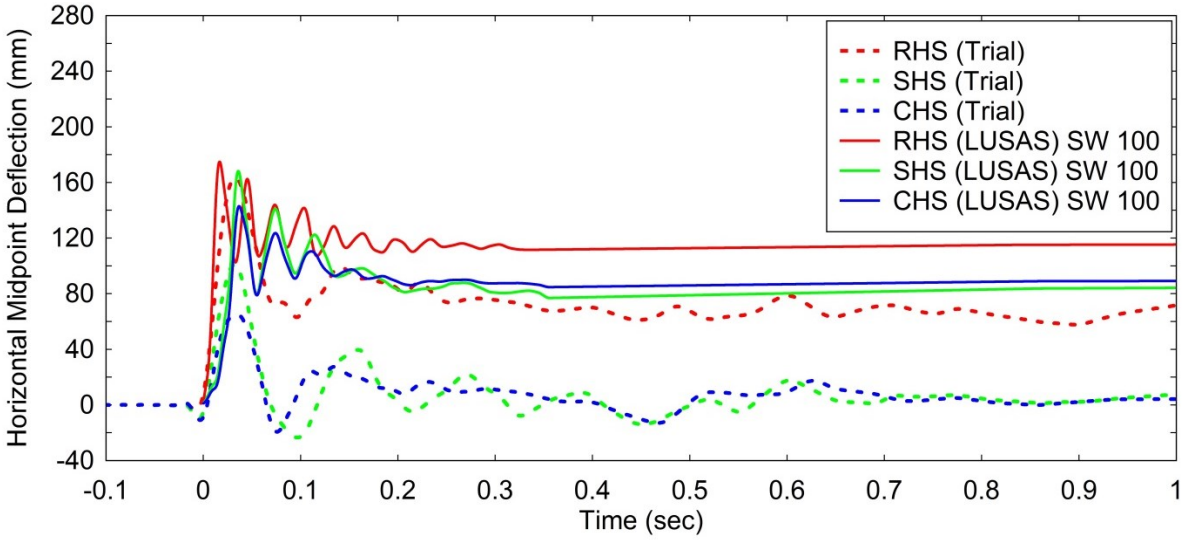

Figure 4.5.10: Trial 4(1): Rig 2 Horizontal Midpoint Deflections

The midpoint deflection curves of the modelled columns have been smoothed using fast Fourier transform smoothing with an average smoothing window of 100 (SW100). The peak deflection of the modelled RHS correlates reasonably well with the actual RHS deflection (trial = 163.65mm, modelled = 174.8mm). There is a larger difference between the final deflections for the trial (72mm)

and modelled (115mm) RHS. The modelled CHS and SHS both over-predict the response of the actual columns. This is due to assumptions in the pressure and temperature variation around the surface and length of each column section. Further development of these models would lead to accurate pressure variations and a more reasonable match to the actual column response.

Fig4.5.11 shows the actual and modelled midpoint deflections of the RHS, SHS and CHS in rig 2 during trial 6. The columns were subject to low thermal and high compressive loads prior to the blast arrival. There is observable correlation between the peak deflections of the modelled and trial RHS and SHS: RHS trial = 115.6mm, model = 149.6mm, SHS trial = 102.5, model = 142.3mm. After the peak deflections the response of the column models over-predicts the actual response. Comparing Fig.4.5.11 to Fig. 4.5.10 the higher thermal load applied in trial 4 has a more significant effect on the column response than the high compressive load (and low thermal) applied in trial 3. This is evident for both the actual and modelled column response.

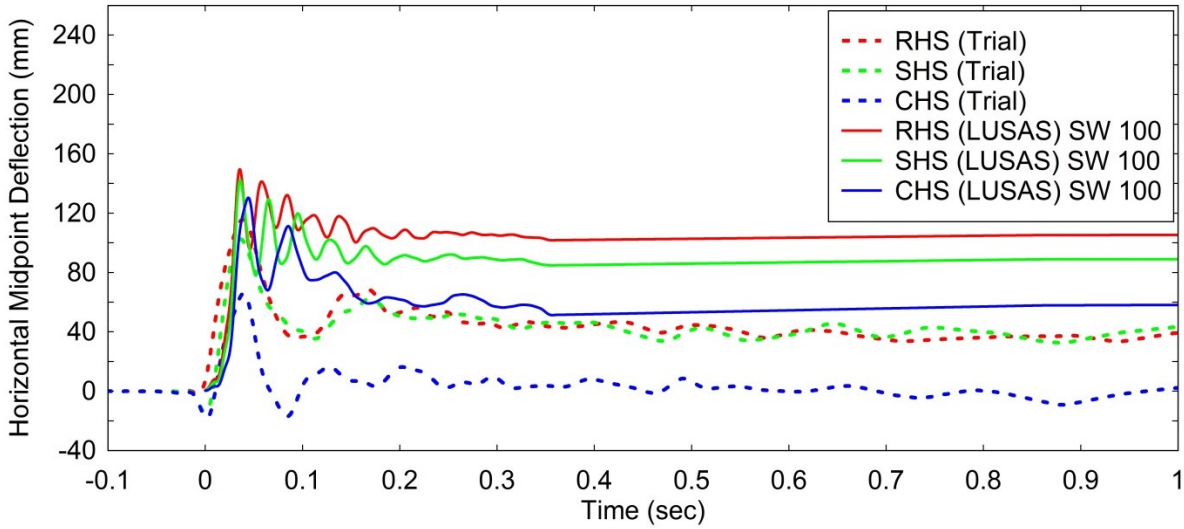

Figure 4.5.11: Trial 6: Rig 2 Horizontal Midpoint Deflections

Fig4.5.12 shows the actual and modelled midpoint deflections of the RHS, SHS and CHS in rig 3 during trial 6. The columns were subject to high compressive loading but no thermal load prior to the blast arrival. Actual peak and final deflections of the RHS are much higher than the modelled deflections. There is reasonable correlation between the peak deflections of the modelled and trial SHS: (model = 103.2mm), (trial = 86.2mm). The final deflections (at one second) of the modelled and trial SHS also correlated reasonably well (model = 19.9mm, trial = 26.8mm).

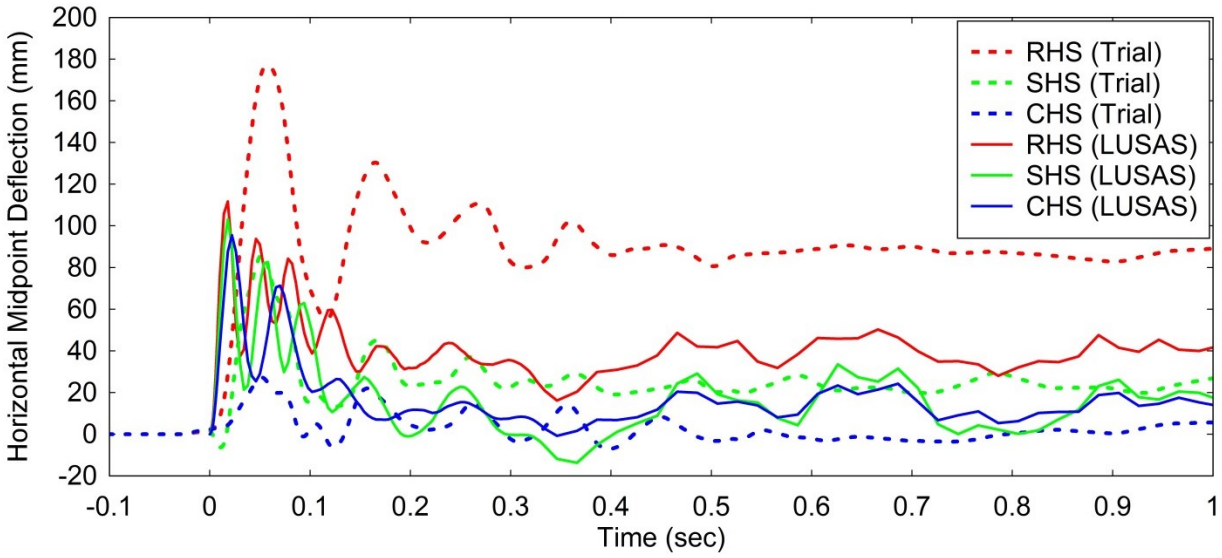

Figure 4.5.12: Trial 6: Rig 3 Horizontal Midpoint Deflections

Figs.4.5.6 to 4.5.12 show results with reasonable correlation, over-prediction and under-prediction from the predictive computational models in comparison to the actual response of the trial columns. Key similarities evident between the computational and actual column response include higher deflections of the RHS in comparison to the SHS and CHS, and larger deflections of columns with higher thermal load. Reasonable correlation is shown between the response of modelled and trial RHS providing verification for the use of the computational methods adopted throughout the research project.

4.5.3 ABT Trial Computational Analysis Summary

The novel ABT trials were successful in recording and observing the thermo-mechanical response of steel columns under combined compression and long duration thermal and blast loading. Experimental trials combining compression, high thermal and long duration blast loads on full scale structural elements had not previously been achieved. The large amount of data recorded during the trials will be used in the many future research applications and the trials have set a precedent for further research in this field. The recorded data was used to develop non-linear FEA models of the structural steel columns replicating the structural response observed during the trials. The response of the column models replicated the response of the actual trial columns well, but with some discrepancies between trials and models. The highly complex pressure loads, temperature loads and changing material and structural properties observed during each trial demonstrate the difficulty in accurately modelling the response of the columns. The overall trends such as deflections increasing with higher thermal load and compressive load in combination with the long duration blast load (opposed to blast alone) were replicated by the computational models. The

trend of RHS exhibiting the largest deflections, followed by SHS then CHS was also replicated by the computational models.

Chapter 5

Resistance Functions

5.1 Theoretical Basis

5.1.1 Development of Resistance Functions

Resistance functions or curves are typically used to describe the elastic and plastic response of structures to blast loading. The resistance R_m, describes the point at which permanent failure occurs in a structure. This can vary for different failure mechanisms, such as column buckling, elastic/plastic failure, lateral torsional buckling or local buckling. For the purpose of this research, R_m refers to the maximum (lateral) elastic deformation of the column before plastic failure occurs. The gradient and extent of the curve beyond R_m describes the ductility of the structure under the specific load set; the extent to which the structure deforms before complete collapse is reached. Fig. 5.1.1 shows the resistance curves of a typical bi-linear and tri-linear structural response of a column subject to blast load. This research adopts the simplified bi-linear resistance curve with findings from the parametric study dictating the gradient of the elastic and post-elastic curves.

The procedure used in the development of the resistance curves for this research involved initially calculating the elastic limit of the structural column section under blast loading. The times at which each column in the study reached this elastic limit were calculated from each deflection-time history graph detailed in 4.4.6. The equivalent applied pressures at the times of elastic limit were back calculated from the applied blast pressure histories: the applied blast pressures at these times are converted to equivalent resistance (R_m) for each column loading scenario by multiplying the blast pressure by the exposed area of the column. The post elastic (ductility) curve is subsequently determined by the deflection history beyond the elastic deflection limit until the peak plastic deflection, or maximum ductility is reached. The detailed calculation procedure used to develop

the resistance functions is shown in 5.1.1. The resistance functions can be used in fast running SDOF analysis codes to determine damage levels to structures subject to blast loads.

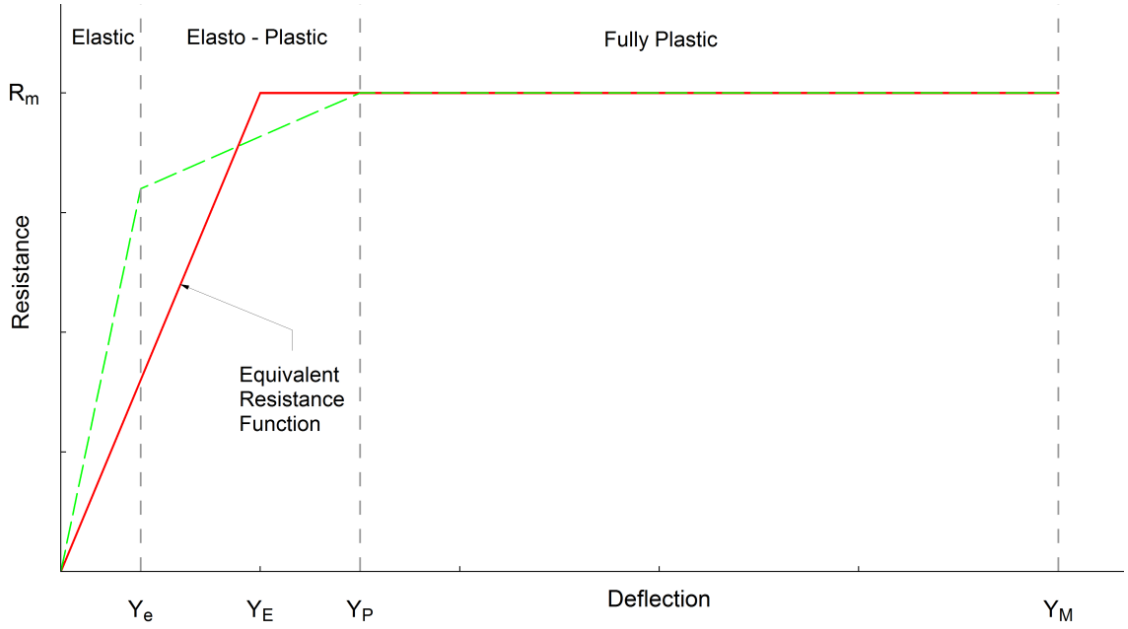

Figure 5.1.1: Resistance Function Tri and Bi-Linear Structural Response

5.1.1.1 Steel Column Calculations under Blast Load

The following details the calculation procedure performed on a CHS193.7x5 S275 structural steel column subject to blast load. The length of the column is 4m with pinned ends. This column length and section type was chosen as it is a typical size and length used in building construction and the relatively thin walls of the column (5mm) allow rapid absorption of thermal load and subsequent structural degradation.

Equations 5.1 to 5.4 detail the classification of the column section performed in accordance with BS EN 1993-1-1:2005, (Bsi, 2005b) and (BSi, 2000). The CHS193.7x5 in S275 steel is a class one section (plastic). Class one sections typically have sufficient ductility to form plastic hinges with sufficient rotation capacity of "not less than the required at the hinge locations" (Bsi, 2005b), this correlates with parametric study results which show plastic hinge formation in the column section under several loading scenarios (Fig.5.1.2). Under high temperatures the section classification may change with reducing yield stress values.

$$\epsilon = \sqrt{\frac{235}{275}} = 0.924 \tag{5.1}$$

$$\frac{d}{t} = \frac{193.7}{5} = 38.74 \tag{5.2}$$

$$50\epsilon^2 = 42.72 \tag{5.3}$$

$$\frac{d}{t} \leq 50\epsilon^2 (Class\ 1) \quad (5.4)$$

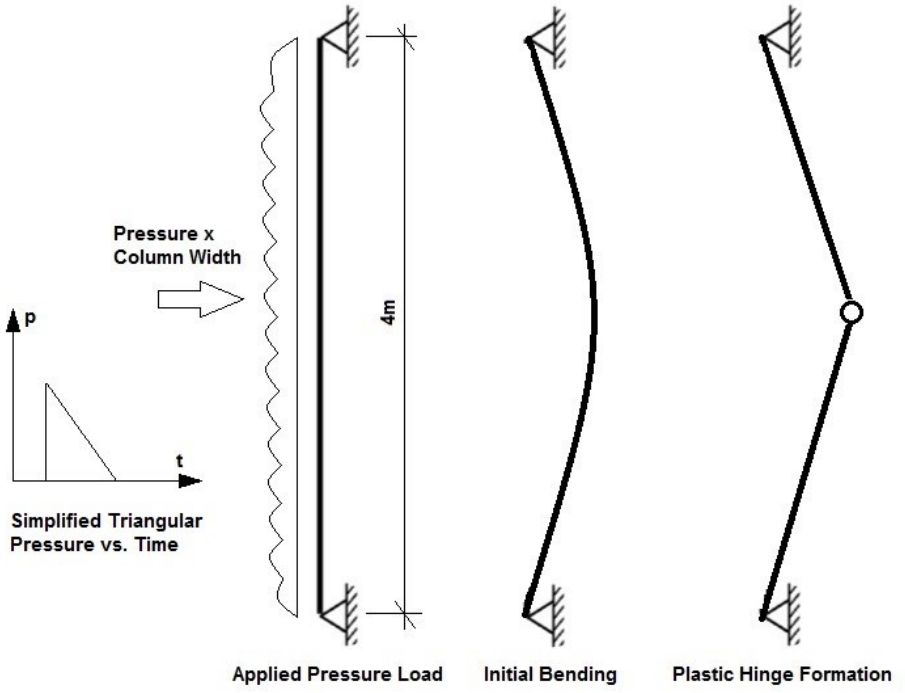

Figure 5.1.2: Pinned End Column with Horizontal Blast Load

The complex non-linear blast loading is simplified to a triangular load applied on the front face of the column. The equations 5.5 to 5.22 detail the column design (Mays, 2009) to a blast load with a peak (applied) pressure (p_{max}) of 198.8kPa (=198.8x10^{3}N/m^2) (2 x incident pressure) and duration (t_d) of 1.25sec. This pressure and duration are used as they are typical values used in the parametric study (Table 4.4). To produce the resistance curves for each loading scenario in the parametric study the peak pressures and durations for each scenario were used to calculate the theoretical resistance. The required resistance to the applied blast load is shown in equations 5.5 and 5.6. A simplification is adopted assuming the blast pressure is applied in a normal direction to the full front face of the CHS (4m x 194mm):

$$R_m = 0.5 p_{max} \times A \quad \text{(Category 2, (UFC, 2008))} \quad (5.5)$$

$$R_m = 0.5 \times 198.8 kN/m^2 \times (4m \times 0.194m) = \mathbf{77.14kN} \quad (5.6)$$

The maximum resistance can be calculated from the bending moment resistance using eq. 5.7:

$$R_m = \frac{8M_p}{L} \quad (5.7)$$

Rearranging eq. 5.7 the required bending moment resistance is calculated using eq. 5.8:

$$M_p = \frac{R_m L}{8} \tag{5.8}$$

$$M_p = \frac{77.14 \times 4}{8} = \mathbf{38.57kNm} \tag{5.9}$$

The column stiffness k_e is calculated using 5.10:

$$k_e = \frac{384EI}{5{L_{eff}}^3} \tag{5.10}$$

E = 205 GPa, I = 1320x10^{-8} (m^4),

As the column is pinned an effective length (L_{eff}) of 1 x L is used.

$$k_e = \frac{384 \times 205{\times}10^9{\times}1320{\times}10^{-8}}{5 \times 4^3} = \mathbf{3247.2x10^3 N/m} \tag{5.11}$$

The design bending moment resistance of the column section is calculated using eq. 5.12:

$$M_{Rd} = f_{yd,dyn} \left[\frac{W_{el}+W_{pl}}{2}\right] \tag{5.12}$$

The dynamic design strength of the steel ($f_{yd,dyn}$) is calculated using eq. 5.13 and eq. 5.14 (Mays, 2009).

$$f_{yd,dyn} = \frac{\left(f_y + \frac{1}{4}(f_{ult} - f_y)\right)}{\gamma_{M0,acc}} \tag{5.13}$$

The partial factor for accidental loading: $\gamma_{M0,acc}$ = 1 (BS EN 1993-1-1)

$$f_{yd,dyn} = \frac{\left(275 + \frac{1}{4}(410-275)\right)}{1} = \mathbf{309x10^3\ N/mm^2} \tag{5.14}$$

Using the plastic and elastic modulus of the column section (W_{el} = 136x10^{-6} (m^3), W_{pl} = 178x10^{-6} (m^3) (Tata, 2016), the design bending moment resistance of the column was calculated using eq.5.15:

$$M_{Rd} = 309 \times 10^6 \left[\frac{136{\times}10^6 + 178{\times}10^{-6}}{2}\right] = \mathbf{48513Nm = 48.51kNm} \tag{5.15}$$

The natural period of the structural column is calculated using equation 5.16:

$$T = 2\pi\sqrt{\frac{K_{lm}M}{k_e}} \tag{5.16}$$

From (Biggs, 1964)the load mass factor K_{lm} = **0.78** for elastic failure (0.66 for plastic failure).

The mass M = 23.3kg/m x 4m = **93.2kg**

Therefore T (the natural period) is:

$$T = 2\pi\sqrt{\frac{0.78 \times 93.2}{3247.2\times10^3}} = 0.0297\,\text{sec} = \mathbf{29.7}\boldsymbol{msec} \tag{5.17}$$

The frequency f, is therefore:

$$f = \frac{1}{T} = \frac{1}{.0297sec} = 33.7Hz \tag{5.18}$$

The design resistance R_m is therefore:

$$R_m = \frac{8M_{rd}}{L} = \frac{8 \times 48.51}{4} = \mathbf{97.02}\boldsymbol{kN} \tag{5.19}$$

The design resistance per unit length (R_u) is:

$$R_u = \frac{97.02}{4} = \mathbf{24.26}\boldsymbol{kN/m} \tag{5.20}$$

The applied peak pressure per unit length (p):

$$p = 198.8 \times \frac{10^3N}{m^2} \times\ 0.194m = \mathbf{38.57}\boldsymbol{kN/m} \tag{5.21}$$

From Figure 3-54 in (UFC, 2008) using a ratio of r_u/p = 24.26 /38.57 = **0.63** and a ratio of t_d/T = 1.25 x 10^3msec / 29.7msec = **42.1**, the ductility ratio is $\mu = \chi_m/\chi_e$ = **100+**. As the value for ductility (μ) is higher than the values on the chart, ductility is set at the maximum of 20. A ductility limit of 20 is specified as the column section is designed under protection category two (protection of structure from collapse): (Mays, 2009), (UFC, 2008). Equation 5.21 is used to calculate the elastic deflection limit (χ_e):

$$\chi_e = \frac{R_m}{k_e} = \frac{97.02kN}{3247.2N/m} = 0.0299m = \mathbf{29.9}\boldsymbol{mm} \tag{5.22}$$

Therefore, the limits set for the resistance curve are χ_e = 29.9mm at μ = 1, and χ_m = 598mm at μ = 20. The process of using these limits to form the resistance curves from the column deflection time histories in the parametric study is detailed below:

1. Find time the column deflects to 29.9mm from deflection-time history (if reached).
2. Find equivalent applied pressure at relative time calculated in step one from the applied blast pressure curves.
3. Convert pressure to resistance (R_m) by multiplying by exposed column area.
4. Find equivalent applied pressure loads at the peak deflections (if beyond 29.9mm)

5. Find ductility by converting equivalent peak pressure to equivalent load and multiplying by exposed column area

The above calculations and resistance curve development procedure were adopted for all the different loading regimes investigated within the parametric study. A limitation to this method of determining the resistance curves is the imposed gradient on the linear increase of blast pressure used within the load curves in the FEA analysis. A small gradient was adopted in increase of the applied blast pressure from zero to peak pressure (opposed to use of an instantaneous increase). This was to encourage convergence during the non-linear analysis. If an instantaneous increase was adopted there would be no time step between zero applied blast pressure and peak, therefore the equivalent pressure at the time of elastic limit would be difficult to determine.

5.2 Derived Output and Implementation

Figs 5.2.1 to 5.2.7 show the resistance curves for columns subject to blast, and blast and thermal loads with a range of peak pressures. Each figure shows the theoretical idealised resistance curve for the structural column, the resistance curve for the blast only analysis and the resistance curve for the blast and thermal analysis. The blast only resistance curves describes the structural response of a column subject to long duration blast load only from explosive events. The equivalent blast and thermal load resistance curves describes the structural response of a column under the same long duration blast load following an intense thermal load radiated from the explosive event. Figures 5.2.1 and 5.2.2 show the resistance curves for columns with blast loads of peak pressures = 185kPa and 282kPa. The elastic limit (resistance = R_m) is not reached for these particular blast only cases. The blast and thermal elastic limit (R_m), is typically lower than the equivalent blast only limit for all loading regimes. As peak pressures increase both the blast only and blast and thermal resistance curves show an increased resistance (R_m) to the same elastic deflection limit and a larger plastic deformation. This indicates an increased yield strength with the higher pressures.

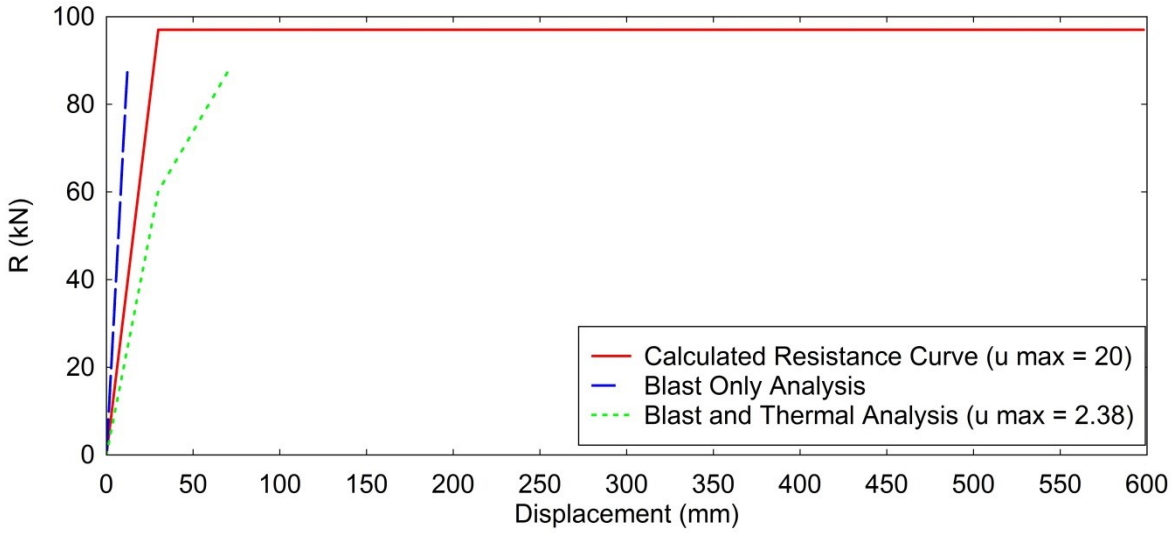

Figure 5.2.1: Resistance Curve: 185kPa Peak Pressure

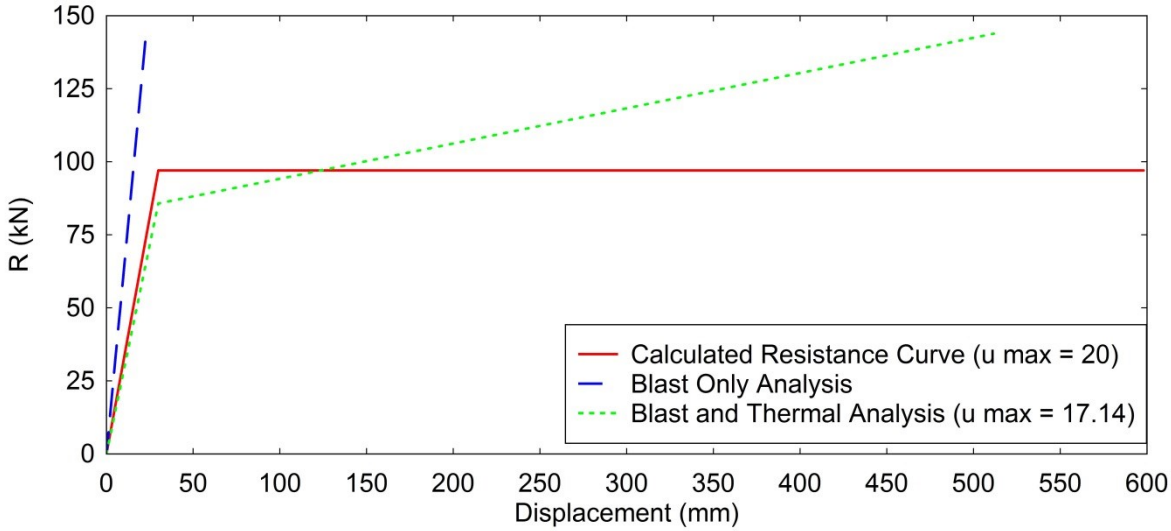

Figure 5.2.2: Resistance Curve: 282kPa Peak Pressure

A full set of resistance curves for varying peak pressures are detailed in Appendix E. The maximum ductility (μ) is shown for each peak pressure. Fig.5.2.7 shows the resistance curves for a column with 290kPa peak pressure applied and fully pinned connections at either end (Figs.5.2.1 to 5.2.6 show the resistance curves for columns with a "roller" top connection). Comparing Fig.5.2.7 to Fig.5.2.2 (282kPa peak pressure, fully pinned), the ductility of the column under combined thermal and blast load with fully pinned ends is much lower than with a roller top end connection. The resistance R_m, at the equivalent elastic deflection limit, is higher for the pinned end case. A

limitation with Figs.5.2.1 to 5.2.7 is minimal direct correlation to the applied thermal load for each case.

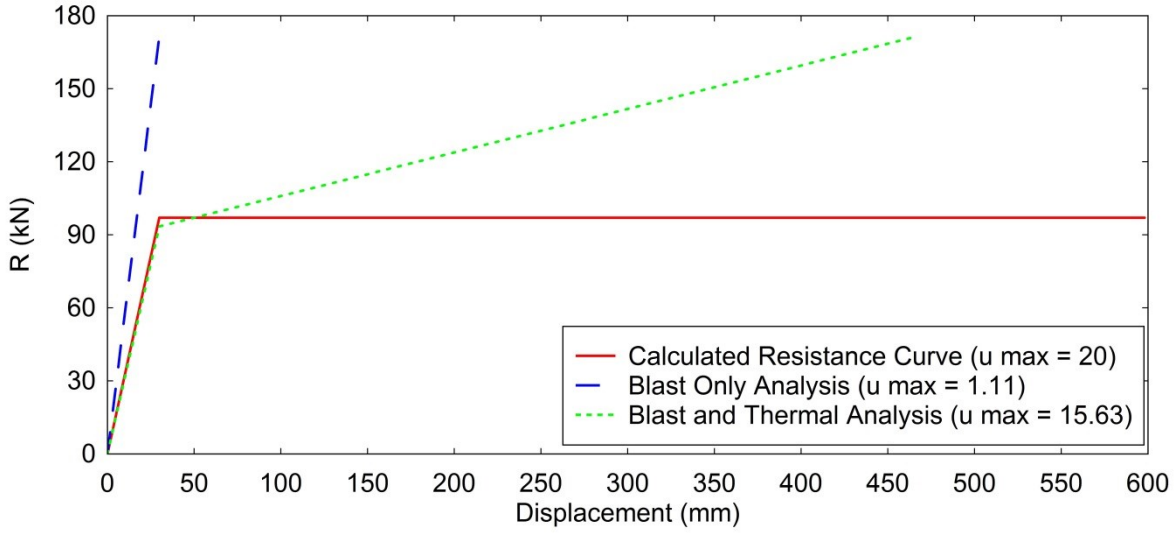

Figure 5.2.3: Resistance Curve: 329.4kPa Peak Pressure

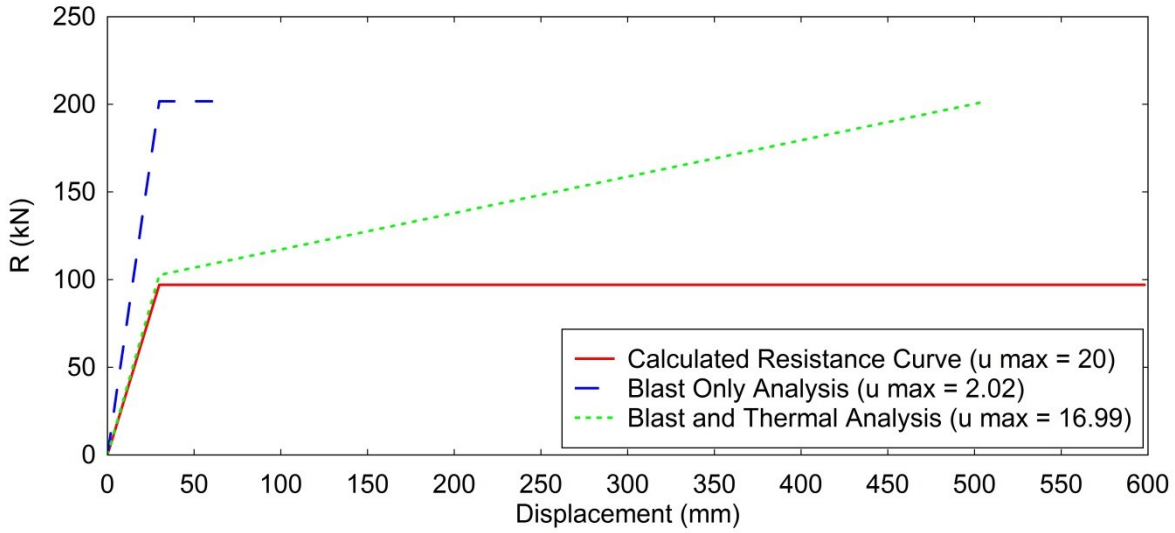

Figure 5.2.4: Resistance Curve: 385kPa Peak Pressure

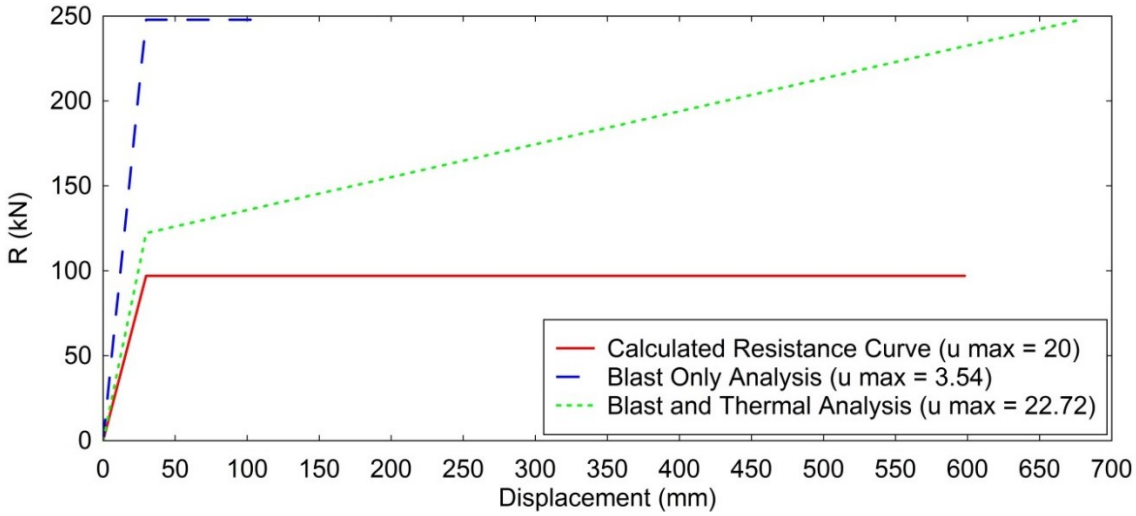

Figure 5.2.5: Resistance Curve: 478kPa Peak Pressure

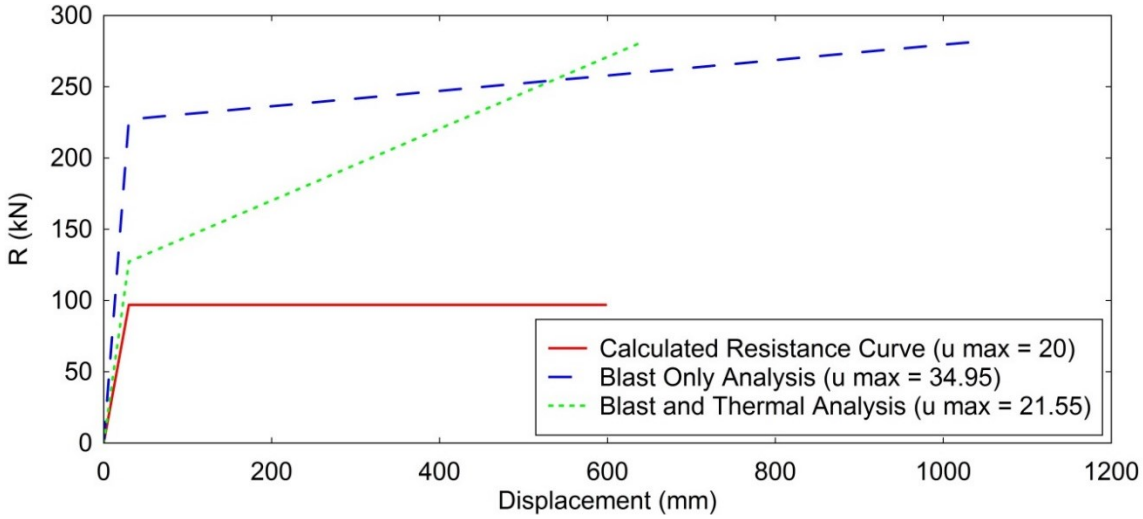

Figure 5.2.6: Resistance Curve: 536kPa Peak Pressure

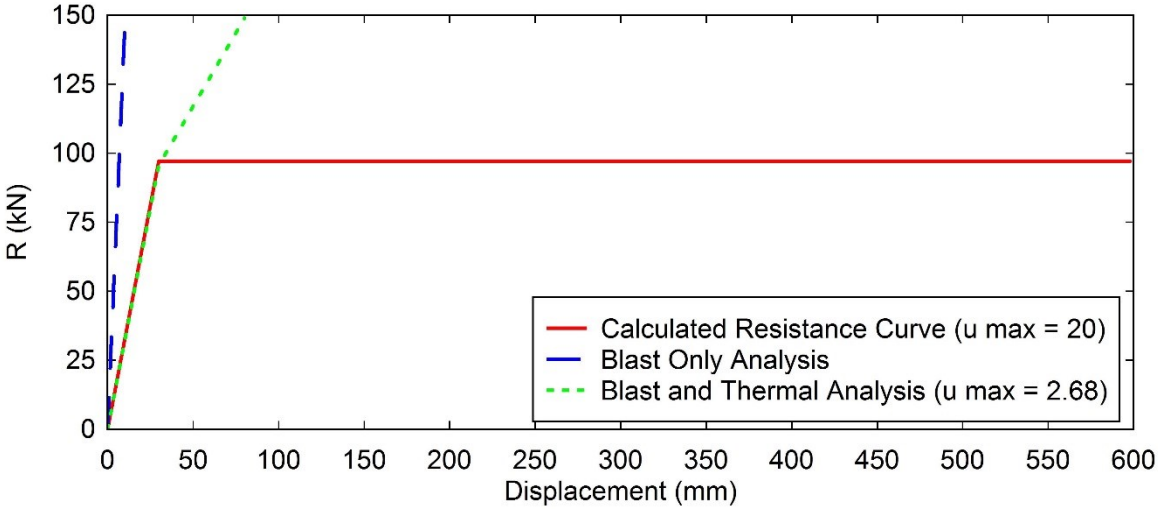

Figure 5.2.7: Resistance Curve (Pinned): 290kPa Peak Pressure

Table 5.1 shows the values for the natural period *T* (sec) and stiffness k_e (N/m) of the columns under the blast only and blast and thermal load conditions with varying peak pressures and temperatures. The natural period is calculated using equation 5.16 for each column under the separate blast and combined blast and thermal loading regimes. The stiffness of the column k_e relates the resistance (R_m) to the equivalent elastic deformation reached.

Table 5.1: Natural Period and Stiffness of Columns

Peak Pressure (kPa)	Equivalent Peak Temperature (°C)	Natural Period T (sec)		Stiffness k_e (N/m)	
		Blast Only	Combined	Blast Only	Combined
66.4	1464	0.0205	0.0421	6.86E+06	1.62E+06
95.1	1525	0.0205	0.0454	6.82E+06	1.39E+06
96.6	1465	0.0205	0.045	6.81E+06	1.42E+06
107.1	1738	0.0205	0.0425	6.83E+06	1.59E+06
109.7	1701	0.0205	0.042	6.86E+06	1.63E+06
111.5	1668	0.0203	0.0416	6.94E+06	1.66E+06
112.0	1536	0.0206	0.0416	6.79E+06	1.66E+06
127.9	1674	0.0203	0.0396	6.96E+06	1.83E+06
136.2	1594	0.0205	0.0396	6.82E+06	1.83E+06
153.1	1708	0.0203	0.0374	6.95E+06	2.05E+06
153.6	1682	0.0201	0.0405	7.12E+06	1.75E+06
182.4	1904	0.0205	0.0371	6.82E+06	2.09E+06
182.5	1762	0.0205	0.0365	6.84E+06	2.16E+06
184.8	1866	0.0198	0.0377	7.30E+06	2.02E+06
198.7	2013	0.0203	0.0344	7.00E+06	2.42E+06
198.8	1873	0.0204	0.0356	6.92E+06	2.26E+06
203.8	1827	0.0204	0.0355	6.90E+06	2.27E+06
260.9	1998	0.0211	0.027	6.46E+06	3.93E+06
281.7	2126	0.0213	0.0316	6.30E+06	2.87E+06
290.3	2084	0.0216	0.0256	6.13E+06	4.38E+06
329.3	2247	0.0224	0.0299	5.73E+06	3.21E+06
329.4	2091	0.0224	0.0303	5.74E+06	3.13E+06
384.9	2166	0.0206	0.0289	6.76E+06	3.44E+06
477.9	2370	0.0186	0.0265	8.30E+06	4.09E+06
536.4	2504	0.0194	0.0259	7.61E+06	4.26E+06

Under the combined blast and thermal loads the stiffness changes due to the increased temperature and decreased Young's Modulus of the steel. Figs.5.2.8 to 5.2.11 show the stiffness (k_e) and natural period (T) of the columns under varying blast only and combined loading regimes. Best fit polynomial curves are shown indicating trends in the results, Appendix J details the polynomial coefficients used for each curve. The stiffness and natural period are shown in relation

to the applied peak pressures and temperatures. With increasing peak pressures the blast only case exhibits little variation in the natural period until very high peak pressures at which slight changes above and below 0.0205sec are observed. The natural period of the columns under combined blast and thermal loading regimes decreases with increasing peak temperature and pressure. The columns under the combined loading regimes show an increased stiffness with increased peak pressures and temperatures; whereas the blast only loaded columns maintain a relatively high stiffness until the extreme peak pressures and temperatures are reached.

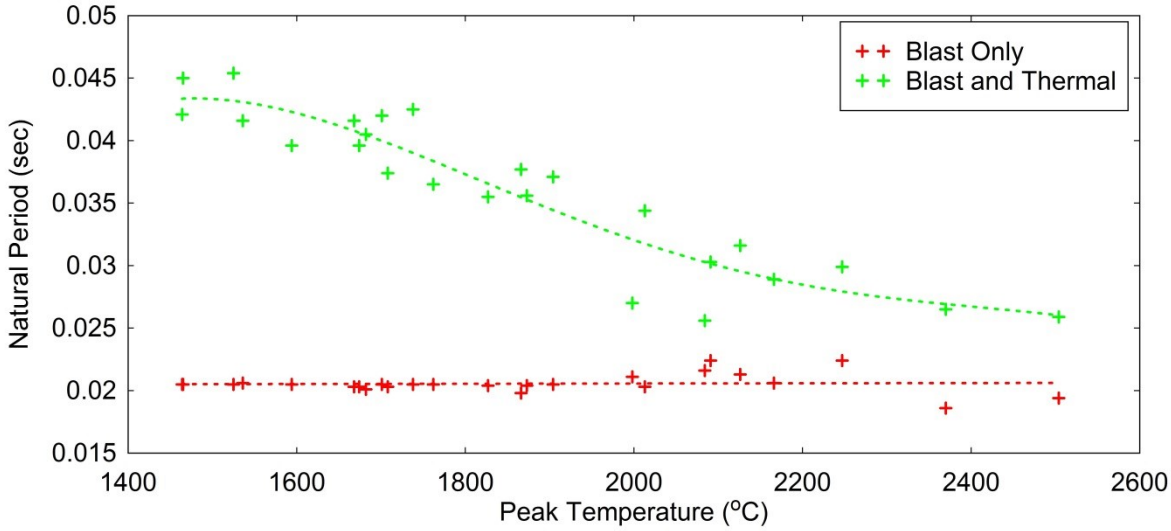

Figure 5.2.8: Natural Period Vs Peak Temperature

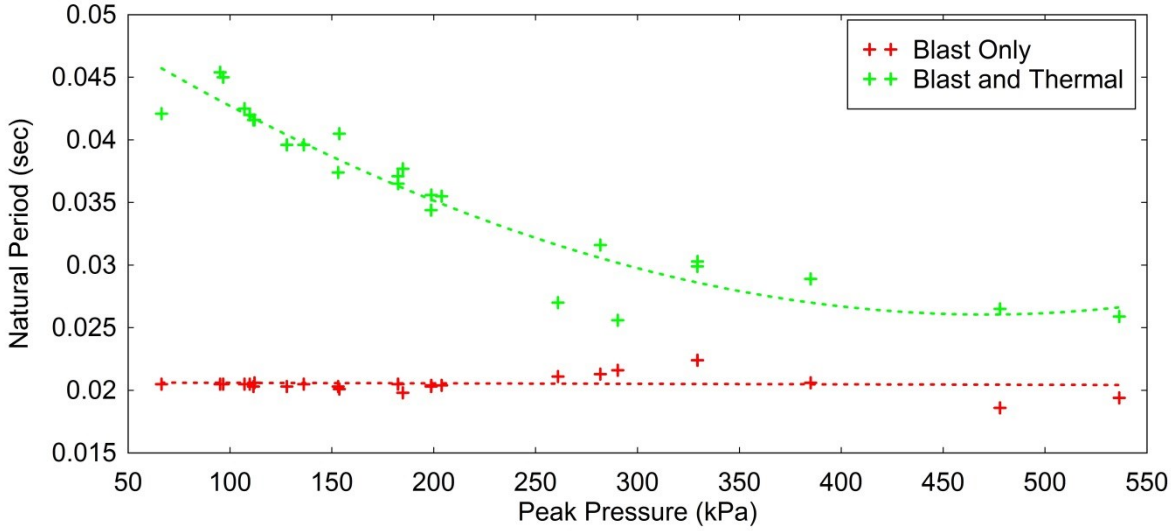

Figure 5.2.9: Natural Period Vs Peak Pressure

The relationship between stiffness and natural period to temperature increase shown in the combined loaded cases appears to be counter-intuitive. With increasing temperatures the Young's Modulus of steel decreases and therefore the stiffness decreases and natural period increases. In relation to this research increasing peak temperatures correlate to shorter distances to the blast centre (and hence higher pressures). At shorter distances the duration of the applied thermal load prior to the arrival of the blast is shorter than at far distances. Therefore the thermal energy has less time to absorb through the steel and the average Young's Modulus across the thickness of the steel is higher than at further distances (and lower peak temperatures) prior to the blast arrival.

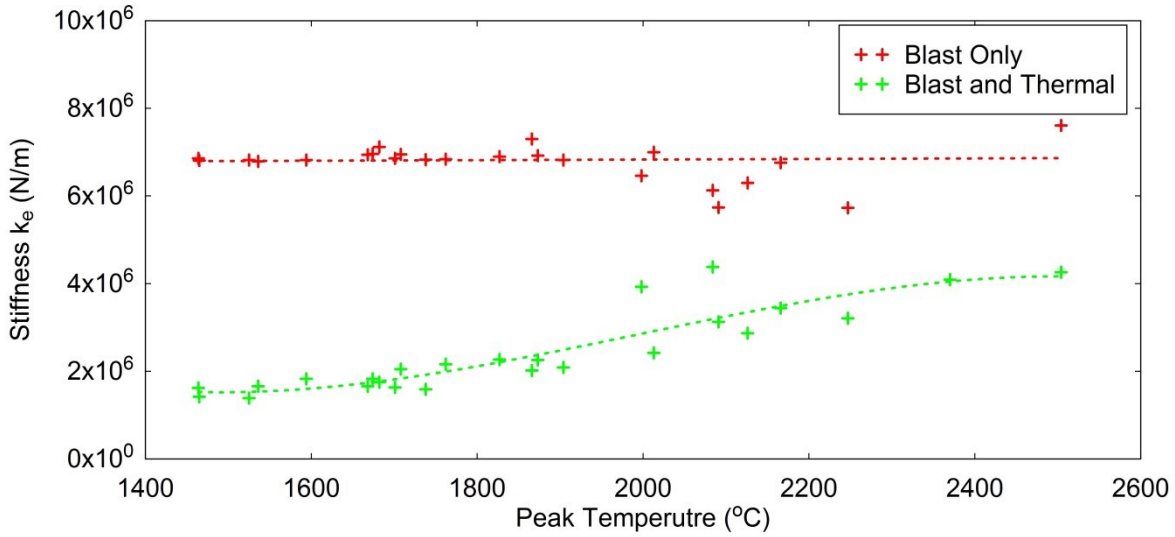

Figure 5.2.10: Stiffness Vs Peak Temperature

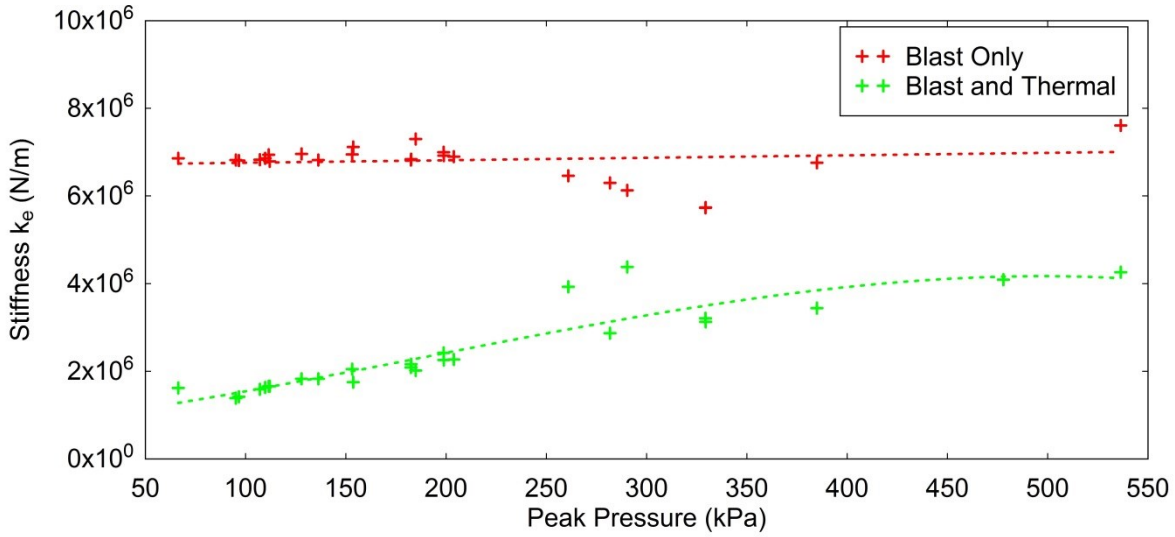

Figure 5.2.11: Stiffness Vs Peak Pressure

Figs.5.2.12 to 5.2.15 show the resistance curves for the combined blast and thermal loading regimes for a range of peak pressures and temperatures. The figures are divided into peak pressure ranges:

95 – 136kPa (Fig.5.2.12), 153 – 198.8kPa (Fig.5.2.13) and 282 – 536kPa (Fig.5.2.14). Typically, the columns exhibit higher maximum ductility and resistance (R_m) at higher peak pressures; however, this is not observed in the middle distance (153 – 198.8kPa) of peak pressures. This trend reversal highlights the difficulty in de-coupling the effects of blast and thermal load in relation peak pressure alone. Fig.5.2.15 shows the resistance curves in relation to peak temperature. Similarly to peak pressures, the maximum ductility and resistance, R_m increase with increasing peak temperatures. The higher ductility at the high pressures and temperatures indicate greater plastic response. This is due to ultimate strength reduction at high temperatures and the increased damage exhibited by columns close to the centre of explosive events.

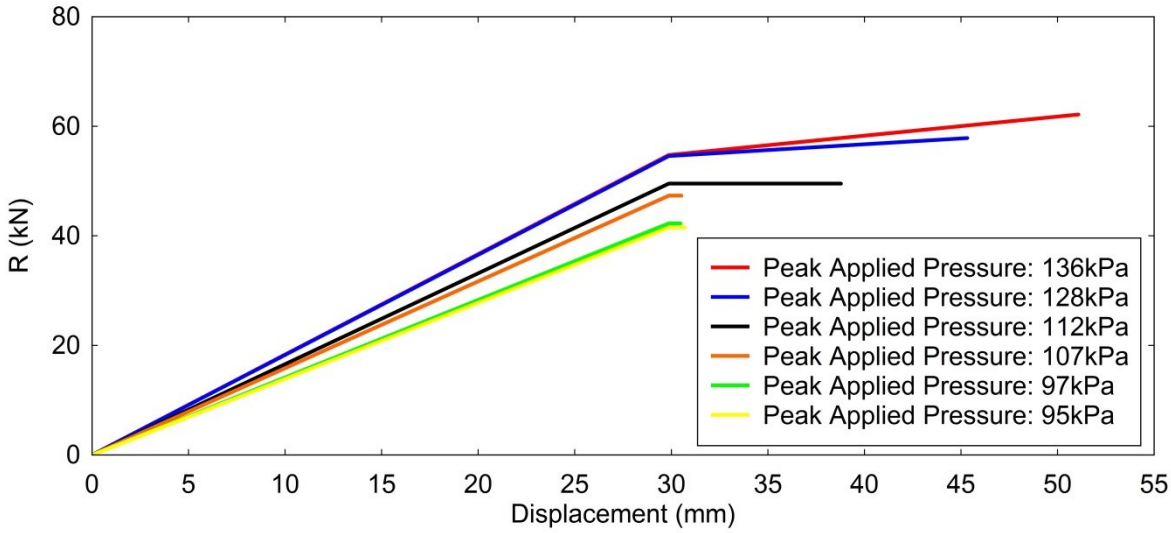

Figure 5.2.12: Resistance Curve: Blast and Thermal: 95-136kPa Peak Pressure

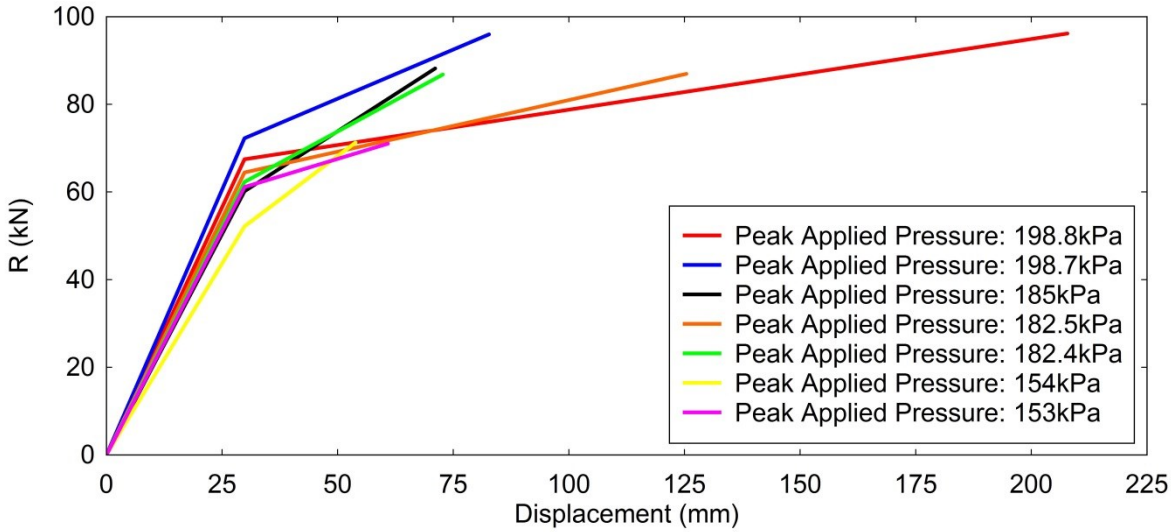

Figure 5.2.13: Resistance Curve: Blast and Thermal: 153-198.8kPa Peak Pressure

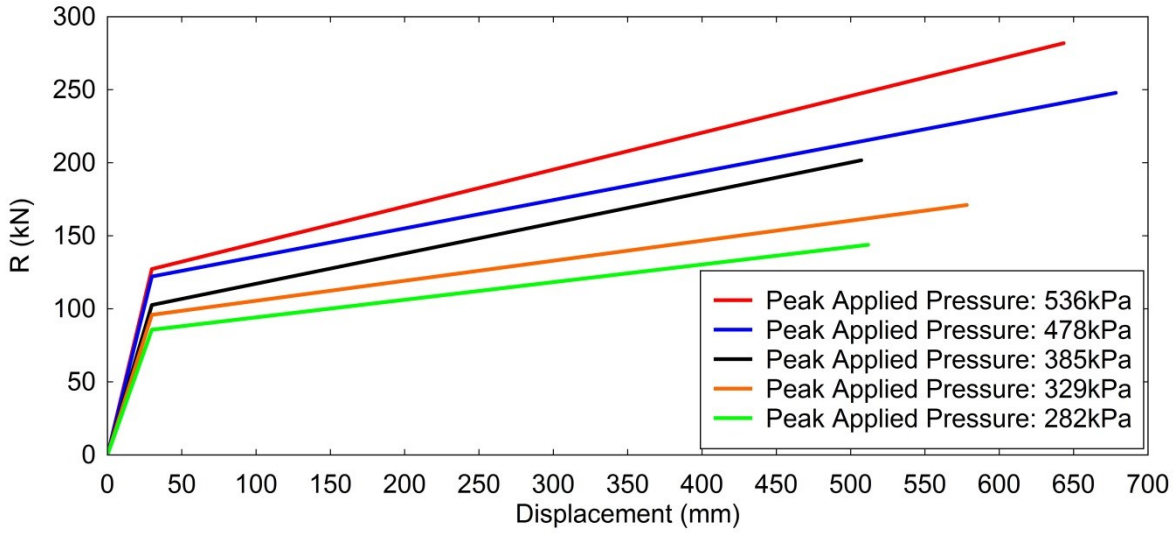

Figure 5.2.14: Resistance Curve: Blast and Thermal: 282-536kPa Peak Pressure

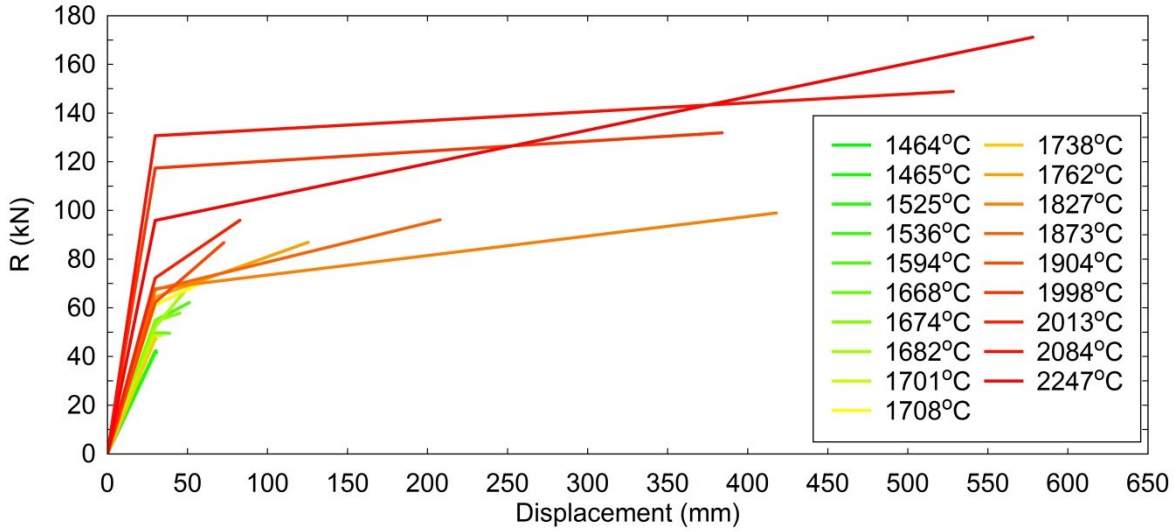

Figure 5.2.15: Resistance Curve: Blast and Thermal: Varying Peak Temperatures

5.3 Resistance Curves Summary

The resistance curves shown in Figs.5.2.1 to 5.2.7 and Figs.5.2.12 to 5.2.15 are used to represent the structural response of a 4m length column (CHS 193.7x5) subject to separate blast and combined blast thermal loading regimes (as detailed in 4.4). The resistance curves shown are for one specific column section and length; therefore variances to the column length, section type, loading regimes and end restraint conditions would modify the shape of the curves. The effect of each parameter should be carefully considered when adopting the curves into predictive algorithms

and for their use in further research. The resistance curves presented in 5.2 show a synergistic response of the steel column when subject to the combined loading regimes. The resistance R_m is typically lower and the ductility typically higher when subject to the combined loads compared to blast loads alone.

Chapter 6

Conclusions and Future Work

Synergistic response of steel structures to combined thermal and long duration blast loading from explosive events is a complex subject due to the non-linear coupled interaction of two separate loading regimes, the thermal material degradation and the thermo-mechanical response of the structure. There is little current available research into the synergistic response of steel structures to blast and thermal loads due to previous limitations in experimental trials and only recent developments in fully coupled thermal and structural finite element analyses. The numerical methods adopted in the non-linear analysis performed during this research have provided a sound platform for the initial research question to be answered.

The novel experimental trials have provided an original contribution to this field of research, by producing extensive data sets and forming the foundations for further thermal and blast experimental trials. The open air arena trials were successful in the recording of pressure and thermal data within a fireball of a high explosive event; this had not been previously achieved. The experimental trials undertaken in the ABT combining compression, thermal and long duration blast loads using ceramic heating elements was successfully developed and undertaken enabling the objectives of the research project to be met. The experimental trials have also enabled verification to the numerical modelling procedures adopted throughout the research project.

The research project answered the following question which was originally set out in the aims:

"To what extent does the intense thermal load from an explosive event degrade a steel structure and how does the thermomechanical behaviour exhibited by the structure alter the response to the subsequent blast load".

In order to answer this question the following steps were undertaken throughout the research project:

i) A literature review was undertaken to expand the initial understanding of the research area and determine what aspects of the question, if any, had been previously researched. The review included an in depth investigation of literature to determine the extent and duration of emitted thermal radiation from explosive events and the equivalent long duration blast loads. The review also detailed the structural and material response to thermal loads from fires, structural and material response to blast loads, experimental simulation of explosive thermal loading and the limited existing research on the synergistic response of structures to thermal and blast loading.(Objectives 1 & 2)

ii) A series of experimental trials were performed to record the intense temperatures and pressures within, and on the edge of an explosive fireball. The response of thin steel plates to the thermal and blast loads from the explosive fireball was also recorded. (Objective 3)

iii) Predictive structural models were developed to investigate the response of steel columns to intense thermal and long duration blast loads. The loading regimes used in these models were calculated from historical texts detailed in the literature review. The structural models were subject to a range of structural and thermal loading regimes as part of the full parametric study. (Objective 4)

iv) A series of innovative experimental trials were performed observing the response of structural steel columns to combined compressive, thermal and long duration blast loads within the Air Blast Tunnel (ABT). Computational models of the columns in the experimental trials were developed. The response of the model columns were analysed and compared to the actual column response providing verification for the computational methods used throughout the research project. The trials have also provided a large set of valuable data which can be used in future research projects. (Objective 5)

v) Using results and data from the parametric studies a series of resistance curves were produced to describe the generic response of structural columns under a range of peak pressures and temperatures. These resistance curves will enable the improved analysis of whole buildings and structures using SDOF based techniques. (Objective 6)

This chapter discusses the research findings from the numerical and experimental results in relation to the research question. The implications and uses of the research results in practical situations, assumptions made and subsequent limitations reached are also detailed. Future research directions are also discussed.

6.1 Research Findings

The primary findings from the project were targeted to satisfy the original research question in order to advance the knowledge and understanding of this complex topic. Results and conclusions drawn from the parametric studies showed that, beyond reasonable doubt, steel structures do exhibit a synergistic response when subject to the intense thermal and long duration blast loads from explosive events. The computational methods adopted for the parametric studies were verified by development of computational models of the experimental trial subjects (plates and columns), and the comparison to the actual response of the plates and columns during the trials.

The extent of the thermal degradation of the steel structures before the arrival of the blast load was determined by examining the results of the parametric studies and resistance curves. From observing the deflection-time history results it is noted that peak and final deflections of the columns under blast load were less than the columns under the combined thermal and blast load. The larger peak deflections indicated a reduction in the Young's modulus and higher final deflections indicated a reduction in yield strength. This is concurrent with the known response of steel under high temperatures. Resistance curves presented also provide evidence of a reduced Young's Modulus and yield strength. A direct comparison of blast only resistance curves and the blast and thermal resistance curves, for each loading set indicate a reduced yield (direct relation to resistance R_m), and a reduced Young's modulus (direct relation to gradient of initial elastic region)

Results from the parametric studies showed at regions close to an explosive event the blast load is dominant. This is due to a shortened period of time for the prior thermal load to absorb through the steel, coupled with very high peak pressures typical at short distances to explosive events. Further away from the centre of explosive events the potential for a synergistic response increases. This increase is due to a high thermal load of longer duration (before the blast arrival) which can raise the temperature of the steel and cause significant degradation of the steel properties. With increasing distances the potential synergistic response decreases as the thermal loads and blast loads decrease. Other findings from the parametric study indicate some steel structures may deform towards the centre of the explosive event before the arrival of the blast. This is due to expansion of the steel near the surface facing the blast; as the surface temperature increases, steel incident to the thermal load expands. Steel expands against the end supports and the cooler steel facing away from the blast therefore deforming towards the theoretical explosive centre before the blast arrival.

Parameters investigated as part of the full parametric study included end connections, compressive load, thermal conductivity and finite element mesh sensitivity. It was observed that a column with

a roller top connection exhibited larger deflections than a column with a pinned top connection. An increase in applied compressive loads corresponded to a decrease in lateral deflection of the columns. This appears counter-intuitive; however, the applied stiffness of the end connections was dominant in dictating the column response compared to the applied compressive load. One and two storey compressive loads were applied to columns with one and two storey equivalent spring stiffness top connections. The study into thermal conductivity showed that columns with higher thermal conductivities exhibited a small increase in the structural response. A study investigating models with one and two element thickness showed a negligible difference in the response of the columns with one or two elements. Therefore the use of one element thick column models was justified for the majority of the parametric study.

The arena trials provided large data sets of thermal flux, temperature and pressure histories within and on the edge of a conventional explosive fireball. By observing the response of steel plates and comparing to predictive numerical models a conclusion was made that no synergistic response was exhibited in the steel plates at 4m from the centre, but a potential synergistic response was observed at 6m from the explosive centre. Findings from the combined ABT trials include larger observed column deflections under combined thermal and blast load compared to blast only and larger observed deflections under high compression and blast load compared to low or no compression. Other findings from the combined ABT trials included larger observed deflections of the RHS compared to the SHS or CHS and larger observed deflections of the columns with wings compared to column with no wings. By using the innovative insulated thermal boxes with ceramic heating elements on a drop down rig in the ABT, the trials have set a benchmark for future thermal and blast trials.

6.2 Practical Implications

In the wake of events such as disasters at Buncefield oil refinery (2005), (Burgan, 2009), (Atkinson, 2011b), the West Texas fertiliser factory (2013) and the Tianjin warehouse (2015) there has been an increasing need to understand the behaviour of buildings under intense thermal and long duration blast loads typical of events of this magnitude. Other events such as the terrorist attack on the World Trade Centre (2001) highlight the requirement to better understand the behaviour of buildings under long duration thermal loads (such as fires) combined with blast and impact loading. This research project investigated the response of steel structures to intense thermal loads and long duration blast loads numerically, and long duration thermal and blast loads experimentally. The findings from the numerical and experimental research can be used to directly improve our understanding of such complex events and the ability to analyse structures under these loading

regimes. The resistance curves presented can be used in SDOF analysis programs. Resistance curves developed from the numerical studies provide a tangible and practical output from this research project.

6.3 Research Limitations

A limitation of this research was the link between the main parametric study and experimental trials. The parametric study investigated the combination of intense thermal loads and long duration blast loads typical of explosive events akin to those at Buncefield, Tianjin and West Texas; however for practical issues the experimental trials investigated the combinations of long, lower duration thermal loads with long duration blast loads.

The use of complex non-linear coupled (thermal and structural) analysis was adopted throughout this research project. In order to develop models representing, as close as possible, real life structures and loads, a series of assumptions were made regarding the complex interactions, behaviours, parameters and variables. These assumptions were made due to a lack of current, existing research in the field and a limited time in which to complete this research project. These assumptions included the method of direct transference of radiant thermal load to the surface of the steel column and the use of the Johnson-Cook material model with specific parameters for the structural steel under high temperatures and strain rates. Further limitations include relating the results from the investigated structural type (column) and section type (CHS) to other structural forms and sections. This research specifically investigated the response of structural steel; therefore it would be unsuitable to relate the conclusions drawn in this project to buildings and structures constructed from other materials such as concrete, masonry or timber.

During the production of the resistance curves the elastic deflection limit was calculated for the CHS under blast loads. In order to determine resistance, a non-theoretical gradient was applied to the initial blast load as part of the non-linear analysis (as opposed to an instant increase in peak pressure). Therefore, at the point when the column reached the theoretical elastic limit a series of back-calculations were performed to find the equivalent time on the increasing blast load gradient. The non-theoretical gradient enabled the finite element analyses to run without convergence issues at times of high loading; however, by introducing the gradient to the analysis a limitation was also introduced regarding the accuracy of the applied blast load at the initial stages.

6.4 Future Research Directions

To minimise the assumptions and limitations described in 6.3, suggestions for the future direction of this research are made in 6.4.1 to 6.4.8. It is the intention that the research directions detailed will further refine and develop the conclusions made during this project and advance the accuracy of the output data particularly with reference to resistance curves.

6.4.1 Heat Transfer from Explosive Events to Structural Surfaces

The transfer of the thermal load from explosive events to the surface of structures is a complex field. Radiation is the primary mechanism of transferring thermal load from the initial explosive heat flash and combustion products. Thermal load is also transferred through convection of the combustion products. Further research into the transfer of thermal load from a range of explosive sizes is necessary to improve the understanding of this mechanism. This would be achieved by undertaking further conventional explosive fireball trials and performing thermo-fluid simulations leading to an improved understanding of thermal transfer from conventional explosive events.

6.4.2 Material Model Investigation of Structural Steels under High Strain Rate and High Temperature Loading

During the computational analysis the most appropriate material model was selected to represent the structural steel under high strain, high strain rate and high temperature loading scenarios. The Johnson-Cook (Johnson, 1983) model was adopted using parameters from previous research into steel under similar loading (Schwer, 2007) & (Özel, 2007). To improve the accuracy of the material model the model parameters could be developed which directly relate to the loading regimes in question. This can be done by high strain rate and high temperature testing of structural steels. A Split-Hopkinson bar (Kolsky, 1949) used in conjunction with a furnace (or similar) for heating steel samples could be adopted to investigate the behaviour of structural steel under these extreme loading regimes. By investigating a range of temperatures, strains and strain rates the parameters for the structural steel model under a range of loading regimes can be developed and subsequently adopted into more accurate material models. The material model adopted for the parametric study and ABT trial modelling used a constant strain rate of $80s^{-1}$ (van Netten, 1997), typical for steel structures under long duration blast loads. The use of a complex material modeller interface to model structural steel under varying strain rates during a non-linear analysis could be further investigated.

6.4.3 Different Column Sections under Intense Thermal and Long Duration Blast Loads

A 4m length, 193.7mm diameter, 5mm thick CHS (typical column size and section) was investigated during the parametric study as its relative thinness allowed for rapid thermal absorption and it is a section which is typically used in construction. Therefore the displacements, stresses and resistance curves presented directly relate to the performance of this section. Investigations into other section sizes and types would develop a broader response spectrum. Sections with a thicker gauge are likely to have a reduced synergistic response as the heat would not penetrate as (relatively) far. A square or rectangular hollow section would potentially absorb more heat as the facing surfaces may be perpendicular to the radiating thermal energy. Thinner sections such as cold formed profiles (as used for secondary elements) could also be investigated as they are more susceptible to both thermal and blast damage.

6.4.4 Different Structural Forms under Intense Thermal and Long Duration Blast Loads

This research investigated the intense loading regimes from explosive events on structural columns. As part of the parametric study and experimental trials the columns had varying end connections and compressive loading. To broaden the data sets different structural forms could be investigated such as individual load carrying beams, slabs, frames or connections. Researching the combined effect of blast/thermal loads and different structural loads such as vertical dead and live distributed loads on beams, lateral stability loads on frames or tension/compression loads in bracing elements would also broaden the knowledge and understanding of this field of research.

As shown in the parametric studies the form of the structural connection has a significant effect on the failure mechanism of the structure under investigation. Thermal load can weaken and alter the behaviour of steel connections to subsequently change the response of the connected beams or columns. Experimental and numerical studies on typical pinned and fixed connections under combined high temperature and blast loading regimes could be used directly to improve the accuracy of the resistance functions and used as non-linear supports in numerical modelling of beams and columns.

6.4.5 Different Structural Materials under Intense Thermal and Long Duration Blast Loads

This research project has investigated the effect of intense thermal and long duration blast loads on structural steel. Steel was chosen for this research due to a relatively high level of thermal

conductivity and its wide use in construction. Further studies into other construction materials will broaden the research field such as the response of plain and reinforced concrete in the form of columns, beams and flat slabs. The response of flat slabs is of interest due to the large exposed area, relative thin structural depth and subsequent effect on supporting structures. It is likely that steel reinforcement would not degrade to the same extent as the steel columns investigated in this research project as the concrete would afford a large degree of thermal protection. The response of concrete to these thermal loads is a relatively un-researched area.

Aluminium is a material which is used less for primary structural elements but is widely used for secondary structural elements such as cladding and curtain wall mullions. As secondary elements are fixed to the external skin of a building there is a high chance they will be subject to the combined intense thermal loading and blast loading from explosive events. Commonly used aluminium alloys typically have lower yield strength (200-600MPa) than structural steel and a higher thermal conductivity (237 W/m.^{o}K); therefore the response of an aluminium section to the combined loading regimes is likely to be greater than that of an equivalent steel section.

Studies into masonry and glass response to the intense thermal and long duration blast regimes would deepen the knowledge of masonry and glass breakage to blast loading. The intense thermal load may introduce stresses into the brittle materials which could alter the response to a subsequent blast load and therefore alter the breakage and fragment distribution.

6.4.6 Holistic Response of a Whole Building to Intense Thermal and Long Duration Blast Loads

Potential research avenues investigating individual materials, structural forms and section types are detailed in 6.4.4 to 6.4.6. Further research could also investigate the holistic response of a whole building to combined thermal and blast loading. Experimental trials investigating the response of whole buildings to these loading regimes would be an innovative and pioneering study and would provide a wealth of valuable data to many researchers and practitioners.

6.4.7 Fire Loads Combined With Short and Long Duration Blast Loads

This research project predominantly focused on the response of structures to intense thermal and long duration blast loads from explosive events. A similar and equally important area of research is the investigation of structures to long duration fire loads and short and long duration blast loads. These situations could arise from a fire in a building which reaches a gas tank or fires indirectly caused by explosive events such as car bombs, which are subsequently followed by other explosions. There are many avenues this research could take in terms of materials, structural forms

and loading regimes. Fire engineering and blast engineering are currently large independent fields of research; however the area of combined fire and blast is a relatively small field in which there are many avenues for new and interesting studies.

6.5 Concluding Remark

The synergistic response of steel structures to combined intense thermal and long duration blast loads is very complex and difficult to predict due to the range of varying processes and parameters involved. This research project has formed initial, original conclusions from a specific series of parameters and assumptions. Resistance curves have been produced to enable the analysis of whole buildings to combined loading regimes. Innovative, novel, experimental trials have been undertaken providing this, and future research projects with large and useful data sets. The results from the parametric studies have shown that there is a synergistic response to intense thermal and long duration blast loads from explosive events. It is the intention that this project will act as a springboard for further research into this area which can both improve the accuracy of current conclusions and broaden the research field to wider areas beyond those investigated in this project.

Appendices

Appendix A: Scientific Formulae

Thermal Load Calculations

Stefan Boltzmann Constant:

$$\sigma = \frac{2\pi^5 k^4}{15\, h^3 c^2}$$ = 1.36 x 10^{-12} (cal/cm^2/sec/deg^4)

(A.1)

= 5.6704x10^{-8} (J/sec/m^2/k^4)

K = Boltzmann Constant, h = Planck Constant, c = Speed of Light

Fireball Maximum Power and Time to Maximum:

$$P_{max} = 3.18W^{0.56}$$ (kT/sec)

(A.2)

$$t_{max} = 0.0417W^{0.44}$$ (sec)

(A.3)

W = Explosive Yield, ρ(h) = Air Density at Given Explosive Height, ρ(0) = Air Density at Sea Level

Radiant Exposure:

$$Q = \frac{E_{tot}\tau}{4\pi D^2}$$ (cal/cm^2)

(A.4)

τ = Transmittance, D= Distance from Explosive Centre

$$E_{tot} = fW$$

(A.5)

f = Thermal Energy Ratio

Structural Deflections to Thermal Loads

Mid-span Deflection of a Slender Beam under Constant Thermal Load:

$$\delta = \frac{2l}{\pi}\sqrt{\varepsilon_T + \frac{\varepsilon_T^2}{2}}$$ (mm)

(A.6)

ε_T = Thermal Strain, l = Length

Deflection Due to Thermal Gradient:

$$y(x) = -\frac{\emptyset}{k^2}\left(\frac{\cosh kl-1}{\sinh kl}\sinh kx - \cosh kx + 1\right) \text{ (mm)}$$

(A.7)

Φ = Beam Curvature, l = Length , x = Distance along Beam Length

(Solved using Newton Raphson)

$$K = \sqrt{\frac{P}{EI}}$$

(A.8)

P = Axial Force, E =Young's Modulus, I = Second Moment of Area

Displacements of cylinder to thermal flux relative end (fixed):

$$w(\theta, Z) = \frac{Z\alpha}{h\rho C}\int_O^\infty \Phi(\theta, t)\, dt \text{ (mm)}$$

(A.9)

α = Coefficient of Thermal Expansion, h = Thickness, ρ = Density, C = Heat Capacity, Φ(θ,t) Incident Flux, Z = Midpoint l/2.

Johnson-Cook Formula for Steel Material:

First bracket: Strain Hardening

Second Bracket: Strain Rate Hardening

Third Bracket: Stress Softening from High Temperatures

$$\sigma_y = \left[A + B(\varepsilon_{eff}^p)^N\right](1 + C\ln\dot{\varepsilon})[1 - (T_H)^M] \text{ (MPa)}$$

(A.10)

σ_y = Yield Stress, ε_{eff}^p= Effective Plastic Strain, A = Elastic Yield Stress, B & N = Strain Hardening Parameters, T_H = Homologous Temperature, M = Material Parameter

Strain Rate Dependent Material Plasticity (Based on the Perzyna Model):

$$\sigma_y' = \left[1 + \left(\frac{\dot{\varepsilon}^{pl}}{\Upsilon}\right)^m\right]\sigma_y \text{(MPa)}$$

(A.11)

σ_y' = Yield Stress Considering Strain Rate Effect, $\dot{\varepsilon}^{pl}$ = Equivalent Plastic Strain Rate, ϒ = Viscosity Parameter, m = Strain Rate Hardening Parameter, σ_y = Static Yield Strength

Appendix B: Compression and Temperature –Time Histories for Columns in ABT Trials

Temperature – Time Histories

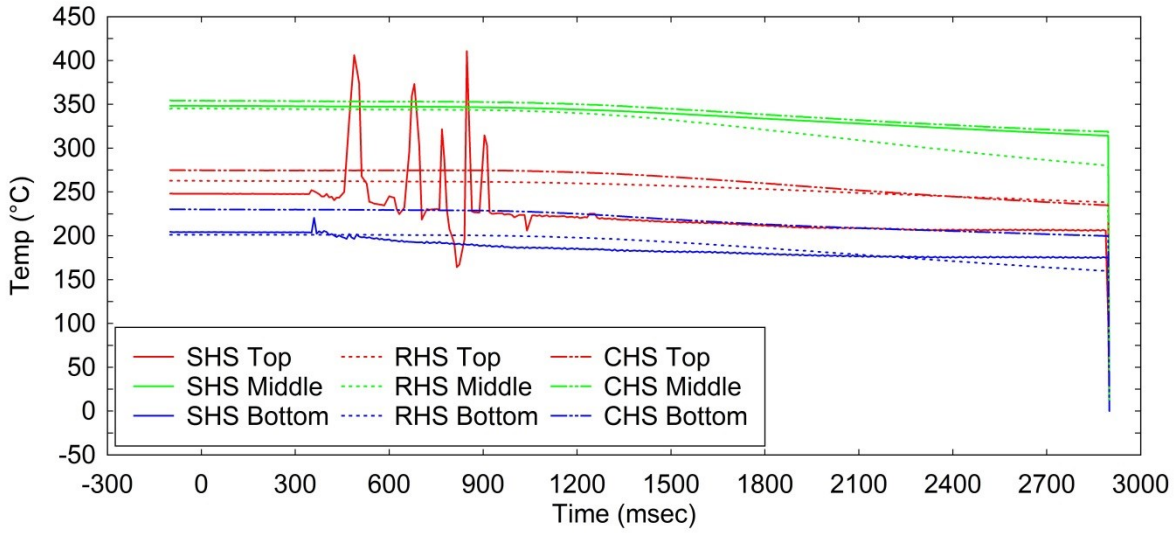

Figure B.1: Post Shot Recorded Temperature (Trial 1(5), Rig 2, 8000 Decimated)

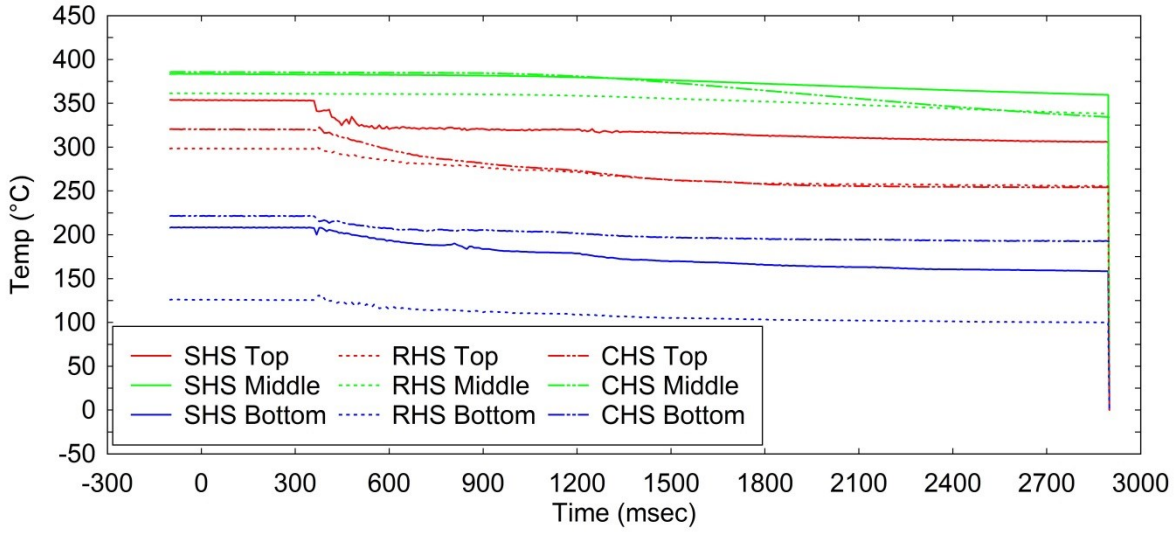

Figure B.2: Post Shot Recorded Temperature (Trial 1(5), Rig 3, 8000 Decimated)

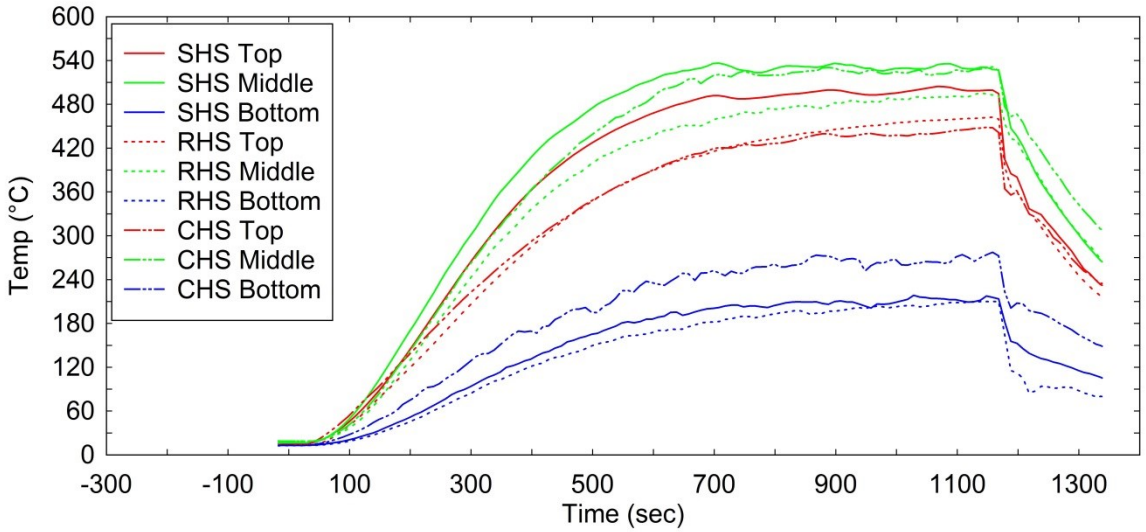

Figure B.3: Pre Shot Recorded Temperature (Trial 3(4), Rig 3, 1000 Decimated)

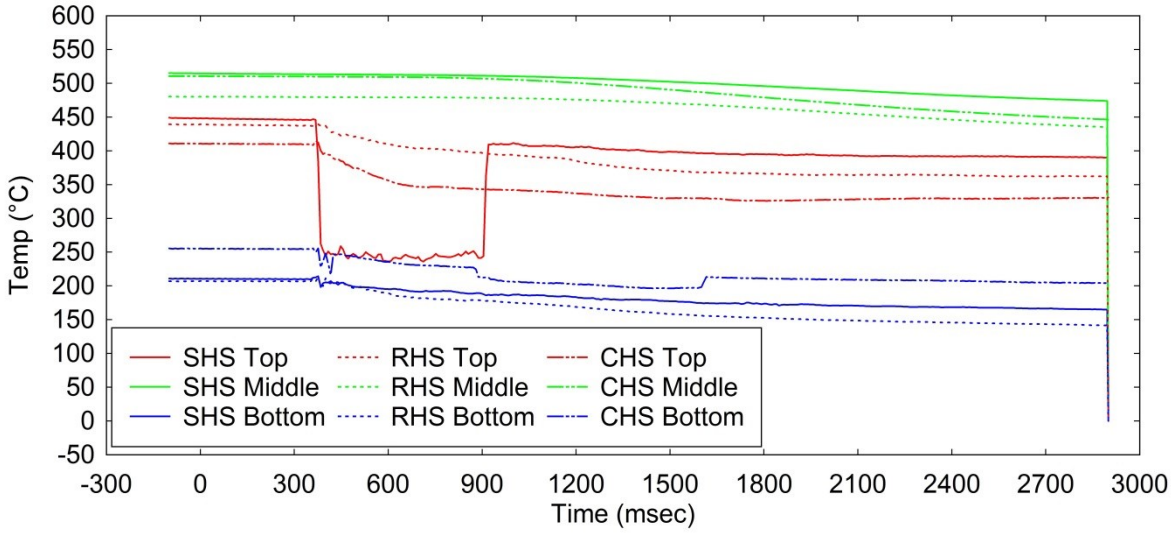

Figure B.4: Post Shot Recorded Temperature (Trial 3(4), Rig 3, 8000 Decimated)

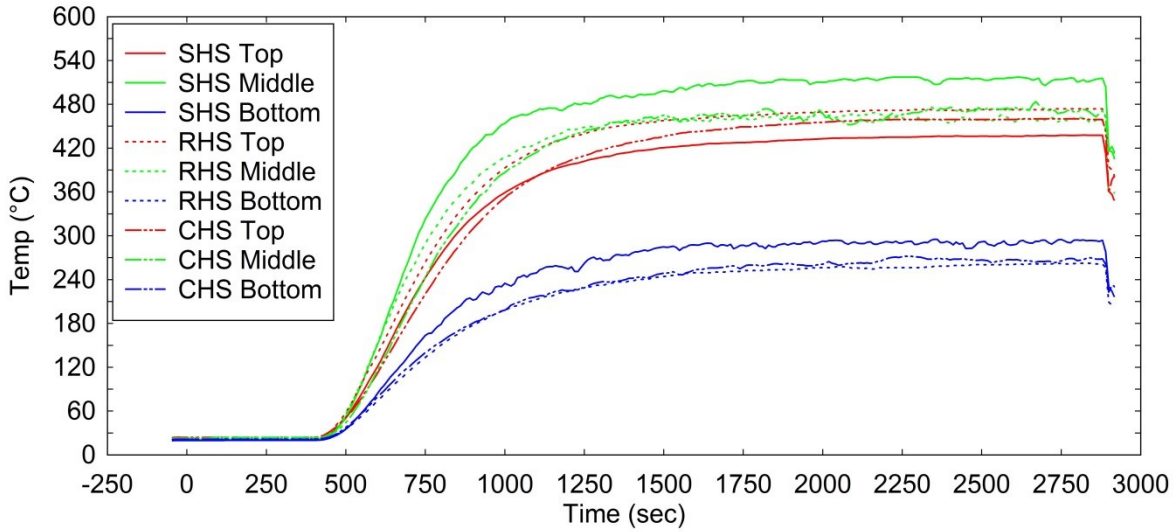

Figure B.5: Pre Shot Recorded Temperature (Trial 4(1), Rig 2, 8000 Decimated)

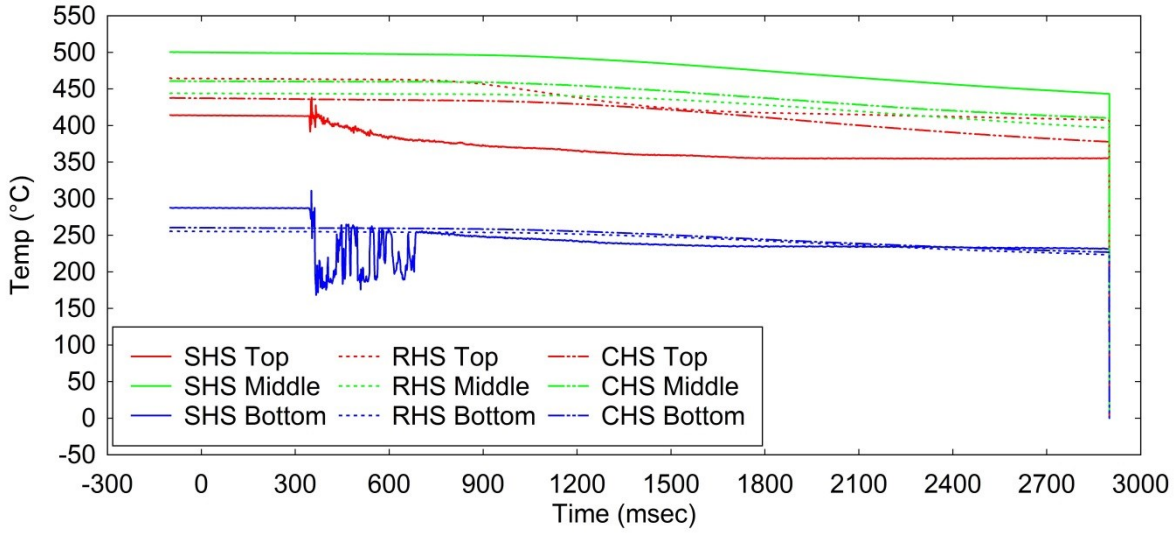

Figure B.6: Post Shot Recorded Temperature (Trial 4(1), Rig 2, 1000 Decimated)

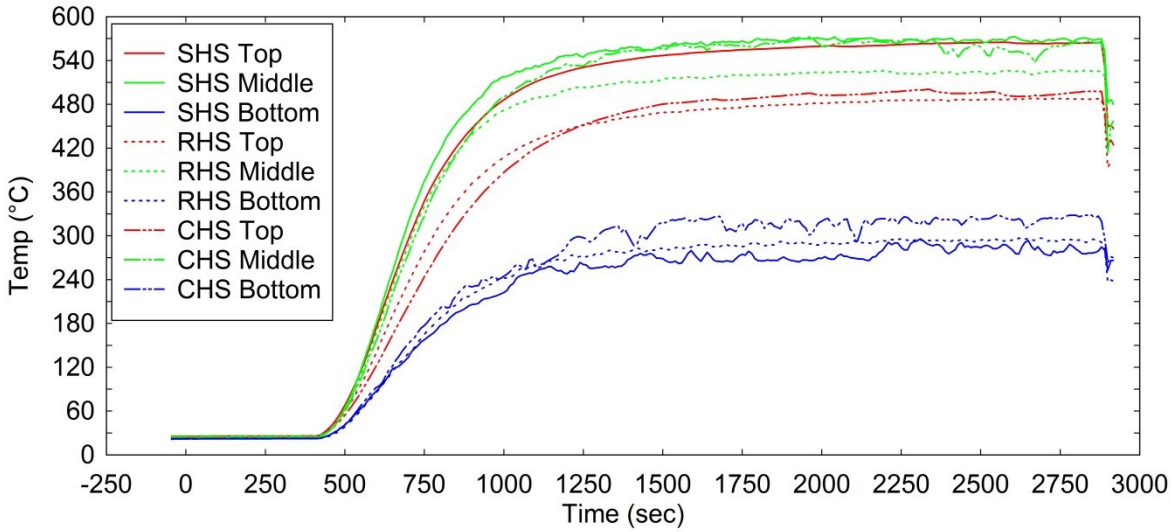

Figure B.7: Pre Shot Recorded Temperature (Trial 4(1), Rig 3, 1000 Decimated)

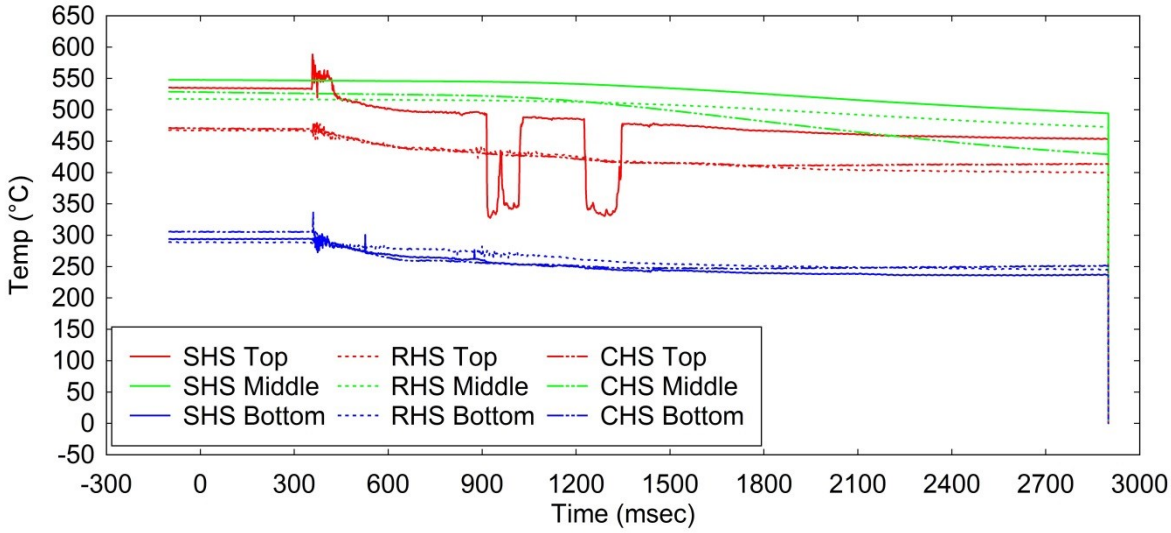

Figure B.8: Post Shot Recorded Temperature (Trial 4(1), Rig 3, 1000 Decimated)

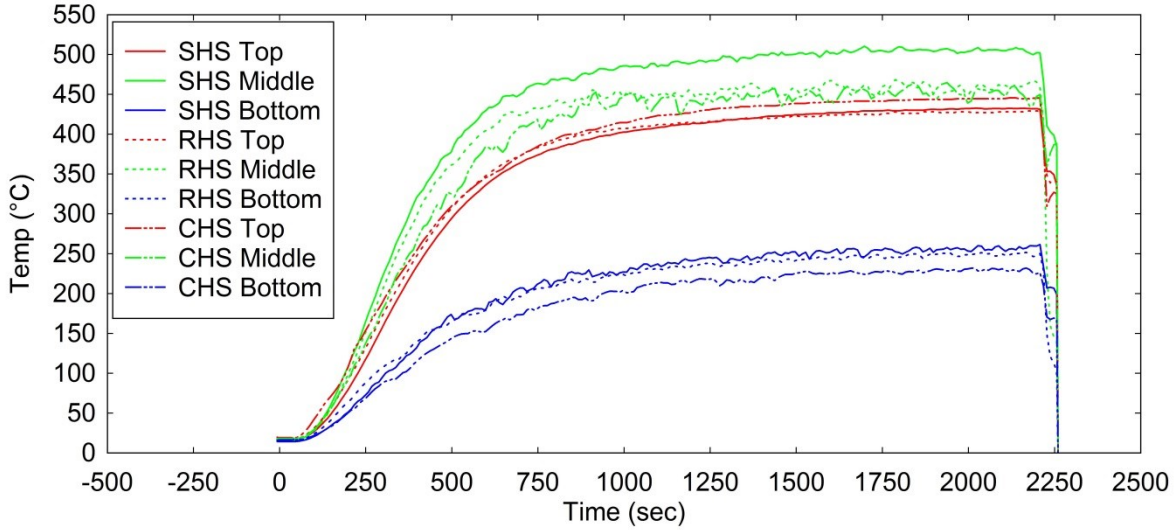

Figure B.9: Pre Shot Recorded Temperature (Trial 5(3), Rig 2, 1000 Decimated)

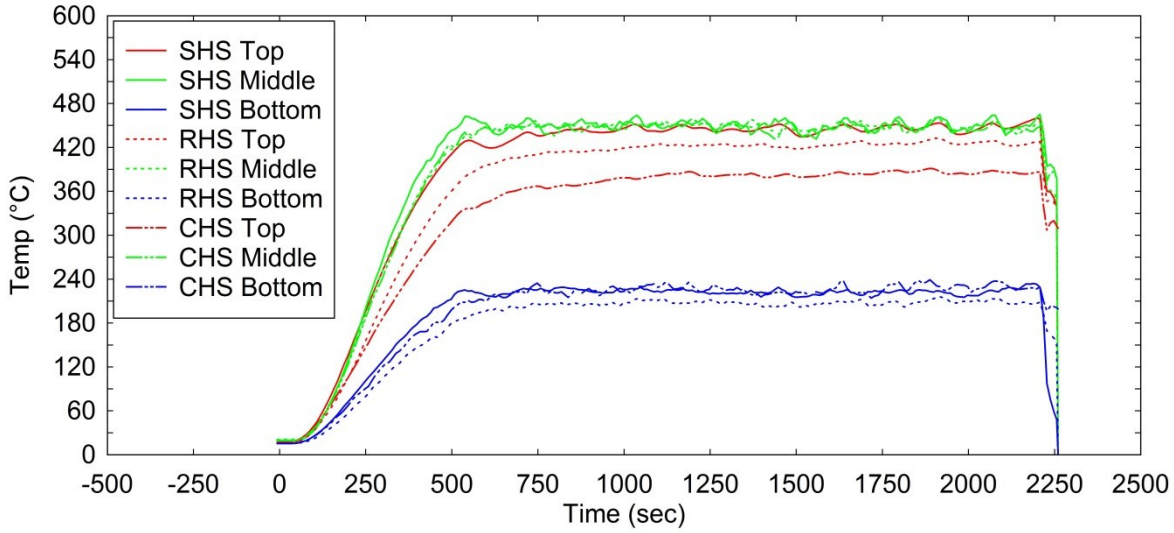

Figure B.10: Pre Shot Recorded Temperature (Trial 5(3), Rig 3, 1000 Decimated)

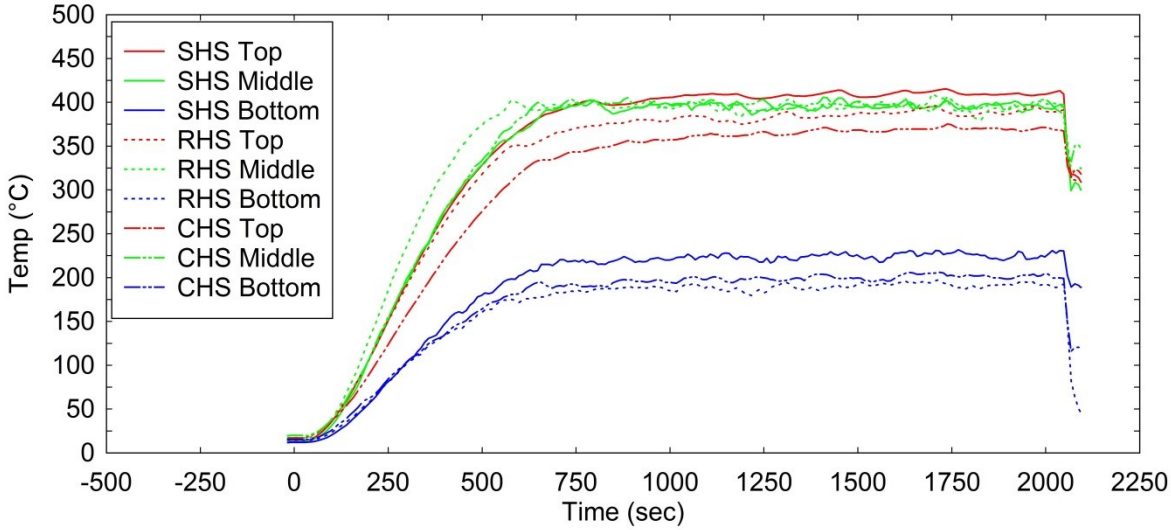

Figure B.11: Pre Shot Recorded Temperature (Trial 6(6), Rig 2, 1000 Decimated)

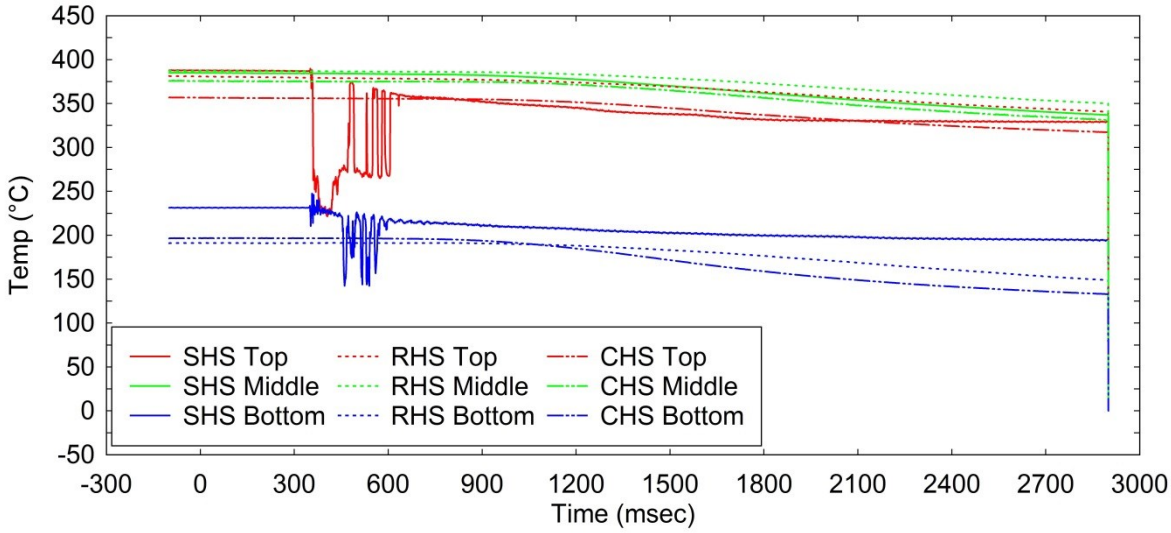

Figure B.12: Post Shot Recorded Temperature (Trial 6(6), Rig 2, 1000 Decimated)

Compression – Time Histories

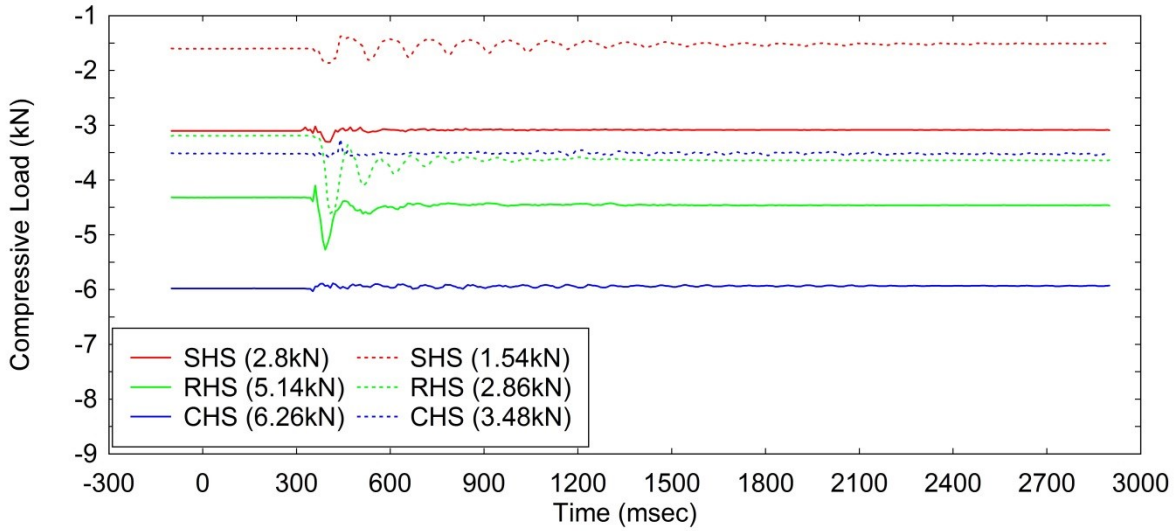

Figure B.13: Post Shot Recorded Compression (Trial 1(5), 8000 Decimated)

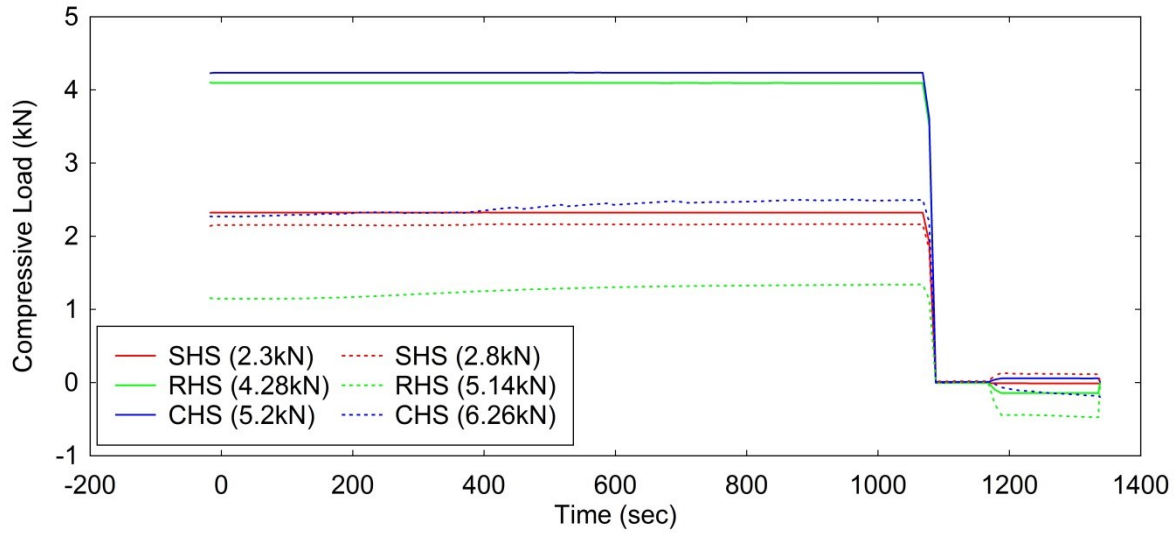

Figure B.14: Pre-Shot Recorded Compression (Trial 3(4) 1000 Decimated)

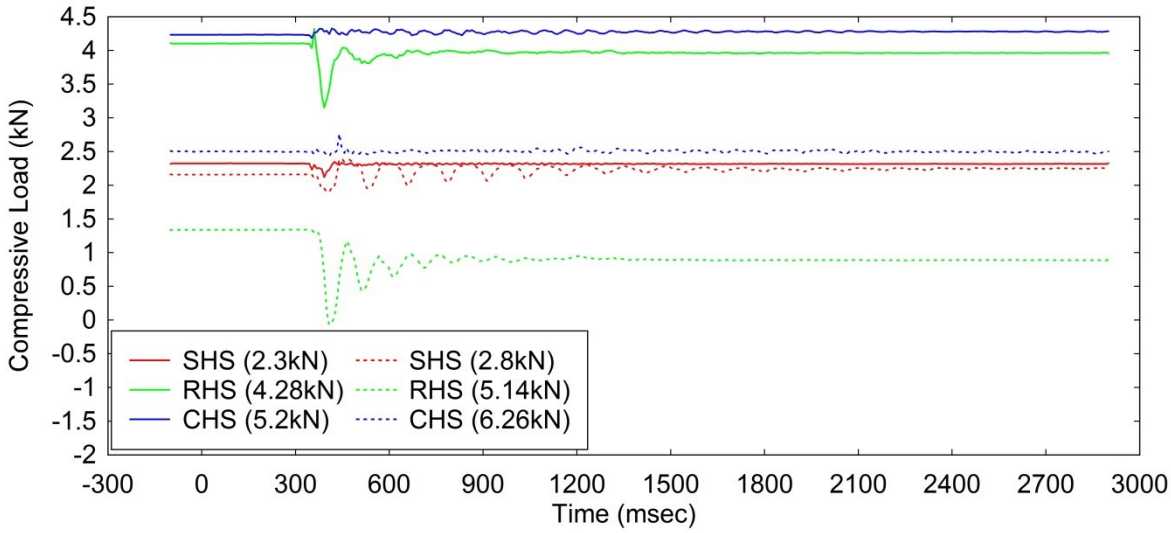

Figure B.15: Post-Shot Recorded Compression (Trial 3(4) 8000 Decimated)

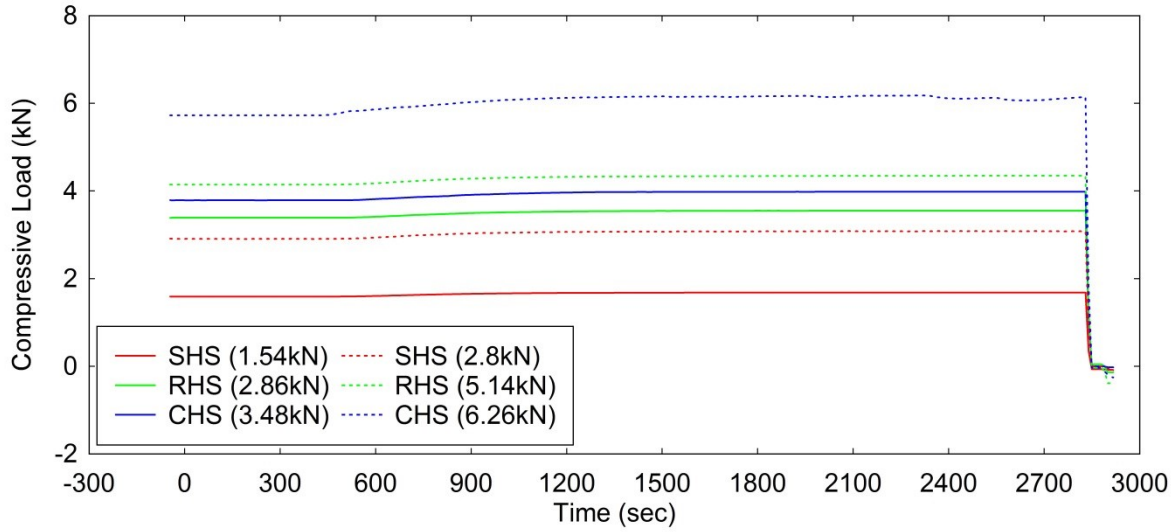

Figure B.16: Pre-Shot Recorded Compression (Trial 4(1) 1000 Decimated)

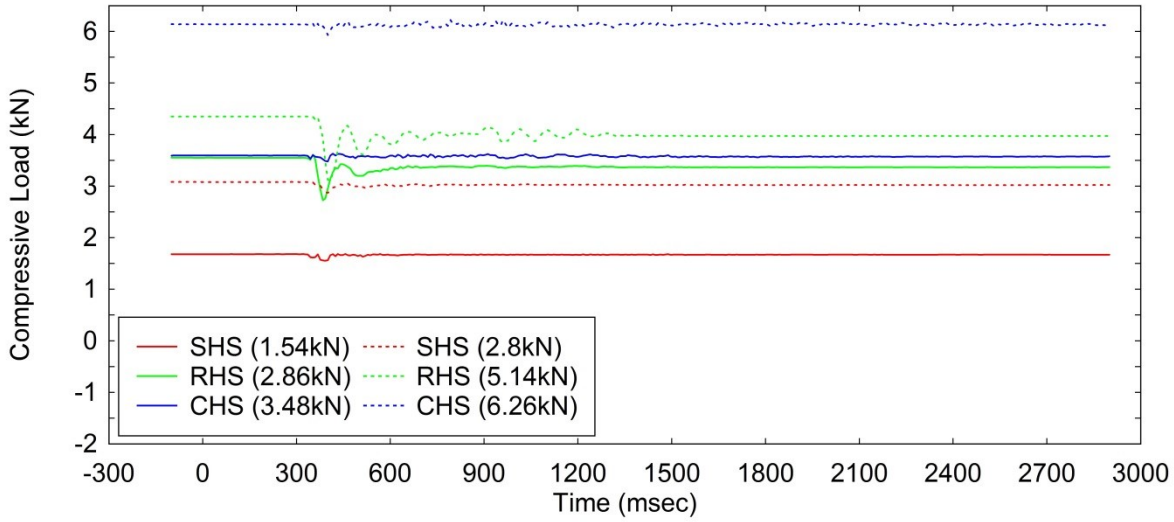

Figure B.17: Post-Shot Recorded Compression (Trial 4(1) 8000 Decimated)

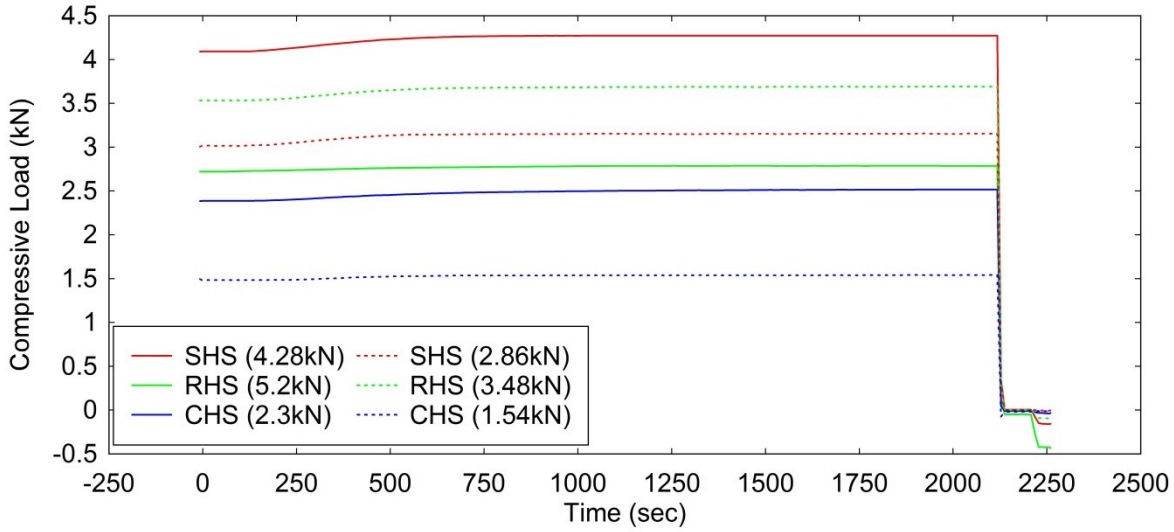

Figure B.18: Pre-Shot Recorded Compression (Trial 5(3) 1000 Decimated)

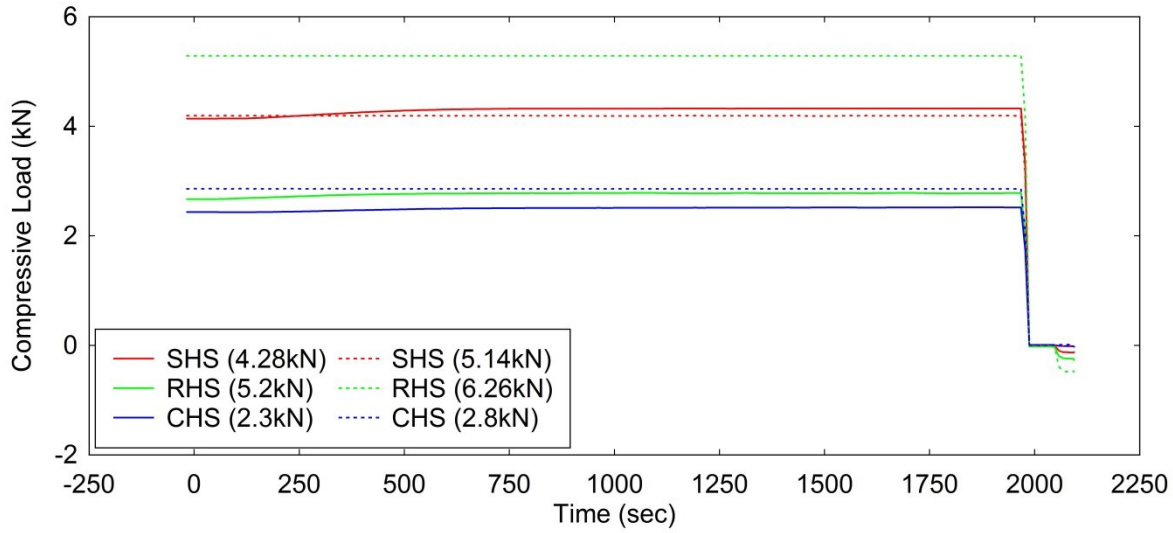

Figure B.19: Pre-Shot Recorded Compression (Trial 6(6) 1000 Decimated)

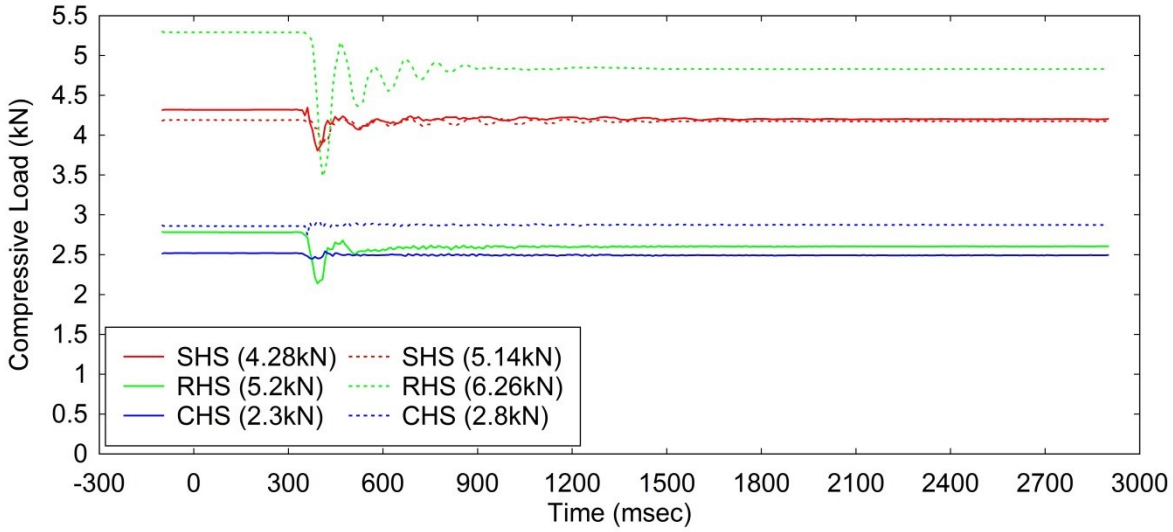

Figure B.20: Post-Shot Recorded Compression (Trial 6(6) 8000 Decimated)

Appendix C: Pressure-Time Histories for Explosive Events Investigated in Parametric Study

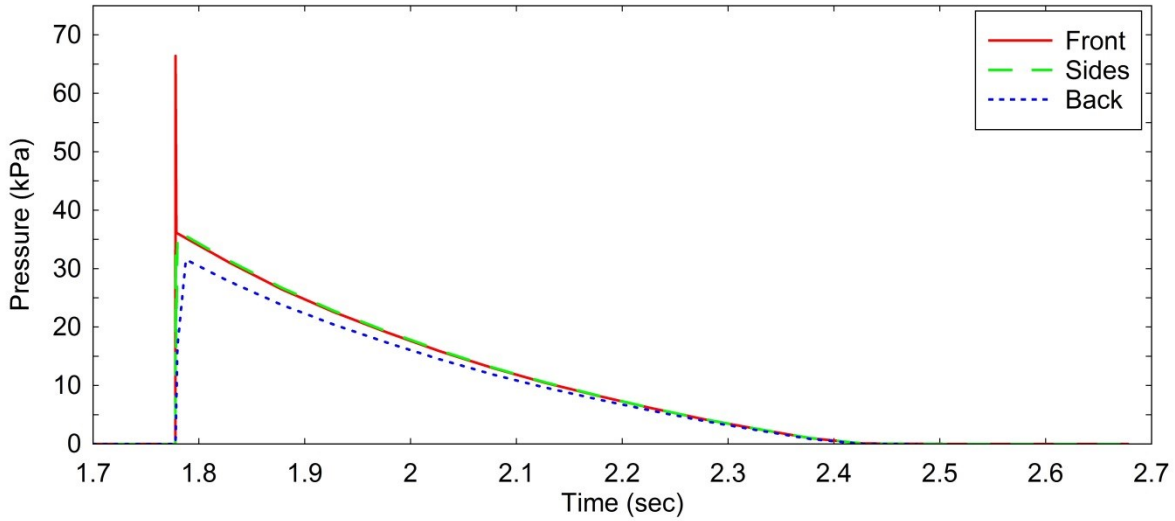

Figure C.1: Applied Pressure – Time History: 66.4kPa Peak Pressure

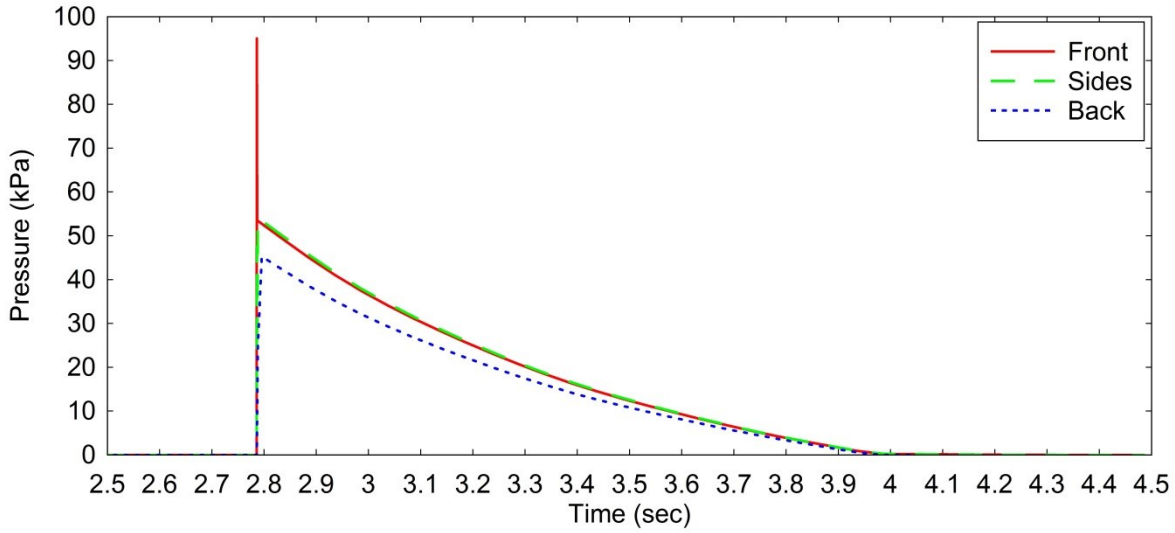

Figure C.2: Applied Pressure – Time History: 95.1kPa Peak Pressure

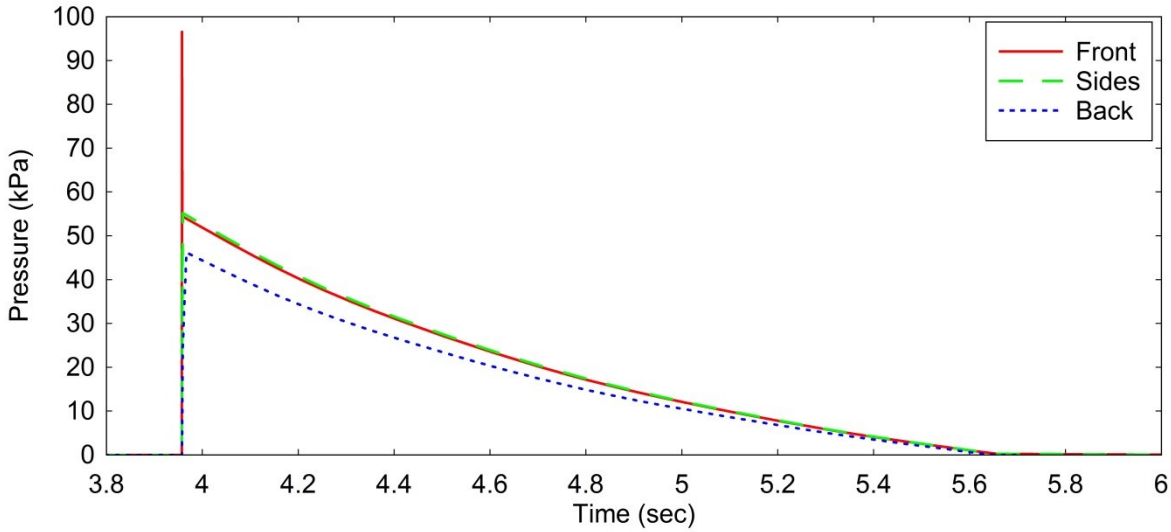

Figure C.3: Applied Pressure – Time History: 96.6kPa Peak Pressure

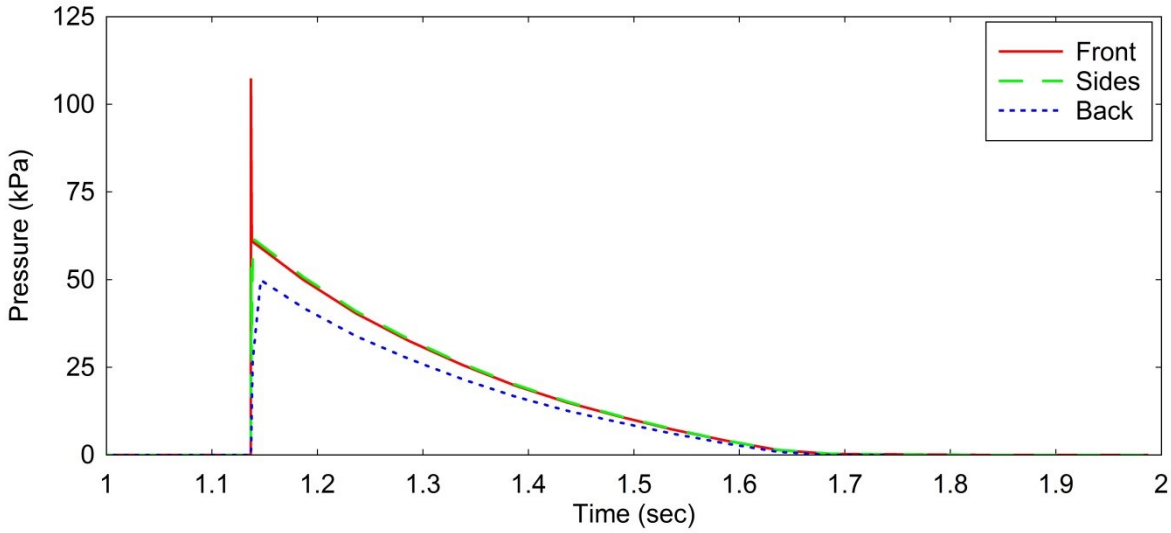

Figure C.4: Applied Pressure – Time History: 107.1kPa Peak Pressure

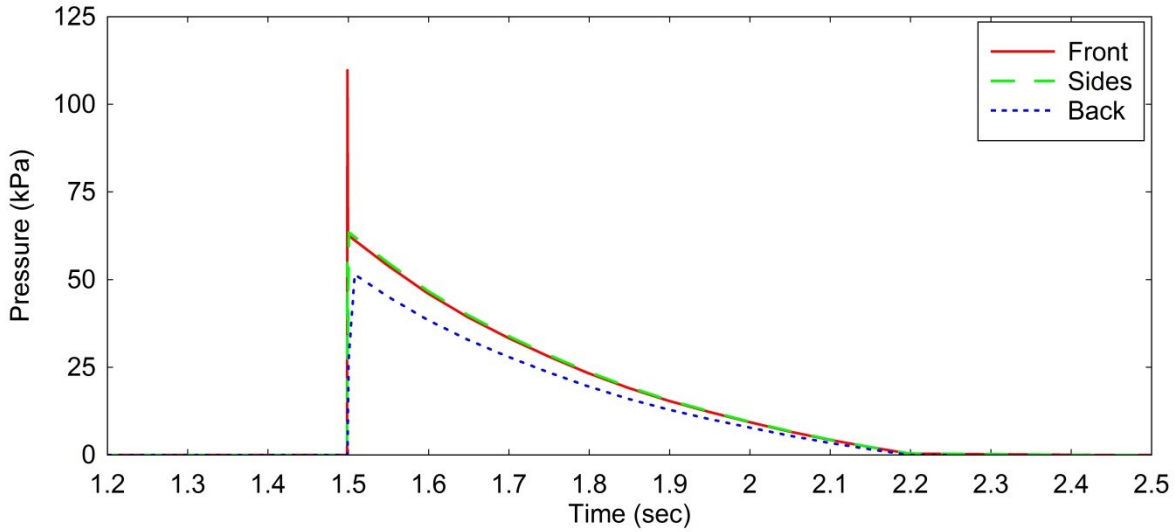

Figure C.5: Applied Pressure – Time History: 109.7kPa Peak Pressure

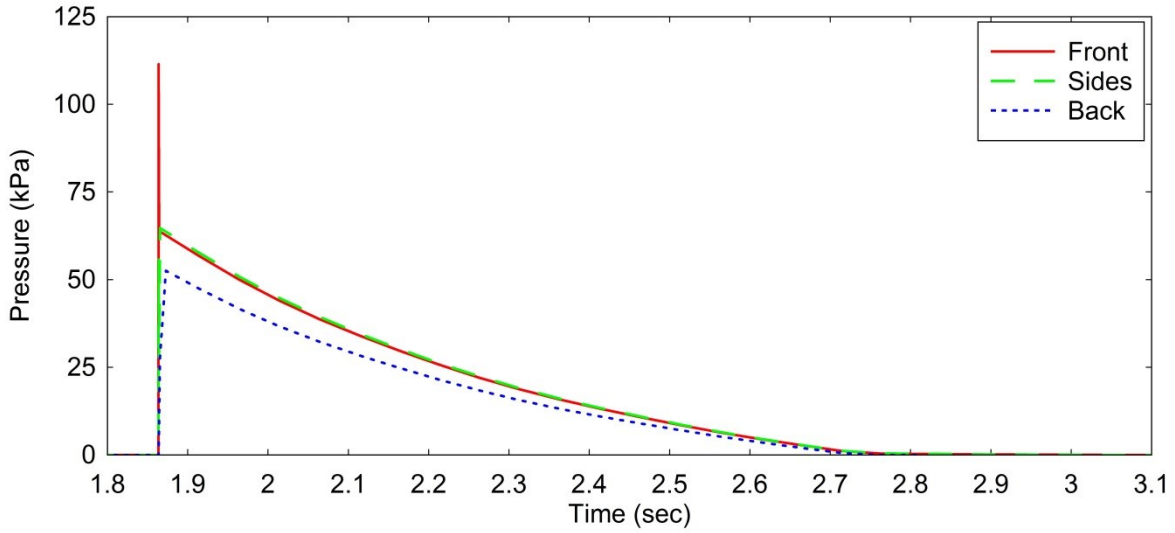

Figure C.6: Applied Pressure – Time History: 111.5kPa Peak Pressure

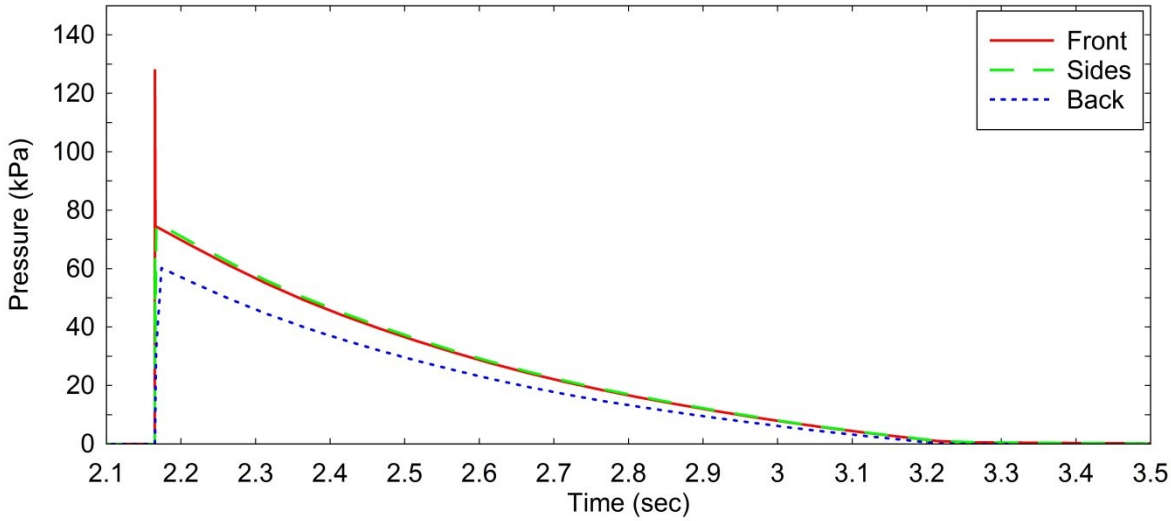

Figure C.7: Applied Pressure – Time History: 127.9kPa Peak Pressure

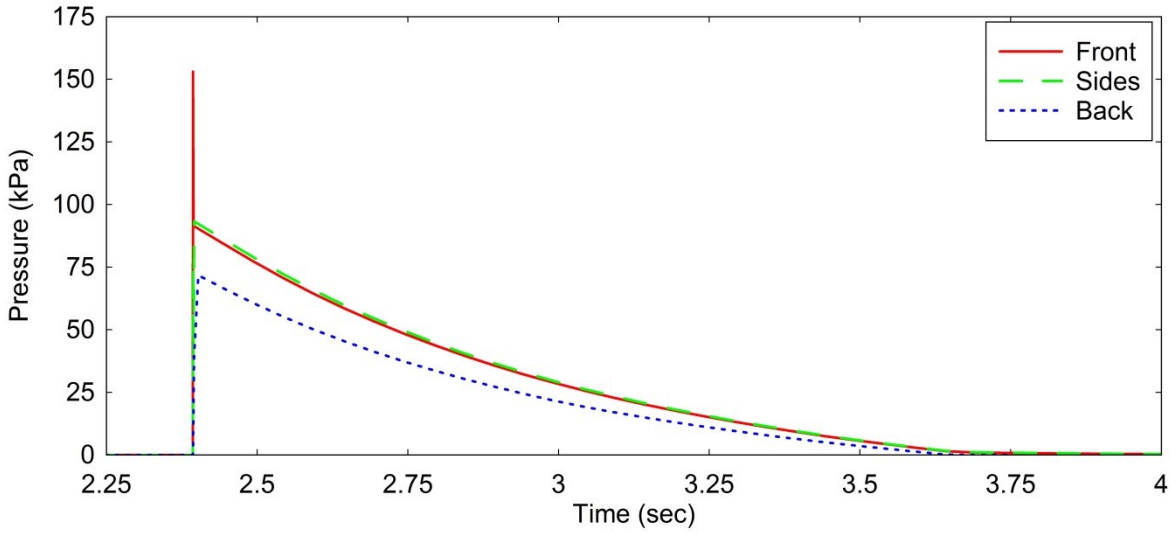

Figure C.8: Applied Pressure – Time History: 153.1kPa Peak Pressure

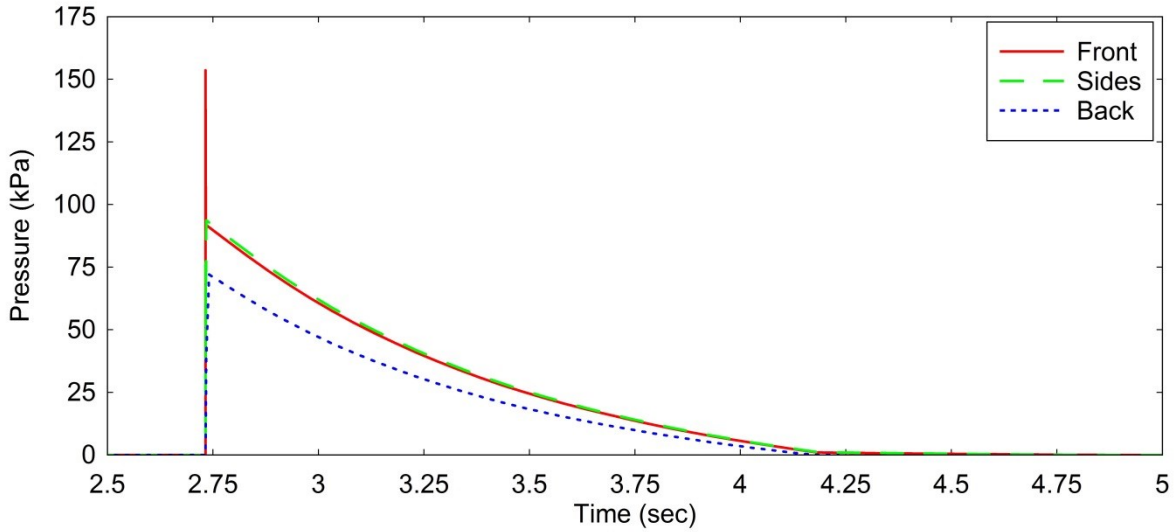

Figure C.9: Applied Pressure – Time History: 153.6kPa Peak Pressure

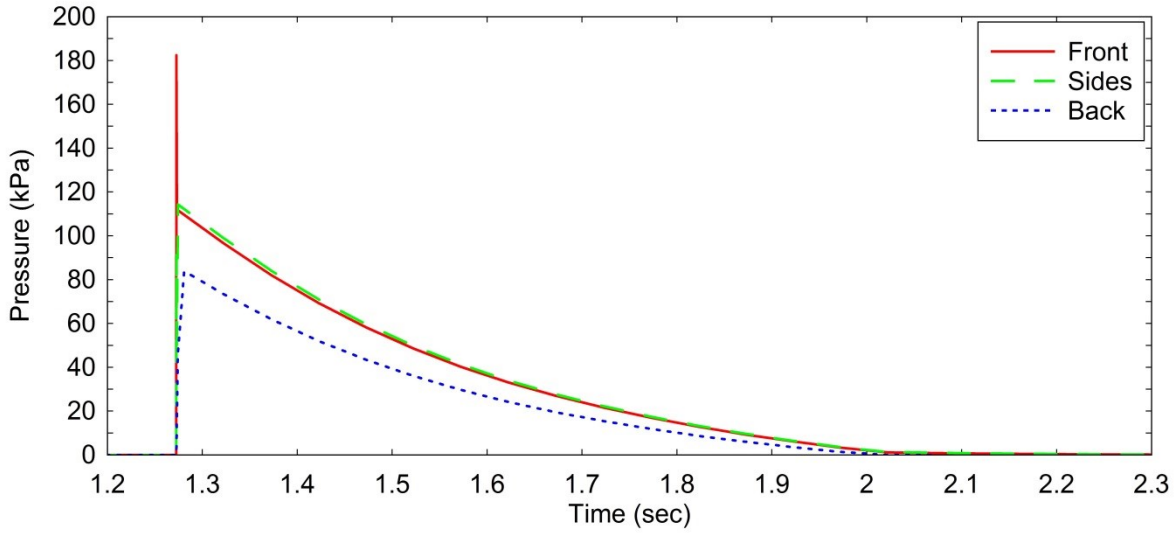

Figure C.10: Applied Pressure – Time History: 182.4kPa Peak Pressure

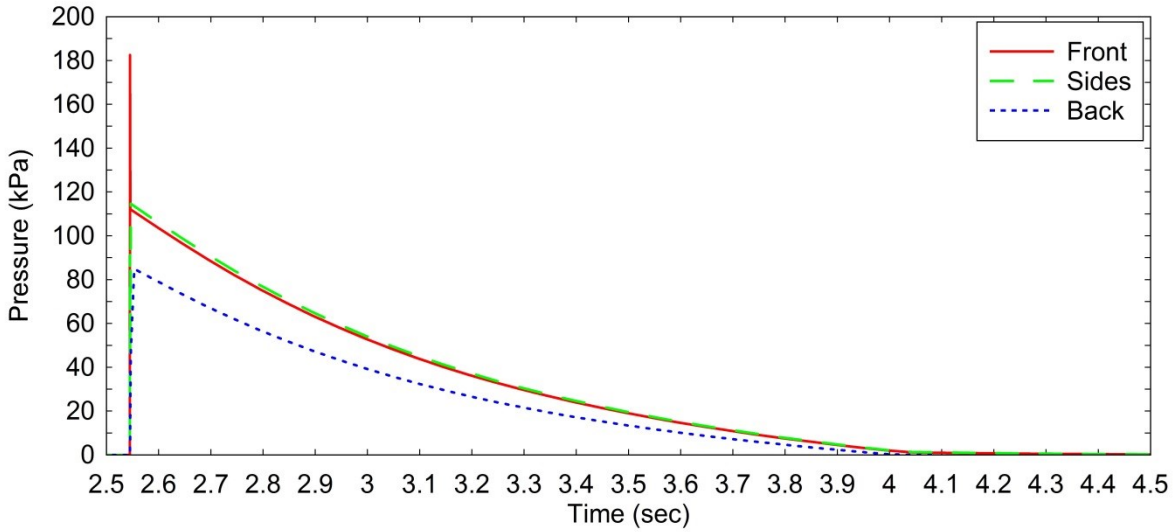

Figure C.11: Applied Pressure – Time History: 182.5kPa Peak Pressure

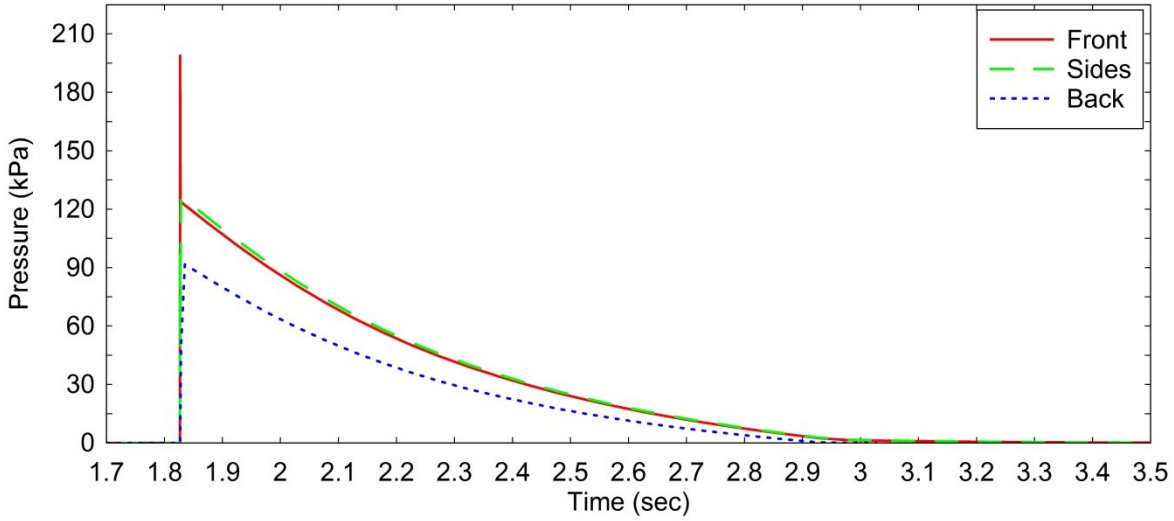

Figure C.12: Applied Pressure – Time History: 198.8kPa Peak Pressure

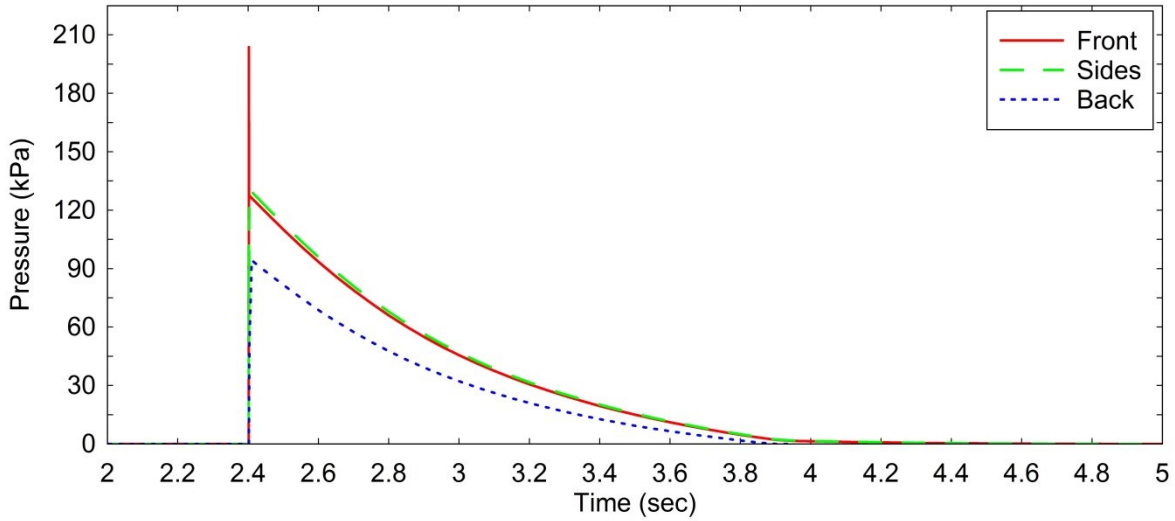

Figure C.13: Applied Pressure – Time History: 203.8kPa Peak Pressure

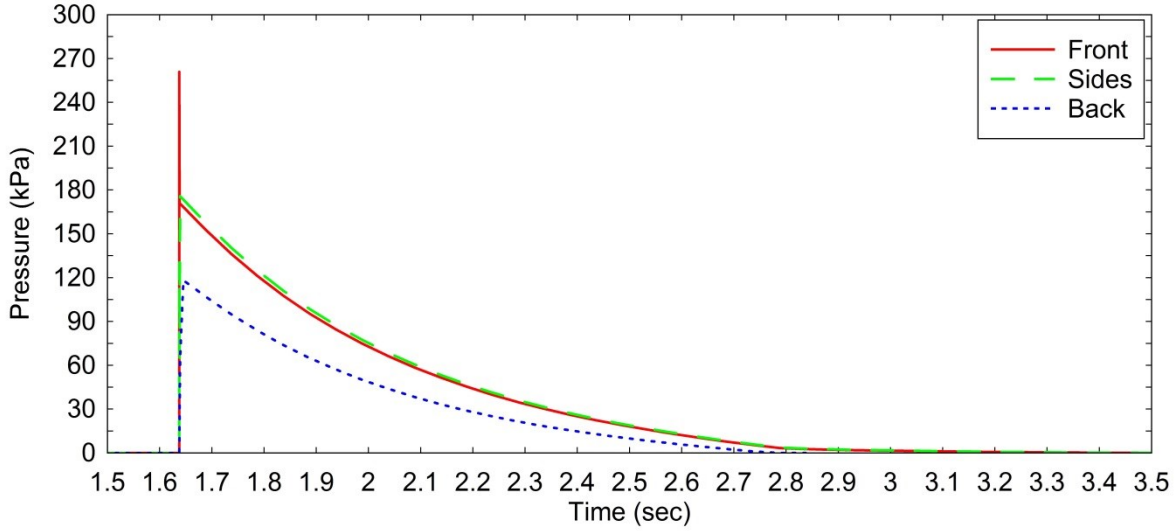

Figure C.14: Applied Pressure – Time History: 260.9kPa Peak Pressure

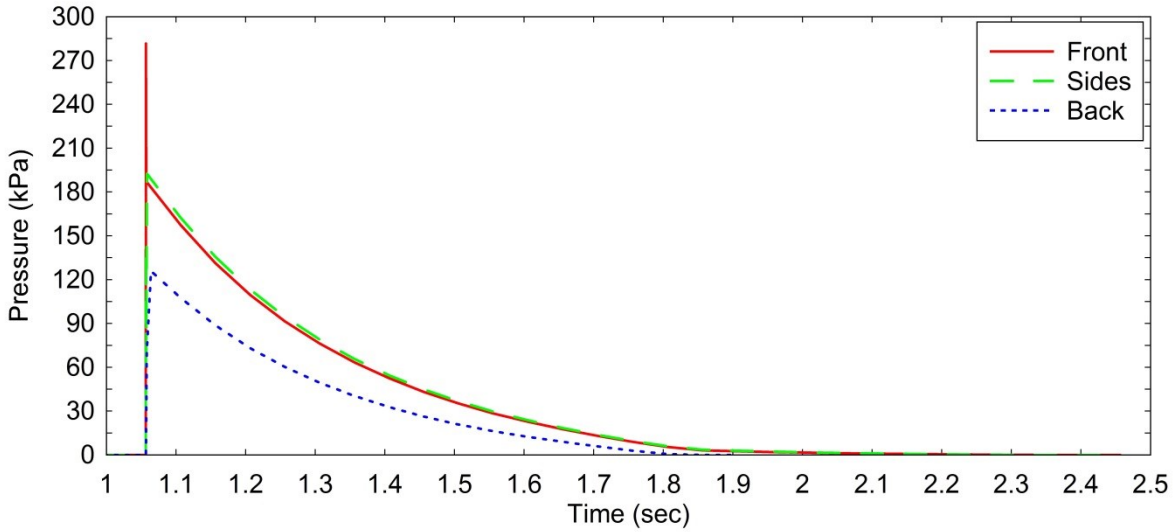

Figure C.15: Applied Pressure – Time History: 281.7kPa Peak Pressure

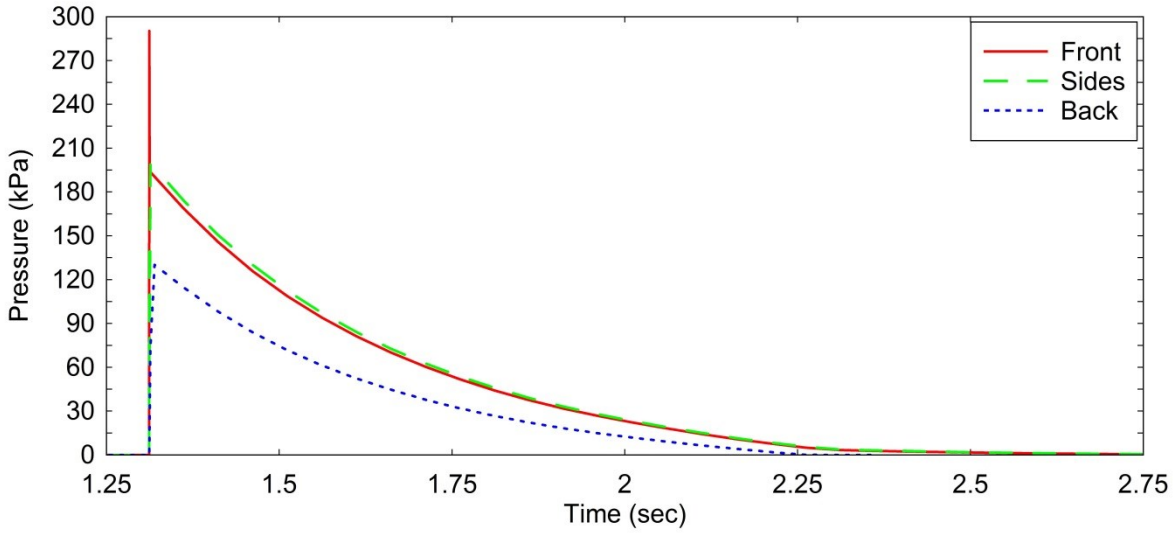

Figure C.16: Applied Pressure – Time History: 290.3kPa Peak Pressure

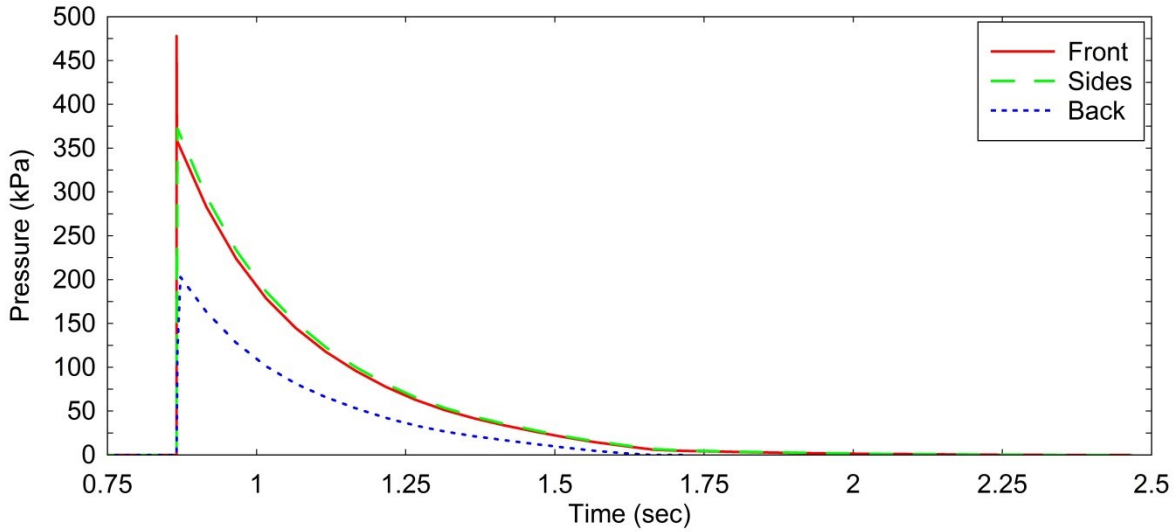

Figure C.17: Applied Pressure – Time History: 477.9kPa Peak Pressure

Appendix D: Deflection & Stress –Time Histories for Columns in Parametric Studies

Midpoint Deflection & Stress Histories (Roller Top)

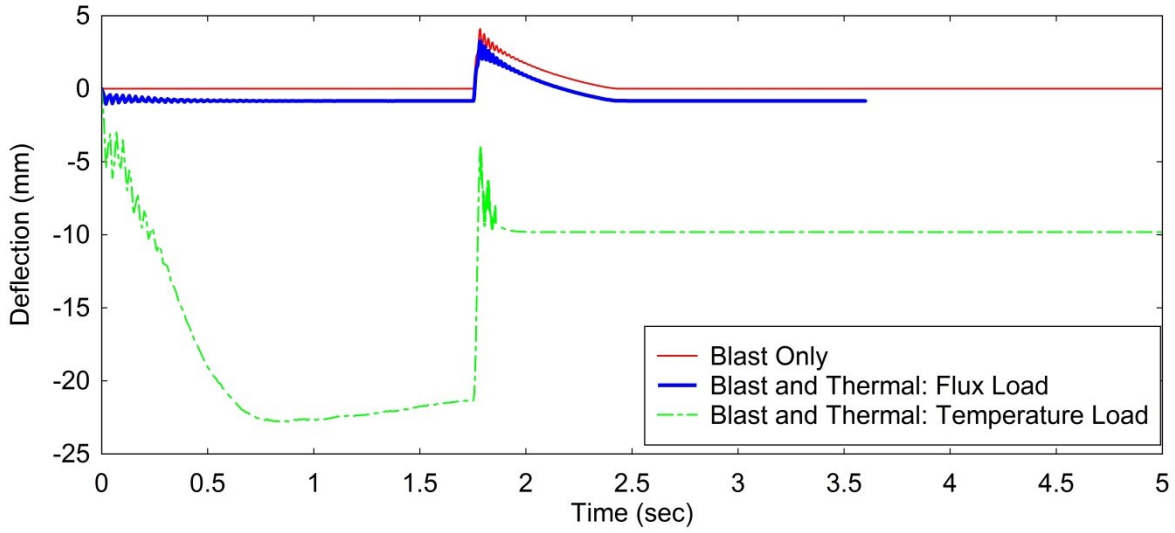

Figure D.1: Midpoint Deflection: 66.4kPa Peak Pressure

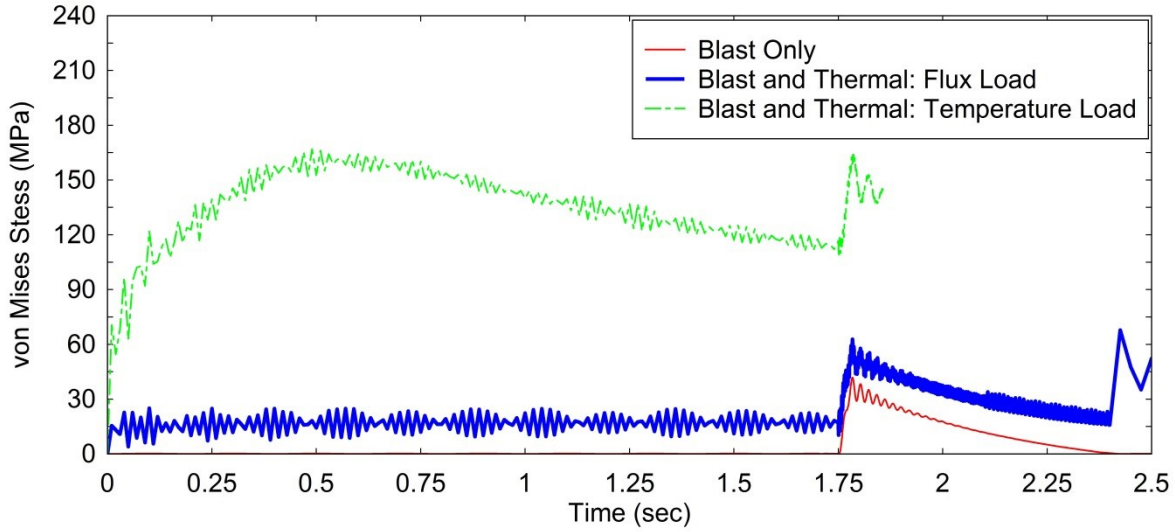

Figure D.2: Midpoint Stress: 66.4kPa Peak Pressure

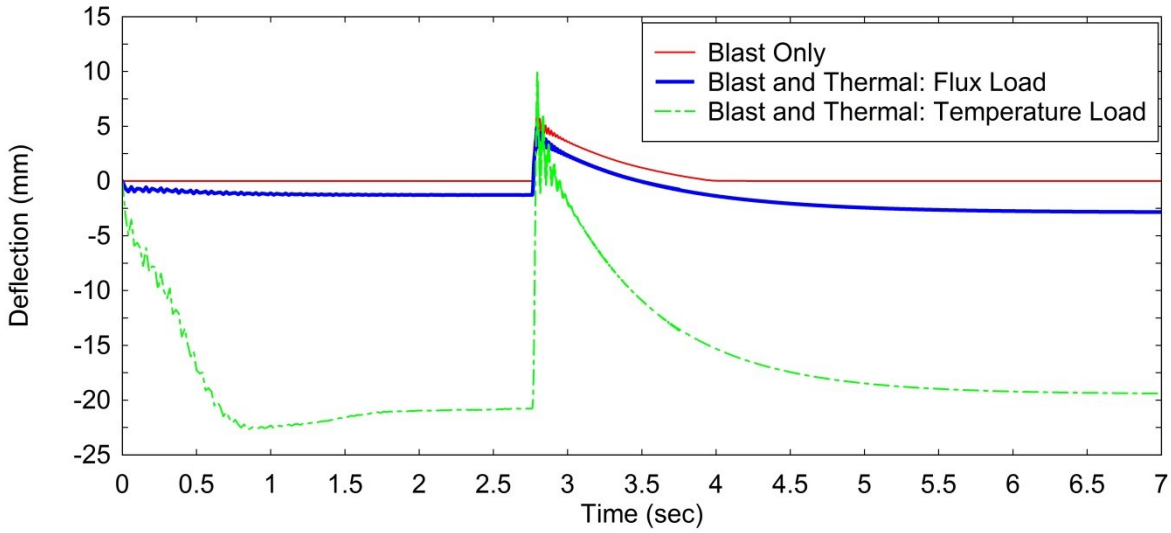

Figure D.3: Midpoint Deflection: 95.1kPa Peak Pressure

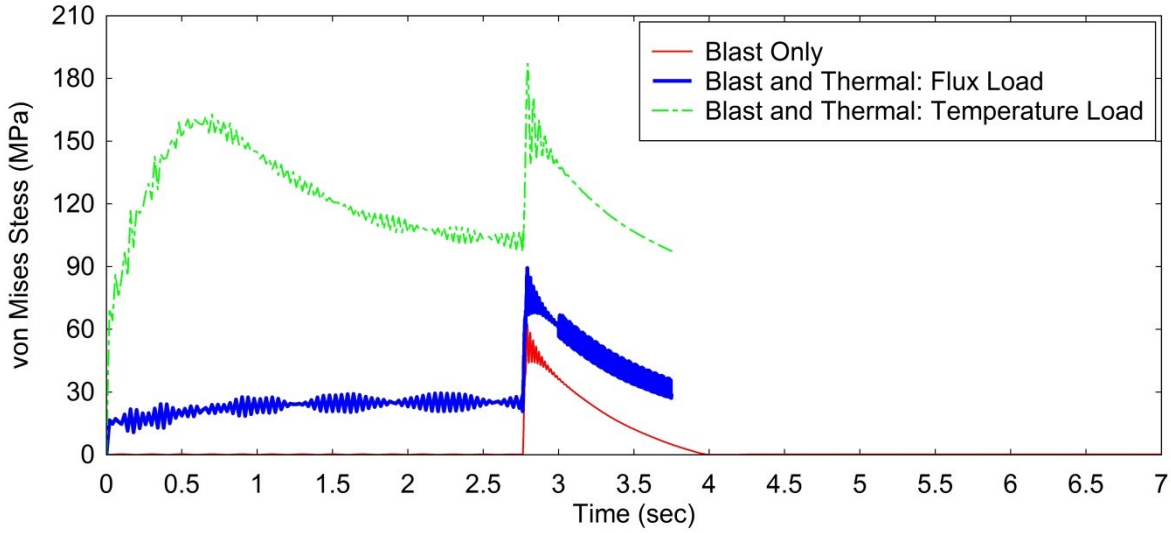

Figure D.4: Midpoint Stress: 95.1kPa Peak Pressure

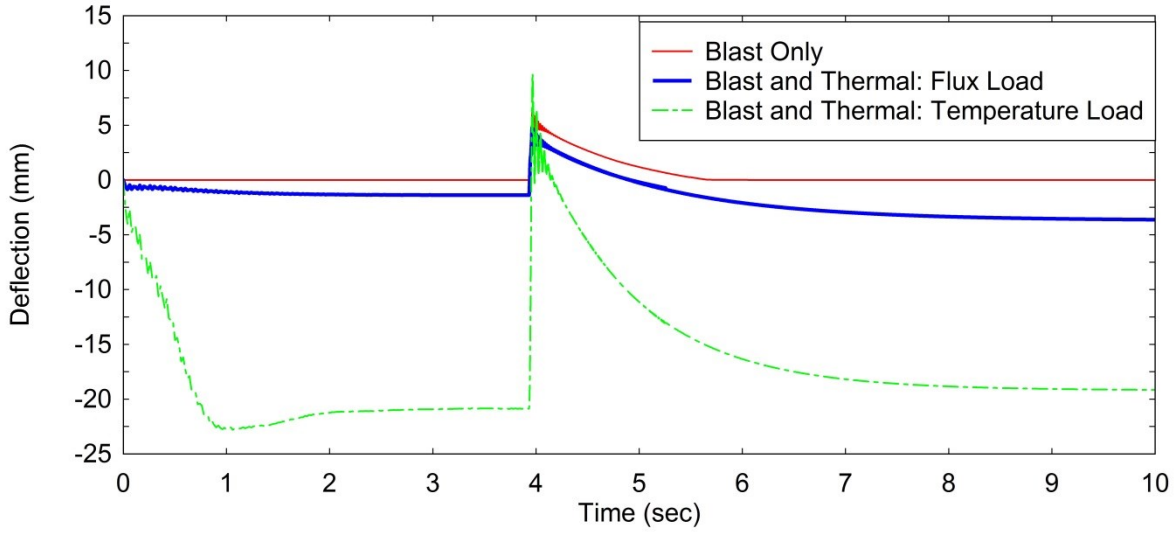

Figure D.5: Midpoint Deflection: 96.6kPa Peak Pressure

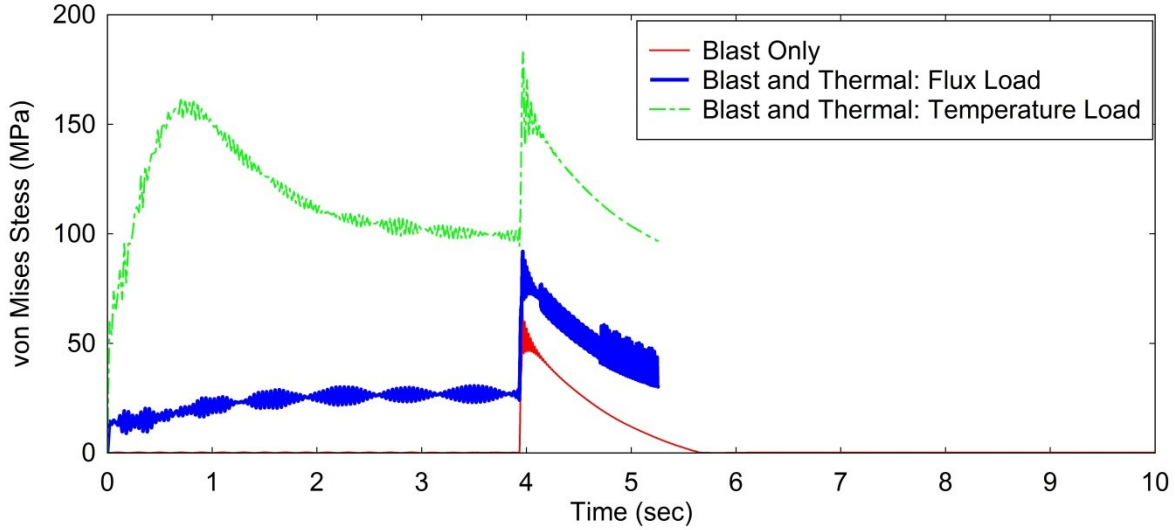

Figure D.6: Midpoint Stress: 96.6kPa Peak Pressure

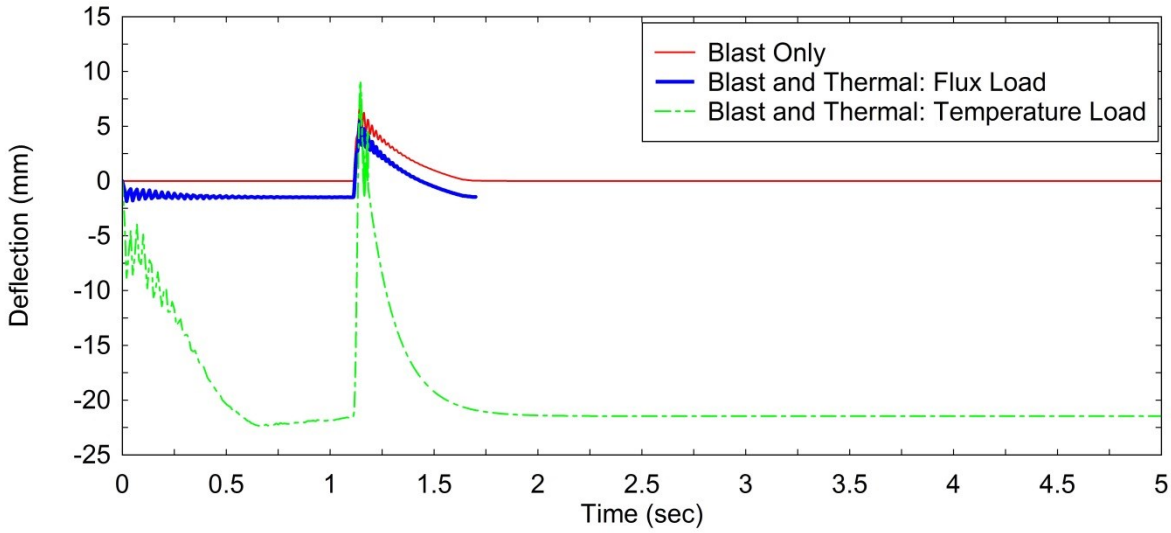

Figure D.7: Midpoint Deflection: 107.1kPa Peak Pressure

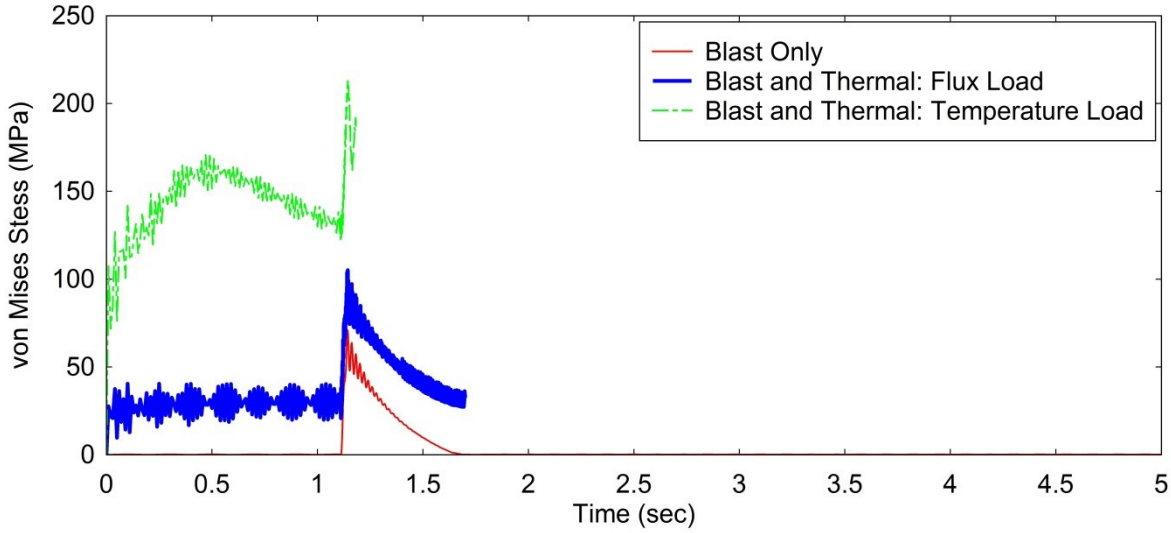

Figure D.8: Midpoint Stress: 107.1kPa Peak Pressure

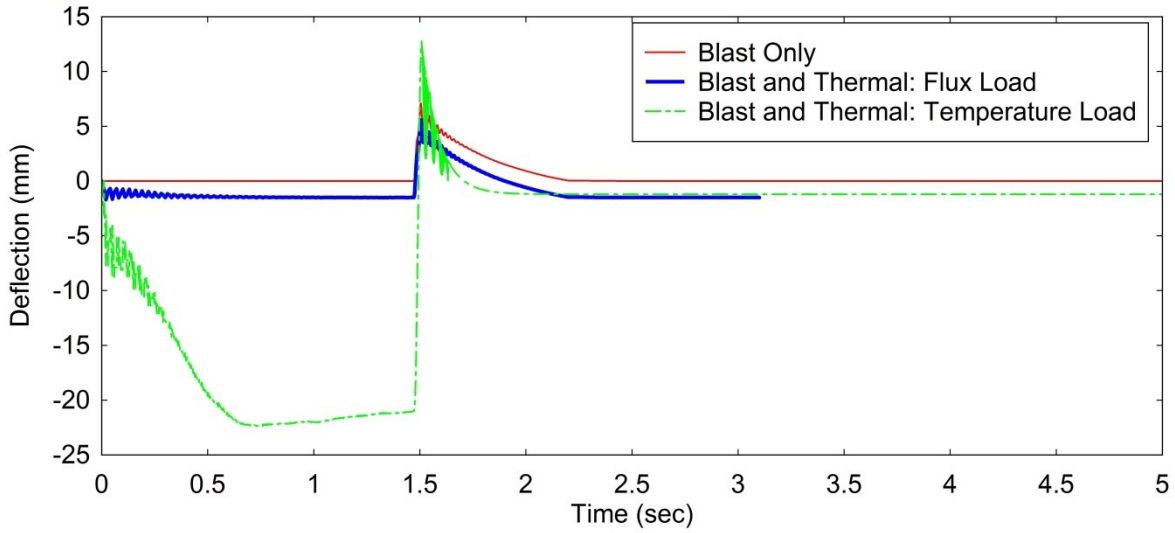

Figure D.9: Midpoint Deflection: 109.7kPa Peak Pressure

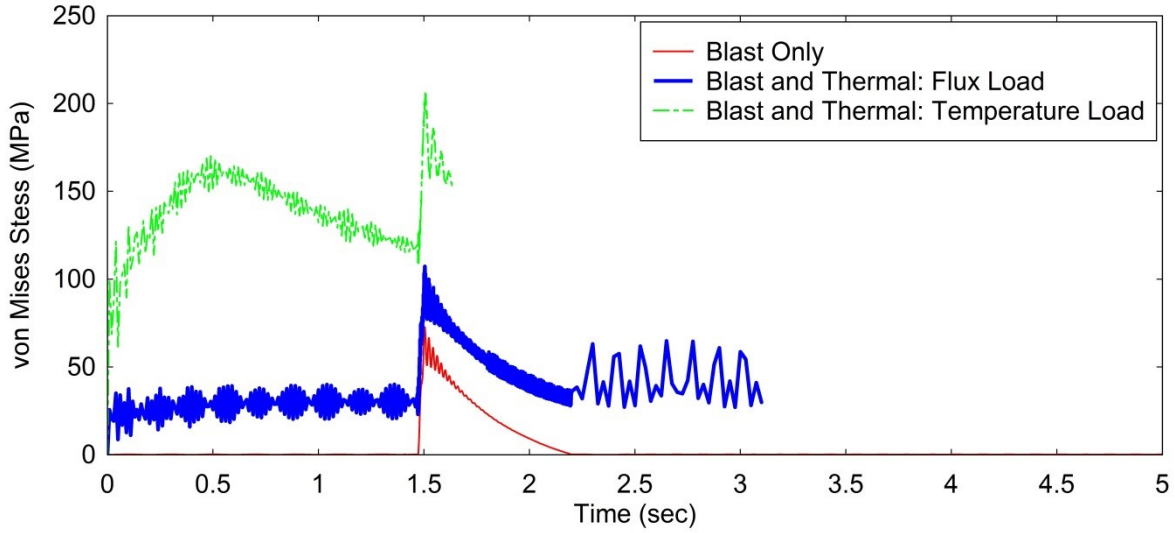

Figure D.10: Midpoint Stress: 109.7kPa Peak Pressure

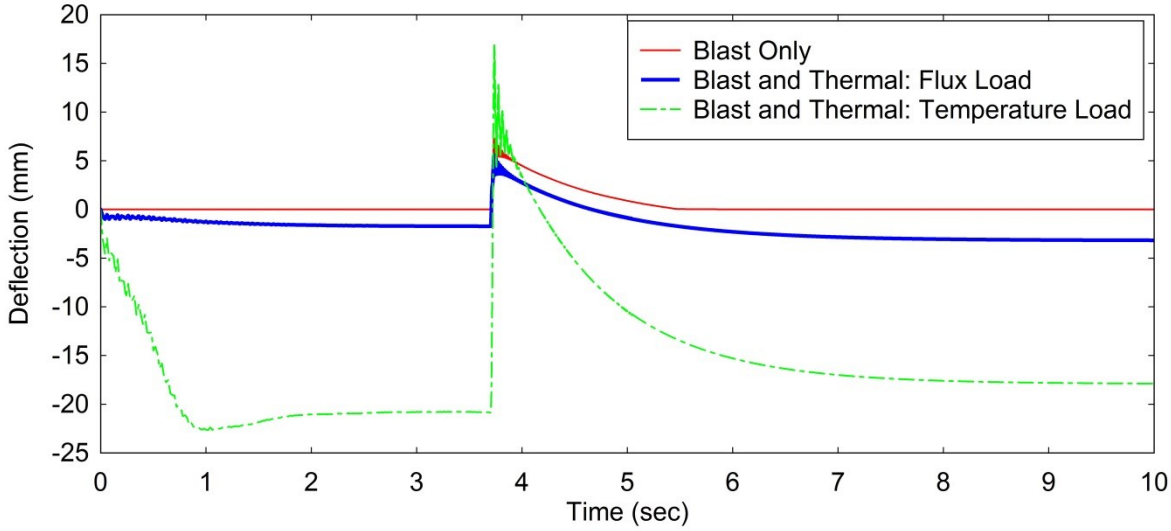

Figure D.11: Midpoint Deflection: 112kPa Peak Pressure

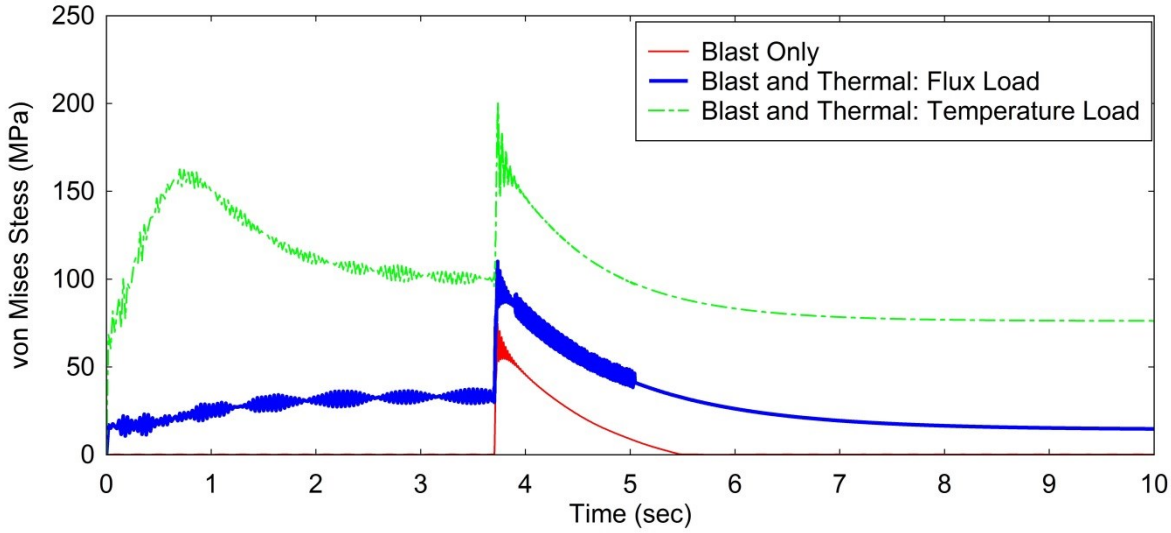

Figure D.12: Midpoint Stress: 112kPa Peak Pressure

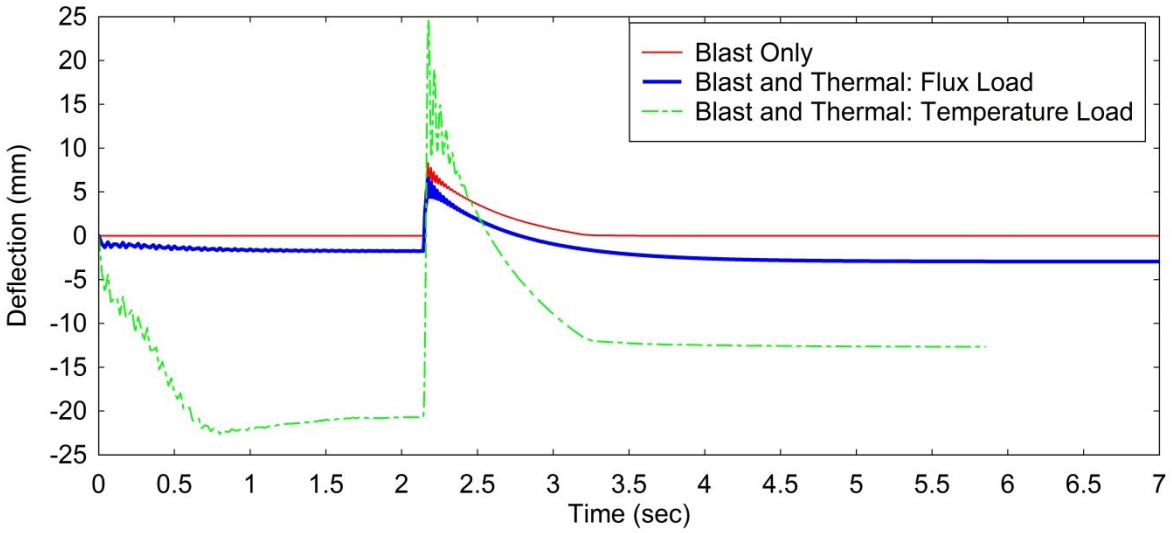

Figure D.13: Midpoint Deflection: 127.9kPa Peak Pressure

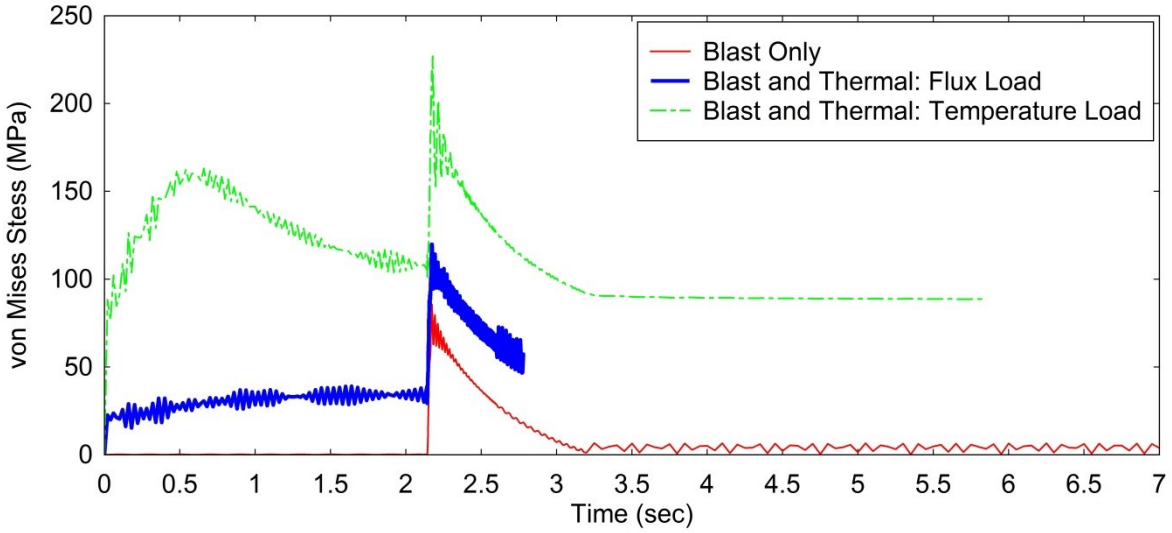

Figure D.14: Midpoint Stress: 127.9kPa Peak Pressure

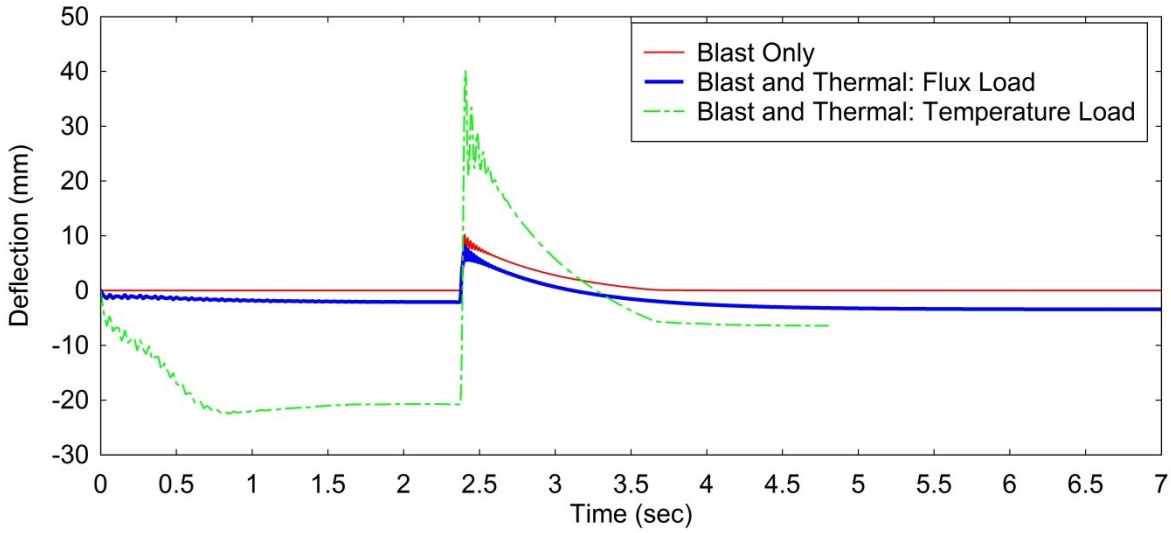

Figure D.15: Midpoint Deflection: 153.1Pa Peak Pressure

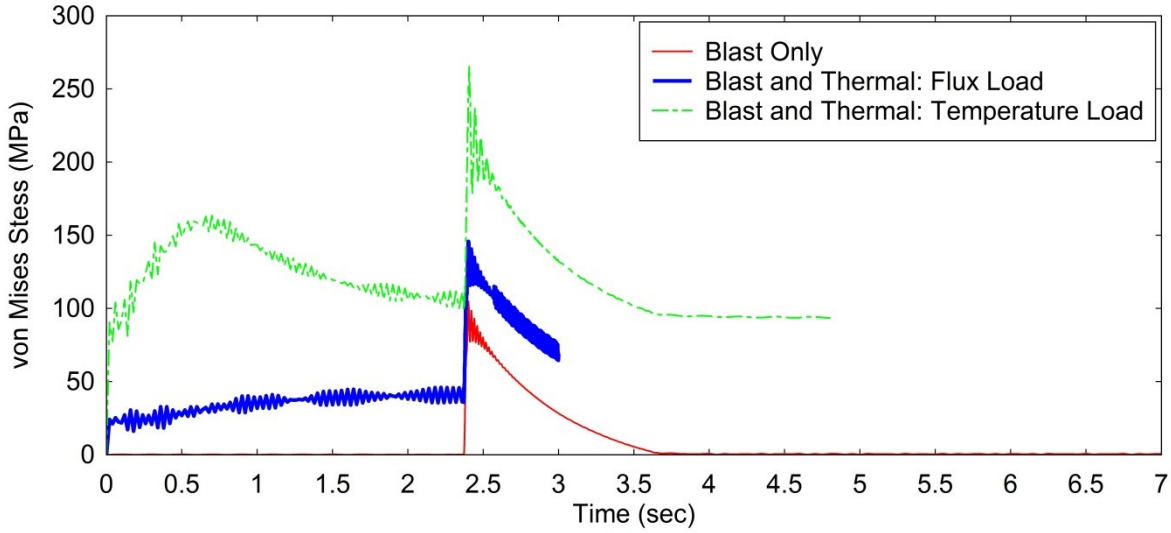

Figure D.16: Midpoint Stress: 153.1Pa Peak Pressure

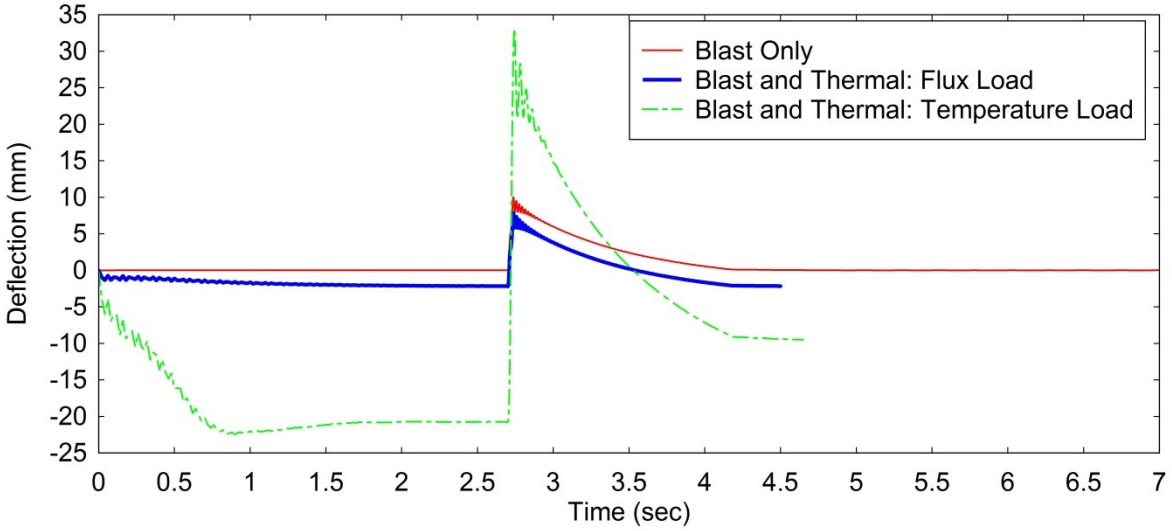

Figure D.17: Midpoint Deflection: 153.6Pa Peak Pressure

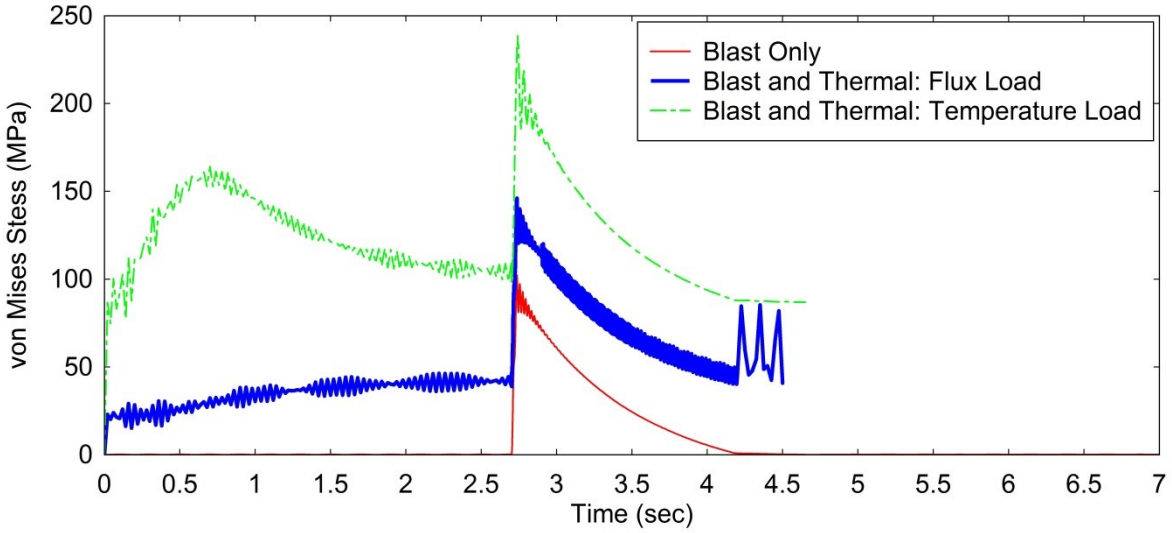

Figure D.18: Midpoint Stress: 153.6Pa Peak Pressure

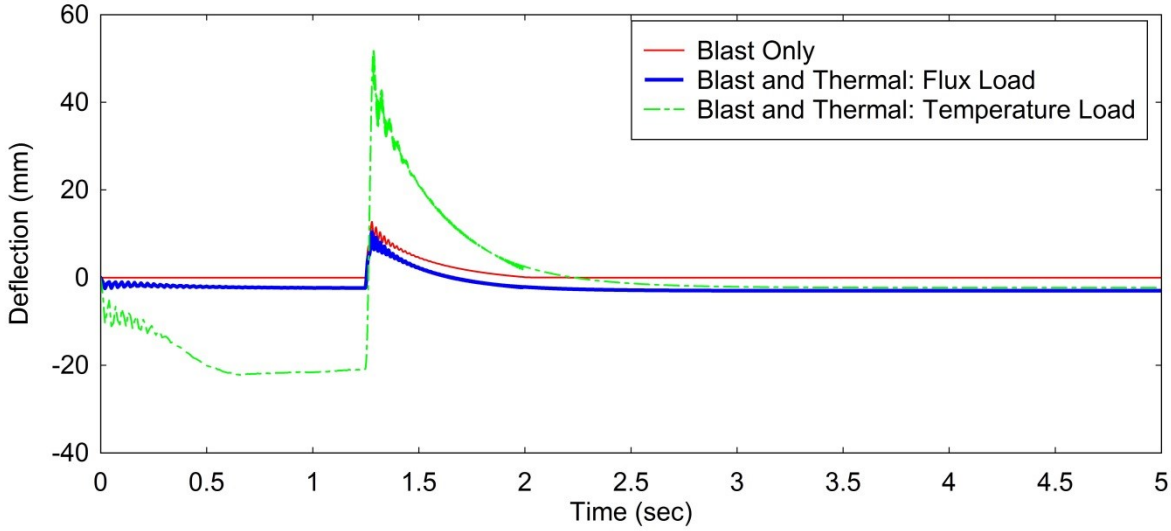

Figure D.19: Midpoint Deflection: 182.4kPa Peak Pressure

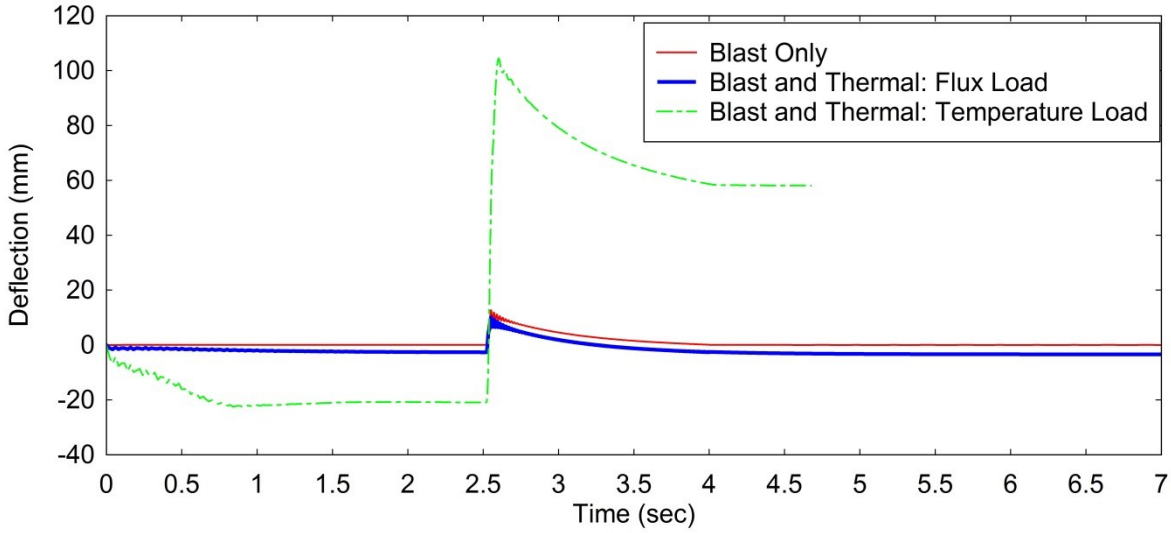

Figure D.20: Midpoint Deflection: 182.5kPa Peak Pressure

]

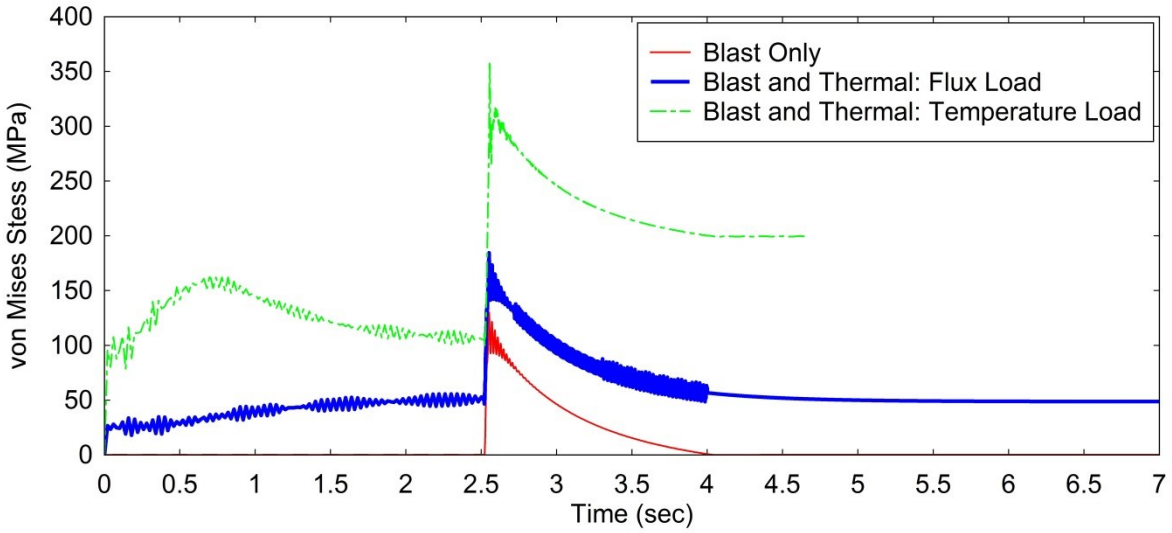

Figure D.21: Midpoint Stress: 182.5kPa Peak Pressure

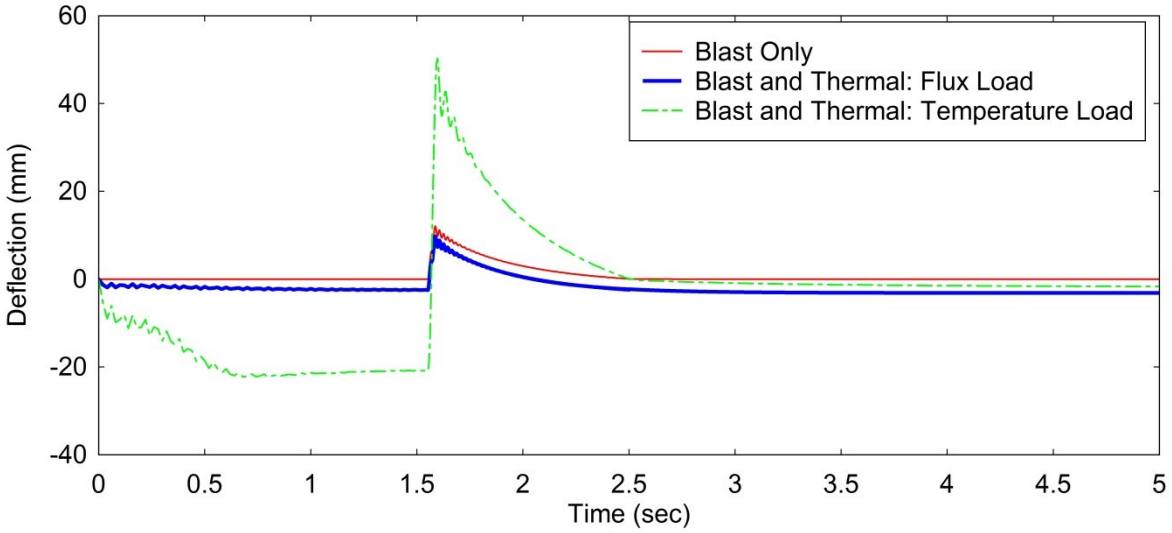

Figure D.22: Midpoint Deflection: 184.8kPa Peak Pressure

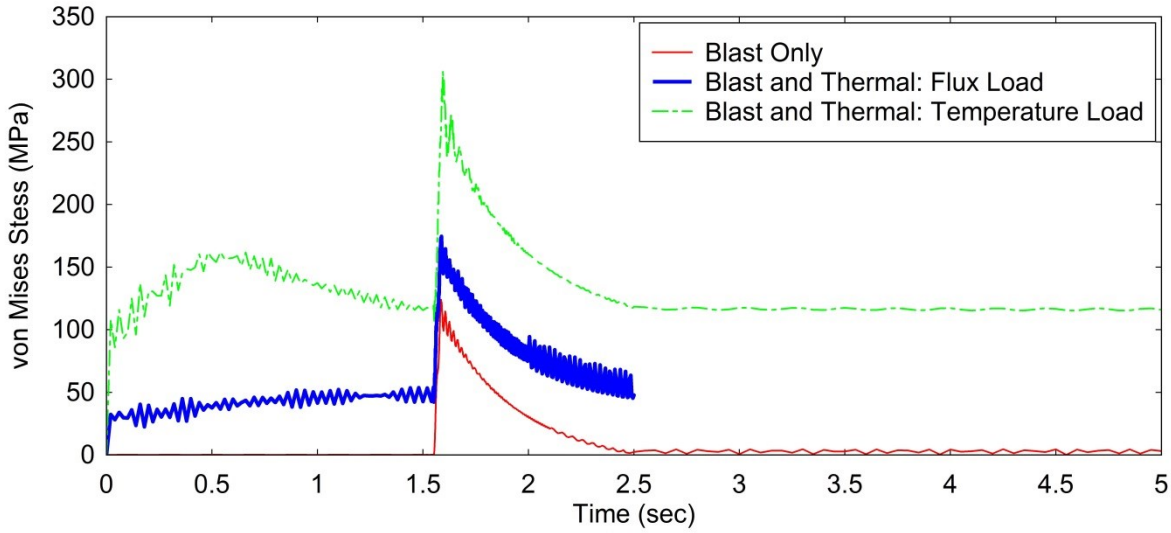

Figure D.23: Midpoint Stress: 184.8kPa Peak Pressure

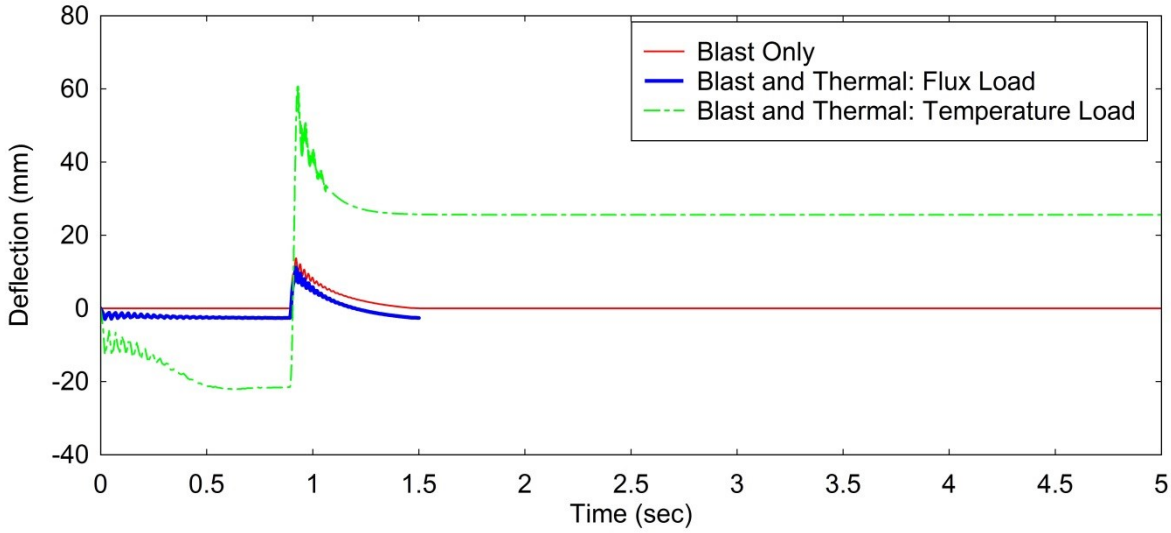

Figure D.24: Midpoint Deflection: 198.7kPa Peak Pressure

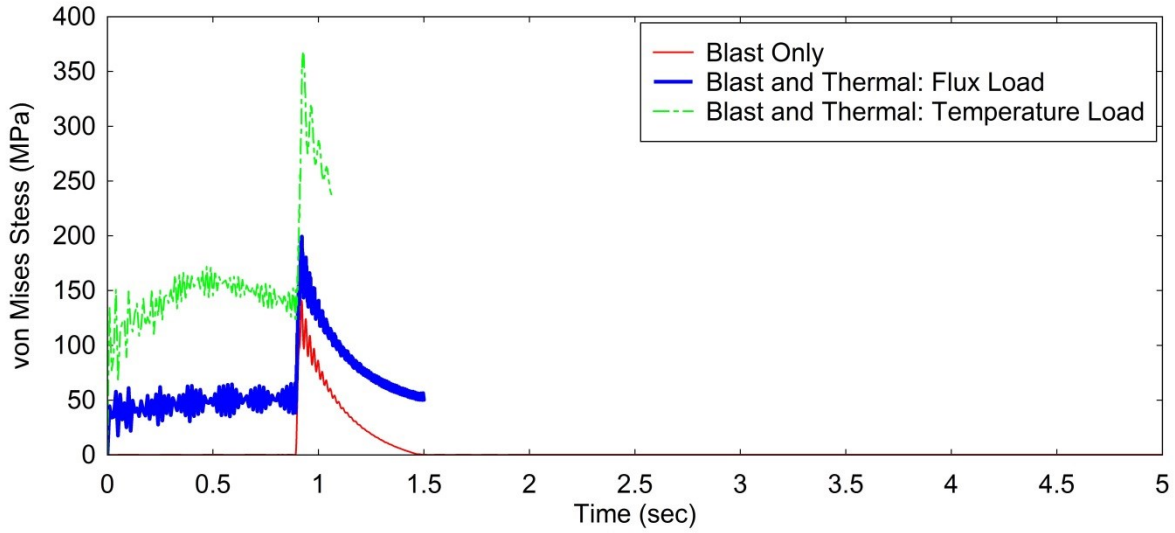

Figure D.25: Midpoint Stress: 198.7kPa Peak Pressure

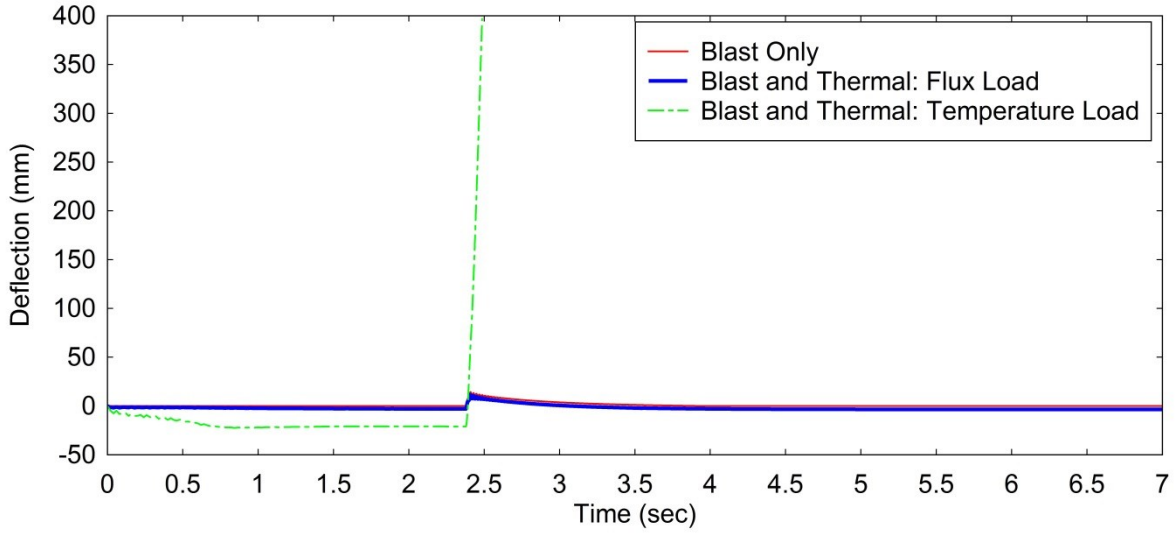

Figure D.26: Midpoint Deflection: 203.8kPa Peak Pressure

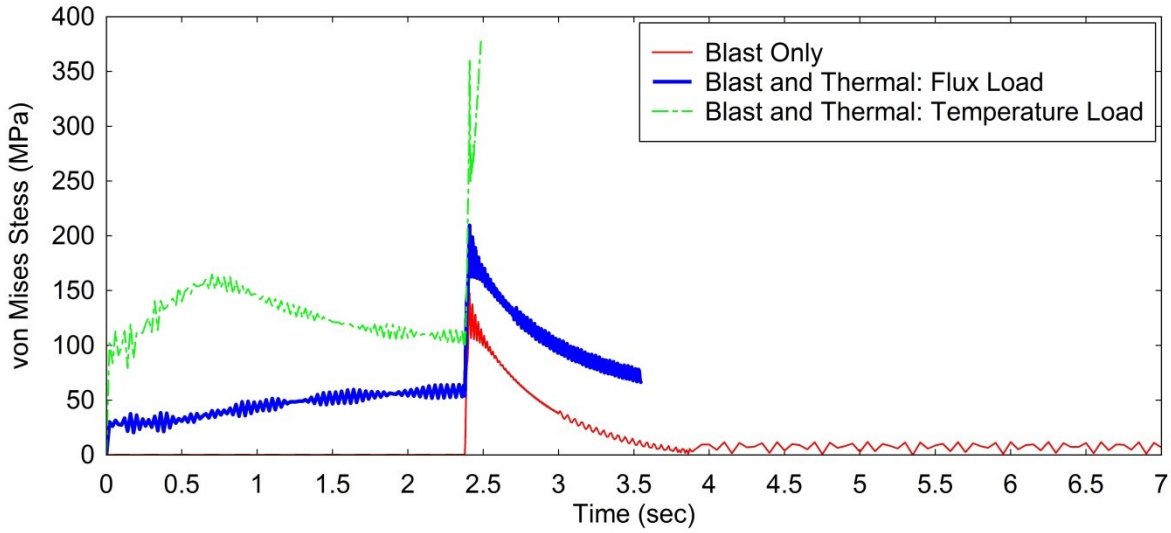

Figure D.27: Midpoint Stress: 203.8kPa Peak Pressure

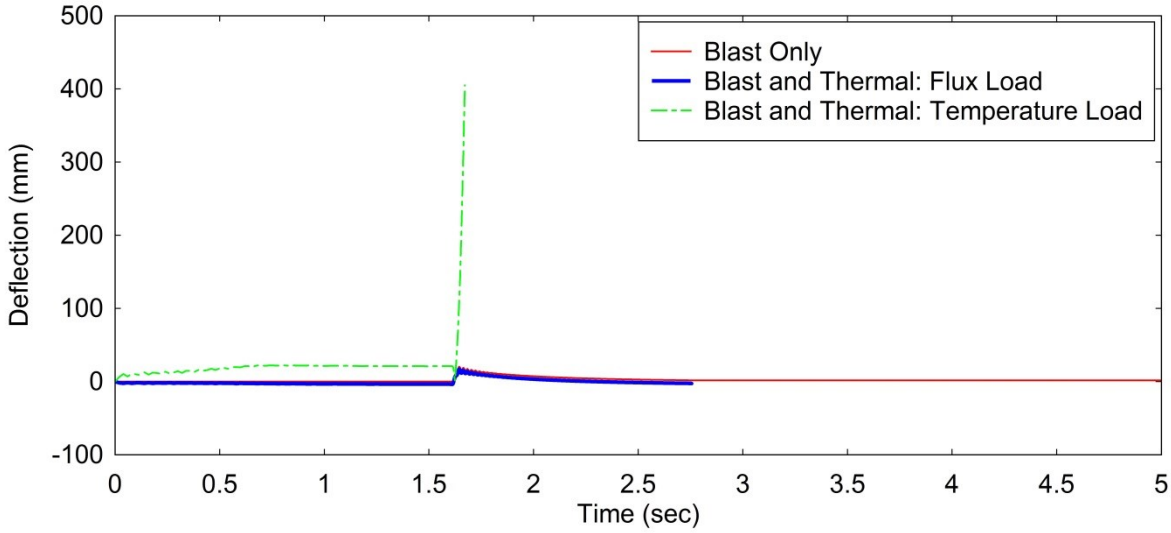

Figure D.28: Midpoint Deflection: 260.9kPa Peak Pressure

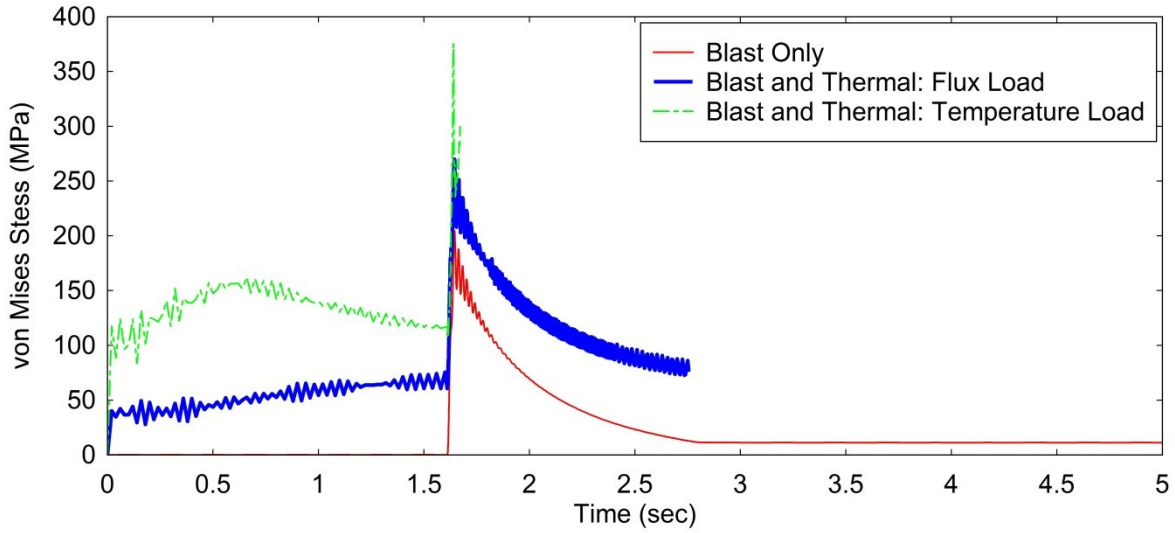

Figure D.29: Midpoint Stress: 260.9kPa Peak Pressure

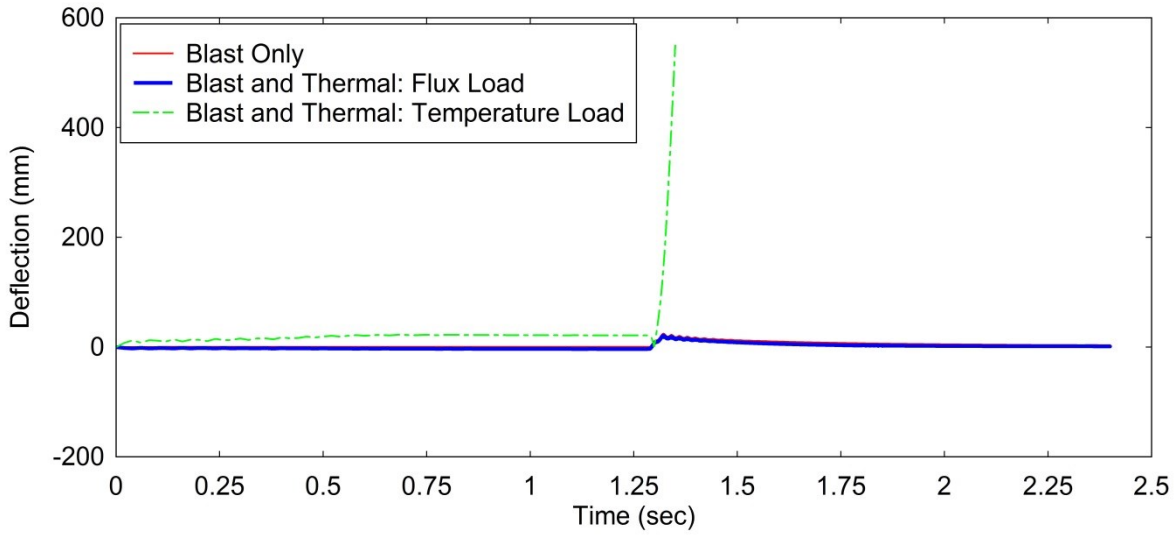

Figure D.30: Midpoint Deflection: 290.3kPa Peak Pressure

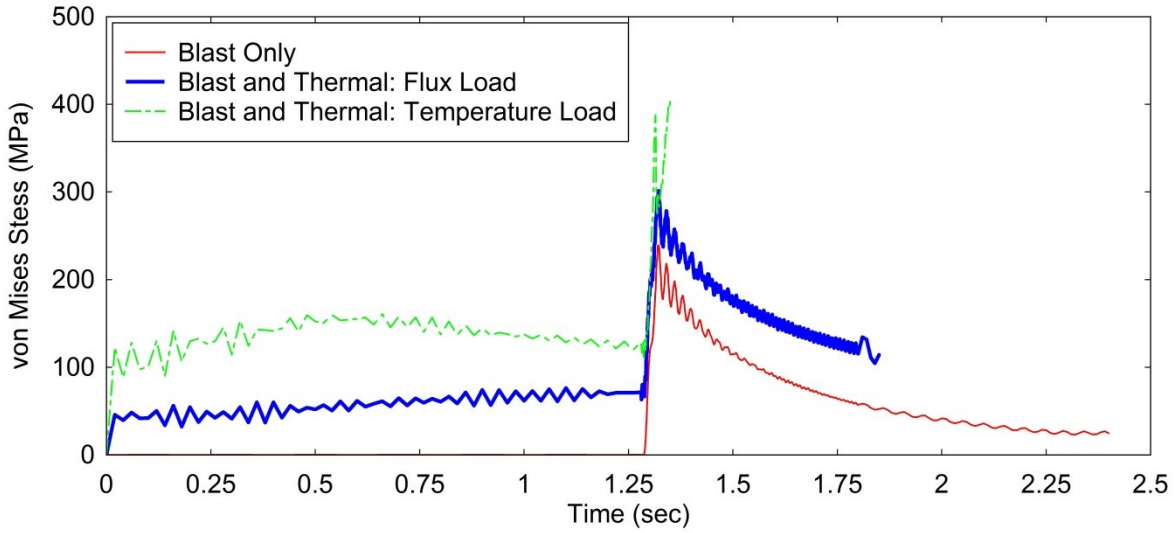

Figure D.31: Midpoint Stress: 290.3kPa Peak Pressure

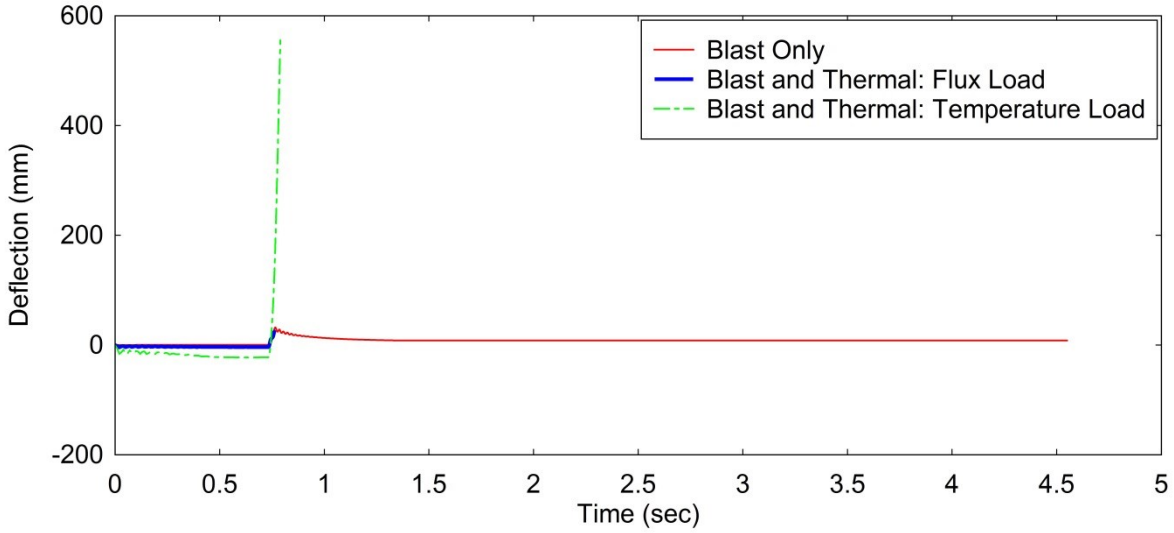

Figure D.32: Midpoint Deflection: 329.3kPa Peak Pressure

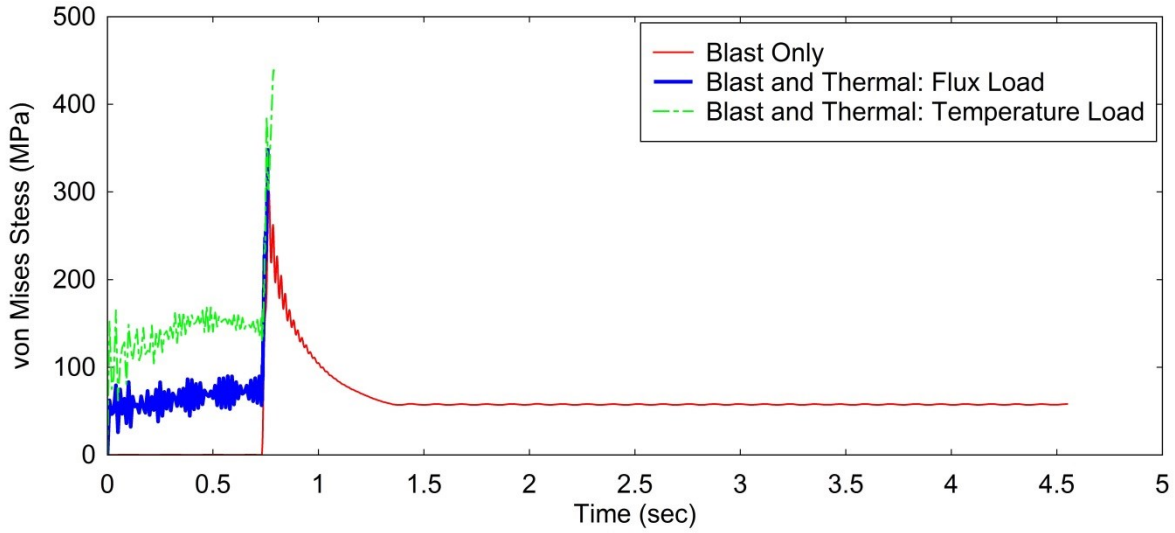

Figure D.33: Midpoint Stress: 329.3kPa Peak Pressure

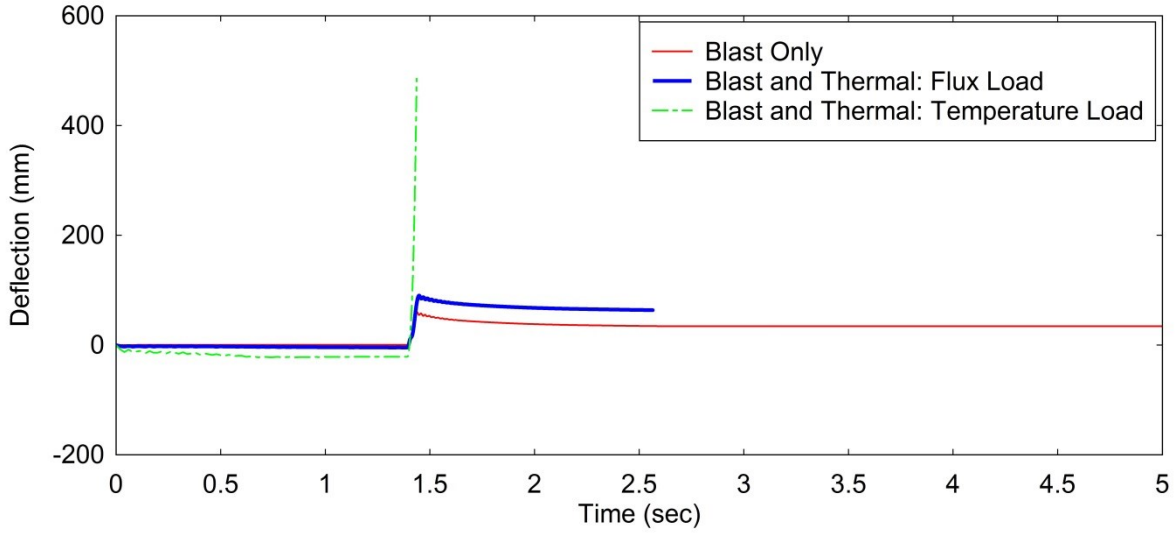

Figure D.34: Midpoint Deflection: 384.9kPa Peak Pressure

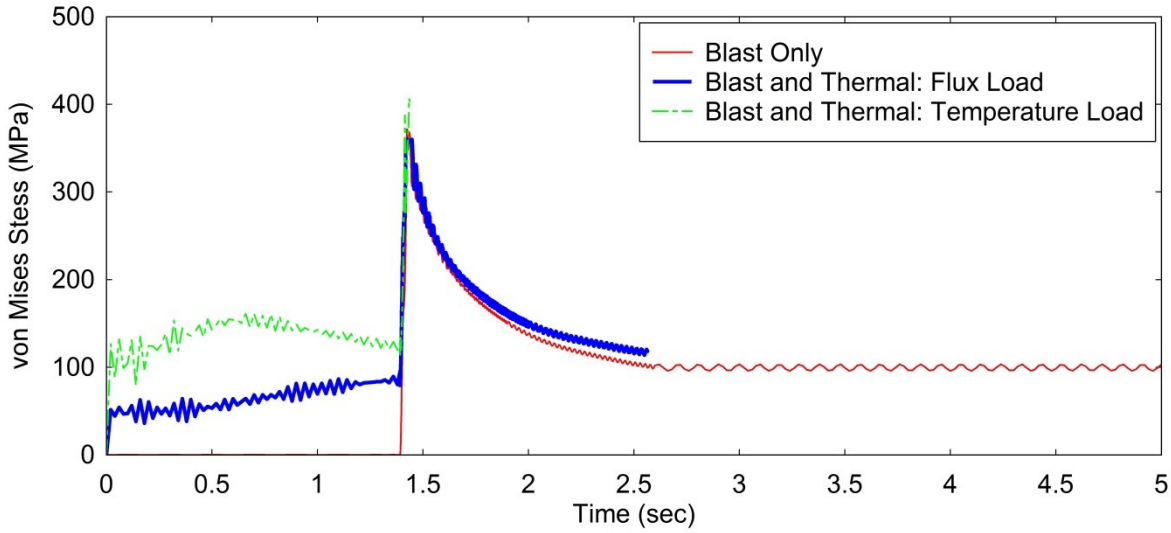

Figure D.35: Midpoint Stress: 384.9kPa Peak Pressure

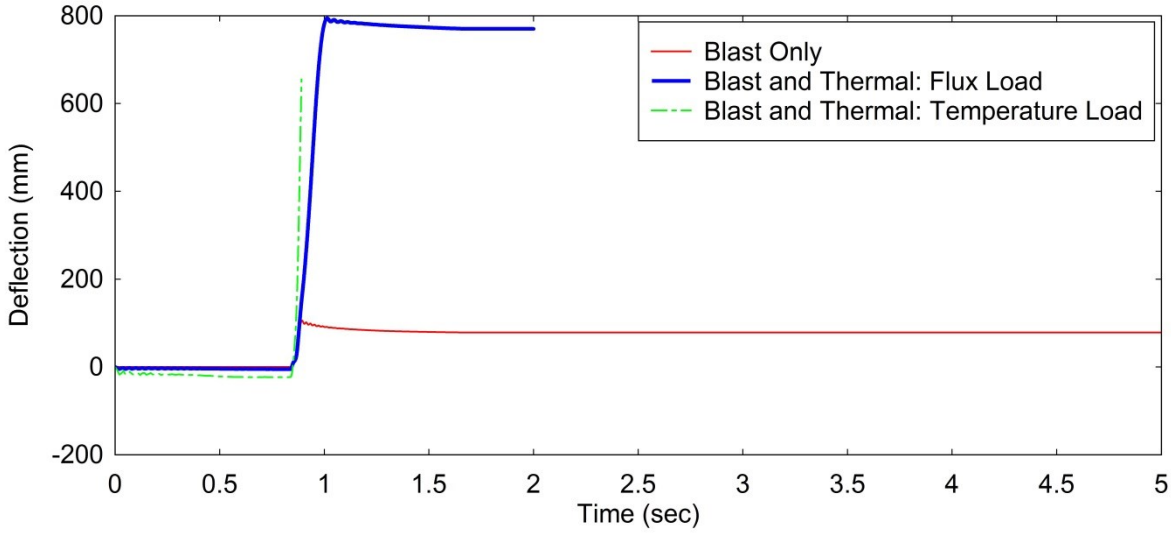

Figure D.36: Midpoint Deflection: 477.9kPa Peak Pressure

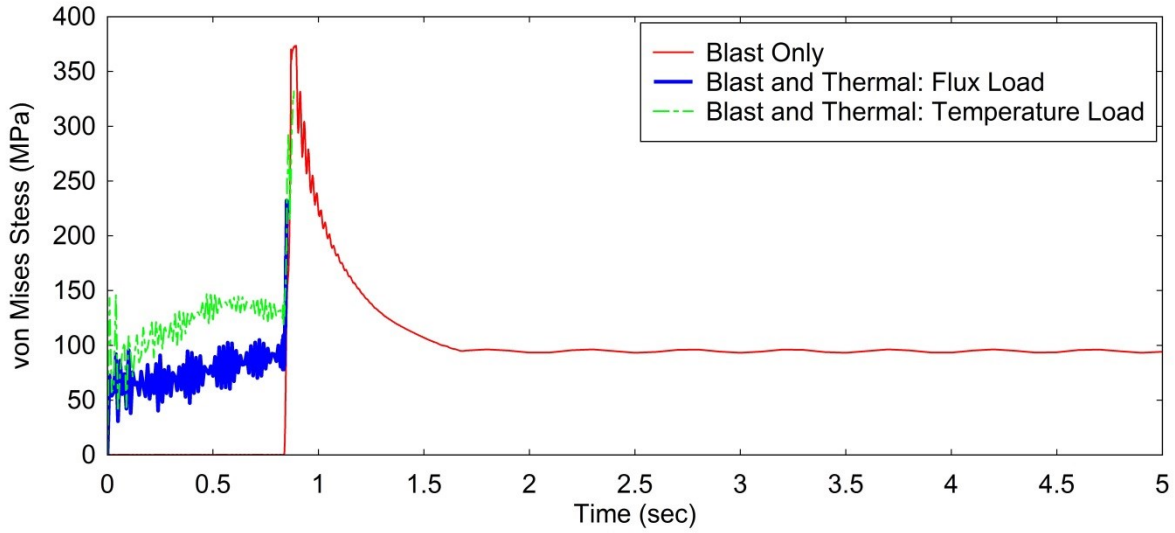

Figure D.37: Midpoint Stress: 477.9kPa Peak Pressure

Midpoint Deflection and Stress Histories (Varying Compressive Load)

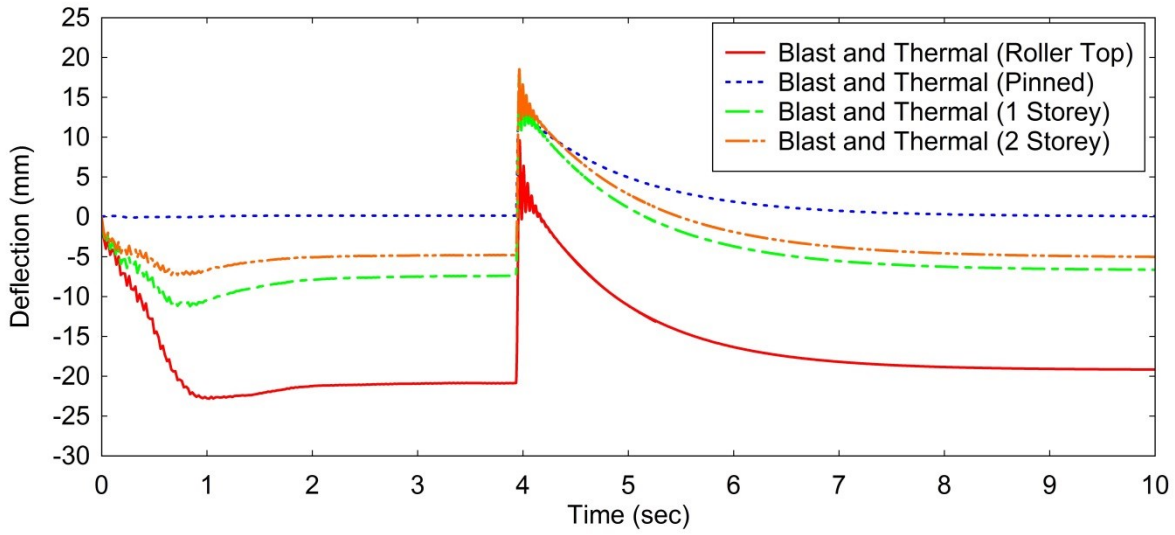

Figure D.38: Midpoint Deflection: Blast and Thermal, Varying Compression: 96.6kPa Peak Pressure

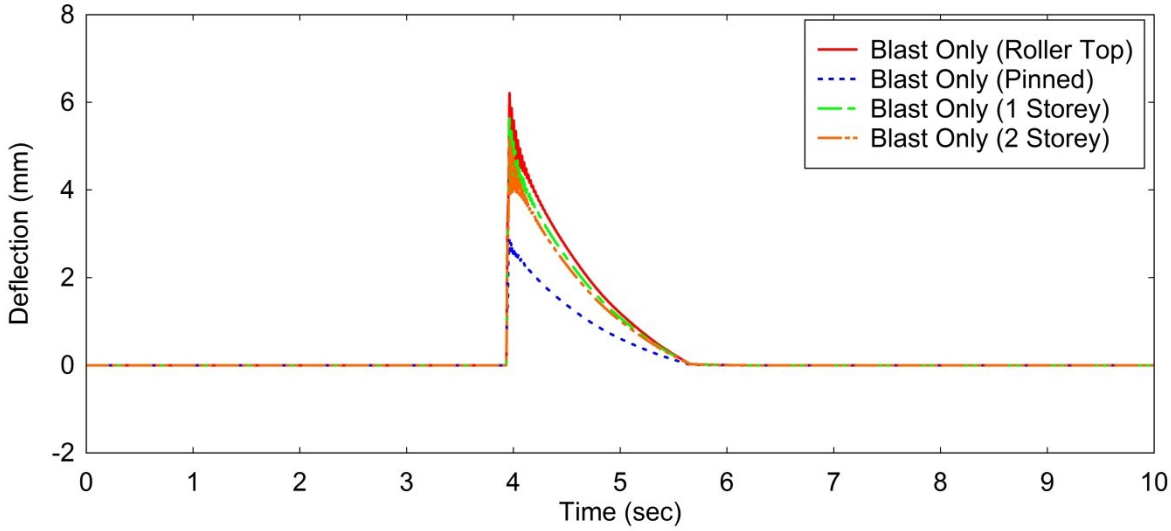

Figure D.39: Midpoint Deflection: Blast Only, Varying Compression: 96.6kPa Peak Pressure

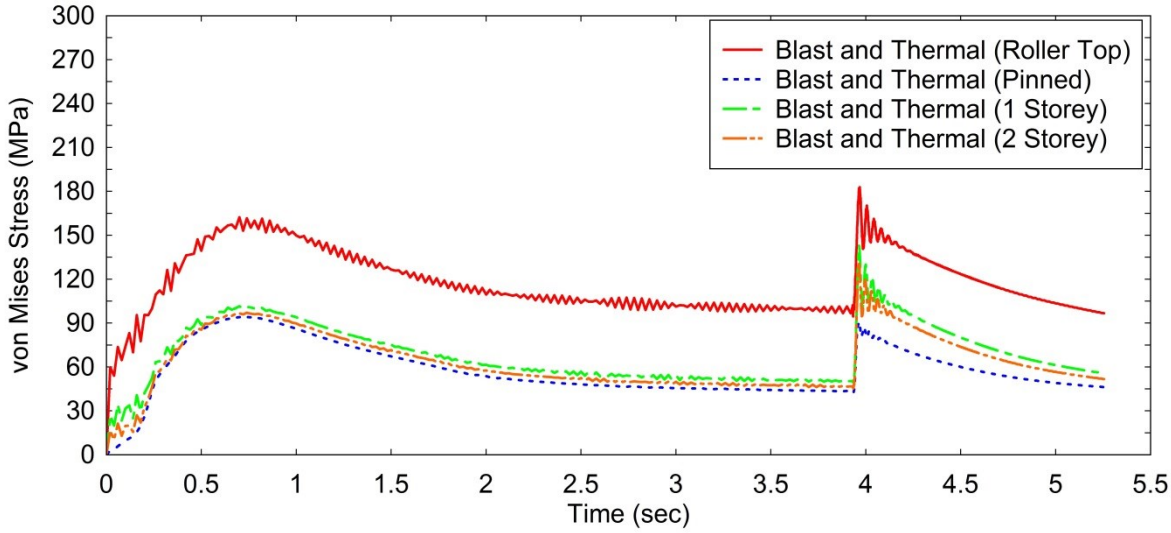

Figure D.40: Midpoint Stress: Blast and Thermal, Varying Compression: 96.6kPa Peak Pressure

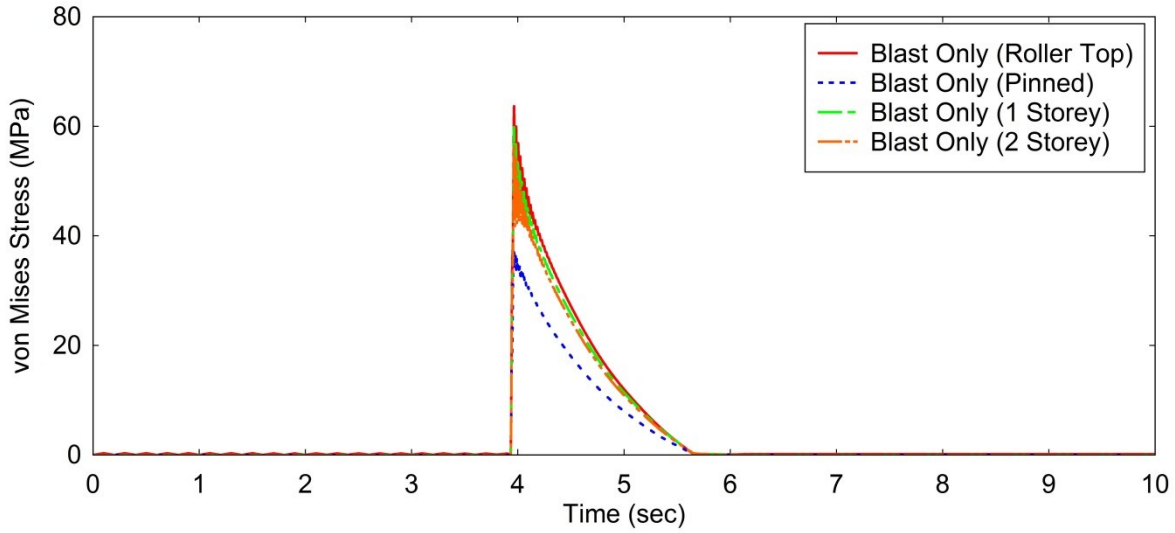

Figure D.41: Midpoint Stress: Blast Only, Varying Compression: 96.6kPa Peak Pressure

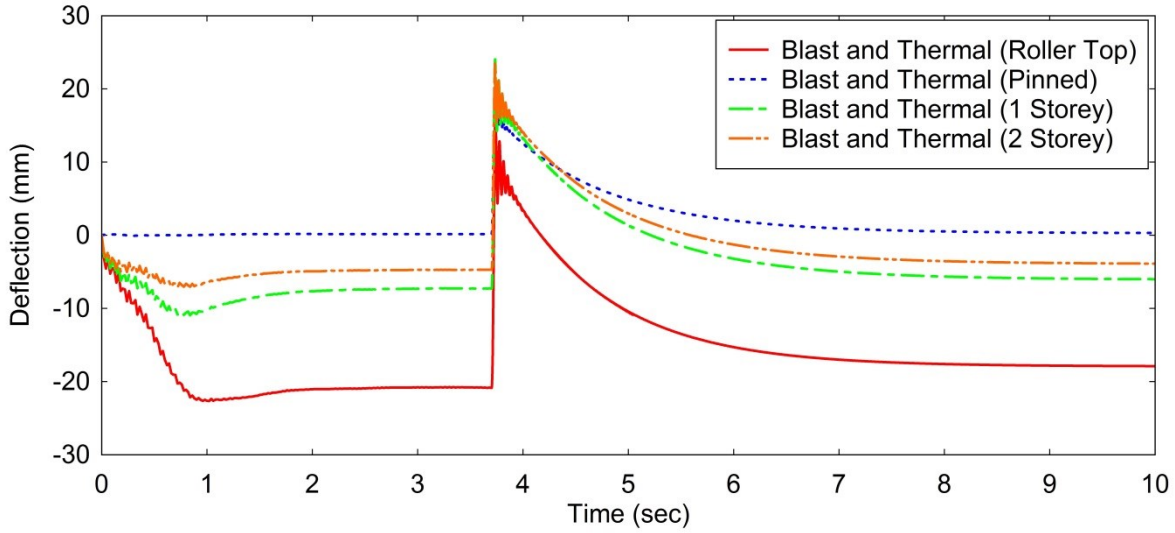

Figure D.42: Midpoint Deflection: Blast and Thermal, Varying Compression: 112kPa Peak Pressure

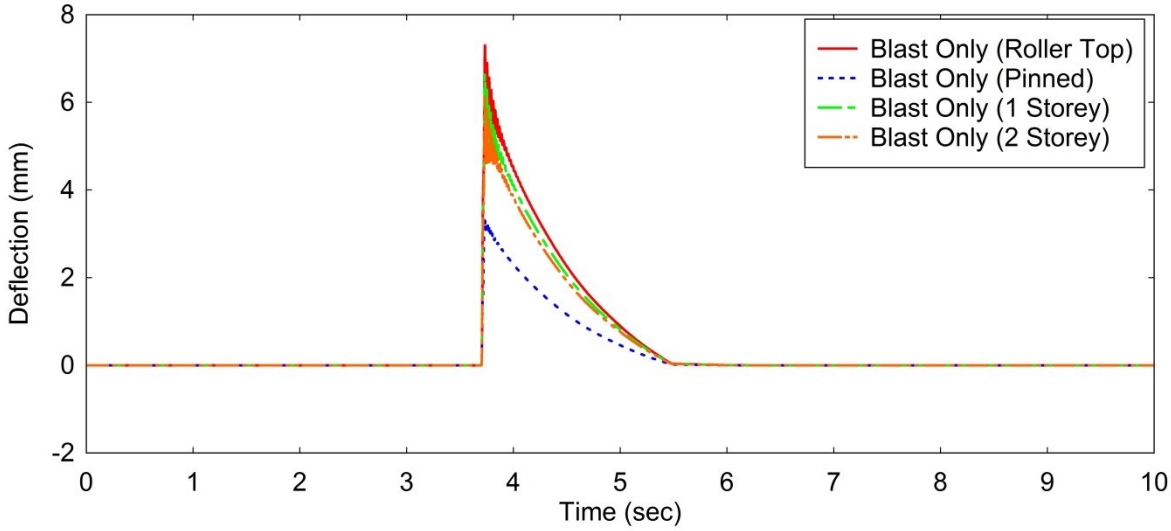

Figure D.43: Midpoint Deflection: Blast Only, Varying Compression: 112kPa Peak Pressure

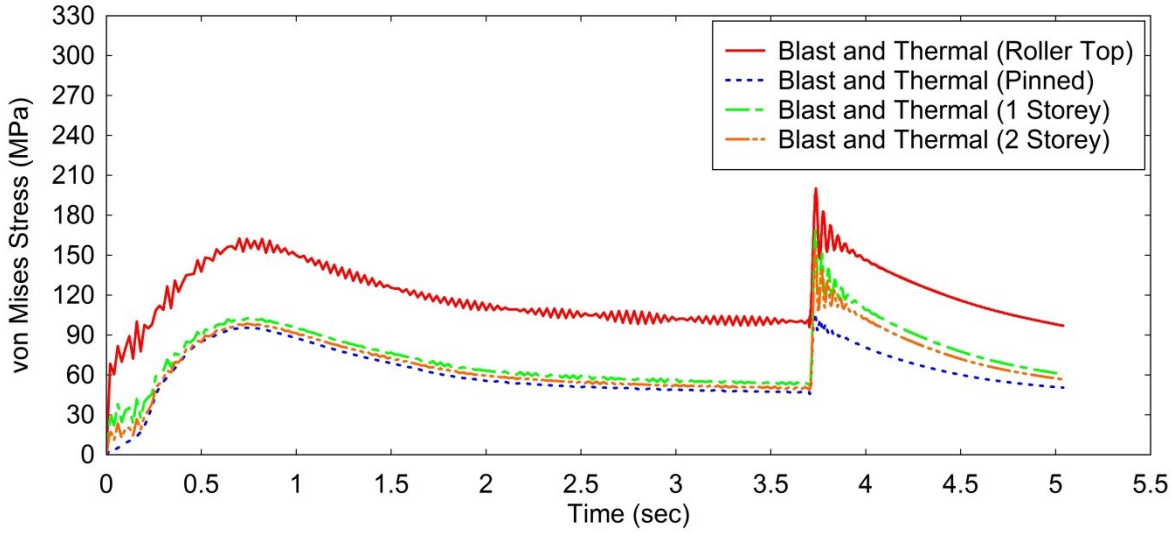

Figure D.44: Midpoint Stress: Blast and Thermal, Varying Compression: 112kPa Peak Pressure

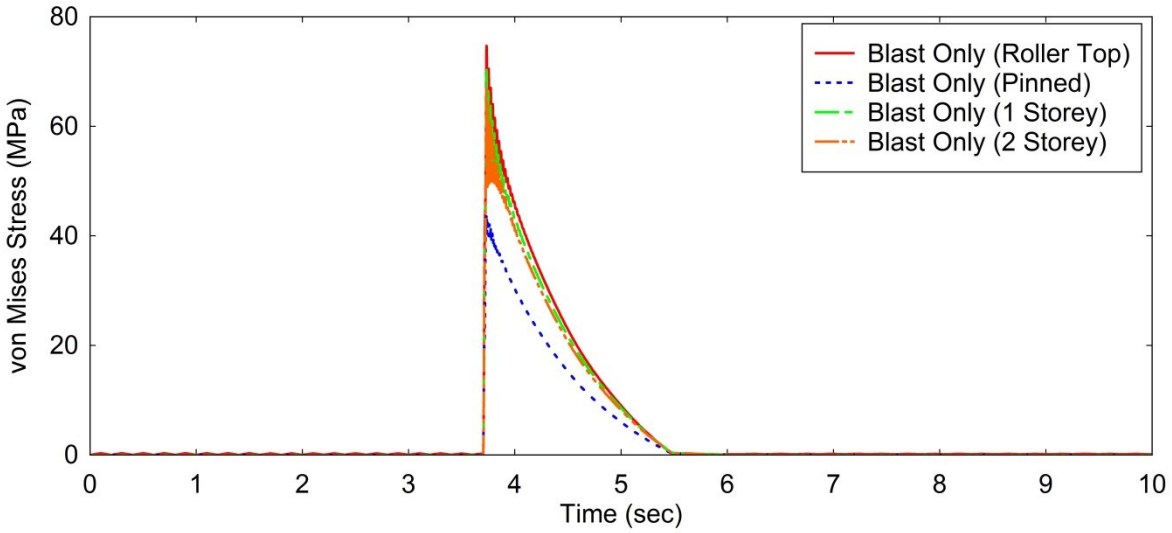

Figure D.45: Midpoint Stress: Blast Only, Varying Compression: 112kPa Peak Pressure

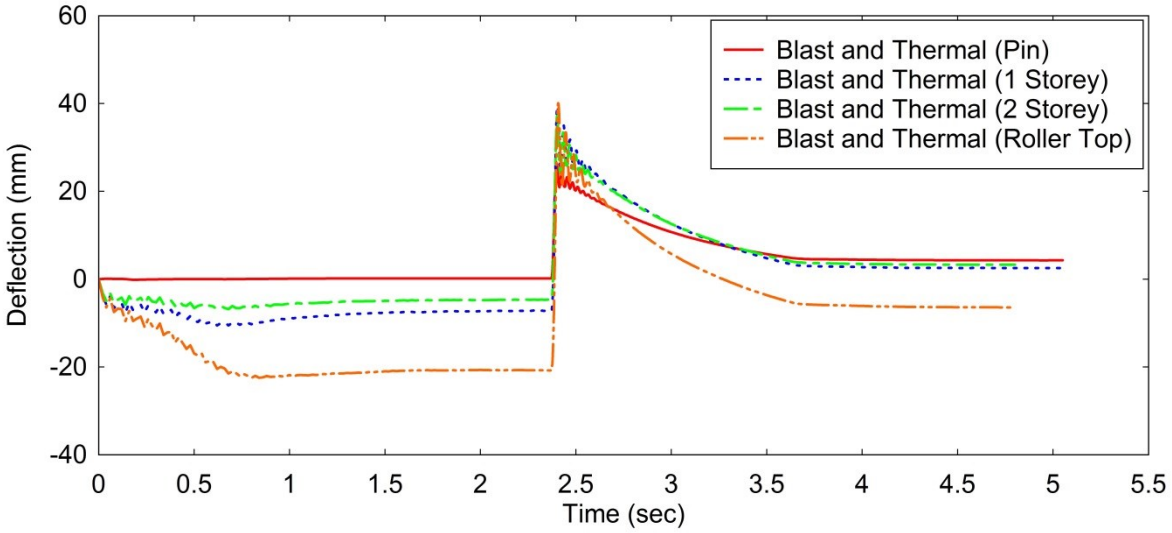

Figure D.46: Midpoint Deflection: Blast and Thermal, Varying Compression: 153.1kPa Peak Pressure

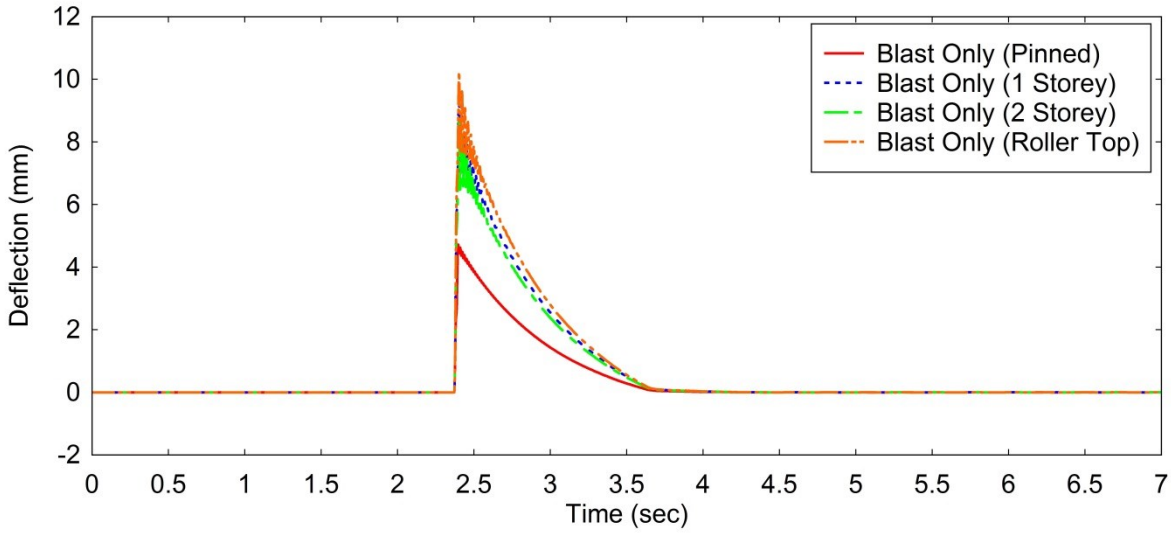

Figure D.47: Midpoint Deflection: Blast Only, Varying Compression: 153.1kPa Peak Pressure

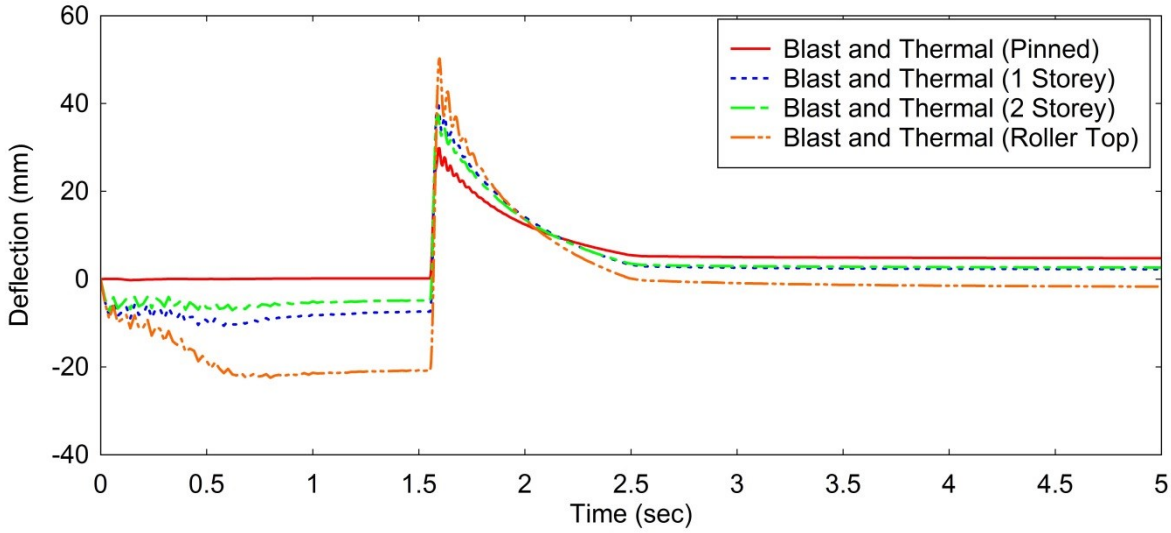

Figure D.48: Midpoint Deflection: Blast and Thermal, Varying Compression: 184.8kPa Peak Pressure

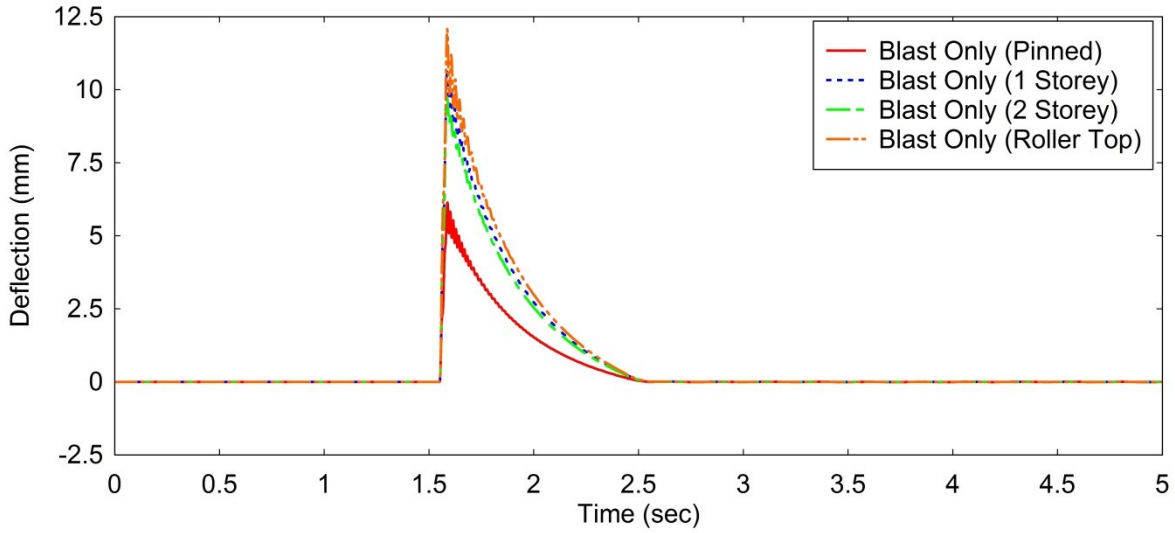

Figure D.49: Midpoint Deflection: Blast Only, Varying Compression: 184.8kPa Peak Pressure

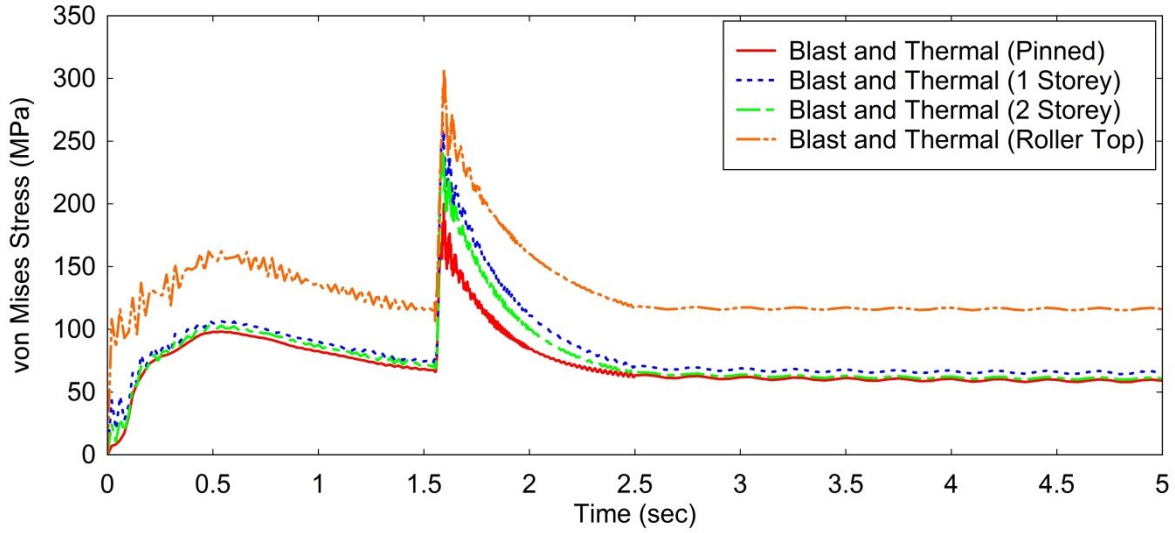

Figure D.50: Midpoint Stress: Blast and Thermal, Varying Compression: 184.8kPa Peak Pressure

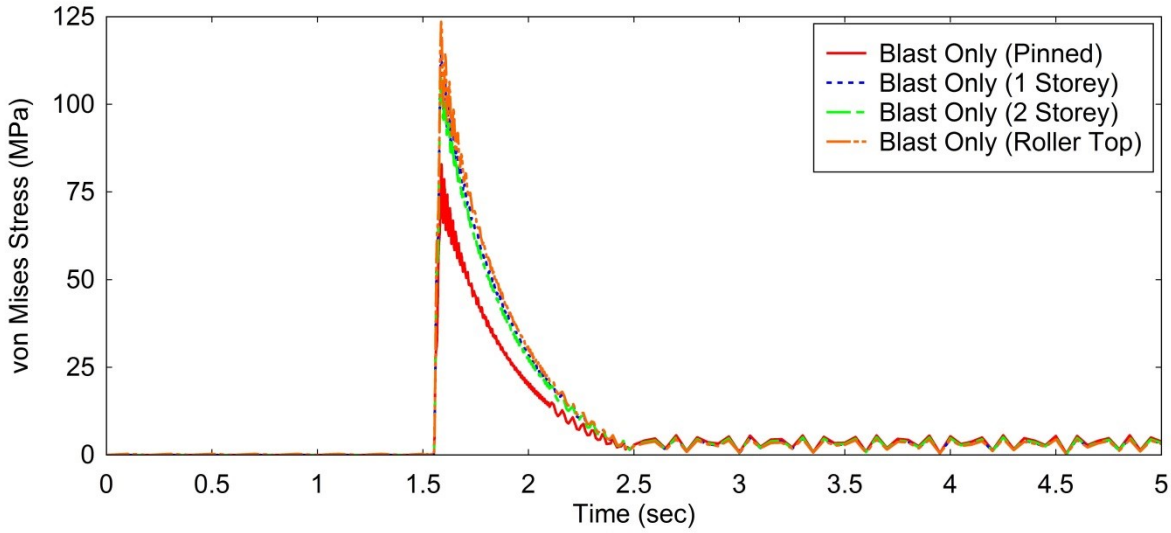

Figure D.51: Midpoint Stress: Blast Only, Varying Compression: 184.8kPa Peak Pressure

Midpoint Deflection Histories (Varying Thermal Conductivity

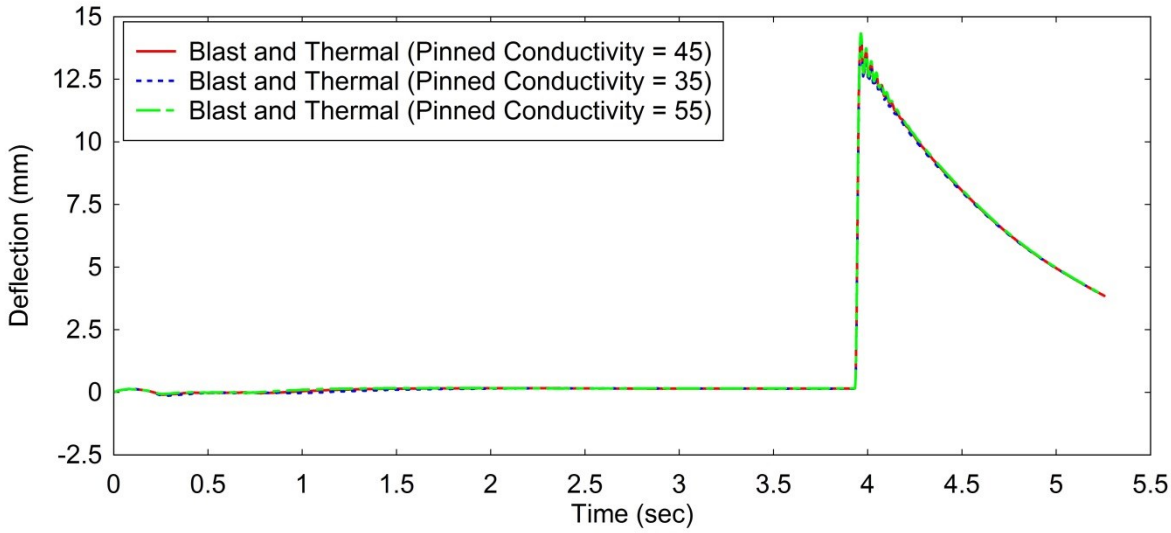

Figure D.52: Midpoint Deflection: Blast & Thermal, Varying Conductivity (W/m.^{o}K): 96.6kPa Peak Pressure

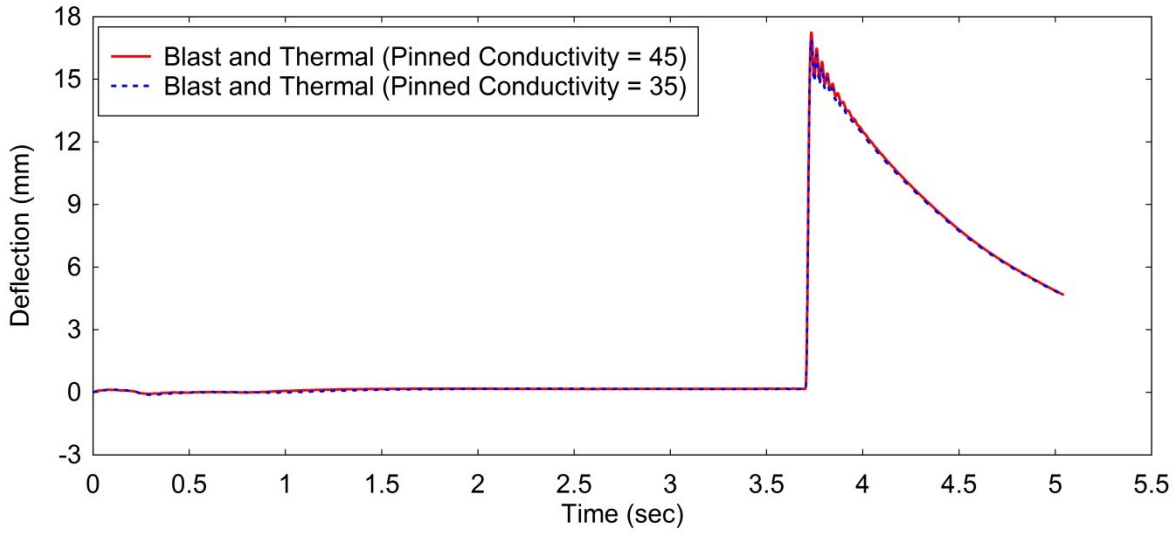

Figure D.53: Midpoint Deflection: Blast & Thermal, Varying Conductivity (W/m.°K): 112kPa Peak Pressure

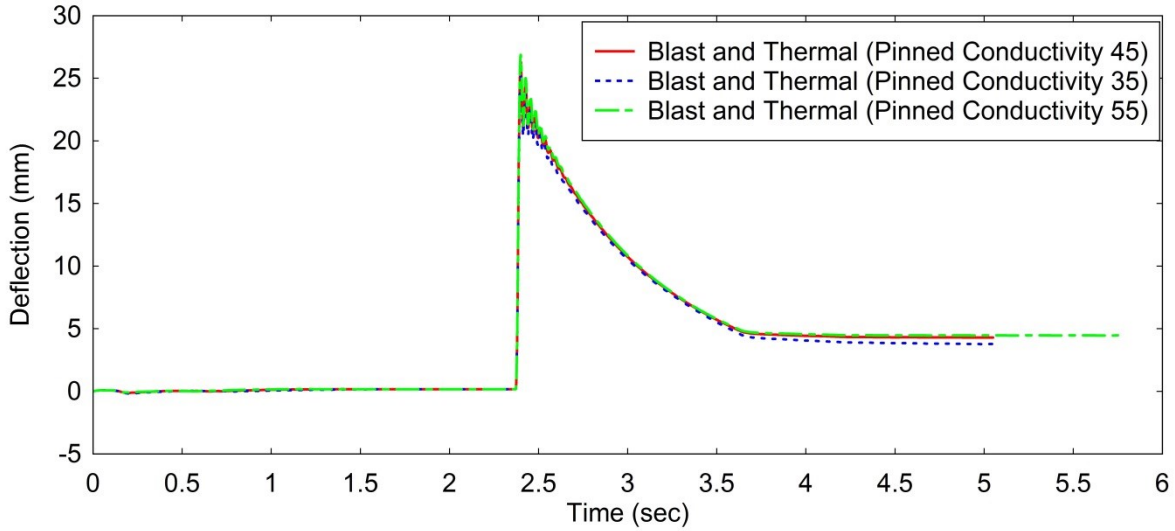

Figure D.54: Midpoint Deflection: Blast & Thermal, Varying Conductivity (W/m.°K): 153.1kPa Peak Pressure

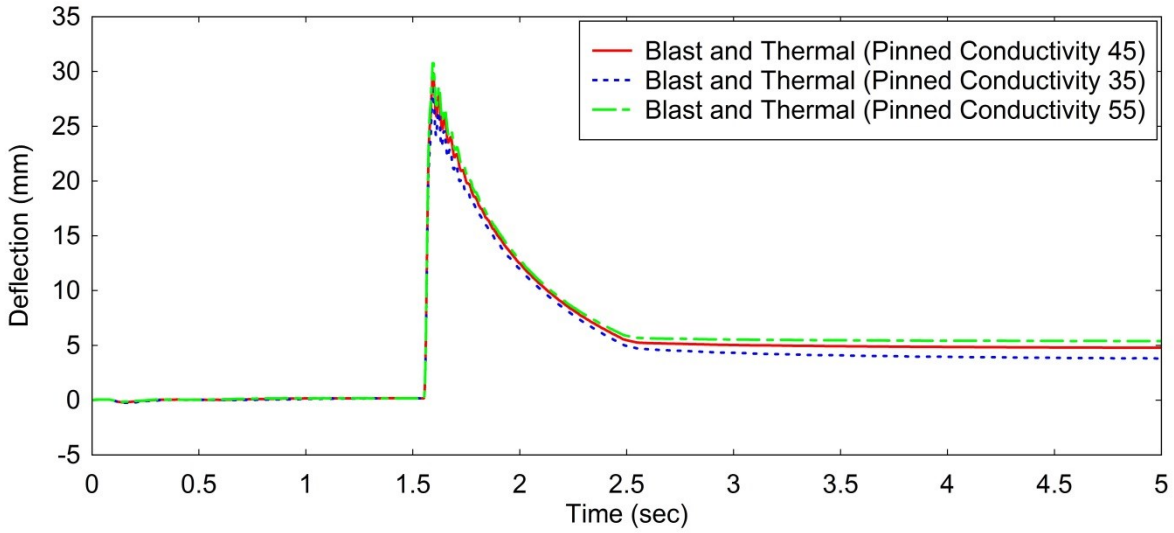

Figure D.55: Midpoint Deflection: Blast & Thermal, Varying Conductivity (W/m.°K): 184.8kPa Peak Pressure

Appendix E: Resistance Curves

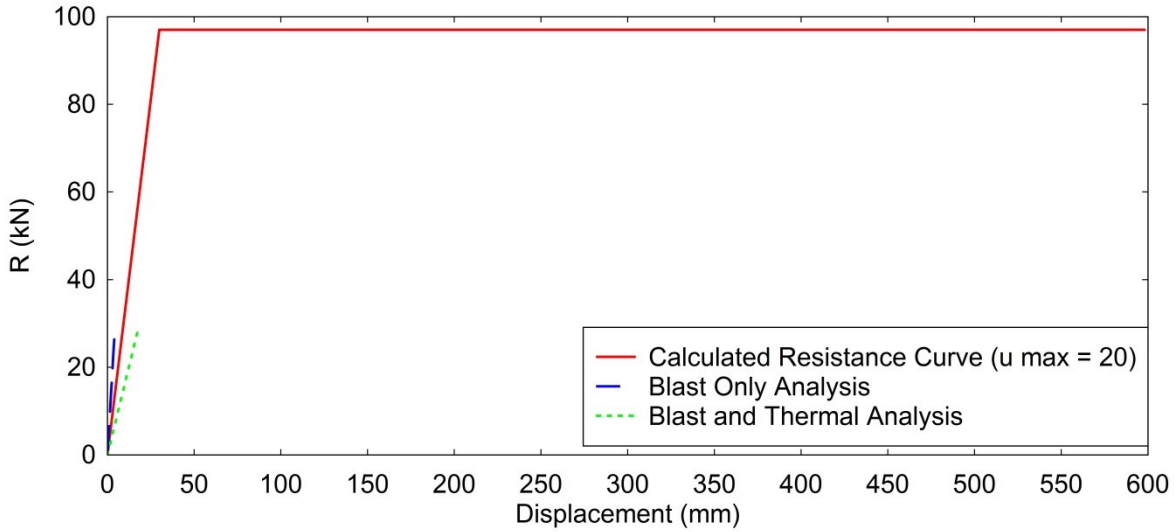

Figure E.1: Resistance Curve: 66.4kPa Peak Pressure

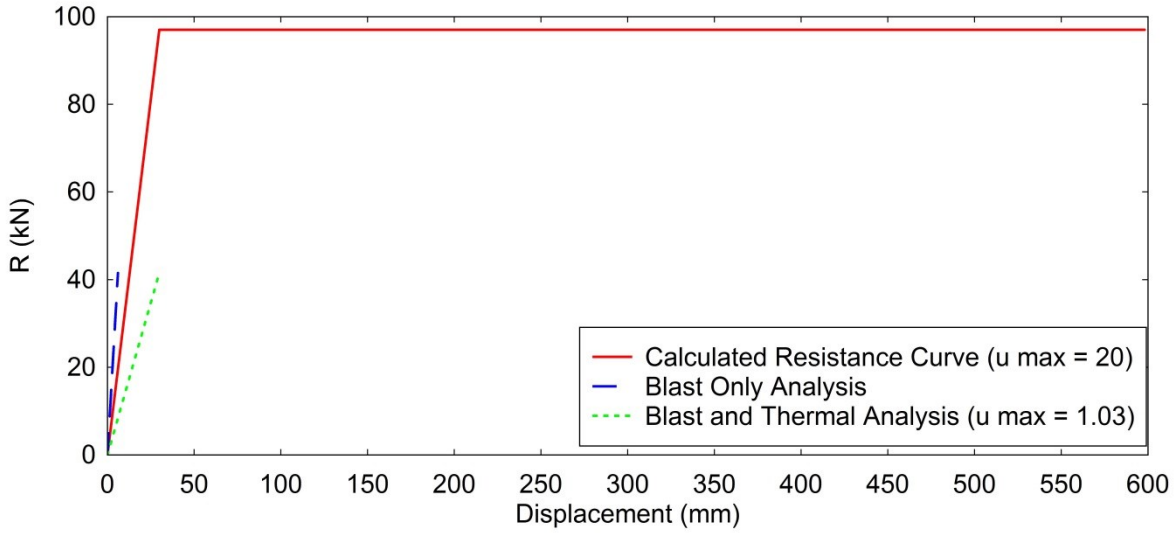

Figure E.2: Resistance Curve: 95.1kPa Peak Pressure

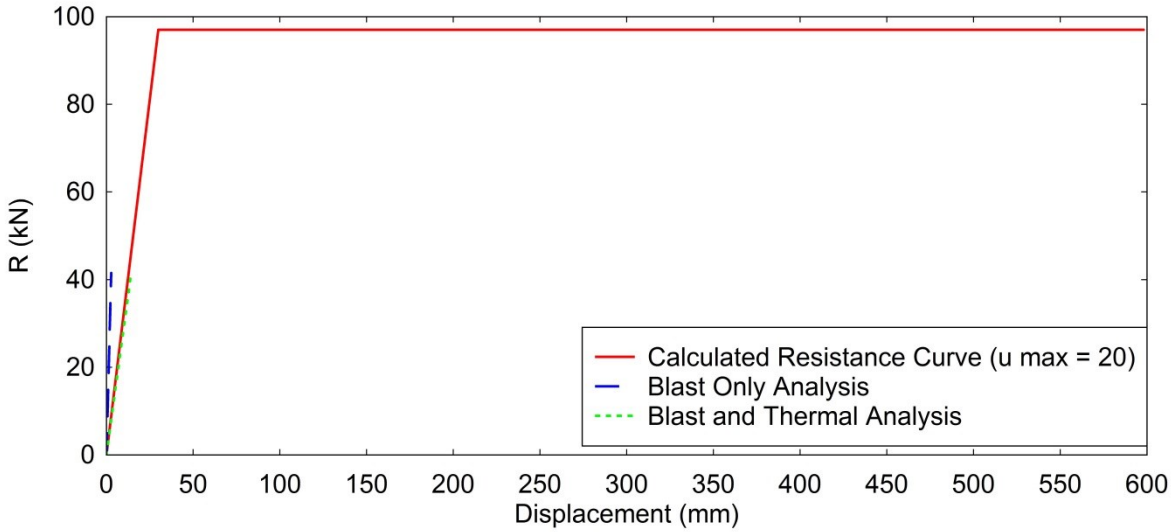

Figure E.3: Resistance Curve: 95.1kPa Peak Pressure (Pinned)

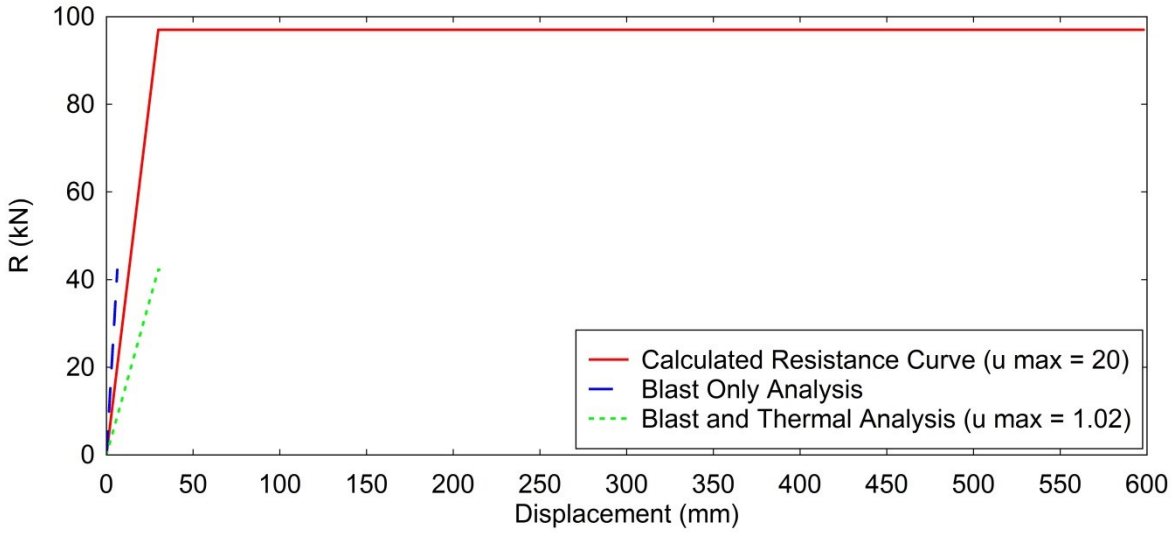

Figure E.4: Resistance Curve: 96.6kPa Peak Pressure

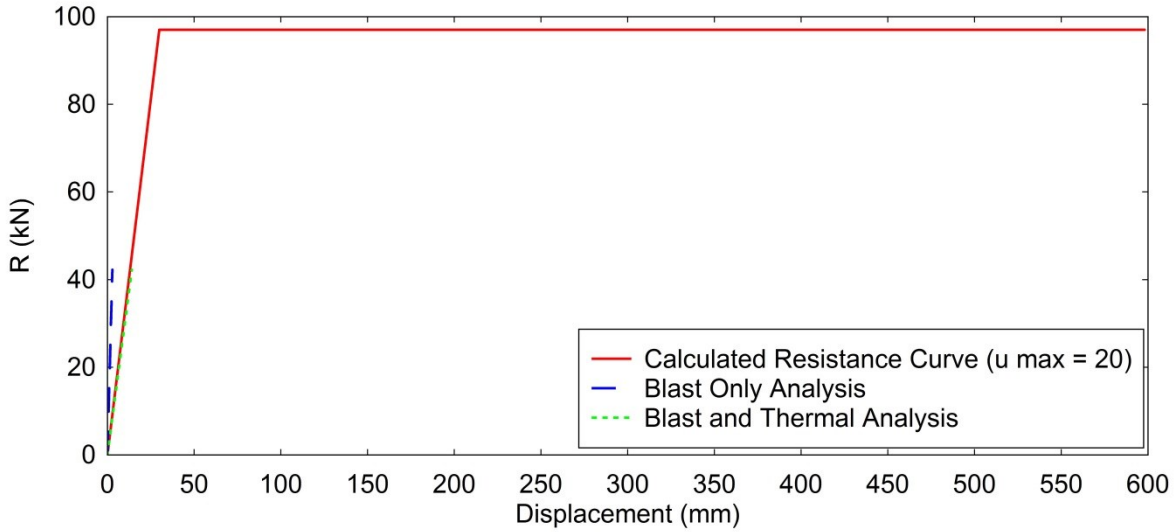

Figure E.5: Resistance Curve: 96.6kPa Peak Pressure (Pinned)

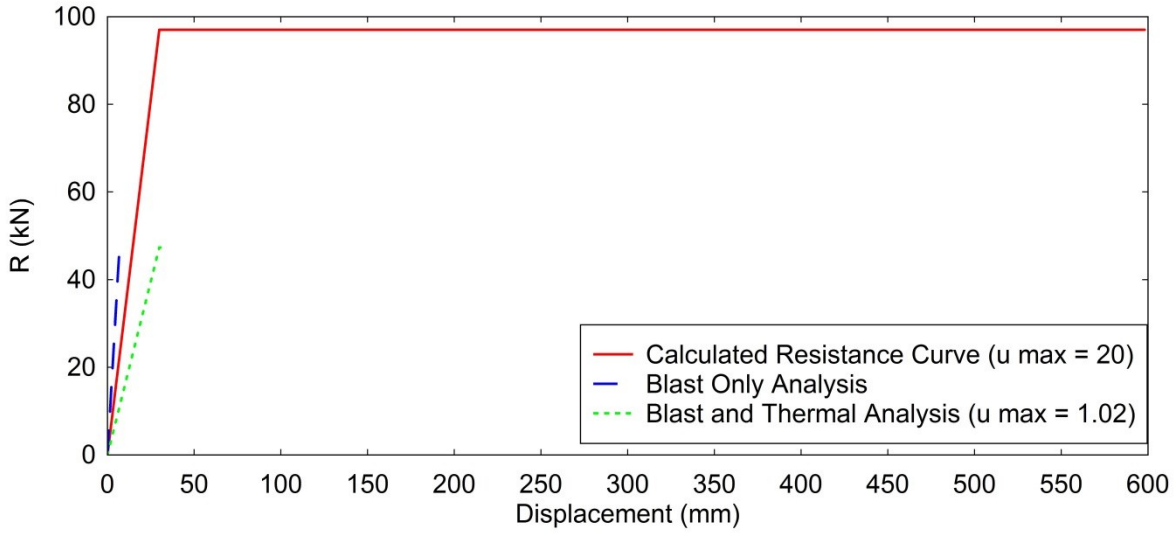

Figure E.6: Resistance Curve: 107.1kPa Peak Pressure

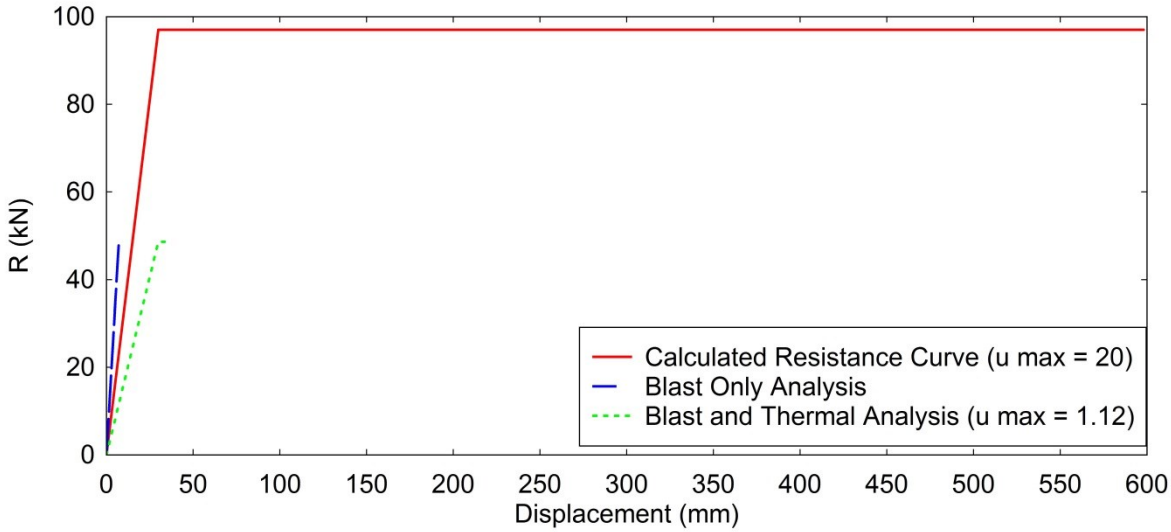

Figure E.7: Resistance Curve: 109.7kPa Peak Pressure

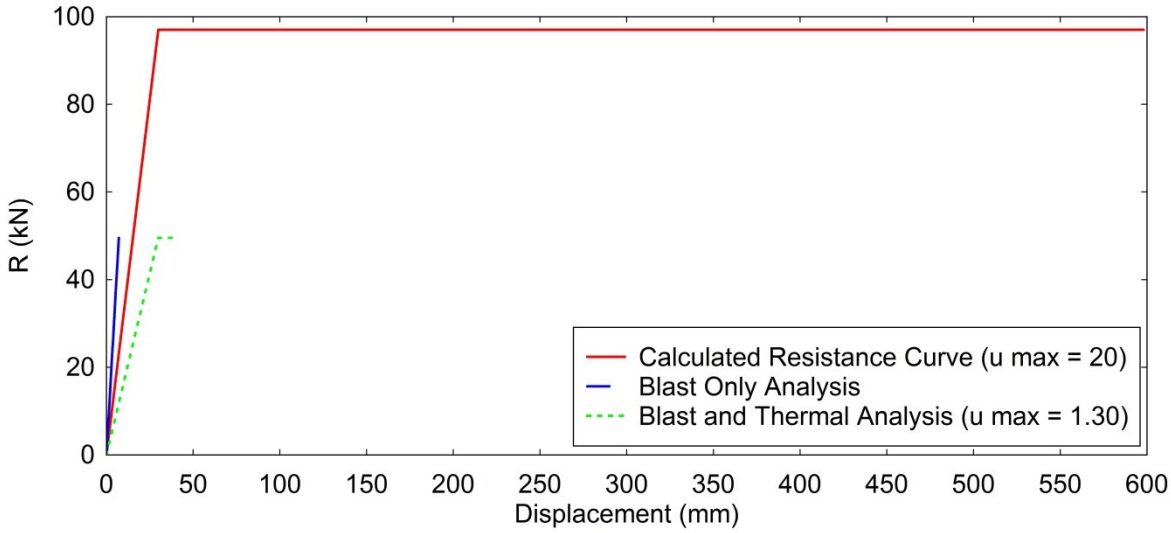

Figure E.8: Resistance Curve: 111.5kPa Peak Pressure

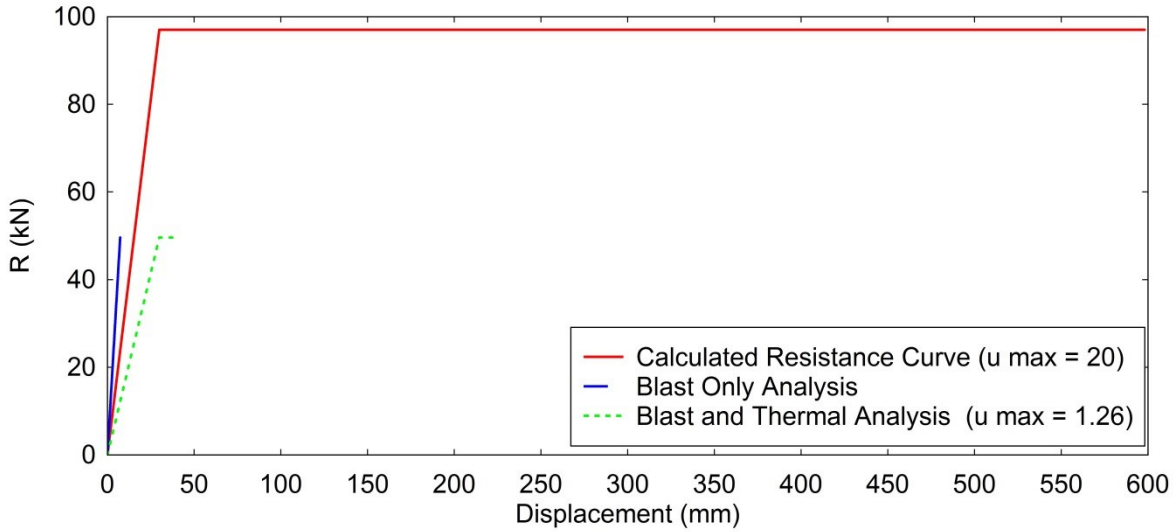

Figure E.9: Resistance Curve: 112kPa Peak Pressure

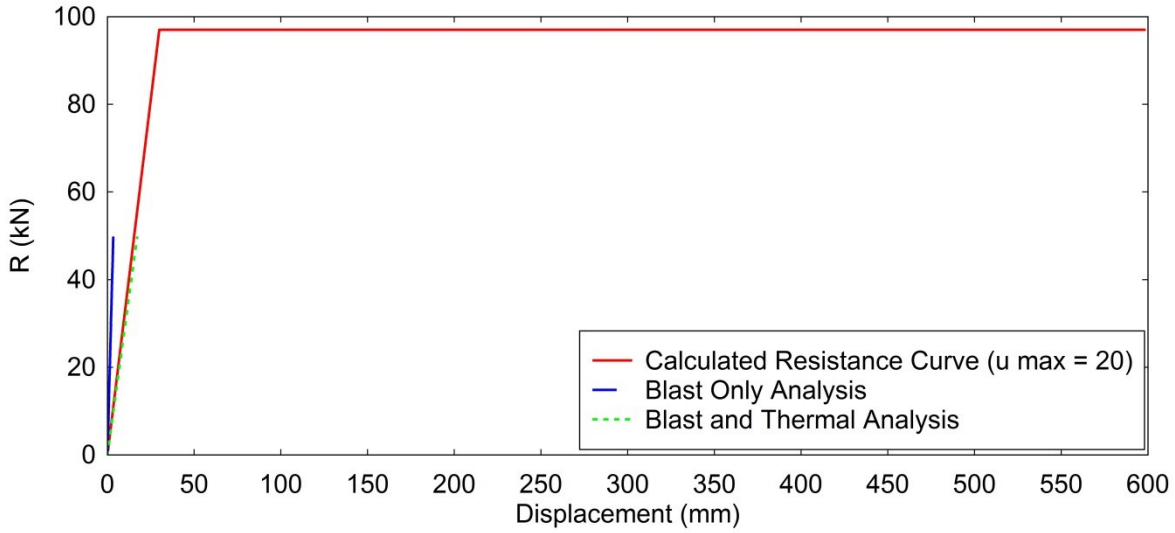

Figure E.10: Resistance Curve: 112kPa Peak Pressure (Pinned)

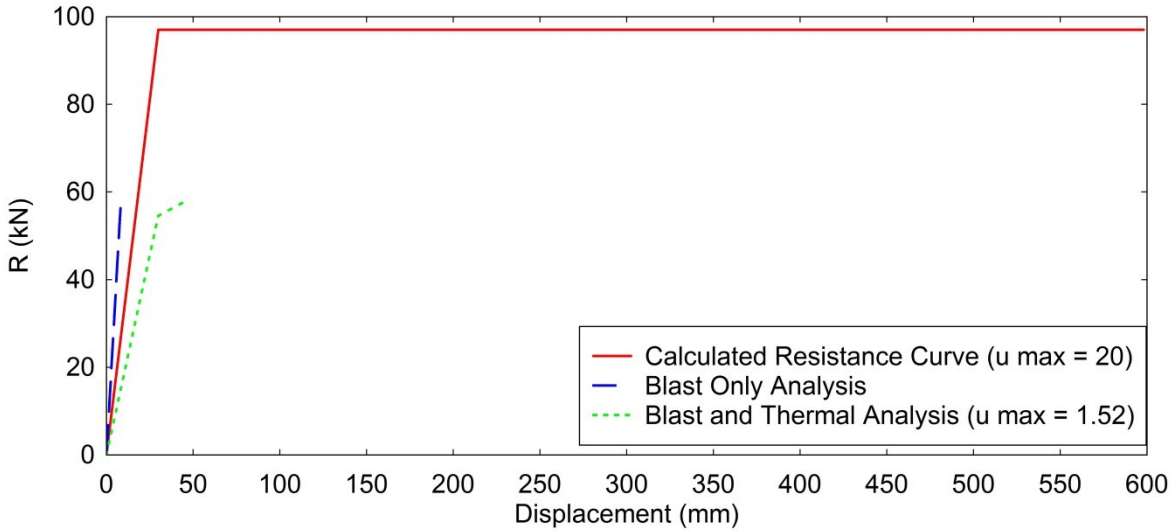

Figure E.11: Resistance Curve: 127.9kPa Peak Pressure

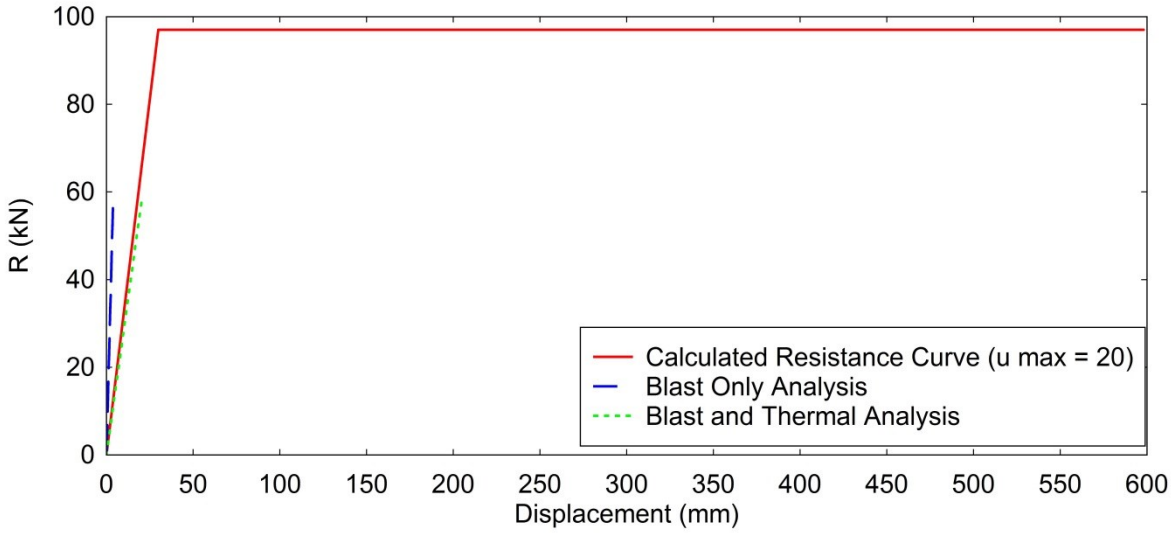

Figure E.12: Resistance Curve: 127.9kPa Peak Pressure (Pinned)

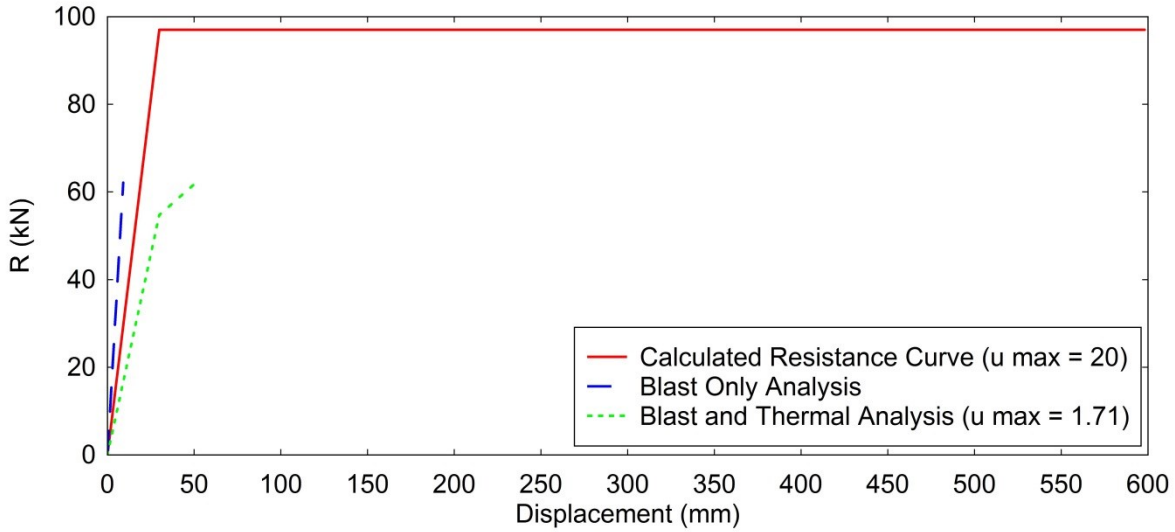

Figure E.13: Resistance Curve: 136.2kPa Peak Pressure

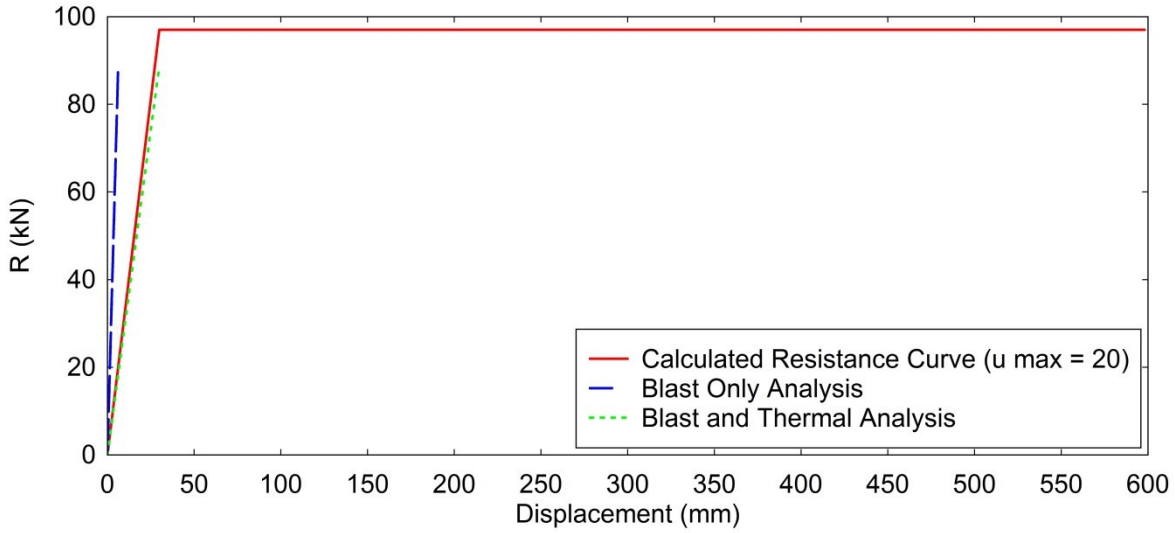

Figure E.14: Resistance Curve: 142.8kPa Peak Pressure (Pinned)

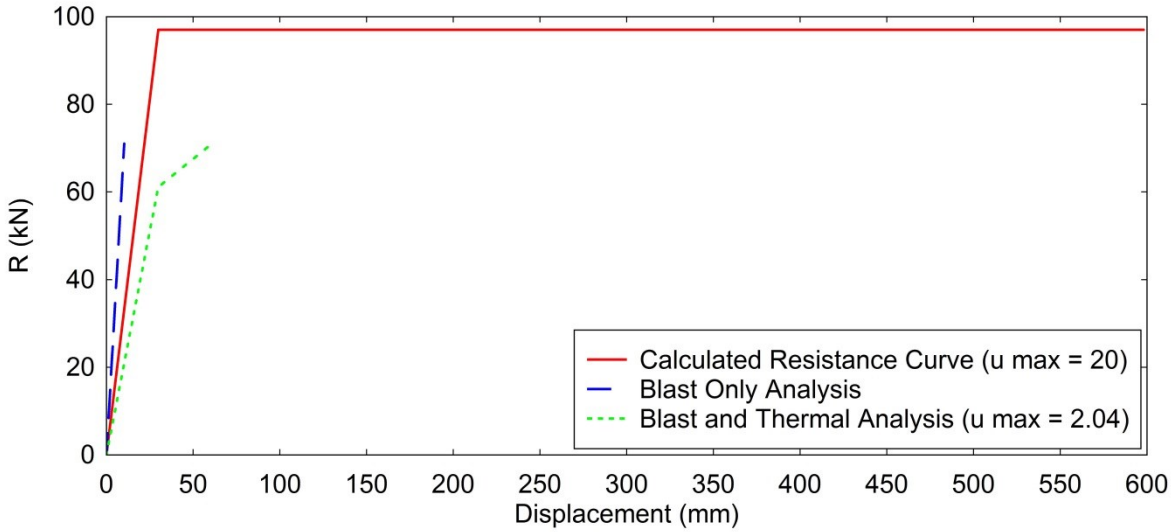

Figure E.15: Resistance Curve: 153.1kPa Peak Pressure

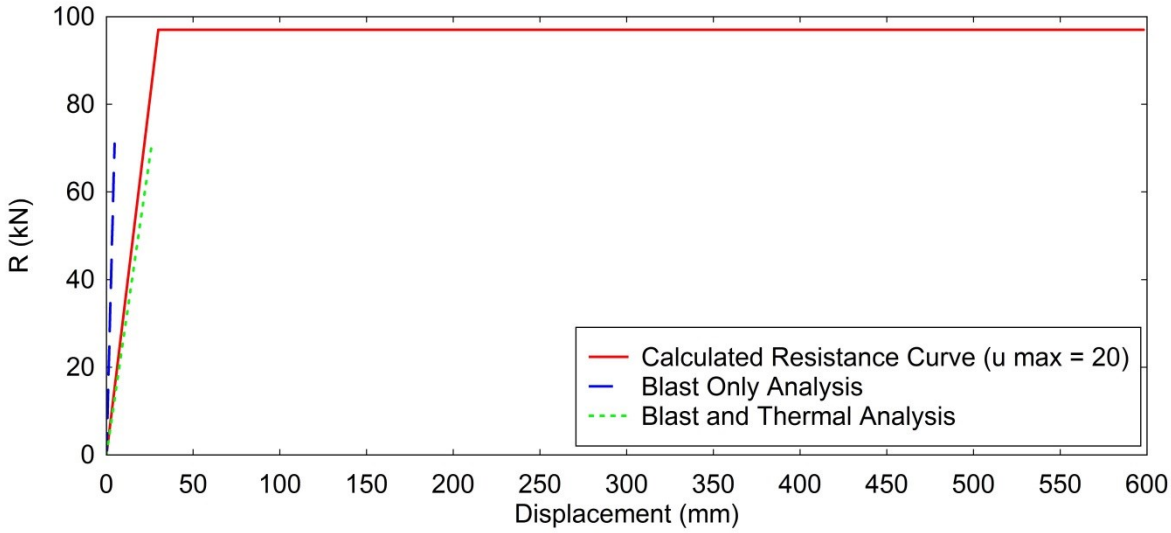

Figure E.16: Resistance Curve: 153.1kPa Peak Pressure (Pinned)

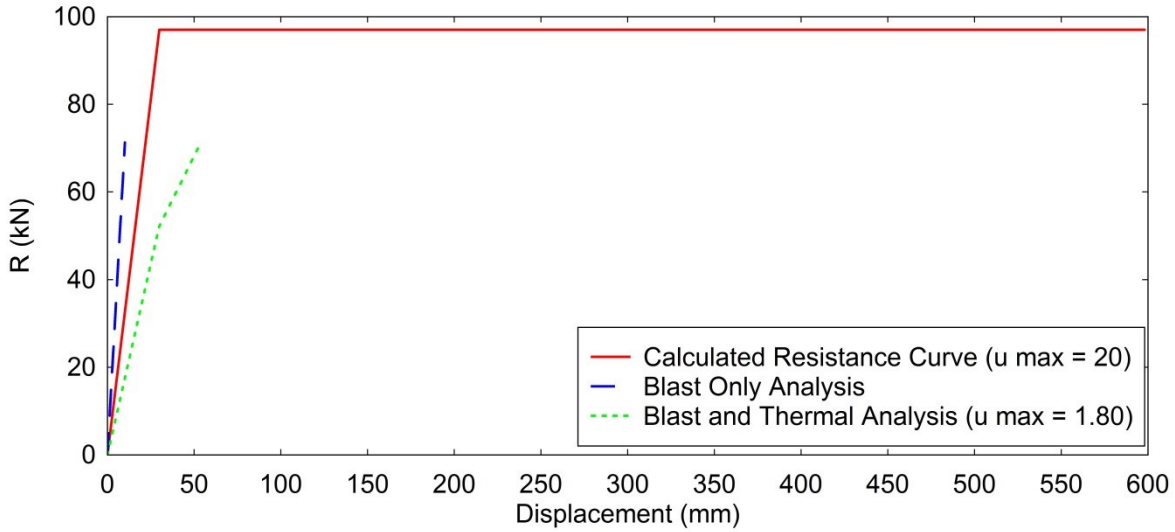

Figure E.17: Resistance Curve: 153.6kPa Peak Pressure

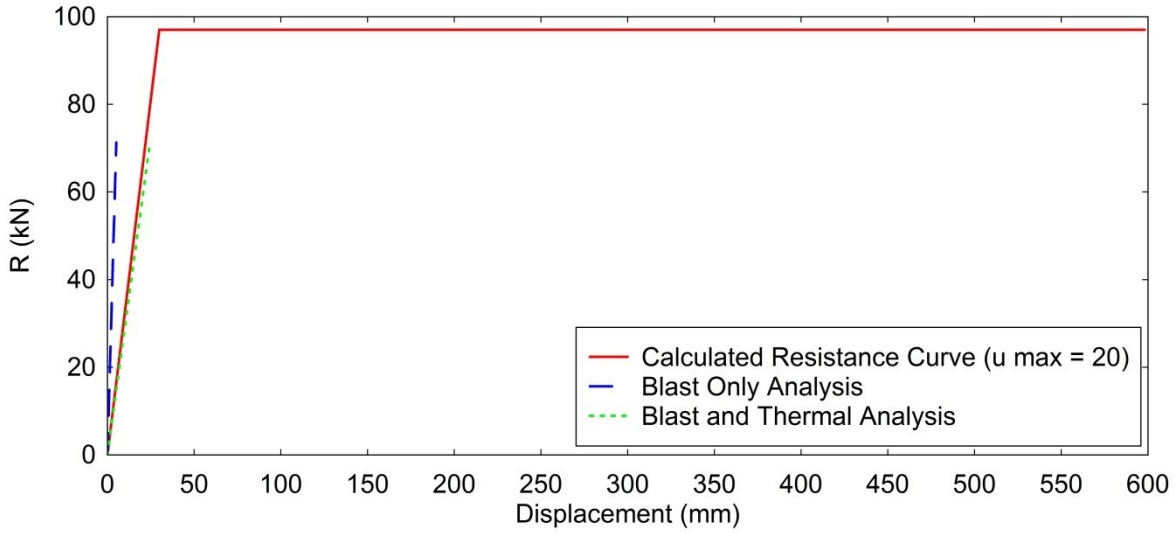

Figure E.18: Resistance Curve: 153.6kPa Peak Pressure (Pinned)

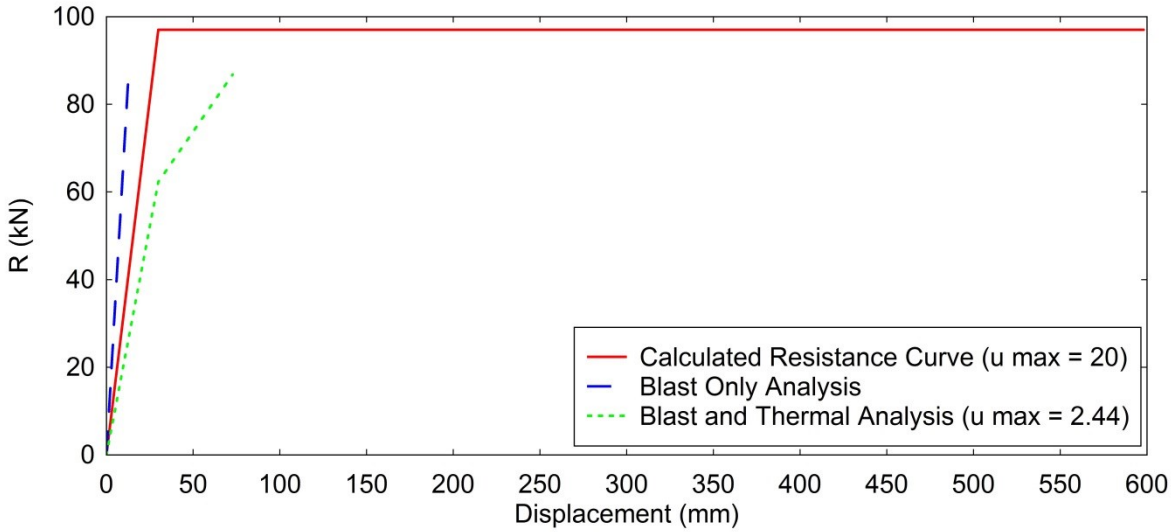

Figure E.19: Resistance Curve: 182.4kPa Peak Pressure

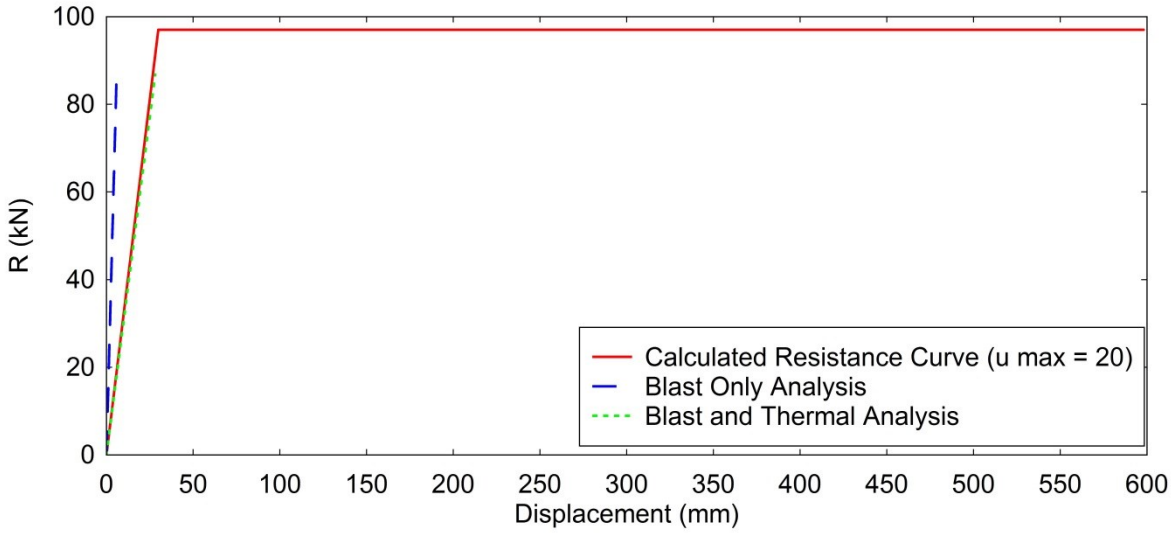

Figure E.20: Resistance Curve: 182.4kPa Peak Pressure (Pinned)

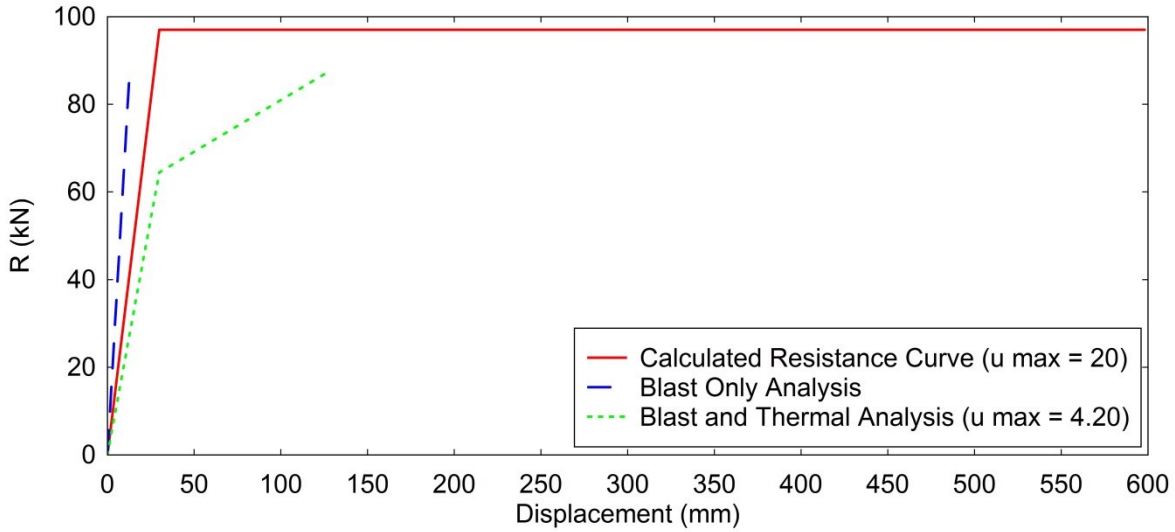

Figure E.21: Resistance Curve: 182.5kPa Peak Pressure

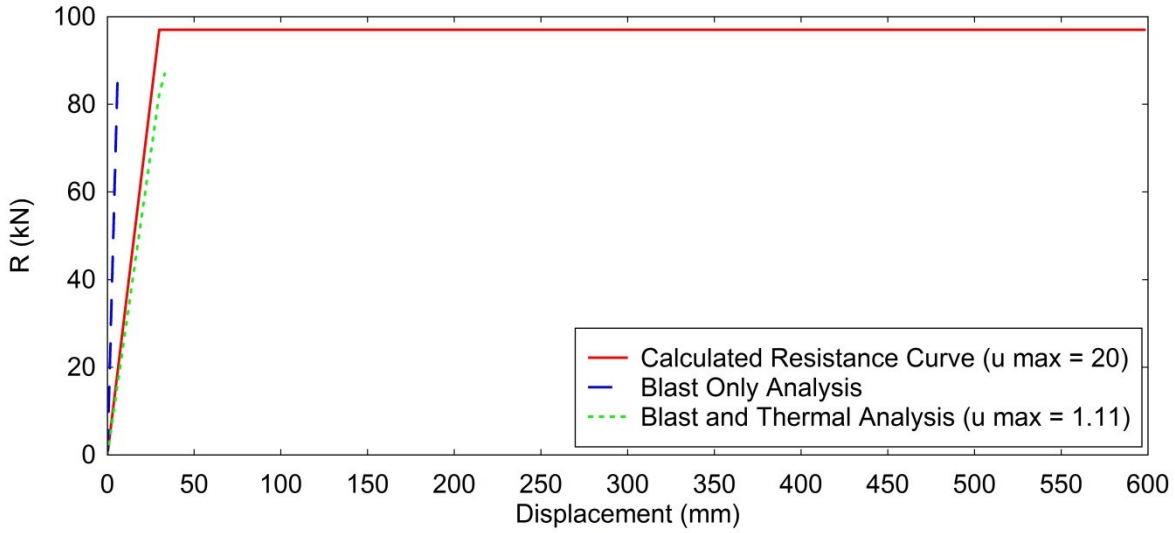

Figure E.22: Resistance Curve: 182.5kPa Peak Pressure (Pinned)

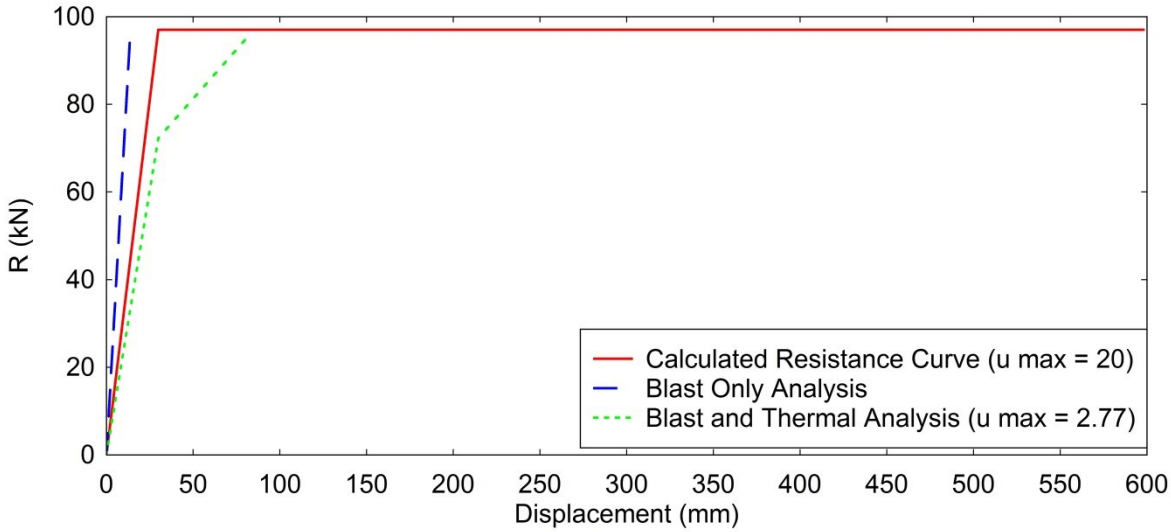

Figure E.23: Resistance Curve: 198.7kPa Peak Pressure

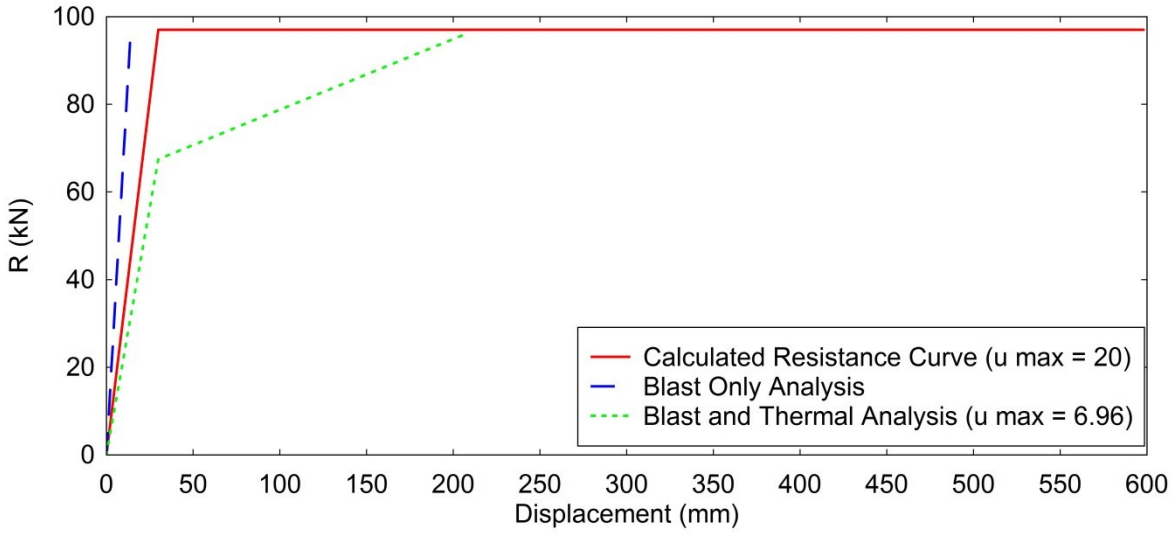

Figure E.24: Resistance Curve: 198.8kPa Peak Pressure

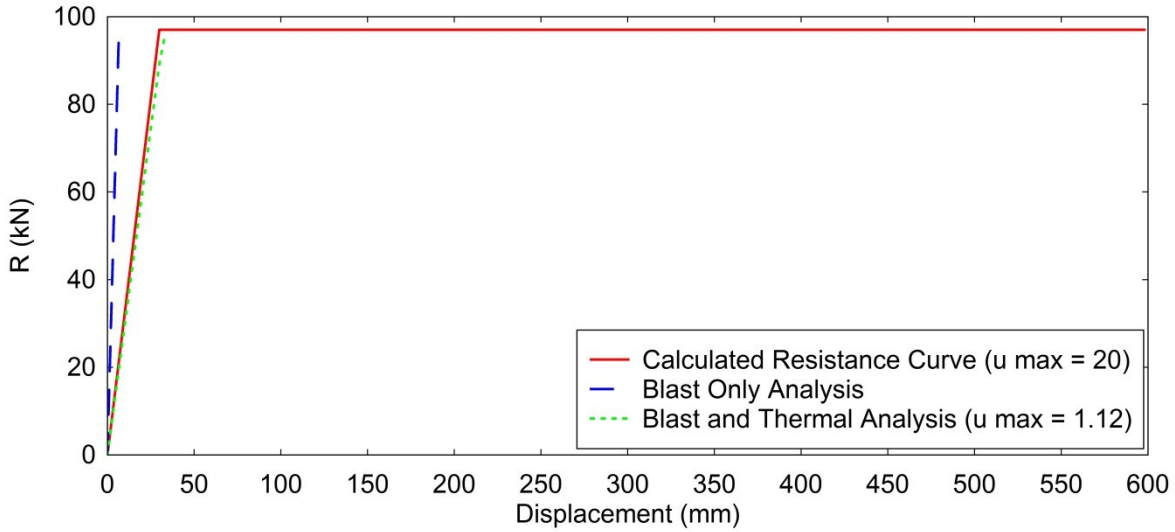

Figure E.25: Resistance Curve: 198.8kPa Peak Pressure (Pinned)

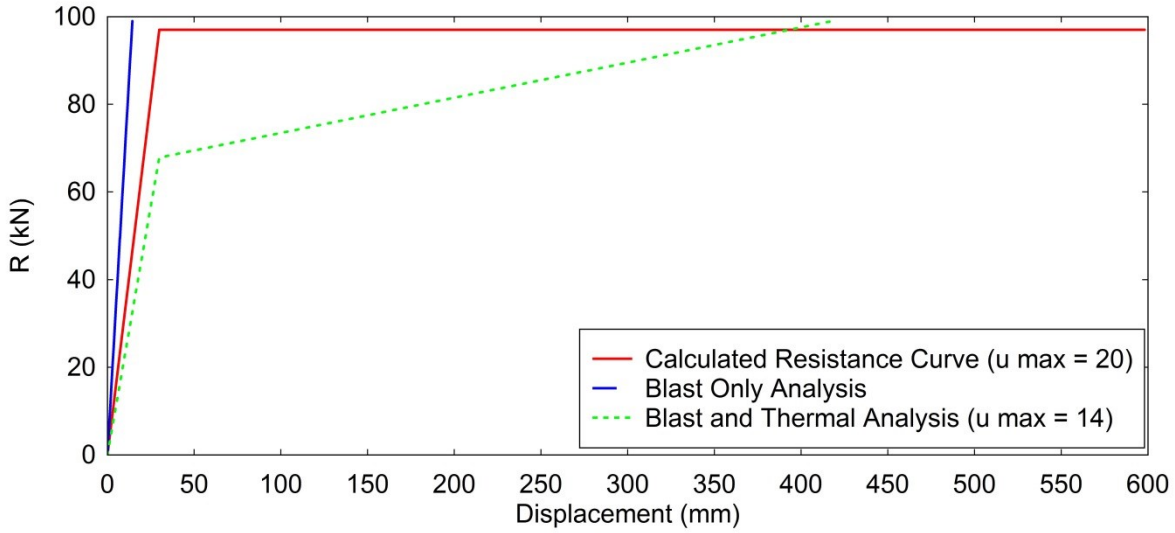

Figure E.26: Resistance Curve: 203.8kPa Peak Pressure

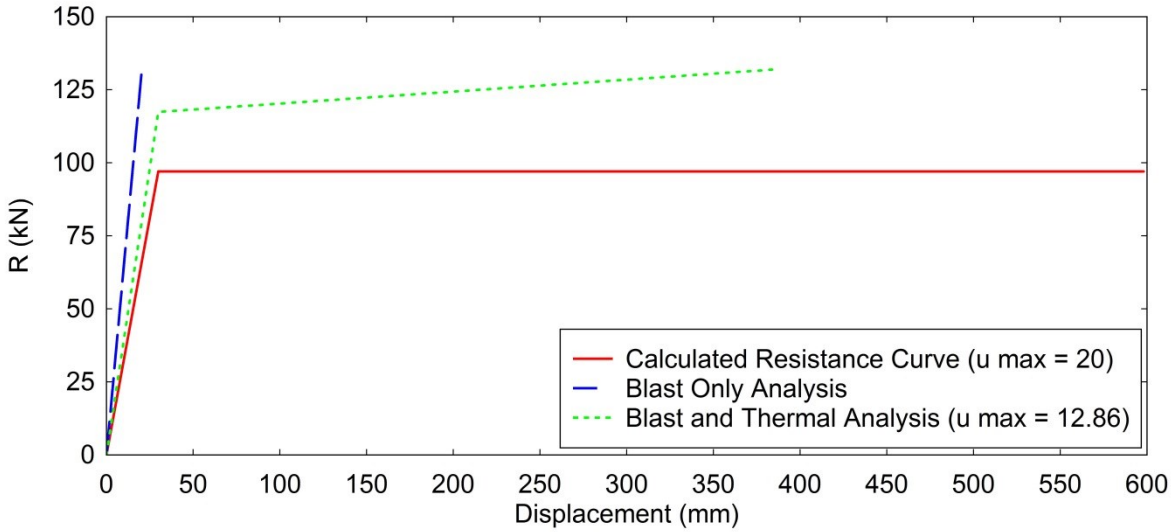

Figure E.27: Resistance Curve: 260.9kPa Peak Pressure

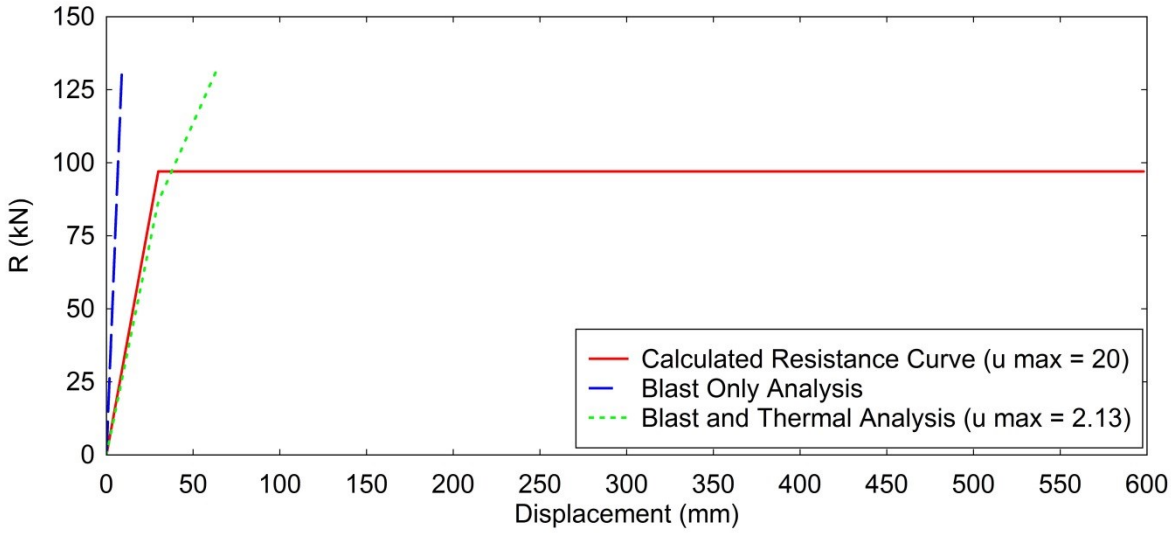

Figure E.28: Resistance Curve: 260.9kPa Peak Pressure (Pinned)

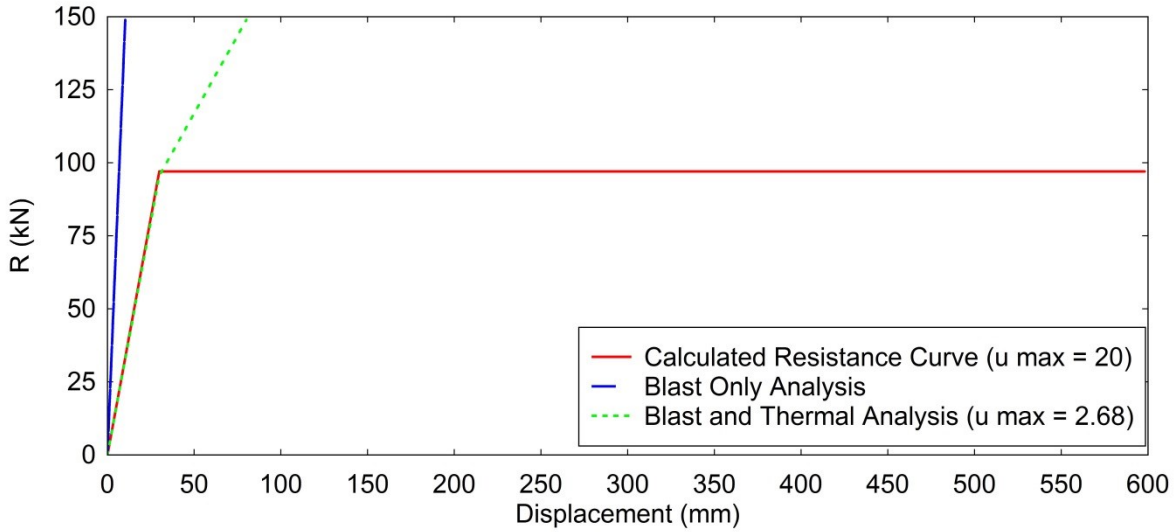

Figure E.29: Resistance Curve: 290.3kPa Peak Pressure (Pinned)

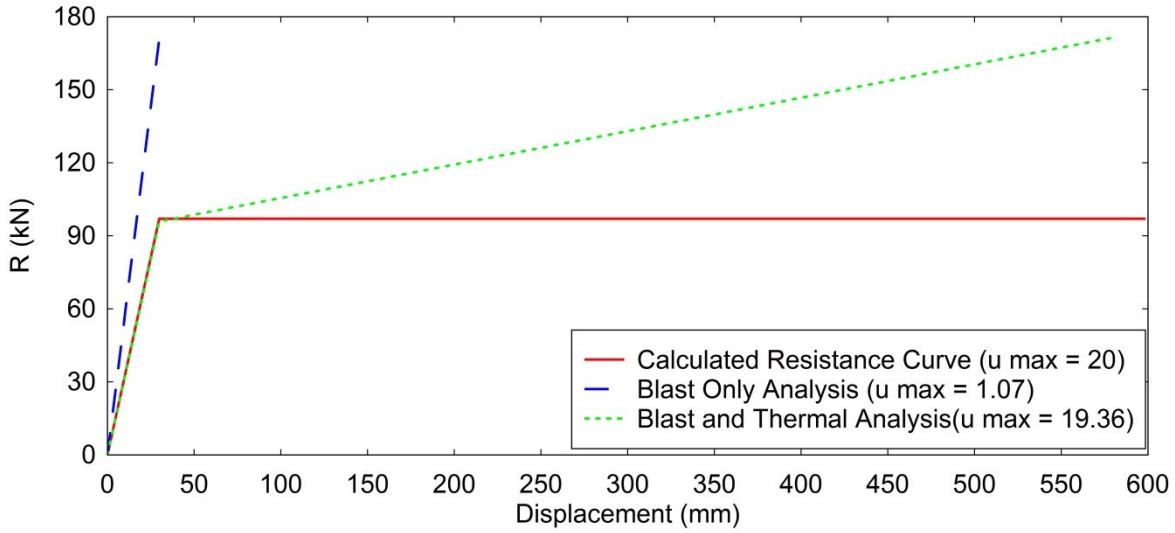

Figure E.30: Resistance Curve: 329.2kPa Peak Pressure

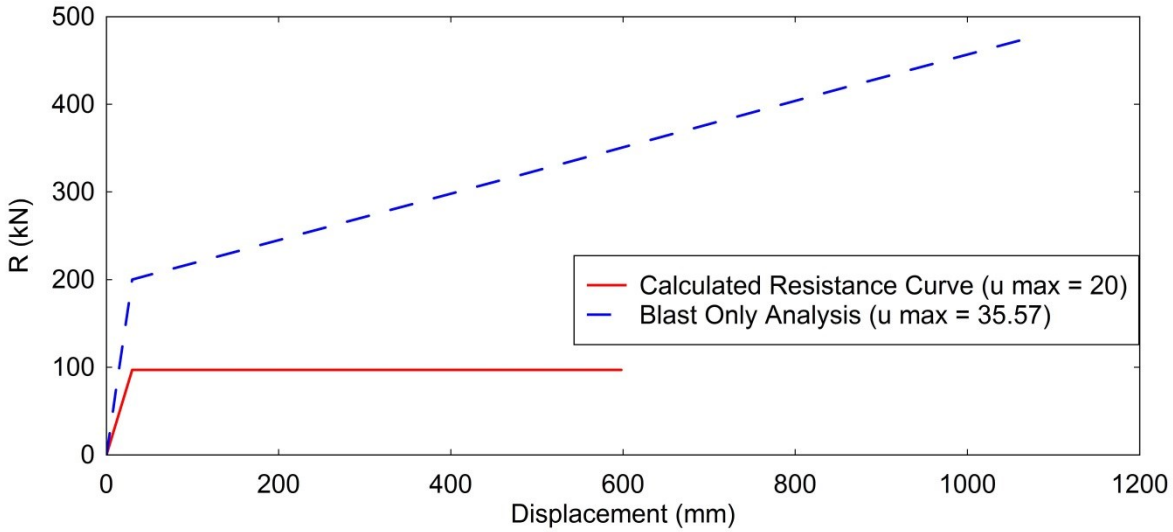

Figure E.31: Resistance Curve: 912.7kPa Peak Pressure (No Thermal)

Appendix F: ISIEMS Paper: Gauging the Fireball: Simulation and Testing

Gauging the Fireball: Simulation and Testing

Laurence G. Clough[1], PhD Researcher
Simon K. Clubley[1], Lecturer in Civil Engineering
[1]Infrastructure Group, Faculty of Engineering & the Environment,
University of Southampton, Southampton, SO17 1BJ

ABSTRACT

Little is known of the effects of combined blast and thermal loading on structures within an explosive fireball. This paper documents and discusses results from temperature, flux, strain and pressure gauges within a fireball of a conventional open arena trial using a 41kg TNT equivalent yield explosive. Plans to simulate an intense thermal fireball environment using a bespoke thermal tile are outlined.

INTRODUCTION

These arena trials were conducted to gauge data across the thermal spectrum from within the fireball of a conventional explosive; this data would set a benchmark for further tests and parametric studies to be undertaken. It was the intention not only to gauge thermal information from the fireball but also to observe the effects of the intense pressure and thermal loading on 2mm thick steel plates. Using the steel plates would allow differentiation between thermal and blast effects at a close distance from the burst centre. This data will become a vital part of a larger project involving the synergistic response of structures to both thermal and blast loading in extreme environments.

Conventional sized explosions do not often produce enough thermal output to considerably affect a structure. Therefore in order to quantify the thermal effect of larger explosions it is necessary to simulate such thermal yields. Much previous work has been undertaken in this field using various simulation devices and techniques to improve the accurate representation of the environment within a thermal fireball [1]. Throughout the development of these simulation devices problems such as disadvantageous combustion products and accurate fluence levels have been encountered. Therefore a bespoke thermal tile has been developed in order to eliminate the previous problems whilst producing a very high flux environment over a very short period of time

METHODOLOGY

Gauging the Fireball from a 41kg TNT eq. Explosive Event

Novel heavy structural boxes were designed and built in order to withstand the intense loading environment within the fireball. The boxes were fitted with a series of gauges and a 2mm thick steel plate. Previous experience showed that gauges closer than 4m from the explosion would have a high probability of not surviving the explosive event and that the fireball would extend no further than 8m radius. In order to provide a range of measurements the instrumentation was therefore set up at three radial locations; 4, 6 and 8m from the centre of the burst (Fig. 1a). The boxes were positioned at a height of 1m from the ground to the plate centre. The 2mm thick steel plates were bolted with a collar to a 12.5mm gauge structural steel box which in turn was mounted onto circular hollow sections (CHS). Thermal flux gauges, thermo-couples, pressure gauges, strain gauges (on steel plates) and temperature indicating labels were attached to the boxes.

Due to the volatile and unpredictable nature of the environment within the fireball it was necessary to use several types of gauges strategically positioned on the boxes in order to differentiate the effects. The thermal flux gauges and one set of thermo-couples were set up pointing vertically out of the top of the boxes, the (reflected) pressure gauges were positioned at the front of the boxes (adjacent to the plate) and the strain gauges and a set of second thermo-couples were positioned inside the boxes on the back of the steel plates (Fig.1b and Fig.2). The temperature indicating labels were adhered to several surfaces including the front surface of the CHS, the rear surface of the boxes, the inside faces of the boxes and the rear of the 2mm plates.

There were two sets of three boxes at each radial location. One set was fully instrumented with all the gauges and the other partially instrumented with just the temperature labels and pressure gauges at 4m and 8m, and no instrumentation at 6m. For the first trial the instrumented boxes faced the blast with the non-instrument facing away. For the second upcoming trial the box orientation will be reversed. The objective behind the different orientations was to attempt to distinguish the effects on the steel plates due to pressure from those due to temperature.

Several high speed cameras were used to observe the propagation of the fireball over time. After the trial the plate deformations were recorded and several non-tested plates of equal thickness and strength were statically tested to determine their tensile strengths.

Figures 1a and 1b. Photos of Structural Boxes.

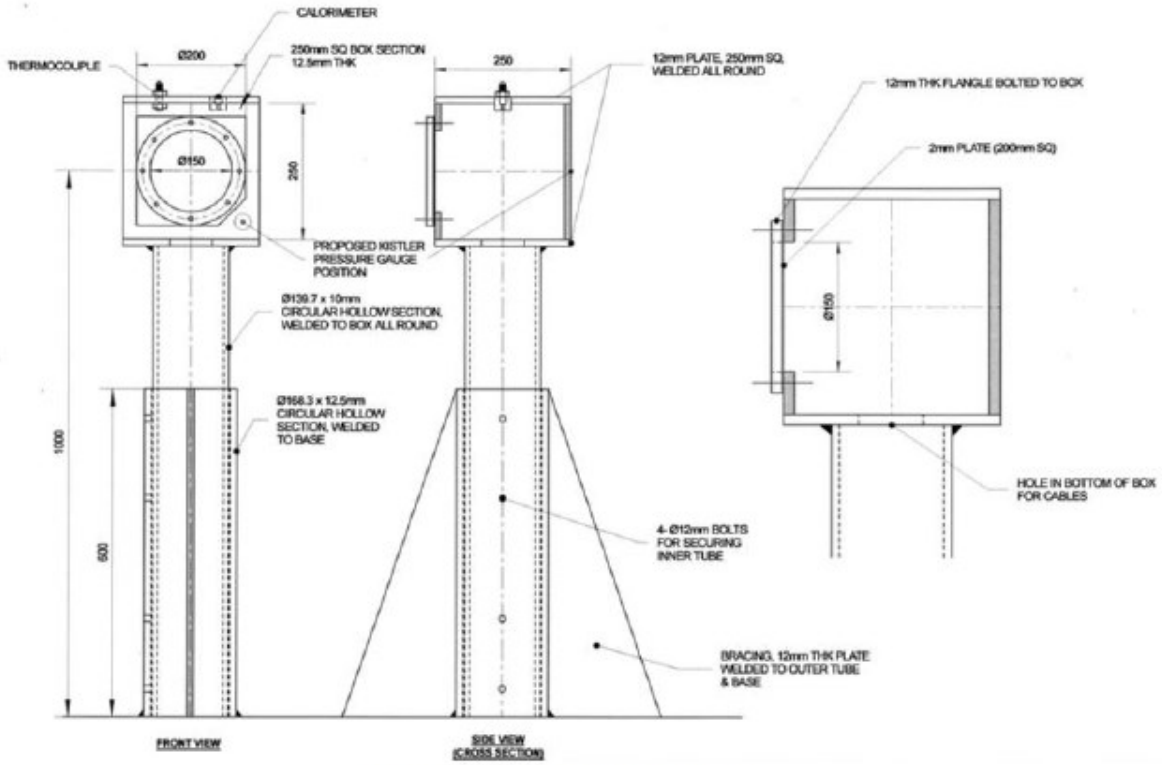

Figure 2. Drawing of Structural Boxes.

RESULTS AND DISCUSSION

Initial Observations

Immediately after the explosive event observations regarding the response of the plates and the temperature indicating labels were made. All three plates facing the blast had experienced deformations (0 to 11mm), the closest plate with the largest (11mm). There was no visible permanent deformation on the plates facing away from the blast. The

permanent deflections on the steel plates facing the blast were caused mainly by the blast pressure; however, these initial observations do not show the deformation history that may have occurred in either set (see strain gauge data).

The temperature labels showed the spectrum of temperatures reached within the fireball, the highest (at 4m) was approximately 200°C, reducing to approximately 70°C at 8m. The labels also helped to show the peak temperature on the inside of the plates, 46°C at 4m. Despite the relatively slow response times of the temperature labels they allow a valuable comparison to be made with the thermo-couples and flux gauges. All the gauged structural boxes survived the trial, indicating that the fabricated boxes are fit for purpose for future thermal tile testing.

Three high speed cameras were directed towards the propagating fireball across the arena pad. Fig.3 shows a still from one of the cameras at 5.39msec after ignition. The cameras revealed the total life span of the fireball to be approximately 1sec and it reached its maximum at 24msec. The cameras show the fireball reaching the 4m and 6m boxes at approximately 3.2msec and 16msec but not expanding as far as the 8m box. The fireball extends just beyond the 6m box, leading to an approximate maximum diameter of 12.5m. The shockwave was at the fireball front at 0.8msec then subsequently overtook it (1.2msec). This data is used as a comparison to the gauge data.

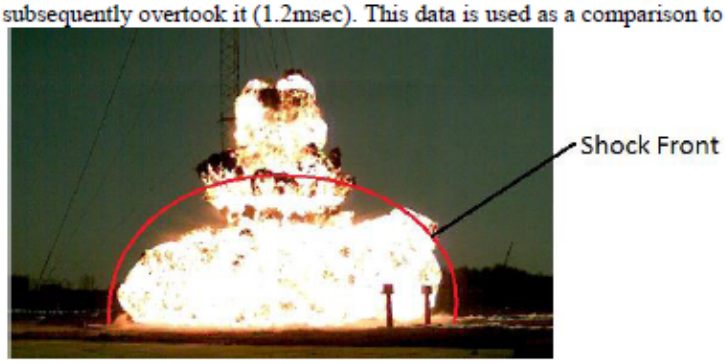

Figure 3. Fireball at 5.39msec after Ignition.

The steel used in the trials was Hot Rolled Steel BSEN 10111:DD11 (Steel for Forming). This steel was chosen due to its lower yield strength and higher ductility than a typical structural steel (275N/mm^2) hence ensuring the plates have a significant response to the explosive event. The 2mm steel plates were statically tested to determine the yield strength (YS), ultimate tensile strength (UTS) and Young's modulus (YM). The results of these tests showed a YS (0.2% Proof) of 162N/mm^2, an UTS of 266 N/mm^2 and a YM of 202x10^3 N/mm^2.

Gauge Data: Reflected Pressure

Two sets of reflected pressure gauges were positioned at 4m and 8m radial locations; one set facing towards the blast and the other facing away. Fig.4 shows the reflected pressure of the facing gauges at 4m over a short time frame at the start of the event. The peak recorded reflected pressure was 4040.45kPa, the impulse was 1.41kPa.s and the duration was 1.2msec with a time of arrival (TOA) of 2.95msec. The 4m gauge recorded a double peak pressure, which can be explained by several hypotheses:

- The second shock is from a reflected pressure of the ground which is more prominent due to its close proximity to the burst.
- The first shock is the main blast pressure and the second is the effect of ground shock on the gauge.
- The first shock is actually the shock from ignition of the initial explosive products, which disappears close to the burst and the second peak is the actual region of compressed air.
- The initial peak is due to 2kg of PE4 being ignited just before the 39kg of TNT.
- The second peak is from the reflection of the compressed air behind the front ("second shock").

Data from the second trial will help to resolve this phenomenon. The flat top of the peak pressure is due to the gauges only being able to record pressure up to 4MPa. Extrapolating the lines to form peaks the recorded pressure would be approximately 5MPa, which compares to the predicted reflected pressure of 5.4MPa at this range from Kingery and Bulmash [2]. For the second set of trials the pressure gauges will be re-calibrated to record over 4MPa.

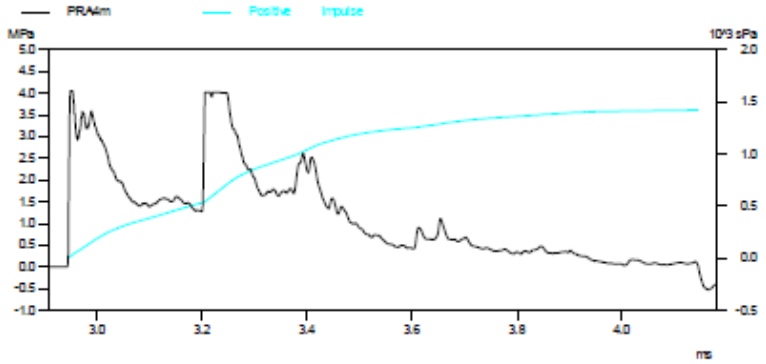

Figure 4. Reflected Pressures at 4m Facing Blast.

Fig. 5 shows the recorded reflected pressures at 8m facing the blast. The 8m facing gauges recorded a peak reflected pressure of 1237.6kPa and an impulse of 0.43kPa.s. The duration was 2.28msec and TOA was 8.34msec. Comparing these with predicted values for pressure (680kPa), impulse (0.403kPa.s), duration (7.47msec) and TOA (7.7msec), the pressure and duration differ considerably but TOA and impulse are similar. The double peak at 4m no longer exists, confirming that the phenomenon observed at 4m is restricted to areas very close to the centre of the burst.

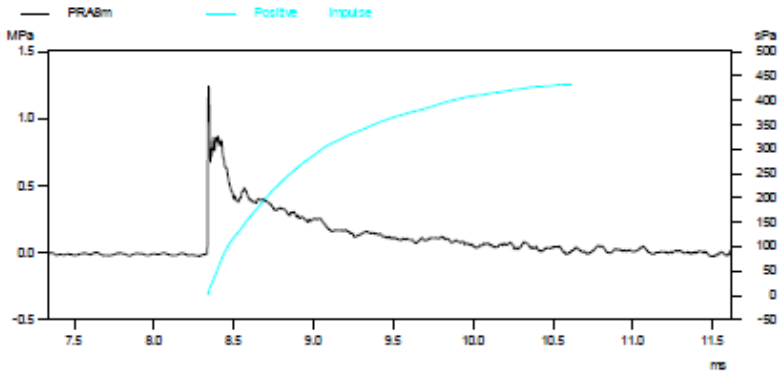

Figure 5. Reflected Pressures at 8m Facing Blast.

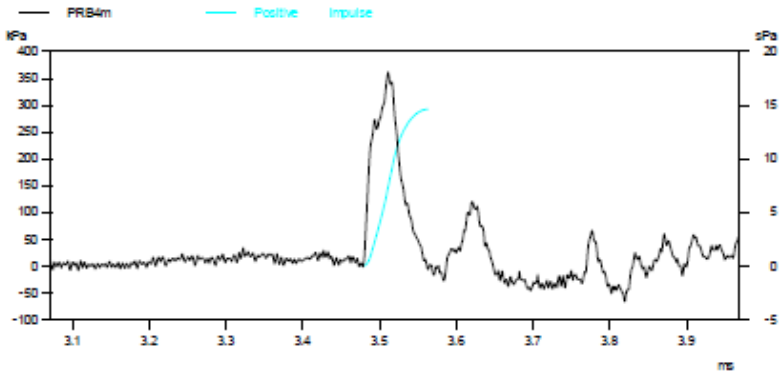

Figure 6. Reflected Pressures at 4m Facing Away From Blast.

Figs.6 and 7 show the reflected pressure at 4m and 8m facing away from the blast. At 4m the peak reflected pressure was 360.4kPa, impulse was 0.01kPa.s and duration was 0.09ms with a TOA of 3.48msec. At 8m the peak reflected pressure was 155.72kPa, impulse was 0.02kPa.s and duration was 0.45ms with a TOA of 9.03msec. After the initial impulse there are many later perturbations as the compressed air at the back of the box is reflected and diffracted.

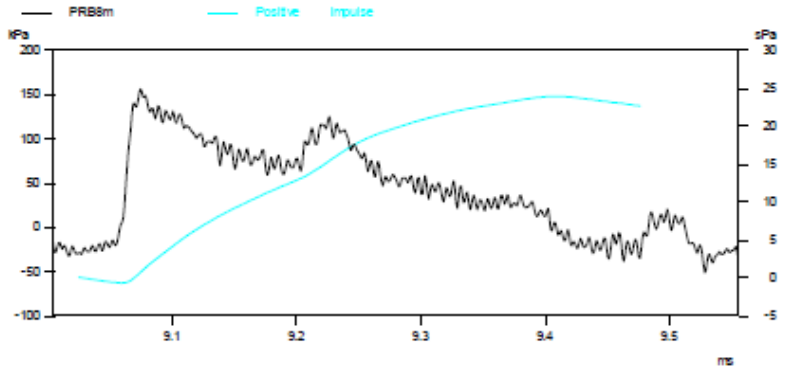

Figure 7. Reflected Pressures at 8m Facing Away From Blast.

Temperature (Thermo-Couples)

The varying temperatures across the fireball were measured using thermocouples placed inside and outside of the boxes. Fig. 8 shows the external recorded temperatures. An initial high temperature increase is followed by a low temperature drop into negative values. This event occurs at approximately 25msec, which is similar to the plots for flux and strain, where comparable rapid increases at approximately 25msec occur. An explanation for these extreme recordings is that a part of the explosive event caused an electrical disturbance to the gauge data at 25msec.

At 4m the temperature peaks at 480°C with a rise time of approximately 140msec. The temperature then slowly drops over several seconds. At 6m the peak temperature was 105°C with a rise time of approximately 410msec. At 8m the peak temperature was 74.5°C with a rise time of 480msec. The atmospheric temperature was 16.4°C at time of detonation; therefore the estimated time for the temperature at each box to return to this was 5.1sec at 4m, 9.6sec at 6m and 6.8sec at 8m. The temperatures recorded by the thermocouples are the temperatures of the thermocouples themselves not the actual air temperature. The rate at which the apparent temperature drops should therefore be taken as the cooling rate for the thermocouples. The external surfaces of the plates were assumed to be the same temperature. For the second trial the length of time recorded by the gauges will be increased.

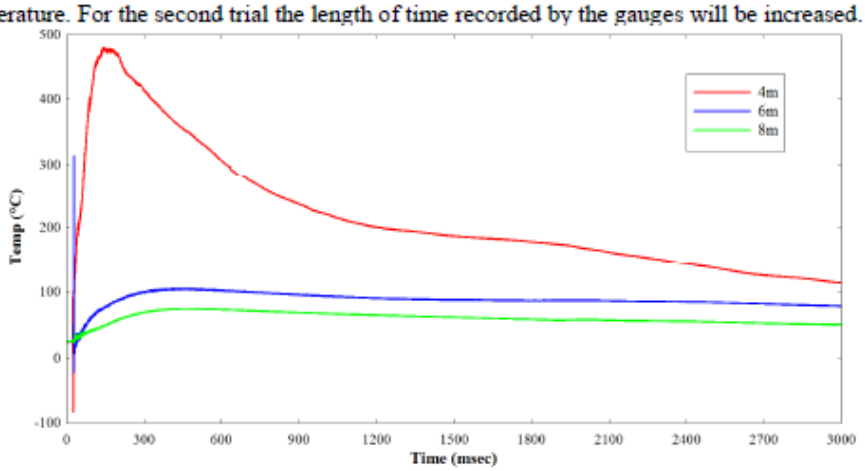

Figure 8. External Recorded Thermocouple Temperatures.

Fig.9 shows the internal recorded temperatures from the thermocouples placed on the rear face of the 2mm steel plates. The temperatures slowly rise to 36°C at 4m, 33.5°C at 6m and 32°C at 8m. Each of these temperatures was reached after 3 seconds. The curves of the plot suggest that the temperatures will not increase significantly more. It is also difficult to estimate the total rise and fall time and the actual peak temperatures reached. For the second trial, the gauges will be calibrated to read data for a longer period of time.

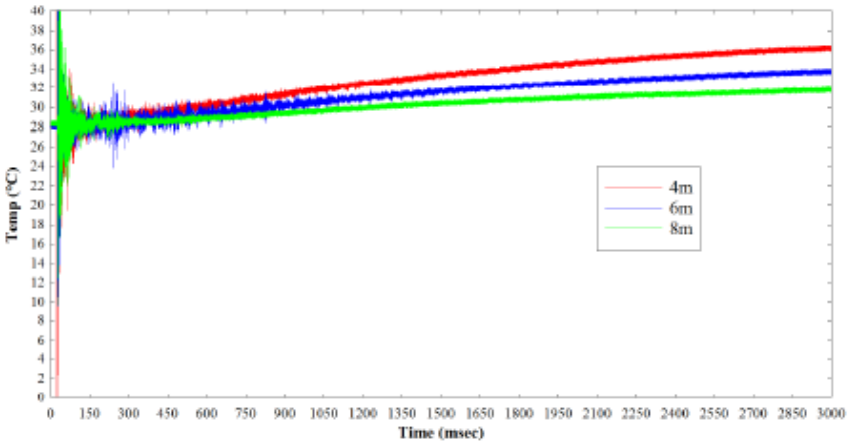

Figure 9. Thermocouple Temperatures on Back of Steel Plate.

Flux Gauges

Fig.10 shows the recorded flux. The peak flux recorded at 4m was 145 Watts/cm^2 at 32msec and the time to return to zero was approximately 500msec. The peak flux at 6m was 85 W/cm^2 at 55msec and the time to return to zero was approximately 450msec. The peak flux at 8m was approximately 30 W/cm^2 at 180msec and the time to return to zero was roughly 600msec. None of the recorded fluxes follow a triangular pulse shape similar to an applied impulse. The delay to the peak recorded flux increases with distance from the source. Comparing the flux with the recorded temperatures from the thermocouples, the flux gauges give a better representation of the thermal energy in the air during the event. This is due to the design of the flux gauge, where a cooling disc prevents the gauge itself from heating too much, allowing a better representation of the real atmosphere than the thermocouples which are left to heat and cool without intervention.

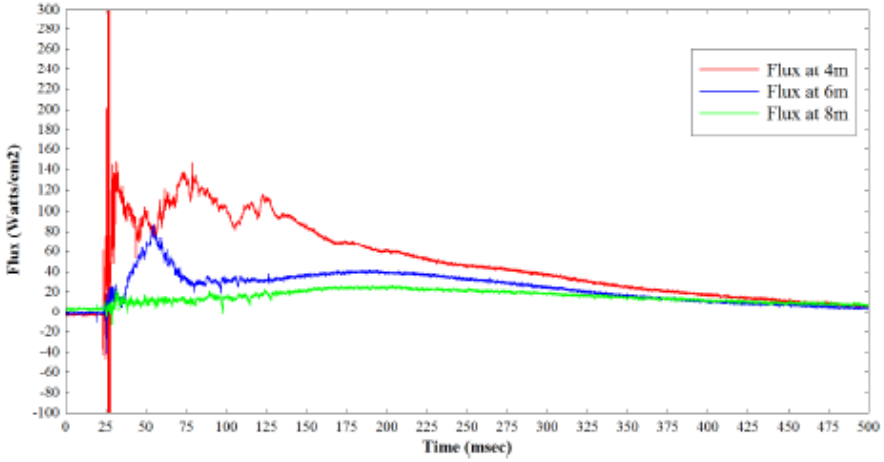

Figure 10. Recorded Flux.

Strain Gauges

The strain gauges were fixed to the back of the 2mm steel plates facing the blast at 4m, 6m and 8m radial locations in order to record any elastic and plastic strains observed in the plates. As previously identified, a potential electrical disturbance at an early stage of the test (25msec) produced extreme readings that were not representative of real strains. Fig. 11 shows the recorded strains from the strain gauge (Rosette type) at the 4m location (largest deformations). The Rosette gauge has three separate individual gauges aligned in different directions; vertical (Red), horizontal (blue) and 45° (green).

Due to the electrical disturbance the initial high and low strain values are difficult to determine. Using the Young's Modulus of $202x10^3 N/mm^2$ the strain values can be converted to equivalent stresses and the ultimate and yield strengths of the steel plates can be converted to equivalent strains to be compared to the plots. If the dynamic increase factors (DIF) are used (assuming yield is reached between 1 and 10msec) a factor of 1.6 can be applied to the yield stress and a factor of 1.05 can be applied to the ultimate tensile strength, giving $259.2N/mm^2$ yield (1283μstrain) and $279.3N/mm^2$ ultimate tensile strength (1383μstrain).

The vertical gauge on the plate at 4m recorded the strain settling at +700μstrain which has an equivalent stress of $141.4N/mm^2$. This is lower than the yield strength of $259.2N/mm^2$ (1283μstrain). The post-trial observations show the plate suffered permanent plastic deformations. This indicates that the strain in the plate would have exceeded 1283μstrain and then settled below the yield strength at $141.4N/mm^2$.

The horizontal strain gauge did not show the same magnitude as the vertical, indicating that the stresses experienced were not radially isotropic. The horizontal strain settles at -315μstrain, which is equivalent to a stress of $63.63N/mm^2$. The gauge at 45° settled at -125μstrain indicating an equivalent stress of $25.25N/mm^2$

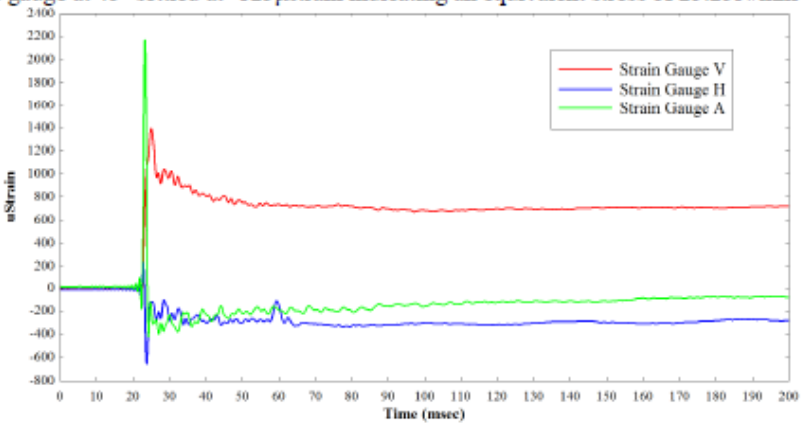

Figure 11. Strain Gauge Readings on Rear of Plate at 4m.

At the 6m radial location the steel plate experienced permanent deflections although not to the same magnitude as the plate at 4m. Fig.12 shows the strain gauge readings on the steel plate at 6m. The vertical strain gauge settled at -15μstrain, which is an equivalent stress of $3.0N/mm^2$. The horizontal strain gauge settled at +200μstrain, (equivalent stress of $40.4N/mm^2$) and the angled strain gauge settled at +30μstrain, (equivalent stress of $6.0N/mm^2$) Although these stresses are low, the plot shows that higher stresses were experienced prior to the plates settling which caused the plate to deform beyond its plastic limit. The peak strain for the horizontal (blue) gauge can be ignored and the curve extrapolated back to give a maximum strain of approximately 1250μstrain.

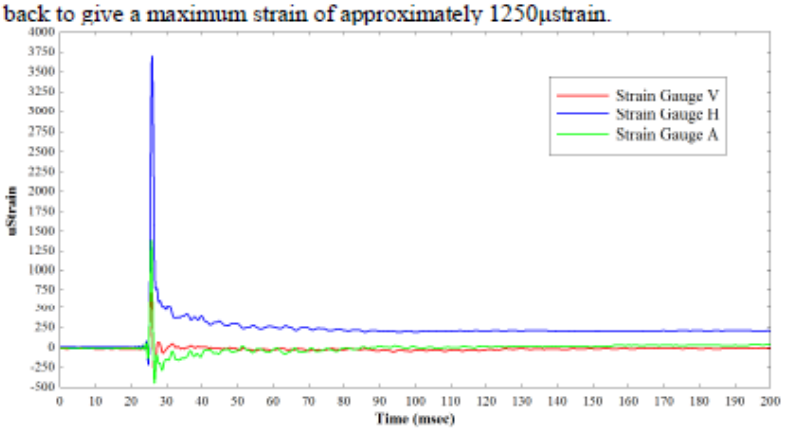

Figure 12. Strain Gauge Reading on Rear of Plate at 6m.

Due to a fault with the gauge data for the plate at 8m the full strain gauge plot is excluded from this report. However Fig. 13 shows the combined maximum strains experienced by each plate at 4m, 6m and 8m from the centre of the burst. The observed higher strains on the 8m plate are likely to be attributed to the gauge fault. The strain plots at

4m, 6m and 8m show oscillations, which may be due to the plates vibrating or an electrical disturbance with the gauges. The recorded oscillations were 10500Hz at 4m, 1000Hz at 6m and 700Hz at 8m; these are comparable to the natural frequency of a 150mm x 2mm thick square plate in its first mode of vibration of 814Hz.

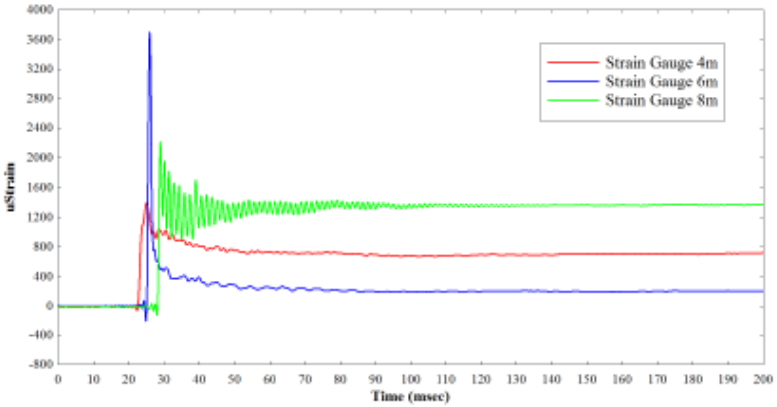

Figure 13. Max Strain Gauge Readings on Rear of Plates at 4m, 6m & 8m.

Deflected Shapes

Fig.14 shows the deflected shape of the plates at 4m and 6m recorded with a Vernier calliper. Fig.15 is a photo of the deformed plate at 4m. The maximum deflection recorded at 4m was 11mm, and at 6m was 6mm. The separate lines for each plate refer to the deflection profile in the X (horizontal) and Y (vertical) directions across the plate. (Note: A polynomial fit has been used to smooth the profile). The deformations of the plate at 8m were not measured as the Vernier callipers were not sufficiently sensitive to register such small deformations. The deflection plots show that the plate at 4m does not deform evenly; this uneven deformation is visible by naked eye.

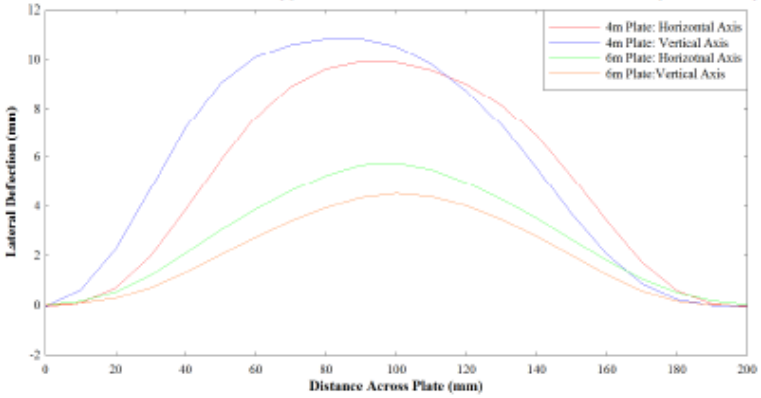

Figure 14. Lateral Deflection of Plates at 4m and 6m.

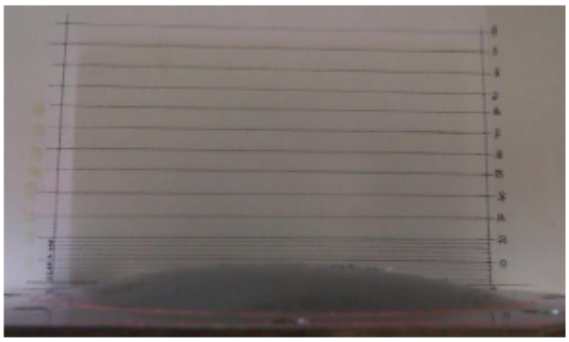

Figure 15. Photo of Deformations on Plate at 4m.

Discussion

During the explosive event the thermal load reached the plates after the blast wave, hence the synergistic effect involving the degradation of the steel due to thermal load prior to arrival of the blast wave did not occur. The thermal load was also too low to have reduced the capacity of the plates alone. The 2mm steel plate experienced deformations and the recorded strains exceeded the equivalent yield values of the steel. However an unloaded full size structural element with thicker gauge and higher strength steel would not see such stresses and deformations; therefore it is likely that such an element would not have yielded in this trial. This conjecture can be endorsed by the zero damage observed on the structural boxes. Lighter, thinner gauge structures such as cladding panels are more likely to fail in such an environment.

At 4m from the burst centre a double pressure peak was recorded. The explanation for the double peak is yet to be discovered but it does shed more light on the complex environment within a fireball. The gauge data recorded during the trial has provided us with a better understanding of the environmental spectrum from within a conventional fireball. Using this information a full parametric study into the synergistic response of structures within a thermal fireball can start to be formed.

To observe how structures can be affected by the thermal load from an explosion the research project will investigate fireballs of varying sizes. The thermal load from larger explosions will have a more detrimental effect on structures compared with the arena trial. Due to practical constraints surrounding the size of explosions that can be tested the thermal loads from such events will be replicated by other means. In order to do so a bespoke thermal tile has been developed to simulate such events.

THERMAL TILES

The simulation of thermal fireballs of explosive events has been well documented over recent decades. The ideal simulation profile of a large yield fireball is a steep flux increase followed by a slower parabolic decay; this flux profile would be applied over a full structural element. Previous simulation devices fall into two categories; large scale thermal simulators which produce lower accuracy rectangular pulse shapes and small scale simulators which can produce very accurate thermal profiles. Large scale simulators such as aluminium oxide jets can be used on full scale structural elements but issues such as thermal products, smoke, ventilation etc. have shown that combining the thermal simulator with a blast load is problematic. Small scale simulators such as solar lamps and Xenon heat flash lamps can only be used on small samples and are therefore more effective for investigating material responses as opposed to structural responses [1].

A new thermal tile is being developed that when ignited produces an extremely high thermal flux over a very short period of time. The tiles are made of a compound of titanium and boron and will be cast in a wax medium which holds the combustibles together until ignition. Due to the volatility of the tiles they need to be produced and tested in highly stable conditions. It is the intention to perform a trial which involves mixing the compound, forming the tile and igniting it using Nichrome wire. If this is successful then a series of experiments will be undertaken in order to benchmark the thermal tiles to assess their suitability to reproduce the expected thermal fluxes across a fireball from a large yield explosive event. The experiments will also be used to evaluate the tiles' suitability to be used within the large blast tunnel. The thermal tiles are based on a previous series of trials named the "Hi-Therm Simulator". These trials used the same Titanium-Boron compound but with different forming materials.

Previous Thermal Tile Research (Design Construct and Test of the Hi-Therm Simulator) [3]

The Defence Special Weapons Agency (DSWA, US) have developed and tested thermal tiles. The intention of this testing programme was to demonstrate if the thermal tiles could work as a high thermal simulator and be successfully combined with a subsequent blast wave. The targeted peak flux to reach was 150cal/cm^2/sec (628W/cm^2/sec), and a thermal fluence between 50 and 450 cal/cm^2. It was also imperative that combustion products from the tiles would not detrimentally interact with the later blast wave.

The concept of the thermal tiles involves combining two metallic elements which when ignited produce a highly exothermic reaction with temperatures exceeding 3000°K. Unlike other thermal simulators there is no requirement for oxygen to enable the two metals to react. To fabricate the tiles the metallic elements are combined in powder form, acetone is then added to the dry powder to form slurry which is poured into 12" x 12" aluminium trays. A palladium cladded aluminium wire embedded within the tile is ignited and produces localised temperatures of approximately 2665°K. This high temperature then initiates the Boron/Titanium reaction. Fig.16 is a diagram of the thermal tile.

Several series of tests were conducted by the DSWA. It was observed that when the trials were initially undertaken using small tiles a reasonable emittance (155Cal/cm2/sec) was recorded and there was little observable

particulate ejecta. However, when larger trials were undertaken the recorded fluxes were less (40cal/cm^2/sec) due to increased products obscuring the radiation. It was also noted that there was a rapid increase in the recorded flux when the particulate fireball impacted against the gauges. This lends itself to the reasoning that the increase in flux was produced by conduction and convection through the particulates, as opposed to the ideal process of radiation. The full scale series of tests did not meet the requirements that had been set out and therefore left the opportunity for further development and testing. An outcome of the trials was the recommendation to use a higher density (low porosity) mixture and eliminate the volatile constituents.

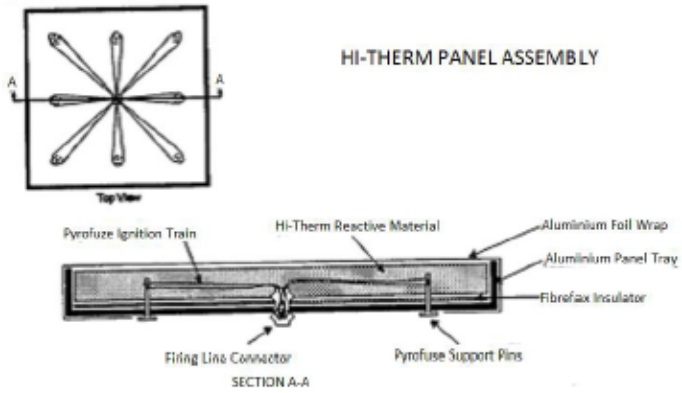

Figure 16. Previous Thermal Tile Configuration.

CONCLUSIONS AND RECOMMENDATIONS

This report describes a novel approach to recording information within a fireball. The temperatures, fluxes and pressures recorded from within the fireball help to form an understanding of the full environmental spectrum across a fireball, including phenomena such as the recorded double pressure peak at 4m.

The synergistic pattern with the highest potential damage criteria is for a structure to be subject to a high thermal load which decays the properties of the structure so that when a later blast wave arrives there is considerably more damage than would occur in the absence of a thermal load. In these arena trials the blast wave reaches the plates before the thermal load increases the plate's temperature so the worst case synergistic response does not occur. However, the external and internal thermocouples show the plates experience a temperature gradient from the thermal fireball. This gradient would induce stresses from the thermal expansion of the external face.

The temperatures, fluxes and pressures recorded in the trials will be used in correlation with data from the thermal tile experimentation and computational analysis on coupled (thermal and blast) structural elements to investigate the full potential synergistic response of structures subject to larger yield explosives. The thermal tiles are scheduled for testing during summer 2013, weather permitting. This paper has set the ground for these sets and future papers will document the results from the trials.

ACKNOWLEDGEMENTS

The author would like to express gratitude to UK MOD for use of the facilities and help of staff at MOD Shoeburyness. All data reported herein is property of the MOD. The assistance of C.Tilbury and G.Evans is gratefully acknowledged with respect to the preparation and undertaking of the trials and Dr. S. Clubley, Dr. J. Severn and J. Atwal-Patel for their support during the entirety of the project. The assistance of R.Collins and R.Keys is also gratefully acknowledged.

REFERENCES

1. Simon, K., Wenig, P., Serra J.J., *Twentieth International Symposium on Military Aspects of Blast and Shock*, Oslo, Norway, 2008, pp. unknown.
2. Kingery, C.N., and Bulmash, G., "Airblast Parameters from TNT Spherical Air Burst and Hemispherical Surface Burst", US Army Ballistic Research Laboratory, Technical Report No. ARBRL-TR-02555.
3. Zavitsanos, P.D, et al. "Design Construct and Test of Hi-Therm Simulator", General Sciences Incorporated, Technical Report No. DNA-TR-94-113.

Appendix G: SUSI Paper: Response of Steel Plates to Thermal and Blast Load from Within the Fireball of an Explosive Event

Response of steel plates to thermal and blast load from within the fireball of an explosive event

L.G.Clough[1], S.K.Clubley[1]
[1]*Infrastructure Group, Faculty of Engineering & the Environment, University of Southampton, UK*

Abstract

Little is known of the effects of combined blast and thermal loading on structures within an explosive fireball. This paper documents and discusses the response of 2mm thick steel plate within a fireball of a 41kg TNT equivalent explosive. This continues the study of work investigating the synergistic response of structures to blast and thermal loads. Results from a coupled thermal and structural Finite Element Analysis (FEA) of the plates are compared with the response recorded by strain gauges and final deflected shapes. Conclusions regarding any potential synergistic response from the plates are made along with the suitability of the numerical model to be used for further coupled studies on full structural elements.

Keywords: blast, thermal, synergistic, structural response, steel

1 Introduction

Two 41kg TNT eq. arena trials were conducted in which six Heavy Structural Boxes (HSB) were placed at 4m, 6m and 8m radial locations within and on the edge of the fireball. Thin gauge (2mm) steel plates were fixed to gauged boxes with one set of fully instrumented boxes facing the blast and another (un-instrumented) facing away. The box orientation was rotated for the second trial to record the pressure/time histories on the front and rear of the boxes. Design of the trials and results from the first trial are documented in [1]. Data from the trials are discussed and compared with the FEA of the plates. Future improvements for explosive trials using the structural boxes are suggested.

The 2mm thick steel plates were modelled using a coupled (thermal and structural) non-linear, FEA software, LUSAS [2]. The models were developed to replicate the behaviour of the plates under the recorded pressures and temperatures from trials and predicted pressures from Air3D [3]. Thermal only, blast only and combined models were developed to distinguish any potential synergistic response. The plates facing towards and away from the blast were also modelled in order to help differentiate between the thermal and blast effects. The process of building and running the plate models are presented along with discussions on the deformed shapes and stresses shown in the plates.

2 Experimental Trial Design

The trials were conducted as part of an on-going programme of research. The paper "Gauging the Fireball: Simulation and Testing" [1] describes in detail the design of the arena trials and novel heavy structural boxes. This paper briefly describes the design but readers are encouraged to refer to [1] for the full trial description.

The 41kg TNT eq. explosive trials were undertaken on an open air arena (Fig.1). The HSBs were designed to withstand pressures of approximately 5MPa and temperatures in the region of 500°C, to ensure they would not be damaged within the fireball of the explosion. K-Type thermocouples and Seqouia thermal flux gauges were fixed to the top of one set of the boxes. Endevco 8510c-100 pressure gauges were positioned on the front face of two of the boxes at 4m and 8m radial locations. The 150mm diameter, 2mm thick circular plate was fixed with a circular collar to the front of the box. Strain gauges and thermocouples were fixed to the rear of the steel plates to measure the deformations and temperature gradient. Figs. 2a & b shows images of the HSBs.

Data cables from the gauges were fed through a hole in the base of the boxes into circular hollow sections (CHS) which the boxes were mounted upon. For the second trial the box orientation was rotated through 180 degrees.

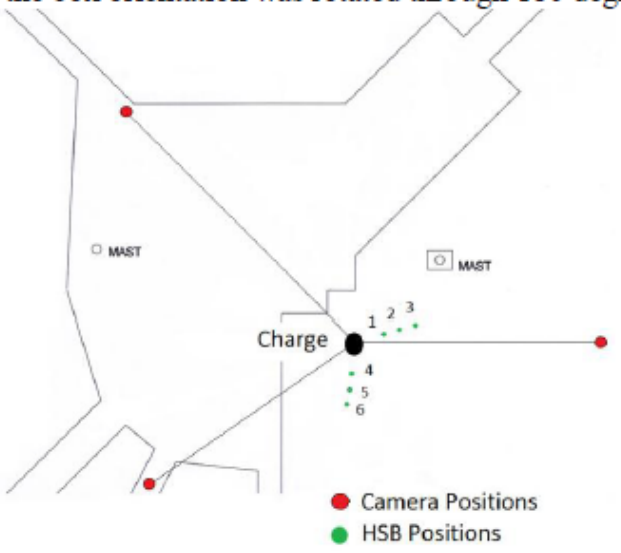

Figure 1: Plan of arena trial


Figure 2a: Heavy structural boxes (HSB). Figure 2b: Front of HSB

The steel used was Hot Rolled Steel for Forming (BSEN 10111:DD11), this has a lower strength than a typical structural steel, with a yield strength 162MPa and ultimate strength of 266MPa. The Young's modulus was 202GPa. Low strength steel was selected to increase the likelihood of a plastic response. Table 1 shows coupon tensile test data from the steel plate samples.

Table 1: Tensile test data

Sample	Yield Strength / 0.2% Proof Stress (MPa)	Ultimate Tensile Strength (MPa)	Fracture (MPa)	Young's Modulus (GPa)
1.1	160 / 165 (Low Strain Rate)	260	204	212
2.1	152 / 156	266	260	213
3.1	160 / 167	269	266	200
1.2	156 / 164	267	260	213
2.2	152 / 154	266	260	183
3.2	162 / 167	270	266	188
Average	157 / 162	266	253	202

3 Trial Results

The following section describes and compares the gauge results from both trials compared with numerical models. Fig.3a & b shows still images immediately after detonation taken by phantom high speed cameras (1 frame / 200μs). The fireball reached a maximum diameter of approximately 12.5m at 39msec.


Figure 3a: Fireball at 5.39msec after ignition. Figure 3b: Fireball at 39msec

3.1 Temperature

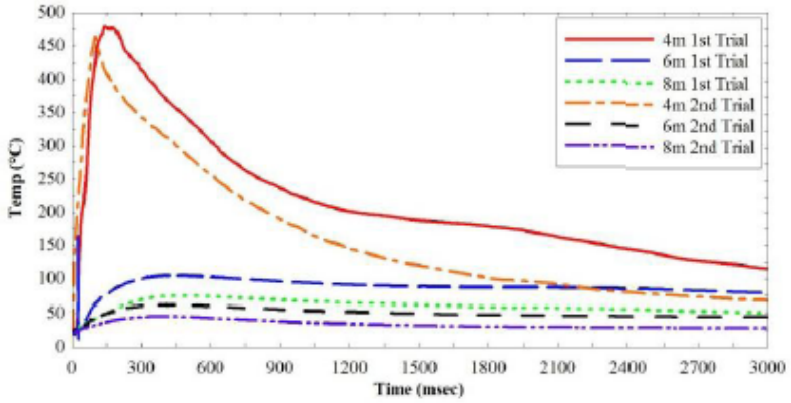

Figure 4: External temperature at 4m, 6m & 8m radial positions.

Fig.4 shows the recorded temperatures from the first and second trials. The temperature profiles for each trial are comparable. At 4m the peak temperature is higher and the temperature decrease is slower for the first (480°C) than the second trial (465°C). At 6m the peak temperatures were 106°C and 64°C for the first and second trial respectively. At 8m the peak temperature for the first trial was 75°C compared to 46°C for the second. The differing values are likely due to the uneven propagation and highly volatile nature of the fireball.

Fig.5 shows the recorded internal temperatures behind the steel plates. Initial temperatures of 28.1°C and 23.8°C were recorded during the first and second trials respectively. These recorded temperatures are aligned in Fig.5 to observe the differential over time. The temperature increase to 3secs at 4m was 8.2°C and 3.75°C for the first trial and second trial respectively. The difference in temperature increase between the two trials can be attributed to the plate orientation. The plates faced towards the charge in the first trial and away during the second trial. The thermal load from any explosive fireball can be transferred through the air by both radiation and convection. Shadowing severely affects the heat transfer through radiation but less so through convection. The lower temperature on the plates facing away is due to shadowing of both radiated and convected thermal energy.

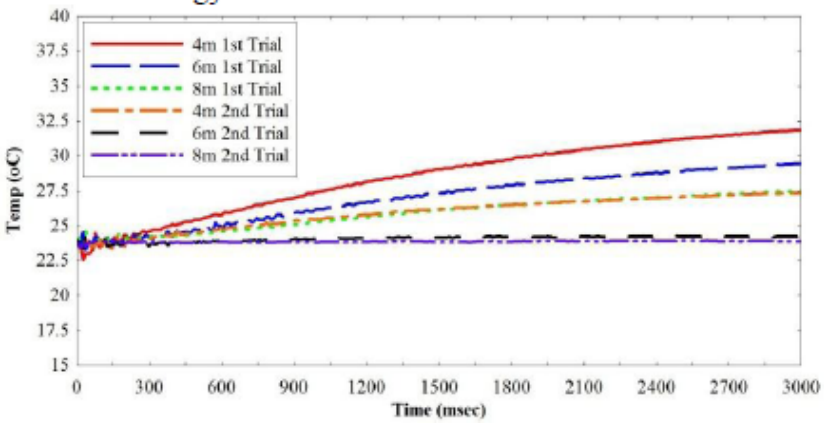

Figure 5: Internal temperature at 4m, 6m & 8m radial positions

3.2 Flux Gauges

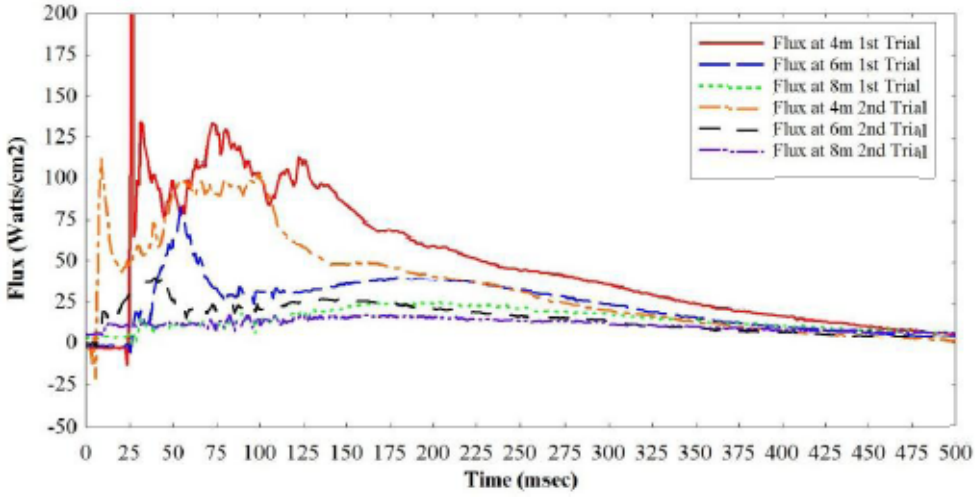

Figure 6: Recorded flux vs. time at 4m, 6m & 8m radial positions.

Fig.6 shows the recorded thermal flux for both trials. At 4m the peak flux recorded for the first and second trials were 145W/cm^2 and (approximately) 115W/cm^2. At 6m the peak flux values were 85W/cm^2 and 40W/cm^2 for the first and second trials. At 8m the flux was approximately 30W/cm^2 and 18W/cm^2 for the two trials. Significantly higher flux values were recorded across the spectrum of the fireball during the first trial than the second trial. As the flux gauges were pointing vertically from the box they would not have been subject to the same radiation flux that the facing plates would have experienced. Future trials will use flux gauges at the front of the boxes.

3.3 Reflected Pressure

The pressure gauges were placed on the front of the boxes adjacent to the plates. Computational fluid dynamics (CFD) simulations were performed using Air3D [3] in order to compare the pressure/time history plots. Fig. 7 shows the reflected pressures for each trial at 4m and 8m.

The recorded peak reflected pressures at 4m facing the blast were 4.04MPa (Trial 1) and 4.29MPa (Trial 2), the predicted values were 5.72MPa (2D) and 2.66MPa (3D). The difference between the 2D and 3D model values are due to the rarefaction of the blast wave around the side of the box. The 2D model assumes an infinitely wide box and therefore there is no diffraction and clearing around the box sides. The 3D model allows rarefaction and therefore the front peak reflected pressure is less. The double peak phenomena was observed at 4m facing the blast which is speculated at being from the combustion products hitting the gauge followed by the region of compressed air.

The recorded peak reflected pressures at 8m facing the blast were 0.82MPa (Trial 1) and 1.14MPa (Trial 2), the predicted values were 0.77MPa (2D) and 0.47MPa (3D). Fast Fourier transform smoothing of the high peak for Trial 2 gives a value of approximately 0.85MPa.

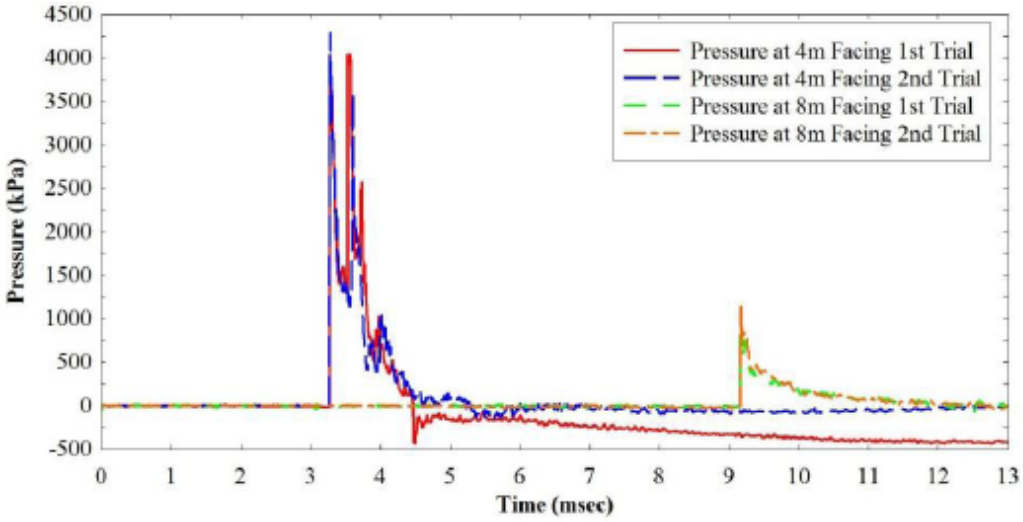

Figure 7: Reflected pressure at 4m, 6m & 8m radial positions

The correlations between blast pressures for both trials are reasonable, showing good reproducibility between the tests. Both gauges at 4m show a double peak, the most suitable explanation for which is the pressure from the detonation of the products followed by the compressed air. At 8m a second peak can also be seen at 20msec, this phenomenon is termed the "second shock" or "termination shock" when a smaller pressure front has been reflected back off the explosive products and propagates out behind the main shock front.

At 4m facing away the peak reflected pressures recorded were approximately 0.28MPa for Trial 1 and 0.32MPa for Trial 2. The predicted Air3D (3D) peak pressure was 0.35MPa. During the first trial at 4.5msec the gauge appears to fail and records unrealistic negative pressure readings thereafter.

3.4 Recorded Strain

Fig.8 shows the maximum recorded strains in the steel plates. The strain gauge plots show a significant difference between the two trials. This is due to the zero visible deflection exhibited by the plates facing away in the second trial. The maximum strain experienced by the plate at 4m settled at 750μstrain whereas the equivalent strain experienced by the plate at 4m from the second trial settled just above 300μstrain, as the plates facing away experienced no permanent deformations this value can be attributed to a gauge fault.

At 25msec there was a significant electrical disturbance which considerably affected the strain gauge results for both trials. This resulted in the plots showing unrealistic peak strains at this time. For the plate at 4m in the first trial, if the line is extrapolated back towards that event we see that it curves up to approximately 1300μstrain this is equivalent to 262MPa stress (approximate yield strength). The other curves show a similar pattern; therefore we can deduce that the peak plate deformations were larger than the final settled deformations.

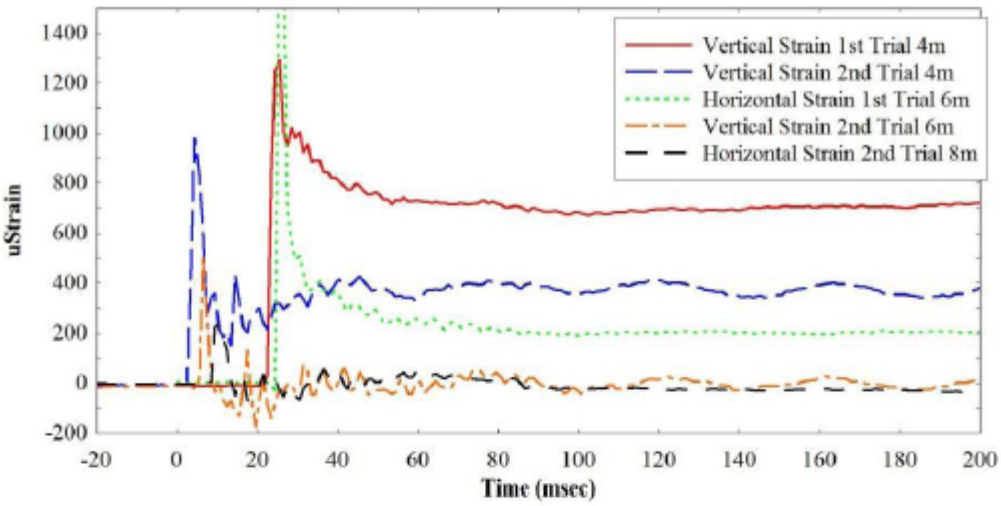

Figure 8: Maximum strain at 4m, 6m & 8m radial positions

The strains recorded by the individual gauges rotated at 0°, 45° and 90° within each rosette gauge were different indicating non-homogenous plate deformations. This may be attributed to varying tightness of bolt, inaccuracy of plate dimensions or a non-planar wave hitting the plates. There are noticeable oscillations indicating a dynamic response of the plates.

3.5 Deflected Shapes

Fig.9 shows a plot of the deflected shape of the plates for both trials at 4m and 6m facing the blast, recorded manually with a Vernier calliper. The profile lines are 10^{th} order polynomial fits to the deflections measured across the plates vertically and horizontally. The maximum deflection at 4m was 10.5mm for trial one and 7.5mm for trial two. The maximum deflection at 6m was 5.25mm for trial one, the deformations in the plate at 6m from the second trial and 8m for both trials were too small to be measured accurately with the Vernier calliper. No permanent deformations were observed on the plates facing away from the blast.

The magnitude of the deformations in the plates facing the blast during the second trial was significantly less than the first trial. Similar patterns regarding the drop in magnitude between the two trials have been noted in other gauges. Reasons for the difference could be due to the unknown and volatile nature of the fireball, reproducibility of trial and fixity of bolts.

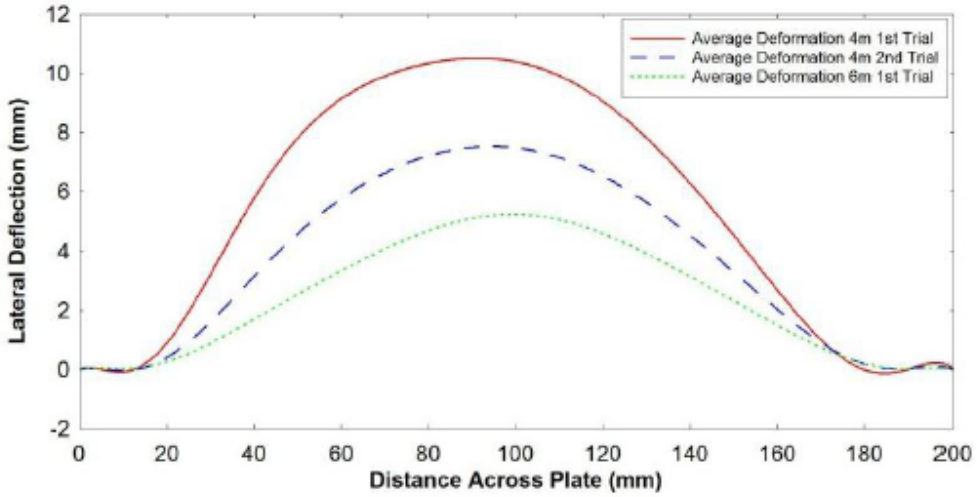

Figure 9: Average maximum plate deflections at 4m and 6m radial positions.

4 Numerical Modelling

The FEA software LUSAS was used to construct the models of the 2mm thick steel plate from the arena trials (Fig.10). The element used was a HX8M linear solid element with a fast multifrontal direct solver, suitable for a coupled thermal and structural non-linear analysis. The non-linear solver used was total Lagrangian. Data from the recorded and predicted pressure vs. time histories were normalised then applied as load curves in LUSAS relating to the peak values inputted as a global distributed loads or prescribed temperatures.

The specified yield strength of the modelled steel was 264MPa with a plastic elongation phase of 20% strain. The yield strength is taken from the static tensile tests multiplied by a dynamic increase factor (DIF) of 1.6 to take account of the high velocity load applied [4]. The temperature loads used in the models were taken directly from the recorded values and the pressure loads were taken both from the CFD predictions and gauges.

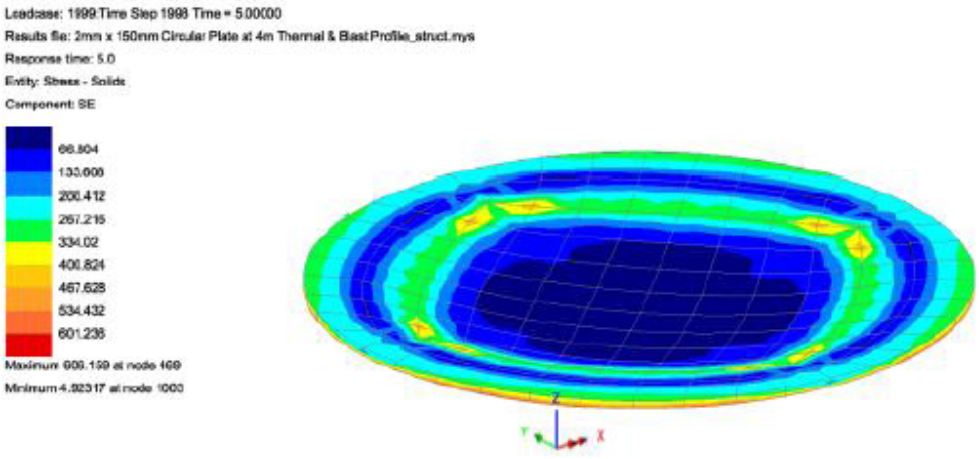

Figure 10: Extract from LUSAS modelling of 2mm circular plate

5 Model Results and Analysis

The following deflections and stresses are taken at the centre of the modelled plates at the position of maximum deflected shape and equivalent stress.

5.1 4m Plate Facing Blast (Recorded Trial Pressures)

Fig. 11 shows the deflection profile history at 4m facing the blast. The deflection history profile of the plate with the combined thermal and blast loads is equal to the deflection history of the plate with the blast load only indicating that at this distance from the centre there are minimal synergistic effects. The plate in the thermal only model deflects to a peak of 6mm then settles at 1.5mm. The thermal load is applied much later than the blast pressure; therefore in the combined model the plate has already deformed and reached its peak stress from the blast pressure by the time the thermal load is applied causing no further damage.

The recorded final deflection of the plates from the trials was: 10.5mm (1st) and 7.5mm (2nd). The final deflected shapes predicted by the numerical models were approximately 8.5mm (1st) and approximately 7.5mm (2nd). Despite the predicted and numerical values not matching for the 1st trial the 2nd trial values were equal. The overall comparability of the predicted and actual values gives confidence for using LUSAS for the preferred non-linear, coupled analysis on whole structural sections. The reasons for the difference in the modelled and recorded deflections can be attributed to fixity of plates, volatility of fireball environment and accurate representation of loads within fireball.

The stress response of the plate to the blast and the combined loads is almost identical to the deflected profile. The peak stress reached is approximately 350MPa.

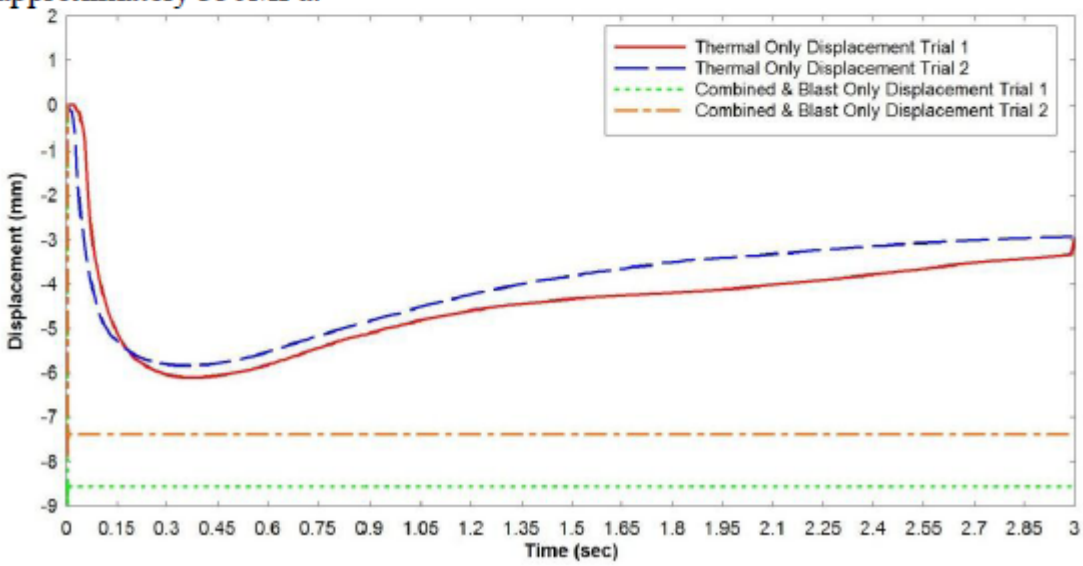

Figure 11: Displacement at 4m facing blast combined & thermal

5.2 6m Plate Facing Blast (Using Air3D Pressures)

Figs.12 and 13 show the modelled deflected shapes of the plate facing the blast at 6m. There were no pressure gauges at this location therefore the pressure used in conjunction with the recorded temperature was taken from the CFD analysis. The blast only displacement is similar to the actual final deflected shape. The 2D final deformation was approximately 5.5mm, which is very close to the 6mm actual permanent deflection.

The combined pressure and temperature deflected plot has several interesting features. A notable high deformation of approximately 2.75mm (2D) followed by a decrease and a noticeable harmonic response (380Hz) followed by a second increase in deformation (peaking at 2.25mm) in line with the increase in temperature. If the deflection is extrapolated from 3sec the final deflected shape would be nearer 1.5mm.

This graph is the best evidence that there may have been some type of synergistic response in the plates in this trial. It is difficult to model the response of the plates more precisely as the exact time of arrival of the blast and thermal loads is unknown at this location.

The thermal only graph follows a similar trend to the thermal and blast (without the initial deflection from blast) peaking at approximately 1.65mm. There is a significant difference between trial 1 and trial 2 response. There is a difference in the recorded temperatures between the two trials but the observed response is unusual compared to the difference in temperatures. The plots of stress follow similar patterns at the deflections with peak values of 385MPa for the combined thermal and blast case.

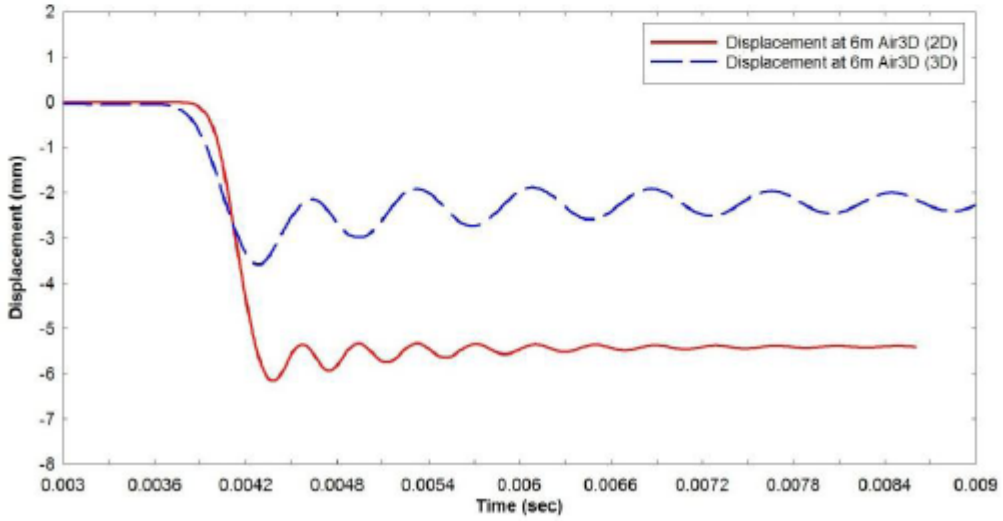

Figure 12: Displacement at 6m facing blast only

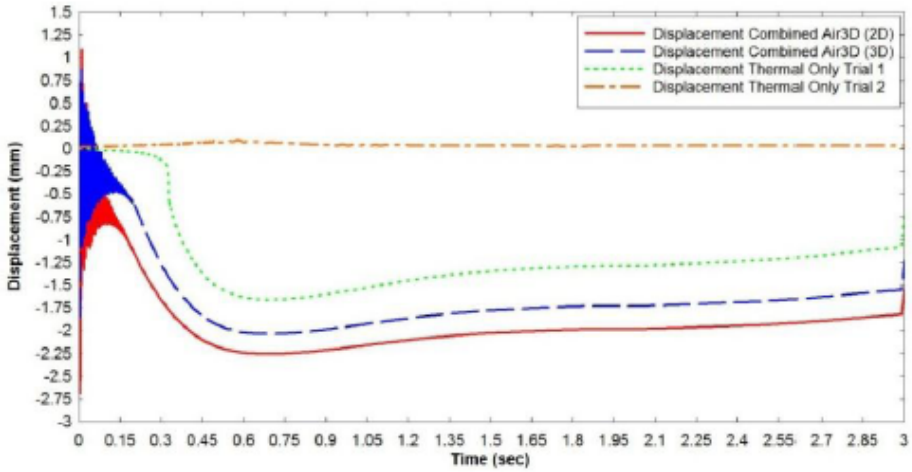

Figure 13: Displacement at 6m facing blast combined and thermal

5.3 8m Plate Facing Blast (1st and 2nd Trial Pressures & Air3D)

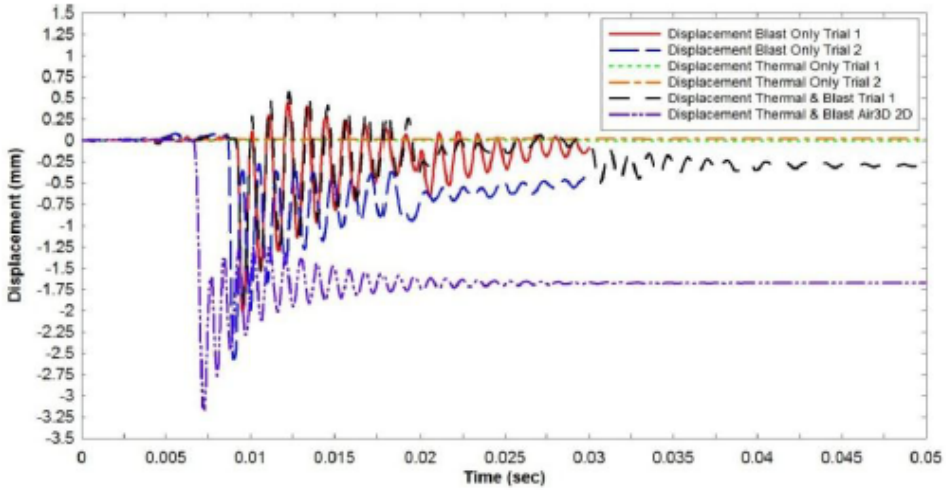

Figure 14: Displacement at 8m facing, combined, thermal and blast only

Fig.14 shows the plot of deflections for the plates at 8m facing the blast. After each trial there was no visible permanent deflection on the plates. The combined thermal and blast peaks at 2mm then settles to 0.3mm, a second peak is observed at 0.03sec, this could be due the second shock. The thermal only plot shows opposing responses for the first and second trial. The profile of the stress plots were identical to the displacement, with peak stresses of approximately 275MPa for both the combined and blast only cases, which corresponds to the yield stress of the steel with a DIF applied. The peak stresses from the Air3D pressure models were 190MPa before settling in a similar profile to the deflected shape.

6 Conclusions

In this paper results from trials gauging the fireball of a 41kg TNT explosive event have been presented. The structural response of 2mm thick plates within

the fireball are described alongside the numerical analysis of the plates to observe any thermal and blast synergistic response. The plates at 4m displayed minimal synergistic response as the deformations and stresses initially caused by the blast wave did not increase upon arrival of the later thermal load.

Synergistic response was observed in the numerical models of the plates at 6m. The plates had lower stresses from the blast and were subsequently heated. It was difficult to confirm if such a response occurred in the actual plates as there were no pressure gauges at 6m and the strain gauges did not show movement after the first 100msec. The plates at 8m did not experience any permanent deformations but numerical models show elastic deformations and oscillations. LUSAS proved a suitable analytical tool for modelling the actual deformations in the non-linear coupled environment.

It has proved difficult to accurately measure the deflection time history of the plates using strain gauges, therefore the use of accelerometers, laser deflection meters and high speed cameras will be adopted for future work. The heavy structural boxes performed well and survived the trials. Further developments are required to provide flux gauges and/or thermocouples on the front of the boxes which will record the direct thermal radiation and convection. Once the boxes have been improved they will be used again for future combined thermal & long duration blast experimentation.

This paper shows that there is minimal synergistic response in structures subject to explosions of a size equivalent to 41kg TNT. Features of fireball development such as a double pressure peak relating to expansion of combustion products and region of compressed air have been highlighted. The deformed shape of the plates from the numerical analysis correlates well with the experimental results. The benchmarking of the numerical tool to actual results has provided the researcher with the confidence in the tool for use with full structural elements exposed to large yield explosive environments.

Acknowledgements

The author acknowledges that all results and data recorded and discussed in this paper are MoD results obtained at MoD facilities.

References

[1] Clough, L.G., Gauging the Fireball: Simulation and Testing. *Proc. of the 15th International Symposium on Interaction of the Effects of Munitions with Structures*, Clubley. S.K., Potsdam, Germany, 2013.
[2] LUSAS, www.lusas.co.uk
[3] Rose, T.A., *An Approach to the Evaluation of Blast Loads on Finite and Semi-Infinite Structures*. PhD Thesis, Cranfield University, Royal Military College of Science.
[4] Yandzio, E. & Gough, C., *Protection of Buildings Against Explosions,* The Steel Construction Institute: Ascot, pp. 60, 1999.

Appendix H: IStructE Young Researcher's Conference Poster Presentation

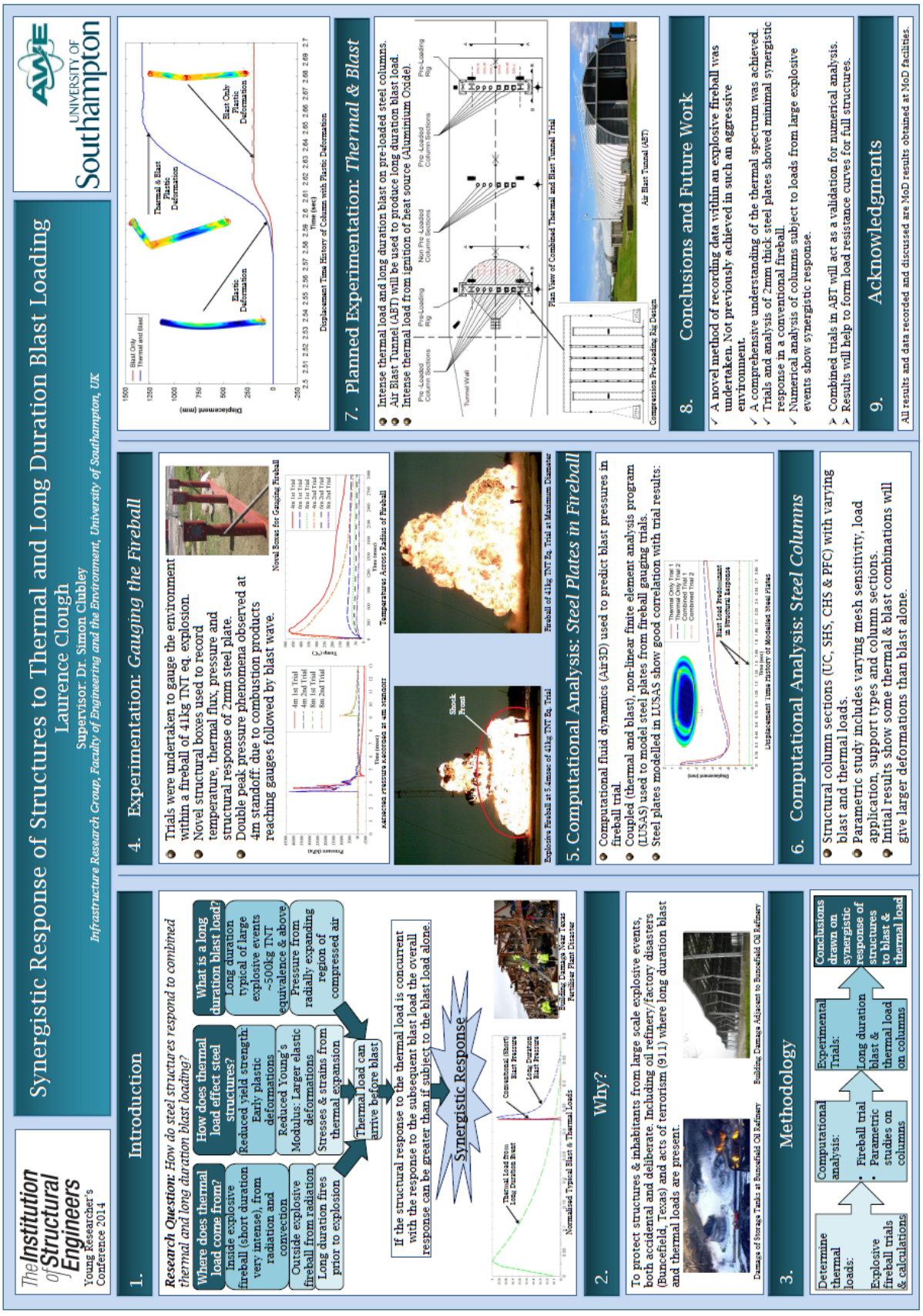
The Institution of Structural Engineers
Young Researcher's Conference 2014
Synergistic Response of Structures to Thermal and Long Duration Blast Loading
Laurence Clough
Supervisor: Dr. Simon Clubley
Infrastructure Research Group, Faculty of Engineering and the Environment, University of Southampton, UK
University of Southampton
1. Introduction
Research Question: How do steel structures respond to combined thermal and long duration blast loading?
Where does thermal load come from?
Inside explosive fireball (short duration very intense), from radiation and convection
Outside explosive fireball from radiation
Long duration fires prior to explosion
How does thermal load effect steel structures?
Reduced Yield strength
Early plastic deformations
Reduced Young's Modulus: Larger elastic deformations
Stresses & strains from thermal expansion
Thermal load can arrive before blast
What is a long duration blast load?
Long duration typical of large explosive events ~500kg TNT equivalence & above
Pressure from radially expanding region of compressed air
If the structural response to the thermal load is concurrent with the response to the subsequent blast load the overall response can be greater than if subject to the blast load alone.
Synergistic Response
Normalised Typical Blast & Thermal Loads
Conventional (Short) Blast Pressure
Long Duration Blast Pressure
Thermal Load from Long Duration Event
Building Damage Near Texas Fertiliser Plant Disaster
2. Why?
To protect structures & inhabitants from large scale explosive events, both accidental and deliberate. Including oil refinery/factory disasters (Buncefield, Texas) and acts of terrorism (9/11) where long duration blast and thermal loads are present.
Damage of Storage Tanks at Buncefield Oil Refinery
Building Damage Adjacent to Buncefield Oil Refinery
3. Methodology
Determine thermal loads:
Explosive fireball trials & calculations
Computational analysis:
Fireball trial
Parametric studies on columns
Experimental Trials:
Long duration blast & thermal load on columns
Conclusions drawn on synergistic response of structures to blast & thermal load
4. Experimentation: Gauging the Fireball
Trials were undertaken to gauge the environment within a fireball of 41kg TNT eq. explosion.
Novel structural boxes used to record temperature, thermal flux, pressure and structural response of 2mm steel plate.
Double peak pressure phenomena observed at 4m standoff: due to combustion products reaching gauges followed by blast wave.
Novel Boxes for Gauging Fireball
Temperature Across Radius of Fireball
Explosive Fireball at 5.4msec of 41kg TNT Eq. Trial
Fireball of 41kg TNT Eq. Trial at Maximum Diameter
Shock Front
5. Computational Analysis: Steel Plates in Fireball
Computational fluid dynamics (Air3D) used to predict blast pressures in fireball trial.
Coupled (thermal and blast), non-linear finite element analysis program (LUSAS) used to model steel plates from fireball gauging trials.
Steel plates modelled in LUSAS show good correlation with trial results:
Thermal Only Trial 1
Thermal Only Trial 2
Combined Trial 1
Combined Trial 2
Blast Load Predominant in Transient Response
Displacement Time History of Modelled Steel Plates
6. Computational Analysis: Steel Columns
Structural column sections (UC, SHS, CHS & PFC) with varying blast and thermal loads.
Parametric study includes varying mesh sensitivity, load application, support types and column sections.
Initial results show some thermal & blast combinations will give larger deformations than blast alone.
7. Planned Experimentation: Thermal & Blast
Intense thermal load and long duration blast on pre-loaded steel columns.
Air Blast Tunnel (AST) will be used to produce long duration blast load.
Intense thermal load from ignition of heat source (Aluminium Oxide).
Displacement (mm)
Blast Only
Thermal and Blast
Thermal & Blast Plastic Deformation
Elastic Deformation
Blast Only Plastic Deformation
Displacement Time History of Column with Plastic Deformation
Time (sec)
Pre-Loaded Column Sections
Pre-Loading Rig
Non Pre-Loaded Column Sections
Tunnel Wall
Plan View of Combined Thermal and Blast Tunnel Trial
Compression Pre-Loading Rig Design
Air Blast Tunnel (AST)
8. Conclusions and Future Work
A novel method of recording data within an explosive fireball was undertaken. Not previously achieved in such an aggressive environment.
A comprehensive understanding of the thermal spectrum was achieved.
Trials and analysis of 2mm thick steel plates showed minimal synergistic response in a conventional fireball.
Numerical analysis of columns subject to loads from large explosive events show synergistic response.
Combined trials in AST will act as a validation for numerical analysis.
Results will help to form load resistance curves for full structures.
9. Acknowledgments
All results and data recorded and discussed are MoD results obtained at MoD facilities.

Appendix J: Best Fit Curves

Deflections: Exponential Decay Curve Fit Equations

Peak Pressure (kPa)	Load Type	Exponential Fit Equation
107.1	Temperature	$y=-21.46+8.641x10^{4}e^{-7.04x}$
66.4	Temperature	$y=-9.818+1.374x10^{20}e^{-25.2x}$
198.7	Temperature	$y=25.58+2.051x10^{5}e^{-9.556x}$
109.7	Temperature	$y=-1.208+1.299x10^{9}e^{-12.17x}$
182.4	Temperature	$y=-2.307+2663e^{-3.158x}$
182.4	Thermal Flux	$y=-3.011+1120e^{-3.581x}$
182.4 Pinned	Temperature	$y=2.071+1019e^{-2.907x}$
182.4 Pinned	Thermal Flux	$y=0.1356+617.4e^{-3.585x}$
111.5	Temperature	$y=-17.12+1244e^{-2.045x}$
111.5	Thermal Flux	$y=-3.189+234.7e^{-1.819x}$
281.7	Thermal Flux	$y=-0.07563+6739e^{-5.638x}$
184.8	Thermal Flux	$y=-3.156+1112e^{-2.865x}$
127.9	Thermal Flux	$y=-2.943+372.4e^{-1.741x}$
127.9 Pinned	Thermal Flux	$y=-0.6777+181.6e^{-1.682x}$
95.1	Temperature	$y=-2.872+217.8e^{-1.243x}$
95.1	Thermal Flux	$y=-19.45+1344e^{-1.446x}$
95.1 Pinned	Temperature	$y=0.1082+615.5e^{-1.374x}$
95.1 Pinned	Thermal Flux	$y=-0.5477+175.4e^{-1.411x}$
290.3	Thermal Flux	$y=1.117+9161e^{-4.763x}$
290.3 Pinned	Thermal Flux	$y=-5.367+417.6e^{-2.16x}$
153.1	Thermal Flux	$y=-3.447+407.7e^{-1.531x}$
153.1 Pinned	Thermal Flux	$y=-0.7157+207e^{-1.31x}$
96.6	Temperature	$y=-19.2+1435e^{-1.036x}$
96.6	Thermal Flux	$y=-3.697+154.6e^{-0.7611x}$
96.6 Pinned	Temperature	$y=0.06608+633.7e^{-0.9727x}$
96.6 Pinned	Thermal Flux	$y=-0.5328+180.6e^{-0.9979x}$
329.4	Thermal Flux	$Y= 8.628+7229e^{-3.862x}$
182.5	Thermal Flux	$y=-3.427+1059e^{-1.766x}$
182.5 Pinned	Thermal Flux	$y=0.4872+617.8e^{-1.796x}$
112	Temperature	$y=-17.92+1404e^{-1.046x}$
112	Thermal Flux	$y=-3.191+266.9e^{-0.9497x}$
112 Pinned	Temperature	$y=0.2814+613.6e^{-0.9783x}$
112 Pinned	Thermal Flux	$y=-0.5689+174.1e^{-1.009x}$
203.8	Thermal Flux	$y=-3.537+1474e^{-1.964x}$
136.2	Temperature	$y=-14.7+1627e^{-1.074x}$
136.2	Thermal Flux	$y=-3.372+374.4e^{-1.044x}$

Blast and Thermal: Roller Top (Parameters vs. Scaled Distance)

Peak Defection		
y = A2 + (A1-A2)/(1 + exp((x-x0)/dx))		
Parameter	**Value**	**Standard Error**
A1	641.33301	52.90855
A2	26.73009	21.26511
x0	237.03969	6.3099
dx	20.26222	4.45757
span	614.60292	61.11538
EC50	8.81E+102	5.56E+103
Reduced Chi-Sqr	3721.46777	
Residual Sum of Squares	78150.82312	
Adj. R-Square	0.93328	

Final Deflection		
y = a/(1 + exp(-k*(x-xc)))		
Parameter	**Value**	**Standard Error**
a	568.58039	38.4269
xc	242.48305	5.18715
k	-0.07581	0.01929
Reduced Chi-Sqr	4451.99869	
Residual Sum of Squares	97943.97117	
Adj. R-Square	0.93144	

Peak Stress		
y = A1 + (A2-A1)/(1 + 10^((LOGx0-x)*p))		
Parameter	**Value**	**Standard Error**
A1	73.28162	11.70695
A2	301.98499	10.54711
LOGx0	285.73201	5.09214
p	-0.01697	0.00315
span	228.70337	18.31744
EC20	--	--
EC50	5.40E+285	1.#INF
EC80	1.75E+250	1.#INF
Reduced Chi-Sqr	319.33173	
Residual Sum of Squares	6386.63467	
Adj. R-Square	0.95836	

Final Stress		
y = A1 + (A2-A1)/(1 + 10^((LOGx0-x)*p))		
Parameter	**Value**	**Standard Error**
A1	86.92868	18.1484
A2	443.40279	55.82135
LOGx0	243.97573	11.11026
p	-0.01924	0.00766
span	356.47411	63.81589
EC20	1.85E+275	1.#INF
EC50	9.46E+243	1.#INF
EC80	4.83E+212	1.#INF
Reduced Chi-Sqr	1648.2057	
Residual Sum of Squares	21426.67415	
Adj. R-Square	0.84801	

Blast and Thermal: Pinned Top (Parameters vs. Scaled Distance)

Peak Deflection		
y = A0 + A1*x + A2*x^2 + A3*x^3 + A4*x^4 + A5*x^5		
Parameter	**Value**	**Standard Error**
a0	2909.86579	7845.44097
a1	-26.18291	138.01013
a2	0.0393	0.96279
a3	2.87E-04	0.00333
a4	-1.12E-06	5.71E-06
a5	1.14E-09	3.89E-09
Reduced Chi-Sqr	2.99602	
Residual Sum of Squares	17.97613	
Adj. R-Square	0.99255	

Final Deflection		
y = A0 + A1*x + A2*x^2 + A3*x^3 + A4*x^4 + A5*x^5		
Parameter	**Value**	**Standard Error**
a0	17406.38	6535.71052
a1	-274.683	114.97049
a2	1.72324	0.80206
a3	-0.00537	0.00277
a4	8.31E-06	4.76E-06
a5	-5.11E-09	3.24E-09
Reduced Chi-Sqr	2.0792	
Residual Sum of Squares	12.47519	
Adj. R-Square	0.99173	

Peak Stress		
y = a*(1 + x)^b		
Parameter	**Value**	**Standard Error**
a	2.46E+11	3.61E+11
b	-3.80401	0.26757
Reduced Chi-Sqr	356.84786	
Residual Sum of Squares	3568.47862	
Adj. R-Square	0.95769	

Final Stress		
y = y0 + A*exp(R0*x)		
Parameter	**Value**	**Standard Error**
y0	52.81395	2.7439
A	2.97E+16	1.26E+17
R0	-0.15235	0.01986
Reduced Chi-Sqr	74.73143	
Residual Sum of Squares	672.5828	
Adj. R-Square	0.98088	

Blast Only: Roller Top (Parameters vs. Scaled Distance)

Peak Deflection		
y = a-b*c^x		
Parameter	**Value**	**Standard Error**
a	8.16929	0.65383
b	-86895.43282	24277.45813
c	0.96108	0.00152
Reduced Chi-Sqr	5.35E+00	
Residual Sum of Squares	107.00201	
Adj. R-Square	0.98949	

Final Deflection		
y = y0 + A*exp(R0*x)		
Parameter	**Value**	**Standard Error**
y0	-0.48404	0.48489
A	2.00E+06	973481.3039
R0	-0.0592	0.00281
Reduced Chi-Sqr	3.90085	
Residual Sum of Squares	81.91785	
Adj. R-Square	0.98663	

Peak Stress		
y = y0 + A/(sqrt(2*PI)*w*x)*exp(-(ln(x/xc))^2/(2*w^2))		
Parameter	**Value**	**Standard Error**
y0	59.72296	7.21915
xc	159.90168	1.93813
w	0.32885	0.01839
A	50587.95837	1276.61704
Reduced Chi-Sqr	239.09219	
Residual Sum of Squares	5020.936	
Adj. R-Square	0.98499	

Final Stress (Very weak)		
y = A0 + A1*x + A2*x^2 + A3*x^3 + A4*x^4		
Parameter	**Value**	**Standard Error**
a0	2584.67781	1051.08381
a1	-27.59044	16.63714
a2	0.10644	0.09371
a3	-1.76E-04	2.23E-04
a4	1.05E-07	1.90E-07
Reduced Chi-Sqr	3252.38807	
Residual Sum of Squares	65047.7614	
Adj. R-Square	0.76558	

Blast Only: Pinned Top (Parameters vs. Scaled Distance)

Peak Deflection		
y = A0 + A1*x + A2*x^2 + A3*x^3 + A4*x^4 + A5*x^5		
Parameter	**Value**	**Standard Error**
a0	807.70346	601.36175
a1	-12.545	10.57863
a2	0.07835	0.0738
a3	-2.43E-04	2.55E-04
a4	3.72E-07	4.38E-07
a5	-2.24E-10	2.98E-10
Reduced Chi-Sqr	0.0176	
Residual Sum of Squares	0.10562	
Adj. R-Square	0.9967	

Peak Stress		
y = A0 + A1*x + A2*x^2 + A3*x^3 + A4*x^4 + A5*x^5		
Parameter	**Value**	**Standard Error**
a0	14255.88618	8586.67979
a1	-227.07332	151.04935
a2	1.45188	1.05375
a3	-0.00461	0.00364
a4	7.26E-06	6.25E-06
a5	-4.52E-09	4.25E-09
Reduced Chi-Sqr	3.5889	
Residual Sum of Squares	21.53338	
Adj. R-Square	0.99638	

Resistance Curves Polynomial Distributions

Curve	Coefficients	Correlation Coefficient
Natural Period vs. Peak Temp (Blast Only)	C(00) = 0.0206401907692 C(01) = -3.963030066e-007	0.0612747827299
Natural Period vs. Peak Temp (Combined)	C(00) = 0.0522862198056 C(01) = -0.0001050962413 C(02) = 9.1441879879e-008 C(03) = 2.8555439218e-011	0.953104454411
Natural Period vs. Peak Pressure (Blast Only)	C(00) = 0.0203841467202 C(01) = 9.22236722159e-008	0.0329259856187
Natural Period vs. Peak Pressure (Combined)	C(00) = -0.816721696234 C(01) = 0.00176750947479 C(02) = -1.32044423831e-006 C(03) = 4.24949968804e-010 C(04) = -5.02544591973e-014	0.931417171797
Stiffness vs. Peak Temperature (Blast Only)	C(00) = 6699962.2373 C(01) = 65.9198915427	0.0358515512889
Stiffness vs. Peak Temperature (Combined)	C(00) = 35986596.3394 C(01) = -57714.0203072 C(02) = 30.9045674196 C(03) = -0.00516405764453	0.902673191421
Stiffness vs. Peak Pressure (Blast Only)	C(00) = 6702685.64325 C(01) = 565.402610547	0.133170281372
Stiffness vs. Peak Pressure (Combined)	C(00) = 836126.004964 C(01) = 5611.10416271 C(02) = 17.8887207601 C(03) = -0.0315422977418	0.922802683935

Glossary of Terms

Blast and Thermal Radiation Terminology

Symbol	Derived Quantity	SI Units
A	Radiating Area	m^2
a_0	Speed of Sound (In Ambient Conditions)	$m.s^{-1}$
b	Waveform Parameter	Dimensionless
c	Velocity of Light	$m.s^{-1}$
D	Distance from Explosive Centre	m
f	Thermal Energy Ratio	Dimensionless
i_r	Reflected Impulse	$N/m^2.s = kg.m^{-1}.s^{-1}$
i_s	Positive Phase Impulse	$N/m^2.s = kg.m^{-1}.s^{-1}$
i_s^-	Negative Phase Impulse	$N/m^2.s = kg.m^{-1}.s^{-1}$
p_0	Atmospheric Pressure	$N/m^2 = kg.m^{-1}.s^{-2}$
p_r	Reflected Peak Overpressure	$N/m^2 = kg.m^{-1}.s^{-2}$
p_s	Peak Static Overpressure	$N/m^2 = kg.m^{-1}.s^{-2}$
p_{so}^-	Peak Negative Overpressure	$N/m^2 = kg.m^{-1}.s^{-2}$
P	Total Radiant Power	$Cal/s = kg.m^2.s^{-3}$
P_{max}	Maximum Power	$Cal/s = kg.m^2.s^{-3}$
Q	Radiant Exposure	$Cal/cm^2 = kg.s^{-2}$
R	Radius	m
R_s	Radius of First Thermal Pulse	m
t	Time	sec
t_{min}	Time to First Minimum	sec

t_{max}	Time to Maximum Power	sec
t_d	Positive Phase Duration	sec
T	Temperature	$^oC = -273.15^oK$
T_s	Temperature of First Thermal Pulse	$^oC= -273.15^oK$
U_s	Velocity	$m.s^{-1}$
W	Explosive Size	kg (TNT Eq.)
Z	Scaled Distance	$m/T^{1/3}$
ε	Emissivity	Dimensionless
η	Ambient Density Ratio	Dimensionless
λ	Wavelength	m
ρ	Density of Air	$kg.m^{-3}$
ρ_o	Density of Air at Sea Level	$kg.m^{-3}$
σ	Stefan Boltzmann Constant	$Cal/s/cm^2/k^4=kg.s.^oK$
τ	Transmittance	Dimensionless

Structural Terminology

Symbol	**Derived Quantity**	**SI Units**
d	Depth	m
E	Young's Modulus	$N/m^2 = kg.m^{-1}.s^{-2}$
F_e	Equivalent Structural Force	$kN = kg.m.s^{-2}$
F(t)	Impulse	$kN.s = kg.m.s^{-1}$
f(y)	Stress	$N/m^2 = kg.m^{-1}.s^{-2}$
I	Second Moment of Area	$cm^4 = m^4$
k	Translational Spring Stiffness	$N/m = kg.s^{-2}$
KE	Kinetic Energy	$J = kg.m^2.s^{-2}$
k_e	Equivalent Structural Stiffness	$N/m = kg.s^{-2}$
K_l	Load Factor	Dimensionless
K_m	Mass Factor	Dimensionless
K_s	Stiffness Factor	Dimensionless
K_{lm}	Load-Mass Factor	Dimensionless
$K_{y,\theta}$	Effective Yield Strength Factor	Dimensionless
$K_{p,\theta}$	Proportional Limit Factor	Dimensionless

$K_{e,\theta}$	Slope of Linear Elastic Range	Dimensionless
L	Length	m
M	Mass	kg
M_e	Equivalent Structural Mass	kg
P_{cr}	Euler Buckling Load	kN = $kg.m.s^{-2}$
R_m	Resistance Function	kN = $kg.m.s^{-2}$
t_d	Duration of Impulse	s
T	Natural Period of Structure	s
ΔT_y	Yield Temperature	^oC
ΔT_{cr}	Critical Buckling Temperature	^oC
$T_{,y}$	Thermal Gradient	^oC /m
U	Strain Energy	N.m = $kg.m^2.s^{-2}$
x_{st}	Static Displacement	m
α	Coefficient of Thermal Expansion	$m/m.^oC = {}^oC^{-1}$
δ	Deflection	m
ε_m	Mechanical Strains	Dimensionless
ε_T	Thermal Strains	Dimensionless
ε_Φ	Thermal Gradient Strain	Dimensionless
θ	Temperature	^oC
θ_g	Gas Temperature in Fire Compartment	^oC
λ	Slenderness Ratio	Dimensionless
σ_{dyn}	Dynamic Yield Strength	MPa = $kg.m^{-1}.s^{-2}$
σ_y	Yield Strength	MPa= $kg.m^{-1}.s^{-2}$
Φ	Curvature	m^{-1}
ω	Natural Frequency	s^{-1}

References

ATKINSON, G. 2011a. Blast Damage to Storage Tanks and Steel Clad Buildings. *Process Safety and Environmental Prtection: Transactions of the Institution of Chemical Engineers,* 89**,** 382 - 390.

ATKINSON, G., CUSCO, L. 2011b. Buncefield: A Violent, Episodic Vapour Cloud Explosion. . *Process Safety & Environmental Protection: Transactions of the Institution of Chemical Engineers* 89**,** 360-370.

BETHE, H. A. 1964. Theory of the Fireball. Los Alamos, New Mexico: Los Alamos Scientific Laboratory.

BIGGS, J. M. 1964. *Introduction to Structural Dynamics,* New York, McGrawHill.

BORGARTZ, B. O. 1985. AWRE Foulness Combined Blast and Thermal Radiation Simulator Installation of the TRS in the Blast Tunnel. *MABS 9* London, England: Atomic Weapon Research Establishment.

BRODE, H. L. 1954. Numerical Solutions of Spherical Blast Waves. Santa Monica, California, U.S.A: The RAND Corporation.

BRODE, H. L. 1963. Thermal Radiation from Nuclear Explosion. Santa Monica, California: The RAND Corporation.

BRODE, H. L. 1964. Fireball Phenomenology. Santa Monica, California: The RAND Corporation.

BSI 1991. Specification for Patented Cold Drawn Steel Wire for Mechanical Springs.

BSI 1996. Loading for Buildings. *Part 1: Code of Practice for Dead and Imposed Loads.*

BSI 1998. Continuously hot-rolled low carbon steel sheet and strip for cold forming - Technical delivery conditions. British Standards Institute.

BSI 2000. Structural Use of Steelwork in Buildings. *Part 1: Code of Practice for Design - Rolled and Welded Sections.*

BSI 2003. Structural Use of Steelwork in Buildings *Code of Practice for Fire Resistant Design.*

BSI 2004. Hot Rolled Products of Structural Steels. *General Technical Delivery Conditions.* British Standards Institute.

BSI 2005a. Eurocode 1: Actions on Structures: General Actions. *Wind Actions.*

BSI 2005b. Eurocode 3: Design of Steel Structures. *General Rules and Rules for Buildings.* British Standards Institute.

BSI 2005c. Eurocode 3: Design of Steel Strucutures: General Rules. *Structural Fire Deisgn.* British Standards Institute.

BSI 2006. Cold Formed Welded Structural Hollow Sections of Non-Alloy and Fine Grain Steels. *Technical Delivery Requirements.*

BSI 2009. Metallic Materials. Tensile Testing. . *Method of Test at Ambient Temperature.*

BSI 2013. Eurocode 1: Actions on Structures, General Actions. *Part1-2: Actions on Structures Exposed to Fire.* British Standards Insitute.

BURGAN, B. 2001. *Elevated Temperature and High Strain Rate Properties of Offshore Steels,* Ascot, UK, HSE.

BURGAN, B. 2009. Buncefield Explosion Mechanism Phase 1. Steel Construction Institute.

BUTTERWORTH, D. 1977. Introduction to Heat Transer. British Standards Institution.
CERAMICX. 2015. *Ceramicx: Ceramic Heating Elements* [Online]. Gortnagrough, Co. Cork, Ireland. Available: http://www.ceramicx.co.uk/ceramic-elements/ [Accessed 4th August 2015].
CHEN, H., LIEW, J. 2005. Explosion and Fire Analysis of Steel Frames Using Mixed Element Approach. *Journal of Engineering Mechanics,* 131**,** 606–616.
CHOPRA, A. K. 2014. *Dynamics of Structures*, Prentice Hall.
CLOUGH, L. G., CLUBLEY, S.K. 2013. Gauging the Fireball: Simulation and Testing. *Internation Symposium on Interaction of Effects of Munitions with Structures.* Potsdam, Germany.
CLOUGH, L. G., CLUBLEY, S.K. 2014. Response of Steel Plates to Thermal and Blast Load from Within the Fireball of an Explosive Event. *Structures under Shock and Impace.* New Forest, UK.
CLUBLEY, S. K. 2013. Steel Sections Subject to Long Duration Blast. *ICE Proceedings, Journal of Structures and Buildings,* 166**,** 273-281.
CLUBLEY, S. K. 2014. Non-linear long duration blast loading of cylindrical shell structures. *Engineering Structures,* 59**,** 113-126.
COOKE, G. M. E. 1988. An Introduction to the Mechanical Properties of Structural Steel at Elevated Temperatures. *Fire Safety Journal,* 13**,** 45 - 54.
CVERNA, F. 2002. *Thermal Properties of Metals,* Ohio, ASM Materials Properties Database Committee.
DAVISON, B., OWENS, G.W. 2012. *The Steel Designers' Manual*, Steel Construction Institute.
DOLAN, P. J. 1972. *Capabilities of Nuclear Weapons,* Washington, DC, Defence Nuclear Agency.
FREEMAN, B. E. 1963. Thermal Phenomena in the Fireball. Kirtland Air Force Base, New Mexico: Air Force Special Weapons Center.
GILLIE, M., USMANI, A., ROTTER, M., 2004. Bending and Membrane Action in Concrete Slabs. *Fire and Materials,* 28**,** 138-157.
GLASSTONE, S., DOLAN, P.J. 1977. *The Effects of Nuclear Weapons,* Washington, DC, United States Department of Defense and Energy Research and Development Administration.
GRATIAS, S. 1983. Synergy of Thermal and Blast Effects. *MABS 8.* Spiez, Switzerland: Centre d'Etudes de Gramat.
GRATIAS, S. 1987. Combined Thermal and Blast Effects Integration of a Thermal Radiation Simulator Inside the 2.4m Diameter Shock Tube at C.E.G. *MABS 10* Bad Reichenhall, Germany: Centre d'Etudes de Gramat.
GREGORY, F. H., PEARSON, R. J. 1982. Analytical and Experimental Studies of the Response of a Cylinder to Nuclear Thermal/Blast Loads. Ballistic Research Labs., Aberdeen Proving Ground, MD, U.S.
GRIFF, N., PROCTOR. J.F. 1972. A Facility for Simulation of Thermal Radiation Airblast Interaction Effects. *MABS 3* Schwetzingen, Germany: Naval Ordance Laboratory.
HETHERINGTON, J., SMITH, P., 1994. *Blast and Ballistic Loading of Structures*, CRC Press.
INCROPERA, F. P., ET AL. 2007. *Introduction to Heat Transfer*, John Wiley & Sons.
IST. 2015. *IST Spring Calculator* [Online]. Sheffield, UK: Institute of Spring Technology. Available: http://www.springcalculator.com/scp/ [Accessed 24th July 2015].
IZZUDDIN, B. A., SONG, L., ELNASHAI, A.S., DOWLING, P.J. 2000. An Integrated Adaptive Environment for Fire and Explosion Analysis of Steel Frames — Part II: Verification and Application. *Journal of Constructional Steel Research,* 53**,** 87-111.
JOHNSON, G. R., COOK, W.H. 1983. A Constitutive Model and Data for Metals Subjected to Large Strains, High Strain Rates and High Temperatures. *Proceedings of the 7th International Symposium on Ballistics* 7.
KINGERY, C. N., BULMASH, G. 1984. Airblast Parameters from TNT Spherical Air Burst and Hemispherical Surface Burst. Maryland, U.S.A: Ballistic Research Laboratory.
KIRBY, B. R. 1998. The Behaviour of a Multi-Storey Steel Framed Building Subjected to Fire Attack: Experimental Data. Rotherham: British Steel., Swinden Technology Centre,.

KITCHENS, C. W. J., LOTTERO, R.E., MARK, A., AND TEEL, G.D. 1981. Blast Wave Modification During Combined Thermal / Blast Simulation Testing. *MABS 7.* Medicing Hat, Alberta, Canada: Ballistic Research Laboratory.

KODUR, V. K. R., DWAIKAT, M.M.S. 2009. Response of Steel Beam–Columns Exposed to Fire. *Engineering Structures,* 31**,** 369-379.

KOLSKY, H. An Investigation of the Mechanical Properties of Materials at Very High Rates of Loading. Physics Society, 1949 London. 676-700.

LAASRAOUI, A., JONAS, J.J. 1991. Prediction of Steel Flow Stresses at High Temperatures and Strain Rates *Metallurgical Transactions A,* 22**,** 154 - 1558.

LIEW, R. J. Y. 2007. Survivability of Steel Frame Structures Subject to Blast and Fire. *Journal of Constructional Steel Research,* 64**,** 854-866.

LUSAS 2011. User Reference Manual. Surrey, UK.

LUSAS 2013. LUSAS: Finite Element Analysis Software. 14.7-10 ed. London, England: FEA Ltd.

MAYS, G., SMITH, P., CORMIE, D. 2009. *Blast Effects on Buildings,* London, England, ICE Publishing.

NASSR, A. A., RAZAQPUR, A.G., TAIT, M.J., CAMPIDELLI, M., FOO, S. 2013. Strength and Stability of Steel Beam Columns under Blast Load. *International Journal of Impact Engineering,* 55**,** 34 - 38.

NGO, T., MENDIS, P., GUPTA, A., RAMSAY. J., 2007. Blast Loading and Blast Effects on Structures - An Overview. *Electronic Journal of Structural Engineering***,** 16.

OPALKA, K. O. 1989. Large Blast and Thermal Simulator Advanced Concept Driver Design by Computational Fluid Dynamics. Aberdeen Proving Ground, Maryland: US Army Ballistic Research Laboratory.

OUTINEN, K., MAKELAINEN, P.,. Mechanical Properties of Structural Steel at Elevated Temperatures and After Cooling Down. *In:* MOSS, P., ed. Structures in Fire: Second Internation Workshop, 2002 Christchurch, NZ.

ÖZEL, T., KARPAT, Y., 2007. Identification of Constitutive Material Model Parameters for High-Strain Rate Metal Cutting Conditions Using Evolutionary Computational Algorithms. *Materials and Manufacturing Processes,* 22.

PEARSON, R. J., WISNIEWSKI, H.L., SZABADOS, P.D. 1981. Synergism in Nuclear Thermal / Blast Loading. *MABS 7* Medicine Hat, Alberta, Canada: Ballistic Research Laboratory.

PENNEY, W. 1987. An Essay on the Damaging Effects of the Heat Flash from Nuclear Explosives. UK: Records of the Atomic Weapons Establishment.

QUIEL, S., MARJANISHVILI, S. Steel Column Subjected to Fire Following an Explosion. 15th ISIEMS, 2013 Potsdam, Germany.

QUIEL, S. E., MARJANISHVILI, S. M., 2012. Fire Resistance of a Damaged Steel Building Frame Designed to Resist Progressive Collapse. *Journal Of Performance Of Constructed Facilities***,** 402 - 409.

RANKINE, W. J. M. 1870. On the Thermodynamic Theory of Waves of Finite Longitudinal Disturbance. *Proceedings of the Royal Society of London,* 18**,** 80-83.

ROSE, T. A. 2001. *An Approach to the Evaluation of Blast Loads on Finite and Semi-Infinite Structures.* PhD PhD Thesis, Cranfield University, Royal Military College of Science.

SCHWER, L. Optional Strain-Rate Forms for the Johnson Cook Constitutive Model and the Role of the Parameter Epsilon. LS-DYNA User Forum: Impact, 2007 Frankenthal.

SHEPHERD, P. G., BURGESS, I. W. 2011. On the Buckling of Axially Restrained Steel Columns in Fire. *Engineering Structures,* 33**,** 2832 - 2838.

SIMON, K., WENIG, P., SERRA, J.J. 2008. Reproducibility of Flux and Fluence Levels in Nuclear Thermal Testing. *MABS 20.* Oslo, Norway: Armed Forces Scientific Institute for Protection Technologies.

SONG, L., IZZUDDIN, B.A., ELNASHAI, A.S., DOWLING, P.J. 2000. An Integrated Adaptive Environment for Fire and Explosion Analysis of Steel Frames — Part I: Analytical Models. *Journal of Constructional Steel Research,* 53**,** 63 - 85.

STEPANOV, K. L., STANCHITS, L. K., STANKEVICH YU. A. 2011. Modeling of Explosion Thermal Radiation. *Journal of Engineering Physics and Thermophysics,* Volume 84**,** pp 179-206.

TATA 2016. Tatal Steel Sections Interactive Blue Book. Tata Steel Europe Ltd.

TEEL, G. D., AND OERTEL, F.H. 1981. Testing to Combined Blast and Thermal Effects at the BRL. *MABS 7* Medicine Hat, Alberta, Canada: Ballistics Research Laboratory.

UFC 2008. Structures to Resist the Effects of Accidental Explosions. United Facilities Criteria (UFC).

USMANI, A. S., ROTTER, J.M., LAMONT, S., SANAD, A.M., GILLIE, M. 2001. Fundamental Principles of Structural Behaviour Under Thermal Effects. *Fire Safety Journal,* 36**,** 721-744.

VAN NETTEN, A. A., DEWEY, J.M. 1997. A Study of Blast Wave Loading on Cantilevers. *Shock Waves* 7**,** 175-190.

VEDANTAM, K., BAJAJ, D., BRAR, N.S., HILL, S., 2005. Johnson - Cook Strength Models For Mild and DP 590 Steels. *In:* FURNISH, M. D. (ed.) *Shock Compression of Condensed Matter.* American Institute of Physics.

WANG, Y., BURGESS, I. W., WALD, F., GILLIE, M. 2013. *Performance Based Fire Engineering of Structures*, Taylor & Francis.

YANDZIO, E., GOUGH, C. 1999. Protection of Buildings against Explosions. Ascot, Berkshire, England: The Steel Construction Institute.

ZAVITSANOS, P. D., ET AL. 1998. Design, Construct and Test of the Hi-Therm Simulator. Souderton, PA, U.S.A: General Sciences, Incorperated.

ZEMIC. 2015 *http://www.zemiceurope.com/* [Online]. Zemix Europe B.V. - Loads Cells & Sensors. [Accessed 30th January 2016].